

Meinhard T. Schobeiri

# Gas Turbine Design, Components and System Design Integration



Springer

# Gas Turbine Design, Components and System Design Integration

Meinhard T. Schobeiri

# Gas Turbine Design, Components and System Design Integration



Springer

Meinhard T. Schobeiri  
Texas A&M University  
College Station, TX  
USA

ISBN 978-3-319-58376-1      ISBN 978-3-319-58378-5 (eBook)  
DOI 10.1007/978-3-319-58378-5

Library of Congress Control Number: 2017943214

© Springer International Publishing AG 2018

This work is subject to copyright. All rights are reserved by the Publisher, whether the whole or part of the material is concerned, specifically the rights of translation, reprinting, reuse of illustrations, recitation, broadcasting, reproduction on microfilms or in any other physical way, and transmission or information storage and retrieval, electronic adaptation, computer software, or by similar or dissimilar methodology now known or hereafter developed.

The use of general descriptive names, registered names, trademarks, service marks, etc. in this publication does not imply, even in the absence of a specific statement, that such names are exempt from the relevant protective laws and regulations and therefore free for general use.

The publisher, the authors and the editors are safe to assume that the advice and information in this book are believed to be true and accurate at the date of publication. Neither the publisher nor the authors or the editors give a warranty, express or implied, with respect to the material contained herein or for any errors or omissions that may have been made. The publisher remains neutral with regard to jurisdictional claims in published maps and institutional affiliations.

Printed on acid-free paper

This Springer imprint is published by Springer Nature  
The registered company is Springer International Publishing AG  
The registered company address is: Gewerbestrasse 11, 6330 Cham, Switzerland



## Preface to the First Edition

Gas turbines today are the integral parts of power generation, transportation, petrochemical and diverse industrial processing systems. Although the design and application of gas turbines in any of the above areas and their operational requirements are different, they share the same underlying physics. The physics of turbomachinery components and systems was discussed in details in the first and the second enhanced edition of my textbook, *Turbomachinery Flow Physics and Dynamic Performance*. The book found a world-wide positive echo among the turbomachinery community including industry and academia. This motivated me to write the current textbook about the gas turbine design, where I spent more than forty years on almost all aspects of gas turbine design R&D in the industry, NASA G.R.C, DOE, and academia. While in the book *Turbomachinery Flow Physics* the aerothermodynamics, heat transfer and performance aspects of almost all thermal turbomachines were discussed in very detail, the current book deals with the aerothermodynamics design of gas turbine components and their integration into a complete gas turbine system.

Designing a gas turbine requires a team work of several groups that are specialized in aero-thermodynamics, heat transfer, computational fluid dynamics, combustion, solid mechanics, vibration, rotordynamics and system control to name just a few. It is beyond the scope of any text book to treat the above areas in a detailed fashion. Available gas turbine handbooks do not treat the above areas in depth and breadth, so that they do cannot be considered a working platform for gas turbine designer. They may, however, be able to provide the reader an overview of the subject. Considering the above, the current book is concentrated on a detailed aerothermodynamics, design and off-design performance aspects of individual components as well as the system integration and its dynamic operation.

Design of gas turbines was from very beginning based on sound physics rather than empiricism. The first gas turbine manufactured around 1900 was not even able to rotate, because the turbine power was much less than the required compressor power. The reason was the poor efficiencies of both the turbine and the compressor component. The failed tests showed that the prerequisite for a successful gas turbine design is the full understanding of its underlying viscous flow physics and its mathematical description. The mathematical structure that describes the three dimensional viscous flow in very details was already derived by C.L.M.H. Navier in 1821 and twenty years later by G.G. Stokes . However, the solution of the Navier-Stokes partial differential equations was at that time out of reach. It was due to L.Prandtl's 1904 groundbreaking boundary layer theory that provided an approximate solution to Navier-Stokes equations. The simplification of the Navier-Stokes equations through boundary layer theory made possible to calculate total pressure loss

coefficient of compressor and turbine blades, define the rotating stall and surge limit of compressors, define the range of the laminar separation of the boundary layer in low pressure turbines and many other aerodynamic aspects of gas turbine operation. In the meantime, the introduction of high speed computers and advanced computational methods has significantly contributed to an exponential growth of information covering almost all aspects of turbomachinery design. This situation has lead to a growing tendency in technical specialization. A factor in the context of specialization is the use of “black boxes” in engineering in general and in turbomachinery in particular. During my 40 years of turbomachinery R&D experience, I have been encountering engineers who can use commercial codes for calculating the complex turbomachinery flow field without knowing the underlying physics of the code they use. This circumstance constituted one of the factors in defining the framework of the book *Turbomachinery Flow Physics* mentioned previously, which aims at providing the students and practicing turbomachinery design engineers with a solid background in turbomachinery flow physics and performance. Built upon a physical basis that contains a minimum of empirical correlations, I have been teaching turbomachinery courses in the past thirty years and educated several generations of highly qualified turbomachinery engineers that are working in US gas turbine manufacturing companies. The current book provides the interested students and the young engineers working in the industry with a material they can use for preliminary design of gas turbines. It is also intended to help instructors of turbomachinery courses around the world to assign gas turbine components as project modules that can be integrated into a complete system.

The current book consists of 18 Chapters that are grouped into three parts. Part I encompassing Chapters 1 through 6 deals with aero-thermodynamics of gas turbine design.

Part II of this book include Chapters 7 through 10 starts with the treatment of cascade and stage efficiency and loss determination from a physically plausible point of view. I refrained from presenting recipe-types of empirical formulas that have no physical foundation. Chapter 8 deals with the calculation of incidence and deviation. Chapter 9 treats in detail the compressor and turbine blade design procedures. Radial equilibrium is discussed in Chapter 10, which concludes Part II.

Part III of the book is entirely dedicated to design, off-design and dynamic performance of turbomachinery components and systems. Particular attention is paid to gas turbine components, their individual modeling, and integration into the gas turbine system. It includes Chapters 11 to 16. Chapter 11 introduces the basic physics of non-linear dynamic simulation of turbomachinery systems and its theoretical background. Starting from a set of general four dimensional partial differential equations in temporal-spatial domain, two-dimensional equation sets are derived that constitute the basis for component modeling. The following Chapters 12, 13 and 14 deal with generic modeling of turbomachinery components and systems in which individual components ranging from the inlet nozzle to the compressor, combustion chamber, turbine, and exhaust diffuser are modeled. In modeling compressor and turbine components, non-linear adiabatic and diabatic expansion and compression calculation methods are presented.

Gas turbine design requires several preliminary steps. These steps were discussed in Chapter 17. Chapter 18 deals with the dynamic simulation of different gas turbine types that are subject to adverse dynamic operations. Seven representative case studies conclude this chapter. In preparing Part III, I tried to be as concrete as

---

possible by providing detailed simulation of existing gas turbine engines and their individual component.

In typing several thousand equations, errors may occur. I tried hard to eliminate typing, spelling and other errors, but I have no doubt that some remain to be found by readers. In this case, I sincerely appreciate the reader notifying me of any mistakes found; the electronic address is given below. I also welcome any comments or suggestions regarding the improvement of future editions of the book.

My sincere thanks are due to many fine individuals and institutions. First and foremost, I would like to thank the faculty of the Technische Universität Darmstadt, from whom I received my entire engineering education. I finalized major chapters of this book during my sabbatical in Germany where I received the Alexander von Humboldt Prize. I am indebted to the Alexander von Humboldt Foundation for this Prize and the material support for my research sabbatical in Germany. My thanks are extended to Prof. Bernd Stoffel, Prof. Ditmar Hennecke, Professor Pelz and Dipl. Ing. Bernd Matyschok for providing me with a very congenial working environment. I truly enjoyed interacting with these fine individuals. NASA Glenn Research Center sponsored the development of the nonlinear dynamic code GETRAN which I used to simulate cases in Part III. I wish to extend my thanks to Mr. Carl Lorenzo, Chief of Control Division, Dr. D. Paxson, and the administration of the NASA Glenn Research Center. I also thank Dr. Richard Hearsey for providing me with a three-dimensional compressor blade design. I also would like to extend my thanks to Dr. Arthur Wennerstrom for providing me with the updated theory on the streamline curvature method.

I am also indebted to the TAMU administration for partially supporting my sabbatical that helped me in finalizing the book.

Last but not least, my special thanks go to my family, Susan and Wilfried for their support throughout this endeavor.

M.T. Schobeiri

September 2016  
College Station, Texas  
tschobeiri@mengr.tamu.edu

# Table of Content

<b>Preface to the First Edition</b> .....	V
<b>Table of Content</b> .....	IX
<b>Nomenclature</b> .....	XVII
<b>1 Introduction, Gas Turbines, Applications, Types</b> .....	1
1.1 Power Generation Gas Turbines .....	1
1.2 Compressed Air Energy Storage Gas Turbines, CAES.....	6
1.3 Power Generation Gas Turbine Process .....	8
1.4 Significant Efficiency Improvement of Gas Turbines .....	10
1.5 Ultra High Efficiency Gas Turbine .....	14
1.6 Aircraft Gas Turbines .....	17
1.7 Aircraft-Derivative Gas Turbines .....	19
1.8 Gas Turbines Turbocharging Diesel Engines .....	22
1.9 Gas Turbine Components, Functions .....	24
1.9.1 Group 1: Inlet, Exhaust, Pipe .....	25
1.9.2 Group 2: Heat Exchangers, Combustion Chamber.....	26
1.9.3 Group 3: Compressor, Turbine Components .....	29
References .....	30
<b>2 Gas Turbine Thermodynamic Process</b> .....	31
2.1 Gas Turbine Cycles, Processes .....	31
2.1.1 Gas Turbine Process .....	32
2.2 Improvement of Gas Turbine Thermal Efficiency .....	39
2.2.1 Minor Improvement of Gas Turbine Thermal Efficiency ..	40
2.2.2 Major Improvement of Gas Turbine Thermal Efficiency ..	41
2.1.3 Compressed Air Energy Storage Gas Turbine .....	45
References .....	47
<b>3 Thermo-Fluid Essentials for Gas Turbine Design</b> .....	49
3.1 Mass Flow Balance .....	49
3.2 Balance of Linear Momentum.....	51
3.3 Balance of Moment of Momentum .....	53
3.4 Balance of Energy .....	56
3.4.1 Energy Balance Special Case 1: Steady Flow .....	57
3.4.2 Energy Balance Special Case 2: Steady Flow .....	58
3.5 Application of Energy Balance to Gas Turbines Components ...	58
3.5.1 Application: Accelerated, Decelerated Flows .....	59
3.5.2 Application: Combustion Chamber, Heat Exchanger.....	60

3.5.3	Application: Turbine, Compressor	63
3.5.3.1	Uncooled turbine	63
3.5.3.2	Cooled turbine	64
3.5.3.3	Uncooled compressor	65
3.5.3.4	Cooled Compressor	66
3.6	Irreversibility and Total Pressure Losses	67
3.6.1	Application of Second Law to Turbomachinery Components	69
3.7	Flow at High Subsonic and Transonic Mach Numbers	71
3.7.1	Density Changes with Mach Number, Critical State	72
3.7.2	Effect of Cross-Section Change on Mach Number	77
3.7.3	Compressible Flow through Channels	84
3.7.4	The Normal Shock Wave Relations	92
3.7.5	The Oblique Shock Wave Relations	98
3.7.6	Detached Shock Wave	102
3.7.7	Prandtl-Meyer Expansion	102
	References	105
<b>4</b>	<b>Theory of Turbomachinery Stages</b>	<b>107</b>
4.1	Energy Transfer in Turbomachinery Stages	107
4.2	Energy Transfer in Relative Systems	108
4.3	General Treatment of Turbine and Compressor Stages	109
4.4	Dimensionless Stage Parameters	113
4.5	Relation Between Stage parameter, Radial Equilibrium	115
4.6	Effect of Degree of Reaction on the Stage Configuration	118
4.7	Effect of Stage Load Coefficient on Stage Power	120
4.8	Unified Description of a Turbomachinery Stage	121
4.8.1	Unified Description of Stage with Constant Mean Diameter	121
4.8.2	Generalized Dimensionless Stage Parameters	122
4.9	Special Cases	124
4.9.1	Case 1, Constant Mean Diameter	125
4.9.2	Case 2, Constant Meridional Velocity Ratio	125
4.10	Increase of Stage Load Coefficient, Discussion	126
	References	128
<b>5</b>	<b>Turbine and Compressor Cascade Flow Forces</b>	<b>129</b>
5.1	Blade Force in an Inviscid Flow Field	129
5.2	Blade Forces in a Viscous Flow Field	134
5.3	The Effect of Solidity on Blade Profile Losses	140
5.4	Relationship Between Profile Loss Coefficient and Drag	140
5.5	Optimum Solidity	142
5.5.1	Optimum Solidity, by Pfeil	143
5.5.2	Optimum Solidity by Zweifel	144
5.6	Generalized Lift-Solidity Coefficient	146
5.6.1	Lift-Solidity Coefficient for Turbine Stator	148
5.6.2	Turbine Rotor	152
	References	155

<b>6</b>	<b>Losses in Turbine and Compressor Cascades</b>	157
6.1	Turbine Profile Loss	158
6.2	Viscous Flow in Compressor Cascade	160
6.2.1	Calculation of Viscous Flows	160
6.2.2	Boundary Layer Thicknesses	161
6.2.3	Boundary Layer Integral Equation	162
6.2.4	Application of Boundary Layer Theory to Compressor	164
6.2.5	Effect of Reynolds Number	168
6.2.6	Stage Profile Losses	168
6.3	Trailing Edge Thickness Losses	168
6.4	Losses Due to Secondary Flows	174
6.4.1	Vortex Induced Velocity Field	176
6.4.2	Calculation of Tip Clearance Secondary Flow Losses	179
6.4.3	Calculation of Endwall Secondary Flow Losses	182
6.5	Flow Losses in Shrouded Blades	186
6.5.1	Losses Due to Leakage Flow in Shrouds	186
6.6	Exit Loss	192
6.7	Trailing Edge Ejection Mixing Losses of Gas Turbine Blades	194
6.7.1	Calculation of Mixing Losses	194
6.7.2	Trailing Edge Ejection Mixing Losses	199
6.7.3	Effect of Ejection Velocity Ratio on Mixing Loss	199
6.7.4	Optimum Mixing Losses	201
6.8	Stage Total Loss Coefficient	201
6.9	Diffusers, Configurations, Pressure Recovery, Losses	202
6.9.1	Diffuser Configurations	203
6.9.2	Diffuser Pressure Recovery	204
6.9.3	Design of Short Diffusers	207
6.9.4	Some Guidelines for Designing High Efficiency Diffusers	210
	References	211
<b>7</b>	<b>Efficiency of Multi-Stage Turbomachines</b>	213
7.1	Polytropic Efficiency	213
7.2	Isentropic Turbine Efficiency, Recovery Factor	216
7.3	Compressor Efficiency, Reheat Factor	219
7.4	Polytropic versus Isentropic Efficiency	221
	References	223
<b>8</b>	<b>Incidence and Deviation</b>	225
8.1	Cascade with Low Flow Deflection	225
8.1.1	Conformal Transformation	225
8.1.2	Flow Through an Infinitely Thin Circular Arc Cascade	234
8.1.3	Thickness Correction	240
8.1.4	Optimum Incidence	240
8.1.5	Effect of Compressibility	242
8.2	Deviation for High Flow Deflection	243
8.2.1	Calculation of Exit Flow Angle	245
	References	247

<b>9</b>	<b>Blade Design</b>	249
9.1	Conformal Transformation, Basics	249
9.1.1	Joukowski Transformation	251
9.1.2	Circle-Flat Plate Transformation	251
9.1.3	Circle-Ellipse Transformation	252
9.1.4	Circle-Symmetric Airfoil Transformation	253
9.1.5	Circle-Cambered Airfoil Transformation	255
9.2	Compressor Blade Design	256
9.2.1	Low Subsonic Compressor Blade Design	257
9.2.2	Compressors Blades for High Subsonic Mach Number.	263
9.2.3	Transonic, Supersonic Compressor Blades	264
9.3	Turbine Blade Design	265
9.3.1	Steps for Designing the Camberline	266
9.3.2	Camberline Coordinates Using Bèzier Function	269
9.3.3	Alternative Calculation Method.	271
9.4	Assessment of Blades Aerodynamic Quality	272
	References	275
<b>10</b>	<b>Radial Equilibrium</b>	277
10.1	Derivation of Equilibrium Equation	278
10.2	Application of Streamline Curvature Method	286
10.2.1	Step-by-step solution procedure	288
10.3	Compressor Examples	292
10.4	Turbine Example, Compound Lean Design	295
10.4.1	Blade Lean Geometry	296
10.4.2	Calculation of Compound Lean Angle Distribution	297
10.4.3	Example: Three-Stage Turbine Design	299
10.5	Special Cases	302
10.5.1	Free Vortex Flow	302
10.5.2	Forced vortex flow	303
10.5.3	Flow with constant flow angle	304
	References	305
<b>11</b>	<b>Nonlinear Dynamic Simulation of Components and systems</b>	307
11.1	Theoretical Background	308
11.2	Preparation for Numerical Treatment	315
11.3	One-Dimensional Approximation	315
11.3.1	Time Dependent Equation of Continuity	315
11.3.2	Time Dependent Equation of Motion	317
11.3.3	Time Dependent Equation of Total Energy	318
11.4	Numerical Treatment	323
	References	324
<b>12</b>	<b>Generic Modeling of Turbomachinery Components and Systems</b>	325
12.1	Generic Component, Modular Configuration	327
12.1.1	Plenum the Coupling Module	327
12.1.2	Group1 Modules: Inlet, Exhaust, Pipe	329
12.1.3	Group 2: Heat Exchangers, Combustion Chamber	330

---

12.1.4	Group 3: Adiabatic Compressor, Turbine . . . . .	332
12.1.5	Group 4: Diabatic Turbine and Compressor Components . . . . .	334
12.1.6	Group 5: Control System, Valves, Shaft, Sensors . . . . .	336
12.2	System Configuration, Nonlinear Dynamic Simulation . . . . .	336
12.3	Configuration of Systems of Non-linear Partial Differential Equations . . . . .	340
	References . . . . .	340
<b>13</b>	<b>Modeling of Inlet, Exhaust, and Pipe Systems . . . . .</b>	<b>343</b>
13.1	Unified Modular Treatment . . . . .	343
13.2	Physical and Mathematical Modeling of Modules . . . . .	343
13.3	Example: Dynamic behavior of a Shock Tube . . . . .	345
13.3.1	Shock Tube Dynamic Behavior . . . . .	347
	References . . . . .	351
<b>14</b>	<b>Modeling of Recuperators, Combustion Chambers . . . . .</b>	<b>353</b>
14.1	Modeling Recuperators . . . . .	354
14.1.1	Recuperator Hot Side Transients . . . . .	355
14.1.2	Recuperator Cold Side Transients . . . . .	355
14.1.3	Coupling Condition Hot, Cold Side . . . . .	356
14.1.4	Recuperator Heat Transfer Coefficient . . . . .	357
14.2	Modeling Combustion Chambers . . . . .	358
14.2.1	Mass Flow Transients . . . . .	359
14.2.2	Temperature Transients . . . . .	360
14.2.3	Combustion Chamber Heat Transfer . . . . .	362
14.3	Example: Startup and Shutdown of a Combustion Chamber . . . . .	364
14.4	Modeling of Afterburners . . . . .	367
	References . . . . .	368
<b>15</b>	<b>Modeling the Compressor Component, Design and Off-Design . . . . .</b>	<b>369</b>
15.1	Compressor Losses . . . . .	370
15.1.1	Profile Losses . . . . .	372
15.1.2	Diffusion Factor . . . . .	373
15.1.3	Generalized Maximum Velocity Ratio for Stator and Rotor . . . . .	377
15.1.4	Compressibility Effect . . . . .	379
15.1.5	Shock Losses . . . . .	383
15.1.6	Correlations for Boundary Layer Momentum Thickness . . . . .	392
15.1.7	Influence of Different Parameters on Profile Losses . . . . .	393
15.1.7.1	Mach Number Effect . . . . .	393
15.1.7.2	Reynolds number effect . . . . .	394
15.2	Compressor Design and Off-Design Performance . . . . .	395
15.2.1	Stage-by-stage and Row-by-Row Adiabatic Compression Process . . . . .	395
15.2.1.1	Stage-by-stage calculation of compression . . . . .	395
15.2.1.2	Row-by-row adiabatic compression . . . . .	397
15.2.1.3	Off-design efficiency calculation . . . . .	401



15.3	Generation of Steady State Performance Map	404
15.3.1	Inception of Rotating Stall	406
15.3.2	Degeneration of Rotating Stall into Surge	408
15.4	Compressor Modeling Levels	409
15.4.1	Module Level 1: Using Performance Maps	410
15.4.1.1	Quasi dynamic modeling using maps:	412
15.4.1.2	Simulation Example:	413
15.4.2	Module Level 2: Row-by-Row Adiabatic Calculation	415
15.4.3	Active Surge Prevention by Adjusting the Stator Blades	416
15.4.4	Module Level 3: Row-by-Row Diabatic Compression	417
15.4.4.1	Description of diabatic compressor module:	418
15.4.4.2	Heat transfer closure equations:	420
	References	422
<b>16</b>	<b>Turbine Aerodynamic Design and Off-design Performance</b>	<b>427</b>
16.1	Stage-by-Stage and Row-by-Row Adiabatic Design	429
16.1.1	Stage-by-Stage Calculation of Expansion Process	430
16.1.2	Row-by-Row Adiabatic Expansion	431
16.1.3	Off-Design Efficiency Calculation	436
16.1.4	Behavior Under Extreme Low Mass Flows	438
16.1.5	Example: Steady Design and Off-Design	441
16.2	Off-Design Calculation Using Global Turbine Characteristics	443
16.3	Modeling the Turbine Module for Dynamic Performance	445
16.3.1	Module Level 1: Using Turbine Performance map	445
16.3.2	Module Level 2: Row-by-Row Adiabatic Expansion	446
16.3.3	Module Level 3: Row-by-Row Diabatic Expansion	447
16.3.3.1	Description of diabatic turbine module:	449
16.3.3.2	Description of diabatic turbine module,	451
16.3.3.3	Heat transfer closure equations	453
	References	454
<b>17</b>	<b>Gas Turbine Design, Preliminary Considerations</b>	<b>455</b>
17.1	Gas Turbine Preliminary Design Procedure	456
17.2	Gas Turbine Cycle	457
17.3	Compressor Design, Boundary Conditions, Design Process	458
17.3.1	Design Process	458
17.3.2	Compressor Blade Aerodynamics	462
17.3.3	Controlling the Leakage Flow	463
17.3.4	Compressor Exit Diffuser	463
17.3.5	Compressor Efficiency and Performance Maps	463
17.3.6	Stagger Angle Adjustment During Operation	465
17.4	Combustion Chambers	466
17.4.1	Combustion Design Criteria	468
17.4.2	Combustion Types	468
17.5	Turbine Design, Boundary Conditions, Design Process	470
17.5.1	Steps of a Gas Turbine Design Process	470

17.5.2 Mechanical Integrity, Components Vibrational .....	475
References .....	475
<b>18 Simulation of Gas Turbine Engines .....</b>	<b>477</b>
18.1 State of Dynamic Simulation, Background .....	478
18.2 Gas Turbine Configurations .....	478
18.3 Gas Turbine Components, Modular Concept .....	481
18.4 Levels of Gas Turbine Engine Simulations .....	486
18.4.1 Zeroth Simulation Level .....	486
18.4.2 First Simulation Level .....	486
18.4.3 Second Simulation Level .....	486
18.4.4 Third Simulation Level .....	486
18.5 Non-Linear Dynamic Simulation Case Studies .....	487
18.5.1 Case Studies: Compressed Air Energy Storage Plant ...	488
18.5.1.1 Case Study: Emergency Shutdown .....	491
18.5.1.2 Case Study 1: Grid Fluctuation Response ....	493
18.5.2 Case Study 2: Dynamic Simulation of a Gas Turbine Under Adverse Operation condition .....	493
18.5.3 Case Studies: Dynamic Simulation of a Split-Shaft Gas Turbine under Adverse Operation condition .....	498
18.5.4 Case Studies: Maximizing the Off-Design Efficiency of a Gas Turbine by Varying the Turbine Stator Stagger Angle .....	503
18.5.4.1 Dynamic Change of Stagger Angle, when Engine is Running .....	504
18.5.5 Case Study 3: Simulation of a Multi-Spool Gas Turbine .....	506
References .....	509

# Nomenclature

<b>A</b>	acceleration, force vector
$A_c$	cold side blade surface area
$A_h$	hot side blade surface area
$b$	trailing edge thickness
$c$	blade chord length
$c$	complex eigenfunction, $c = c_r + ic_i$
$c$	speed of sound
$c_{ax}$	blade axial chord length
$C_D$	cascade drag coefficient
$C_f$	friction coefficient
$C_i$	constants
$C_L$	blade lift coefficient
$C_L^*$	camberline lift coefficient
$c_p, c_v$	specific heat capacities
$d$	projected trailing edge thickness $d = b/\sin\alpha_2$
$D$	diffusion factor
$D$	dimensionless trailing edge thickness
$D_e$	equivalent diffusion factor
$D_h$	hydraulic diameter
$D_m$	modified diffusion factor
$e$	specific total energy
$e_i$	orthonormal unit vector
$E_\lambda$	Planck's spectral emissive power
$f$	slot thickness/trailing edge thickness ratio $f = s/b$
$f_C$	reheat factor for multistage compressors
$f_T$	recovery factor for multistage turbines
$f_\infty$	recovery factor for turbines with infinite number of stages
$F$	auxiliary function
<b>F</b>	force vector
$g$	blade geometry function
$G$	blade geometry parameter
$G$	circulation function
$G_i$	auxiliary functions
$h$	height
$h$	specific static enthalpy
$H$	specific total enthalpy
$H$	immersion ratio
$H_{12}$	form factor, $H_{12} = \delta_1/\delta_2$

---

$H_{13}$	form factor, $H_{32} = \delta_3/\delta_2$
$i$	incidence angle
$I$	moment of inertia
$k$	thermal conductivity
$K$	specific kinetic energy
$l, m$	coordinates introduced for radial equilibrium
$l_m$	specific shaft work
$L$	stage power
$m$	mass
$\dot{m}$	mass flow
$\dot{m}_c$	cooling mass flow
$M$	Mach number
$\mathbf{M}$	vector of moment of momentum
$\mathbf{M}_a$	axial vector of moment of momentum
$n$	number of stations
$n$	polytropic exponent
$\mathbf{n}$	normal unit vector
$Nu$	Nusselt number
$p, P$	static, total pressure
$P$	total pressure $P = p + \rho V^2/2$
$Pr$	Prandtl number
$Pr_e$	effective Prandtl number
$Pr_t$	turbulent Prandtl number
$q$	specific thermal energy (heat per unit of mass)
$q_c$	cold side specific heat rejected from stage
$q_h$	hot side specific heat transferred to the stage
$q'$	specific heat transferred to stator blades
$q''$	specific heat transferred to rotor blades
$\dot{\mathbf{q}}$	heat flux vector
$Q$	thermal energy (heat)
$\dot{Q}$	thermal energy flow (heat flow)
$\dot{Q}_c$	thermal energy flow (heat flow), blade cold side
$\dot{Q}_h$	thermal energy flow (heat flow), blade hot side
$\dot{Q}'$	thermal energy flow (heat flow) to/from stator blades
$\dot{Q}''$	thermal energy flow (heat flow) to/from rotor blades
$r$	degree of reaction
$r_i$	radius of stage stream surface
$\mathbf{r}$	radius vector
$R$	radius in conformal transformation
$R$	density ratio, $R = \rho_3/\rho_2$
$R$	radiation

---

$R$	radius of the mean flow path
$Re$	Reynolds number
$R_w$	thermal resistance
$s$	specific entropy
$s$	slot thickness
$s$	blade spacing
$S_i$	cross section at station $i$
$St$	Stanton number
$Str$	Strouhal number
$t$	time
$t$	thickness
$\mathbf{t}$	tangential unit vector
$T$	static temperature
$T$	tangential force component
$\mathbf{T}$	stress tensor, $\mathbf{T} = e_i e_j \tau_{ij}$
$T_o$	stagnation or total temperature
$T_c$	static temperature on blade cold side
$T_h$	static temperature on blade hot side
$T_w$	blade material temperature
$u$	specific internal energy
$u$	velocity
$\mathbf{U}, \mathbf{V}, \mathbf{W}$	rotational, absolute, relative velocity vectors
$v$	specific volume
$V$	volume
$\bar{\mathbf{v}}$	mean velocity vector
$V_{\max}$	maximum velocity on suction surface
$W$	mechanical energy
$\dot{W}$	mechanical energy flow (power)
$\dot{W}_{sh}$	shaft power
$\mathbf{X}$	state vector
$x_i$	coordinates
$Z_i$	individual stage loss coefficient

## Greek Symbols

$\alpha$	heat transfer coefficient
$\alpha, \beta$	absolute and relative flow angles
$\alpha_{st}$	stagnation angle in conformal transformation
$\gamma$	blade stagger angle
$\gamma$	specific circulation function
$\gamma$	shock angle
$\Gamma$	circulation vector
$\delta$	deviation angle
$\delta_1, \delta_2, \delta_3,$	boundary layer displacement, momentum, energy thickness

---

$\Delta_1, \Delta_2$	dimensionless displacement, momentum thickness
$\varepsilon$	loss coefficient ratio
$\varepsilon$	convergence tolerance
$\varepsilon'$	dimensionless parameter for stator blades heat transfer
$\varepsilon''$	dimensionless parameter for rotor blades heat transfer
$\zeta$	total pressure loss coefficient
$\eta$	efficiency
$\eta$	velocity ratio
$\theta$	segment angle
$\Theta$	blade flow deflection angle
$\Theta$	shock expansion angle
$\Theta$	temperature ratio
$\kappa$	isentropic exponent
$\kappa$	ratio of specific heats
$\lambda$	stage load coefficient
$\lambda$	wave length
$\Lambda$	load function
$\mu$	mass flow ratio
$\mu$	absolute viscosity
$\mu, \nu, \phi$	velocity ratios
$\nu$	kinematic viscosity
$\nu_m$	straight cascade stagger angle
$\xi$	distance ratio $\xi = x/b$
$\pi$	pressure ratio
$\Pi$	stress tensor, $\Pi = e_i e_j \pi$
$\rho$	density
$\sigma$	cascade solidity $\sigma = c/s$
$\tau$	temperature ratio
$\tau_o, \tau_w$	wall shear stress
$\phi$	stage flow coefficient
$\Phi$	dissipation function
$\Phi, \psi$	potential, stream function
$X$	complex function
$\psi$	isentropic stage load coefficient
$\Psi$	stream function
$\omega$	angular velocity
$\Omega$	Rotation tensor

### Subscripts, superscripts

a, t	axial, tangential
c	compressible
c	cold side
C	compressor
C, S, R	cascade, stator, rotor
ex	exit

---

F	flame
F	fuel
Fi	film
G	combustion gas
h	hot side
in	inlet
max	maximum
P, S	blade pressure, suction surface
s	isentropic
s	shock
t	turbulent
w	wall
—	time averaged
∕	random fluctuation
~	deterministic fluctuation
*	dimensionless
+	wall functions
/, //	stator, rotor

**Abbreviations**

NACA	National Advisory Committee for Aeronautics
NASA	National Aeronautics and Space Administration
TPFL	Turbomachinery Performance and Flow Research Laboratory at Texas A&M University

# 1 Introduction, Gas Turbines, Applications, Types

Gas turbines are engines within which the chemical energy of the fuel is converted either into mechanical energy in terms of shaft power or into kinetic energy. Gas turbines that produce shaft power are power *generation gas turbines*. Gas turbines that convert the fuel energy into kinetic energy are used for generation of thrust to propel an aircraft. The conversion of fuel energy into shaft power or propulsive force, requires interaction of several components of the engine, within each of them a chain of energy conversion takes place.

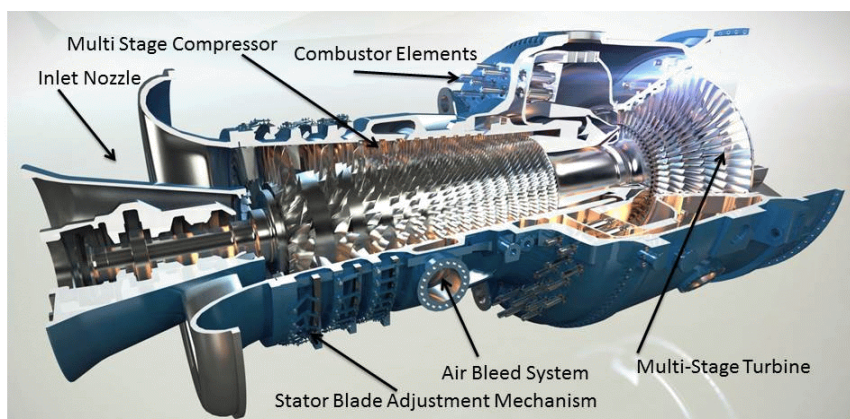


Figure 1.1: Alstom heavy duty power generation gas turbine GT13E2 with gross output of 202.7 MW and a combined cycle efficiency of 53.5%.

## 1.1 Power Generation Gas Turbines

Consider a power generation gas turbine shown in Figure 1.1. Air from the environment enters the inlet nozzle, where its total pressure is *partially converted into kinetic energy*. After passing through the inlet, air enters a multi-stage compressor, where its total pressure continuously increases to reach the design pressure ratio at the exit of the compressor. The increase of total pressure is accomplished by supplying mechanical energy through the turbine. In this case, one is dealing with a *partial conversion of mechanical energy into potential energy*. Based on the compression pressure ratio, the working medium air leaves the compressor exit at a relatively high total temperature and total pressure. It enters the combustion chamber, where fuel is added. Within the combustion chamber an intensive combustion process takes place, where the *chemical energy of the fuel is converted into thermal energy*. The resulting combustion gas enters a multi-stage turbine, where its total energy is,



to a great extent, converted into mechanical energy. The process of energy conversion continues within the exit diffuser (not visible in Figure.1.1), where the kinetic energy of the exiting gas is partially converted into potential energy. The energy conversion process that takes place in individual components is always associated with certain total pressure losses causing entropy increase that leads to efficiency decrease. The energy conversion process discussed above is inherent to all power generation gas turbine irrespective of their power size, types and configurations. Similar components are found in Figure 1.2 and all power generation gas turbines .

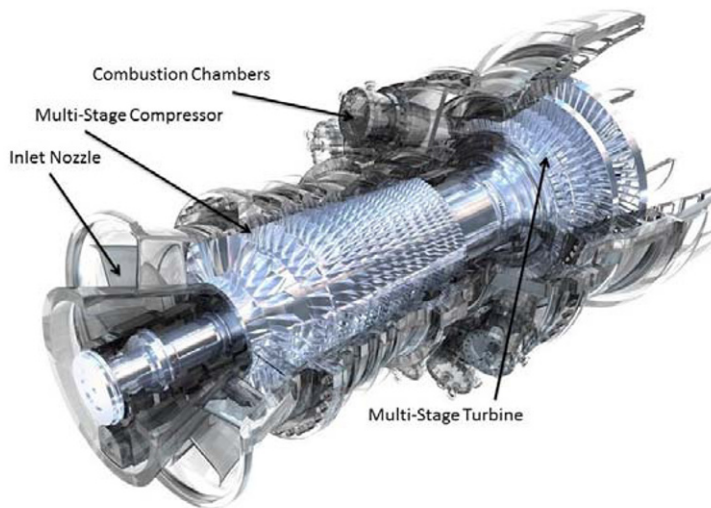


Figure 1.2: A General Electric heavy duty gas turbine with its major components.

The gas turbine configurations shown in Figure 1.1 and 1.2 are characterized by having one multi-stage compressor, one multi-stage turbine and one shaft that carries both compressor and turbine blades. The pressure increase inside the compressor is established by several stages, each of which comprises a stator and a rotor blade row. Total pressure increase is established by compressor rotor row only, while the stator row increases static pressure thus reducing velocity. The stator also provides the necessary flow deflection for the rotor row which receives mechanical energy input from the turbine. Figure 1.3 shows a Siemens SGT5-4000F gas turbine with the compressor and turbine stages. Its annular type combustion chamber has several fuel injectors that are distributed equidistantly in circumferential direction. The annular configuration of the combustion chamber serves a more uniform temperature

distribution for the following turbine component. The multi-stage turbine that follows the combustion chamber provides the power necessary to drive the compressor unit and the generator for producing the electricity.

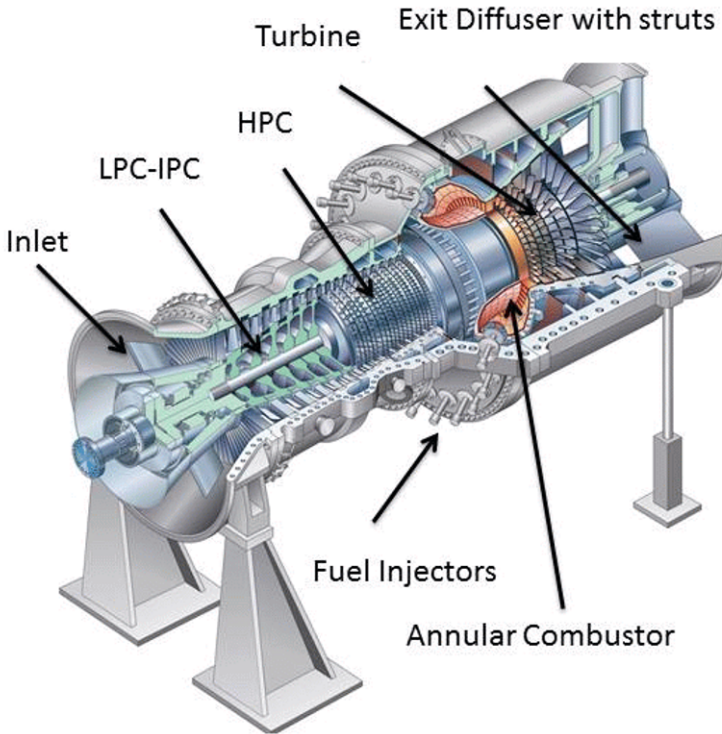


Figure 1.3: Siemens power generation gas turbine SGT5-4000F with a multi-stage compressor, an annular combustor with a set of fuel injectors and a multi-stage turbine.

Siemens gas turbines SGT5-4000F have a gross power output of 292 MW, a gross efficiency of 39.8%, a gross heat rate of 9038 kJ/kWh, a compressor pressure ratio of 18.2 by 15 stages, an exhaust temperature of 580.0 C and an exhaust mass flow 688kg/s. In Combined Cycle configuration the plant produces a net power of 423 MW at a net efficiency of 58.4% and a net heat rate of 6164 kJ/kWh

The gas turbines shown in Figures 1.1-1.3 share a common characteristic: the number of their compressor stages is three-to four times larger than the number of their turbine stages. This phenomenon is explained in terms of different flow characteristics in these two components. While the pressure inside a compressor blade channel is continuously increasing, the one inside a turbine blade channel is

decreasing. In compressor case, the blade boundary layer is exposed to a positive pressure gradient causing the fluid particles to decelerate, eventually come to standstill and reverse the direction. This is the triggering mechanism of what is termed rotating stall. In turbine case, however, the fluid particles inside the turbine blade channel and within its boundary layer are subject to a negative pressure environment that causes the particle to accelerate. As a result, turbine blades can be subject to a much stronger pressure gradient than the compressor blades. This statement is visualized by comparing a compressor cascade with a turbine cascade. As Figure 1.4 shows, the deflection of the turbine cascade is approximately  $\Theta_T \approx 4 \times \Theta_C$ . A

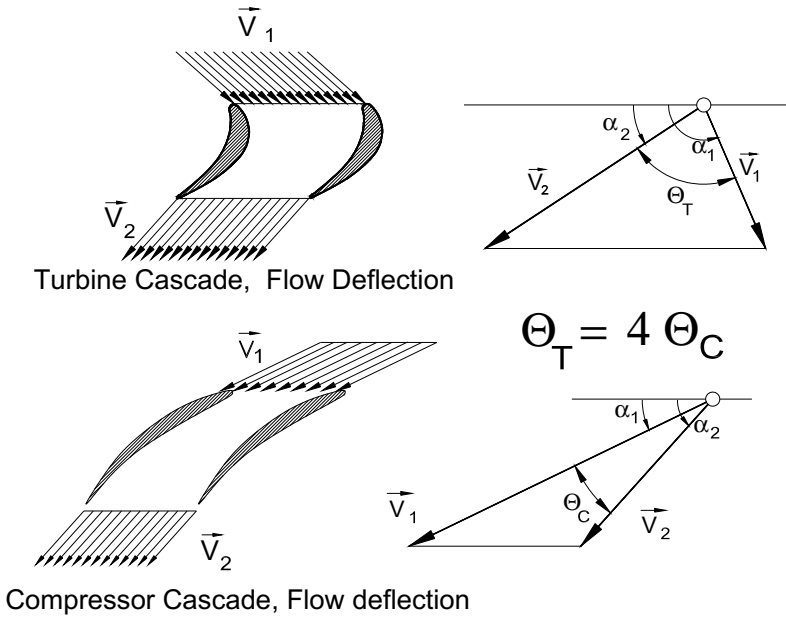


Figure 1.4: Flow deflection in a compressor and a turbine cascade.

quantifying parameter to describe this phenomenon is the stage load coefficient defined as  $\lambda = \Delta H / U^2$  with  $\Delta H$  as the specific total enthalpy of the stage and  $U$  the circumferential velocity of the rotor blade in the mid-section. Assume a single stage turbine with  $\lambda = 2$  has to process a pressure ratio of  $\pi_T = 1.7$ . For an axial compressor to supply this pressure ratio four stages are needed, each with pressure ratio of  $\pi_C = 1.14$ . In contrast to the axial compressors with relatively low pressure ratio per stage, radial compressors can be designed with a single stage exceeding pressure ratios above 5. These type of compressors can be applied to gas turbines of small power size. As an example, a small gas turbine OP16 by OPRA, is shown in Figure 1.5. The rotor carries a single stage centrifugal compressor with a pressure

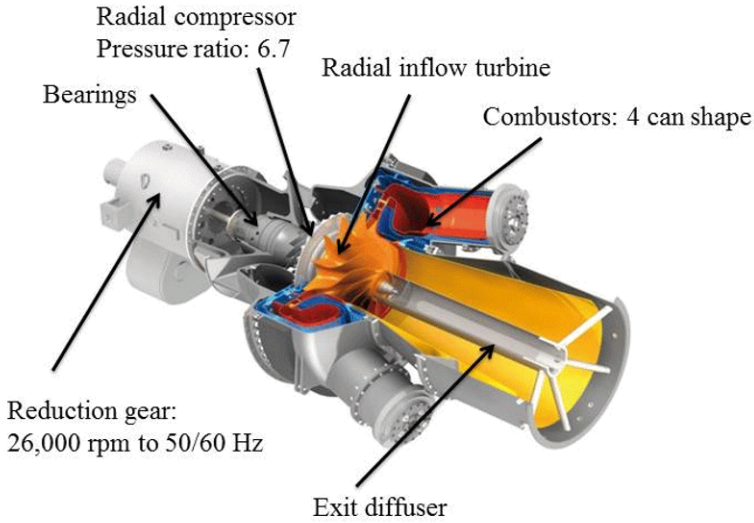


Figure 1.5: OP16 gas turbine with centrifugal compressor and centripetal turbine.

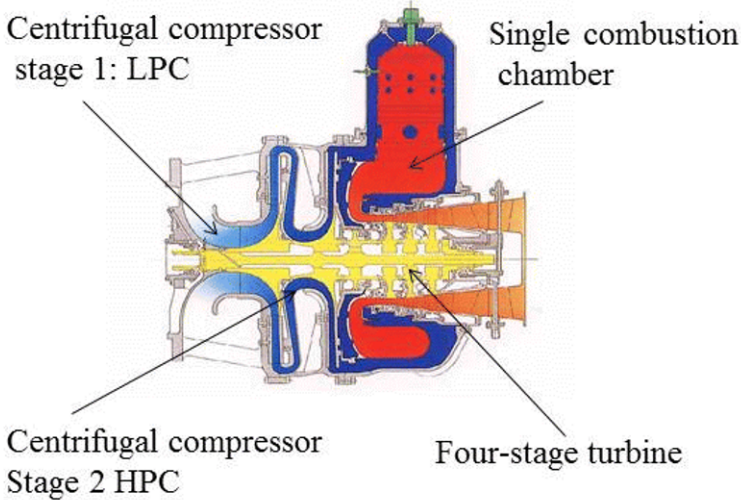


Figure 1.6: A Kawasaki small gas turbine with two centrifugal compressors, a four stage turbine and a single combustion chamber.

ratio of  $\pi_c = 6.7$ . The compressor is driven by a single stage centripetal turbine that produces a net power of 2MW at a gross efficiency of 26%. This 2 MW class engine is suitable for oil and gas, marine, industrial and commercial power applications.

To obtain a higher pressure ratio, two or more centrifugal compressors can be arranged and operated in series. A small Kawasaki gas turbine, M1A-13/17, with 1.5 MW power is shown in Figure 1.6. It has a two stage centrifugal compressor, a single combustion chamber and a four stage turbine. For small size engines, the centrifugal compressor is the appropriate pressure supplier, but it cannot be used for large power generation gas turbines or aero-engines. As will be explained in detail in Chapter 4, the mechanism of pressure generation by a centrifugal compressor is based on the difference in the circumferential kinetic energies from exit to inlet,  $U_{exit}^2 - U_{inlet}^2$ . Since the power is directly proportional to the mass flow, large engines require large amount of mass flow. In order for a centrifugal compressor to provide the same amount of mass flow as an axial compressor, its exit diameter must be substantially larger than the inlet mean diameter. This makes the use of centrifugal compressors impractical for installation into the large power generation gas turbines. For aero-engines, a disproportionately large outer diameter increases the drag force and thus the fuel consumption.

## 1.2 Compressed Air Energy Storage Gas Turbines, CAES

The first compressed air energy storage (CAES) plant was designed and manufactured by Brown Boveri & Cie (BBC), installed in Huntorf Germany and commissioned 1978. It comprises of a compressor train that pumps air into a large underground cavern, an electric/generator and a gas turbine unit. The plant was designed to cover the peak-load demand in a highly efficient manner. Its gas turbine unit distinguishes itself from all other conventional turbines. The conventional gas turbines require up to two thirds of the turbine power to drive the compressor, leaving about one third as the net power for electricity generation. In contrast, the CAES-gas turbine uses the pre-compressed air stored in an underground cavern. During the high electric energy demand the compressed air is directed to the combustion chamber, where fuel is added. Thus, the entire thermal energy of the combustion gas is transferred to the shaft.

Figures 1.7 show the schematics of the CAES Huntorf with more details presented in [1]. The plant has been operating reliably since 1978 as an emergency power generator to cover the peak electric energy demand. It consists of (1) a compressor train, (2) an electric motor/generator unit, (3) gas turbine, and (4) underground compressed air storage. During a period of eight hours of low electric energy demand (night), the electric motor operating at 60MW drives the compressor train that pumps air into an underground salt cavern with a storage volume of 310,000 m<sup>3</sup> more than 600 m deep below the ground at a maximum pressure of about 70 bar. The compressor train consists of an axial low pressure compressor with 20 stages and a high pressure unit with 6 radial impellers operating at 7622 rpm. The compressed air has a relatively high exit temperature and must be cooled down before entering the storage cavern. The HPC has two inter-cooler and one after-cooler.

During the compression mode, the turbine valve VT is closed, while the

compressor valve VC is open. During the power generation mode, the compressor valve VC is closed, while the turbine valve VT opens. During high electric energy demand, the cavern exit valves open, and air after passing through a pre-heater enters the high pressure (HP)-combustion chamber, where fuel is added. The lean combustion gas expands in HP-turbine, and exits into the low pressure (LP)-combustion chamber, where the remaining fuel is added. The gas turbine operates and delivers 290 MW for about two hours.

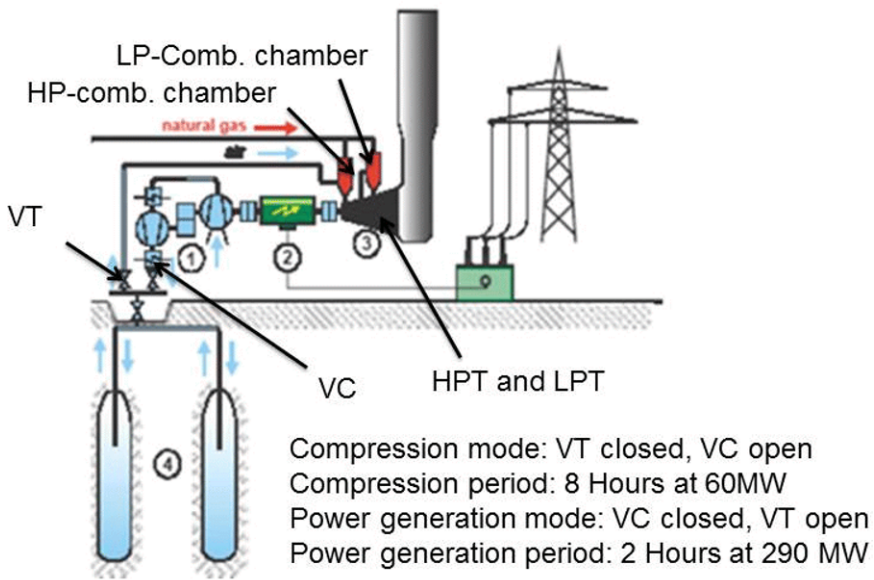


Figure 1.7: Compressed air storage facility Huntorf, Germany

The core component of this and the more advanced Soyland CAES facility is the gas turbine shown in Figure 1.8. It consists of a high pressure (HP) combustion chamber followed by a multi-stage HP-turbine followed by a low pressure (LP) combustion chamber and a multi-stage LP-turbine. A detailed dynamic performance and efficiency study of this CAES-gas turbine operating in power generation mode compared to the one with only one combustion chamber and one multi-stage turbine gave a substantial increase of efficiency. Although this standard efficiency improvement method was used in CAES plant design, until late eighties it did not find its way into the power generation gas turbine design. The reason for not applying this very effective method to gas turbines was in first place the inherent problem of the integration of the typical BBC-large volume silo-type combustion chambers into a compact gas turbine engine. Adding another conventional large volume combustion chamber such as those in CAES raised a number of unforeseeable design integrity and operational reliability concerns that deterred engine manufacturer. However,

taking advantage of the well known reheat concept and its successful application to CAES-Huntorf, seemed to be a viable solution for improving the BBC gas turbine efficiencies. The adoption of this concept occurred after the merger between the Swedish company Asea and Brown Boveri, Switzerland in 1988.

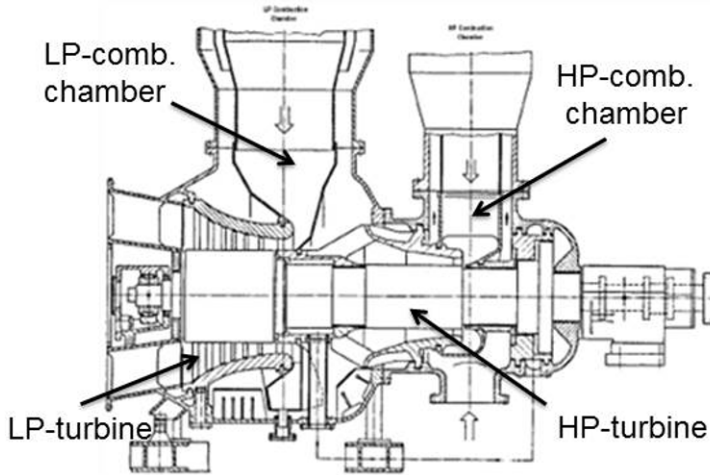


Figure 1.8: CAES Soyland from [1].

### 1.3 Power Generation Gas Turbine Process

Worldwide prior to 1986, the thermal efficiency of gas turbines, based on the turbine inlet temperature (TIT) ranged from  $\eta_{BL} = 32\% - 35\%$ . Achieving higher efficiency required a substantial increase of TIT necessitating extensive cooling of the front turbine stages. Studies in [2] and [3] show that a significant efficiency improvement can be achieved by introducing the reheat concept used in CAES-turbine design. The thermodynamic process in Figure 1.9 shows the thermal efficiency as a function of pressure ratio (top) and specific gas turbine work (bottom) with TIT as a parameter. As seen, for each TIT, there is an optimum pressure ratio that increases with rising the turbine inlet temperature. Increasing the pressure ratio beyond this optimum point will reduce the efficiency. Given a certain maximum compressor stage pressure ratio as a limit (1.15-1.25), any increase in overall pressure ratio requires adding more stages. In practice, the compressor is designed with a pressure ratio less than the optimum but with  $\eta_{th} \approx \eta_{th_{opt}}$ . Figure 1.9 explains this process: using a temperature

ratio of  $\Theta = 4$ , its optimum pressure ratio is close to  $\pi_{opt} \approx 19$  (red circle). Its optimum efficiency, however, is very close to the one at  $\pi = 15$  (circle marked green). To provide the difference of  $\Delta \pi = 4$ , at least 7 stages, each with a  $\pi_{stage} = 1.22$  are necessary to arrive at  $\pi_{opt} \approx 19$ . Considering Figure 1.9 (bottom), it should be noted that the maximum efficiency and maximum specific gas turbine work are at two different pressure ratios as shown in Figure 1.10. In fact, moving toward smaller pressure ratios as discussed above is not only saving a significant number of stages, but it also moves the specific GT-work to higher level which is desirable for integrating the gas turbine into a combined cycle (CCGT).

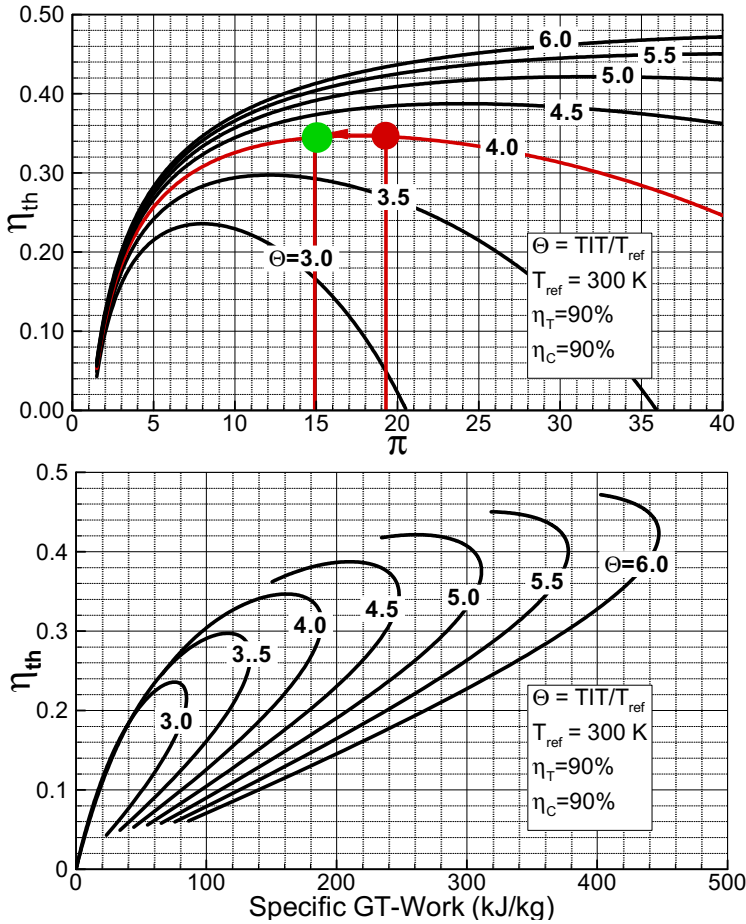


Figure 1.9: Efficiency improvement of conventional gas turbines.



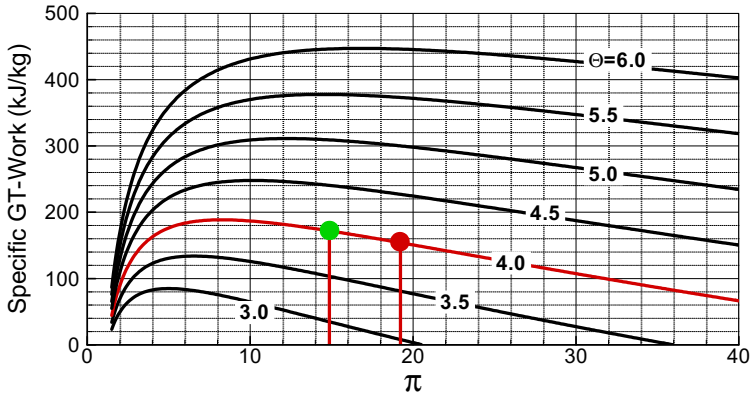


Figure 1.10: Specific GT-work as a function of pressure ratio with TIT as parameter.

1.4 Significant Efficiency Improvement of Gas Turbines

A schematic representation of the reheat concept mentioned previously is given in Figure 1.11 in terms of T-S-diagrams for a baseline gas turbine (a) and a gas turbine with reheat stage (b). To apply the reheat concept, first the optimum pressure ratio and the corresponding design pressure ratio must be obtained. This ratio is for the

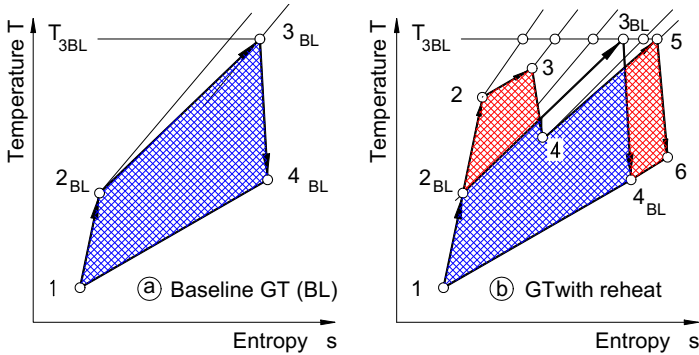


Figure 1.11: Performance comparison of a conventional and a reheat gas turbine.

same baseline temperature almost twice the baseline pressure ratio. Using a gas turbine with an efficiency of 36% as the baseline GT, a reheat stage was added as shown in Figure 1.11. The blue hatched area in Figure 1.11 (a) represents the performance of the baseline GT, whereas the area hatched in blue and red represents

the performance of a GT with a reheat stage. It should be noted that the turbine inlet temperature for the baseline GT and the GT with reheat are the same. This is a very important aspect that enables a gas turbine design with a high efficiency but at a lower temperature; for example 1200 °C. Figure 1.12 shows quantitatively the efficiency improvement using the reheat concept. The blue curve represents the efficiency of a relatively advanced GT up to 1986. The green curve exhibits the efficiency of a generic reheat gas turbine. This curve includes the predicted efficiency of 40.5% already reported in [4]. While the pressure ratio of this generic gas turbine and the one of ABB-GT24/26 are identical, the turbine inlet temperature is by 4°C lower than the turbine inlet temperature of GT24/26 [4].

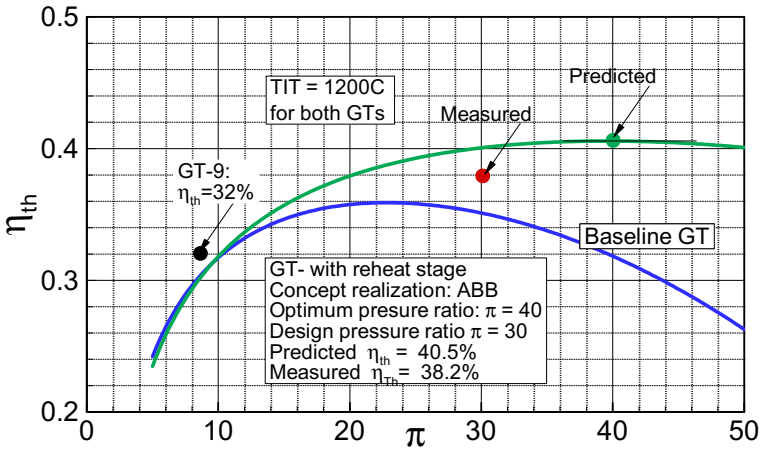


Figure 1.12: Efficiency comparison between a conventional (blue curve) and a reheat gas turbine (green curve).

As seen, the new reheat gas turbine has an efficiency increase of 8.5% compared to the one of GT-9 and 4.5% compared to the baseline of a more advanced gas turbine in the same period of time. The corresponding measured efficiency for GT24 reported in [4] was 38.2%. The difference of 2.3% was attributed to numerous failures associated with compressor blade distress in the form of cracking [4]. The failures occurred at the start of the engine operation. Although the difference of 2.3% is not insignificant, an enormous improvement of thermal efficiency was achieved despite the facts that: (a) The compressor pressure ratio is far greater than the one of conventional GT one  $\pi_{opt_{GT24}} \approx 2 \times \pi_{opt_{BL}}$  causing the compressor efficiency to decrease. The latter is because of reduced blade height associated with an increase in secondary flow losses. (b) The introduction of a second combustion chamber inherently causes additional total pressure losses.

The application of the reheat concept to large gas turbines started in 1990 by ABB and completed in 1995 with two engines, GT24, designed for 60Hz markets (USA and the others) and GT26 for 50Hz (Europe). The first gas turbine GT24 was installed 1995 at Gilbert (USA), [4]. The new element of this advanced technology is the fuel injector of the sequential combustion system. This system was first introduced by BBC at Beznau, Switzerland in 1948. As reported by Frutschi [5]. The plant is still operational after almost half a century, has a turbine inlet temperature of 600 °C, and an efficiency of 30%, which is remarkably high for this very low turbine inlet temperature.

Figure 1.13 shows the gas turbine GT-24/26 with all components. It has a compressor with 22 stages and a pressure ratio of 30/1, a reheat stage with a pressure ratio of 30/15 and two combustion chambers. The first combustion chamber has a firing temperature of approximately 1232°C at the high-pressure reheat turbine (HPT). Since the blade material starts melting at about 1200°C, hot gas components must be cooled well below the melting point. As a result, the blades of the single-stage HPT and the first and second stages of the four stage low-pressure turbine (LPT) are air cooled. The first annular combustor with EV-burners is followed by the

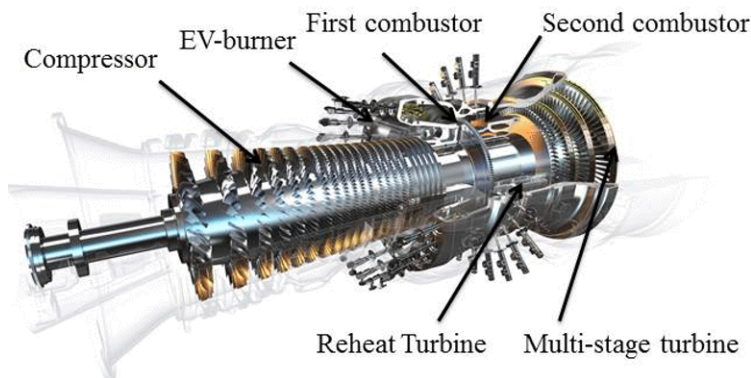


Figure 1.13: GT-24/26 with its components.

HP-reheat turbine followed by second combustor, followed by a four-stage LPT. The combustors have EV (environmental) swirl burners. As reported in [6] and shown in Figure 1.14, the EV burner consists of two half cone shells, which are displaced parallel to the axis, with two tangential slots. The swirl strength of the flow entering through the tangential slots is increasing in axial direction and is adjusted such, that a vortex breakdown of the core flow occurs close to the burner exit.

The phenomenon of vortex breakdown, stability, and its application to combustion chambers started mid eighties at Brown Boveri & Cie and reported, among others, in the papers by Keller et al. [7] and Schobeiri [8] and found its application into the gas turbine GT-9 in late nineties as reported by Keller et al. [9].

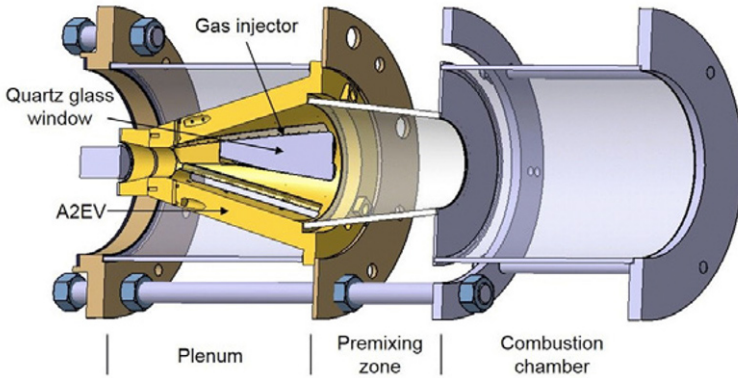


Figure 1.14: EV-burner test section.

As reported in [6], in the EV premix burner no specific flame stabilizer hardware exists which is exposed – as in conventional premix burners - upstream to the ignitable mixture and downstream to the flame stabilization zone. As a result the EV burner has an inherent safety against autoignition or flame flashback events.

A series of performance tests reported in [4] measured the characteristics of GT-24(60Hz). It also contains the performance data of GT-26(50Hz). Both versions have a compression ratio of 30/1, but different mass flow rates, powers and efficiencies. These are listed in Table 1. The updated values marked with (\*) are from [10].

Table 1.1: Performance data for GT24 and 26 from [4].

Characteristics	GT-24 (60Hz)	GT-26 (50Hz)
TIT (°C)	1235	1235
Pressure ratio	30.0 (35.4)*	30.0, (35.0)
Efficiency %	37.9 (40.0)*	38.2 (41.0)*
Baseload output (MW)	166 (235)*	241 (345)*
Heat Rate (kJ/kWh)	9495	9490
Mass flow rate (kg/s)	378	610
Exhaust temperature (°C)	610	610

## 1.5 Ultra High Efficiency Gas Turbine With Stator Internal Combustion

In Section 1.4, it was shown that by keeping a moderate level of TIT, major efficiency improvement could be achieved by changing the design technology. This section shows the concept of a new technology that is capable of further increasing the GT-efficiency. The new technology, the Ultra High Efficiency Gas Turbine With Stator Internal Combustion, UHEGT, deals with a new concept for the devolvement of power and aircraft gas turbine engines, where the combustion process takes place within the turbine stator rows, leading to a distributed combustion. The UHEGT-concept allows eliminating the combustion chamber resulting in high thermal efficiencies which cannot be achieved by any gas turbine engines of conventional design. The concept of the UHEGT was developed by Schobeiri described in [2] and [3]. A detailed study in [3] shows that the UHEGT-concept drastically improves the thermal efficiency of gas turbines from 5% to 7% above the current highest efficiency of 40.5% set by GT24/26 at full load. To demonstrate the innovative claim of the UHEGT-concept, a study was conducted comparing three conceptually different power generation gas turbine engines: GT-9, a conventional gas turbine (single shaft, single combustion chamber), a gas turbine with sequential combustion (concept realization by ABB:GT24/26), and a UHEGT. The evolution of

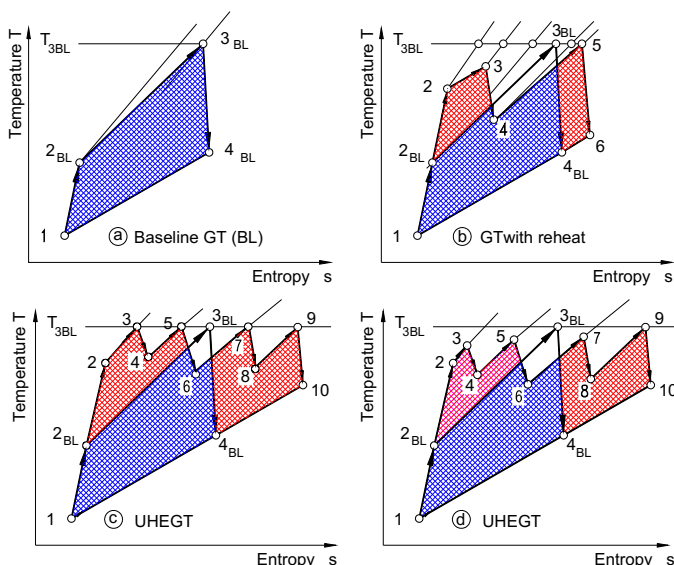


Figure 1.15: T-s diagrams of three different gas turbines.

the gas turbine process that represents the efficiency improvement is shown in Figure 1.15. Starting with the base load process, Figure 15(a), the first improvement is shown in Figure 1.15(b), where the red hatched areas add to the T-s area leading to a substantial increase of thermal efficiency. The stator internal combustion represented by the UHEGT-concept shown in Figure 1.15 (c), shows a further increase of the T-s area and thus the thermal efficiency. In Figure 1.15(c) the stator inlet temperature is kept constant. However, as shown in Figure 1.15(d) the stator inlet temperature might be less than the maximum desired one within the first two stages.

A quantitative calculation of each process is presented in Figure 1.16. It compares the thermal efficiency and specific work of baseline GT, the GT24/26, and

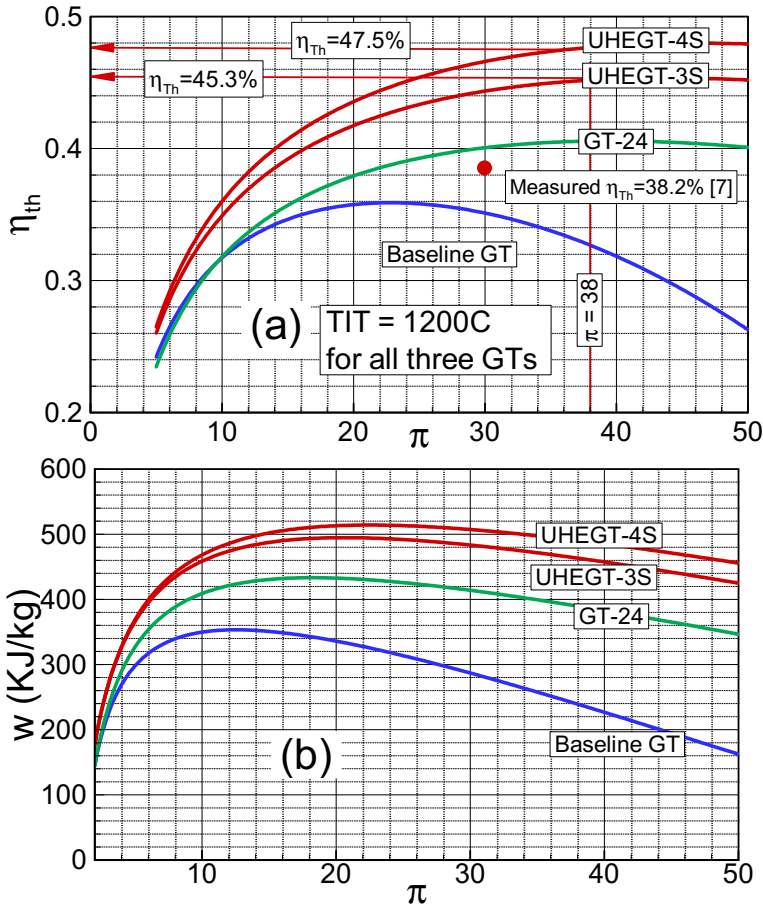


Figure 1.16: Comparison of (a) thermal efficiencies and (b) specific work for Baseline GT, GT24/26 and UHEGT.

a UHEGT with three and four stator-internal combustion, UHEGT-3S and UHEGT-4S, respectively. Maximum temperature, TIT, for all cycles are the same and equal to 1200 C. As shown in Figure 1.6a, for the UHEGT-3S a thermal efficiency above 45% is calculated. This exhibits an increase of at least 5% above the efficiency of the current most advanced gas turbine engine which is close to 40%. Increasing the number of stator internal combustion to 4, curve labeled with UHEGT-4S, can raise the efficiency above 47% which is an enormous efficiency increase compared to any existing gas turbine engine. It should be noted that UHEGT-concept substantially improves the thermal efficiency of gas turbines, where the pressure ratio is optimized corresponding to the turbine inlet temperature. This gives UHEGT a wide range of applications from small to large size engines. Figure 1.17 summarizes the impact of technology change on thermal efficiency. It is remarkable that the efficiency increase of the UHEGT of 7.5% above the best existing GTs has been achieved without substantially raising the TIT.

### Impact of Technology Change on GT-Thermal Efficiency

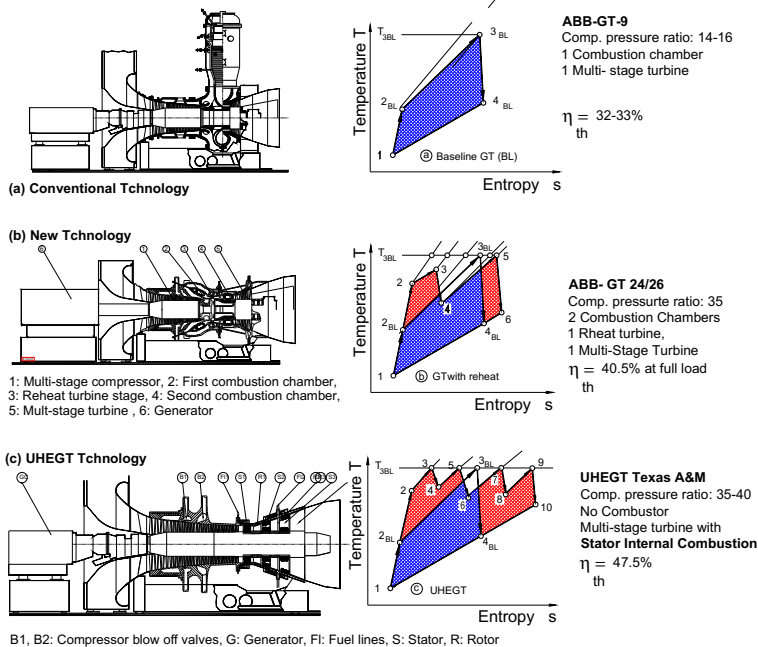


Figure 1.17: Technology change: Substantial increase of thermal efficiency at a moderate level.



## 1.6 Aircraft Gas Turbines

Besides power generation, gas turbines play an important role in transportation. Aircraft gas turbines are the main propulsion systems of large, medium, and small size aircrafts. As an example, a high bypass ratio aircraft gas turbine engine is shown in Figure. 1.18.

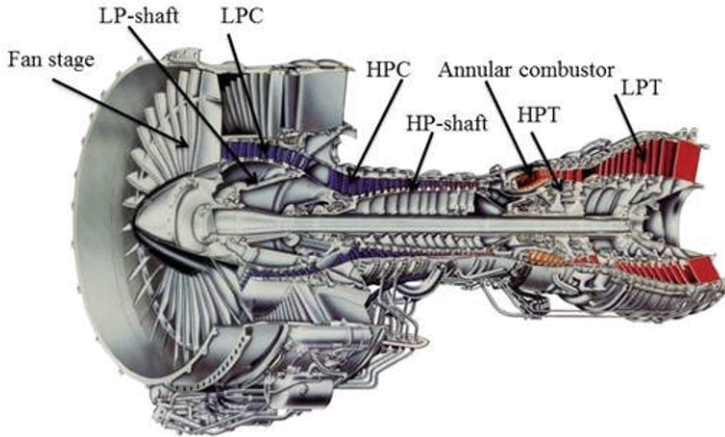


Figure 1.18: Twin spool, high bypass ratio aircraft engine (Pratt& Whitney).

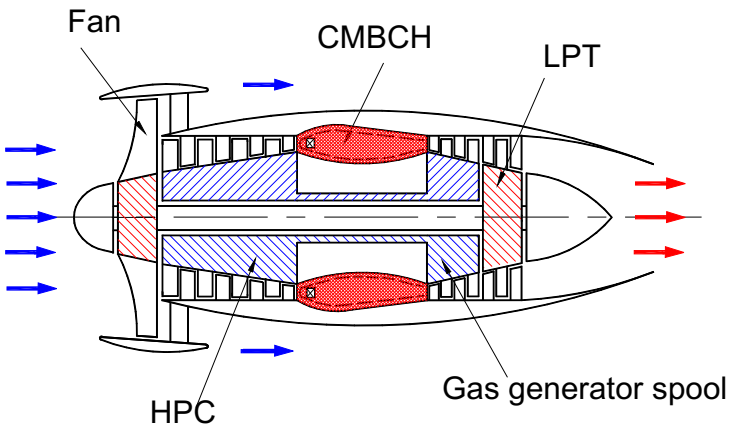


Figure 1.19: Sketch of the two independently rotating spool.

The twin spool engine consists of a fan stage, a multi-stage LPC, a combined IPC and



HPC, an annular combustion chamber, followed by the HPT followed by the LPT and two concentric shafts. The schematic of the concentric shaft arrangement is given in Figure 1.19. The fan stage generates a pressure ratio around 1.3 and is driven by the LPT. The HPT drives the IPC-HPC compressor stages, while sharing the external shaft with the latter. The configuration of HPC and HPT constitutes the gas generator spool. The pre-compressed air from the fan stage enters the LPC and after the final compression through the HPC-stages, it enters the combustion chamber where fuel is added. The engine produces a maximum thrust of 19 kN. The gas generator spool provides the high-pressure, high temperature combustion gas to drive the LPT. After exiting from the LPT, the combustion gas expands in the exhaust nozzle. Its kinetic energy is used for producing additional thrust. Figure 1.20 shows the GT- schematics and the process diagrams of a single shaft power generation gas turbine and a twin-spool aircraft engine. While in Figure 1.20(a), the total energy of the combustion gas is converted into the mechanical energy, in Figure 1.20(b) a major portion of the combustion gas total energy is used to power the gas generating turbine.

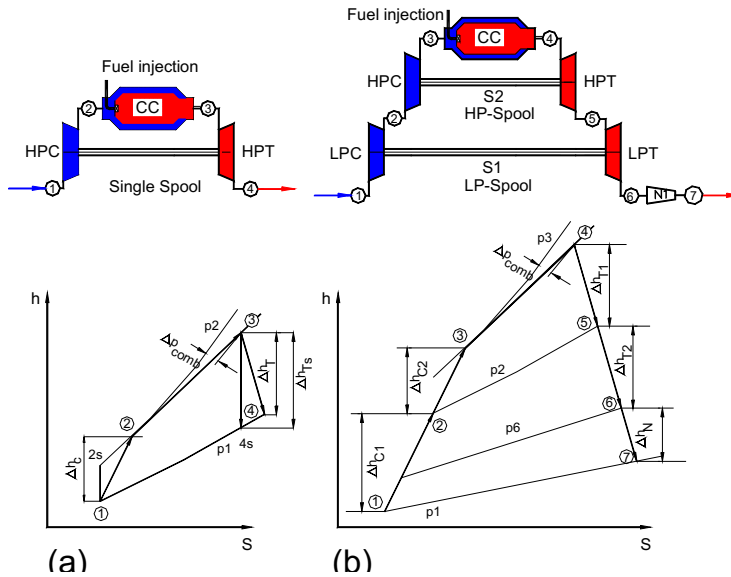


Figure 1.20: H-s-diagram of a single spool power generation gas turbine (a) and a twin-spool aircraft engine (b).

Another advanced aircraft engine is the Rolls Royce Trent 1000, a three-spool engine shown in Figure 1.21. It consists of, LP-, IP-, and HP-spools with the corresponding LPC-LPT, IPC-IPT, and HPC-HPT shafts. As reported in [11], the turbofan engine has a bypass ratio of 11:1, one LPC-stage, eight IPC, and six HPC-stages. The turbine side consists of a single-stage HPT, a single-stage IPT and a six-stage LPT. The compressors deliver an overall pressure ratio of 52:1 with an air mass flow rate of 1290 kg/s. The maximum thrust of the engine is 240-350 kN and thrust-to-weight ratio is 6.189:1. The three spools rotate at different speeds: HP-spool 13391rpm, IP-spool 8937 rpm and LP-spool 2683 rpm. Following temperature limits are listed in [11]: (a) Maximum temperature during ground starts and shutdown: 700 °C, (b) Maximum during in-flight relights: 900 °C, (c) Maximum for take-off (5 min. limit): 900 °C, (d) Maximum Continuous (unrestricted duration): 850 °C, (e) Maximum over-temperature (20 second limit): 920 °C.

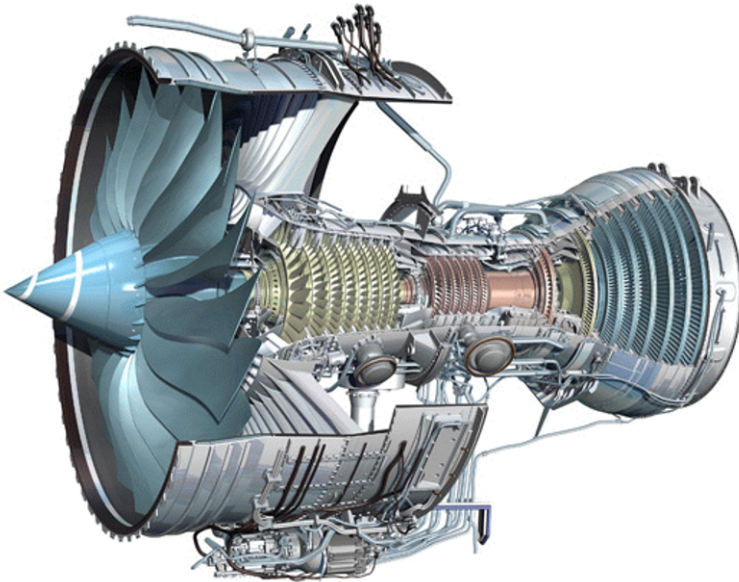


Figure 1.21: Three spool aircraft engine RR Trent 1000.

## 1.7 Aircraft-Derivative Gas Turbines

Aircraft engines have much higher power density compared to power generation ones. With relatively minor design changes, they can be used as emergency power generators. They also can be used as propulsive units in high speed ships, trains and tanks. A twin spool fan engine can be modified to produce power by removing the fan stage, keeping the gas generator HPC and modifying the LPT in such a way that it can

generate power. As a representative example, Figure 1.22, a General Electric LM6000-PF+ shows how an aircraft engine can be converted into a power generation one. There are numerous derivatives of different aircraft engine types by different

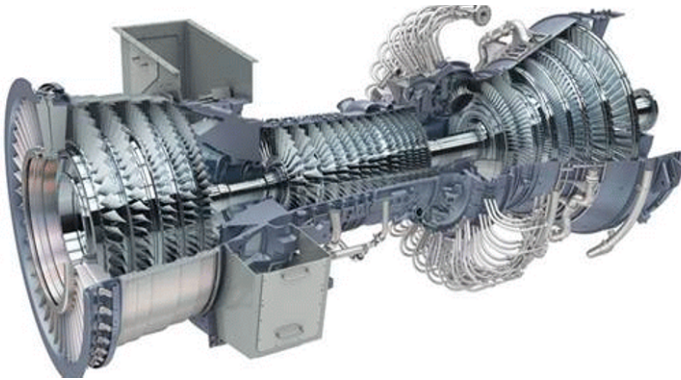


Figure 1.22: Aero-derivative gas turbine GE, the LM6000-PF+ .

manufacturers, where the LPT has been modified as a free turbine to generate power.

A different, and more complex derivative is the GE-LMS-100 shown in Figure 1.23. This engine is a modular combination of MS6000 IFA LP-compressor, CF6-80C2 Hp-compressor and CF6-80E HP-turbine. To increase the thermal efficiency, the well proven intercooling technology, first introduced by BBC in 1948, was used. The technology was applied to a dual shaft gas turbine Beznau, Switzerland [5].

Modular design of GE-LMS-100: Power 100 MW, Pressure ratio: 42:1, Mass flow: 208.65kg/s, Core speed from 8000-9000 rpm, Power shaft speed: 3600 rpm

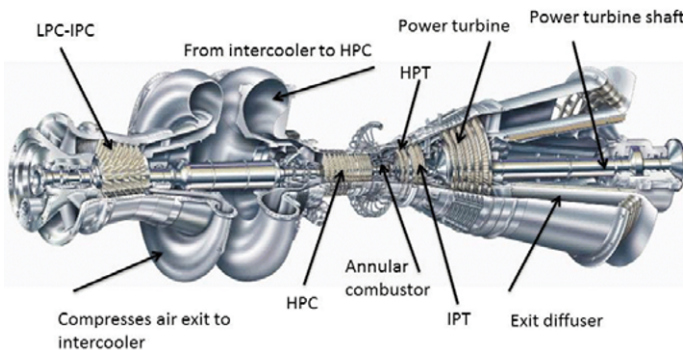


Figure 1.23: Aero-derivative gas turbine by GE, the LMS100.

For the LMS-100 gas turbine, intercooling the air that exits from the LPC has resulted in an efficiency of 45% .

Figure 1.24 shows the schematic of an intercooled twin spool aero-derivative with the corresponding temperature-entropy diagram. At the exit of the low pressure compressor LPC, the compressed air is intercooled from  $T_2$  to  $T_3$ , before entering the high pressure HPC. As seen, the temperature  $T_3$  is slightly above the inlet temperature of LPC. The difference  $\Delta T = T_3 - T_1$  is due to the temperature of the cooling fluid and the cooling efficiency. The subsequent compression by HPC results in a temperature  $T_4$  that corresponds to the pressure ratio and the efficiency of the HPC.

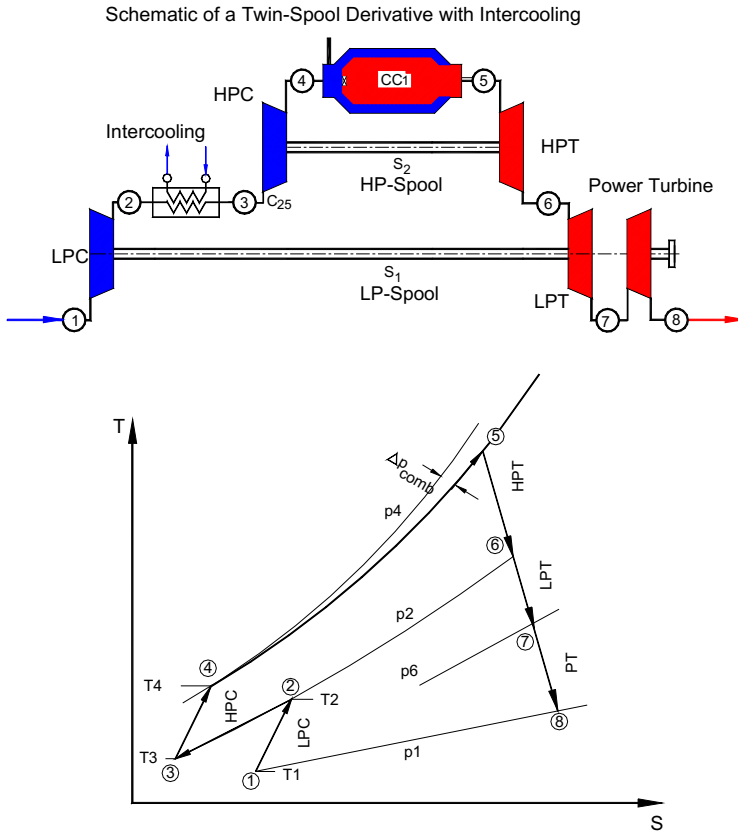


Figure 1.24: Twin spool aero-derivative gas turbine with intercooling, T-s diagram.

Figure 1.25 summarizes different configurations of derivatives that can be constructed from twin-spool core engines. These are among others, twin spool

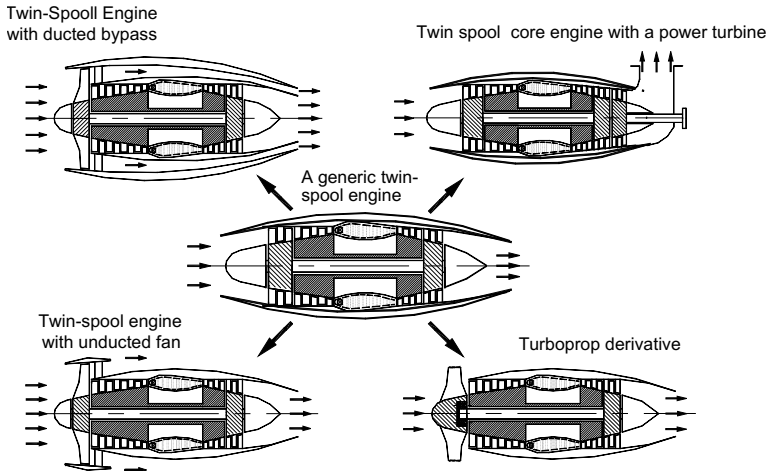


Figure 1.25: Different Aero-derivative configurations.

engines with ducted bypass, twin spool core engine with a power turbine, unducted fan engine and turboprop derivatives.

## 1.8 Gas Turbines Turbocharging Diesel Engines

Turbochargers belong to the category of small size gas turbines. They are applied to cars, trucks and large ship Diesel engines. Their function is to increase the effective mean piston pressure of internal combustion engines and therefore raise their thermal efficiencies. As an example, a typical turbocharger for large Diesel engines of 10 MW is shown in Fig. 1.26. The turbocharger consists of an air filter, inlet nozzle, a radial compressor stage, driven by a single stage axial turbine. Exhaust gas from Diesel engine enters the turbine, where its total energy is partially converted into the shaft power. The turbine drives the compressor stage, which is usually a single stage radial compressor. The compressor sucks air from the environment, compresses and delivers it to the piston, thereby substantially increasing the mean effective piston pressure and thermal efficiency of the engine. For large Diesel engines running at 1200-1800 rpm, high efficiency of 50% are achieved by turbocharging. This is about 10% above the current best efficiency of gas turbines and 10% below the combined cycle systems. The turbine power generally covers the compressor power and the bearing friction losses. During the engine transient operations, however, there is always a mismatch between the turbine and the compressor power but it disappears after a dynamic equilibrium has been reached between these two components.

Figure 1.27 shows a turbocharger for a car with Diesel engine. Major car

manufacturers recently introduced smaller size turbochargers to increase the mean piston pressure.

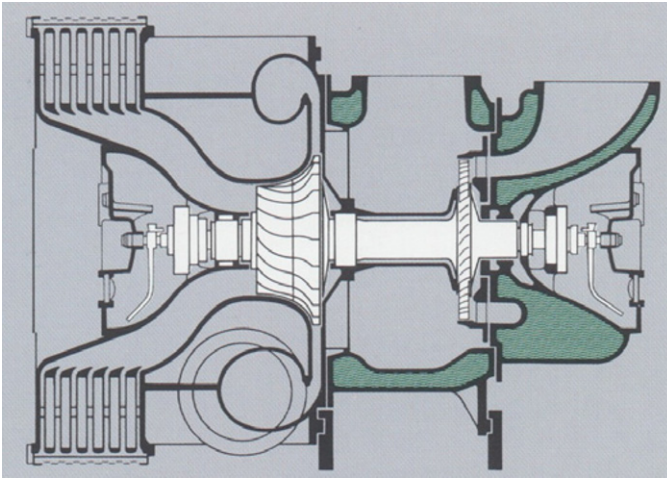


Figure 1.26: Turbocharger of a large Diesel engine of 10MW Power, compressor pressure ratio: 4.0:1 (ABB).

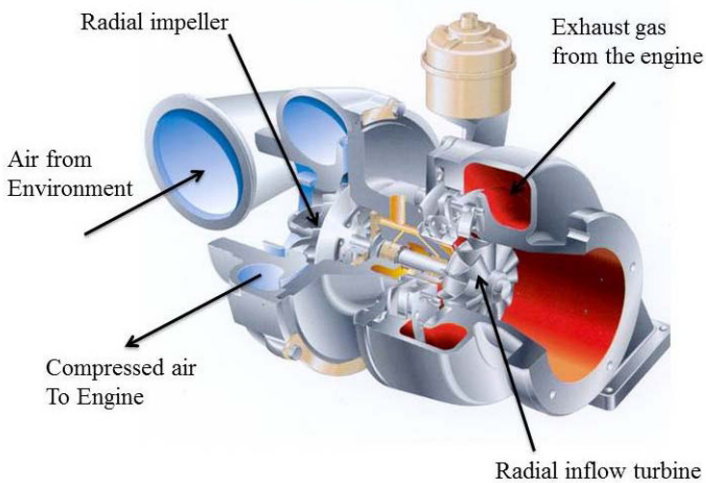


Figure 1.27: Turbocharger for a small Diesel engine, manufactured by Borg Warner, Germany.

## 1.9 Gas Turbine Components, Functions

Gas turbine systems used for power generation, thrust generation or for turbocharging consist of several components, [12],[13],[14] and[15]. Each component is designed to perform a defined function within the system. Inlet nozzles, exit diffusers, combustion chambers, compressors, and turbines are a few component examples.

A component may consist of several *sub-components*. A turbine or a compressor stage exhibits such a sub-component. Figure 1.28 exhibits an advanced gas turbine with sequential combustors and other components. Figure 1.29 illustrates a decomposition of a twin-spool engine into its major components. It consists of (1) a high pressure-spool that encompasses the multistage high pressure compressor, a combustion chamber, and the high pressure turbine component, (2) a *low pressure-spool* shaft connects the low pressure compressor with the low pressure turbine component, (3) the combustion chamber, (4) an inlet diffuser and exit nozzle. The two spools are connected aerodynamically. The mass flow, with high kinetic energy exiting from the last stage of the HP-turbine stage, impinges on the first stator of the LP-turbine, and is further expanded within the LP-component and the following thrust nozzle, that provides the required kinetic energy for thrust generation. Besides the major components shown in Figures 1.28 and 1.29, there are several other components such as pipes that serve the transport of mass flow from compressor to

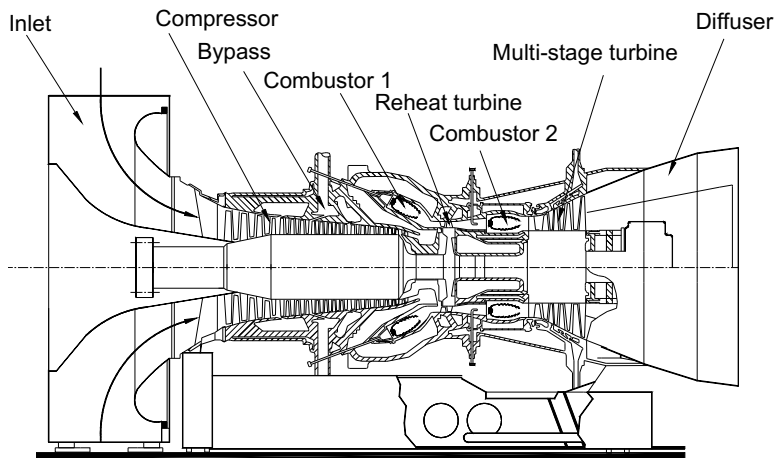


Figure 1.28: Gas turbine components.

turbine for cooling purposes, valves with the operation ramp defined by the control system, control systems, lubrication systems, bearings, electric motors for power supply, etc. The components shown in Figure 1.28 and 1.29 are categorized in groups based on their respective functions.

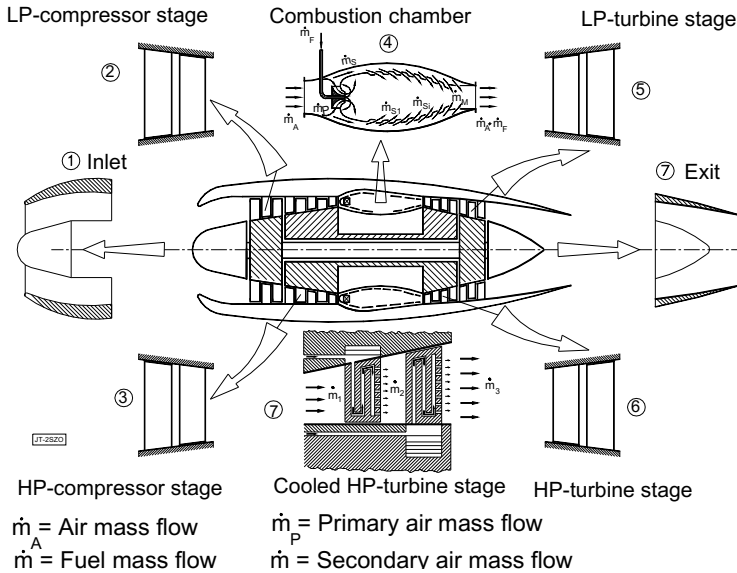


Figure 1.29: Decomposition of a twin-spool engine.

### 1.9.1 Group 1: Inlet, Exhaust, Pipe

Group 1 includes those components in which no transfer of thermal energy with the surrounding environment takes place. Their function consists, among other things, of

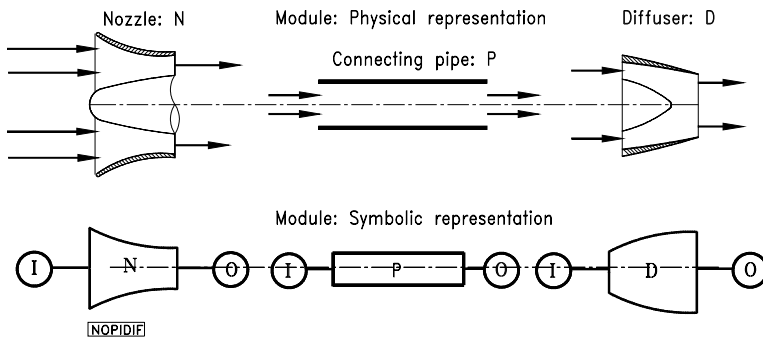


Figure 1.30: Component and modular representation of inlet nozzle N, connecting pipe P, and Diffuser D

transporting the mass, accelerating the mass flow through the nozzle, and reducing the kinetic energy through a diffuser. Figure 1.30 exhibits the physical representation of the component's nozzle, pipe, and diffuser. Each module is surrounded by an inlet



and an outlet plenum. These plena serve as the coupling element between two or more modules. Detailed physical and mathematical modeling of these modules are presented in Chapter 13.

### 1.9.2 Group 2: Heat Exchangers, Combustion Chamber, After- Burners

Group 2 includes those components within which the processes of thermal energy exchange or heat generation take place. Heat exchangers are encountered in different forms such as recuperators, regenerators, inter-coolers, and after-coolers.

**Recuperators** are used to improve the thermal efficiency of small power generation gas turbines. While hot gas from the exhaust system enters the low pressure side (hot side) of the recuperator, compressor air enters the high pressure

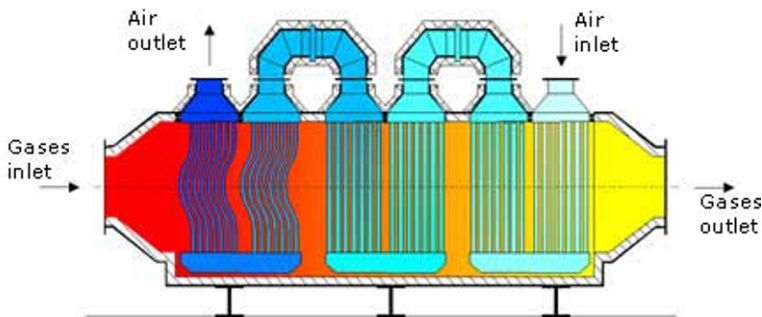


Figure 1.31: A gas turbine recuperator with gas and air side tubes made by Kalfrisa..

side (cold side). By passing over a number of contact surfaces, the hot side of the recuperator transfers thermal energy to the compressor air that passes through the recuperator cold side. After exiting the recuperator air side, preheated air enters the following combustion chamber. As Figure 1.31 shows, low temperature air enters the recuperator tubes that are exposed to the hot gas. Heat is transferred from hot gas to the air through convection, conduction and radiation increasing the temperature of air. The air at higher temperatures enter the combustion chamber and the exhaust gas exits the recuperator at lower pressure (for detail see Chapter 14)

**Combustion Chambers** of power generation and aircraft engines share the same function. They convert the chemical energy of the fuel into thermal energy. There are different type of combustion chambers such as silo type, annular and tubular combustion chambers. The silo type was the standard combustion chamber for all Brown Boveri gas turbines from GT-8 to GT-13. Figure 1.32 exhibits the gas turbine GT-9 with the silo type combustion chamber. It generally consists of a primary combustion zone, a secondary zone, and a mixing zone. The primary zone, surrounded by  $n$  rows of ceramic segments, separates the primary combustion zone from the secondary zone and protects the combustion chamber casing from being

exposed to high temperature radiation. The actual process of combustion occurs in the primary zone. The mixing in of the secondary air passing through mixing nozzles and holes reduces the gas temperature in the mixing zone to an acceptable level for the gas turbine that follows. The rows of segments in the combustion zone are subjected to a severe thermal loading due to direct flame radiation. Film and convective cooling on both the air and the gas sides cools these segments. The air mass flows required to cool these hot segments flow through finned cooling channels, thereby contributing to the convection cooling of the segments on the air side. The cooling air mass flow exiting from the  $j^{\text{th}}$  segment row, effects a film cooling process on the gas side within the boundary layer in the next row of segments. At the end of that process, the cooling air mass flow is mixed with the primary air mass flow, thus, reducing the exit temperature.

## BBC-GT-9 with Silo Combustion chamber

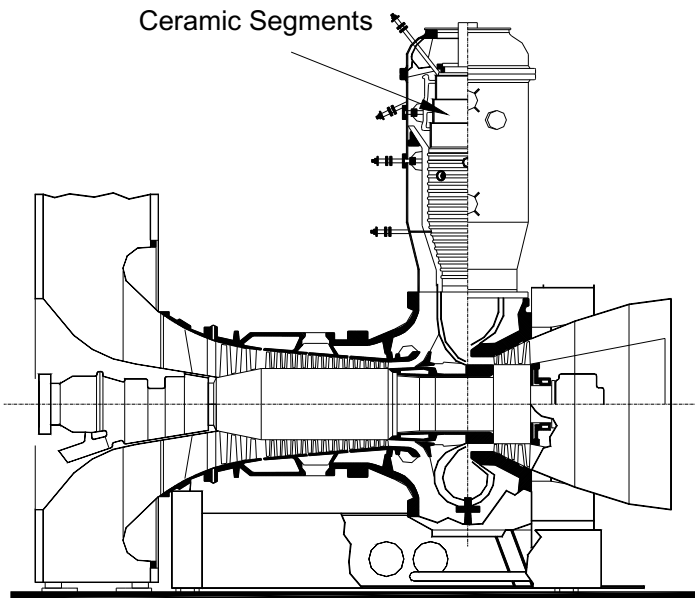


Figure 1.32: Gas turbine BBC-GT-9 with a silo type combustion chamber.

An updated version of this combustion chamber type is implemented into Alstom GT-11N shown in Figure 1.33, where the traditional BBC-injectors are replaced by the dry-Nox injectors. The configuration of the internal segments are kept the same. The new fuel injectors are similar to the one shown in Figure 1.14.



Figure 1.33: Gas turbine Alstom GT-11N with a silo type combustion chamber

Annular combustion chamber is another type of combustion chamber. A generic configuration of this component is shown in Figure 1.34. Feature common to all types

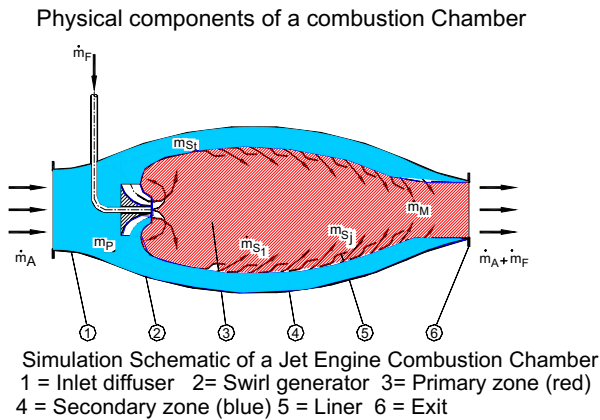


Figure 1.34: Schematic of an annular combustion chamber.

of combustion chambers are the inlet diffuser, swirl generator, primary and secondary combustion zones (Details in Chapter 14).

### 1.9.3 Group 3: Compressor, Turbine Components

This group includes components within which an exchange of mechanical energy (shaft power) with the surroundings takes place. The representatives of this group are compressors and turbines. As an example, Fig. 1.35 shows a turbine with the compression expansion diagrams, the row-by-row arrangements and the velocity diagrams. The row-by-row adiabatic compression and expansion processes are described by the conservation laws in conjunction with the known stage characteristics as discussed in Chapter 15. These components are comprehensively treated in Chapter 15.

In addition to the axial design, there are compressors and turbines with radial blade design. These, however are applied to gas turbines with small power sizes as well as to turbochargers shown in Figures 1.5, 1.6, 1.26 and 1.27. Radial compressors are generally used for higher pressure ratios but small mass flow rates. Details of radial compressor design are found in Chapter 16.

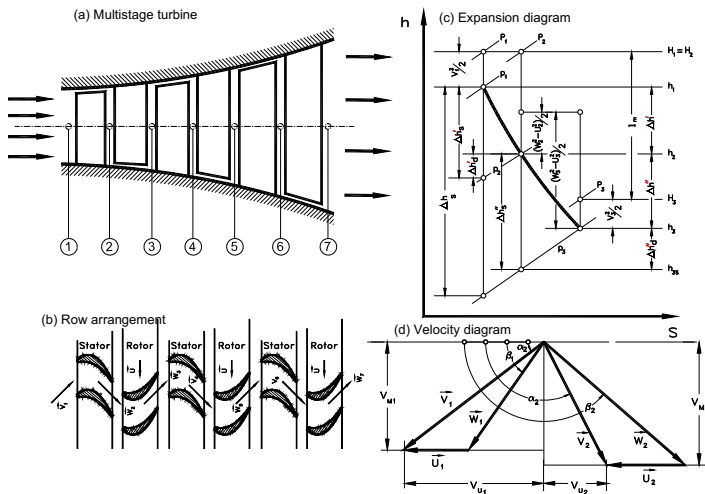


Figure 1.35: Schematic of a multi-stage turbine, row arrangement, expansion diagram and the velocity diagram.

## References

- 1.. Schobeiri, M.T., 1982, "Dynamisches Verhalten der Luftspeichergasturbine Huntorf bei einem Lastabwurf mit Schnellabschaltung," Brown Boveri, Technical Report, TA-58.
2. Schobeiri, M.T., 2012, "Turbomachinery Flow Physics and Dynamic Performance," Second and Enhanced Edition, 725 pages with 433 Figures, Springer-Verlag, New York, Berlin, Heidelberg, ISBN 978-3-642-24675-3, Library of Congress 2012935425.
3. Schobeiri, Meinhard T., Ghoreyshi Seyed M., UHEGT, the Ultra-high Efficiency Gas Turbine Engine with Stator Internal Combustion ASME Transactions Journal of Eng. Gas Turbines Power. 2015; 138(2): 021506-021506-14. GTP-15-1351, doi: 10.1115/1.4031273.
4. EPRIGEN, 1998, Thermal Performance of the ABB GT24 Gas Turbine in Peaking Service at the Gilbert Station of GPU Energy, EPRIGEN, Palo Alto, CA.
5. Frutschi, H.U., 1994, "Advanced Cycle System with new GT24 and GT26 Gas Turbines, Historical Background," ABB Review 1/94.
6. Döbbeling, K., Hellat, J, Koch, H., 2005, "25 Years of BBC/ABB/ALSTOM Lean Premix Combustion Technologies," ASME PaperGT2005-68269.
7. Keller, J., Egli, W., and Althaus, R., 1988, "Vortex breakdown as a fundamental element of vortex dynamics," Z. Angew. Math. Phys. 39, 404.
8. Schobeiri, M.T., 1989, "On the Stability Behavior of Vortex Flows in Turbomachinery," (in German) Zeitschrift für Flugwissenschaften und Weltraumforschung, 13(1989) pp. 233-239.
9. Keller, J.J., Sattelmayer, T., and Thueringer, F., "Double-cone burners for gas turbine type 9 retrofit application," 19th International Congress on Combustion Engines (CIMAC, Florence, 1991).
10. Gas Turbine World, 2014-15 Handbook, Volume 31.
11. European Aviation Safety Agency, EASA, Certificate Data Sheet Number : E.036, Issue : 04, September 2013, Type : Rolls-Royce Plc, Trent 1000 Series Engines
12. Schobeiri, M. T., Abouelkheir, M., Lippke, C., 1994, "GETRAN: A Generic, Modularly Structured Computer Code for Simulation of Dynamic Behavior of Aero-and Power Generation Gas Turbine Engines," an honor paper, ASME Transactions, *Journal of Gas Turbine and Power*, Vol. 1, pp. 483-494.
13. Schobeiri T., 1986: "A General Computational Method for Simulation and Prediction of Transient Behavior of Gas Turbines." ASME-86-GT-180.
14. Schobeiri M. T., 1985 "Aero-Thermodynamics of Unsteady Flows in Gas Turbine Systems." Brown Boveri Company, Gas Turbine Division Baden Switzerland, BBC-TCG-51.
15. Schobeiri M.T., 1985b "COTRAN, the Computer Code for Simulation of Unsteady Behavior of Gas Turbines." Brown Boveri Company, Gas Turbine Division Baden Switzerland, BBC-TCG-53-Technical Report.

## 2 Gas Turbine Thermodynamic Process

The first step toward designing a new gas turbine is to generate its thermodynamic cycle diagram. This diagram provides the essential information about the connection between the turbine inlet temperature  $TIT$ , the compressor pressure ratio  $\pi_c$  and the gas turbine thermal efficiency  $\eta_{th}$ . Starting with a simple GT-cycles, in the following sections methods are introduced to determine the GT-efficiency and its improvement by changing the gas turbine configurations and cycles.

### 2.1 Gas Turbine Cycles, Processes

The simplest gas turbine cycle is the Brayton cycle, which is an ideal cycle. In this cycle, the components compressor, combustion chamber and turbine are represented by an isentropic compression with an efficiency  $\eta_c = 100\%$ , an isobaric heat addition with total pressure loss coefficient  $\zeta_{cmbc} = 0.0$ , an isentropic expansion with  $\eta_T = 100\%$  and an isobaric heat rejection with the loss coefficient  $\zeta = 0.0$ . In addition, the ideal cycle does not account for different properties of the working media through the components. It assumes calorically perfect gases for all components, meaning that the specific heat at constant pressure  $c_p$  and constant volume  $c_v$  and thus their ratio  $\kappa = c_p/c_v \neq f(T)$  are not function of temperature. The flow through a GT-component, however, is associated with total pressure losses that are sources of entropy increase and thus the reduction of efficiency. Furthermore, it considers real gases with  $c_p, c_v = f(T)$ . Figure 2.1 compares the ideal cycle with a real one.

As the ideal cycle Fig. 2.1(a) shows, the divergence of the isobars ensures that, with increasing the pressure ratio, the difference  $(\Delta h_T - \Delta h_C)$  becomes larger. This results in higher GT-efficiency. In a real gas turbine, Fig. 2.1(b), however, the above difference continuously increases with increasing the pressure ratio, it reaches a maximum and by further increasing the pressure ratio, the efficiency decreases as shown later in this chapter. The compressor aerodynamics explains this phenomenon: With a given limit for compressor stage loading, increasing the pressure ratio requires adding more stages. This in turn results in smaller blade heights that are associated with higher secondary flow losses (see details in Chapter 6) causing the stage efficiency to drop. As a result, the compressor requires more power from the turbine leading to smaller difference  $(\Delta h_T - \Delta h_C)$ . Consequently, the thermal efficiency will drop, once its maximum  $\eta_{th_{max}}$  has been reached. This statement will be quantitatively substantiated in the following section. In addition to the major differences discussed above, the ideal cycle shown in Fig. 2.1(a) is actually a closed cycle with a constant mass flow  $\dot{m}_{cycle} = \dot{m}_{air} = const.$  However, the real cycle, Fig. 2.1(b) is an open cycle with the fuel mass flow added in combustion chamber. Thus

the turbine mass flow is the sum of compressor mass flow and the fuel mass flow injected into the combustion chamber.

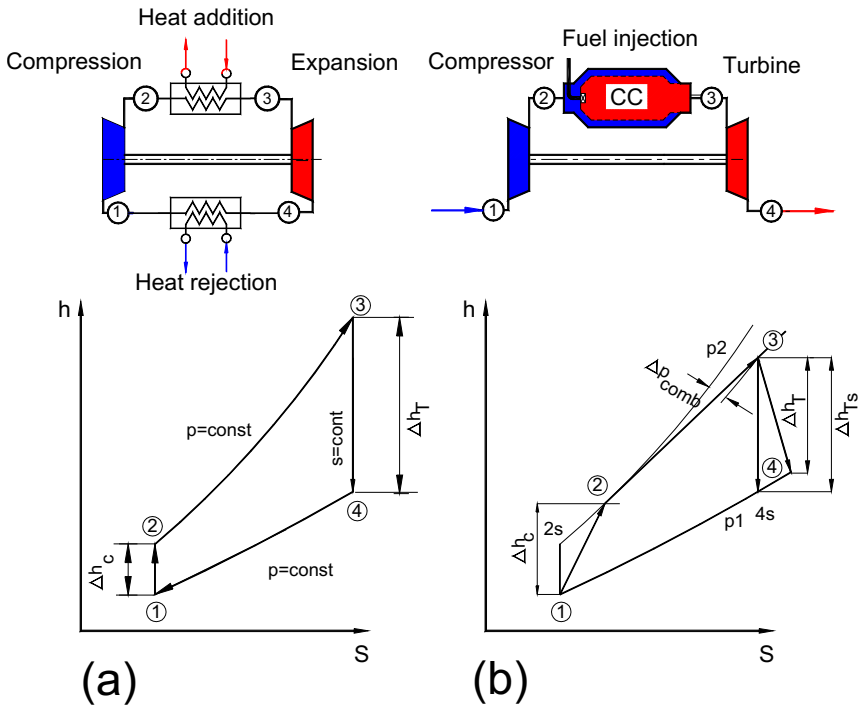


Fig. 2.1: Simple gas turbine configuration with the corresponding thermodynamics process: (a) ideal cycle, (b) real cycle.

### 2.1.1 Gas Turbine Process

Accurate prediction of the thermal efficiency of a gas turbine engine requires the knowledge of the compressor, combustion chamber, and turbine efficiencies as well as the bearing losses and the losses in auxiliary systems. Furthermore, detailed knowledge of the amount of mass flows with their extraction and injection pressures for cooling the turbine blades and the rotor discs are necessary. In addition, a detailed gas table that accounts for thermodynamic properties of humid air as well as the properties of the combustion gas must be implemented into the calculation procedure. Assuming air and combustion gas as calorically perfect gases results in significant errors. Fig. 2.2 exhibits a schematic diagram that shows the compressor component with the inlet nozzle and three cooling mass flow extractions and two blow off-valves for surge protection. Mass flow through P1 extracted from plenum 4 cools the second turbine stage; mass flows through P2 cools the first turbine stage and finally, mass

flow through P3 reduces the combustion chamber exit temperature before it enters the turbine. At stations 6, 7, 8, and 11 humid air is mixed with combustion gas resulting in a local change of water/air and fuel/air ratios, thus changing the entire thermodynamic properties including the special gas constant  $R$ .

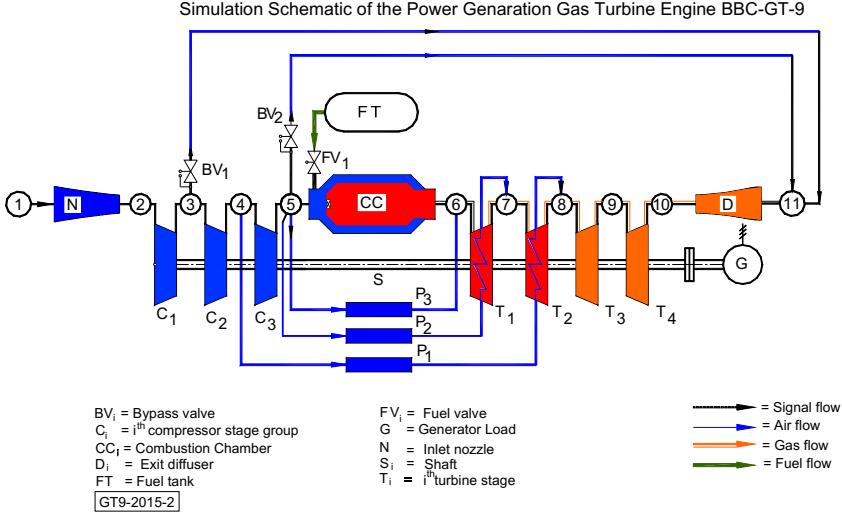


Fig. 2.2: Schematic of a single spool gas turbine illustrating the mass flow extraction from compressor for different cooling purposes.

The above schematic reflects the configuration of a gas turbine system, whose aero-thermodynamic properties at any point are already known. However, this information is unknown if one intends to design a completely new gas turbine. In the absence of the above information, reasonable assumptions relative to component efficiencies can be made to qualitatively determine the thermal efficiency and its trend with regard to parameter variation. In the following section, a simple thermal efficiency calculation procedure is derived that is appropriate for varying different parameters and determining their impacts on thermal efficiency. For this purpose we consider a gas turbine with a recuperator with a given effectiveness  $\eta_R$  that can be varied from 0 to 1. The gas turbine with without a recuperator ( $\eta_R = 0$ ) has the simplest cycle and the one with  $\eta_R = 1$  has an ideal recuperation.

The gas turbine with its corresponding process is sketched in Fig. 2.3. It consists of a compressor, a recuperator, a combustion chamber and a turbine. Exhaust gas from the turbine is diverted into the recuperator gas side, heating up the compressed air before it enters the combustion chamber. The individual processes are compression, fuel addition and combustion, heat exchange in recuperator and expansion in turbine. Air from the environment is sucked into the compressor at station (1), it is compressed and exits the compressor at station (2), which is the entry point of the recuperator cold side. By passing through the recuperator, heat is



transferred from the recuperator hot side to the cold side through convection and conduction. The addition of heat gradually increases the compressor air temperature that enters the combustion chamber at station (5). Entering the combustion chamber, first the fuel is injected through fuel nozzles. Within the combustion chamber a thorough mixing of the fuel mass flow with the compressor air takes place. The subsequent ignition raises the combustion gas temperature to the designed turbine inlet temperature TIT at station (3). During the expansion process within the turbine a major portion the total energy of the combustion gas is converted into mechanical energy. After expansion combustion gas leaves the turbine at station (4). The exhaust gas enters the hot side of the recuperator, where its heat is partially transferred through convection and conduction to the recuperator cold side.

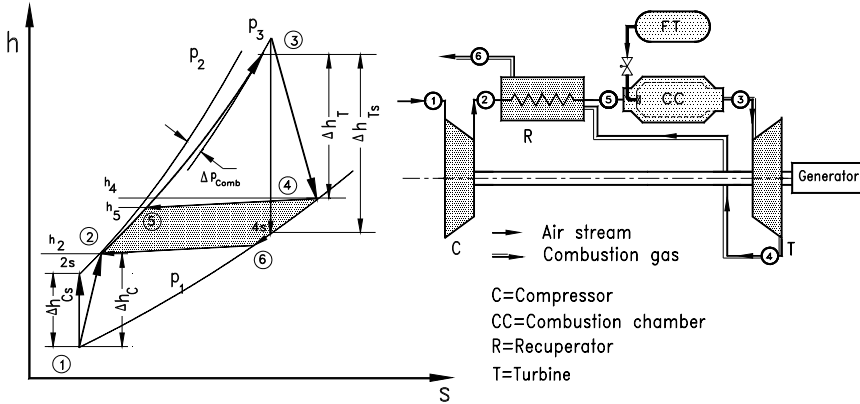


Fig. 2.3: Simple sketch of a gas turbine with recuperator.

The compressor and turbine enthalpy differences are calculated from:

$$l_C = h_2 - h_1 = \frac{h_{2s} - h_1}{\eta_c} \quad (1)$$

$$l_T = h_3 - h_4 = (h_3 - h_{4s}) \eta_T$$

with  $l_C$ ,  $l_T$  as the compressor and turbine specific mechanical energy. We introduce the following definitions for the recuperator air- and gas-side ( $RA$ ,  $RG$ ), as well as combustion chamber ( $CC$ ) pressure loss coefficients:

$$\zeta_{RA} = \frac{\Delta P_{RA}}{P_2}, \text{ with } \Delta P_{RA} = P_2 - P_5$$

$$\zeta_{RG} = \frac{\Delta P_{RG}}{P_1}, \text{ with } \Delta P_{RG} = P_4 - P_6$$

$$\zeta_{CC} = \frac{\Delta P_{CC}}{P_2}, \text{ with } \Delta P_{CC} = P_5 - P_3$$
(2)

The thermal efficiency is defined as

$$\eta_{in} = \frac{L_{net}}{\dot{Q}_{in}} = \frac{L_T - L_C}{\dot{Q}_{in}} = \frac{\dot{m}_T l_T - \dot{m}_C l_C}{\dot{Q}_{in}} \quad (3)$$

with  $L_T$ ,  $L_C$  as the turbine and compressor power and  $\dot{Q}_{in} = \dot{m}_{Fuel} \Delta H_{Fuel}$  as the fuel power: The specific net power  $L_{net}$  is calculated from:

$$\frac{L_{net}}{\dot{m}_1} = \frac{L_T - L_c}{\dot{m}_1} = \frac{\dot{m}_3 l_T - \dot{m}_1 l_C}{\dot{m}_1} = (1 + \beta) l_T - l_c \quad (4)$$

with the fuel air ratio  $\beta = \dot{m}_f / \dot{m}_1$ . Replacing the specific turbine mechanical energy  $l_T$  by the enthalpy difference from Eq. (2.1), we find:

$$\begin{aligned} \frac{\dot{m}_3}{\dot{m}_1} l_T &= (1 + \beta) (h_3 - h_4) = \eta_T (1 + \beta) (h_3 - h_{4s}) \\ \frac{\dot{m}_3}{\dot{m}_1} l_T &= \eta_T (1 + \beta) \bar{c}_{PT} (T_3 - T_{4s}) \\ \frac{\dot{m}_3}{\dot{m}_1} l_T &= \eta_T (1 + \beta) \bar{c}_{PT} T_3 \left( 1 - \frac{T_{4s}}{T_3} \right) \end{aligned} \quad (5)$$

In order to invoke the effect of turbine inlet temperature in the efficiency diagram, the enthalpy difference in Equation (2.5) is expressed in terms of temperature difference. Thus the isentropic enthalpy difference is written in terms of a product of averaged specific heat at constant pressure and the isentropic temperature difference. The specific heat in Eq.(2.5) exhibits an averaged value between the two given temperatures:

$$\bar{c}_{PT} = \frac{h_3 - h_{4s}}{T_3 - T_{4s}} \quad (6)$$

The temperature ratio in Eq. (2.5) can be related to the pressure ratio as follows:

$$\frac{T_3}{T_{4s}} = \left( \frac{p_3}{p_4} \right)^{\left( \frac{k-1}{k} \right)_T} = \pi_T^{\left( \frac{k-1}{k} \right)_T} = \pi_T^{m_T}, \quad \text{with } m_T \equiv \left( \frac{k-1}{k} \right)_T \quad (7)$$

with  $\kappa = \bar{c}_p / \bar{c}_v$  as the averaged specific heat ratio. The subscript  $T$  in Eq. (2.7) refers to *Turbine*. Thus, with Eq. (2.7), Eq. (2.5) becomes:

$$\frac{\dot{m}_3}{\dot{m}_1} l_T = \eta_T (1 + \beta) \bar{c}_{PT} T_3 \left( 1 - \pi_T^{-m_T} \right) \quad (8)$$

Because of the pressure losses across the combustion chamber, the turbine and compressor pressure ratios are not the same ( $\pi_T \neq \pi_c$ ). Implementing the pressure losses of the combustion chamber and recuperator air side, we find:

$$\pi_T = \frac{p_3}{p_4} = \frac{p_2 - \Delta p_{RA} - \Delta p_{cc}}{p_1 + \Delta p_{RA}} = \frac{p_2}{p_1} \left( \frac{1 - \zeta_{RA} - \zeta_{cc}}{1 + \zeta_{RA}} \right) = \pi_c \frac{1 - \zeta_{RA} - \zeta_{cc}}{1 + \zeta_{RA}} \quad (9)$$

We set the fraction on the right hand side of Eq. (2.9):

$$\epsilon = \frac{1 - \zeta_{RA} - \zeta_{cc}}{1 + \zeta_{RA}} \quad (10)$$

and arrive at:

$$\pi_T = \epsilon \pi_c, \text{ for } \epsilon = 0, \zeta_{RA} = \zeta_{CC} = \zeta_{RA} = 0 \text{ and for } \epsilon < 0, \zeta_{RA} \neq 0, \zeta_{cc} \neq 0 \quad (11)$$

For parameter variation, following values may be used:  $\zeta_{RA} \approx \zeta_{RG} \approx 2 - 5\%$ ,  $\zeta_{cc} \approx 3 - 5\%$ . Following exactly the same procedure defined by Eqs. (2.4) through (2.11), we find the compressor specific work as:

$$l_C = \frac{1}{\eta_C} \bar{c}_{Pc} T_1 \left( \pi_C^{m_C} - 1 \right), \text{ with } m_C = \left( \frac{k-1}{k} \right)_C \quad (12)$$

with the subscript C in Eq. (2.12) referring to compressor. Inserting Eqs. (2.8) and (2.12) into Eq. (2.4), we arrive at:

$$\eta_{th} = \frac{\eta_T \bar{c}_{PT} \frac{T_3}{T_1} \left[ 1 - (\epsilon \pi_c)^{-m_T} \right] (1 + \beta) - \frac{1}{\eta_c} \bar{c}_{Pc} \left( \pi_c^{m_c} - 1 \right)}{\bar{c}_{Pcc} \left[ (1 + \beta) \frac{T_3}{T_1} - \frac{T_5}{T_1} \right]} \quad (13)$$

The turbine inlet temperature  $T_3$ , the environmental temperature  $T_1$ , and thus their ratio  $T_3/T_1$  is considered as a known parameter. This parameter can also be used for parametric studies. Therefore it is desirable to express the ratio  $T_5/T_1$  in terms of  $T_3/T_1$ . We find this ratio by utilizing the recuperator effectiveness  $\eta_R$ .

$$\eta_R = \frac{h_5 - h_2}{h_4 - h_2} \cong \frac{T_5 - T_2}{T_4 - T_2} \quad (14)$$

From compressor and turbine energy balance, Eq. (2.1) we find

$$\begin{aligned} T_2 &= T_1 + (T_{2s} - T_1) \frac{1}{\eta_c} = T_1 + T_1 \left( \pi_c^{m_c} - 1 \right) \frac{1}{\eta_c} \\ T_4 &= T_3 - (T_3 - T_{4s}) \eta_T = T_3 - T_3 \left[ 1 - (\epsilon \pi_c)^{-m_T} \right] \eta_T \end{aligned} \quad (15)$$

Equation (2.15) in dimensionless form yields:

$$\begin{aligned} \frac{T_2}{T_1} &= 1 + \frac{1}{\eta_c} \left( \pi_c^{m_c} - 1 \right) \\ \frac{T_4}{T_1} &= \frac{T_3}{T_1} - \frac{T_3}{T_1} \eta_T \left[ 1 - (\epsilon \pi_c)^{-m_T} \right] \end{aligned} \quad (16)$$

Introducing the temperature ratio  $\Theta = T_3/T_1$ , the temperature ratio  $T_4/T_1$  Eq. (2.16) becomes:

$$\frac{T_4}{T_1} = \Theta \left\{ 1 - \left[ 1 - (\epsilon \pi_c)^{-m_T} \right] \eta_T \right\} \quad (17)$$

To determine the temperature ratio  $T_5/T_1$ , we re-arrange Eq. (2.14)

$$\frac{T_5}{T_1} = \eta_R \left( \frac{T_4}{T_1} - \frac{T_2}{T_1} \right) + \frac{T_2}{T_1} \quad (18)$$

Using Eqs. (2.16) and (2.17), Eq. (2.18) is re-arranged as

$$\frac{T_5}{T_1} = \eta_R \left[ \Theta \left\{ 1 - \left[ 1 - (\epsilon \pi_c)^{-m_T} \right] \eta_T \right\} - 1 - \frac{1}{\eta_c} \left( \pi_c^{m_c} - 1 \right) \right] + 1 + \frac{1}{\eta_c} \left( \pi_c^{m_c} - 1 \right) \quad (19)$$

Introducing Eq. (2.19) and the definition  $\Theta = T_3/T_1$  into Eq. (2.13), the thermal efficiency equation for a gas turbine with a recuperator is written as:

$$\eta_{th} = \frac{\bar{c}_{PT} \eta_T \theta \left[ 1 - (\epsilon \pi_c)^{-m_T} \right] (1 + \beta) - \frac{1}{\eta_c} \bar{c}_{Pc} (\pi_c^{m_c} - 1)}{\bar{c}_{PCC} \left\{ \theta (1 + \beta - \eta_R) - \left[ 1 + \frac{1}{\eta_c} (\pi_c^{m_c} - 1) \right] [1 - \eta_R] + \theta \eta_R \eta_T [1 - (\epsilon \pi_c)^{-m_T}] \right\}} \quad (20)$$

From Eq. (2.20) special cases are obtained. Setting  $\eta_R = 0$  gives the thermal efficiency of a gas turbine without recuperator. The ideal case of Brayton cycle is obtained by setting all loss coefficients equal to zero, all efficiencies equal to unity, and  $\bar{c}_{PC} = \bar{c}_{PCC} = \bar{c}_{PT} = \text{const.}$  Equation (2.20) properly reflects the effects of individual parameters on the thermal efficiency and can be used for preliminary parameter studies. As an example, Fig. 2.4 shows the effect of pressure ratio, the turbine inlet temperature, and the component efficiency on thermal efficiency for four different cases.

In the following, standard gas turbine cycles are presented for large power size gas turbines (5 MW and above) with axial compressors and small size GTs (below 5 MW) with radial compressors. The latter has always a recuperator attached to the exit of the compressor. Figures 2.4 (a) and (b) show the impact of compressor and turbine efficiency on thermal efficiency of a simple gas turbine cycles such as the one presented in Fig. 2.1, for temperature ratios of  $\Theta = TIT/T_{ref} = 3.5 - 5.0$  with  $TIT$  as the turbine inlet temperature. For each turbine inlet temperature, there is one optimum pressure ratio. While Fig. 2.4(a) with  $\eta_C = \eta_T = 85\%$  represents the older generation of gas turbines, Fig. 2.4(b) with  $\eta_C = \eta_T = 90\%$  represents the recent progress in the area of compressor and turbine design and the impact of their efficiency improvement on the thermal efficiency. For temperature ratios up to  $\Theta = 4.5$  pronounced efficiency maxima are visible within a limited  $\pi$ -range. Approaching higher inlet temperature, however, this range widens significantly.

As shown in Chapter 1, Figs. 1.9 and 1.10 and in accord with the findings in Fig. 2.4(a,b), if reaching the optimum pressure ratio is not associated with a noticeable thermal efficiency increase ( $\Delta \eta_{th} > 0.5\%$ ), then it is recommended to choose a lower pressure ratio but with an efficiency close to the optimum one. Figure 2.4(a) justifies this recommendation. It shows that the optimum pressure ratio of  $\pi_{opt} = 18$  (red circle) has almost the same  $\eta_{th}$  as the one with  $\pi_{opt} = 14$ . To provide the difference of  $\Delta \pi = 4$ , at least 7 stages must be added to the compressor with very short blade heights of rear stages. As the aerodynamics loss calculation shows (Chapter 6) the shorter a turbine or a compressor blade is the higher is the secondary flow loss. Higher secondary flow loss, however, results in lower overall compressor efficiency. The case presented in Fig. 2.4(b) shows the same tendency as in Fig. 2.4(a) with regard to the selection of pressure ratio. The temperature ratio  $\Theta = 4.0$  corresponds to a turbine inlet temperature of  $T_3 = 1,200K$  at a compressor inlet temperature of  $T_1 = 300.0K$ .

Figures 2.4(c,d), indicate that higher thermal efficiencies at a substantially lower pressure ratio can be achieved by utilizing recuperators. This is particularly suitable

for small gas turbines with power ranging from 50 kW (so called “micro-turbines”) to 2MW. The required low maximum pressure ratio can easily be achieved by a single-stage centrifugal compressor. Comparing cases with and without recuperator in Fig. 2.4 shows that thermal efficiency increases with increasing the component efficiency.

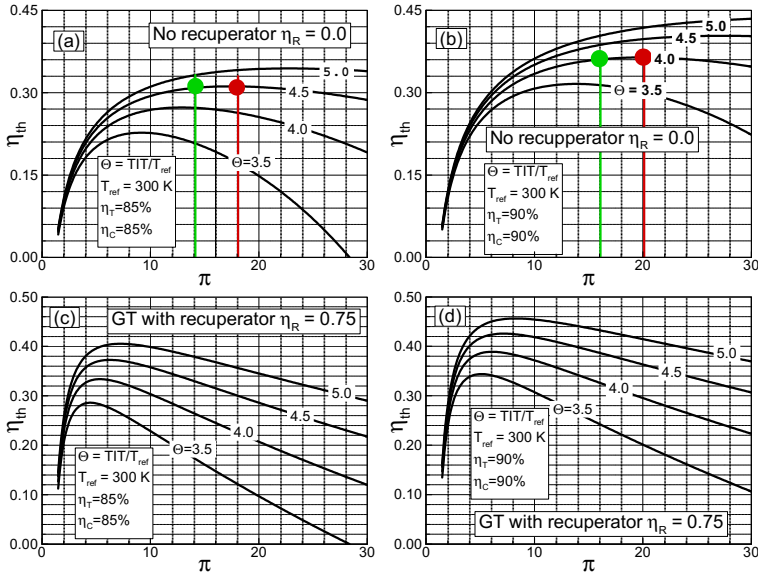


Fig. 2.4: Thermal efficiency of a gas turbine without a recuperator (a), (b) and with a recuperator (c), (d) as a function of compressor pressure ratio with the turbine inlet temperature ratio as a parameter for two different sets of compressor and turbine efficiencies.

## 2.2 Improvement of Gas Turbine Thermal Efficiency

The above parameter study indicates that for a conventional gas turbine with a near-optimum pressure ratio with or without the recuperator, the turbine inlet temperature is the parameter that determines the level of thermal efficiency. For small size gas turbines recuperator is an inherent component of the gas turbine. For large power generation gas turbines, however, it is not a practical option. Using a recuperator in a large gas turbine requires significantly lower pressure ratio that requires a large volume recuperator. As a result in order to improve the thermal efficiency of conventional gas turbines, increasing the turbine inlet temperature seems to be the only option left. Considering this fact, in the last three decades, gas turbine manufacturers have been concentrating their efforts to improve their cooling technology that is essential for increasing the turbine inlet temperature (TIT) of

conventional gas turbines. Considering the current level of TIT, In the following, two different methods are discussed that improve the gas turbine efficiency. The first method deals with minor improvements of  $\eta_{th}$  of conventional gas turbines. The second method, however, presents new technologies that substantially increase the gas turbine efficiency without increasing the turbine inlet temperature.

### 2.2.1 Minor Improvement of Gas Turbine Thermal Efficiency

**Intercooling:** One of the method to increase the thermal efficiency of gas turbines is intercooling the compressor air when it exits the LPC or the combined LPC and IPC. This method is effective for compressor pressure ratios above 40. The Intercooling occurs at a pressure ratio of  $\pi_{IC} = \sqrt{\pi_C}$  with  $\pi_C$  as the design

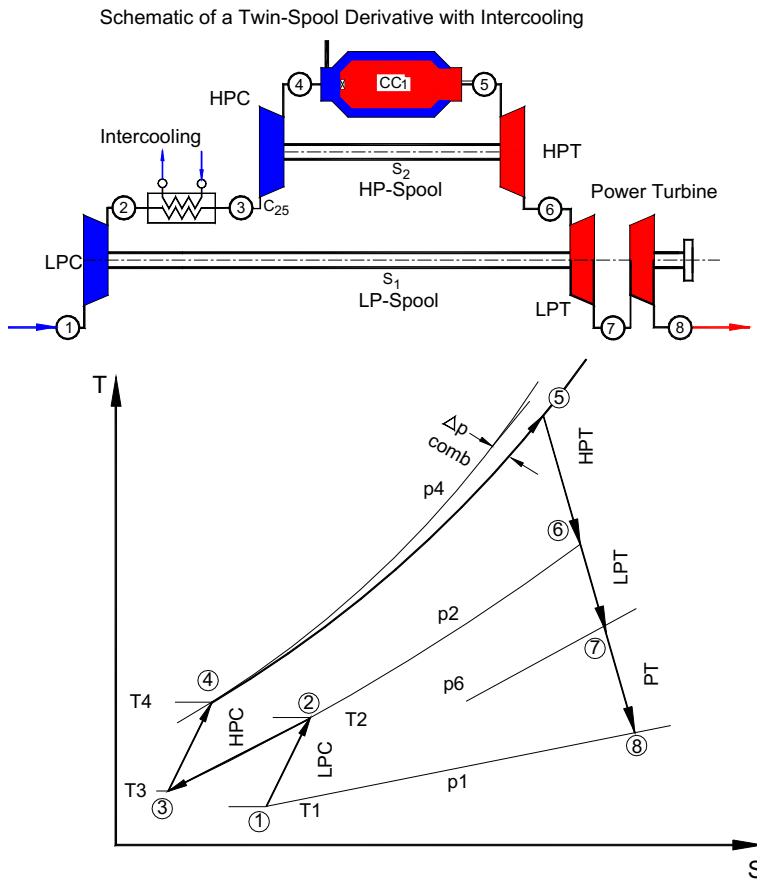


Fig. 2.5: Operation diagram of a power generation gas turbine with an intercooler, a twin spool core and a power shaft.

compressor pressure ratio. As an example, the case of GE-LMS100 which is an aircraft derivative with an efficiency of 45% presented in Chapter 1 shows the improving effect of intercooling on thermal efficiency. The intercooling process of such a gas turbine is shown in Fig. 2.5. Considering the additional expenses due to the design, manufacture and installation of the intercooler, for conventional gas turbine design with the pressure ratio  $\pi_c < 40$ , intercooling as an efficiency augmentation method seems not be a practical alternative.

**Refrigeration of Inlet Air:** As Fig. 2.4 shows, keeping the TIT and reducing the compressor inlet temperature increases the thermal efficiency. Based on the capacity of the installed refrigeration system the compressor inlet temperature can be lowered by over 20C. In calculating the thermal efficiency, one has to include the amount of the energy required for refrigeration process in the energy balance.

**Evaporating Cooling:** Another method to cool air before entering the compressor is using the evaporative cooling. This cooling technique is used in hot regions with low humidity. Its cooling effectiveness is limited by the relative humidity of the environment.

## 2.2.2 Major Improvement of Gas Turbine Thermal Efficiency

**Reheat:** An effective method for substantially increasing the thermal efficiency without a significant increase in turbine inlet temperature is the application of the well known reheat principle as a classical method for thermal efficiency augmentation. Although this standard efficiency improvement method is routinely applied in steam turbine power generation, it did not find its way into the aircraft and the power generation gas turbine design. As discussed in Chapter 1, the Compressed Air Energy Storage (CAES) gas turbine was the first to utilize the reheat concept. The gas turbine has two combustion chambers designed and manufactured by Brown Boveri & Cie (BBC), installed in Huntorf Germany and commissioned 1978. The successful operation of this gas turbine was the basis for a major technology change that has lead to a new gas turbine type GT24/26 by the Swiss manufacturer ABB. The development of this new engine started 1990 and completed 1995. The gas turbine GT24 designed for 60Hz market (USA) and GT26 for 50Hz (Europe). Figure 2.6 shows a schematic arrangement of the gas turbine 24/26. The application of the reheat concept, increased the efficiency of GT-9 from 32% to 40.5%.

The T-s-diagram of the gas turbine GT24/26 compared to a conventional baseline design is presented in Fig. 2.7. Starting with the blue hatched baseline process, Fig. 2.7(a), the red hatched reheat process, Fig. 2.7(b) exhibits an addition to the area enclosed by the baseline T-s diagram. This addition translates into a substantial increase of the efficiency as shown in Fig. 2.8. It shows quantitatively the efficiency improvement using the reheat concept. The blue curve represents the efficiency of a relatively advanced GT up to 1986. The green curve exhibits the efficiency of a generic reheat gas turbine.



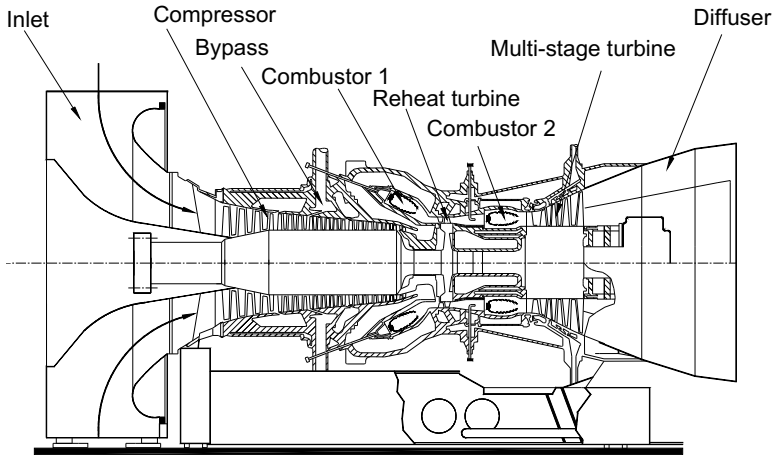


Fig. 2.6: Schematic arrangement of the gas turbine GT-24/26. The application of the reheat concept increased the efficiency of GT-9 from 32% to 40.5%.

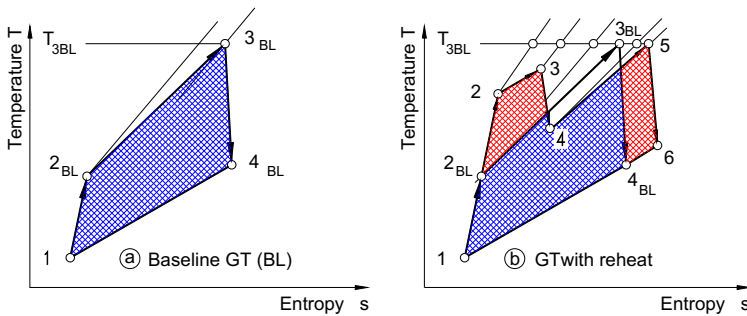


Fig. 2.7: The T-s-diagram of a gas turbine with a reheat stage compared with a conventional baseline design; (a) baseline GT, (b) GT with a reheat turbine stage and two combustion chambers.

The green curve includes the predicted efficiency of 40.5% already reported in [1] and [2]. It should be noted that the turbine inlet temperatures for the baseline GT and the GT with reheat are the same. This is a very important aspect that enables a gas turbine design with a high efficiency but at a lower temperature for example 1200 oC. The major efficiency increase shown in Fig. 2.8, gave rise to further increase  $\eta_{th}$  by introducing a new technology discussed in the following section.

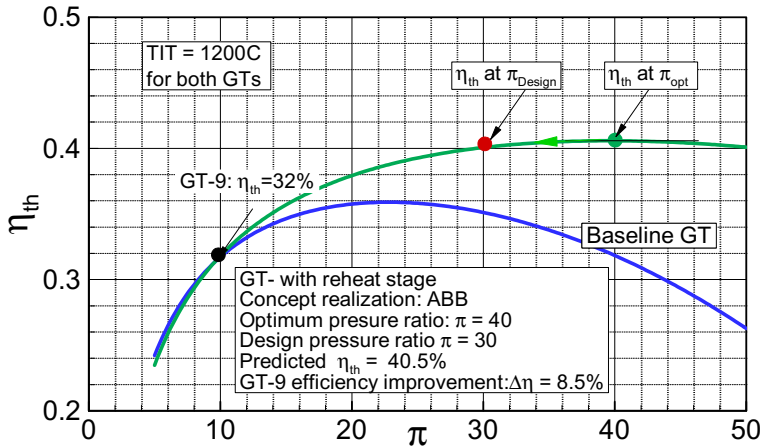


Fig. 2.8: Major efficiency improvement using the reheat concept.

**New Technology:** Major efficiency improvement requires a major technology change. As shown in [3], and [4], major improvement can be achieved by using the UHEGT-technology (Ultra High Efficiency Gas Turbine technology) that utilizes stator internal combustion. This technology eliminates the combustion chambers altogether and places the combustion process inside the stator and rotor blade passages. Figures 2.9 and 2.10 show the T-s-diagram and the schematic and a composition of the UHEGT-components

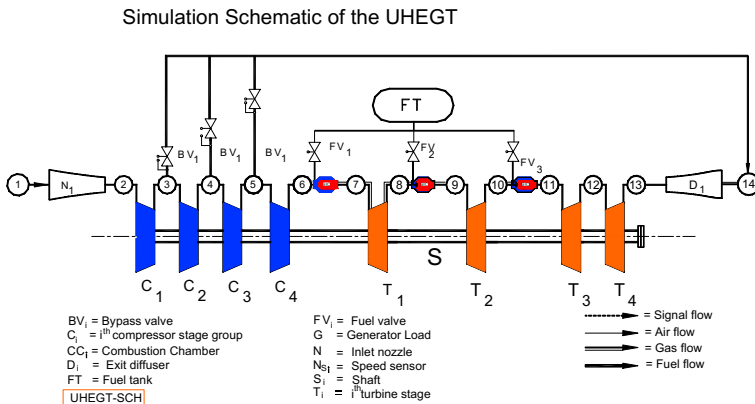


Fig. 2.9: Schematic diagram of an Ultra High Efficiency gas turbine.

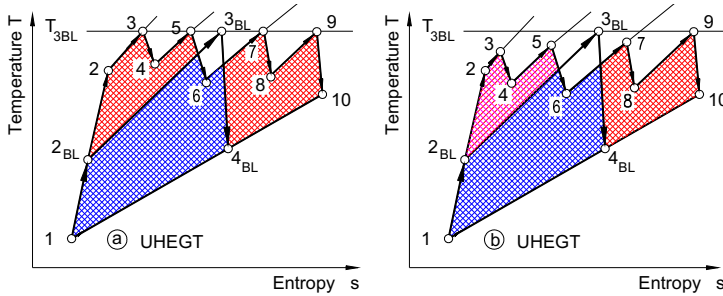


Fig. 2.10: T-s-diagrams for the Ultra High Efficiency Gas Turbine, (a) with constant TIT, (b) with variable TIT.

As shown in Fig. 2.9, a air enters the inlet nozzle and is compressed through the LPC (C1 and C2), IPC (C3) and HPC(C4). It leaves the compressor at a pressure ratio

of 40/1. The high pressure air enters the first turbine stator with an array of fuel injection nozzles that are distributed circumferentially. A portion of the total fuel mass flow is injected into the axial gap upstream of the first stator row. Combustion starts upstream of the first stator row and the stator blade channels. Combustion gas exits the first stator row entering the first rotor row the rotational motion of the rotor causes a strong mixing of unburned fuel particles with the rest of combustion gas resulting in a complete combustion. After exiting the first rotor row the lean combustion gas enters the second stator row, where the second portion of the fuel is added. After completing the same combustion process in the second stage, combustion gas enters the third stage turbine, where the injection process takes place similar to the first to stages. The process of fuel injection and subsequent combustion is associated with the simultaneous energy extraction from the combustion gas and generation of turbine shaft power. The process is shown in Fig. 2.10. As in Fig. 2.7, the above T-s-diagram includes the baseline process (hatched blue area and the addition of sequential reheat-expansion process (hatched red). Figure 2.10(a) represents the process with the same TIT after each combustion. Based on the design requirement, the TIT may have a variable distribution.

Figure 2.11 shows the comparison of UHEGT with GT24/26 and a baseline Gas turbine. In Fig. 2.11 gas turbines with three and four stator internal combustion, UHEGT-3S and UHEGT-4S, respectively are shown. The turbine inlet temperature TIT, for all cycles is the same and equals to 1200 C. As discussed in Chapter 1, Fig. 1.16, for UHEGT-3S a thermal efficiency above 45% is calculated. This exhibits an increase of at least 5% above the efficiency of the most advanced gas turbine engine which is close to 40%. Increasing the number of stator internal combustion to 4, curve labeled with UHEGT-4S, can raise the efficiency above 47% which is an enormous efficiency increase compared to any existing gas turbine engine. It should be noted that UHEGT-concept substantially improves the thermal efficiency of gas turbines, where the pressure ratio is optimized corresponding to the turbine inlet temperature.

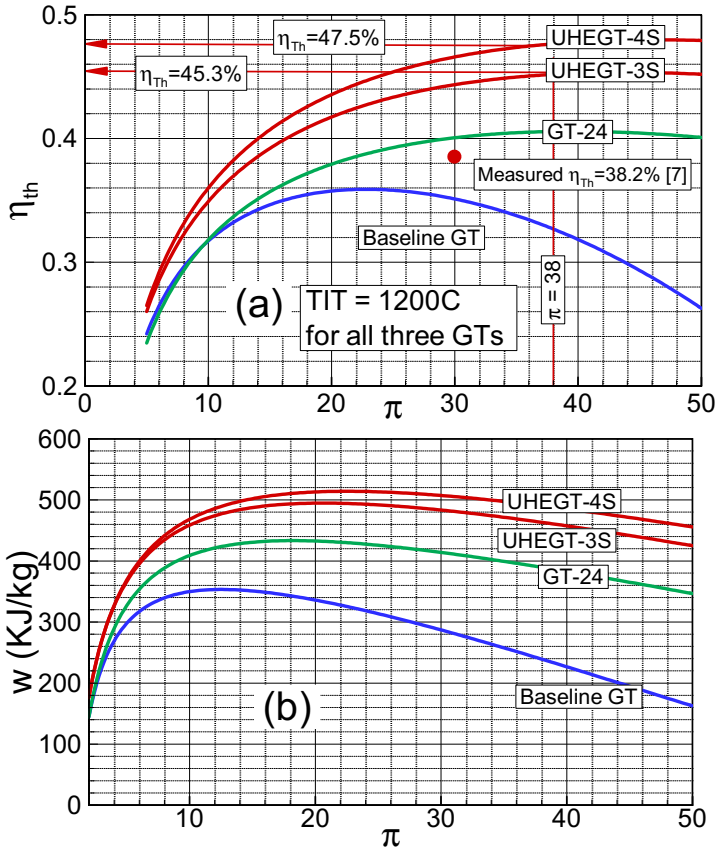


Fig. 2.11: Comparison of (a) thermal efficiencies and (b) specific work for Baseline GT, GT24/26 and UHEGT.

This gives UHEGT a wide range of applications from small to large size engines.

### 2.1.3 Compressed Air Energy Storage Gas Turbine

Compressed Air Energy Storage (CAES) power plants [5], [6],[7] are utilized to efficiently cover the peak electric energy demand. As an example the CAES Huntorf in Germany that we briefly discussed in Chapter 1 is shown in Fig. 2.12. It consists of a compressed air generator unit, which is a compressor train consisting of a low pressure compressor, LPC, and an integrated IPC- HPC. The LPC consists of an axial low pressure compressor with 20 stages and the IPC- HPC has 6 radial impellers operating at 7622 rpm. The compressed air has a relatively high exit temperature and

must be cooled down before entering the storage cavern. The LPC has one intercooler and the IPC-HPC has two intercoolers and one after-cooler.

The shaft of LPC and IPC-HPC are connected via a gear transmission. The power generation unit consists of a high pressure combustion chamber CC1 followed by a HPT, followed by a low pressure combustion chamber CC2 followed by a LPT. The air generator and the power generation units are connected with an electric motor/generator via two couplings. During the compression mode, the generator is decoupled from the turbine side and the electric motor/generator drives the compressor train. In this mode the compressor valve VC is open and the turbine valve VT is closed. During a period of eight hours of low electric energy demand (night), the electric motor operating at 60MW drives the compressor train that pumps air into an underground salt cavern with a storage volume of 310,000 m<sup>3</sup> more than 600 m deep below the ground at a maximum pressure of about 70 bar. During the power generation mode the electric motor is decoupled from the compressor shaft, the electric motor functions as generator. In this mode the compressor valve VC is closed and turbine VT is open.

In power generation mode, compressed air enters the combustion chamber, where approximately 50% of the total fuel mass flow is added generating a lean combustion gas. The lean combustion gas expands in HP-turbine, and exits into the

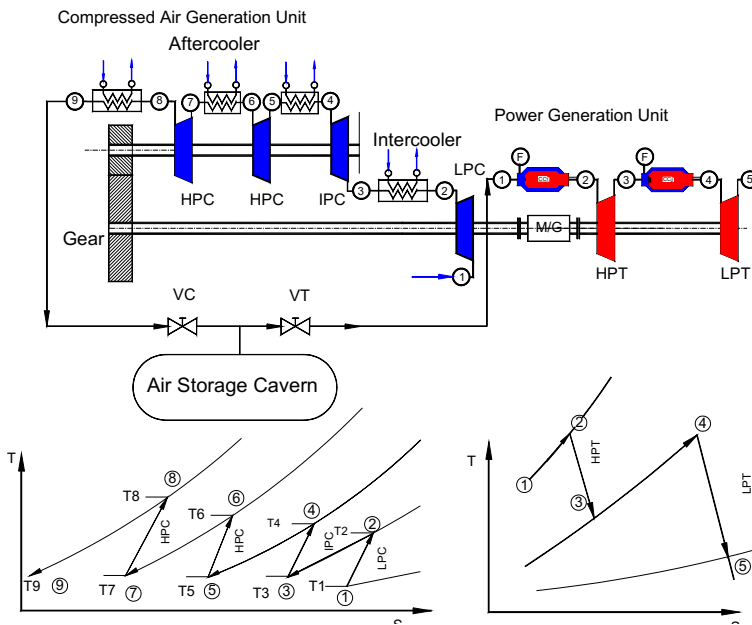


Fig. 2.12: Operation schematic of a Compressed Air Energy Storage Facility.

low pressure (LP)-combustion chamber, where the remaining fuel is added. The gas

turbine delivers 290 MW for about two hours.

Due to the short duration operation, the power generation unit undergoes a cyclic transient operation. To account for unforeseeable problems that may arise from a transient operation, precautionary actions must be taken in early stage of design. A sudden generator trip is one of the scenarios that can endanger the integrity of the power plant. In case of a generator trip the fuel and shutdown valves have to be activated within a very short period of time to prevent the shaft rotational speed from exceeding its limit. After closing the valves, the high pressure, high temperature combustion gases that are enclosed inside both combustion chambers with expand into the turbines that are running without any load on their shaft. As a result, the shaft rotational speed start raising, approaching a maximum and then decreasing. This maximum strongly depends on the closing ramp of the fuel and shutdown valves.

## References

1. Schobeiri, M.T., 2005, "Turbomachinery Flow Physics and Dynamic Performance," First Edition, Springer-Verlag, New York, Berlin, Heidelberg.
2. Schobeiri, M.T., 2012, "Turbomachinery Flow Physics and Dynamic Performance," Second and Enhanced Edition, 725 pages with 433 Figures, Springer-Verlag, New York, Berlin, Heidelberg, ISBN 978-3-642-24675-3, Library of Congress 2012935425.
3. Schobeiri, M.T., 2015, "UHEGT, the Ultra-High Efficiency Gas Turbine Engine with Stator Internal Combustion, Patent Protection No. 62/046,542.
4. Schobeiri, Meinhard T., Ghoreyshi Seyed M., UHEGT, the Ultra-high Efficiency Gas Turbine Engine with Stator Internal Combustion ASME Transactions Journal of Eng. Gas Turbines Power. 2015; 138(2):021506-021506-14. GTP-15-1351, doi: 10.1115/1.4031273.
5. Schobeiri, M.T., 1982, "Dynamisches Verhalten der Luftspeichergasturbine Huntorf bei einem Lastabwurf mit Schnellabschaltung," Brown Boveri, Technical Report, TA-58.
6. Schobeiri, M. T. and Haselbacher, H., 1985, "Transient Analysis of GAS Turbine Power Plant, Using the Huntorf Compressed Air Storage Plant as an Example," ASME Paper No. 85-GT-197.
7. Schobeiri, T., 1986, "A General Computational Method for Simulation and Prediction of Transient Behavior of Gas Turbines," ASME Paper No. 86-GT-180.1982, ".

### 3 Thermo-Fluid Essentials for Gas Turbine Design

As seen in the previous chapters, gas turbines consist of many components within which a chain of conversion of energy takes place. Design of a modern gas turbine engine with its components requires solid knowledge of aero-thermodynamic, heat transfer, combustion and solid mechanics design of these components. Aero-thermodynamics is the very basic tool for design, off-design and dynamic calculations of gas turbine components and hence the gas turbine system. The subject aero-thermodynamics and its application to engineering is treated comprehensively by Schobeiri, [1], [2] and [3]. Special attention was paid in [3] to applications of aero-thermodynamics to turbomachinery components.

In the following sections, we summarize the aero-thermodynamics conservation laws essential for applying to the gas turbine components. By arriving at the final conservation equations for the general unsteady flow cases, in [3] we extensively used Reynolds Transport Theorem. In the following sections, we assume steady flow dropping the unsteady terms. For an in-depth study of these laws, we refer to Chapter 4 in [3]. We start with the mass flow balance, which will be followed by the linear momentum, angular momentum, and the energy balance.

#### 3.1 Mass Flow Balance

To obtain the mass flow balance using the continuity equation in integral form for steady flow, we take an arbitrary system with a control surface that may consist of one or more inlets, one or more exits, and may include porous walls, as shown in Fig. 3.1. Assuming a steady state, for such a case the mass flow balance is expanded as:

$$\begin{aligned} \int_{S_{in1}} \rho \mathbf{V} \cdot \mathbf{n} dS + \int_{S_{in2}} \rho \mathbf{V} \cdot \mathbf{n} dS + \int_{S_{out1}} \rho \mathbf{V} \cdot \mathbf{n} dS + \\ \int_{S_{out2}} \rho \mathbf{V} \cdot \mathbf{n} dS + \int_{S_{out3}} \rho \mathbf{V} \cdot \mathbf{n} dS + \int_{S_{Wall}} \rho \mathbf{V} \cdot \mathbf{n} dS = 0 \end{aligned} \quad (3.1)$$

As shown in Fig. 3.1 and by convention, the normal unit vectors,  $\mathbf{n}_{in}$ ,  $\mathbf{n}_{out}$ ,  $\mathbf{n}_{Wall}$ , point away from the region bounded by the control surface. Similarly, the tangential unit vectors,  $\mathbf{t}_{in}$ ,  $\mathbf{t}_{out}$ ,  $\mathbf{t}_{Wall}$ , point in the direction of shear stresses. For the case presented in Fig. 3.1, the integral over the solid wall surface disappears. An example, where the integral over the wall surface does not vanish, is a film cooled turbine blade

with discrete film cooling hole distribution along the blade suction and pressure surfaces as shown in Fig. 3.2. To apply the mass flow balance to a turbine or cascade blade channel, the control volume should be placed in such a way that it includes quantities that we consider as known, as well as those we seek to find.

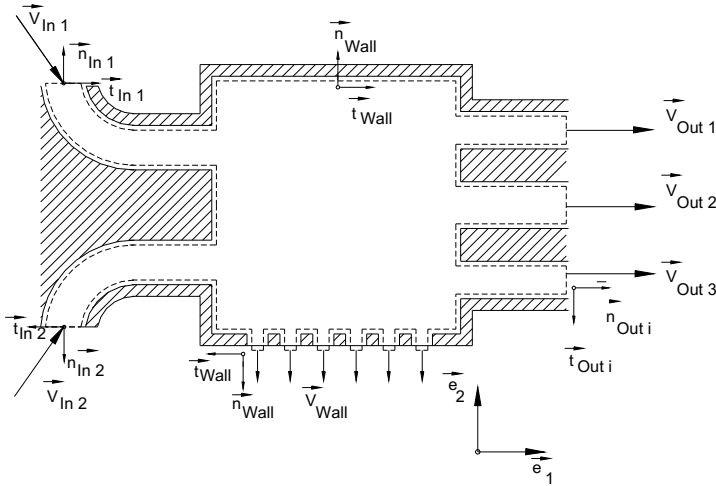


**Fig. 3.1** Control volume, unit normal and tangential vectors

For the turbine cascade shown in Fig. 3.2, the appropriate control surface consists of the surfaces AB, BC, CD, and DA.

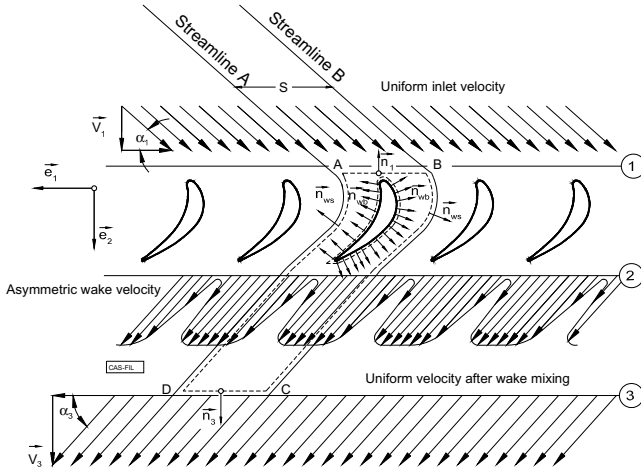


**Fig. 3.2:** Flow through a rectilinear turbine cascade with discrete film cooling holes.



The two surfaces, BC and DA, are portions of two neighboring streamlines. Because of the periodicity of the flow through the cascade, the surface integrals along these streamlines will cancel each other. As a result, the mass flow balance reads:

$$\int_{S_{in}} \rho \mathbf{V} \cdot \mathbf{n} dS + \int_{S_{out}} \rho \mathbf{V} \cdot \mathbf{n} dS + \int_{S_{Wall}} \rho \mathbf{V} \cdot \mathbf{n} dS = 0 \quad (3.2)$$

The last surface integral accounts for the mass flow injection through the film cooling holes. If there is no mass diffusion through the wall surfaces, the last integral in Eq. (3.2) will vanish leading to:

$$\int_S \rho \mathbf{V} \cdot \mathbf{n} dS = \int_{S_{in}} \rho \mathbf{V} \cdot \mathbf{n} dS + \int_{S_{out}} \rho \mathbf{V} \cdot \mathbf{n} dS = 0 \quad (3.3)$$

### 3.2 Balance of Linear Momentum

The momentum equation in integral form applied to a control volume determines the integral flow quantities such as blade lift and drag forces, average pressure, temperature, and entropy. We consider a steady flow through an arbitrary system with an inlet, an exit, a porous wall and solid walls and place the control volume inside it as shown in Fig. 3.3

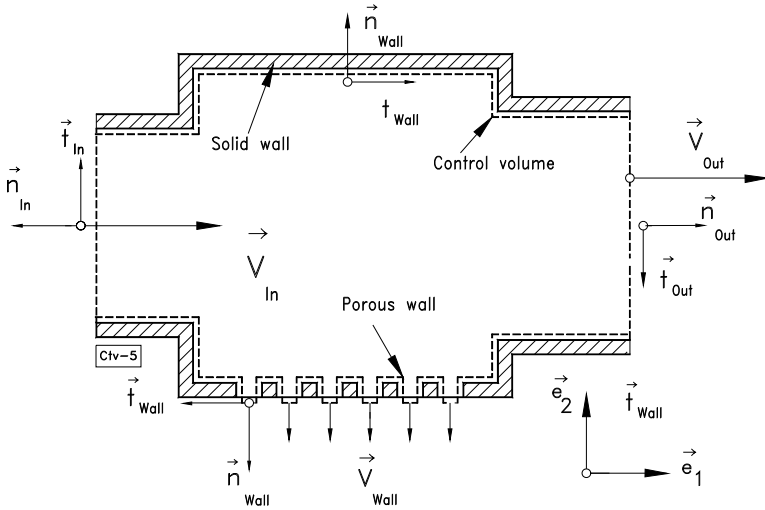


**Fig. 3.3:** Control volume, single inlet, single and outlet and porous wall.

Using the final results for calculating the linear momentum balance from [3] we find the reaction force acting on any system as:

$$\mathbf{F}_R = \int_{S_{Cin}} \mathbf{V} d\dot{m} - \int_{S_{Cout}} \mathbf{V} d\dot{m} - \int_{S_{Cwall}} \mathbf{V} d\dot{m} + \int_{S_{Cin}} (-n\mathbf{p})dS + \int_{S_{Cin}} (-\boldsymbol{\tau})dS + \int_{S_{Cout}} (-n\mathbf{p})dS + \int_{S_{Cout}} (-\boldsymbol{\tau})dS + \mathbf{G} \quad (3.4)$$

with the reaction force  $\mathbf{F}_R$  as the flow force acting in the opposite direction as the reaction force:

$$\mathbf{F}_R = -\mathbf{F}_{Flow} = - \int_{S_{Cw}} (-n\mathbf{p})dS - \int_{S_{Cw}} (-\boldsymbol{\tau})dS = \int_{S_{Cw}} (n\mathbf{p})dS + \int_{S_{Cw}} (\boldsymbol{\tau})dS \quad (3.5)$$

The vector equation (3.4) can be decomposed into three components. An order of magnitude estimation suggests that the shear stress terms at the inlet and outlet are, in general, very small compared to the other terms. It should be pointed out that the wall shear stress is already included in the resultant force  $\mathbf{F}_R$ . Also the time dependent term, [3], is dropped here for steady state assumption. For applying Eq. (3.4) to a turbine or a compressor blade, Fig. 3.4 exhibits an appropriate control volume.

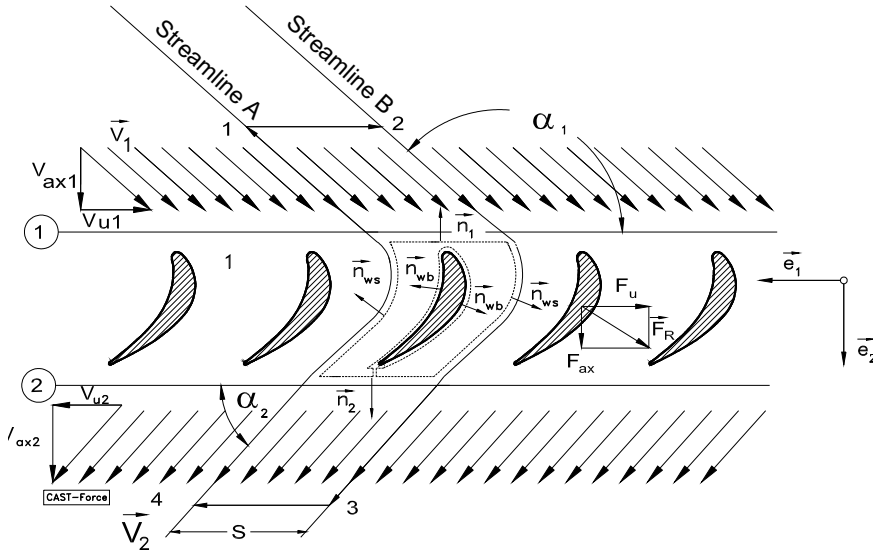


**Fig. 3.4:** Reaction force vector  $\mathbf{F}_R$  on a turbine blade with its components  $F_u$  and  $F_{ax}$  in circumferential and axial components.

### 3.3 Balance of Moment of Momentum

The conservation law of moment of momentum for a steady flow is given in the flowing section. Detail derivation of general time dependent conservation of moment of momentum is presented in [3]. The blade reaction force  $\mathbf{F}$  may have components in axial, circumferential and radial directions. Acting on the blade surface at the position vector  $\mathbf{R}$ , the force  $\mathbf{F}$  generates a reaction moment of momentum  $\mathbf{M}_\theta$  which may have also three components. The only component that is responsible for power generation is the axial moment  $M_{axial}$ , which is the projection of  $\mathbf{M}_\theta$  in axial direction. The reaction moment of momentum  $\mathbf{M}_\theta$  is:

$$\begin{aligned}
 \mathbf{M}_\theta = & - \frac{\partial}{\partial t} \left( \int_{V_c} \mathbf{X} \times \mathbf{V} dm \right) + \int_{S_1} (\mathbf{X} \times \mathbf{V}) d\dot{m} - \int_{S_2} (\mathbf{X} \times \mathbf{V}) d\dot{m} \\
 & \int_{S_1} (\mathbf{X} \times (-n\mathbf{p}) dS)_1 + \int_{S_1} (\mathbf{X} \times (-\tau\mathbf{t}) dS)_1 + \\
 & \int_{S_2} (\mathbf{X} \times (-n\mathbf{p}) dS)_2 + \int_{S_2} (\mathbf{X} \times (-\tau\mathbf{t}) dS)_2 + \\
 & \int_{V_c} \mathbf{X} \times \mathbf{g} dm
 \end{aligned} \tag{3.6}$$

Equation (3.6) describes the moment of momentum in general form. The first integral on the right-hand side expresses the angular momentum contribution due to the unsteadiness. The second and third term represents the contribution due to the velocity momenta at the inlet and exit. The forth and sixth term are formally the contributions of pressure momenta at the inlet and exit. The shear stress integrals, the fifth and seventh terms, representing the moment due to shear stresses at the inlet and exit, are usually ignored in practical cases. For applications to turbomachines, Eq. (3.6) can be used to determine the moment that the flow exerts on a turbine or compressor cascade. Of practical interest is the *axial moment*  $M = M_a$  which acts on the cascade with respect to the axis of rotation. The moment  $M = M_a$  is equal to the component of the moment vector parallel with the axis of surfaces of revolution.

Figure 3.5 is a graphic representation of the quantities involved in the equation of moment of momentum. As shown in Fig. 3.5, the axial moment vector is the projection of the vector  $\mathbf{M}_\theta$  on the machine axis  $\mathbf{e}_2 \cdot \mathbf{M}_\theta$  and then allocating the same direction to arrive e at the axial vector:

$$\mathbf{M} = \mathbf{M}_a = \mathbf{e}_2 (\mathbf{e}_2 \cdot \mathbf{M}_\theta) \tag{3.7}$$

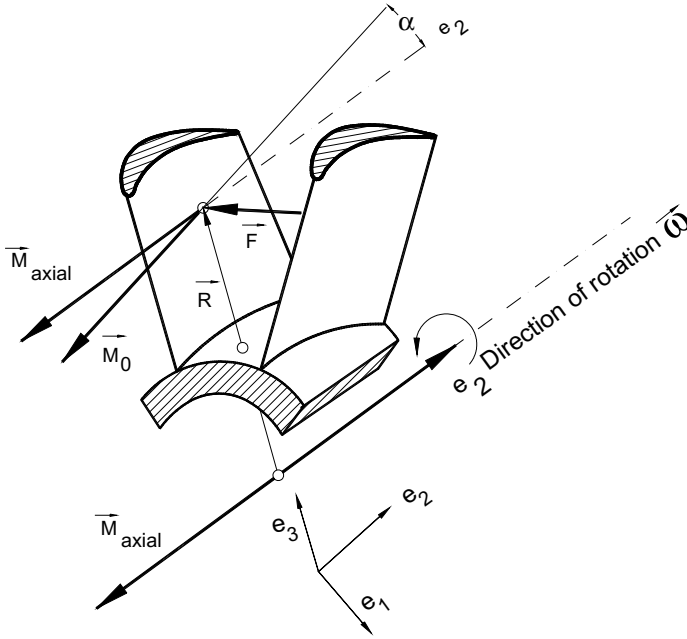


**Fig. 3.5:** Illustration of the axial moment by projecting the reaction moment  $\mathbf{M}_0$  in axial direction  $\mathbf{e}_2$ .

Neglecting the contribution of the shear stress terms at the inlet and exit but not along the wall surfaces,  $S_w$ , and performing the above scalar multiplication, the pressure contributions vanish identically. Furthermore, the moment contribution of gravitational force will vanish. With these assumptions, Eq. (3.7) reduces to:

$$\mathbf{M}_a = - \frac{\partial}{\partial t} \left( \int_{V_0} \mathbf{X} \times \mathbf{V} d\mathbf{m} \right) + \mathbf{e}_2 \left[ \int_{S_1} (R_1 V_{u1}) d\dot{m} - \int_{S_2} (R_2 V_{u2}) d\dot{m} \right] \quad (3.8)$$

with  $V_u$  as the absolute velocity component in circumferential direction. For steady flow, Eq. (3.8) reduces to:

$$\mathbf{M}_a = \mathbf{e}_2 \left[ \int_{S_1} (R_1 V_{u1}) d\dot{m} - \int_{S_2} (R_2 V_{u2}) d\dot{m} \right] \quad (3.9)$$

For the case where the velocity distributions at the inlet and exit of the channel are fully uniform and the turbomachine is rotating with the angular velocity  $\boldsymbol{\omega}$ , the power consumed (or produced) by a compressor (or by a turbine) stage is calculated by:

$$P = \omega \cdot \mathbf{M}_a = \omega \cdot e_2 \dot{m} (R_1 V_{u1} - R_2 V_{u2}) = \dot{m} (U_1 V_{u1} - U_2 V_{u2}) \quad (3.10)$$

Although the application of conservation laws are extensively discussed in the following chapters, it is found necessary to present a simple example of how the moment of momentum is obtained by utilizing the *velocity diagram* of a single-stage axial compressor. Figure 3.6 represents a single stage axial compressor with the constant hub and tip diameters.

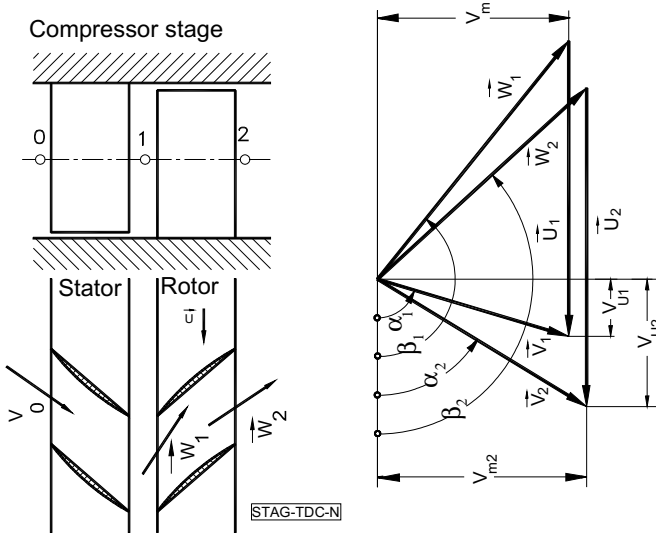


**Fig. 3.6:** A single stage axial compressor with its velocity diagram. The circumferential velocity difference  $|(V_{u2} - V_{u1})|$  is responsible for the compressor total pressure increase and thus the power consumption.

We consider the flow situation at the mid-section. The flow is first deflected by the *stator row*. Entering the rotor row, the fluid particle moves through a rotating frame, where the rotational velocity  $U$  is superimposed on the relative velocity  $W$ . The constant radii at the inlet and exit of the mid-section result in  $\omega R_1 = \omega R_2 = U_1 = U_2 = U$  simplifying Eq. (3.10) to  $P = \dot{m} U (V_{u1} - V_{u2})$ . The expression in the parenthesis,  $(V_{u1} - V_{u2})$ , is shown in the velocity diagram, Figure 3.5. It states that the compressor power consumption is related to the flow deflection expressed in terms of the circumferential velocity difference. The larger the difference  $(V_{u1} - V_{u2})$  is, the higher the pressure ratio that the compressor produces. However, for each type of compressor design (axial, radial, subsonic, super sonic) there is always a limit to this difference, which is dictated by the flow separation, as we will see later. For the case where no blades are installed inside the channel and the axial velocity distributions at the inlet and exit of the channel are fully uniform, Eq.

(3.9) is reduced to:

$$R_1 V_{u1} = R_2 V_{u2} = \text{const.} \quad (3.11)$$

This is the so called free vortex flow. It states that the strength of a vortex in an inviscid flow environment is conserved. Assuming an inviscid flow through the exit diffuser of a gas turbine, the existence of a vortex helps the boundary layer stay attached.

### 3.4 Balance of Energy

The conservation law of energy in integral form, that we discuss in the following sections, is based on the thermodynamic principals, primarily first law of thermodynamics for open systems and time dependent control volume. It is fully independent from conservation laws of fluid mechanics. However, it *implicitly* contains the irreversibility aspects described by the dissipation process. The contribution of the irreversibility is *explicitly* expressed by using the *Clausius* entropy equation, known as the second law of thermodynamics. The energy equation is applied to a variety of turbomachine components and describes a *chain of energy conversion process* that usually takes place in a thermo-fluid dynamics system such as the one shown in Fig. 3.7. As an example, Fig. 3.7 shows a high performance gas turbine with several components to which we apply the energy equation.

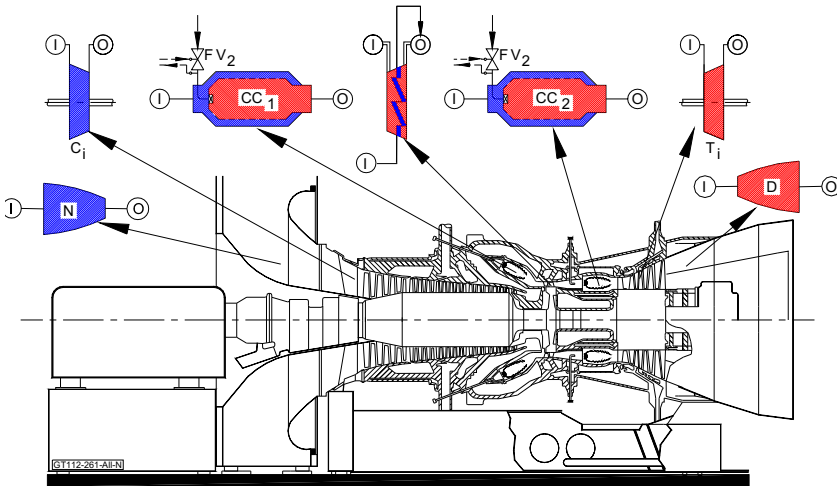


**Fig. 3.7:** A modern power generation gas turbine with a single shaft, two combustion chambers, a multi-stage compressor, a single stage reheat turbine and a multi-stage turbine.

A detailed derivation of the energy equation is presented in [3], from which we take the final result:

$$\begin{aligned} \dot{Q} + \dot{W}_{Shaft} = & \int_{v(t)} \frac{\partial}{\partial t} \left( \rho \left( u + \frac{1}{2} V^2 + gz \right) \right) dv + \\ & \dot{m}_{Out} \left( h + \frac{1}{2} V^2 + gz \right)_{Out} - \\ & \dot{m}_{In} \left( h + \frac{1}{2} V^2 + gz \right)_{In} \end{aligned} \quad (3.12)$$

For a fixed control volume, the volume integral can be rearranged as:

$$\int_{v(t)} \frac{\partial}{\partial t} \left( \rho \left( u + \frac{1}{2} V^2 + gz \right) \right) dv = \int_{VC} \frac{\partial(\rho e)}{\partial t} dv = \frac{\partial}{\partial t} \int_{VC} (\rho e) dv \quad (3.13)$$

We set  $\int_{CV} \rho e dv = E_{CV}$ , and since  $E_{CV}$  can only change with time, the partial derivative is replaced by the ordinary one,  $\partial/\partial t \equiv d/dt$ . As a result, we obtain:

$$\dot{Q} + \dot{W}_{Shaft} = \frac{dE}{dt} + \dot{m}_{Out} \left( h + \frac{1}{2} V^2 + gz \right)_{Out} - \dot{m}_{In} \left( h + \frac{1}{2} V^2 + gz \right)_{In} \quad (3.14)$$

Equation (3.14) exhibits the general form of energy equation for an open system with a fixed control volume. For technical applications, several special cases are applied which we will discuss in the following.

### 3.4.1 Energy Balance Special Case 1: Steady Flow

If a power generating machine such as a turbine, or a power consuming machine such as a compressor, operates in a steady design point, the first term on the right-hand side of Eq. (3.14) disappears,  $dE/dt = 0$ , which leads to:

$$\dot{Q} + \dot{W}_{Shaft} = \dot{m}_{Out} \left( h + \frac{1}{2} V^2 + gz \right)_{Out} - \dot{m}_{In} \left( h + \frac{1}{2} V^2 + gz \right)_{In} \quad (3.15)$$

Equation (3.15) is the energy balance for a turbomachine with thermal energy (heat) addition or rejection  $\dot{Q}$  (kJ/s) per unit of time and the shaft power is supplied or consumed  $\dot{W}_{shaft}$ .

### 3.4.2 Energy Balance Special Case 2: Steady Flow, Constant Mass Flow

In many applications, the mass flow remains constant from the inlet to the exit of the machine. Examples are uncooled turbines and compressors where no mass flow is added during the compression or expansion process. In this case, Eq. (3.15) reduces to:

$$\dot{Q} + \dot{W}_{shaft} = \dot{m} \left[ \left( h + \frac{1}{2} V^2 + gz \right)_{out} - \left( h + \frac{1}{2} V^2 + gz \right)_{in} \right] \quad (3.16)$$

Now, we define the *specific total enthalpy*

$$H \equiv h + \frac{1}{2} V^2 + gz \quad (3.17)$$

and insert it into Eq. (3.16), from which we get:

$$\dot{Q} + \dot{W}_{shaft} = \dot{m} (H_{out} - H_{in}) \quad (3.18)$$

In Eq. (3.16) or (3.18), the contribution of  $\Delta gz$  compared to  $\Delta h$  and  $\Delta V^2$  is negligibly small. Using the above equation, the energy balance for the major components of the gas turbine engine shown in Fig. 3.7 can be established as detailed in the following section.

## 3.5 Application of Energy Balance to Gas Turbines Components

The gas turbine engine shown in Fig. 3.7 consists of a variety of components, to which the energy balance in different form can be applied. These components can be categorized in three groups. The first group entails all those components that serve either the mass flow transport from one point of the engine to another or the conversion of kinetic energy into the potential energy and vice versa. Pipes, diffusers, nozzles, and throttle valves are representative examples of the first group. Within this group no thermal or mechanical energy (shaft work) is exchanged with the surroundings. We in thermodynamic sense these components are assumed adiabatic. The second group contains those components, within which thermal energy is generated or exchanged with the surroundings. Combustion chambers or heat exchangers are typical examples of these components. Thermodynamically speaking, in this case we are dealing with diabatic systems. Finally, the third group includes components within which thermal and mechanical energy is exchanged. In the following sections, each group is treated individually.



### 3.5.1 Application: Accelerated, Decelerated Flows

Nozzles, turbine stator cascades, throttle and, to some extent, pipes are examples of accelerated flows. Diffuser and compressor cascades decelerate the flow. For these devices, Eq. (3.18) reduces to:

$$H_{out} - H_{in} = 0, \text{ or } H_{out} = H_{in} = \text{Const} \quad (3.19)$$

The h-s-diagrams of the pipe, nozzle, and diffuser are shown in Fig. 3.8.

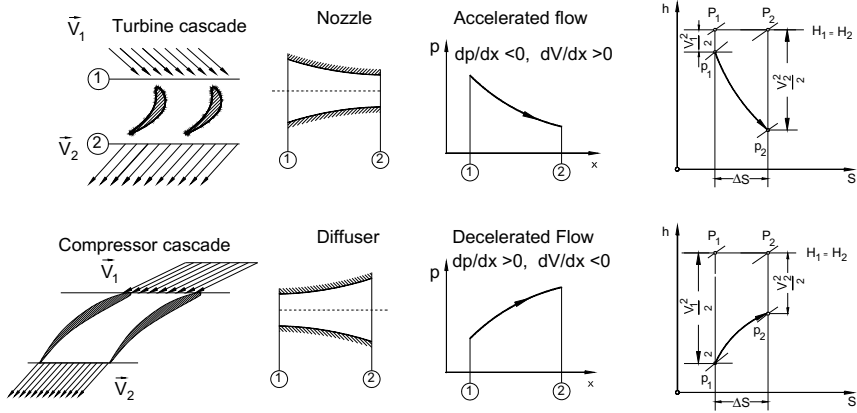


**Fig. 3.8:** Energy transfer in accelerated and decelerated flows with  $P$  as the total pressure and  $p$  the static pressure.

As this figure shows, the viscous flow causes entropy increase which results in a reduction of the total pressure from  $P_1$  to  $P_2$ . The total pressure is the sum of static pressure, dynamic pressure and the pressure due to the change of height:

$$P = p + \frac{1}{2} \rho V^2 + \rho g z \quad (3.20)$$

Neglecting the contribution of  $\Delta g z$  results in the following relation for total pressure loss:

$$\Delta P = P_{in} - P_{out} = \left( p + \frac{1}{2} \rho V^2 \right)_{in} - \left( p + \frac{1}{2} \rho V^2 \right)_{out} \quad (3.21)$$

The area under the process reflects the irreversibility due to the internal friction which results in total pressure drop. As discussed in Section 3.6.1 the total pressure difference  $\Delta P$  is directly related to the entropy increase  $\Delta s$  caused by the viscosity of the fluid.

### 3.5.2 Application: Combustion Chamber, Heat Exchanger

As indicated, combustion chambers or heat exchangers are typical examples of the components belonging to the group, within which heat generation or heat transfer takes place. The energy for this components balance is a special case of Eq. (3.18) with the shaft power  $\dot{W}_{Shaft} = 0$ :

$$\dot{Q} = \dot{m}(H_{Out} - H_{In}) \quad (3.22)$$

As a result, the total enthalpy at the exit is the sum of the inlet total enthalpy plus the heat added to the system. Introducing the specific thermal energy,  $q = \dot{Q}/\dot{m}$  (kJ/kg), we find

$$H_{Out} = H_{In} + q \quad (3.23)$$

Figure. 3.9 shows a schematic of a gas turbine combustion chamber, where the combustion air and fuel are mixed leading to an increased exit temperature and enthalpy.

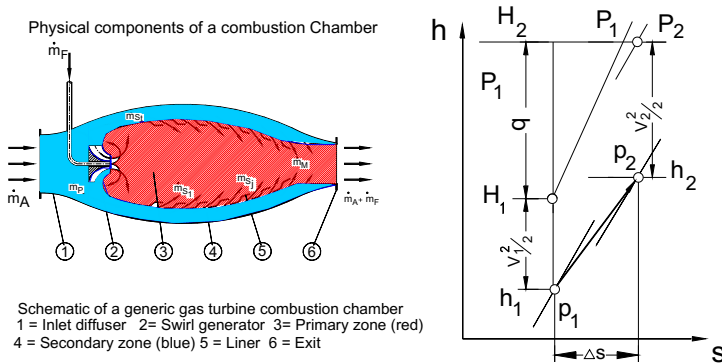


**Fig. 3.9:** Schematic of a gas turbine combustion chamber with h-s diagram, fuel and air mass flow  $\dot{m}_{fuel}$ ,  $\dot{m}_{air}$ , primary and secondary air mass flow  $\dot{m}_p$ ,  $\dot{m}_s$  and  $q = \dot{Q}/\dot{m}$  as the specific thermal energy (kJ/kg) added by the fuel, P: total pressure, p: static pressure.

The combustion process is shown in Fig. 3.9, where a simplified model of a combustion chamber is presented. The flow and combustion process within the combustion chamber is associated with entropy increases due to the heat addition and internal friction inside the chamber  $\Delta s = \Delta s_q + \Delta s_f$ . The internal friction, the wall friction, and particularly the mixing process of the primary and secondary air mass flows  $\dot{m}_p$ ,  $\dot{m}_s$ , cause pressure decreases of up to 5%. The thermal energy per unit mass flow is shown in Fig. 3.9 as  $q$ . It corresponds to the total enthalpy difference.

$$q = H_2 - H_1.$$

Another components within which a heat exchange takes place are recuperators. These components are mostly used in small gas turbines (see Chapter 2). Figure 3.10 shows the mechanism of the heat transfer from the hot side of the recuperator to the cold side. Heat from the gas turbine exhaust system is diverted into the hot side of a recuperator, thereby increasing the compressor exit temperature before it enters the combustion chamber. Figure 3.10 exhibits three sketches: Sketch (a) represents the physical component, where heat is transferred from the hot side to the cold side. The metal tubing that separates the hot side from the cold side is simplified by a solid wall between the two sides. Sketch (b) serves the numerical simulation, where the solid wall is subdivided into several segments.

To obtain the temperature distribution from the inlet to the exit of the recuperator on both sides, energy equation in conjunction with continuity and momentum equation is applied to each segment. Expressing the enthalpy in terms of specific heat and temperature, the energy equations for the hot and the cold sides are given as:

$$\begin{aligned}\dot{Q}_{h_k} &= \dot{m}_h (c_{p,h,i} T_{h,i} - c_{p,h,i+1} T_{h,i+1}) \\ \dot{Q}_{c_k} &= \dot{m}_c (c_{p,c,i} T_{c,i} - c_{p,c,i+1} T_{c,i+1})\end{aligned}\quad (3.24)$$

In Eq. (3.24) the indices  $h$  and  $c$  refer to hot and cold side respectively. The index  $k$  refers to the position between  $i$  and  $i+1$ . The  $c_p$  is the specific heat at constant pressure and  $T_i$  represents the temperature of the segment on the hot, cold side respectively. The thermal energy flow portions  $\dot{Q}_{h_k}$  and  $\dot{Q}_{c_k}$  assume positive (heat addition) or negative signs (heat rejection) based on the direction of the heat flow that pertains to the individual volume elements. They are calculated using the heat transfer coefficient and the temperature difference:

$$\dot{Q}_c = \bar{\alpha}_c A_c \Delta \bar{T}_c, \quad \dot{Q}_h = \bar{\alpha}_h A_h \Delta \bar{T}_h \quad (3.25)$$

In Eq. (3.25),  $\bar{\alpha}_c$ ,  $\bar{\alpha}_h$  are the averaged heat transfer coefficients,  $\Delta \bar{T}_c$ ,  $\Delta \bar{T}_h$  the mean temperature and  $A_c$ ,  $A_h$  the contact surfaces on the cold and hot sides, respectively.

The mean temperatures are:

$$\Delta \bar{T}_h = \bar{T}_{S_h} - \bar{T}_{\infty_h}, \quad \Delta \bar{T}_c = \bar{T}_{S_c} - \bar{T}_{\infty_c} \quad (3.26)$$

The subscripts  $S$  and  $\infty$  in Eq. (3.26) refer to the *surface temperature* and the temperature outside the boundary layer, respectively. In case of steady operation of the recuperator both energy flows are equal, however in transient operation there is a non-zero difference  $\dot{Q}_h - \dot{Q}_c \neq 0$  that represents the amount of energy stored inside the recuperator tubing.

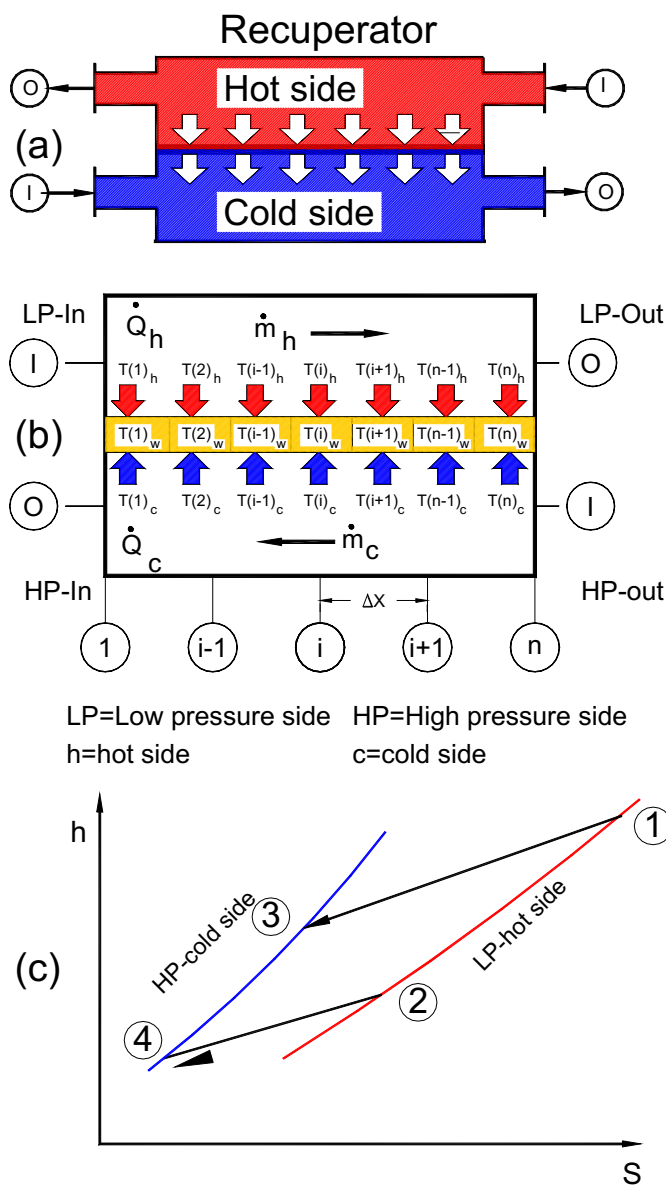


**Fig. 3.10:** A schematic of (a) recuperator component with hot and cold side, (b) discrete segments, and (c) h-s diagram.

### 3.5.3 Application: Turbine, Compressor

Within this group, mechanical and thermal energy transfers to/from surroundings take place. Turbines and compressors are two representative examples. The energy balance in general form is:

$$\dot{Q} + \dot{W}_{Shaft} = \frac{dE}{dt} + \dot{m}_{Out}(h + \frac{1}{2}V^2 + gz)_{Out} - \dot{m}_{In}(h + \frac{1}{2}V^2 + gz)_{In} \quad (3.27)$$

We distinguish in the following cases, where we consider steady flow only. Thus, the first term on the right-hand side,  $dE/dt = 0$ , disappears.

**3.5.3.1 Uncooled turbine.** We start with adiabatic (uncooled) turbine component, where no heat exchange between the turbine blades with the surroundings, in this case the turbine working medium, takes place:  $\dot{Q} = 0$ . The mass flows at the inlet and exit are the same. Figure. 3.11 shows a turbine stage, which consists of a stator and a rotor row.

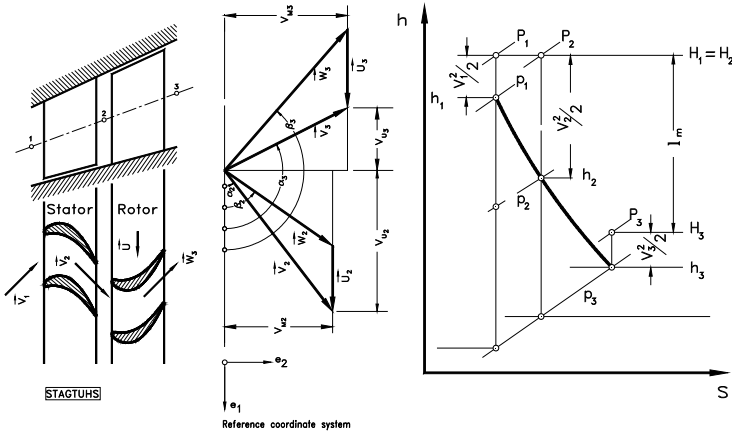


**Fig. 3.11:** Turbine stage consisting of a stator and a rotor row (left), velocity diagram (middle), h-s-diagram (right), P: total pressure, p: static pressure.

The stator row with several blades deflects the flow to the following rotor row, which turns with angular velocity  $\omega$ . The process of conversion of total energy into mechanical energy takes place within the rotor. Following the nomenclature in Fig. 3.11, we introduce the specific stage mechanical energy  $l_m = \dot{W}_{Shaft}/\dot{m}$ . Considering the h-s-diagram in Fig. 3.11, for adiabatic turbine,  $\dot{Q} = 0$ , Eq. (3.27) reduces to:

$$-l_m = H_3 - H_1 = (h_3 - h_1) + \frac{1}{2}(V_3^2 - V_1^2) \quad (3.28)$$

The negative sign of  $l_m$  indicates that energy is rejected from the system (to the surroundings). The h-s-diagram in Fig. 3.11 shows the expansion process within the

stator, where the total enthalpy within the stator  $H_1 = H_2$  remains constant. Changes of the total enthalpy occur within the rotor, where mechanical energy is produced. In addition, the *stage velocity diagram* is also shown in Fig. 3.11. This diagram shows the velocity deflection within both stator and rotor blades. As we saw from Eq. (3.10), the stage power is given by:

$$P = \omega \cdot M_a = \omega \cdot e_2 \dot{m} (R_1 V_{u1} - R_2 V_{u2}) = \dot{m} (U_1 V_{u1} - U_2 V_{u2}) \quad (3.29)$$

Dividing the above equation by the mass flow, we find:

$$\frac{P}{\dot{m}} = l_m = U_1 V_{u1} - U_2 V_{u2} \quad (3.30)$$

This equation can be found using the energy Equation (3.28) by replacing the static enthalpies in Eq. (3.28) by the kinetic energies and trigonometric relations from the velocity diagram shown Fig. 3.11.

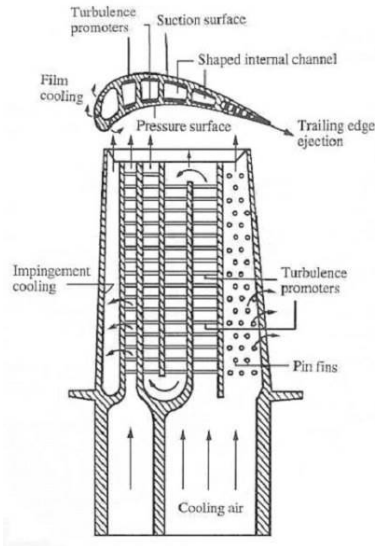


**Fig. 3.12:** A cooled turbine blade with internal cooling channels and external film cooling holes.

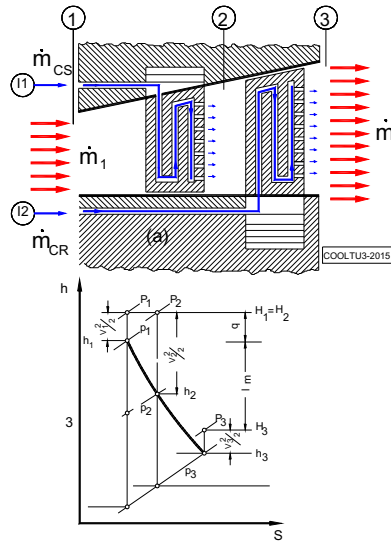


**Fig. 3.13:** simplified schematic of a cooled turbine stage with

**3.5.3.2 Cooled turbine:** The turbine inlet temperature of advanced gas turbine are close to the melting point of the blade material. This requires a rigorous cooling of

the first three turbine rows. We consider a cooled (diabatic) gas turbine blade, Fig. 3.12, where a heat exchange between the turbine material and the cooling medium takes place. The schematic of such a gas turbine blade is shown in Fig. 3.13 (right). In order to protect the blades from excessive thermal stresses, substantial amount of heat must be removed from the blades. One of the cooling methods currently used introduces cooling air from compressor into the turbine cooling channels. A portion of the cooling air enters the blade internally and passes through several channels, Fig. 3.12. Inside these channels, intensive heat transfer from the blade material to the cooling medium takes place resulting in a substantial reduction of the blade surface temperature. To intensify the heat transfer, the channels have internal pin fins and turbulators causing an increase in local turbulence level. The locally created turbulent flow will have strong velocity fluctuations that transport mass, momentum and energy to the boundary layer within the channels. This increases the heat removal from the blade material. The cooling air may exit the blade through a slot at the trailing edge. This cooling method is termed internal cooling. The cooling air may also exit arrays of holes on the blade surface including the blade tip creating a protective film very close to the blade surface. The film constitutes a buffer between the hot gas and the blade material.

The process of expansion and heat transfer is depicted in the h-s diagram shown in Fig. 3.13. Assuming a steady flow through the turbine and neglecting the energy by gravitational force, the energy equation reads:

$$\dot{Q} + \dot{W}_{shaft} = \dot{m}_{out}(h + \frac{1}{2}V^2) - \dot{m}_{in}(h + \frac{1}{2}V^2) \quad (3.31)$$

If we assume for this particular type of cooling scheme, the cooling mass flows through the stator and rotor have the same value,  $\dot{m}_{CS} = \dot{m}_{CR}$  and join the main turbine mass flow, then the turbine stage inlet and exit mass flows are the same,  $\dot{m}_{in} = \dot{m}_{out} = \dot{m}$ . With this assumption, we introduce the specific heat  $q \equiv \dot{Q}/\dot{m}_{in}$  which is transferred from the stator and rotor blades to the cooling mass flows,  $\dot{m}_{CS}$  and  $\dot{m}_{CR}$ . Considering the negative signs of the specific mechanical energy  $l_m$  and the heat  $q$ , we obtain from Eq. (3.31) for the cooled turbine stage:

$$q + l_m = (h + \frac{1}{2}V^2)_{in} - (h + \frac{1}{2}V^2)_{out} \quad (3.32)$$

The h-s diagram in Fig. 3.13 shows the specific stage mechanical energy  $l_m$  and the heat transferred from the turbine stage blade material  $q$ . From this diagram we can see that the turbine specific stage mechanical energy has been reduced by the amount of the heat rejected from the blades.

**3.5.3.3 Uncooled compressor.** Figure. 3.14 shows a compressor stage which consists of a stator and a rotor row.

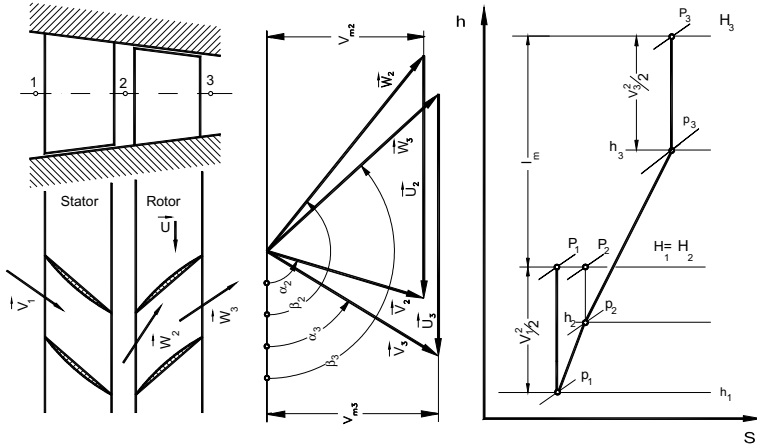


**Fig. 3.14:** Compressor stage consisting of a stator and a rotor row (left), velocity diagram (middle) and h-s-diagram (right), P: total pressure, p:static pressure.

Similar to the turbine stage, the stator row with several blades deflects the flow to the following rotor row, which is turning with an angular velocity  $\omega$ . The process of conversion of total energy into mechanical energy takes place within the rotor. As in the case of a turbine component, we follow the nomenclature of Fig. 3.14 for mechanical energy transfer and introduce the specific stage mechanical energy  $l_m = \dot{W}_{shaft} / \dot{m}$ . Considering an adiabatic and steady state compressor operation

shown in Fig. 3.14, the energy equation (3.27) modifies as:

$$l_m = H_3 - H_1 \quad (3.33)$$

The positive sign of  $l_m$  indicates that energy is consumed by the system (from the surroundings).

**3.5.3.4 Cooled Compressor.** Gas turbines with conventional design and pressure ratios  $\pi_c$  around 20 do not need cooling. Even non-conventional gas turbines such as GT24/26 described in Chapter 2 can operate at high pressure ratio without compressor air cooling. For higher compression ratio, however, compressor cooling is required. Compressed air energy storage plant described in Chapter 2 and the gas turbine GE-LMS100 are two representative examples, where intercooling cooling is applied. Figure 3.15 shows process of compressor air cooling through an intercooler and three aftercoolers. The last aftercooler positioned between the plena (8) and (9) reduces the temperature and thus the specific volume of the humid air that enters the air storage cavern.



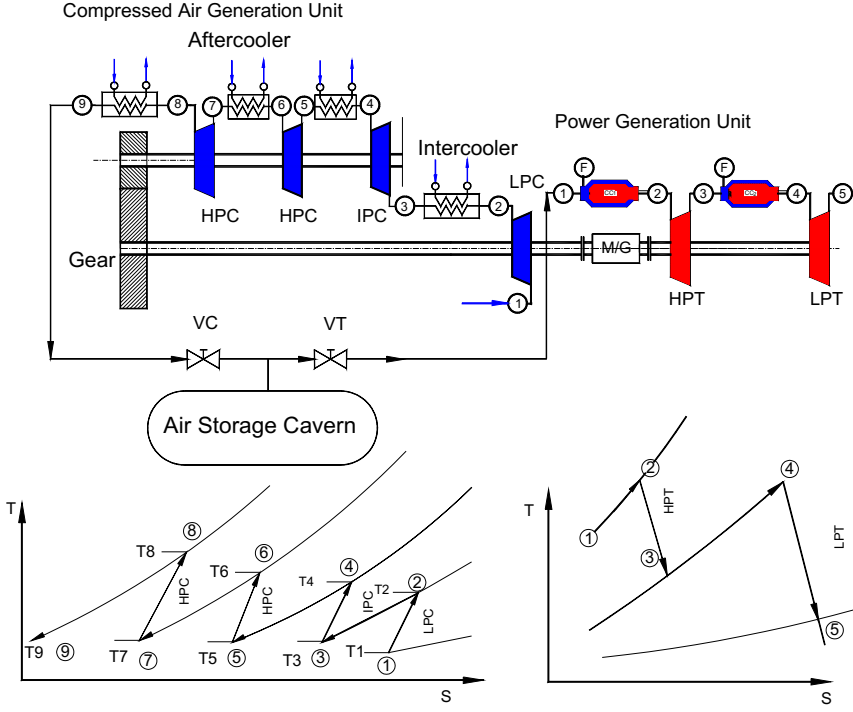


**Fig. 3.15:** Cooling of the compressor air of Compressed Air Energy Storage plant in Huntorf, Germany.

### 3.6 Irreversibility and Total Pressure Losses

The total pressure losses within a component can be calculated using the second law of thermodynamics:

$$ds = \frac{\delta q}{T} = \frac{du + p dv}{T} = \frac{dh - v dp}{T} \quad (3.34)$$

Using the generalized thermodynamic relations, we find:

$$ds = \frac{c_v}{T} dT + \left( \frac{\partial p}{\partial T} \right)_v dv \quad (3.35)$$

or in terms of  $c_p$ :

$$ds = \frac{c_p}{T} dT - \left( \frac{\partial v}{\partial T} \right)_p dp \quad (3.36)$$

With:

$$dh = c_p dT + \left( v - T \left( \frac{\partial v}{\partial T} \right)_p \right) dp \quad (3.37)$$

For the working media used in thermal turbomachines such as steam, air, and combustion gases, the thermodynamic properties can be taken from appropriate gas and steam tables. In general, the specific heats at constant pressure  $c_p$  and constant specific volume  $c_v$  are functions of temperature. Figure 4.15 shows the specific heat at constant pressure as a function of temperature with the *fuel/air ratio*  $\mu$  as parameter. The dry air is characterized by  $\mu = 0$  and no moisture. As seen at lower temperatures, changes of  $c_p$  are not significant. However, increasing the temperature results in higher specific heat. In the case of combustion gases, the addition of fuel in a combustion chamber causes a change in the gas constant  $R$  and additional increase in  $c_p$ . At moderate pressures, the ideal gas relation can be applied

$$pv = RT ; \quad \frac{\partial v}{\partial T} = \frac{R}{p} \quad (3.38)$$

With this relation, the entropy change can be obtained using Eq. (3.35) in terms of enthalpy or internal energy,

$$ds = \frac{c_p}{T} dT - R \frac{dp}{p}, \quad ds = \frac{c_v}{T} dT + R \frac{dv}{v} \quad (3.39)$$

Assuming lower temperatures where  $c_p$  and  $c_v$  can be approximated as constant, the entropy change is calculated by integrating Eq. (3.39):

$$\Delta s = c_p \ln \left( \frac{T_2}{T_1} \right) - R \ln \left( \frac{p_2}{p_1} \right) = c_p \ln \left[ \left( \frac{T_2}{T_1} \right) \left( \frac{p_1}{p_2} \right)^{\frac{\kappa-1}{\kappa}} \right] \quad (3.40)$$

$$\Delta s = c_v \ln \left( \frac{T_2}{T_1} \right) + R \ln \left( \frac{v_2}{v_1} \right) = c_v \ln \left[ \left( \frac{T_2}{T_1} \right) \left( \frac{v_2}{v_1} \right)^{\kappa-1} \right] \quad (3.41)$$

Equations (3.40) and (3.41) are valid under perfect gas assumption,  $c_p$  and  $c_v \neq f(T)$ , for estimating the entropy changes. For dry or moist air as working media in compressors, and combustion gases as the working media in turbines and combustion chambers, appropriate gas tables must be used in order to avoid significant errors. In using the energy equation, gas table should be used for fuels that are used in gas turbine design. Considering the working media air or combustion gas as calorically perfect gas ( $c_p, c_v, \kappa = \text{const.}$ ) leads to substantial errors. This is particularly true for combustion chamber and turbine. Figure 3.16 shows the specific heat at constant

pressure as a function of temperature  $c_p = f(T)$  with the fuel/air ratio  $\mu = \dot{m}_{fuel}/\dot{m}_{air}$  as a parameter. As the figure shows, even for a relatively low turbine inlet temperature TIT=1000K, an error from 18% to 30% will result if working with calorically perfect air.

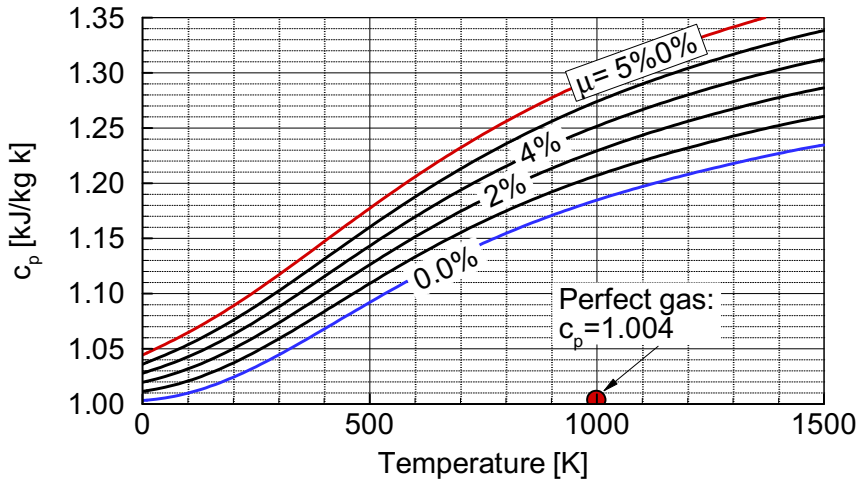


**Fig. 3.16:** Specific heat at constant pressure for dry air and combustion gases with different fuel/air ratios.

### 3.6.1 Application of Second Law to Turbomachinery Components

To calculate the entropy increase as a result of an irreversible process, a simple nozzle or turbine stator flow is considered. The expansion process is shown in Fig. 3.17.

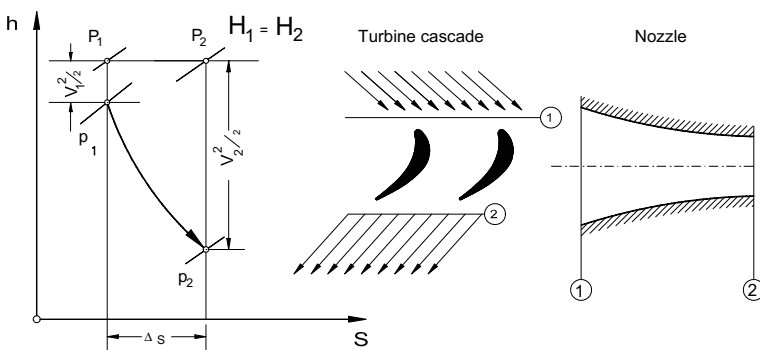


**Fig. 3.17** Total pressure loss and entropy increase in a nozzle and a turbine cascade, P: total pressure, p:static pressure.

The entropy change is obtained using the second law:

$$\Delta s = c_p \ln \left( \frac{T_2}{T_1} \right) - R \ln \left( \frac{p_2}{p_1} \right) \quad (3.42)$$

where  $p_1, p_2$  and  $T_1, T_2$  are static pressures and temperatures. These quantities can be related to the total quantities by the following simple modification:

$$\frac{p_2}{p_1} = \frac{\left( \frac{p_2}{p_{o2}} \right)}{\left( \frac{p_1}{p_{o1}} \right)} \quad (3.43)$$

Introducing the temperature relation by applying the isentropic relation with  $p v^\kappa = \text{const.}$ ,

$$\left( \frac{p_2}{p_{o2}} \right) = \left( \frac{T_2}{T_{o1}} \right)^{\frac{\kappa}{\kappa-1}}, \quad \text{and} \quad \left( \frac{p_1}{p_{o1}} \right) = \left( \frac{T_1}{T_{o1}} \right)^{\frac{\kappa}{\kappa-1}} \quad (3.44)$$

and inserting Eq. (3.44) into Eq. (3.43) leads to:

$$\frac{p_2}{p_1} = \frac{\left( \frac{T_2}{T_{o2}} \right)^{\frac{\kappa}{\kappa-1}}}{\left( \frac{T_1}{T_{o1}} \right)^{\frac{\kappa}{\kappa-1}}} \left( \frac{p_{o2}}{p_{o1}} \right) \quad (3.45)$$

If we assume that the fluid is a perfect  $c_p \neq f(T) = \text{const.}$ , then we may set  $T_{o1} = T_{o2}$ . With this assumption Eq. (3.45) simplifies as:

$$\frac{p_2}{p_1} = \left( \frac{T_2}{T_1} \right)^{\frac{\kappa}{\kappa-1}} \left( \frac{p_{o2}}{p_{o1}} \right) \quad (3.46)$$

The entropy changes obtained form:

$$\Delta s = c_p \ln \left( \frac{T_2}{T_1} \right) - R \frac{\kappa}{\kappa-1} \ln \left( \frac{T_2}{T_1} \right) - R \ln \left( \frac{p_{o2}}{p_{o1}} \right) \quad (3.47)$$

With:

$$c_p = R \frac{\kappa}{\kappa-1} \quad (3.48)$$

the first two terms on the right hand side of (3.47) cancel each other leading to:

$$\Delta s = R \ln \left( \frac{p_{o1}}{p_{o2}} \right) = -R \ln \left( \frac{p_{o2}}{p_{o1}} \right) = -R \ln \frac{p_{o1} - \Delta p_o}{p_{o1}} \quad (3.49)$$

Thus, the entropy change is directly related to the total pressure loss. We introduce the total pressure loss coefficient  $\zeta$ :

$$\zeta = \frac{\Delta p_o}{p_{o1}} \quad (3.50)$$

then we have:

$$\Delta s = -R \ln(1 - \zeta) \quad (3.51)$$

or

$$\zeta = 1 - e^{\frac{-\Delta s}{R}} \quad (3.52)$$

If the total pressure loss coefficient is known, the entropy change can be calculated using Eq. (3.52). For compressor or turbine components, different loss correlations are available that are based on experimental investigations. We will discuss a few of these correlations later.

### 3.7 Flow at High Subsonic and Transonic Mach Numbers

The turbine component of gas turbines may operate at higher subsonic, transonic, or supersonic Mach ranges. This is particularly true when the components operate at off-design conditions that may cause an increase in exit flow velocity. A typical example is the flow through a subsonic turbine stator blade shown in Fig. 3.18.

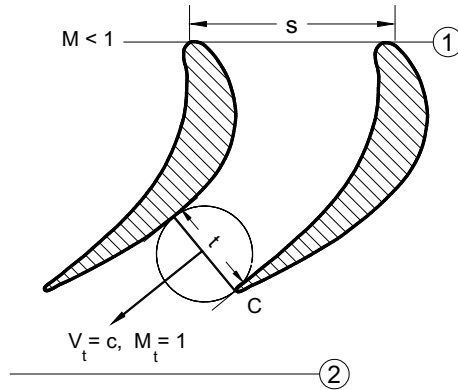


**Fig. 3.18:** Guided flow through a turbine cascade from inlet station (1) to the throat(t). The working medium is accelerated from subsonic  $M < 1$  to sonic flow  $M = 1$ .

Similar situations may occur in blade channels of turbine or compressor rotors, inlet

guide vanes, and nozzles.

Figure 3.18 depicts a purely *convergent channel*. An increase in flow velocity at the exit of a turbine stator, shown in Fig. 3.18, necessitates an increase of the inlet pressure. Since the flow velocity is a function of the pressure difference across the turbine cascade, it will increase continuously until the speed of sound is reached. This happens at the smallest cross section, namely the blade *throat*  $t$ . For a convergent blade channel, as shown in Fig. 3.18, no further acceleration can take place with increasing the pressure difference between the inlet (1) and the exit (2). By reaching the speed of sound at the throat, the critical condition is established and the turbine blade channel is *choked*. If a higher velocity than the speed of sound is desired, then the blade geometry must change. In the following sections, we introduce the basic physics necessary to describe the flow behavior at high subsonic and transonic Mach numbers and their effect on channel geometry and thermodynamic properties.

### 3.7.1 Density Changes with Mach Number, Critical State

The changes in fluid density and the flow Mach number are closely related. To find the corresponding relationships, we apply the energy equation for an adiabatic system to a large adiabatic container, Fig. 3.19, where the exit diameter  $d$  is assumed to be negligibly small compared to the container diameter  $d \ll D$ .

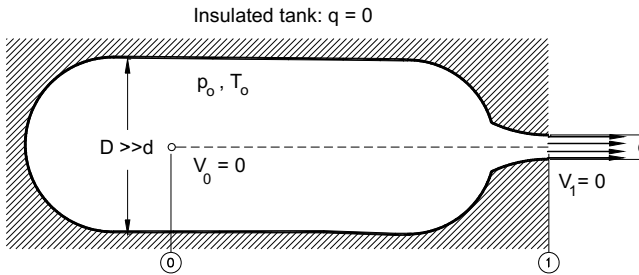


**Fig. 3.19:** An adiabatic system consisting of a large container and a convergent nozzle.

For the system in Fig. 3.19, the energy equation is written as:

$$H \equiv h_t = h_0 + \frac{1}{2}V_0^2 = h_1 + \frac{1}{2}V_1^2 = \text{const.} \quad (3.53)$$

Since in this chapter we are dealing with one-dimensional flow, the velocity subscripts refer to the stations and not to the velocity components as we did in previous chapters. Thus, the subscript  $0$  and  $t$  refers to the *stagnation* condition, where the velocity is assumed to be zero. Assuming a perfect gas, we introduce, for enthalpy, the temperature and rewrite Eq. (3.53) in terms of total temperature:

$$\frac{T_t}{T} = 1 + \frac{1}{2c_p} \frac{1}{T} V^2 \quad (3.54)$$

The specific heats at constant pressure and volume are related by the specific gas

constant:

$$c_p - c_v = R, \frac{c_p}{c_v} = \kappa, M = V/c \text{ and } c = \sqrt{\kappa R T} \quad (3.55)$$

Using the above relations, the total temperature ratio as a function of the Mach number  $M$  read:

$$\frac{T_t}{T} = 1 + \frac{1}{2} (\kappa - 1) M^2 \quad (3.56)$$

To obtain similar relationship for the density ratio, we assume an isentropic process described by:

$$p v^\kappa = p_t v_t^\kappa = \text{con.} \quad (3.57)$$

that we combine with the equation of state for ideal gases,

$$v = \frac{p}{RT} \quad (3.58)$$

Thus, eliminating the specific volume results in:

$$\frac{p_t}{p} = \left( \frac{T_t}{T} \right)^{\frac{\kappa}{\kappa-1}} \quad (3.59)$$

Introducing Eq. (3.56) into (3.59) results in:

$$\frac{p_t}{p} = \left( 1 + \frac{\kappa - 1}{2} M^2 \right)^{\frac{\kappa}{\kappa-1}} \quad (3.60)$$

Likewise, we obtain the density ratio as:

$$\frac{\rho_t}{\rho} = \left( 1 + \frac{\kappa - 1}{2} M^2 \right)^{\frac{1}{\kappa-1}} \quad (3.61)$$

Equation (3.61) expresses the ratio of stagnation point density relative to the density at any arbitrary point in the container including the exit area. Assuming air as a perfect gas with  $\kappa = 7/5$  at a temperature of  $T = 300^\circ\text{K}$ , the ratios  $\Delta\rho/\rho_t = (\rho_t - \rho)/\rho_t$ ,  $\Delta p/p_t = (p_t - p)/p_t$ , and  $\Delta T/T_t = (T_t - T)/T_t$  from Eqs. (3.56), (3.60) and (3.61), are plotted in Fig. 3.20.

In this figure, we find that for very small Mach numbers,  $M < 0.1$ , the density change,  $\Delta\rho/\rho_t$ , is small and the flow is considered incompressible. Increasing the Mach number, however, results in significant changes of the density ratio. In practical applications, flows with  $M < 0.3$  are still considered incompressible. Increasing the Mach number above  $M > 0.3$  results in higher density changes that cannot be neglected as Fig. 3.20 shows. Thus, the flow is considered as compressible with a noticeable change of density. If the velocity approaches the speed of sound, i.e.  $V = c$  and  $M = 1$ , it is called the critical velocity and the flow state is called critical. In this case, the properties in Eqs. (3.56), (3.60) and (3.61) are calculated by setting  $M = 1$ . To distinguish this particular flow state, quantities are labeled with the superscript \*. The critical temperature ratio is:

$$\frac{T_t^*}{T^*} = \frac{(\kappa + 1)}{2} \text{ for } \kappa = 7/5: \frac{T_t^*}{T^*} = 1.2 \quad (3.62)$$

The critical pressure ratio reads:

$$\frac{p_t^*}{p^*} = \left( \frac{\kappa + 1}{2} \right)^{\frac{\kappa}{\kappa-1}} \text{ for } \kappa = 7/5: \frac{p_t^*}{p^*} = 1.893 \quad (3.63)$$

and finally, the critical density ratio is obtained from:

$$\frac{\rho_t^*}{\rho^*} = \left( \frac{\kappa + 1}{2} \right)^{\frac{1}{\kappa-1}} \text{ for } \kappa = 7/5: \frac{\rho_t^*}{\rho^*} = 1.577 \quad (3.64)$$

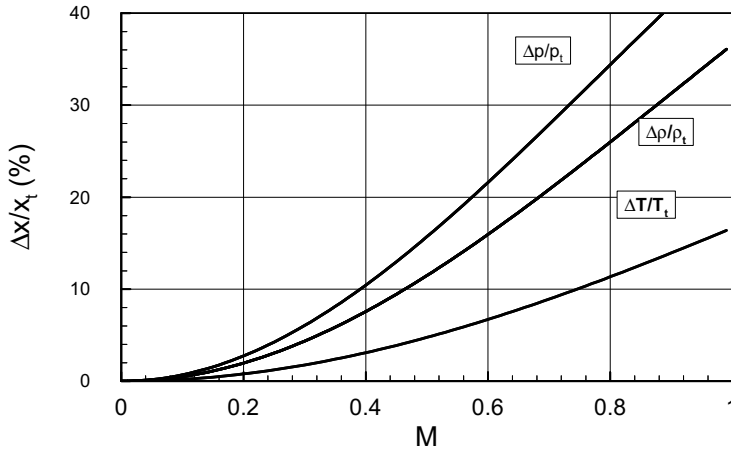


**Fig. 3.20** Density, pressure, and temperature changes as a function of flow mach number.



From Eq. (3.63), it is obvious that in order to achieve the sonic flow ( $M = 1$ ), the critical pressure ratio must be established first. In a system as in Fig. 3.19 with a *convergent exit nozzle* and air as the working medium with  $\kappa = 1.4$ , the critical pressure ratio is  $p_t^*/p^* = 1.893$ . At this pressure ratio the mass flow per unit area has a maximum and the flow velocity at the exit nozzle equals to the speed of sound. Any increase in pressure ratio above the critical one results in a *choking state* at the nozzle throat. In this case, the convergent nozzle produces its own exit pressure, such that the critical pressure ratio is maintained. Equations (3.62) to (3.64) were derived for calorically perfect gases. They indicate, the critical values of the thermodynamics properties for gases are exclusively functions of the substance parameter  $\kappa = c_p/c_v$ . For the working media of gas turbines the specific heats  $c_p, c_v$  are functions of temperature and the chemical composition of the working media gas that determine the specific gas constant.

To calculate the mass flow of a calorically perfect gas through a convergent nozzle in terms of pressure ratios, we first replace the enthalpy in the energy equation by:

$$h = c_p T = \frac{k}{k-1} RT = \frac{k}{k-1} p v = \frac{k}{k-1} \frac{p}{\rho} \quad (3.65)$$

Thus, the energy equation for a calorically perfect gas reads:

$$\frac{V_1^2}{2} + \frac{\kappa}{\kappa-1} \frac{p_1}{\rho_1} = \frac{V_2^2}{2} + \frac{\kappa}{\kappa-1} \frac{p_2}{\rho_2} \quad (3.66)$$

To eliminate the density at the exit, we now apply the isentropic relation to the right-hand side of Eq. (3.66) and arrive at:

$$\frac{V_1^2}{2} + \frac{\kappa}{\kappa-1} \frac{p_1}{\rho_1} = \frac{V_2^2}{2} + \frac{\kappa}{\kappa-1} \frac{p_1}{\rho_1} \left( \frac{p_2}{p_1} \right)^{\frac{(\kappa-1)}{\kappa}} \quad (3.67)$$

We assume that inside the container, because of  $D \gg d$ , the velocity  $V_1$  is negligibly small compared to the velocity at the nozzle exit  $V_2$ . In this case, the static pressure  $p_1$  would represent the total pressure at the same position  $p_1 \equiv p_t$ . We now set  $p_2 \equiv p_e$  and call it the nozzle exit or back pressure. If the actual pressure ratio is less than the critical one,  $p_t/p_e < p_t^*/p_e^*$  and the mass flow exits into the atmosphere, then the nozzle exit pressure is identical with the ambient pressure and the nozzle is not choked. On the other hand, if  $p_t/p_e > p_t^*/p_e^*$ , the convergent nozzle is choked indicating that it has established a back pressure for itself, which corresponds to the critical pressure. With the above assumption, the mass flow through a convergent channel is calculated by:

$$\dot{m} = V\rho A = A \sqrt{\frac{2\kappa}{\kappa-1} p_t \rho_t \left[ \left( \frac{p_e}{p_t} \right)^{\frac{2}{\kappa}} - \left( \frac{p_e}{p_t} \right)^{\frac{\kappa+1}{\kappa}} \right]} = A \Psi \sqrt{\frac{2\kappa}{\kappa-1} p_t \rho_t} \quad (3.68)$$

where the *mass flow function*  $\Psi$  is defined as

$$\Psi = \sqrt{\left( \frac{p_e}{p_t} \right)^{\frac{2}{\kappa}} - \left( \frac{p_e}{p_t} \right)^{\frac{\kappa+1}{\kappa}}} \quad (3.69)$$

thus, the mass flow through the nozzle is calculated by,

$$\dot{m} = A \Psi \sqrt{\frac{2\kappa}{\kappa-1} p_t \rho_t} \quad (3.70)$$

Figure 3.21 shows the mass flow function  $\Psi$  as a function of the pressure ratio for different  $\kappa$ .

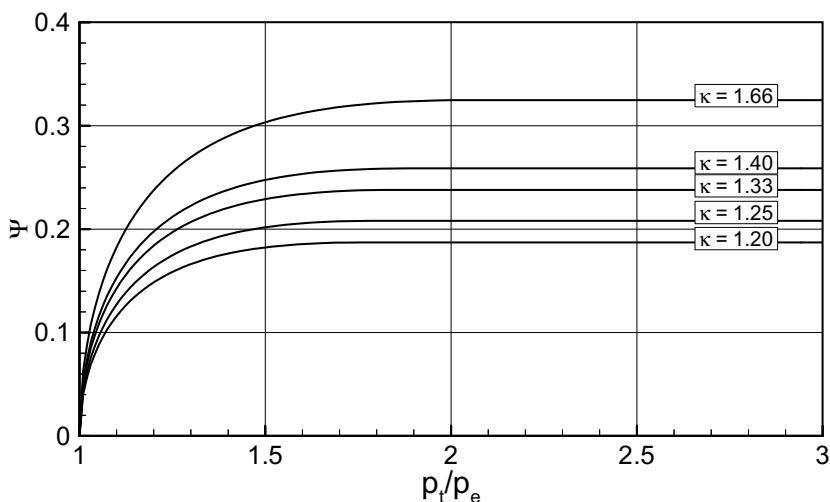


**Fig. 3.21** Flow function  $\psi$  versus the pressure ratio with  $\kappa$  as parameter.

The maximum value of  $\Psi$  is obtained from:

$$\Psi_{\max} = \sqrt{\frac{\kappa-1}{\kappa+1} \left( \frac{2}{\kappa+1} \right)^{\frac{1}{\kappa-1}}} \quad (3.71)$$

Figure 3.21 shows that increasing the pressure ratio results in an increase of the mass

flow function  $\Psi$  until  $\Psi_{max}$  has been reached. Further increase in pressure ratio results in a choking state, where the flow function remains constant.

### 3.7.2 Effect of Cross-Section Change on Mach Number

The influence of the *Mach number* gives rise to further differences between compressible and incompressible flow. However, we first examine the effect that the Mach number has on the relation between the cross-sectional area  $A$  and the velocity  $V$  in an isentropic flow. This relation is obvious in an incompressible flow from the continuity equation:

$$VA = \text{const}; \quad (3.72)$$

as  $A$  becomes large  $V$  must decrease, and vice versa. However, the continuity equation for compressible flow,

$$\rho VA = \text{const} \quad (3.73)$$

contains the additional variable  $\rho$  that changes with the Mach number as shown in Fig. 3.19. We differentiate Eq. (3.73) and divide the result by Eq. (3.73). As a result, we obtain the expression:

$$\frac{dV}{V} + \frac{dA}{A} + \frac{d\rho}{\rho} = 0 \quad (3.74)$$

for isentropic flow, thus  $p = p(\rho)$ , we have from the definition of the speed of sound

$$c^2 = \left( \frac{\partial p}{\partial \rho} \right)_s \quad (3.75)$$

in particular  $dp/d\rho = c^2$  and therefore, from Eq. (3.74)

$$\frac{dV}{V} + \frac{dA}{A} + \frac{dp}{c^2 \rho} = 0. \quad (3.76)$$

Using the component of Euler's equation for one-dimensional flow,

$$V dV = - \frac{dp}{\rho} \quad (3.77)$$

We then obtain the modified Eq.(3.130) as:

$$\frac{dV}{V} + \frac{dA}{A} = \frac{V^2}{c^2} \frac{dV}{V} \quad (3.78)$$

which we reduce to:

$$\frac{dA}{A} = -\frac{dV}{V}(1 - M^2) \quad (3.79)$$

Introducing Eq. (3.79) into (3.77) results in:

$$\frac{dA}{A} = \frac{dp}{\rho V^2}(1 - M^2) \quad (3.80)$$

With Eqs. (3.79) and (3.80) we have established a relationship between the velocity change, the pressure change, and the Mach number. For  $M < 1$  we obtain qualitatively the same behavior as in incompressible flow: a decrease in the cross-sectional area leads to an increase in velocity, leading to a subsonic nozzle flow, Fig. 3.22(left).

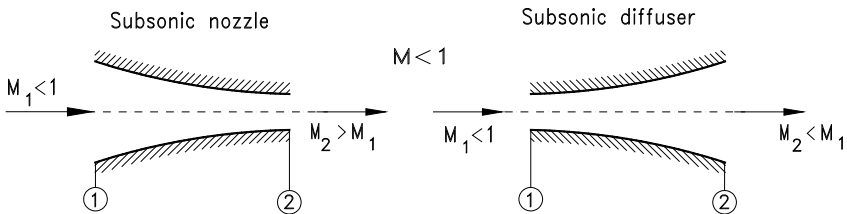


**Fig. 3.22** Left: Subsonic nozzle with  $dA < 0$ ,  $dV > 0$ ,  $dp < 0$ ,  
Right: Subsonic diffuser with  $dA > 0$ ,  $dV < 0$ ,  $dp > 0$ .

On the other hand, an increase in the cross-sectional area ( $dA > 0$ ) corresponds to a decrease in velocity ( $dV < 0$ ), resulting in a subsonic diffuser flow, Fig. 3.22 (right). For  $M = 1$ , we obtain  $dA/dx = 0$  and  $dp = 0$ . For  $M > 1$  Eq. (3.79) and (3.80) show that if the cross-sectional area ( $dA/dx > 0$ ) increases, the velocity must also increase ( $dV/dx > 0$ ), or if the area decreases, so does the velocity. As a result, we have a supersonic nozzle and diffuser shown in Fig. 3.23.

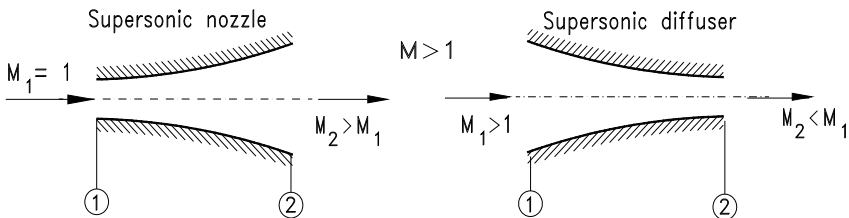


**Fig. 3.23** Left: Supersonic nozzle with  $dA > 0$ ,  $dV > 0$ ,  $dp < 0$ ,  
Right: Supersonic diffuser with  $dA > 0$ ,  $dV < 0$ ,  $dp > 0$ .

Equations (3.78) and (3.79) indicate that in order to reach the sonic speed  $M = 1$ , the area change  $dA/dx$  must vanish. This implies that the cross section must have a minimum. Considering the configurations shown in Fig. 3.22 and Fig. 3.23, channels can be constructed that satisfy the requirements stated in Eq. (3.79) and (3.80). A

generic convergent-divergent nozzle known as the *Laval nozzle* shown in Fig. 3.24 (a), is an example. A similar configuration is used in the so called *control stage* of steam turbines, Fig. 3.24 (b). This channel can accelerate the flow from a subsonic to a supersonic Mach range.

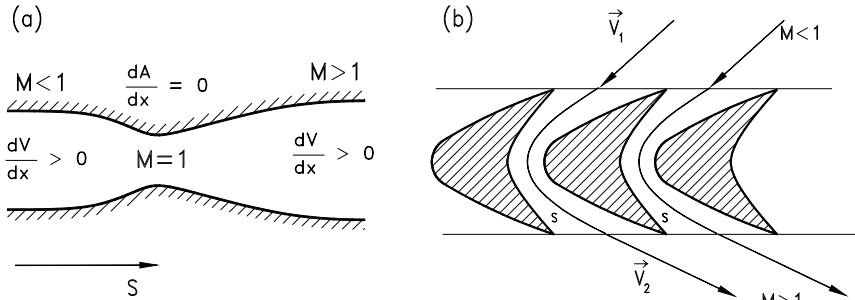


**Fig. 3.24** (a) A generic Laval nozzle operating at the design pressure ratio, (b) Stator row of a control stage of a steam turbine.

The condition for a supersonic flow to be established is that the pressure ratio along the channel from the inlet to the exit must correspond to the nozzle design pressure ratio, which is above the super critical pressure ratio. In this case, the flow is accelerated in the convergent part, reaches the Mach number  $M = 1$  in the *throat*, and is further accelerated in the divergent portion of the nozzle. If the channel pressure ratio is less than the critical pressure ratio, the flow in convergent part is accelerated to a certain subsonic Mach number,  $M < 1$ , and then decelerates in divergent parts. A supersonic diffuser, on the other hand, is characterized by convergent divergent channels with an inlet Mach number  $M > 1$ .

Figure 3.25 shows schematically the flow through an inlet diffuser of a supersonic aircraft. Passing through an oblique shock, the flow enters the inlet and is decelerated from  $M > 1$  to  $M = 1$  at the throat, where the sonic velocity has been reached. Further deceleration occurs at the divergent part of the inlet.

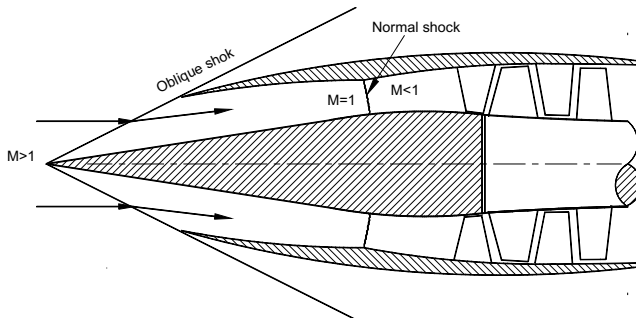


**Fig. 3.25:** Flow through a supersonic inlet: deceleration from  $M > 1$ , to  $M = 1$  at the throat and  $M < 1$  downstream of the throat.

Equation (3.79) and its subsequent integration, along with the flow quantities listed in Table 4.1, indicate the direct relation between the area ratio and the Mach number. These relations can be utilized as a useful tool for estimating the cross section distribution of a Laval nozzle, a supersonic stator blade channel, or a supersonic diffuser. If, for example, the Mach number distribution in the streamwise direction is given,  $M(S) = f(S)$ , the cross section distribution  $A(S) = f(M)$  is directly calculated from Table 4.1. If, on the other hand, the cross section distribution in the streamwise direction is prescribed, then the Mach number distribution, and thus, all other flow quantities can be calculated using an inverse function. Since we assumed the isentropic flow with calorically perfect gases as the working media, important features such as flow separation as a consequence of the boundary layer development under adverse pressure gradient, will not be present. Therefore, in both cases, the resulting channel geometry or flow quantities are just a rough estimation, no more, no less. Appropriate design of such channels, particularly transonic turbine or compressor blades, require a detailed calculation where the fluid viscosity is fully considered.

In order to represent the thermodynamic variables as functions of a Mach number, we use the continuity and energy equations in conjunction with the isentropic relation, and the equation of state for the thermally perfect gases with  $p = \rho RT$ . The isentropic flow parameters as a function of a Mach number are summarized in Table 3.1, which contains two columns. The first column gives the individual parameter ratios at arbitrary sections, whereas the second one gives the ratios relative to the critical state. The gas dynamics relations presented in Table 3.1 are depicted in Fig. 3.26.

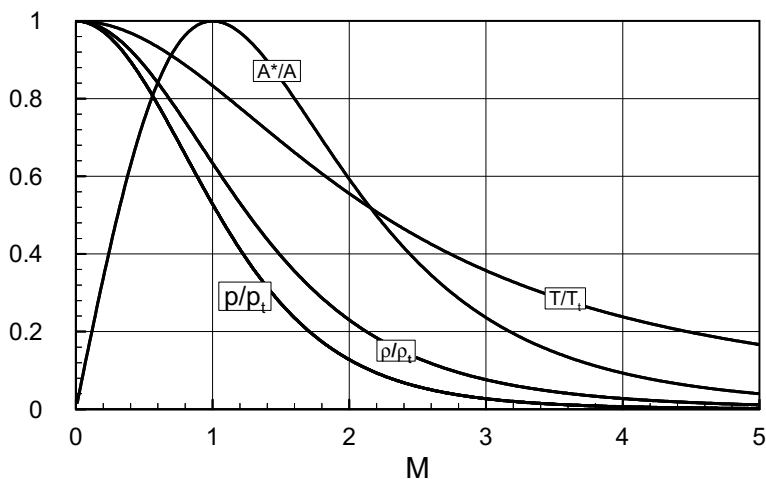


**Fig. 3.26** Area ratio and the thermodynamic property ratios as a function of Mach number for  $\kappa = 1.4$ .

Table 3.1: Summary of the gas dynamic functions

Parameters for any two arbitrary sections	Parameters relative to the critical state
$\frac{A}{A_1} = \frac{1}{M} \left( \frac{1 + \frac{\kappa-1}{2} M^2}{1 + \frac{\kappa-1}{2} M_1^2} \right)^{\frac{1}{2} \left( \frac{\kappa+1}{\kappa-1} \right)}$	$\frac{A}{A^*} = \frac{1}{M} \left( \frac{1 + \frac{\kappa-1}{2} M^2}{\frac{\kappa+1}{2}} \right)^{\frac{1}{2} \left( \frac{\kappa+1}{\kappa-1} \right)}$
$\frac{p}{p_1} = \left( \frac{1 + \frac{\kappa-1}{2} M_1^2}{1 + \frac{\kappa-1}{2} M^2} \right)^{\frac{\kappa}{\kappa-1}}$	$\frac{p}{p^*} = \left( \frac{\frac{\kappa+1}{2}}{1 + \frac{\kappa-1}{2} M^2} \right)^{\frac{\kappa}{\kappa-1}}$
$\frac{T}{T_1} = \frac{1 + \frac{\kappa-1}{2} M_1^2}{1 + \frac{\kappa-1}{2} M^2}$	$\frac{T}{T^*} = \frac{\frac{\kappa+1}{2}}{1 + \frac{\kappa-1}{2} M^2}$
$\frac{h}{h_1} = \frac{1 + \frac{\kappa-1}{2} M_1^2}{1 + \frac{\kappa-1}{2} M^2}$	$\frac{h}{h^*} = \frac{\frac{1+\kappa}{2}}{1 + \frac{\kappa-1}{2} M^2}$
$\frac{V}{V_1} = \frac{M}{M_1} \left( \frac{1 + \frac{\kappa-1}{2} M_1^2}{1 + \frac{\kappa-1}{2} M^2} \right)^{\frac{1}{2}}$	$\frac{V}{V^*} = M \left( \frac{\frac{1+\kappa}{2}}{1 + \frac{\kappa-1}{2} M^2} \right)^{\frac{1}{2}}$
$\frac{\rho}{\rho_1} = \frac{v_1}{v} = \left( \frac{1 + \frac{\kappa-1}{2} M_1^2}{1 + \frac{\kappa-1}{2} M^2} \right)^{\frac{1}{\kappa-1}}$	$\frac{\rho}{\rho^*} = \frac{v^*}{v} = \left( \frac{\frac{1+\kappa}{2}}{1 + \frac{\kappa-1}{2} M^2} \right)^{\frac{1}{\kappa-1}}$

Laval nozzles were first used in steam turbines, but many other applications for these nozzles have been found, for example, in rocket engines, supersonic steam turbines, etc. In the following, we briefly discuss the operational behavior of a generic Laval nozzle, which is strongly determined by the pressure ratio. Detailed discussion of this topic can be found in excellent books by Spurk [4], Prandtl et al. [5] and Shapiro [6]. Starting with the design operating point, where the exit pressure is set equal to the ambient pressure  $p_e = p_a$ , curve ①, that corresponds to the design area ratio (Fig. 3.27a).

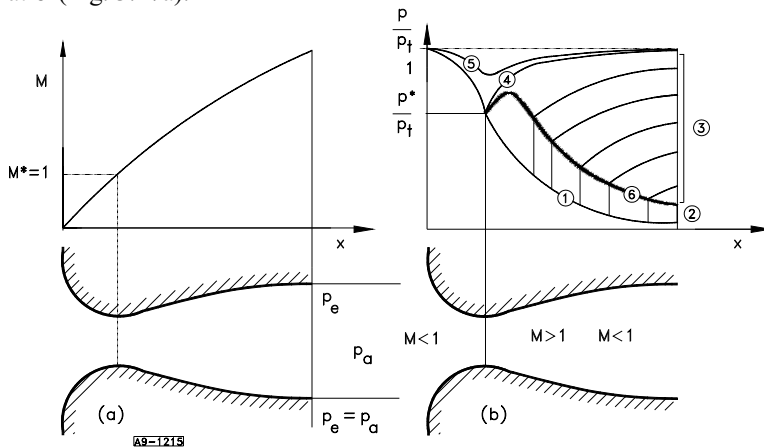


**Fig. 3.27** Operational behavior of a generic Laval nozzle, (a) Expansion to the design exit pressure, (b) Overexpansion.

In this case, the Mach number continuously increases from the subsonic at the inlet to the supersonic at the exit. Increasing the ambient pressure results in an overexpanded jet, because the flow in the nozzle expands above a pressure that does not correspond to its design pressure: point ② with  $p_e < p_a$ . At this pressure condition, the flow pattern inside the nozzle does not change as curve ① indicates. However, outside the nozzle, the flow undergoes a system of *oblique shocks* that emanate from the rim of the nozzle, raising the lower nozzle discharge pressure discontinuously to the ambient pressure. The shock surfaces intersect and are reflected at the jet boundary as steady *expansion waves* (Fig. 3.28).

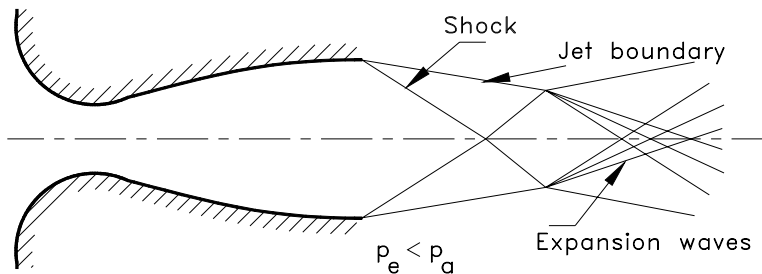


**Fig. 3.28** Overexpanded jet



A rhombic pattern, characteristic of supersonic jets, arises and this is sometimes visible to the naked eye in exhaust jets of rocket engines. If the ambient pressure is further raised, the shock moves into the nozzle and forms a *normal shock wave* in the nozzle, curves ③. This discontinuous pressure increase positions itself in the nozzle just so that the required ambient pressure is reached. Behind the shock, the flow is subsonic. The section of the nozzle behind the shock then works as a subsonic diffuser, which theoretically raises the pressure behind the shock to the ambient pressure. However, in practice, a flow separation occurs and the actual gain in pressure is so small that the pressure behind the shock is actually about the same as the ambient pressure. If the ambient pressure is raised even further, it curves, the shock migrates into the nozzle, and it becomes weaker, since the Mach number in front of the shock becomes smaller. If the ambient pressure is increased such that the shock finally reaches the throat of the nozzle, the shock strength drops to zero and the whole nozzle contains subsonic flow, curve ④. If we increase  $p_a$  even further, the Mach number has a maximum at the throat, but  $M = 1$  is no longer reached, curve ⑤. The geometric locations of all pressure discontinuities are also shown in Fig. 3.27, curve ⑥.

In *under-expanded jets*, the pressure at the nozzle exit  $p_e$  is larger than the ambient pressure  $p_a$  (Fig. 3.29).

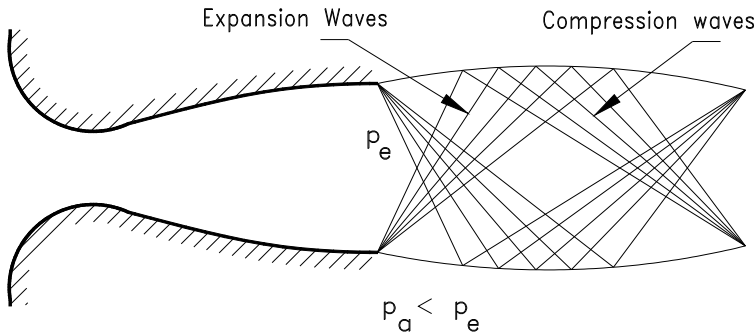


**Fig. 3.29** Under-expanded jet

The pressure is reduced to the ambient pressure through a system of stationary *expansion waves*. The flow in the nozzle remains unaffected by this. The expansion waves penetrate into themselves and are then reflected at the boundary of the jet as *compression waves* and these often reform themselves into a shock. In this manner, a rhombi pattern is set up in the jet again similar to the over-expanded jets.

In a convergent nozzle, no steady supersonic flow can be formed in the above stated manner. As long as the ambient pressure  $p_a$  is larger than the critical pressure  $p^*$ , the pressure in the jet  $p_e$  is the same as the ambient pressure  $p_a$  (Fig. 3.29). If the Mach number,  $M = 1$ , is reached at the smallest cross-section, then  $p_e = p^*$  and the ambient pressure can be decreased below this pressure ( $p_a < p_e$ ). Next, an after-expansion takes place in the free jet and the pressure at the nozzle exit is expanded to the ambient pressure  $p_a$  again through stationary expansion waves (Fig. 3.30).

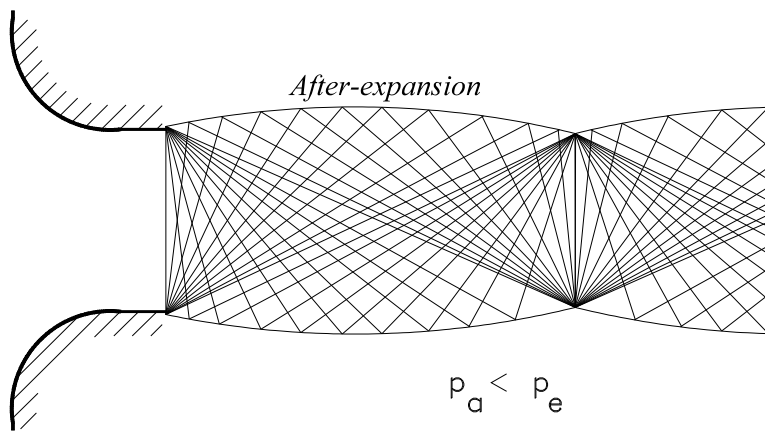


Fig. 3.30 Subsonic nozzle with after expansion

### 3.7.3 Compressible Flow through Channels with Constant Cross Section

This type of flow is encountered in several components of turbomachines such pipes, labyrinth seals, and to a certain degree of simplicity, in combustion chambers and afterburners of supersonic jet engines. In the case of pipes and labyrinth seals, we are dealing with an adiabatic flow process, where the total enthalpy remains constant. However, entropy increases are present due to the internal friction, shocks, or throttling. Combustion chambers and afterburners can be approximated by a constant cross section pipe with heat addition or rejection. The characteristic features of these devices are that the entropy changes are caused by heat addition, such that the friction contribution to the entropy increase can be neglected. This assumption leads to a major simplification that we may add heat to a constant cross section pipe and assume that the impulse remains constant. The constant total enthalpy is described by the *Fanno process*, whereas the constant impulse case is determined by the *Rayleigh process*.

Starting with the Rayleigh process, we will specifically consider the flow in a duct with a constant cross-section, without surface or internal friction, but with heat transfer through the wall. In the absence of the shaft power, Eq. (3.16) is modified to:

$$\frac{V_2^2}{2} + h_2 = \frac{V_1^2}{2} + h_1 + q. \quad (3.81)$$

In the application of the momentum balance, we assume here that the contribution of the friction forces to the total entropy increase compared to the entropy increase by external heat addition is negligibly small, thus the friction in Eq. (3.4) is  $F_r = 0$ . This results in:

$$\rho_2 V_2^2 + p_2 = \rho_1 V_1^2 + p_1 = \rho V^2 + p = \text{const.} \quad (3.82)$$

To find the flow quantities for the Rayleigh process, we present the calculation of a pressure ratio. The other quantities such as velocity ratio, temperature ratio, density ratio, etc., are obtained using a similar procedure. We start with the calculation of the pressure ratio by utilizing the following steps.

**Step 1:** We combine the differential form of the momentum equation,

$$dp + 2\rho VdV + d\rho V^2 = 0 \quad (3.83)$$

with the differential form of continuity equation for a constant cross section,

$$d\rho V + \rho dV = 0 \quad (3.84)$$

and obtain the modified momentum equation. This equation can immediately be found from the 1-D Euler equation.

$$Vdp + VdV = 0 \quad (3.85)$$

We rearrange the modified momentum equation by introducing the Mach number

$$\frac{dp}{p} = -\frac{VdV}{\rho p} = -\frac{VdV}{RT} = -\kappa M^2 \frac{dV}{V} \quad (3.86)$$

**Step 2:** We combine the differential form of the continuity equation (3.84) with the differential form of the equation of state for ideal gases. With this step we eliminate the density from Eq. (3.84), we have

$$\frac{dV}{V} + \frac{dp}{p} = \frac{dT}{T} \quad (3.87)$$

To eliminate the velocity ratio in Eqs. (3.86) and (3.87), we use the definition of the Mach number. Its differentiation yields

$$\frac{dV}{V} = \frac{dM}{M} + \frac{1}{2} \frac{dT}{T} \quad (3.88)$$

**Step 3:** Inserting the velocity ratio (3.88) into momentum equation (3.86) and the equation of motion (3.84), we obtain for the pressure ratio,

$$\frac{2}{\kappa M^2} \frac{dp}{p} - 2 \frac{dM}{M} = \frac{dT}{T} \quad (3.89)$$

We also replace in continuity equation (3.87) the velocity ratio with Eq. (3.88) and find a second equation for temperature ratio,

$$\frac{2dp}{p} + \frac{2dM}{M} = \frac{dT}{T} \quad (3.90)$$

**Step 4:** Equating (3.89) and (3.90), we find

$$\frac{dp}{p} = \frac{2\kappa M dM}{1 + \kappa M^2} \quad (3.91)$$

The above equation can be integrated between any two positions including the one where  $M = 1$

$$\frac{p_2}{p_1} = \frac{1 + \kappa M_1^2}{1 + \kappa M_2^2} \quad (3.92)$$

and for the critical state

$$\frac{p}{p^*} = \frac{1 + \kappa}{1 + \kappa M^2} \quad (3.93)$$

In a similar manner, the temperature ratio calculated as,

$$\frac{dT}{T} = 2 \frac{dM}{M} \left( \frac{1 - \kappa M_1^2}{1 + \kappa M_2^2} \right) \quad (3.94)$$

Considering the initial assumption of calorically perfect gas, the integration gives,

$$\frac{T_2}{T_1} = \frac{h_2}{h_1} = \frac{M_2^2}{M_1^2} \left( \frac{1 + \kappa M_1^2}{1 + \kappa M_2^2} \right)^2 \quad (3.95)$$

and relative to critical state, we have

$$\frac{T}{T^*} = \frac{h}{h^*} = M^2 \left( \frac{1 + \kappa}{1 + \kappa M^2} \right)^2 \quad (3.96)$$

In the same manner, we find the flow quantities such as the velocity, density, and specific volume ratios for the Rayleigh process as functions of the Mach number. These quantities are listed in Table 3.2. With these quantities as functions of a Mach number, the entropy change is determined by using any of the two equations (3.40) or (3.41).

$$\Delta s = c_p \ln \left[ \left( \frac{T_2}{T_1} \right) \left( \frac{p_1}{p_2} \right)^{\frac{\kappa-1}{\kappa}} \right] = c_v \ln \left[ \left( \frac{T_2}{T_1} \right) \left( \frac{v_2}{v_1} \right)^{\kappa-1} \right] \quad (3.97)$$

In terms of critical state:

$$\Delta s = s - s^* = c_p \ln \left[ \left( \frac{T}{T^*} \right) \left( \frac{p^*}{p} \right)^{\frac{\kappa-1}{\kappa}} \right] = c_v \ln \left[ \left( \frac{T}{T^*} \right) \left( \frac{v}{v^*} \right)^{\kappa-1} \right] \quad (3.98)$$

Replacing the temperature and pressure ratios by the corresponding functions listed in Table 3.2, we find

$$\frac{s - s^*}{c_p} = \ln M^2 \left( \frac{k + 1}{1 + \kappa M^2} \right)^{\frac{\kappa+1}{\kappa}} \quad (3.99)$$

The above properties can be determined by varying the Mach number. As mentioned previously, a Rayleigh curve is the locus of all constant momentum processes. It can be easily constructed by varying the Mach number and finding the corresponding, enthalpy, pressure, or entropy ratios. Table 3.2: Summary of steps and equations for construction of Rayleigh and Fanno curves.

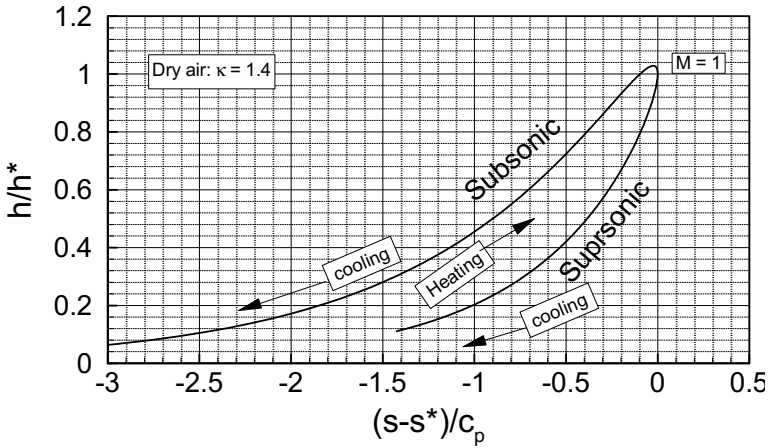
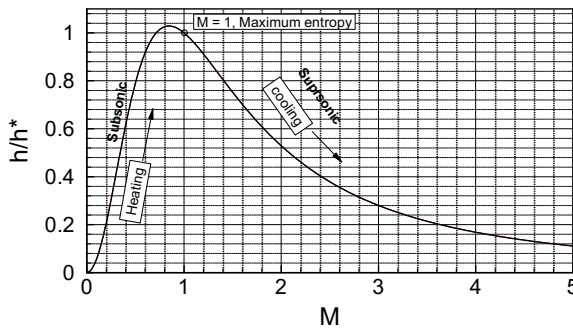


**Fig. 3.31:** Dimensionless  $h$ - $s$  diagram for Rayleigh process for dry air assumed as a perfect gas, upper (subsonic acceleration) branch indicates the heat addition ( $ds > 0$ ) to reach sonic speed ( $M = 1$ ), lower branch (supersonic acceleration) caused by the heat rejection ( $ds < 0$ ).

Table 3.2: Table 3.2: Steps for construction of Rayleigh and Fanno curves.

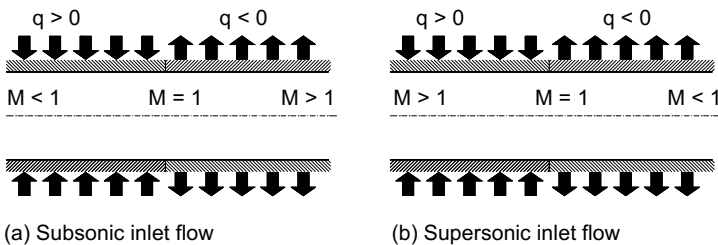
Rayleigh Characteristics	Fanno Characteristics
$\frac{A}{A^*} = 1$	$\frac{A}{A^*} = 1$
① $\frac{p}{p^*} = \left( \frac{\kappa + 1}{1 + \kappa M^2} \right)$	$\frac{p}{p^*} = \frac{1}{M} \left( \frac{\kappa + 1}{2(1 + \frac{\kappa - 1}{2} M^2)} \right)^{1/2}$
② $\frac{T}{T^*} = M^2 \left( \frac{\kappa + 1}{(1 + \kappa) M^2} \right)^2$	$\frac{T}{T^*} = \frac{\frac{\kappa + 1}{2}}{1 + \frac{\kappa - 1}{2} M^2}$
③ $\frac{h}{h^*} = M^2 \left( \frac{\kappa + 1}{(1 + \kappa) M^2} \right)^2$	$\frac{h}{h^*} = \frac{\frac{1 + \kappa}{2}}{1 + \frac{\kappa - 1}{2} M^2}$
④ $\frac{V}{V^*} = \frac{(k + 1) M^2}{1 + \kappa M^2}$	$\frac{V}{V^*} = M \left( \frac{\frac{1 + k}{2}}{1 + \frac{\kappa - 1}{2} M^2} \right)^{\frac{1}{2}}$
⑤ $\frac{\rho^*}{\rho} = \frac{(k + 1) M^2}{1 + \kappa M^2}$	$\frac{\rho^*}{\rho} = M \left( \frac{\frac{1 + k}{2}}{1 + \frac{\kappa - 1}{2} M^2} \right)^{\frac{1}{2}}$
⑥ $\Delta s = c_p \ln \left[ \left( \frac{T}{T^*} \right) \left( \frac{p^*}{p} \right)^{\frac{\kappa - 1}{\kappa}} \right]$	$\Delta s = c_p \ln \left[ \left( \frac{T}{T^*} \right) \left( \frac{p^*}{p} \right)^{\frac{\kappa - 1}{\kappa}} \right]$
$\frac{s - s^*}{c_p} = \ln M^2 \left( \frac{k + 1}{1 + \kappa M^2} \right)^{\frac{\kappa + 1}{\kappa}}$	$\frac{s - s^*}{c_p} = \ln M^2 \left( \frac{\frac{k + 1}{2}}{M^2 (1 + \frac{\kappa - 1}{2} M^2)} \right)^{\frac{\kappa + 1}{2\kappa}}$

Figure. 3.31 shows the Rayleigh curve in terms of enthalpy ratio as a function of dimensionless entropy difference for dry air as a calorically perfect gas. As seen, it has a subsonic upper branch with  $M < 1$ , a supersonic lower branch, with  $M > 1$  joined by the sonic point with  $M = 1$ . Moving along the subsonic upper branch, the addition of heat causes the specific volume and, consequently, the velocity and the Mach number to increase until the speed of sound ( $M = 1$ ) has been reached. Further increase of the Mach number requires cooling the mass flow. If the inlet mach number is supersonic (lower branch), a continuous addition of heat will cause a flow deceleration up to  $M = 1$ . Further deceleration requires a continuous heat rejection along the subsonic upper branch.



**Fig. 3.32:** Change of Mach number in a constant area channel with heat addition, rejection.

Figure 3.32 shows the enthalpy (or temperature) distribution as a function of a Mach number. The flow acceleration and deceleration as a result of heat addition/rejection is illustrated in a fictive channel shown in Fig. 3.33. To emulate the Rayleigh process, we think of a channel that consists of two parts having the same type of heat conductive material and the same cross section.



**Fig. 3.33:** A fictive channel for realization of Rayleigh process, (a) subsonic acceleration with heat addition and rejection, (b) supersonic deceleration with heat addition and rejection.

The parts are joined together by a thin, perfect heat insulating joint such that no heat can flow through it from either side. We assume that the streamwise location of the

joint coincides with the streamwise location of the point with  $M = 1$ . Starting with a subsonic inlet Mach number, Fig. 3.33(a), an amount of heat is added such that the increase in specific volume causes the velocity to increase, Fig. 3.31 (upper branch), and Fig. 3.32. To go beyond the speed of sound, heat needs to be rejected, Fig. 3.31 (lower branch), and 3.32. In the absence of the heat rejection, an increase of velocity is not possible. The channel will choke. Figure 3.33(b) shows the Rayleigh process that starts with a supersonic inlet. To decelerate the flow, heat is added such that the speed of sound is reached. Further deceleration requires a reduction of specific volume which is established by rejecting the heat. As seen, the preceding Rayleigh process was characterized by reversibly adding and rejecting heat at a constant momentum that resulted in flow acceleration or deceleration.

We now consider the case of Fanno process. It is characterized by constant total enthalpy, where no heat is added or rejected from a duct of constant cross-section. The flow is considered as non-isentropic, where internal, as well as, wall friction may exist. As a result, the static enthalpy experiences a continuous decrease, while the velocity increases. To generate the Fanno curve, first the flow quantities are expressed in terms of Mach number in a manner similar to the Rayleigh process presented above. The corresponding relations are summarized in Table 3.1, 1.

Applying the energy, continuity, and impulse to an adiabatic constant cross-section duct flow, we find the pressure ratio from:

$$\frac{p}{p^*} = \frac{1}{M} \left( \frac{\kappa + 1}{2(1 + \frac{\kappa-1}{2}M^2)} \right)^{\frac{1}{2}} \quad (3.100)$$

The other thermodynamic properties are calculated from:

$$\frac{T}{T^*} = \frac{\frac{\kappa + 1}{2}}{1 + \frac{\kappa-1}{2}M^2}, \quad \frac{h}{h^*} = \frac{\frac{1 + \kappa}{2}}{1 + \frac{\kappa-1}{2}M^2}, \quad \frac{\rho^*}{\rho} = M \left( \frac{\frac{1 + \kappa}{2}}{1 + \frac{\kappa-1}{2}M^2} \right)^{\frac{1}{2}} \quad (3.101)$$

Finally, the velocity ratio is given by

$$\frac{V}{V^*} = M \left( \frac{\frac{1 + \kappa}{2}}{1 + \frac{\kappa-1}{2}M^2} \right)^{\frac{1}{2}} \quad (3.102)$$

Taking the pressure and temperature ratios from Eqs. (3.100) and (3.101), we obtain the entropy difference from,

$$s - s^* = \Delta s = c_p \ln \left[ \left( \frac{T}{T^*} \right) \left( \frac{p^*}{p} \right)^{\frac{\kappa-1}{\kappa}} \right] \quad (3.103)$$



or in terms of Mach number, we obtain

$$\frac{\Delta s}{c_p} = \frac{s - s^*}{c_p} = \ln M^2 \left( \frac{\frac{k+1}{2}}{M^2 \left(1 + \frac{\kappa-1}{2} M^2\right)} \right)^{\frac{\kappa+1}{2\kappa}} \quad (3.104)$$

the Fanno curve in an  $h$ - $s$  diagram plotted in Fig. 3.34. This curve is valid for a duct flow without heating, independent of the wall and internal friction.

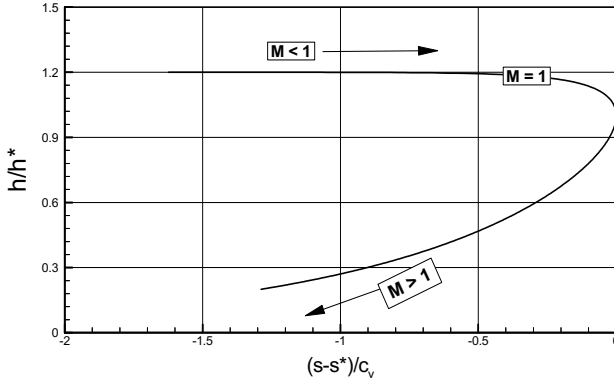


**Fig. 3.34** Fanno curve for ideal two atomic gases ( $\kappa = 1.4$ ).

The upper part of the curve is the subsonic branch and the lower is the supersonic branch. Considering a flow through a long pipe, because of the entropy increase, the static enthalpy, the static pressure, and the density decreases. As a consequence, the velocity increases until the speed of sound with Mach number  $M = 1$  has been reached. A further increase of the velocity pass the speed of sound resulting in  $M > 1$ , requires a decrease in entropy which violates the second law. Therefore, the velocity cannot exceed the speed of sound. Figure. 3.33 shows a typical application of Fanno process. The high pressure side of a steam turbine shaft is sealed against the atmospheric pressure. To reduce the mass flow that escapes from the process through the radial gap between the shaft and the casing, labyrinth seals are installed on the shaft and in the casing, Fig. 3.35 (a).

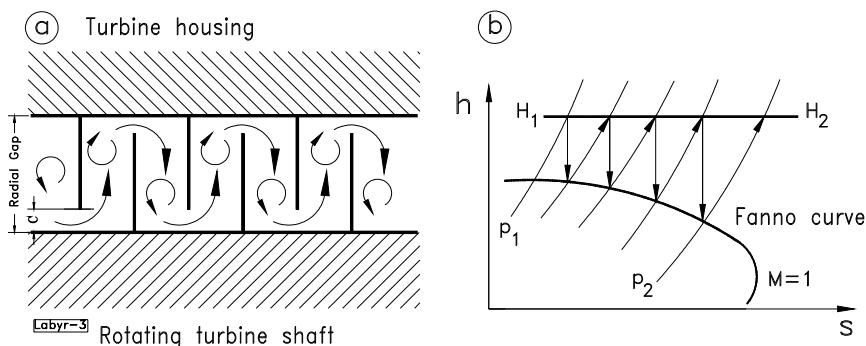


**Fig. 3.35** Flow through a labyrinth seal of turbomachine (a) dissipation of kinetic energy, (b) Fanno process.

High pressure steam enters the gap and expands through the clearance  $C$ , where its potential energy is converted into kinetic energy. By entering the cavity, the kinetic energy is dissipated causing a noticeable pressure decrease. The process of expansion and dissipation repeats in the following cavities resulting in a relatively small mass flow that leaves the turbine. The end points of all expansions through the clearances are located on a Fanno line, which corresponds to a constant total enthalpy.

In Table 3.2, the equations are summarized and steps are marked that are necessary for construction of Rayleigh and Fanno lines. Fanno and Rayleigh curves are constructed using the following steps. In step ① the Mach number is varied and the corresponding thermodynamic properties are calculated from steps ② to ⑤. With the temperature and pressure ratios calculated in steps ① and ②, the entropy can be calculated. These steps were performed to plot Fig. 3.31 and Fig. 3.32. Once the thermodynamic properties are calculated, different versions of Fanno and Rayleigh curves can be constructed easily.

### 3.7.4 The Normal Shock Wave Relations

In explaining the design and off-design behavior of a Laval nozzle, on several occasions, we used the terms normal shock and oblique shock without getting into details of their calculation. This section is intended to cover the basic physics of the shock phenomenon and how to calculate the thermo-fluid states before and after the shock. Detailed discussion of this topic can be found in excellent books by Spurk [2], Prandtl et al.[3] and Shapiro [4].

The normal shock occurs when a supersonic flow encounters a strong perturbation. If a supersonic flow impinges on a blunt body, it will generate a normal shock in front of the body. Behind the shock, the flow velocity becomes subsonic causing the pressure, density and temperature to rise. The transition from supersonic to subsonic velocity occurs within a thin surface with a thickness that has an order of magnitude of the mean free path of the fluid. Thus, in gas dynamics it is approximated as a surface discontinuity with an infinitesimally small thickness. In a normal shock, the velocity vectors before and after the shock are perpendicular to the shock surface. In an oblique shock, however, the velocity vectors are not perpendicular to the shock

surface. In contrast to the normal shock, in oblique shock the velocity after the shock may still be supersonic.

Given the quantities in front of the shock, the quantities behind the shock can be determined using the conservation laws presented in this chapter. We assume that changes in flow quantities up- and downstream of the actual shock compared to the changes within the shock itself is negligibly small. Furthermore, we assume a steady adiabatic flow and, considering the infinitesimal thickness of the shock, we neglect the volume integrals. In addition, we assume that the inlet and exit control surfaces are approximately equal ( $S_1 \approx S_2$ ) and the wall surface  $S_w$  is very small, Fig. 3.36.

In the following, using the conservation laws and the known thermo-fluid quantities in front of the normal shock we develop relations which allow the calculation of the quantities behind the shock. Using the control volume in Fig. 3.36, we apply the continuity equation,

$$\rho_1 V_1 = \rho_2 V_2, \quad (3.105)$$

the balance of momentum,

$$\rho_1 V_1^2 + p_1 = \rho_2 V_2^2 + p_2, \quad (3.106)$$

and the balance of energy,

$$\frac{V_1^2}{2} + h_1 = \frac{V_2^2}{2} + h_2, \quad (3.107)$$

where the subscript 1 denotes the position just in front of the shock and the subscript 2 the position just behind (Fig. 3.36).

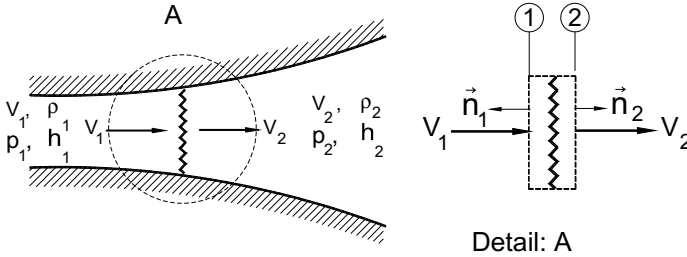


**Fig. 3.36:** Normal shock in divergent part of a supersonic nozzle.

Since the control volume that contains the shock front has an infinitesimally small width, the areas on both sides of the shock front are the same. This is true even if the cross-section of the duct as shown in Fig. 3.36 varies. In addition to the conservation laws, we introduce the equation of state to have the corresponding number of equations necessary to find the unknowns. This can be taken from steam or gas tables

$$p = p(\varrho, h) \quad (3.108)$$

For the perfect gas approximation, the equation of state is reduced to

$$p = \varrho RT \equiv \varrho h \frac{\kappa - 1}{\kappa} \quad (3.109)$$

With Eqs. (3.105) to (3.109), the state behind the shock can be determined. Inserting the continuity Eq. (3.105), into the momentum Eq. (3.106) and energy Eq. (3.107), we find the pressure difference

$$p_2 - p_1 = \varrho_1 V_1^2 \left( 1 - \frac{\varrho_1}{\varrho_2} \right) \quad (3.110)$$

and the enthalpy difference

$$h_2 - h_1 = \frac{V_1^2}{2} \left[ 1 - \left( \frac{\varrho_1}{\varrho_2} \right)^2 \right]. \quad (3.111)$$

After eliminating the velocity  $V_1$  from Eqs. (3.110) and (3.111) we obtain a relationship between the thermodynamic quantities, the so-called *Hugoniot relation*:

$$h_2 - h_1 = \frac{1}{2} (p_2 - p_1) \left( \frac{1}{\varrho_1} + \frac{1}{\varrho_2} \right), \quad (3.112)$$

Using Eq. (3.109), for a perfect gas we find the following relation:

$$\frac{p_2}{p_1} = \frac{\frac{(\kappa + 1)}{(\kappa - 1)} \frac{\varrho_2}{\varrho_1} - 1}{\frac{(\kappa + 1)}{(\kappa - 1)} - \frac{\varrho_2}{\varrho_1}} \quad (3.113)$$

between the pressure and the density ratios. Equation (3.113) indicates that for the following density ratio

$$\frac{\varrho_2}{\varrho_1} = \frac{\kappa + 1}{\kappa - 1} \quad (3.114)$$

the pressure ratio approaches infinity. Figure 3.37 shows the pressure ratios for a normal shock as well as for an isentropic process.

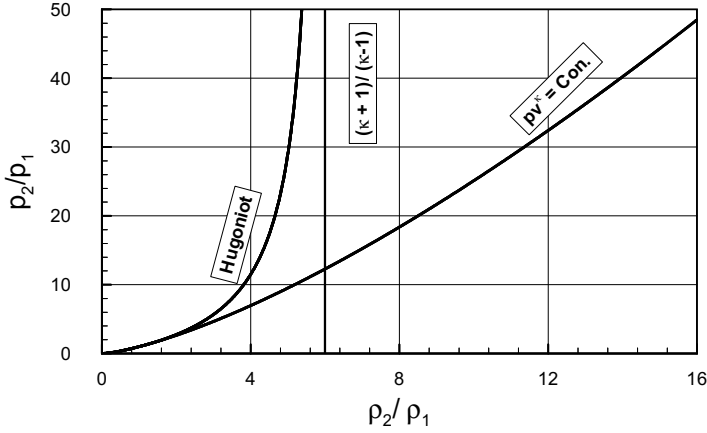


**Fig. 3.37** Shock and isentropic compression.

The working medium used in calculating the Hugoniot curves is air as a two-atomic gas with the specific heat ratio  $\kappa = c_p/c_v = 7/5$ . For comparison purposes, Figure 3.37 also contains the pressure ratio for an isentropic process. While in case of normal shock with  $p_2/p_1 \rightarrow \infty$  the density ratio approaches a finite value of  $(\kappa+1)/(\kappa-1) = 6.0$ , the same ratio results in an infinitely large density ratio  $\rho_2/\rho_1$  for isentropic flow. As we will see in the following, this large pressure ratio caused by a strong shock is associated with a strong entropy increase. The limit for the temperature ratio can also be obtained by using equation of state applied before and after the shock

$$\frac{T_2}{T_1} = \frac{p_2}{p_1} \frac{\rho_1}{\rho_2} \quad (3.115)$$

Setting in Eq. (3.115) the limit  $p_2/p_1 \rightarrow \infty$  results in  $T_2/T_1 = \infty$ . From Eq. (3.110) the velocity can be obtained as:

$$V_1^2 = \frac{p_1}{\rho_1} \left( \frac{p_2}{p_1} - 1 \right) \left( 1 - \frac{\rho_1}{\rho_2} \right)^{-1} \quad (3.116)$$

Introducing the speed of sound  $c^2 = \kappa p/\rho$  for calorically perfect gases, Eq. (3.116) can be modified as:

$$\left( \frac{V_1}{c_1} \right)^2 = M_1^2 = \frac{1}{\kappa} \left( \frac{p_2}{p_1} - 1 \right) \left( 1 - \frac{\rho_1}{\rho_2} \right)^{-1} \quad (3.117)$$

from which we can eliminate  $\varrho_1/\varrho_2$  using the Hugoniot relation (3.113). Thus, we arrive at a quadratic equation for pressure ratio with the Mach number in front of the shock as an independent variable

$$\left(\frac{p_2}{p_1} - 1\right)^2 - 2 \frac{\kappa}{\kappa + 1} (M_1^2 - 1) \left(\frac{p_2}{p_1} - 1\right) = 0, \quad (3.118)$$

Solving Eq. (3.118) results in a trivial solution  $p_2/p_1 = 1$  (no shock) and

$$\frac{p_2}{p_1} = 1 + 2 \frac{\kappa}{\kappa + 1} (M_1^2 - 1). \quad (3.119)$$

Equation (3.119) is an explicit relation between the pressure ratio across the shock and the Mach number  $M_1$ . It shows that, in order to establish a pressure ratio  $p_2/p_1 > 1$  the Mach number  $M_1$  must be greater than one. Even for a transonic Mach number of  $M = 1.1$  a normal shock delivers a pressure ratio of 1.245. In context of compressor design, this pressure ratio is quite significant. To achieve this pressure ratio with a compressor, we need to have at least one compressor stage consisting of a stator and a rotor row. To reduce the number of compressor stages, the compressor designer, whenever possible, takes advantage of pressure increase by normal shocks using transonic and supersonic compressors. These compressors achieve high pressure ratios at lower stage number

Replacing  $p_2/p_1$  in Eq. (3.119) in Hugoniot relation (3.113), we express the density ratio as a function of Mach number:

$$\frac{\varrho_2}{\varrho_1} = \frac{(\kappa + 1)M_1^2}{2 + (\kappa - 1)M_1^2} \quad (3.120)$$

Similarly the temperature ratio is obtained by using Eq. (3.119) and (3.120):

$$\frac{T_2}{T_1} = \frac{p_2}{p_1} \frac{\varrho_1}{\varrho_2} = \frac{(2\kappa M_1^2 - (\kappa - 1))(2 + (\kappa - 1)M_1^2)}{(\kappa + 1)^2 M_1^2}. \quad (3.121)$$

Using Eq. (3.119) and (3.120) in conjunction with the continuity equation, we find the Mach number after the shock

$$M_2^2 = \left(\frac{V_2}{a_2}\right)^2 = V_1^2 \left(\frac{\varrho_1}{\varrho_2}\right)^2 \frac{\varrho_2}{\kappa p_2} = M_1^2 \frac{p_1 \varrho_1}{p_2 \varrho_2}, \quad (3.122)$$

Introducing Eqs. (3.119) and (3.120) into (3.122), we obtain the Mach number behind the shock as:

$$M_2^2 = \frac{\kappa + 1 + (\kappa - 1)(M_1^2 - 1)}{\kappa + 1 + 2\kappa(M_1^2 - 1)}. \quad (3.123)$$

Finally, we obtain the entropy increase due to the normal shock by using the second law applied to a perfect gas:

$$s_2 - s_1 = c_v \ln \left[ \frac{p_2}{p_1} \left( \frac{\rho_2}{\rho_1} \right)^{-\kappa} \right] \quad (3.124)$$

Replacing the pressure and density ratios in Eq. (3.124) by Eqs. (3.119) and (3.120)

$$\frac{s_2 - s_1}{c_v} = \ln \left\{ \left[ 1 + \frac{2\kappa}{\kappa + 1} (M_1^2 - 1) \right] \left[ \frac{(\kappa + 1)M_1^2}{2 + (\kappa - 1)M_1^2} \right]^{-\kappa} \right\} \quad (3.125)$$

we arrive at the entropy relation for normal shock as a function of Mach number  $M_1$ . To estimate the shock strength, Spurk [2] eliminated the density ratio from Eq. (3.124) using Eq. (3.113) and arrived at.

$$s_2 - s_1 = c_v \ln \left\{ \frac{p_2}{p_1} \left( \frac{\frac{\kappa - 1}{\kappa + 1} \frac{p_2}{p_1} + 1}{\frac{\kappa - 1}{\kappa + 1} + \frac{p_2}{p_1}} \right)^{\kappa} \right\} \quad (3.126)$$

As seen from Eq. (3.126) for a strong shock  $p_2/p_1 \rightarrow \infty$ , the entropy difference tends logarithmically to infinity. For a weak shock, Spurk [2] expanded the right-hand side of Eq. (3.126), introduced the shock strength parameter  $p_2/p_1 - 1 = \epsilon$  and found that for a weak shock the entropy increase is of third order with respect to the shock strength:

$$\frac{s_2 - s_1}{c_v} = \frac{\kappa^2 - 1}{12\kappa^2} \epsilon^3 \quad (3.127)$$

The dimensionless thermodynamic properties as well as the Mach number behind the

shock are shown in Fig. 3.38. While temperature, pressure and entropy ratios behind the shock increase with increasing the  $M_1$ , the density ratio as well as the Mach number  $M_2$  approach finite values. As we already saw the density ratio approaches  $(\kappa + 1)/(\kappa - 1) = 6.0$  (for  $\kappa = 1.4$ ). For a very strong shock, the Mach number behind the shock approaches the finite value of

$$M_2 \Big|_{(M_1 \rightarrow \infty)} = \sqrt{\frac{1}{2} \frac{\kappa - 1}{\kappa}} = 0.378 \text{ (for } \kappa = 1.4\text{).} \quad (3.128)$$

### 3.7.5 The Oblique Shock Wave Relations

In the previous section we dealt with the normal shock wave, a special type of shock that is perpendicular to the flow direction. The more prevalent shocks encountered

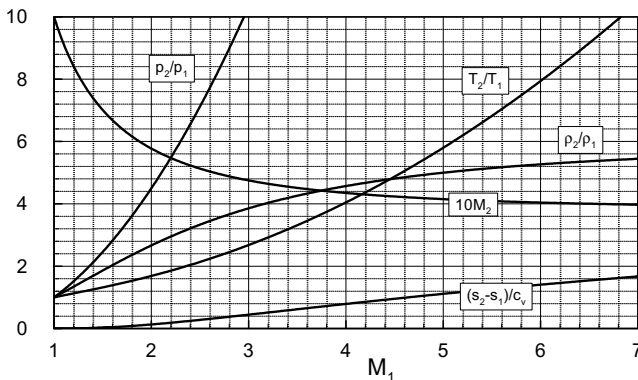


**Fig. 3.38:** Dimensionless thermodynamic properties and the Mach number behind the shock as functions of Mach number ahead of the shock.

in turbomachine flow paths such as transonic turbine or compressor blade channels are the oblique shocks. The basic mechanism of the oblique shock is shown in Fig. 3.39a.

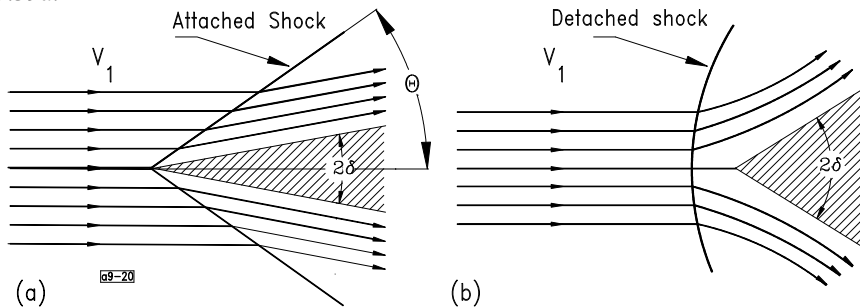


**Fig. 3.39** A qualitative picture of two different shock patterns based on the same supersonic Mach number but different wedge angle  $2\delta$



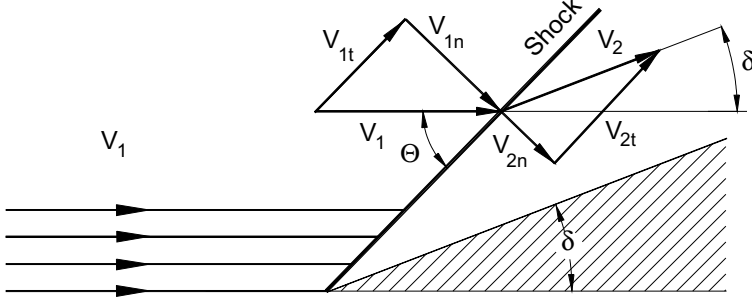


**Fig. 3.40:** Incoming velocity vector  $V_1$  decomposed into normal and tangential components.  $\Theta$  = Shock angle,  $\delta$  = Half wedge angle.

Supersonic flow with uniform velocity  $V_1$  approaches a wedge with a sharp angle  $2\delta$ . A surface discontinuity characterized by an oblique shock wave is formed that builds an angle  $\Theta$  with the flow direction. This particular shock is called the attached shock. Following a streamline by passing through the shock front, the streamline is deflected by an angle which corresponds to the wedge angle  $(2\delta)_a$ . A different shock pattern is observed when the same supersonic flow approaches another wedge with  $(2\delta)_b > (2\delta)_a$ , as shown in Fig. 3.39b. Again, following an arbitrary streamline upstream of the leading edge, a *strong shock* is formed which is detached. Figure 3.39( a) and (b) suggest that, depending on the magnitude of the incoming Mach number and the wedge angle or, generally body bluntness, attached or detached shocks may occur. To establish the corresponding relationships between the Mach number, the wedge angle, and the angle of the oblique shock, we use the same procedure that we applied to the normal shock waves. To do this, we decompose the velocity vector  $V_1$  in front of the shock into a component normal to the shock front  $V_{1n}$ , and a component tangential to the shock front  $V_{1t}$ , as shown in Fig. 3.40. The tangential component is

$$V_{1t} = V_1 \cos \Theta . \quad (3.129)$$

and the normal component follows from

$$V_{1n} = V_1 \sin \Theta , \quad (3.130)$$

Introducing the normal Mach number built with the normal component, we arrive at:

$$M_{1n} = \frac{V_{1n}}{a_1} = M_1 \sin \Theta . \quad (3.131)$$

The thermodynamics properties behind an oblique shock is calculated in a similar manner by using Eqs. (3.119), (3.120) and (3.121) and by replacing  $M_l$ , with  $M_{ln}$ , from (3.131):

$$\frac{p_2}{p_1} = 1 + 2 \frac{\kappa}{\kappa + 1} (M_1^2 \sin^2 \Theta - 1), \quad (3.132)$$

$$\frac{\rho_2}{\rho_1} = \frac{(\kappa + 1) M_1^2 \sin^2 \Theta}{2 + (\kappa - 1) M_1^2 \sin^2 \Theta}, \quad (3.133)$$

$$\frac{T_2}{T_1} = \frac{2\kappa M_1^2 \sin^2 \Theta - (\kappa - 1) \left[ 2 + (\kappa - 1) M_1^2 \sin^2 \Theta \right]}{(\kappa + 1)^2 M_1^2 \sin^2 \Theta}. \quad (3.134)$$

The normal component of the Mach number behind the oblique shock is calculated from:

$$M_{2n} = \frac{V_{2n}}{c_2} = M_2 \sin(\Theta - \delta) \quad (3.135)$$

with  $V_{2n} = V_2 \sin(\Theta - \delta)$  and  $M_2 = V_2 / c_2$ . Relative to the shock front, the normal component  $M_{ln}$ , which might be supersonic, experiences a drastic deceleration resulting in a subsonic normal component  $M_{2n}$  behind the shock. The Mach number  $M_2$ , however, can be supersonic. If we again replace  $M_l$  and  $M_2$  with  $M_{ln}$  and  $M_{2n}$  in the Eq. (3.123) valid for a normal shock, we find:

$$M_2^2 \sin^2(\Theta - \delta) = \frac{\kappa + 1 + (\kappa - 1)(M_1^2 \sin^2 \Theta - 1)}{\kappa + 1 + 2(M_1^2 \sin^2 \Theta - 1)} \quad (3.136)$$

Using the continuity equation, we can transform this into a relation between the shock angle  $\Theta$  and the wedge angle  $\delta$  (Fig. 3.40):

$$\tan \delta = \frac{2 \cot \Theta (M_1^2 \sin^2 \Theta - 1)}{2 + M_1^2 (\kappa + 1 - 2 \sin^2 \Theta)} \quad (3.137)$$

Since the incoming Mach number  $M_1$  and the wedge angle  $\delta$  are supposed to be known, we have with Eqs. (3.136) and (3.137) two equations and two unknowns namely  $\Theta$  and  $M_2$ .

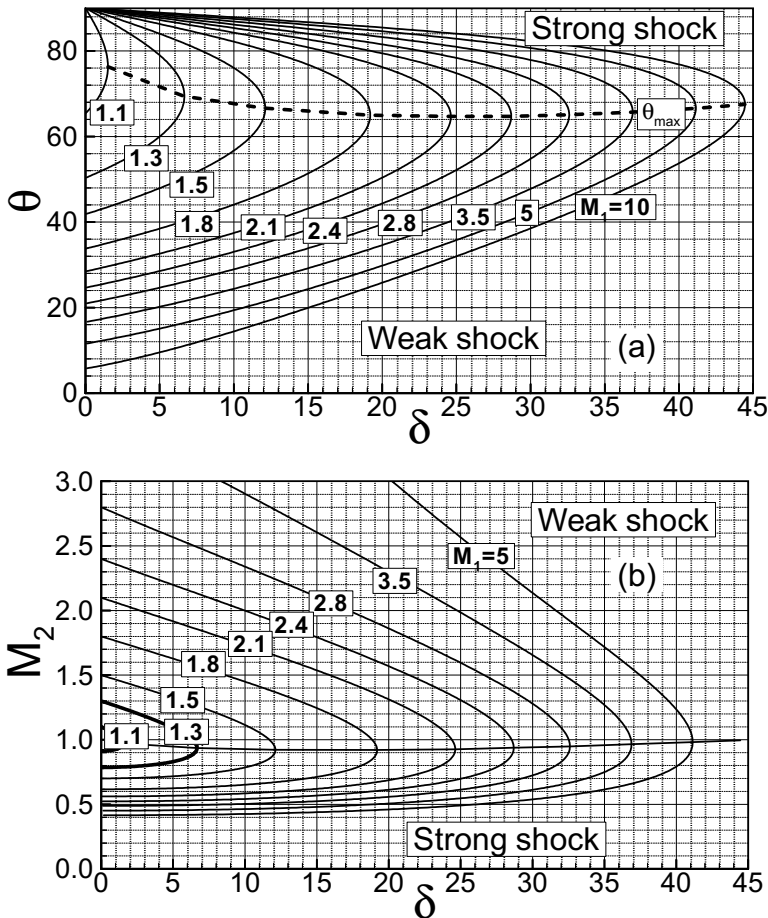


**Fig. 3.41: (a,b):** Shock angle (a) and Mach number (b) as functions of deflection angle with incoming Mach number as parameter.

As shown in Fig. 3.41(a,b) for each given  $\delta$ , two solutions, a *strong shock* and a *weak shock*, can be found based on the magnitude of incoming  $M_1$ . For a given Mach number  $M_1$ , a strong shock is characterized by the shock angle  $\Theta$  that is larger than the maximum shock angle  $\Theta_{max}$  (dashed curve in Fig 3.41a), associated with the maximum deflection  $\delta_{max}$ ; otherwise, the shock is called a *weak shock*. While a strong shock always causes a subsonic flow behind the shock front, in a weak shock the flow velocity behind the shock can be either subsonic or the supersonic. For  $\delta < \delta_{max}$  there are then two possible solutions for the shock angle  $\Theta$ . Which solution actually arises depends on the boundary conditions far behind the shock. Figure 3.41(b) displays the Mach number after the shock. Here again, strong shock leads to a subsonic mach

number after the shock, whereas a weak shock may maintain the supersonic character of the flow.

### 3.7.6 Detached Shock Wave

We now consider deflection angles  $\delta > \delta_{\max}$ ; these lead to flows past “blunt wedges”. If, for a given Mach number  $M_1$  a deflection angle  $\delta$  larger than  $\delta_{\max}$  arises, a *detached shock* is the only possibility. Both strong and weak shocks are then realized in the shock configuration as Fig. 3.41 reveals. Close to the stagnation streamline the wave angle is around  $90^\circ$  (strong shock, subsonic flow behind the shock), while at greater distances from the body the shock deteriorates into a Mach wave ( $\Theta = \mu$ ). It is difficult to calculate the resulting flow behind the shock, since subsonic flow, supersonic flow and flow close to the velocity of sound all appear together (*transonic flow*).

### 3.7.7 Prandtl-Meyer Expansion

Unlike the supersonic flow along a concave surface which was associated with an oblique shock leading to a Mach number  $M_2 < M_1$ , the flow along a convex surface, Fig. 3.42, experiences an expansion process.

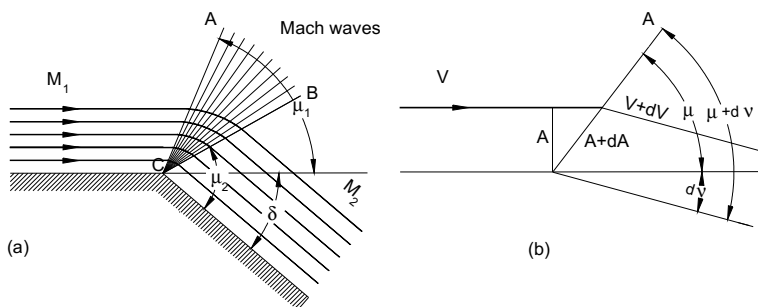


**Fig. 3.42:** Prandtl-Meyer Expansion at a convex corner

The parallel streamlines with the uniform Mach number  $M_1$  passes through a system of expansion or Mach waves, thereby they move apart from each other and accelerate to a new Mach number  $M_2 > M_1$ . The expansion is associated with a deflection of the incoming supersonic flow with the Mach angle  $\mu_1$  to  $\mu_2$ . To calculate the new Mach number, we first consider a supersonic flow around a corner of an infinitesimal deflection,  $dA$ , as shown in Fig. 3.42, and apply the continuity equation (3.79):

$$\frac{dA}{A} = -\frac{dV}{V}(1 - M^2) \quad (3.138)$$

The velocity ratio is expressed in terms of Mach number by utilizing the energy equation

$$\frac{dV}{V} = \frac{dM}{M(1 + \frac{\kappa - 1}{2}M^2)} \quad (3.139)$$

Inserting Eq. (3.139) into (3.138), we obtain:

$$\frac{dA}{A} = \frac{(M^2 - 1)dM}{M(1 + \frac{\kappa - 1}{2}M^2)} \quad (3.140)$$

The geometric relation from Fig. 3.42 reads:

$$\frac{A + dA}{A} = \frac{\sin(\mu + dv)}{\sin\mu} = \frac{\sin\mu \cos dv + \cos\mu \sin dv}{\sin\mu} = 1 + dv \cot\mu \quad (3.141)$$

In Eq. (3.141), we assumed  $dv$  as infinitesimally small allowing to set:  $\cos dv = 1$  and  $\sin dv = dv$ . With this approximation, Eq. (3.141) becomes:

$$\frac{dA}{A} = dv \cot\mu = dv \sqrt{M^2 - 1} \quad (3.142)$$

with  $\mu$  as the Mach angle that can be expressed as  $\sin\mu = 1/M$ . Equating (3.142) and (3.140) leads to:

$$dv = \frac{\sqrt{(M^2 - 1)}dM}{M(1 + \frac{\kappa - 1}{2}M^2)} \quad (3.143)$$

and its subsequent integration gives:

$$v = \sqrt{\frac{\kappa + 1}{\kappa - 1}} \arctan\left(\sqrt{\frac{\kappa + 1}{\kappa - 1}} \sqrt{M^2 - 1}\right) - \arctan\sqrt{M^2 - 1} \quad (3.144)$$

This deflection angle  $v$  as well as the Mach angle  $\mu$  equation are plotted in Fig. 3.43. As shown, each arbitrary supersonic Mach number is uniquely associated with a deflection angle  $v$ . As an example, we assume that in Fig. 3.43 the flow has the Mach number  $M_1 = 1.5$  and turns around a corner with an angle  $\delta = 40^\circ$ . For this Mach number, the corresponding deflection angle  $v_1 = 12.2$  is found. After turning around



The incoming supersonic flow impinges on the sharp leading edge and forms a weak oblique shock, followed by an expansion fan. Passing through the shock front, the Mach number, although smaller, remains supersonic. Expansion waves are formed along the suction surface (convex side) of the blade from the leading edge  $L$  to the point  $e$ , where the subsequent Mach wave at point  $e$  intersects the adjacent blade leading edge. Since the angle  $\Theta$  is known, Mach number  $M_e$  at position  $e$  can easily be calculated from Prandtl-Meyer relation.

## References

1. Schobeiri, M.T.: Fluid Mechanics for Engineers, Graduate Textbook, Springer-Verlag, New York, Berlin, Heidelberg, ISBN 978-642-1193-6 published 2010.
2. Schobeiri, M.T.: Engineering Applied Fluid Mechanics, Graduate Textbook, publisher McGraw Hill, Printing on the market since January 15, 2014
3. Schobeiri, M.T., 2012, "Turbomachinery Flow Physics and Dynamic Performance," Second and Enhanced Edition, 725 pages with 433 Figures, Springer-Verlag, New York, Berlin, Heidelberg, ISBN 978-3-642-24675-3, Library of Congress 2012935425.
4. Spurk, J, 1997, "Fluid mechanics," Springer-Verlag, berlin, Heidelberg, New York.
5. Prandtl, L., Oswatisch, K., Wiegand, K., 1984, "Führer durch die Strömungslehre," 8. Auflage, Branschweig, Vieweg Verlag.
6. Shapiro, A.H., 1954, "The Dynamics and Thermodynamics of Compressible Fluid Flow," Vol. I, Ronald Press Company, New York, 1954.

## 4 Theory of Turbomachinery Stages

### 4.1 Energy Transfer in Turbomachinery Stages

The energy transfer in turbomachinery is established by means of the stages. A *turbomachinery stage* comprises a row of fixed, guide vanes called *stator blades*, and a row of rotating blades termed *rotor*. To elevate the total pressure of a working fluid, *compressor stages* are used that partially converts the mechanical energy into potential energy. According to the conservation law of energy, this energy increase requires an external energy input which must be added to the system in the form of mechanical energy. Figure 4.1 shows the schematic of an axial compressor stage that consists of one stator and two rotor rows. In general, a *compressor component* starts with a rotor row followed by a stator row. Compressor configurations are also found that start with an *inlet guide vane*. To define a unified station nomenclature for compressor and turbine stages, we identify with station number 1 as the inlet of the stator, followed by station 2 as the rotor inlet, and 3, rotor exit. The absolute and relative flow angles are counted counterclockwise from a horizontal line. This convention allows an easier calculation of the off-design behavior of compressor and turbine stages during a transient operation, as we will see later. This angle definition is different the angle conventions used in literature, [1], [2], [3], and [4].

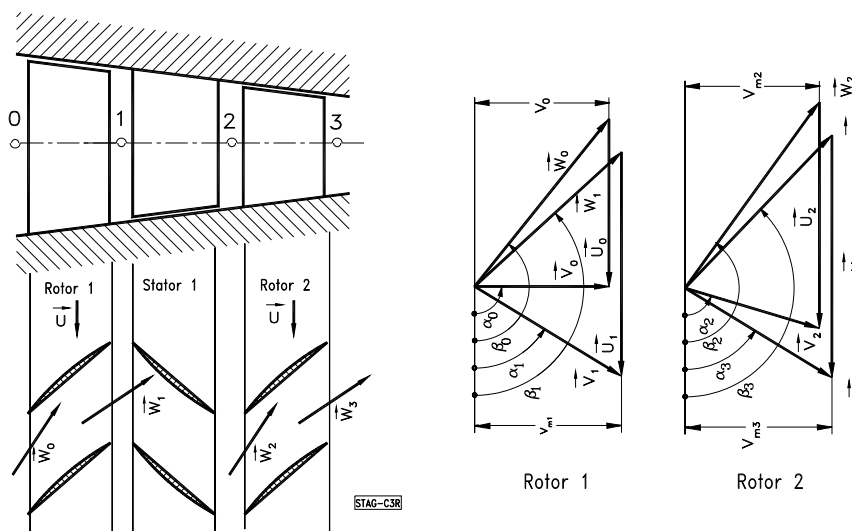


**Fig. 4.1:** An axial compressor stage with a rotor-stator-rotor configuration (left) and velocity diagrams for the first and second rotor (right).



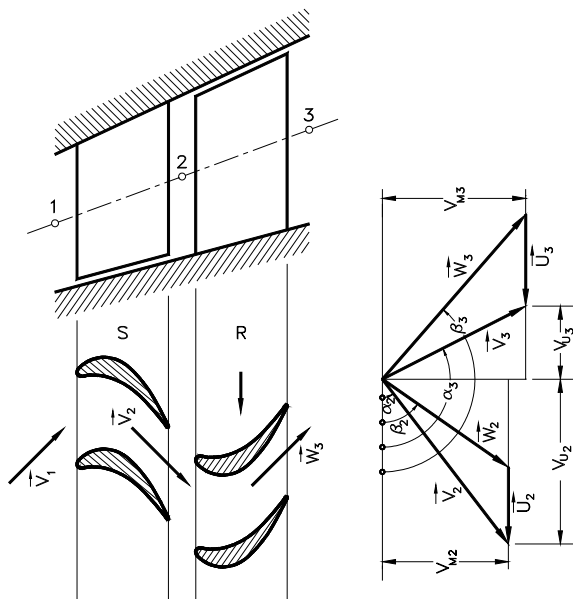


**Fig. 4.2:** An axial turbine stage with velocity diagram.

The working fluid enters the first rotor with an *absolute velocity* in the axial direction, Fig. 4.1 (right), where it is deflected in the direction of the rotor's leading edge.

As a result of the rotational motion of the rotor, a major part of the mechanical energy input is converted into the potential energy of the working medium, causing the total pressure to rise. During the compression process, the absolute velocity within the stator and the relative velocity vector within the rotor decreases. To convert the total energy of a working medium into mechanical energy, *turbine stages* are used. Figure 4.2 exhibits a turbine stage within a multi-stage environment. As shown, the mean diameter and, thus, the flow path cross section increases from inlet to exit. This continuous increase is due to the continuity requirement. The expansion process through a turbine stage causes an increase in specific volume of the working fluid. To keep the axial velocity component nearly the same, the cross section of a turbine stage must increase. Conversely, in compressors, the compression process causes a decrease in specific volume. Keeping the axial velocity component almost the same requires a decrease in cross section in the compression flow direction.

## 4.2 Energy Transfer in Relative Systems

Since the rotor operates in a relative frame of reference (relative system), the energy conversion mechanism is quite different from that of a stator (absolute system). A fluid particle that moves with a relative velocity  $\vec{W}$  within the relative system that rotates with the angular velocity  $\vec{\omega}$ , has an absolute velocity:

$$\mathbf{V} = \mathbf{W} + \boldsymbol{\omega} \times \mathbf{R} = \mathbf{W} + \mathbf{U}, \quad \boldsymbol{\omega} \times \mathbf{R} = \mathbf{U} \quad (4.1)$$

with  $\mathbf{R}$  in Eq. (4.1) as the radius vector of the particle in the relative system. Introducing the absolute velocity vector  $\mathbf{V}$  in the equation of motion, (3.37), and multiplying the results with a relative differential displacement  $d\mathbf{R}$ , we get the energy equation for an adiabatic steady flow within a relative system:

$$d\left(h + \frac{1}{2}\mathbf{W}^2 - \frac{\boldsymbol{\omega}^2 \mathbf{R}^2}{2} + gz\right) = 0 \quad (4.2)$$

or the relative total enthalpy (for details see Chapter 3, Eq. 3.112, 3.113):

$$H_r = h + \frac{1}{2}\mathbf{W}^2 - \frac{\boldsymbol{\omega}^2 \mathbf{R}^2}{2} + gz = \text{const.} \quad (4.3)$$

Neglecting the gravitational term,  $gz \approx 0$ , Eq. (4.3) can be written as:

$$h_1 + \frac{1}{2}\mathbf{W}_1^2 - \frac{1}{2}U_1^2 = h_2 + \frac{1}{2}\mathbf{W}_2^2 - \frac{1}{2}U_2^2 \quad (4.4)$$

Equation (4.4) is the energy equation transformed into a relative system. As can be seen, the transformation of kinetic energy undergoes a change while the transformation of static enthalpy is frame indifferent. With these equations in connection with the energy balance treated in Chapter 3, we can analyze the energy transfer within an arbitrary turbine or compressor stage.

### 4.3 General Treatment of Turbine and Compressor Stages

In this chapter, compressor and turbine stages are treated from a unified physical point of view. Figures 4.3 and 4.4 show the decomposition of a turbine and a compressor stage into their stator and rotor rows. The primes “/” and “//” refer to stator and rotor rows respectively. As seen, the difference between the isentropic and the polytropic enthalpy difference is expressed in terms of dissipation  $\Delta h'_d = \Delta h'_s - \Delta h'$  for turbines and  $\Delta h'_d = \Delta h' - \Delta h'_s$  for compressors. For the stator, the energy balance requires that  $H_2 = H_1$ . This leads to:

$$h_1 - h_2 = \Delta h' = \frac{1}{2}(\mathbf{V}_2^2 - \mathbf{V}_1^2) \quad (4.5)$$

Moving to the relative frame of reference, the relative total enthalpy  $H_{r2} = H_{r3}$  remains constant. Thus, the energy equation for the rotor is according to Eq. (4.4), Fig. 4.4:

$$h_2 - h_3 = \Delta h'' = \frac{1}{2}(\mathbf{W}_3^2 - \mathbf{W}_2^2 + U_2^2 - U_3^2) \quad (4.6)$$

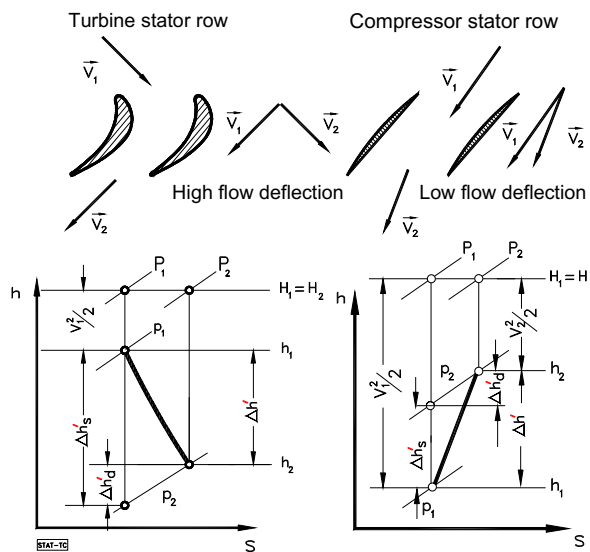


**Fig. 4.3:** Expansion and compression process through a turbine and a compressor stator row.

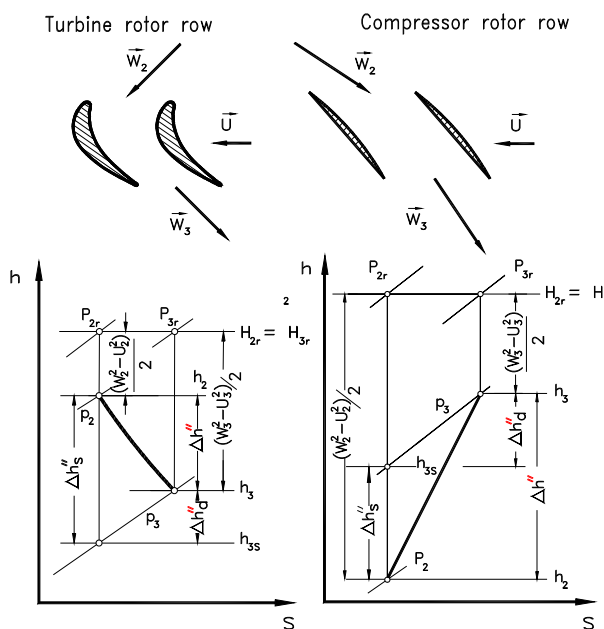


**Fig. 4.4:** Expansion and compression process through a turbine and a compressor rotor row.

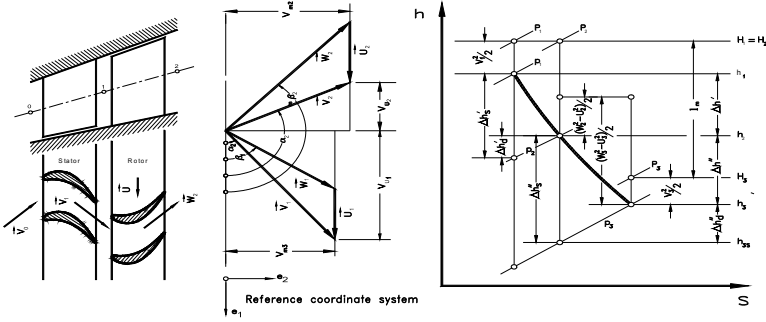


**Fig.4.5:** A turbine stage (left) with the velocity diagram (middle) and the expansion process (right). The direction of the unit vector  $e_1$  is identical with the rotational direction. P: total pressure, p: static pressure.

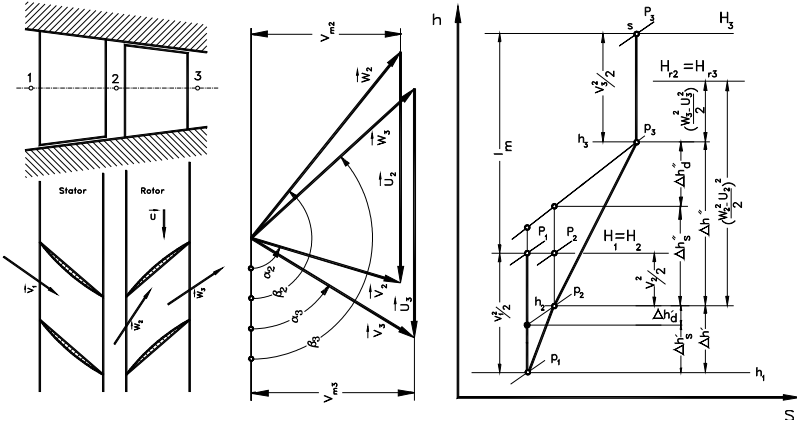


**Fig.5.6:** A compressor stage (left) with the velocity diagram (middle) and the compression  $h$ - $s$ -diagram (right). P: total pressure, p: static pressure.

The stage specific mechanical energy balance requires (Fig. 4.5):

$$l_m = H_1 - H_3 = (h_1 - h_2) - (h_3 - h_2) + \frac{1}{2}(V_1^2 - V_3^2) \quad (4.7)$$

Inserting Eq. (4.5) and (4.6) into (4.7) yields:

$$l_m = \frac{1}{2} \left[ (V_2^2 - V_3^2) + (W_3^2 - W_2^2) + (U_2^2 - U_3^2) \right] \quad (4.8)$$

Equation (4.8), known as the *Euler Turbine Equation*, indicates that the stage work can be expressed simply in terms of absolute, relative, and rotational kinetic energies. This equation is equally applicable to turbine stages that *generate* shaft power and to

compressor stages that *consume* shaft power. In the case of a turbine stage, the sign of the specific mechanical energy  $l_m$  is negative, which indicates that energy is removed from the system (power generation). In compressor cases, it is positive because energy is added to the system (power consumption). Before proceeding with velocity diagrams, it is of interest to evaluate the individual kinetic energy differences in Eq. (4.8). If we wish to design a turbine or a compressor stage with a high specific mechanical energy  $l_m$  for a particular rotational speed, then we have two options: (1) We increase the *flow deflection* that leads to an increase in  $(V_2^2 - V_3^2)$ . (2) We increase the radial difference that leads to a larger  $(U_2^2 - U_3^2)$ . While option (1) is used in axial stages, option (2) is primarily applied to radial stages. These quantities are the characteristics of a stage velocity diagram at the corresponding radial section.

Using the trigonometric relation with the *angle convention* from the velocity diagram in Figs. 4.5 and 4.6, we determine the velocity components and vector relations from:

$$\begin{aligned} V_{m2} &= W_{m2}, \quad V_{m3} = W_{m3} \\ W_2 &= e_1(V_{u2} - U_2) + e_2V_{m2} \\ W_3 &= -e_1(V_{u3} + U_3) + e_2V_{m3} \end{aligned} \quad (4.9)$$

In Eq. (4.9)  $V_m$ ,  $W_m$  and  $V_u$ ,  $W_u$  are the meridional and circumferential components of the absolute and relative velocities, respectively. The corresponding kinetic energy contributions are determined from:

$$\begin{aligned} W_2^2 &= (V_{u2}^2 + V_{m2}^2) + U_2^2 - 2V_{u2}U_2 = V_2^2 + U_2^2 - 2V_{u2}U_2 \\ W_3^2 &= V_{u3}^2 + U_3^2 + 2V_{u3}U_3 + V_{m3}^2 \\ W_3^2 &= V_3^2 + U_3^2 + 2V_{u3}U_3 \end{aligned} \quad (4.10)$$

Incorporating Eq. (4.9) and (4.10) into (4.8) yields the *stage specific work*:

$$l_m = U_2V_{u2} + U_3V_{u3} \quad (4.11)$$

Equation (4.11) is valid for axial, radial, and mixed flow turbines and compressors. A similar relation was obtained in Chapter 4, Eq. (4.46), from the scalar product of moment of momentum and the angular velocity. There, we found the power:  $P = \dot{m}U(V_{u1} - V_{u2})$ . In order to avoid confusions that may arise from different signs, it should be pointed out that in Chapter 4, no angle convention was introduced and the negative sign in Eq. (4.46) was the result of the formal derivation of the conservation law of moment of momentum. This negative sign implies that  $V_{u1}$  and  $V_{u2}$  point in the same direction. The unified angle convention introduced in Figs. 4.1 and

4.2, however, takes the actual direction of the velocity components with regard to a predefined coordinate system.

#### 4.4 Dimensionless Stage Parameters

Equation (4.11) exhibits a direct relation between the specific stage work  $l_m$  and the kinetic energies. The velocities from which these kinetic energies are built can be taken from the corresponding stage velocity diagram. The objective of this chapter is to introduce dimensionless stage parameters that completely determine the stage velocity diagram. These stage parameters exhibit unified relations for compressor and turbine stages respectively.

Starting from a turbine or compressor stage with constant mean diameter and axial components, shown in Fig. 4.7, we define the dimensionless stage parameters that describe the stage velocity diagram of a *normal stage* introduced by Traupel [5]. A normal stage is encountered within the high pressure (HP) part of multi-stage turbines or compressor components and is characterized by  $U_3 = U_2$ ,  $V_3 = V_1$ ,

$V_{m1} = V_{m3}$  and  $\alpha_1 = \alpha_3$ . The similarity of the velocity diagrams allows using the same blade profile throughout the HP-turbine or compressor, thus significantly reducing manufacturing costs.

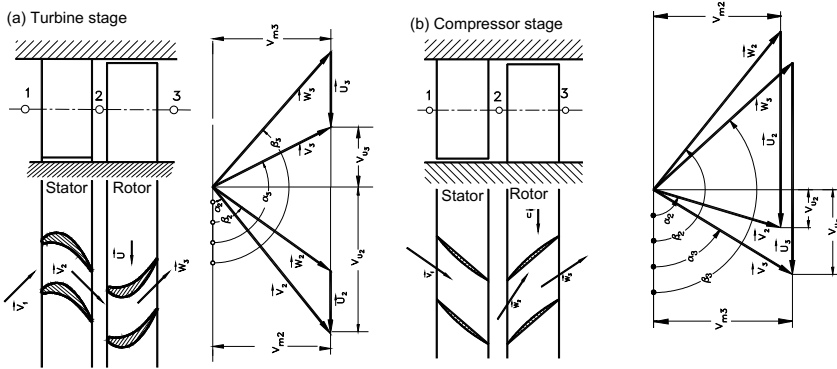


Fig. 4.7: Turbine and compressor stages with the velocity diagrams.

We define the stage flow coefficient  $\phi$  as the ratio of the meridional velocity component and the circumferential component. For this particular case, the meridional component is identical with the axial component:

$$\phi = \frac{V_{m3}}{U_3} \quad (4.12)$$

The stage flow coefficient  $\phi$  in Eq. (4.12) is a characteristic for the mass flow behavior through the stage. The *stage load coefficient*  $\lambda$  is defined as the ratio of the specific stage mechanical energy  $l_m$  and the exit circumferential kinetic energy  $U_3^2$ . This coefficient directly relates the flow deflection given by the velocity diagram with the specific stage mechanical energy:

$$\lambda = \frac{l_m}{U_3^2} \quad (4.13)$$

The stage load coefficient  $\lambda$  in Eq. (4.13) describes the work capability of the stage. It is also a measure for the stage loading. The *stage enthalpy coefficient*  $\psi$  represents the ratio of the isentropic stage mechanical energy and the exit circumferential kinetic energy  $U_3^2$ .

$$\psi = \frac{l_s}{U_3^2} \quad (4.14)$$

The stage enthalpy coefficient represents the stage isentropic enthalpy difference within the stage. Furthermore, we define the *stage degree of reaction*  $r$ , which is the ratio of the static enthalpy difference used in rotor row divided by the static enthalpy difference used in the entire stage:

$$r = \frac{\Delta h''}{\Delta h'' + \Delta h'} \quad (4.15)$$

The degree of reaction  $r$  indicates the portion of energy transferred in the rotor blading. Using Eqs. (4.5) and (4.6), we arrive at:

$$r = \frac{\Delta h''}{\Delta h' + \Delta h''} = \frac{W_3^2 - W_2^2 + U_2^2 - U_3^2}{W_3^2 - W_2^2 + U_2^2 - U_3^2 + V_2^2 - V_1^2} \quad (4.16)$$

Since for the stage type under consideration,  $V_1 = V_3$  and  $U_2 = U_3$ , Eq. (4.16) can be simplified as:

$$r = \frac{W_3^2 - W_2^2}{W_3^2 - W_2^2 + V_2^2 - V_3^2} \quad (4.17)$$

The velocity vectors and the corresponding kinetic energies are determined from the stage velocity diagram in connection with the angle and direction convention as follows:

$$\begin{aligned} V_2 &= e_1(W_{u2} + U_2) + e_2W_{m2}, & V_2^2 &= (W_{u2} + U_2)^2 + W_{m2}^2 \\ V_3 &= -e_1(W_{u3} - U_3) - e_2W_{m3}, & V_3^2 &= (W_{u3} - U_3)^2 + W_{m3}^2 \end{aligned} \quad (4.18)$$

since  $U_2 = U_3 = U$

$$V_2^2 - V_3^2 = W_2^2 - W_3^2 + 2UW_{u2} + 2UW_{u3} \quad (4.19)$$

Using Eqs. (4.18) and (4.19), Eq. (4.17) gives:

$$r = \frac{W_3^2 - W_2^2}{2U(W_{u2} + W_{u3})} = \frac{W_{u3}^2 - W_{u2}^2}{2U(W_{u2} + W_{u3})} \quad (4.20)$$

Re-arranging Equation (4.20) yields the final relationship for the particular stage we introduced above:

$$r = \frac{1}{2} \frac{W_{u3} - W_{u2}}{U} \quad (4.21)$$

#### 4.5 Relation Between Degree of Reaction and Blade Height for a Normal Stage Using Simple Radial Equilibrium

In axial flow compressors or turbines, the working fluid has a rotational and translational motion. The rotating fluid is subjected to centrifugal forces that must be balanced by the pressure gradient in order to maintain the radial equilibrium. Consider an infinitesimal sector of an annulus with unit depth containing the fluid element which is rotating with tangential velocity  $V_u$ .

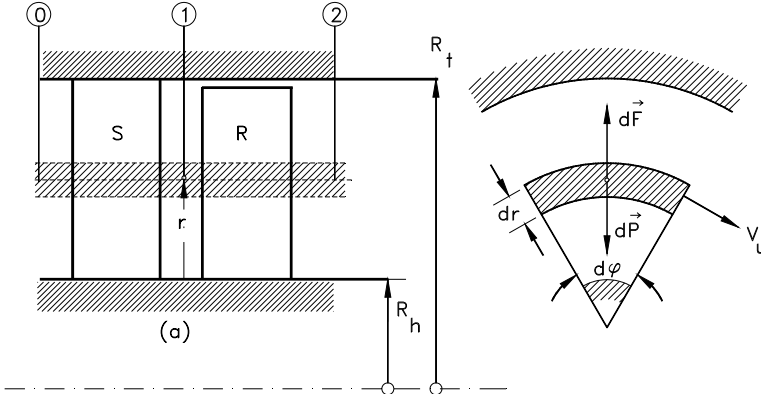


**Fig. 4.8:** Explanation for simple radial equilibrium

The centrifugal force acting on the element is shown in Fig. 4.8. Since the fluid element is in radial equilibrium, the centrifugal force per unit width is obtained from:

$$dF = dm \frac{V_u^2}{R} \quad (4.22)$$

with  $dm = \rho R dR d\phi$ . The centrifugal force is kept in balance by the pressure forces:



$$\frac{dp}{dR} = \rho \frac{V_u^2}{R} \quad (4.23)$$

This result can also be obtained by decomposing the Euler equation of motion (3.46) for inviscid flows in its three components in a cylindrical coordinate system. The Euler equation is expressed as:

$$\mathbf{V} \cdot \nabla \mathbf{V} = -\frac{1}{\rho} \nabla p \quad (4.24)$$

In the radial direction:

$$V_r \frac{\partial V_r}{\partial R} + V_u \frac{\partial V_r}{R \partial \phi} + V_z \frac{\partial V_r}{\partial z} - \frac{V_u^2}{R} = -\frac{1}{\rho} \frac{\partial p}{\partial R} \quad (4.25)$$

The assumptions needed to arrive at Eq. (4.23) are:

$$\frac{\partial V_r}{\partial R} \approx 0, \quad \text{Axial symmetric: } \frac{\partial V_r}{\partial \phi} = 0, \quad \frac{\partial V_r}{\partial z} \approx 0 \quad (4.26)$$

With these assumptions, Eq. (4.24) yields:

$$\frac{1}{\rho} \frac{\partial p}{\partial R} = \frac{V_u^2}{R}, \quad (4.27)$$

Equation (4.27) is identical to Eq. (4.23). Calculation of the static pressure gradient requires additional information from the total pressure relation. For this purpose, we apply the Bernoulli equation neglecting the gravitational term:

$$P = p + \frac{1}{2} \rho V^2 = p + \frac{1}{2} \rho (V_u^2 + V_{ax}^2 + V_r^2) \quad (4.28)$$

with  $V_u$ ,  $V_{ax}$ ,  $V_r$  as the velocity components in circumferential, axial and radial directions. Using Eq. (4.28), the change in radial direction is:

$$\frac{dP}{dR} = \frac{dp}{dR} + \rho V_u \frac{dV_u}{dR} + \rho V_{ax} \frac{dV_{ax}}{dR} + \rho V_r \frac{dV_r}{dR} \quad (4.29)$$

For a constant total pressure  $P = \text{const.}$  and  $V_{ax} = \text{const.}$ , Eq.(4.29) yields:

$$\frac{dp}{dR} + \rho V_u \frac{dV_u}{dR} = 0, \quad \text{or} \quad \frac{dp}{dR} = -\rho V_u \frac{dV_u}{dR} \quad (4.30)$$

Equating (4.30) and (4.23) results in:

$$V_u \frac{dV_u}{dR} + \frac{V_u^2}{R} = 0 \quad (4.31)$$

or

$$\frac{dV_u}{V_u} + \frac{dR}{R} = 0 \quad (4.32)$$

The integration of Eq. (4.32) leads to  $V_u R = \text{const.}$  This type of flow is called free vortex flow and fulfills the requirement to be potential flow,  $\nabla \times \mathbf{V} = \mathbf{0}$ . We use this relation to rearrange the specific stage mechanical energy:

$$l_m = U_2 V_{u2} + U_3 V_{u3} = \omega (R_2 V_{u2} + R_3 V_{u3}) \quad (4.33)$$

At station (2) the swirl is  $R_2 V_{u2} = \text{const.} = K_2$ ; likewise at station 3 the swirl is  $R_3 V_{u3} = K_3$ . Since  $\omega = \text{const.}$ , the specific stage mechanical energy is constant:

$$l_m = (K_2 + K_3)\omega = \text{const.} \quad (4.34)$$

Equation (4.34) implies that for a stage with constant spanwise meridional components and constant total pressure from hub to tip, the specific stage mechanical energy is constant over the entire blade height. To express the degree of reaction in a spanwise direction, we replace the enthalpy differences in Eq. (4.15) by pressure differences. For this purpose, we apply the first law for an adiabatic process through stator and rotor blades expressed in terms of  $\Delta h'' = \bar{v}'' \Delta p''$ ,  $\Delta h' = \bar{v}' \Delta p'$  with  $\bar{v}'$  and  $\bar{v}''$  as the averaged specific volumes in stator and rotor, respectively. It leads to:

$$r = \frac{\bar{v}'' \Delta p''}{\bar{v}'' \Delta p'' + \bar{v}' \Delta p'} = \frac{\Delta p''}{\Delta p'' + \frac{\bar{v}'}{\bar{v}''} \Delta p'} \approx \frac{p_2 - p_3}{p_1 - p_3} \quad (4.35)$$

In the above equation, the ratios of the specific volumes were approximated as  $\bar{v}'/\bar{v}'' \approx 1$ . This approximation is permissible as long as the flow Mach number is within the low subsonic range. For intermediate and high subsonic flow with  $M > 0.4$ , Eq. (4.15) should be used. Considering  $R_2 V_{u2} = \text{const.}$  the integration of Eq. (4.23) for station 1 from an arbitrary diameter  $R$  to the mean diameter  $R_m$  yields,

$$(p_1 - p_{m1}) = \frac{\rho}{2} (V_{um})_1^2 \left( 1 - \frac{R_m^2}{R^2} \right) \quad (4.36)$$

At station (2) we have,  
and finally, at station (3) we arrive at:

$$(p_3 - p_{m3}) = \frac{\rho}{2}(V_{um})_3^2 \left( 1 - \frac{R_m^2}{R^2} \right)_3 \quad (4.38)$$

$$(p_2 - p_{m2}) = \frac{\rho}{2}(V_{um})_2^2 \left( 1 - \frac{R_m^2}{R^2} \right)_2 \quad (4.37)$$

with  $(R_m)_1 = (R_m)_2 = (R_m)_3$ , and  $V_{um3} = V_{um1}$ . Introducing Eqs. (4.36), (4.37) and (4.38) into (4.35), we finally arrive at a simple relationship for the degree of reaction:

$$\frac{1 - r}{1 - r_m} = \frac{R_m^2}{R^2} \quad (4.39)$$

From a turbine design point of view, it is of interest to estimate the degree of reaction at the hub and tip radius by inserting the corresponding radii into Eq. (4.39). As a result, we find:

$$\frac{1 - r_h}{1 - r_m} = \left( \frac{R_m}{R_h} \right)^2, \quad \frac{1 - r_t}{1 - r_m} = \left( \frac{R_m}{R_t} \right)^2 \quad (4.40)$$

Equation (4.40) represents a simple radial equilibrium condition which allows the calculation of the inlet flow angle in radial direction by integrating Eq. (4.32):

$$V_u R = \text{const.}; \quad R = \frac{\text{const.}}{V_u} \quad (4.41)$$

This leads to determination of the inlet flow angle in a spanwise direction,

$$\frac{R_m}{R} = \frac{\cot \alpha_1}{\cot \alpha_{1m}} \quad (4.42)$$

## 4.6 Effect of Degree of Reaction on the Stage Configuration

The distribution of degree of reaction can also be obtained by simply using the velocity ratio for  $r$ . If, for example, the degree of reaction at the mean diameter is set at  $r = 50\%$ , Eq. (4.40) immediately calculates  $r$  at the hub and tip for the simple radial

equilibrium condition  $V_u R = \text{const.}$  as presented above. It should be mentioned that, for a turbine, a negative degree of reaction at the hub may lead to flow separation and is not desired. Likewise, for the compressor,  $r$  should not exceed the value of 100%. The value of  $r$  has major design consequences. For turbine blades with  $r = 0$ , as shown in Fig. 4.9(a) and 4.10, the flow is deflected in the rotor blades without any enthalpy changes. As a consequence, the magnitude of the inlet and exit velocity vectors are the same and the entire stage static enthalpy difference is partially converted within the stator row. Note that the flow channel cross section remains constant.

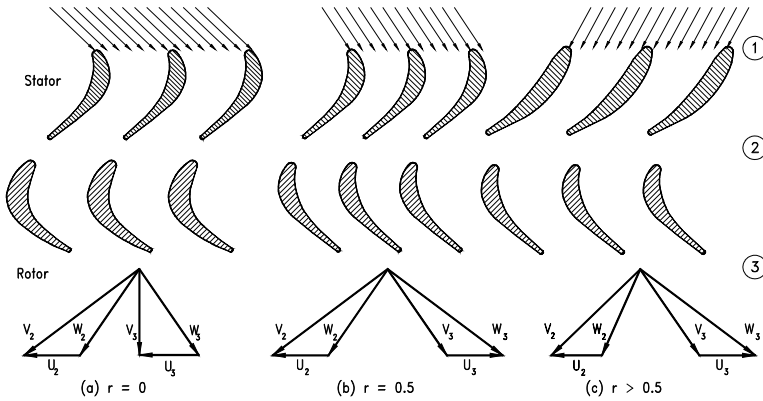


**Fig. 4.9:** Effect of degree of reaction on the stage configuration.

For  $r = 0.5$ , shown in Fig. 4.9(b), a fully symmetric blade configuration is established. Figure 4.9(c) shows a turbine stage with  $r > 0.4$ . In this case, the flow deflection inside the rotor row is much greater than the one inside the stator row. Figure 4.10 shows the flow deflection within a high speed rotor cascade. In the past, mainly two types of stages were common designs in steam turbines. The stage with a constant

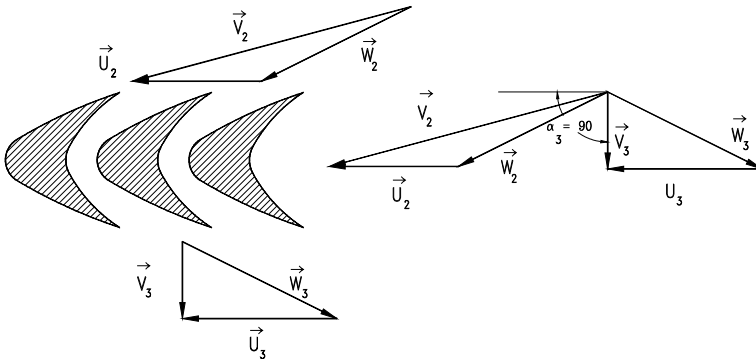


**Fig. 4.10:** Flow through a high speed turbine rotor with a degree of reaction  $r = 0.0$ , note that  $\alpha_3 = 90^\circ$  and  $|W_2| = |W_3|$ .

pressure across the rotor blading called *action stage*, was used frequently. This turbine stage was designed such that the exit absolute velocity vector  $\mathbf{V}_3$  was swirl free. It is most appropriate for the design of single stage turbines and as the last stage of a multi-stage turbine. As we shall see in Chapter 8, the *exit loss*, which corresponds to the kinetic energy of the exiting mass flow, becomes a minimum by using a swirl free absolute velocity. The stage with  $r = 0.5$  is called the *reaction stage*.

## 4.7 Effect of Stage Load Coefficient on Stage Power

The stage load coefficient  $\lambda$  defined in Eq. (4.13) is an important parameter which describes the stage capability to generate/consume shaft power. A turbine stage with low flow deflection, thus, low specific stage load coefficient  $\lambda$ , generates lower specific mechanical energy. To increase the stage mechanical energy  $l_m$ , blades with higher flow deflection are used that produce higher stage load coefficient  $\lambda$ . The effect of an increased  $\lambda$  is shown in Fig. 4.11, where three different bladings are plotted.

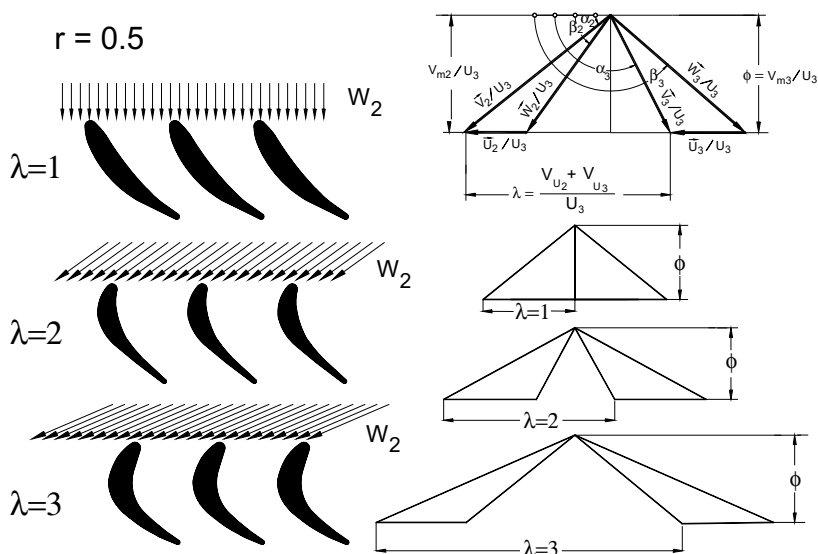


**Fig.5.11:** Dimensionless stage velocity diagram that explains the effect of stage load coefficient  $\lambda$  on flow deflection and blade geometry.

The top blading with the stage load coefficient  $\lambda = 1$  has a low flow deflection. The middle blading has a moderate flow deflection and moderate  $\lambda = 2$  which delivers a stage power twice as high as the top blading. Finally, the bottom blading with  $\lambda = 3$ , delivers three times the stage power as the first one. In the practice of turbine design, among other things, two major parameters must be considered. These are the specific load coefficients and the stage polytropic efficiencies.

Lower deflection generally yields higher stage polytropic efficiency, but many stages are needed to produce the required turbine power. However, the same turbine

power may be established by a higher stage flow deflection and, thus, a higher  $\lambda$  at the expense of the stage efficiency. Increasing the stage load coefficient has the advantage of significantly reducing the stage number, thus, lowering the engine weight and manufacturing cost. In aircraft engine design practice, one of the most critical issues besides the thermal efficiency of the engine, is the thrust/weight ratio. Reducing the stage numbers may lead to a desired thrust/weight ratio. While a high turbine stage efficiency has top priority in power generation steam and gas turbine design, the thrust/weight ratio is the major parameter for aircraft engine designers.

## 4.8 Unified Description of a Turbomachinery Stage

The following sections treat turbine and compressor stages from a unified standpoint. Axial, mixed flow, and radial flow turbines and compressors follow the same thermodynamic conservation principles. Special treatments are indicated when dealing with aerodynamic behavior and loss mechanisms. While the turbine aerodynamics is characterized by negative (favorable) pressure gradient environments, the compression process operates in a positive (adverse) pressure gradient environment. As a consequence, partial or total flow separation may occur on compressor blade surfaces leading to partial stall or surge. On the other hand, with the exception of some minor local separation bubbles on the suction surface of highly loaded low pressure turbine blades, the turbine operates normally without major flow separation or breakdown. These two distinctively different aerodynamic behaviors are due to different pressure gradient environments. Turbine and compressor cascade aerodynamics and losses are extensively treated in Chapters 7 and 16. In this section, we will first present a set of algebraic equations that describes the turbine and compressor stages with constant mean diameter and extend the approach to general cases where the mean stage diameter changes.

### 4.8.1 Unified Description of Stage with Constant Mean Diameter

For a turbine or compressor stage with constant mean diameter (Fig. 4.7), we present a set of equations that describe the stage by means of the dimensionless parameters such as stage flow coefficient  $\phi$ , stage load coefficient  $\lambda$ , degree of reaction  $r$ , and the flow angles. From the velocity diagram with the angle definition in Fig. 4.7, we obtain the flow angles:

$$\begin{aligned}\cot \alpha_2 &= \frac{U_2 + W_{u2}}{V_m} = \frac{1}{\phi} \left( 1 + \frac{W_{u2}}{U} \right) = \frac{1}{\phi} \left( 1 - r + \frac{\lambda}{2} \right) \\ \cot \alpha_3 &= -\frac{W_{u2} - U_2}{V_m} = -\frac{1}{\phi} \left( \frac{W_{u3} - U}{U} \right) = \frac{1}{\phi} \left( 1 - r - \frac{\lambda}{2} \right)\end{aligned}\tag{4.43}$$

Similarly, we find the other flow angles, thus, we summarize:

$$\cot \alpha_2 = \frac{1}{\phi} \left( 1 - r + \frac{\lambda}{2} \right) \quad (4.44)$$

$$\cot \alpha_3 = \frac{1}{\phi} \left( 1 - \frac{\lambda}{2} - r \right) \quad (4.45)$$

$$\cot \beta_2 = \frac{1}{\phi} \left( \frac{\lambda}{2} - r \right) \quad (4.46)$$

$$\cot \beta_3 = -\frac{1}{\phi} \left( \frac{\lambda}{2} + r \right) \quad (4.47)$$

The stage load coefficient can be calculated from:

$$\lambda = \phi (\cot \alpha_2 - \cot \beta_3) - 1 \quad (4.48)$$

The velocity diagram of the last stage of a compressor or a turbine differs considerably from the normal stage. As mentioned in the previous section, to minimize the *exit losses*, the last stage usually has an exit flow angle of  $\alpha_3 = 90^\circ$ . Figure 4.12 compares the velocity diagram of a normal stage with the one in the last stage of the same turbine component. As shown, by changing the exit flow angle to  $\alpha_3 = 90^\circ$ , substantial reduction in exit velocity vector  $\mathbf{V}_3$  and, thus, the exit kinetic energy  $V_3^2$  can be achieved. This subject is treated in Chapter 7 in detail.

#### 4.8.2 Generalized Dimensionless Stage Parameters

In this chapter, we extend the foregoing consideration to compressor and turbine stages where the diameter, circumferential velocities, and meridional velocities are not constant. Examples are axial flow turbine and compressors, Fig. 4.5 and 4.6,

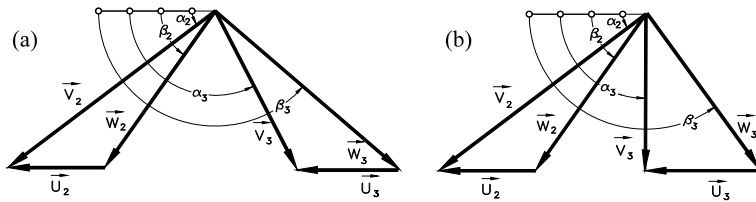


**Fig. 5.12:** Turbine stage velocity diagrams, (a) for a normal stage, (b) for the last stage of a multi-stage turbine.

radial inflow (centripetal) turbines, Figs. 4.13, and centrifugal compressors, 4.14.

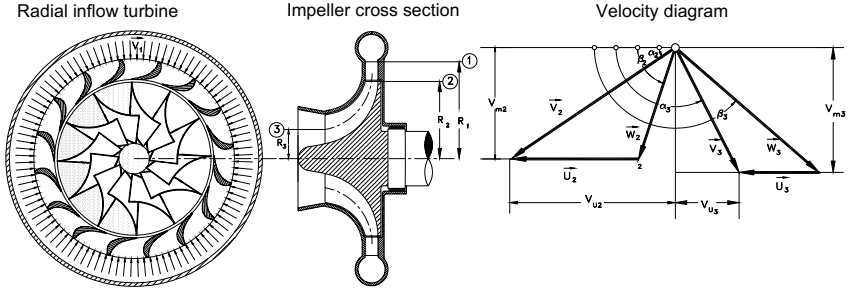


**Fig. 4.13:** A centripetal turbine stage with cross section and velocity diagram.

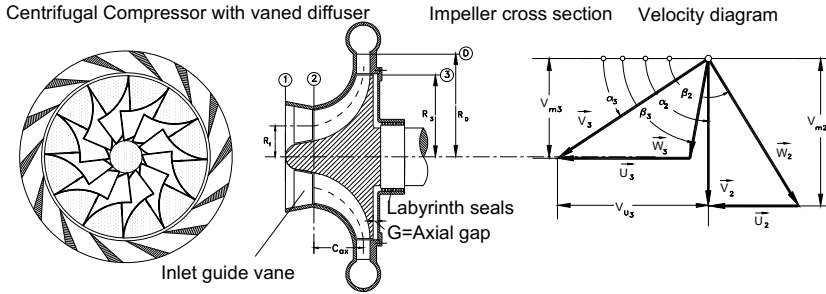


**Fig. 4.14:** A centrifugal compressor stage with cross section and velocity diagram.

In the following, we develop a set of unifying equations that describe the above axial turbine and compressor stages, as well as the centripetal turbine and centrifugal compressor stages shown in Figs. 4.13 and 4.14. We introduce new dimensionless parameters:

$$\mu = \frac{V_{m2}}{V_{m3}}, \quad v = \frac{R_2}{R_3} = \frac{U_2}{U_3}, \quad \phi = \frac{V_{m3}}{U_3}, \quad \lambda = \frac{1_m}{U_3^2}, \quad r = \frac{\Delta h''}{\Delta h' + \Delta h''} \quad (4.49)$$

with  $V_m$ ,  $U$  from the velocity diagrams and  $\Delta h'$ ,  $\Delta h''$  as the specific static enthalpy differences in rotor and stator. The dimensionless parameter  $\mu$  represents the meridional velocity ratio for the stator and rotor respectively,  $v$  the circumferential velocity ratio,  $\phi$  the stage flow coefficient,  $\lambda$  the stage load coefficient and  $r$  the degree of reaction. Introducing these parameters into the equations of continuity, moment of momentum, and the relation for degree of reaction, the stage is completely defined by a set of four equations:

$$\cot \alpha_2 - \cot \beta_2 = \frac{v}{\mu \phi} \quad (4.50)$$



$$\cot\alpha_3 - \cot\beta_3 = \frac{1}{\phi} \quad (4.51)$$

The relation for the specific load coefficient is obtained from

$$\lambda = \phi(\mu v \cot\alpha_2 - \cot\beta_3) - 1 \quad (4.52)$$

and the degree of reaction is:

$$r = \frac{1}{2} \frac{\mu^2 \phi^2 \cot^2 \alpha_2 (v^2 - 1) - 2\mu v \phi \lambda \cot \alpha_2 + \lambda^2 + 2\lambda - \phi^2 (\mu^2 - 1)}{\lambda} \quad (4.53)$$

The four Eqs. (4.50), (4.51), (4.52) and (4.53) contain nine unknown stage parameters. To find a solution, five parameters must be guessed. Appropriate candidates for the first guess are: the diameter ratio  $v = R_2/R_3 = U_2/U_3$ , the stator and rotor exit angles  $\alpha_2$ , and  $\beta_3$ , the exit flow angle  $\alpha_3$  and the stage degree of reaction  $r$ . In addition, the stage flow coefficient  $\phi$  can be estimated by implementing the information about the mass flow and using the continuity equation. Likewise, the stage load coefficient  $\lambda$  can be estimated for turbine or compressor stages by employing the information about the compressor pressure ratio or turbine power. Once the five parameters are guessed, the rest of the four parameters are determined by solving the above equation system. In this case, the four parameters calculated fulfill the conservation laws for the particular compressor or turbine blade geometry for which five stage parameters were guessed. This preliminary estimation of stage parameters, however, is considered the first iteration toward an optimum design. A subsequent loss and efficiency calculation, presented in Chapter 8, will clearly show if the guessed parameters were useful or not. In fact, few iterations are necessary to find the optimum configuration that fulfills the efficiency requirement set by the compressor or turbine designer. All stage parameters in Eqs. (4.50), (4.51), (4.52), and (4.53) can be expressed in terms of the flow angles  $\alpha_2$ ,  $\alpha_3$ ,  $\beta_2$ , and  $\beta_3$ , which lead to a set of four nonlinear equations:

$$\begin{aligned} (1 - v^2)\mu^2\phi^2\cot^2\alpha_2 + 2\mu v\phi\lambda\cot\alpha_2 - \lambda^2 - 2(1 - r)\lambda + (\mu^2 - 1)\phi^2 &= 0 \\ (1 - v^2)\phi^2\cot^2\alpha_3 + 2\phi\lambda\cot\alpha_3 + \lambda^2 - 2(1 - r)\lambda v^2 + (\mu^2 - 1)\phi^2 v^2 &= 0 \\ (1 - v^2)(\mu\phi\cot\beta_2 + v)^2 + 2v\lambda(\phi\mu\cot\beta_2 + v) - \lambda^2 - 2(1 - r)\lambda + (\mu^2 - 1)\phi^2 &= 0 \\ (1 - v^2)(\phi\cot\beta_3 + 1)^2 + 2\lambda(\phi\cot\beta_3 + 1) + \lambda^2 - 2(1 - r)\lambda v^2 + (\mu^2 - 1)\phi^2 v^2 &= 0 \end{aligned} \quad (4.54)$$

## 4.9 Special Cases

Equations (4.50) through (4.54) are equally valid for axial, radial, and mixed flow

turbine and compressor stages. Special stages with corresponding dimensionless parameters are described as special cases as listed below.

#### 4.9.1 Case 1, Constant Mean Diameter

In this special case, the diameter remains constant leading to the circumferential velocity ratio of  $v = U_2/U_3 = 1$ . The meridional velocity ratio  $\mu = V_{m2}/V_{m3} \neq 1$ . The flow angles expressed in terms of other dimensionless parameters are:

$$\begin{aligned}\cot\alpha_2 &= \frac{1}{\phi\mu} \left[ \frac{\lambda}{2} + (1 - r) - (\mu^2 - 1) \frac{\phi^2}{2\lambda} \right] \\ \cot\alpha_3 &= \frac{1}{\phi} \left[ -\frac{\lambda}{2} - (1 - r) - (\mu^2 - 1) \frac{\phi^2}{2\lambda} \right] \\ \cot\beta_2 &= \frac{1}{\mu\phi} \left[ \frac{\lambda}{2} + (1 - r) - (\mu^2 - 1) \frac{\phi^2}{2\lambda} - 1 \right] \\ \cot\beta_3 &= \frac{1}{\phi} \left[ -\frac{\lambda}{2} + (1 - r) - (\mu^2 - 1) \frac{\phi^2}{2\lambda} - 1 \right]\end{aligned}\tag{4.55}$$

The stage load coefficient is calculated from:

$$\lambda = \phi (\mu \cot\alpha_2 - \cot\beta_3) - 1 \text{ for } v = 1 \text{ and } \mu \neq 1\tag{4.56}$$

#### 4.9.2 Case 2, Constant Mean Diameter and Meridional Velocity Ratio

In this special case, circumferential and meridional velocities are equal leading to:  $v = U_2/U_3 = 1$ ,  $\mu = V_{m2}/V_{m3} = 1$ . The flow angles are calculated from:

$$\begin{aligned}\cot\alpha_2 &= \frac{1}{\phi} \left( \frac{\lambda}{2} - r + 1 \right) \\ \cot\alpha_3 &= \frac{1}{\phi} \left( -\frac{\lambda}{2} - r + 1 \right)\end{aligned}\tag{4.57}$$

The stage load coefficient is calculated from:

$$\lambda = \phi (\cot\alpha_2 - \cot\beta_3) - 1 \text{ for } v = 1 \text{ and } \mu = 1\tag{4.58}$$

In the following, we summarize the generalized stage load coefficient for different  $\mu$ ,  $v$ - cases,

$$\begin{aligned}
 \lambda &= \phi \left[ \mu v \cot \alpha_2 - \cot \beta_3 \right] - 1 && \text{for } v \neq 1 \text{ and } \mu \neq 1 \\
 \lambda &= \phi \left[ \mu \cot \alpha_2 - \cot \beta_3 \right] - 1 && \text{for } v = 1 \text{ and } \mu \neq 1 \\
 \lambda &= \phi \left[ v \cot \alpha_2 - \cot \beta_3 \right] - 1 && \text{for } v \neq 1 \text{ and } \mu = 1 \\
 \lambda &= \phi \left[ \cot \alpha_2 - \cot \beta_3 \right] - 1 && \text{for } v = 1 \text{ and } \mu = 1
 \end{aligned} \tag{4.59}$$

#### 4.10 Increase of Stage Load Coefficient, Discussion

Following the discussion in Section 4.3 regarding the increase of the specific stage mechanical energy and the subsequent discussion in Section 4.8, we proceed with Eq. (4.52), where the stage load parameter  $\lambda$  is expressed in terms of  $\mu$ ,  $v$ ,  $\alpha_2$  and  $\beta_3$ :

$$\lambda = \phi(\mu v \cot \alpha_2 - \cot \beta_3) - 1 \tag{4.60}$$

This equation is of particular significance for the first estimation of the stage load coefficient which is responsible for the stage power of a turbine or a compressor. While the stage flow coefficient  $\phi$  can be estimated from the continuity equation and the velocity ratios  $\mu$  and  $v$  can be guessed for the first design iteration, the angles  $\alpha_2$  and  $\beta_3$  follow closely the exit metal angles of stator and rotor.

The effect of flow deflection on stage load coefficient of axial flow turbines was already discussed in Section 4.8. As we saw, turbine blades can be designed with stage load coefficients  $\lambda$  as high as 2 or more. In turbine blades with high  $\lambda$  and Reynolds numbers  $Re = V_{exit} c / \nu > 150,000$ , the governing strong negative pressure gradient prevents the flow from major separation. However, if the same type of blade operates at lower Reynolds numbers, flow separation may occur that results in a noticeable increase in profile losses. For high pressure turbines (HP-turbines), the strong favorable pressure gradient within the blade channels prevents the flow from major separation. However, low pressure turbine (LPT) blades, particularly those of aircraft gas turbine engines that operate at low Reynolds numbers (cruse condition up to  $Re = 120,000$ ), are subjected to laminar flow separation and turbulent re-attachment.

While axial turbine blades can be designed with relatively high positive  $\lambda$ , the flow through axial compressor blade channels is susceptible to flow separation, even at relatively low  $\lambda$ . This is primarily due to a positive pressure gradient in the streamwise direction that causes the boundary layer to separate once a certain deflection limit or a *diffusion factor* (see Chapter 16) has been exceeded. To achieve a higher  $\lambda$  and, thus, a higher stage pressure ratio, a smaller diameter ratio  $v = D_2/D_3 = U_2/U_3$  can be applied. Using a moderate diameter ratio range of  $v = 0.85 - 0.75$  results in a mixed flow configuration. At a lower range of  $v$  such as

$\nu = 0.75 - 0.4$ , centrifugal compressor configuration is designed.

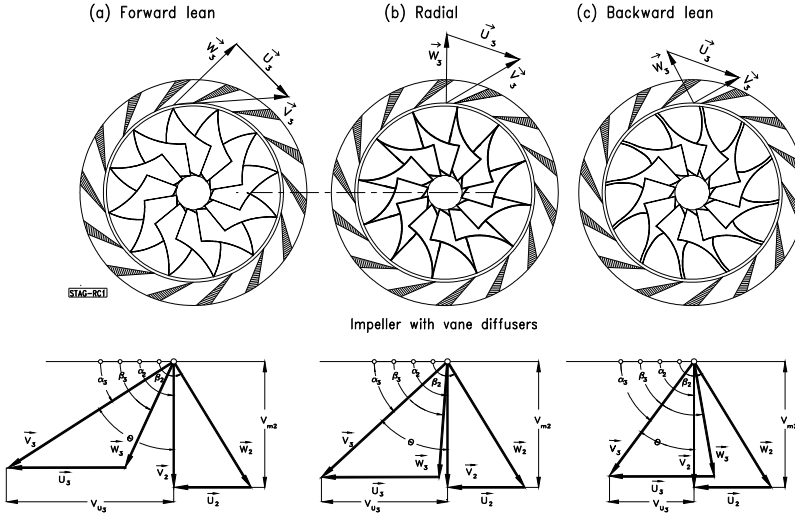


**Fig. 4.15:** Centrifugal compressor stage with velocity diagrams, a) forward lean, b) radial zero lean, c) backward lean.

Figure 4.15 shows, schematically, three centrifugal compressors with three different exit flow angles and the corresponding velocity diagrams. Figure 4.15a exhibits a centrifugal impeller with the trailing edge portion that is forward leaned and has a negative lean angle of  $\Delta\beta = \beta_3 - 90^\circ < 0$ . The reference configuration, Fig. 4.15 b, shows the impeller with a radial exit flow angle  $\beta_3 = 90^\circ$  and, thus,  $\Delta\beta = 0$ . Finally, Fig. 4.15c shows the impeller with backward leaned trailing edge portion with a positive lean angle  $\Delta\beta = \beta_3 - 90^\circ > 0$ . All three impellers have the same diameter ratio  $\nu$  and the same rotational speed  $\omega$ . The  $\lambda$ -behavior of these impellers is shown in Fig. 4.16, where the relative exit flow angle is varied in the range of  $\beta_3 = 80^\circ - 105^\circ$ . As shown, forward lean results in higher deflection  $\Theta$ , larger  $\Delta V_u$  and, thus, higher negative  $\lambda$ , which is associated with a higher profile loss. Backward lean, however, reduces the flow deflection  $\Theta$  and  $\Delta V_u$ . As a result, the stage load coefficient  $\lambda$  reduces. For the comparison, the radial exit case with  $\beta_3 = 90^\circ$  is plotted. In calculating the stage load coefficient  $\lambda$ , the influence of the radius ratio  $\nu = R_2/R_3 = U_2/U_3$  on the stage load coefficient becomes clear.

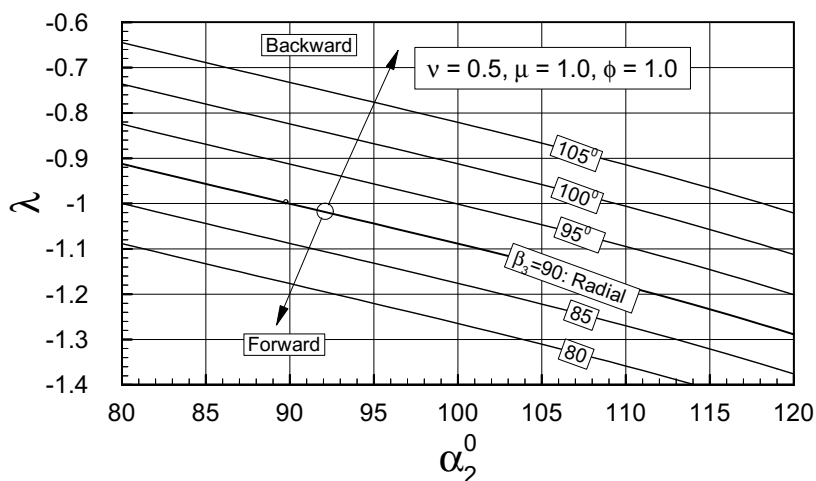


Fig. 4.16: Influence of lean angle on  $\lambda$ : Forward lean with  $\beta_3 < 90^\circ$ , Backward lean  $\beta_3 > 90^\circ$ , Zero lean  $\beta_3 = 90^\circ$ .

## References

1. Vavra, M.H., Aero-Thermodynamics and Flow in Turbomachines, John Wiley & Sons, New York, 1960.
2. Traupel, W., Thermische Turbomaschinen, Bd.I, 1977, Springer-Verlag Berlin Heidelberg New York.
3. Horlock, J.H., Axial Flow Compressors. London, Butterworth 1966.
4. Horlock, J.H., Axial Flow Turbine London, Butterworth 1966.

## 5 Turbine and Compressor Cascade Flow Forces

The last chapter was dedicated to the energy transfer within turbomachinery stages. The stage mechanical energy production or consumption in turbines and compressors were treated from a unified point of view by introducing a set of dimensionless parameters. As shown in Chapter 4, the mechanical energy, and therefore the stage power, is the result of the scalar product between the moment of momentum acting on the rotor and the angular velocity. The moment of momentum in turn was brought about by the forces acting on rotor blades. The blade forces are obtained by applying the conservation equation of linear momentum to the turbine or compressor cascade under investigation. In this chapter, we first assume an inviscid flow for which we establish the relationship between the *lift force* and *circulation*. Then, we consider the viscosity effect that causes friction or drag forces on the blading.

### 5.1 Blade Force in an Inviscid Flow Field

Starting from a given turbine cascade with the inlet and exit flow angles shown in Fig. 5.1, the blade force can be obtained by applying the linear momentum principles to the control volume with the unit normal vectors and the coordinate system shown

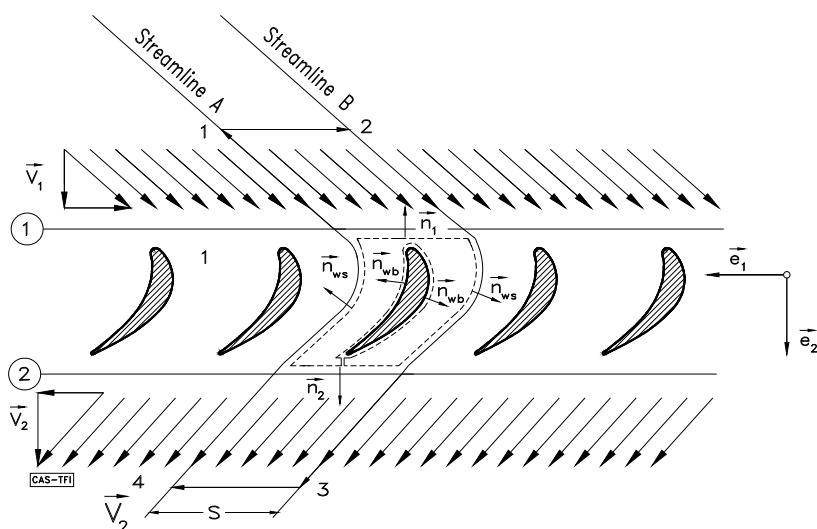


**Fig. 5.1:** Inviscid flow through a turbine cascade. The blades are assumed to have zero trailing edge thickness

in Fig.5.1. As in Chapter 4, the blade force is:

$$\mathbf{F}_i = \dot{m}\mathbf{V}_1 - \dot{m}\mathbf{V}_2 - \mathbf{n}_1 p_1 sh - \mathbf{n}_2 p_2 sh \quad (5.1)$$

with  $h$  as the blade height that can be assumed as unity. The relationship between the control volume normal unit vectors and the unit vectors pertaining to the coordinate system is given by:  $\mathbf{n}_1 = -\mathbf{e}_2$  and  $\mathbf{n}_2 = \mathbf{e}_2$ . The inviscid flow force is obtained by the linear momentum equation where no shear stress terms are present:

$$\mathbf{F}_i = \dot{m}(\mathbf{V}_1 - \mathbf{V}_2) + \mathbf{e}_2(p_1 - p_2)sh \quad (5.2)$$

The subscript  $i$  refers to inviscid flow. The above velocities can be expressed in terms of circumferential as well as axial components;

$$\mathbf{F}_i = -\mathbf{e}_1 \dot{m}[(V_{u1} + V_{u2})] + \mathbf{e}_2 [\dot{m}(V_{\alpha 1} - V_{\alpha 2}) + (p_1 - p_2)sh] \quad (5.3)$$

With  $V_{\alpha 1} = V_{\alpha 2}$  and  $V_{u1} \neq V_{u2}$  from Fig. 5.1, Eq. (5.3) is rearranged as:

$$\mathbf{F}_i = -\mathbf{e}_1 \dot{m}(V_{u1} + V_{u2}) + \mathbf{e}_2(p_1 - p_2)sh = \mathbf{e}_1 F_u + \mathbf{e}_2 F_{\alpha} \quad (5.4)$$

with the circumferential and axial components

$$F_u = -\dot{m}(V_{u1} + V_{u2}) \text{ and } F_{\alpha} = (p_1 - p_2)sh \quad (5.5)$$

The above static pressure difference is obtained from the Bernoulli equation  $p_{01} = p_{02}$ , where the static pressure difference is obtained:

$$p_1 - p_2 = \frac{1}{2} \rho (V_2^2 - V_1^2) = \frac{1}{2} \rho (V_{u2}^2 - V_{u1}^2) \quad (5.6)$$

Inserting the pressure difference along with the mass flow  $\dot{m} = \rho V_{\alpha} sh$  into Eq. (5.5) and the blade height  $h = 1$ , we obtain the axial as well as the circumferential components of the lift force:

$$\left. \begin{aligned} F_{\alpha} &= \frac{1}{2} \rho (V_{u2} + V_{u1}) (V_{u2} - V_{u1}) s \\ F_u &= -\rho V_{\alpha} (V_{u2} + V_{u1}) s \end{aligned} \right\} \quad (5.7)$$

From Eq.(5.2) and considering (5.7), the lift force vector for the inviscid flow is:

$$\mathbf{F}_i = \rho s (V_{u2} + V_{u1}) \left[ -\mathbf{e}_1 V_{\alpha} + \mathbf{e}_2 \frac{V_{u2} - V_{u1}}{2} \right] \quad (5.8)$$

This means that the direction of the blade force is identical with the direction of the vector within the brackets. In the next step, we evaluate the expression in the bracket. First, we calculate the mean velocity vector  $V_{\infty}$ :

$$\mathbf{V}_{\infty} = \frac{\mathbf{V}_1 + \mathbf{V}_2}{2} = \frac{1}{2} \mathbf{e}_1 (V_{u2} - V_{u1}) + \mathbf{e}_2 V_{\alpha} \quad (5.9)$$

and the circulation around the profile shown in Fig. 5.1 is:

$$\Gamma = \oint \mathbf{V} \cdot d\mathbf{c} , \quad (5.10)$$

where  $d\mathbf{c}$  is a differential displacement along the closed curve and  $\mathbf{V}$  is the velocity vector. The closed curve is placed around the blade profile so that it consists of two streamlines that are apart by the spacing  $s$ . Performing the contour integral around the closed curve  $c$ , we find:

$$\Gamma = V_{u1}s + \int_2^3 \mathbf{V} \cdot d\mathbf{c} + V_{u2}s + \int_4^1 \mathbf{V} \cdot d\mathbf{c} \quad (5.11)$$

Since the following integrals cancel each other:

$$\int_2^3 \mathbf{V} \cdot d\mathbf{c} = -\int_4^1 \mathbf{V} \cdot d\mathbf{c} \quad (5.12)$$

We obtain the circulation and thus the circulation vector:



$$\begin{aligned}\Gamma &= (V_{u2} + V_{u1})s \text{ with the direction } \mathbf{e}_3 = -\mathbf{e}_2 \times \mathbf{e}_1 \\ \Gamma &= (\mathbf{e}_2 \times \mathbf{e}_1)s(V_{u2} + V_{u1}) = (-\mathbf{e}_3)s(V_{u1} + V_{u2})\end{aligned}\quad (5.13)$$

We multiply the circulation vector with the mean velocity vector

$$\mathbf{V}_\infty \times \Gamma = \left\{ \frac{1}{2} \mathbf{e}_2 (V_{u2} - V_{u1}) - \mathbf{e}_1 V_{ax} \right\} (V_{u2} + V_{u1})s \quad (5.14)$$

and compare Eq.(5.14) with (5.8) to arrive at the inviscid flow force:

$$\mathbf{F}_i = \rho \mathbf{V}_\infty \times \Gamma \quad (5.15)$$

This is the well-known Kutta-Joukowski lift-equation for inviscid flow. Figure 5.2 exhibits a single blade taken from a turbine cascade with the velocities  $\mathbf{V}_1$ ,  $\mathbf{V}_2$ ,  $\mathbf{V}_\infty$ , as well as the circulation vector  $\Gamma$ , and the force vector  $\mathbf{F}_i$ . As seen, the inviscid flow force vector  $\mathbf{F}_i$  is perpendicular to the plane spanned by the mean velocity vector  $\mathbf{V}_\infty$  and the circulation vector  $\Gamma$ .

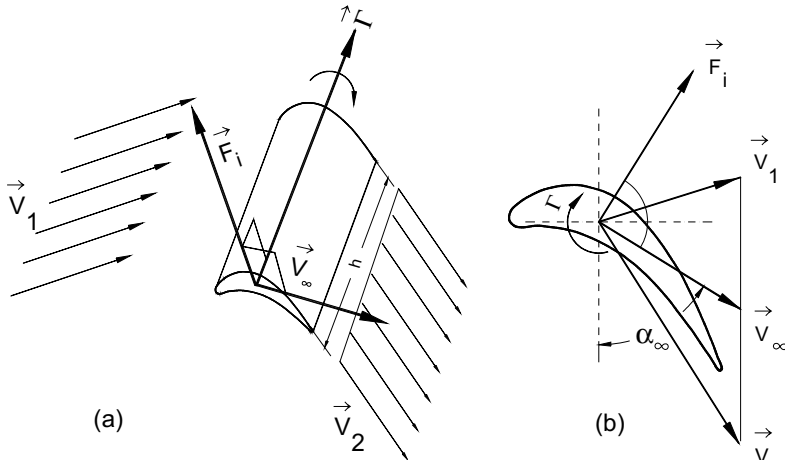


**Fig. 5.2:** (a) A turbine blade in an inviscid flow field with velocity, circulation and lift force vectors, (b) inviscid lift force vector  $\mathbf{F}_i$  perpendicular to the plane by  $\Gamma$  and  $\mathbf{V}_\infty$ .

Equation (5.15) holds for any arbitrary body that might have a circulation around it regardless of the body shape. It is valid for turbine and compressor cascades and exhibits the fundamental relation in inviscid flow aerodynamics. The magnitude of the force vector is obtained from:

$$F_i = \frac{F_{ax}}{\cos \alpha_\infty} = \frac{1}{2} \frac{\rho s (V_{u2} + V_{u1})(V_{u2} - V_{u1})}{\cos \alpha_\infty} \quad (5.16)$$

Expressing  $F_i$  in terms of  $V_\infty$ , the inviscid lift force for a turbine cascade is:

$$F_i = \rho V_\infty (V_{u2} + V_{u1}) s \quad (5.17)$$

Figure 5.3 exhibits the inviscid flow forces acting on a turbine and a compressor cascade.

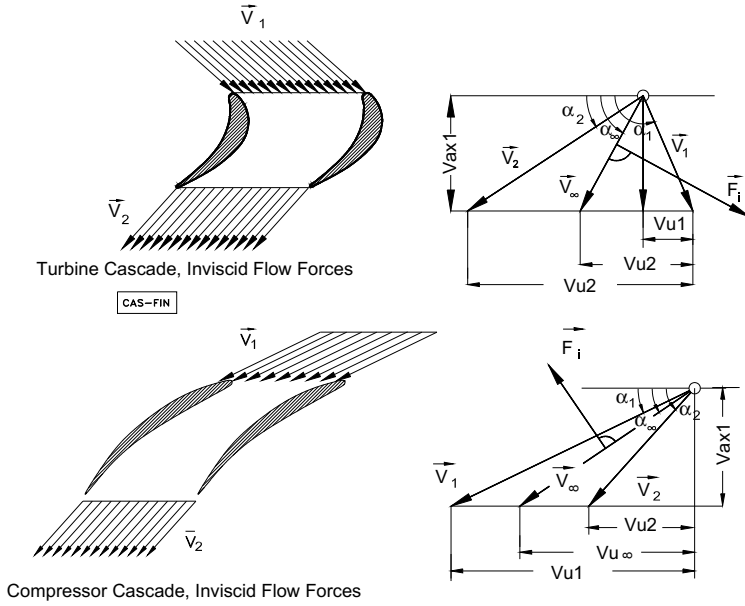


**Fig. 5.3:** Turbine (top) and compressor (bottom) cascade inviscid flow forces.

The flow deflection through the cascades is shown using the velocity diagram for accelerated flow (turbine) and decelerated flow (compressor). As shown in Fig. 5.3, the inviscid flow force (inviscid lift) is perpendicular to the mean velocity vector  $V_\infty$ . The lift force can be non-dimensionalized by dividing Eq. (5.17) by a product of the exit dynamic pressure  $\rho V^2/2$  and the projected area  $A = ch$  with the height  $h$  assumed  $h = 1$ . Thus, the *lift coefficient* is obtained from:

$$C_L = \frac{F_i}{\frac{\rho}{2} V_2^2 c} = \left[ \frac{2 V_\infty (V_{u2} + V_{u1})}{V_2^2} \right] \frac{s}{c} \text{ or} \quad (5.18)$$

$$C_L \sigma = 2 \frac{\sin^2 \alpha_2}{\sin \alpha_\infty} (\cot \alpha_2 - \cot \alpha_1)$$

As shown in section 5.2, the above relationship can be expressed in terms of the cascade flow angles and the geometry.

## 5.2 Blade Forces in a Viscous Flow Field

The working fluids in turbomachinery, whether air, gas, steam or other substances, are always viscous. The blades are subjected to the viscous flow and undergo shear stresses with *no-slip condition* on the suction and pressure surfaces, resulting in boundary layer developments on both sides of the blades. Furthermore, the blades have certain definite trailing edge thicknesses. These thicknesses together with the boundary layer thickness, generate a spatially periodic wake flow downstream of each cascade as shown in Fig. 5.4. The presence of the shear stresses cause drag forces that reduce the total pressure. In order to calculate the blade forces, the momentum Eq. (5.1) can be applied to the viscous flows. As seen from Eq. (5.5) and Fig. (5.4), the circumferential component remains unchanged. The axial component, however, changes in accordance with the pressure difference as shown in the following relations:

$$\begin{aligned} F_u &= -\rho V_{ax} (V_{u2} + V_{u1}) s h \\ F_{ax} &= (p_1 - p_2) s h \end{aligned} \quad (5.19)$$

The blade height  $h$  in Eq. (5.19) may be assumed as unity. For a viscous flow, the static pressure difference cannot be calculated by the Bernoulli equation. In this case, the total pressure drop must be taken into consideration. We define the total pressure loss coefficient:

$$\zeta \equiv \frac{P_{o1} - P_{o2}}{\frac{1}{2} \rho V_2^2} \quad (5.20)$$

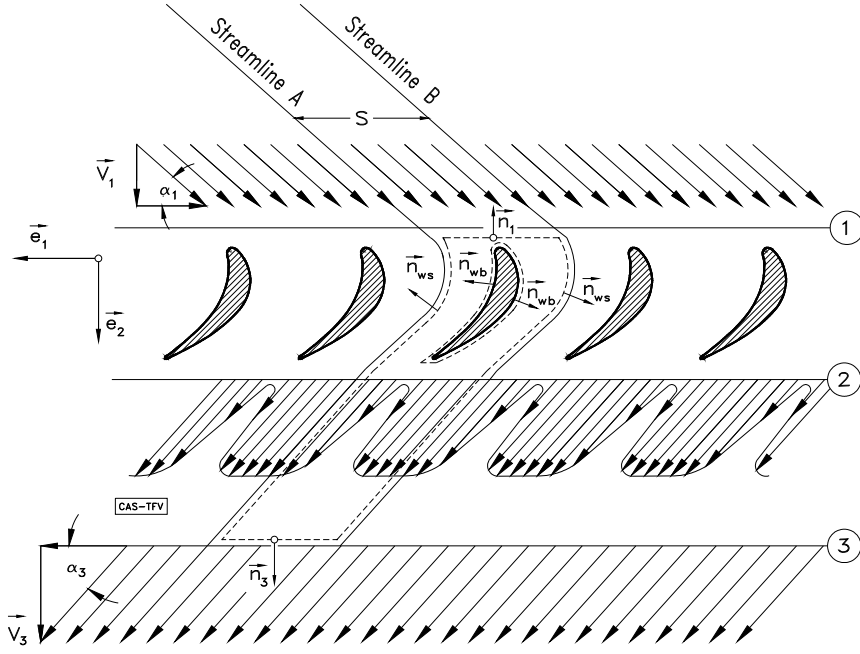


**Fig. 5.4:** Viscous flow through a turbine cascade. Station ① has a uniform velocity distribution. At station ② wakes are generated by the trailing edge- and boundary layer thickness and are mixed out at ③.

with  $P_1 \equiv p_{01}$  and  $P_2 \equiv p_{02}$  as the averaged total pressure at stations 1 and 2. Inserting for the total pressure the sum of static and dynamic pressure, we get the static pressure difference as:

$$p_1 - p_2 = \frac{\rho}{2} (V_2^2 - V_1^2) + \zeta \frac{\rho}{2} V_2^2 \quad (5.21)$$

Incorporating Eq. (5.21) into the axial component of the blade force in Eq. (5.19) yields:

$$F_{ax} = \frac{\rho}{2} (V_2^2 - V_1^2) s + \zeta \frac{\rho}{2} V_2^2 s \quad (5.22)$$

with  $F_{ax}$  as the axial force component per unit height. We introduce the velocity components into Eq. (5.22) and assume that for an incompressible flow the axial components of the inlet and exit flows are the same. As a result, Eq. (5.22) reduces

to:

$$F_{ax} = \frac{\rho}{2} (V_{u2}^2 - V_{ul}^2) s + \zeta \frac{\rho}{2} V_2^2 s \quad (5.23)$$

The second term on the right-hand side exhibits the axial component of the drag force per unit height accounting for the viscous nature of a frictional flow shown in Fig. 5.5. Thus, the axial projection of the drag force is obtained from:

$$D_{ax} = \zeta \frac{\rho}{2} V_2^2 s \quad (5.24)$$

Figure 5.5 exhibits the turbine and compressor cascade flow forces, including the lift and drag forces on each cascade for viscous flow, where the periodic exit velocity distribution caused by the wakes and shown in Fig. 5.4, is completely mixed out resulting in an averaged uniform velocity distribution, Fig. 5.5.

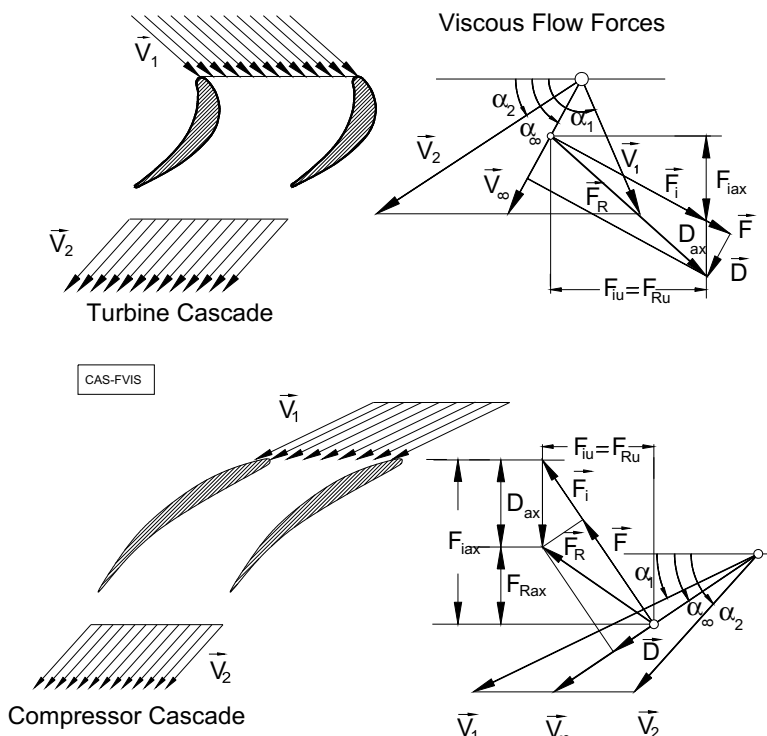


**Fig. 5.5:** Viscous flow forces on turbine cascade (top) and compressor cascade (bottom). The resultant force is decomposed into lift and drag component.

With Eq. (5.24), the loss coefficient is directly related to the drag force:

$$\zeta = \frac{D_{ax}}{\frac{\rho}{2} V_2^2 s} \quad (5.25)$$

Since the drag force  $D$  is in the direction of  $V_\infty$ , its axial projection  $D_{ax}$  can be written as:

$$D_{ax} = \frac{D}{\sin \alpha_\infty} \quad (5.26)$$

Assuming the blade height  $h = l$ , we define the drag and lift coefficients as:

$$C_D = \frac{D}{\frac{\rho}{2} V_2^2 c}, \quad C_L = \frac{F}{\frac{\rho}{2} V_2^2 c} \quad (5.27)$$

introduce the drag coefficient  $C_D$  into Eq. (5.25), and obtain the loss coefficient

$$\zeta = C_D \frac{c}{s} \frac{1}{\sin \alpha_\infty} \quad (5.28)$$

The magnitude of the lift force is the projection of the resultant force  $F_R$  on the plane perpendicular to  $V_\infty$ :

$$F = F_i + D_{ax} \cos \alpha_\infty \quad (5.29)$$

Using the lift coefficient defined previously and inserting the lift force, we find

$$C_L = \frac{2 V_\infty (V_{u2} + V_{u1})}{V_2^2} \frac{s}{c} + \zeta \frac{s}{c} \cos \alpha_\infty \quad (5.30)$$

Introducing the cascade solidity  $\sigma = c/s$  into Eq. (5.30) results in:

$$C_L \frac{c}{s} \equiv C_L \sigma = \frac{2 V_\infty (V_{u2} + V_{u1})}{V_2^2} + \zeta \cos \alpha_\infty \quad (5.31)$$

The lift-solidity coefficient is a characteristic quantity for the cascade aerodynamic loading. Using the flow angles defined in Fig. 5.3, the relationship for the lift-solidity

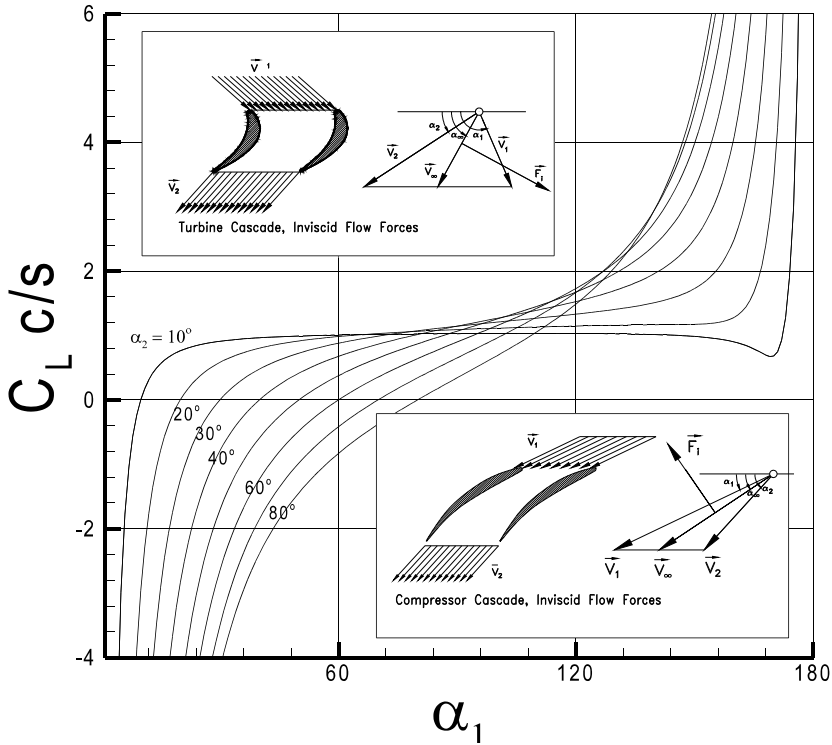


**Fig. 5.6:** Lift-solidity coefficient as a function of inlet flow angle  $\alpha_1$  with the exit flow angle  $\alpha_2$  as parameter for turbine and compressor cascades.

coefficient becomes:

$$C_L \sigma = 2 \frac{\sin^2 \alpha_2}{\sin \alpha_\infty} (\cot \alpha_2 - \cot \alpha_1) + \zeta \cos \alpha_\infty \quad (5.32)$$

with:

$$\cot \alpha_\infty = \frac{1}{2} (\cot \alpha_2 + \cot \alpha_1) \quad (5.33)$$

For a preliminary design consideration, the contribution of the second term in Eq. (5.32) compared with the first term can be neglected. However, for the final design, the loss coefficient  $\zeta$  needs to be calculated from Chapter 7 and inserted into Eq. (5.32). Figure 5.6 shows the results as a function of the inlet flow angle with the exit flow angle as the parameter for turbine and compressor cascades. As an example, a turbine cascade with an inlet flow angle of  $\alpha_1 = 132^\circ$ , and an exit flow of  $\alpha_2 = 30^\circ$

resulting in a total flow deflection of  $\Theta = 102^\circ$ , has a positive lift-solidity coefficient of  $C_L \sigma = 2.0$ . This relatively high lift coefficient is responsible for generating high blade forces and thus, a high blade specific mechanical energy for the rotor. In contrast, a compressor cascade with an inlet flow angle of  $\alpha_1 = 60^\circ$  and an exit flow angle of  $\alpha_2 = 80^\circ$  which result in a total compressor cascade flow deflection of only  $\Theta = 20^\circ$ , has a lift-solidity coefficient of  $C_L \sigma = -0.8$ . This leads to a much lower blade force and thus, lower specific mechanical energy input for the compressor rotor. The numbers in the above example are typical for compressor and turbine blades. The high lift-solidity coefficient for a turbine cascade is representative of the physical process within a highly accelerated flow around a turbine blade, where, despite a high flow deflection, no flow separation occurs. On the other hand, in case of a compressor cascade, a moderate flow deflection, such as the one mentioned above, may result in flow separation. The difference between the turbine and compressor cascade flow behavior is explained by the nature of boundary layer flow around the turbine and compressor cascades. In a compressor cascade, shown in Fig. 5.7 the boundary layer flow is subjected to two co-acting decelerating effects, the wall shear stress dictated by the viscous nature of the fluid and the positive pressure gradient imposed by the cascade geometry.

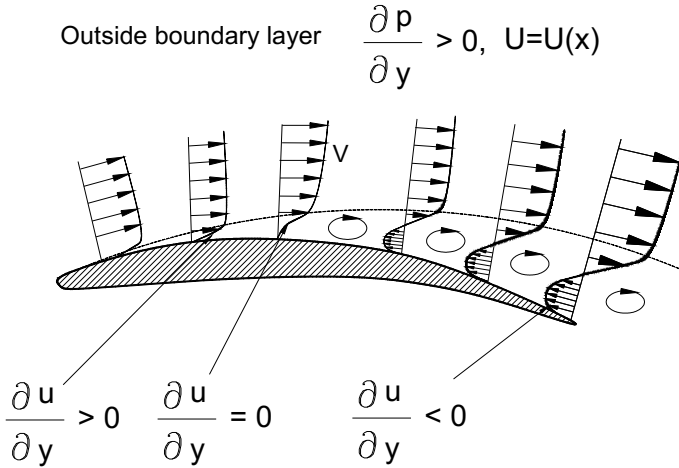


**Fig. 5.7:** Boundary layer development along the suction surface of a compressor cascade.

A fluid particle within the boundary layer that has inherently lower kinetic energy compared to a particle outside the boundary layer, has to overcome the pressure forces due to the governing positive pressure gradient. As a result, this particle continuously decelerates, comes to a rest, and separates. In the case of a turbine



cascade, the decelerating effect of the shear stress forces is counteracted by the accelerating effect of the negative pressure gradient that predominates a turbine cascade flow.

### 5.3 The Effect of Solidity on Blade Profile Losses

Equation (5.32) exhibits a fundamental relation between the lift coefficient, solidity, inlet and exit flow angle, and the loss coefficient  $\zeta$ . At this stage, the question might arise as to how the profile loss  $\zeta$  will change if the solidity  $\sigma$  changes. The solidity has the major influence on the flow behavior within the blading. If the spacing is too small, the number of blades is large and the friction losses dominate. Increasing the spacing, which is identical to reducing the number of blades, at first causes a reduction of friction losses. Further increasing the spacing, decreases the friction losses and also reduces the guidance of the fluid that may result in flow separation leading to separation losses. With definite spacing, there is an equilibrium between the separation and friction losses. At this point, the profile loss  $\zeta = \zeta_{\text{friction}} + \zeta_{\text{separation}}$  is at a minimum. The corresponding spacing/chord ratio has an optimum, which is shown in Fig. 5.8.

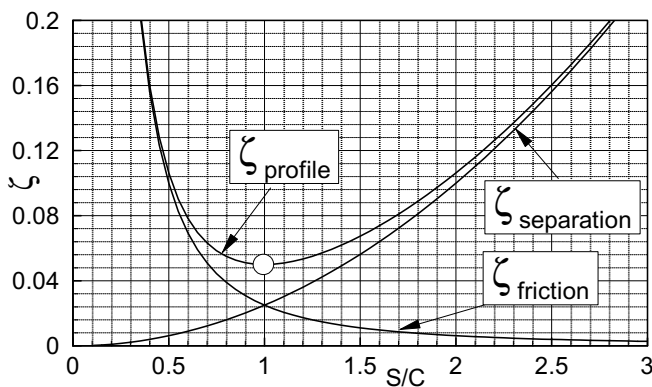


**Fig.5.8:** Profile loss coefficient as a function of spacing/chord ratio. The circle marks the optimum spacing/chord ratio.

### 5.4 Relationship Between Profile Loss Coefficient and Drag

To establish a relationship for turbine cascade profile losses, which is based on a systematic turbine cascade investigations, we define the so-called drag-lift ratio:

$$\epsilon = \frac{C_D}{C_L} \quad (5.34)$$

which is a characteristic for a profile. The drag and the loss coefficients in Eq. (5.28)

$$\zeta = C_D \frac{c}{s} \frac{1}{\sin \alpha_\infty} \quad (5.35)$$

are related to the lift coefficient by Eq. (5.34) as:

$$C_L \frac{c}{s} = \frac{\zeta \sin \alpha_\infty}{\epsilon} \quad (5.36)$$

Expressing the drag coefficient in Eq. (5.35) by the lift coefficient (5.34) and introducing Eq. (5.36) into (5.32) we obtain:

$$\zeta \frac{\sin \alpha_\infty}{\epsilon} - \zeta \cos \alpha_\infty = 2 \frac{\sin^2 \alpha_2}{\sin \alpha_\infty} (\cot \alpha_2 - \cot \alpha_1) \quad (5.37)$$

Rearranging Eq. (5.37) gives a direct relation between the loss coefficient  $\zeta$ , the inlet and exit flow angles and the drag-lift ratio  $\epsilon$ :

$$\zeta = \frac{2\epsilon}{1 - \epsilon \cot \alpha_\infty} \cdot \frac{\sin^2 \alpha_2}{\sin^2 \alpha_\infty} (\cot \alpha_2 - \cot \alpha_1) \quad (5.38)$$

Figure 5.9 shows a typical drag-lift ratio  $\epsilon$  experimentally determined by Pfeil [1] for turbine and compressor cascades.

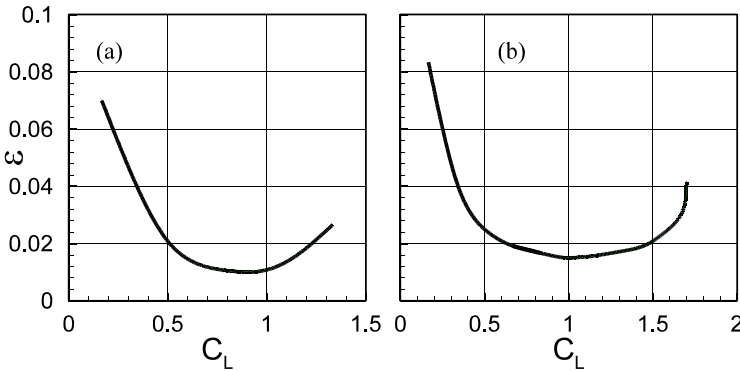


**Fig. 5.9:** Typical drag-lift ratio  $\epsilon$  as a function of the lift coefficient (a) for a turbine cascade and (b) for a compressor cascade, from [1]

## 5.5 Optimum Solidity

To find the optimum solidity for a variety of turbine and compressor cascades, Pfeil [1] performed a series of comprehensive experimental studies where 8 compressor cascades with NACA-profiles and 8 turbine cascades were investigated. The blade profiles ranged from low to high flow deflection. In these studies, Pfeil extended his analysis, among others, to the existing data from Carter and Hounsell [2], and Abbot, et al.[3]. According to the studies in [1], the  $\epsilon$  versus  $C_L$ -diagram in Fig. 5.9 shows that the drag-lift ratios for compressor and turbine cascades have clearly defined optimum ranges. For the turbine cascades presented in [1] and in accord with the finding of Zweifel [4], the optimum lift coefficient range is  $(C_L)_{opt} \approx 0.8-1.05$ , whereas for the compressor cascades  $C_{L_{opt}} \approx 0.9-1.25$ . The experimental

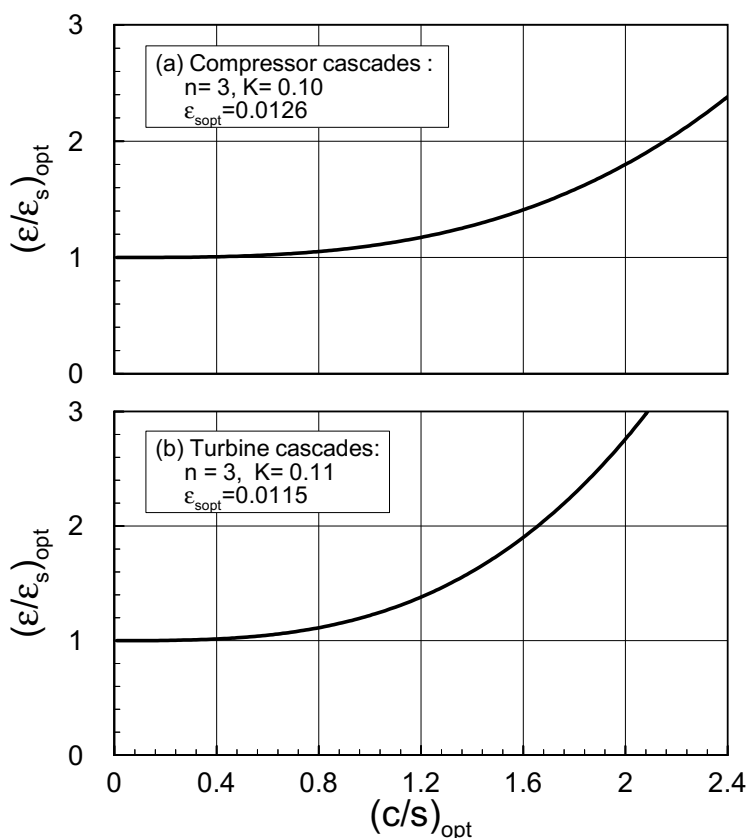


**Fig. 5.10:** Relative drag/lift-ratio as a function of optimum chord-spacing ratio for (a) compressor and (b) turbine cascades, [1]

investigations by Pfeil [1], his analysis of the data and the correlations he obtained from the Results are significant for determining the optimum solidity. The earlier study by Zweifel [4] that has lead to the *Zweifel's criterion* is still used turbine design. In the following, we discuss the procedures by Pfeil and Zweifel.

### 5.5.1 Optimum Solidity, by Pfeil

Investigating the  $\varepsilon$ -behavior of a single profile and building a relative  $\varepsilon$ -ratio, the studies in [1] reveal the following functional relationship:

$$\left( \frac{\varepsilon}{\varepsilon_s} \right)_{opt} = 1 + f \left( \frac{c}{s} \right)_{opt} \quad (5.39)$$

The above relationship is plotted in Fig. 5.10 and can be approximated by:

$$\left( \frac{\varepsilon}{\varepsilon_s} \right)_{opt} = 1 + K \left( \frac{c}{s} \right)_{opt}^n \quad (5.40)$$

with  $\varepsilon_s$  as the drag-lift ratio for a single blade. From experimental investigations for turbine and compressor cascades with hydraulically smooth blade surfaces, the maximum thickness-chord ratios  $(t/c) = 0.15$  for turbine and  $(t/c) = 0.1$  for compressor and the Reynolds number  $Re = 3.5 \times 10^5$ , the values for  $n$ ,  $K$ , and  $(\varepsilon_s)_{opt}$  were evaluated and are given in Fig. 5.10 (a) and (b). Using Eq. (5.41), the optimum profile loss coefficient is calculated by :

$$\zeta = (\varepsilon_s)_{opt} \left[ 1 + K \left( \frac{c}{s} \right)_{opt}^n \right] C_L \frac{c}{s} \frac{1}{\sin \alpha_\infty} \quad (5.41)$$

Figures 5.10 (a) and (b) exhibit the optimum  $\varepsilon$ -ratios as a function of optimum chord-spacing ratio for turbine and compressor cascades investigated in [1]. As seen for up to  $(c/s)_{opt} \approx 0.4$ , the ratio  $(\varepsilon/\varepsilon_s)_{opt}$  is almost constant. Equation (5.32) in conjunction with Eq. (5.41) gives a reasonably accurate estimation for calculating the optimum spacing/chord ratio, which is necessary to determine the blade numbers for compressor and turbine stator and rotor rows, respectively.

### 5.5.2 Optimum Solidity by Zweifel

As we saw in the preceding section, for a given blade geometry with given inlet and exit flow angles, there exist a distinct spacing/chord ratio at which the profile loss coefficient is a minimum. To find this ratio, Zweifel [4] introduced an *ideal tangential blade force*, which is based on an *ideal pressure* distribution shown in Fig. 5.11. As Zweifel [4] states, this ideal pressure distribution has the maximum total pressure over the entire pressure side. On the suction side, the pressure falls instantaneously to  $p_2$  being the lowest pressure possible without pressure rise. This ideal pressure, which of course cannot be realized gives a tangential force per unit of length. The idea of Zweifel is reflected in Fig. 5.11. Thus the ideal pressure distribution acting on the blade and projected in tangential direction is shown as the dashed rectangle, which is the difference between the inlet total pressure and the exit static pressure. For

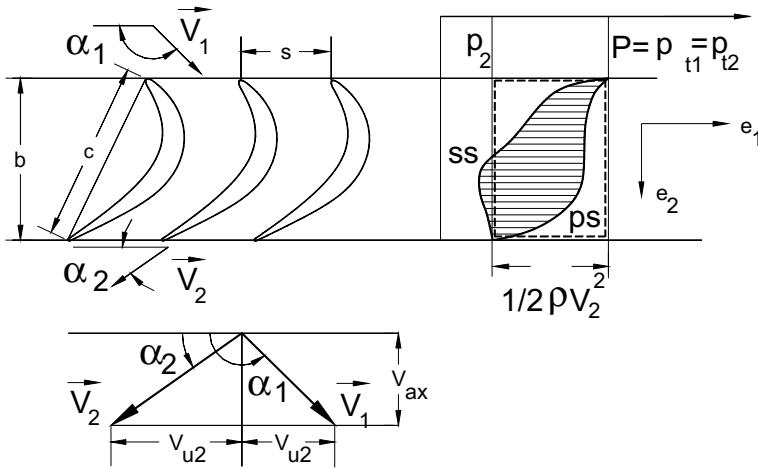


**Fig. 5.11:** Real and ideal pressure distribution around a turbine blade.

comparison, the real pressure distribution projected in tangential direction is also shown in Fig. 5.11. Thus the ideal tangential (circumferential) force per unit of length can be calculated from:

$$F_{u_{id}} = \frac{\rho}{2} V_2^2 b \quad (5.42)$$

The real tangential (circumferential) force is obtained from the momentum equation in circumferential direction using the coordinate system defined in Fig. 5.11:

$$F_u = \dot{m}(V_{u1} + V_{u2}) = \rho V_{ax}(V_{u1} + V_{u2})s \quad (5.43)$$

Dividing Eq. (5.43) by (5.42), Zweifel [4] introduced the following aerodynamic load coefficient:

$$\Psi_T = 2 \sin^2 \alpha_2 (\cot \alpha_2 - \cot \alpha_1) \left( \frac{s}{b} \right) \quad (5.44)$$

which is called the Zweifel number. Zweifel also introduced another load coefficient  $\Psi_A$ , which is a special case of Eq.(5.32), where the profile loss coefficient is ignored leading to:

$$\Psi_A = 2 \frac{\sin^2 \alpha_2}{\sin \alpha_\infty} (\cot \alpha_2 - \cot \alpha_1) \left( \frac{s}{c} \right) \quad (5.45)$$

which is related to  $\Psi_T$ , via  $\Psi_T / \Psi_A = V_{ax} / V_\infty s/b$ . Equation (5.44) is the product of the blade flow deflection and the spacing/chord ratio. If, for example, a turbine or a compressor design requires a certain prescribed  $\Psi_T$ , Eq. (5.44) offers a simple guideline as how to configure the blade deflection and the spacing/chord ratio: a blade with a large deflection (stator:  $\alpha_1, \alpha_2$ , rotor:  $\beta_2, \beta_3$ ) must be associated with a small spacing/chord ratio and vice versa.

The Zweifel number as a function of the inlet flow angle with the exit flow angle as a parameter for a given pair of spacing and chord is plotted in Fig. 5.12 for a low pressure turbine.

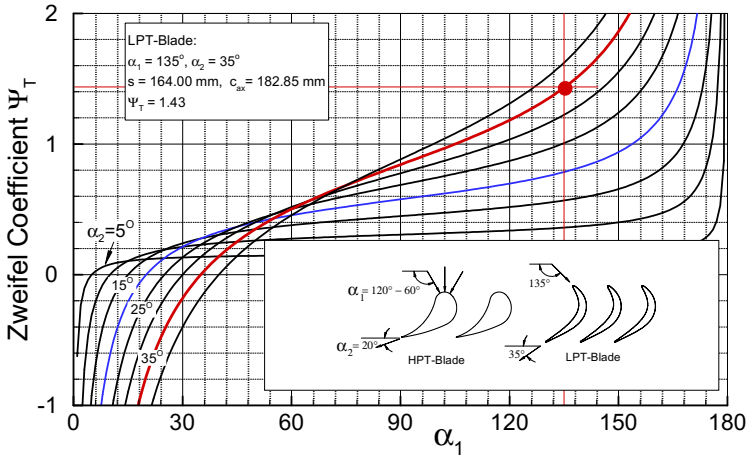


**Fig. 5.12:** Zweifel coefficient as a function of inlet flow angle with exit flow angle as parameter for a given spacing/chord ratio.

Figure 5.12 also includes a high pressure turbine blade, where the inlet flow angle can significantly change during the off-design operation. Usually, the  $s/c$ -ratio

corresponds to the design point operation. However, if the turbine is designed to frequently operate under adverse off-design operations, the s/c-ratio may be chosen, such that an acceptable range of profile loss is maintained.

Based on the experimental results by Christiani [5] and Keller [6] that dealt with turbine and compressor cascade flows at low Mach numbers, Zweifel suggested that for large flow deflections, the profile loss coefficient approaches a minimum for  $\Psi_T = 0.8$ . This would allow the calculation of an optimum spacing/chord ratio from:

$$\frac{s}{b} = \frac{0.4}{\sin^2 \alpha_2 (\cot \alpha_2 - \cot \alpha_1)} \quad (5.46)$$

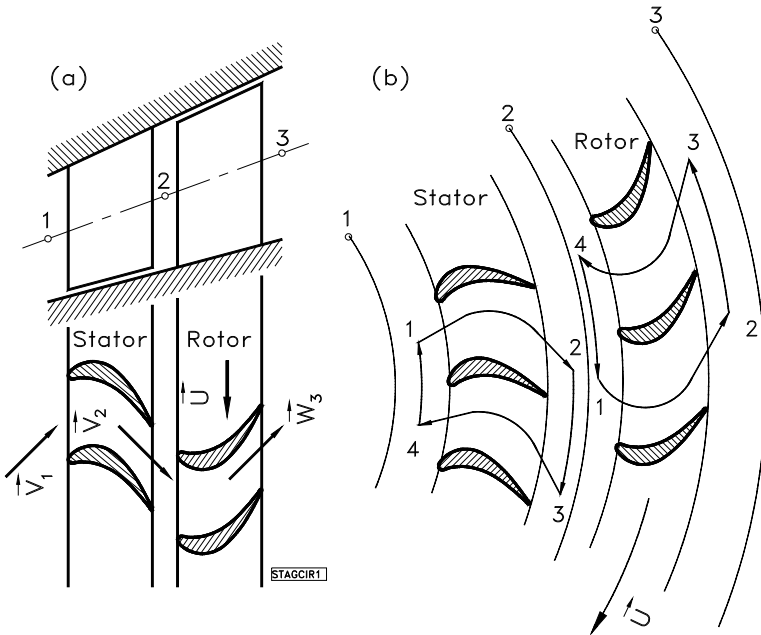
It should be pointed out that Eq. (5.44) and the subsequent Eq. (5.46) are of limited validity. The value of  $\Psi_T = 0.8$  represents only a few cases investigated by Christiani and Keller [5]. More detailed experiments by Pfeil show that the optimum loss coefficients strongly depend of the flow deflection, where  $\Psi_A$  can vary between  $\Psi_A = 0.75$ -1.15. Furthermore, important parameters such as Reynolds number, Mach number and unsteady interaction between stator and rotor blades through the wake impingement and its becalming effect on the blade spacing/chord ratio have to be considered. The latter is comprehensively investigated by Schobeiri and his co-workers [7], [8], [9], [10], and [11].

## 5.6 Generalized Lift-Solidity Coefficient

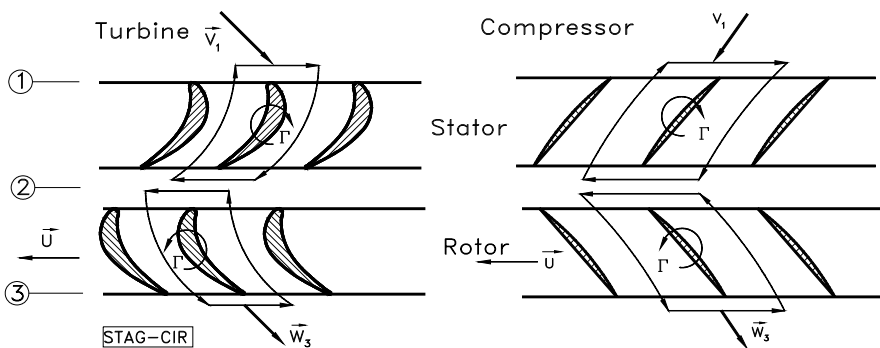
The relationship for lift-solidity coefficient derived in Section 6.2 is restricted to turbine and compressor stages with constant inner and outer diameters. This geometry is encountered in high pressure turbines or compressor components, where the streamlines are almost parallel to the machine axis. In this special case, the stream surfaces are cylindrical with almost constant diameter. However, in general cases such as in intermediate and low pressure stages, as well as radial compressor and turbine stages, the stream surfaces have different radii, as shown in Fig. 6.13. The meridional velocity component might also change from station to station. In order to calculate the blade lift-solidity coefficient correctly, the radius and the meridional velocity changes must be taken into account. In the following sections, the corresponding relations for a turbine stator and rotor are derived. Extending the derivation to compressor stator and rotor leads to the same results.

Figure 6.13 shows a turbine stage with a meridional cross section where the mean radius changes from the inlet at station 1 to the exit at station 3 (Fig 6.13a). The same cross section unfolded exhibits the change of the spacing for the stator and the rotor cascade (6.13b). Before starting with the derivation of the generalized lift-solidity coefficient, we introduce a convention about the direction of the circulation around the stator and rotor blades. The reference configurations are the turbine stator and rotor. To treat both the turbine and compressor stator and rotor in a unified manner, we use the same direction convention that we assume for the reference configuration,

namely turbine stator and rotor. Thus, the generalized lift-solidity coefficients that we obtain for turbine stator is fully identical with the one for compressor stator. Likewise, the lift-solidity coefficient for the turbine rotor is fully identical with the one for compressor rotor. This convention is depicted in Fig. 6.14.



**Fig. 6.13:** A turbine stage with different mean diameter (a), circulation around stator and rotor (b).



**Fig. 6.14:** Unified circulation convention for stator and rotor cascades.



### 5.6.1 Lift-Solidity Coefficient for Turbine Stator

To calculate the lift-solidity coefficient for the turbine stator shown in Fig. 6.13, first the circulation around the stator blade is calculated using Eq. (5.10)

$$\Gamma = \oint_C \mathbf{V} \cdot d\mathbf{c} = V_{u1}s_1 + V_{u2}s_2 + \int_1^2 \mathbf{V} \cdot d\mathbf{c} + \int_3^4 \mathbf{V} \cdot d\mathbf{c} \quad (5.47)$$

The last two integrals in Eq. (5.47) cancel each other resulting in

$$\Gamma = V_{u2}s_2 + V_{u1}s_1 \quad (5.48)$$

As shown in Fig. 6.13, the spacing  $s_1$  is different from  $s_2$ . To establish a relationship between  $s_1$  and  $s_2$ , we may introduce two planes that intersect each other on the machine axis at an angle  $\Delta\theta$ . The angle  $\Delta\theta$  is chosen such that the planes contain at least one blade. The spacings are related through:

$$\frac{s_1}{s_2} = \frac{\Delta\theta r_1}{\Delta\theta r_2} = \frac{r_1}{r_2} \quad (5.49)$$

We introduce the dimensionless meridional velocity ratio and the diameter ratio for the stator

$$\mu = \frac{V_{m1}}{V_{m2}}, \quad v = \frac{r_1}{r_2} = \frac{s_1}{s_2} \quad (5.50)$$

Since  $s_1$  and  $s_2$  are related by  $s_1 = v s_2$ , the circulation  $\Gamma$  in Eq. (5.48) becomes:

$$\Gamma = s_2 (V_{u2} + v V_{u1}) \quad (5.51)$$

Similar to Eq. (5.9), the mean velocity vector is:

$$\mathbf{V}_\infty = \frac{1}{2} (\mathbf{V}_1 + \mathbf{V}_2) \quad (5.52)$$

The velocity vector  $\mathbf{V}_\infty$ , its corresponding components, and angles are presented in Fig. 6.15.

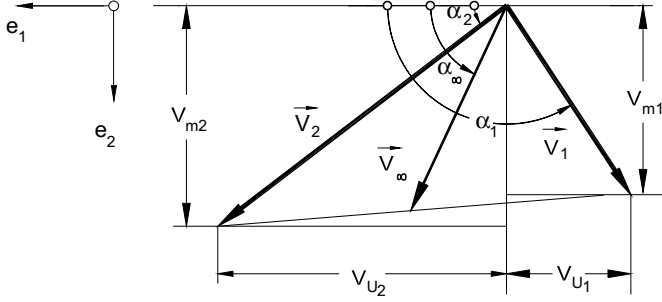


**Fig. 6.15:** Velocity diagram for a turbine stator cascade with different radii at the inlet and exit.

Using the reference coordinate in Fig. 6.15, we express the velocity vector  $\mathbf{V}_\infty$  in terms of its components

$$\mathbf{V}_\infty = \frac{1}{2} (\mathbf{V}_1 + \mathbf{V}_2) = \frac{1}{2} [(-\mathbf{e}_1 V_{u1} + \mathbf{e}_2 V_{m1}) + (\mathbf{e}_1 V_{u2} + \mathbf{e}_2 V_{m2})] \quad (5.53)$$

Rearranging Eq. (5.53) gives:

$$\mathbf{V}_\infty = \frac{1}{2} [\mathbf{e}_1 (V_{u2} - V_{u1}) + \mathbf{e}_2 (V_{m1} + V_{m2})] \quad (5.54)$$

Thus the components in circumferential and meridional directions are:

$$V_{u\infty} = \frac{1}{2} (V_{u2} - V_{u1}) \quad \text{and} \quad V_{m\infty} = \frac{1}{2} (V_{m1} + V_{m2}) \quad (5.55)$$

With  $V_{m\infty}$  from Eq. (5.55),  $V_{m\infty} = V_\infty \sin \alpha_\infty$ , and (5.50) we obtain:

$$V_\infty = |\mathbf{V}_\infty| = \frac{1}{2} \frac{V_{m2}(1 + \mu)}{\sin \alpha_\infty} \quad (5.56)$$

where  $\sin \alpha_\infty$  can be obtained from

$$\cot \alpha_\infty = \frac{V_{u\infty}}{V_{m\infty}} = \frac{V_{u2} - V_{u1}}{V_{m1} + V_{m2}} = \frac{\mu \cot \alpha_1 + \cot \alpha_2}{1 + \mu} \quad (5.57)$$

Introducing Eq. (5.51) and (5.56) into the inviscid lift equation (5.15) , we find:

$$C_L = \frac{F_i}{\frac{1}{2} \rho_\infty V_2^2 c} = \frac{V_{m2}(1 + \mu)}{V_2^2 \sin \alpha_\infty} (V_{u2} + v V_{u1}) \frac{s_2}{c} \quad (5.58)$$

or:

$$C_L \frac{c}{s_2} = \frac{\sin \alpha_2^2}{\sin \alpha_\infty} (1 + \mu) (\cot \alpha_2 - v \mu \cot \alpha_1) \quad (5.59)$$

Equation (5.59) represents the generalized lift-solidity coefficient for a stator cascade with different inlet and exit radii, meridional and circumferential velocity components. Setting  $v = 1$  and  $\mu = 1$ , Eq. (5.59) assumes the same form as Eq. (5.18).

The influence of the diameter ratio  $v$  on the cascade lift coefficient can be seen from Fig. 6.16(a) and (b). It represents the plot of Eq.(5.59). Setting the stator exit flow angle  $\alpha_2 = 70^\circ$  for a compressor cascade, the lift coefficient is plotted as a function of the inlet flow angle  $\alpha_1$  for five different  $v$ -vales. The curve with  $v < 1.0$  corresponds to axial, radial cascades, where the exit diameter is larger than the inlet one. Such diameter ratios are found in radial compressors, intermediate and low pressure turbine units. The curve with  $v = 1$  corresponds to a cascade geometry with constant mean diameter, and finally the case  $v > 1.0$  corresponds to a cascade geometry, where the inlet diameter is larger than the exit one. This type of cascades are encountered in radial inflow turbines. As Fig. 6.16 shows, a compressor cascade with an inlet flow angle  $\alpha_1 = 60^\circ$  and  $v = 1$  gives a lift coefficient  $C_L c/s = -0.41643$ . Reducing the diameter ratio to  $v = 0.8$  results in much smaller lift-solidity coefficient of  $C_L c/s = -0.19081$  and thus a relaxation of the cascade aerodynamic loading. As a consequence, higher deflection may be achieved that leads to a higher stage pressure ratio without separation. For this particular example, keeping the exit flow angle  $\alpha_2 = 70^\circ$ , the cascade flow deflection will increase from 10 to 15.5°. These results are fully compatible with those presented in Chapter 5. In Fig. 6.15(b) the cascade exit flow angle is set  $\alpha_2 = 20^\circ$  which is typical of a conventional turbine stator blades exit angle. For the inlet flow angle of  $\alpha_1 = 90^\circ$  and above, the lift-solidity coefficient is just slightly different from the one shown in Fig. 6.6.

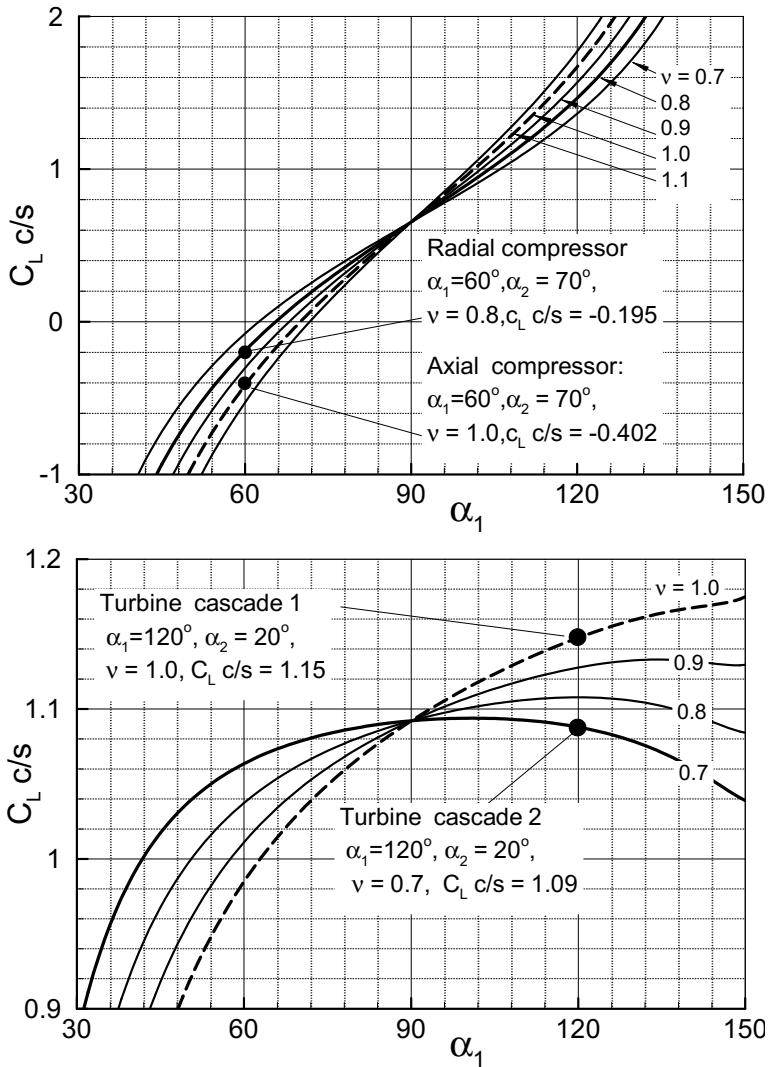


**Fig. 6.16:** Influence of diameter ratio on cascade lift-solidity coefficient, (a) for exit flow angle  $\alpha_2 = 70^\circ$  corresponding to a compressor exit flow angle and (b) for a conventional turbine exit flow angle of  $\alpha_2 = 20^\circ$ .

### 5.6.2 Turbine Rotor

To determine the lift-solidity coefficient of a rotating cascade, two different types of circulations are distinguished. The first one is the *relative circulation* that is constructed by the circumferential components of the relative velocity vectors and the corresponding spacings. This relative circulation is registered by an observer who is placed within the rotating or relative frame of reference. The second one is the *absolute circulation*, which is recorded by an observer located in a stationary or absolute frame of reference. Since the absolute circulation is responsible for energy transfer to/from the rotating cascade, it is used for calculating the lift-solidity coefficient of turbine/compressor rotor cascades.

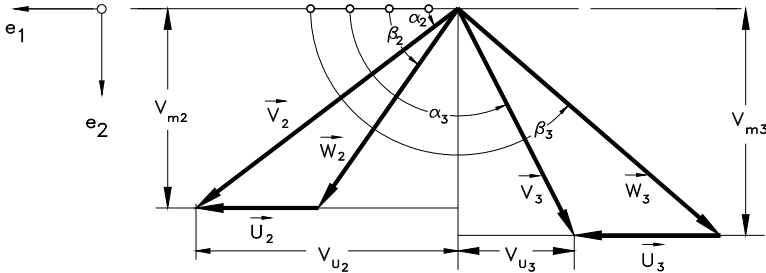


Fig. 6.17: Angle definition to determine the rotor cascade lift coefficient.

Using the nomenclature in Fig. 6.13 in conjunction with the stage velocity diagram, Fig. 6.17, the absolute circulation around the rotor blade is given by:

$$\Gamma = V_{u2}s_2 + V_{u3}s_3 \quad (5.60)$$

Considering the following relations:

$$\mu = \frac{V_{m2}}{V_{m3}}, \quad v = \frac{r_2}{r_3}, \quad \phi = \frac{V_{m3}}{U_3} \quad (5.61)$$

and applying similar procedure as in 6.6.1, the mean velocity is found:

$$V_\infty = \frac{1}{2} \frac{V_{m3}}{\sin \alpha_{\infty R}} (1 + \mu) \quad (5.62)$$

The subscript  $R$  in Eq.(5.62) refers to the rotor. Referring to the angle definition in Fig. 6.17, the absolute velocity components in circumferential direction  $V_{u2}$ ,  $V_{u3}$  can be explained in terms of circumferential component of the relative velocities  $W_{u2}$ ,  $W_{u3}$  and the circumferential velocities  $U_2$ ,  $U_3$ . For the absolute and relative velocity vectors and their components we find:

$$\begin{aligned}
 V_2 &= W_2 + U_2, & V_3 &= W_3 + U_3 \\
 V_{u2} &= W_{u2} + U_2, & V_{u3} &= W_{u3} - U_3
 \end{aligned}
 \tag{5.63}$$

Introducing Eqs. (5.61), (5.62), and (5.63) into the following lift equation:

$$F = \rho_\infty V_\infty \times \Gamma \text{ with } \Gamma = |\Gamma| = V_{u2}s_2 + V_{u3}s_3 \tag{5.64}$$

we obtain the generalized inviscid lift-solidity coefficient for the rotor:

$$C_L = \frac{V_{m3}}{\sin \alpha_{\infty R}} \frac{(1 + \mu)(V_{u2}s_2 + V_{u3}s_3)}{V_3^2 c} \tag{5.65}$$

Replacing the exit velocity by  $V_3 = V_{m3}/\sin \alpha_3$ , we find:

$$C_L = \frac{\sin^2 \alpha_3}{\sin \alpha_{\infty R}} (1 + \mu) \left( v \frac{V_{u2}}{V_{m3}} + \frac{V_{u3}}{V_{m3}} \right) \frac{s_3}{c} \tag{5.66}$$

In Eq. (5.66) we insert the corresponding components from Eq (6.58)

$$C_L = \frac{\sin^2 \alpha_3}{\sin \alpha_{\infty R}} (1 + \mu) \left( \mu v \left( \frac{W_{u2}}{V_{m2}} + \frac{U_2}{V_{m2}} \right) + \frac{W_{u3}}{V_{m3}} - \frac{U_3}{V_{m3}} \right) \frac{s_3}{c} \tag{5.67}$$

For further rearrangement of Eq. (5.67), we implement the following relations

$$\frac{W_{u2}}{V_{m2}} = \cot \beta_2, \quad \frac{W_{u3}}{V_{m3}} = -\cot \beta_3, \quad \frac{U_2}{V_{m2}} = \frac{v}{\phi \mu}, \quad \frac{U_3}{V_{m3}} = \frac{1}{\phi} \tag{5.68}$$

and obtain the final relation for the lift-solidity coefficient for a rotor cascade as:

$$C_L \frac{c}{s_3} = \frac{\sin^2 \alpha_3}{\sin \alpha_{\infty R}} (1 + \mu) \left[ \mu v \cot \beta_2 - \cot \beta_3 + \frac{v^2 - 1}{\phi} \right] \tag{5.69}$$

Equation (5.69) is generally valid for calculating the lift coefficients of radial, mixed, and axial turbines and compressor rotors. The absolute angles  $\alpha_3$  and  $\alpha_{\infty R}$  are related to the relative angles  $\beta_2$  and  $\beta_3$  by the following trigonometric relations:

$$\cot \alpha_2 = \cot \beta_2 + \frac{v}{\mu \phi}, \quad \cot \alpha_3 = \cot \beta_3 + \frac{1}{\phi}, \quad \cot \alpha_{\infty} = \frac{\cot \alpha_3 + \mu \cot \alpha_2}{1 + \mu} \quad (5.70)$$

With Eqs. (5.68) and (5.69), the generalized lift- solidity coefficient can be determined for turbine and compressor cascades with given geometry, flow angles, and velocity ratios. As an example, Fig. 6.17 presents the lift-solidity coefficient for turbine and compressor rotor cascades as a function of rotor relative inlet flow angle  $\beta_2$  with the relative exit flow angle  $\beta_3$  as a parameter.

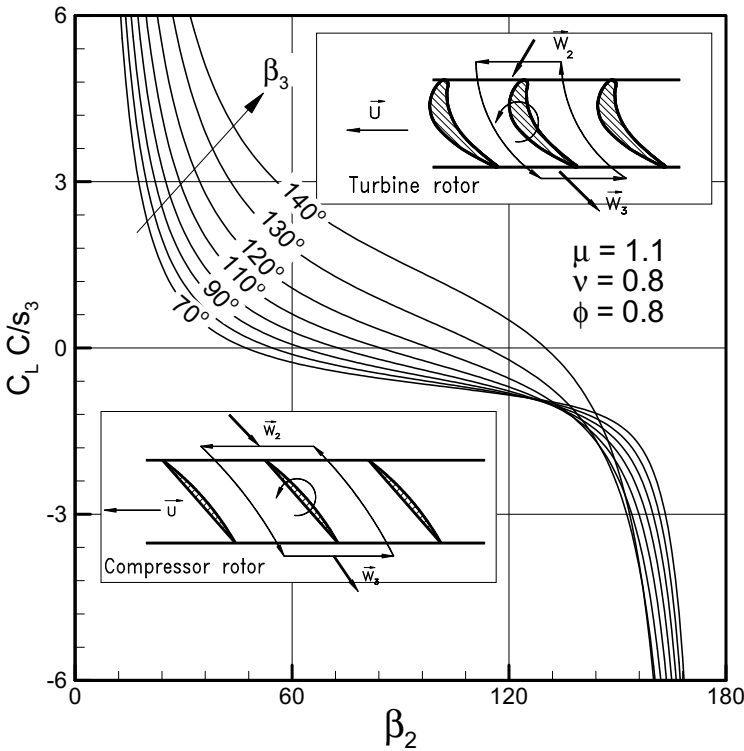


**Fig. 6.18:** Lift-solidity coefficient for turbine and compressor rotor cascade as a function of the relative flow angle  $\beta_3$  with  $\beta_2$  as parameter.

As the figure shows, the positive lift- solidity coefficients represent the values for turbine rotor cascades, whereas the negative ones pertain to the compressor rotor cascades. Keeping the exit flow angle constant and decreasing the relative inlet flow

angle leads to a higher flow deflection and thus a higher lift. In contrast, a higher lift-solidity coefficient for compressor rotor cascades is achieved by increasing the relative inlet flow angle. It should be pointed out that flow deflections above  $\Delta\theta = 20^\circ$  may lead to flow separation along the suction surface of the compressor rotor blade. Equation (5.69) is generally valid for a rotating cascade, where the meridional and circumferential velocity ratios are different from zero. Special case for no-rotating cascade can easily be derived for  $U \rightarrow 0$ , and in the limit  $\phi \rightarrow \infty$  we obtain the term  $(v^2 - 1)/\phi \rightarrow 0$ . In this case the relative flow angles are transformed into absolute flow angles. Considering the sign convention for circulation in Fig. 6.14, the resulting equation corresponds to Eq. (6.54).

## References

1. Pfeil, H., 1969, "Optimale Primärverluste in Axialgittern und Axialstufen von Strömungsmaschinen," *VD-Forschungsheft* 535.
2. Carter, A.D.S., Hounsell, A.F., 1949, "General Performance Data for Aerofoils Having C1, C2 or C4 Base Profiles on Circular Arc Camberlines," National Gas Turbine Establishment (NGTE), Memorandum 62. London H.M. Stationary Office 1949
3. Abbot, J.H., Doenhoff, A.E., Stivers, L.S., 1945, "Summary of Airfoil Data," National Advisory Committee for Aeronautics (NACA) T.R. 824, Washington 1945.
4. Zweifel, O., 1945, "Die Frage der optimalen Schaufelteilung bei Beschaukelungen von Turbomaschinen, insbesondere bei großer Umlenkung in den Schaufelreihen," Brown Boveri und Co., BBC-Mitteilung 32 (1945), S. 436/444.
5. Christiani, 1928, "Experimentelle Untersuchungen eines Trag flächenprofils bei Gitteranordnung," *Luftfahrtforschung*, Vol 2, P. 91.
6. Keller, 1934, "Axialgebläse vom Standpunkt der Tragflächentheorie," Dissertation, ETH Zürich 1923.
7. Schobeiri, M. T. and Öztürk, B., 2003, Ashpis, D., "On the Physics of the Flow Separation Along a Low Pressure Turbine Blade Under Unsteady Flow Conditions," ASME 2003-GT-38917, presented at International Gas Turbine and Aero-Engine Congress and Exposition, Atlanta, Georgia, June 16-19, 2003, also published in ASME Transactions, *Journal of Fluid Engineering*, May 2005, Vol. 127, pp. 503-513.
8. Schobeiri, M. T. and Öztürk, B., 2004, "Experimental Study of the Effect of the Periodic Unsteady Wake Flow on Boundary Layer development, Separation, and Re-attachment Along the Surface of a Low Pressure Turbine Blade," ASME 2004-GT-53929, presented at International Gas Turbine and Aero-Engine Congress and Exposition, Vienna, Austria, June 14-17, 2004, also published in the ASME Transactions, *Journal of Turbomachinery*, Vol. 126, Issue 4, pp. 663-676.



9. Schobeiri, M.T., Öztürk, B. and Ashpis, D., 2005, "Effect of Reynolds Number and Periodic Unsteady Wake Flow Condition on Boundary Layer Development, Separation, and Re-attachment along the Suction Surface of a Low Pressure Turbine Blade," ASME Paper GT2005-68600.
10. Schobeiri, M.T., Öztürk, B. and Ashpis, D., 2005, "Intermittent Behavior of the Separated Boundary Layer along the Suction Surface of a Low Pressure Turbine Blade under Periodic Unsteady Flow Conditions," ASME Paper GT2005-68603.
11. Öztürk, B. and Schobeiri, M. T., 2006, "Effect of Turbulence Intensity and Periodic Unsteady Wake Flow Condition on Boundary Layer Development, Separation, and Re-attachment over the Separation Bubble along the Suction Surface of a Low Pressure Turbine Blade," ASME, GT2006-91293.

## 6 Losses in Turbine and Compressor Cascades

The flow through a turbomachine is generally three-dimensional, viscous, highly unsteady, transitional, turbulent, and compressible. This complex flow is associated with total pressure losses caused by different flow and geometry parameters. To accurately predict the efficiency of a turbomachine, accurate flow calculation is required. The most accurate flow calculation method is the direct numerical simulation (DNS) which solves the Navier-Stokes equations without including any turbulence and transition models. This method is currently being applied to different turbomachinery components with great success. However, for the time being, the computational efforts and the required computation time makes the application of DNS as a design tool impractical. As an alternative, the Reynolds averaged version of the Navier-Stokes equations (RANS) is routinely applied in turbomachinery design. To simulate the flow relatively accurately by RANS, the turbomachinery aerodynamicists have to choose, among a variety of turbulence and transition models, the most suitable one that satisfactorily predicts the efficiency of the turbomachine under design. Since most of these models involve empirical correlations that are derived from simple flow experiments, they deliver efficiencies that significantly differ from the measured efficiency of the machine. To find an acceptable solution, the computer Navier-Stokes codes are frequently *calibrated*. The issue of laminar turbulent transition, turbulence and its modeling is treated in Chapter 19 and more comprehensively in [1].

Before performing a CFD-simulation, however, the aerodynamicists have to estimate the magnitude of major component losses essential for the one-dimensional *meanline* calculations to arrive at the preliminary machine efficiency. For this purpose, different types of loss correlations are used that are of a purely empirical, semi-empirical, or theoretical nature. Such correlations are established by research centers, or individual turbomachinery manufacturers. What is interesting is that, regardless of the different natures of correlations and different design concepts and philosophies the machine designs are based on, their measured efficiencies are not far from the estimated ones. As Traupel [2] correctly indicated, a turbomachinery stage might have an efficiency of 85%, using five different major loss sources each associated with an uncertainty of  $\pm 20\%$ . For a total stage loss coefficient, this leads to an uncertainty of  $\pm 10\%$ . Since the normalized magnitude of the loss coefficient is considered to be  $100\% - 85\% = 15\%$ , the uncertainty in efficiency estimation would be about 1.5% which is acceptable for a preliminary calculation. Considering these facts, the use of loss correlations is always an integral part of the preliminary design process.

In this chapter, we present correlations for major individual loss coefficients that are described by the conservation laws of aero-thermodynamics and based on systematic experiments. Evidently, these correlations are first approximations and

cannot be considered as generally valid. However, they give insight into the mechanism of loss generation from a physical point of view and may be enhanced or corrected to suit the particular design needs. The major aerodynamic losses are:

1. Profile or primary loss
2. Loss due to the trailing edge thickness
3. Secondary flow loss
4. Loss due to trailing edge mixing in cooled gas turbine blades
5. Exit loss
6. Minor loss

Minor losses include disc friction and wetness losses. The latter is specific to steam turbine design. In what follows, physics-based correlations for the first five individual losses are presented that help turbomachinery designers to reliably estimate the losses and the efficiencies of turbomachinery components.

## 6.1 Turbine Profile Loss

For calculation of optimum chord-spacing, we learned that the optimum chord-spacing ratio exists at the point where the total pressure loss is a minimum. We then introduced the total pressure loss coefficient  $\zeta$ , called the *profile loss coefficient*  $\zeta_p$ . The profile losses are caused, among others, by the Reynolds- and Mach-number effects, geometry parameters, such as chord-spacing ratio  $c/s$ , maximum blade thickness-chord ratio  $t/c$ , and surface roughness. In Chapter 6, we presented the profile loss coefficient  $\zeta_p$  by Pfeil [3] and Kirchberg and Pfeil [4] as:

$$\zeta_p = (\epsilon_{opt})_{single} \left[ 1 + K \left( \frac{c}{s} \right)^3 \right] C_L \frac{c}{s \sin \alpha_\infty} \quad (6.1)$$

where  $(\epsilon_{opt})_{single} = 0.0115$  for a maximum blade thickness-chord ratio  $(t/c)_{max} = 0.15$  for turbine,  $(t/c)_{max} = 0.10$  for compressor blading and  $K = 0.11$ . The optimum profile loss coefficient is plotted in Fig. 6.1 as a function of inlet flow angle  $\alpha_1$  with the exit flow angle  $\alpha_2$  as a parameter. In case the actual Reynolds number is different from the one in Fig. 6.1, the loss coefficient can be corrected as shown in Section 6.2.5. For a turbine cascade with a given flow deflection angle  $\theta = \alpha_1 - \alpha_2$ , the optimum spacing/chord ratio  $(s/c)_{opt}$  can be taken from Fig. 6.1 (bottom) and the lift-solidity ratio from Eq. (6.32). If the actual turbine blade has a different maximum blade thickness-chord ratio than  $(t/c)_{max,ref} = 0.15$ , the loss coefficient can be corrected using the following empirical correlation:

$$\frac{\zeta_p}{(\zeta_p)_{t/c=0.15}} = \left( \frac{s/c - (t/c)_{max,ref}}{s/c - t/c} \right)^2 \quad (6.2)$$

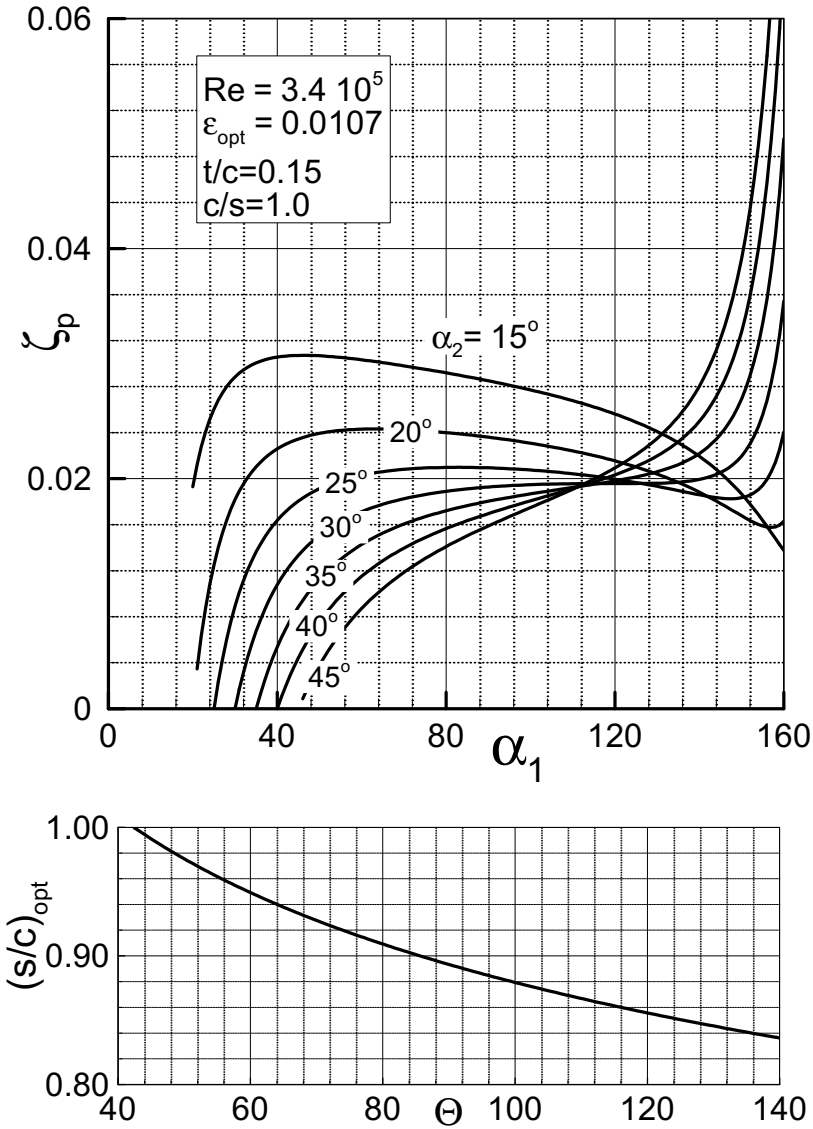


**Fig. 6.1:** Top profile loss coefficient as a function of inlet flow angle with exit flow angle as a parameter, bottom: the optimum spacing chord ratio as a function of the flow deflection angle  $\Theta = \alpha_1 - \alpha_2$ , angles measured in degree.

Equation (6.2) accurately fits the experimental data by Speidel [5]. As Fig. 6.2 shows, the relative loss coefficient increases with increasing the maximum blade thickness. In intermediate and low pressure turbines, because of a relatively high aspect ratio and excessive mechanical stresses at the blade root, the blade thickness distribution

from hub to tip must decrease. In high pressure turbine blade design the implementation of cylindrical blades with relatively thick blade profiles have been the conventional practice. However, in recent years, driven by the need to improve the turbine efficiency, the manufacturers are implementing three-dimensional blades with compound lean and also decreasing blade thickness from hub to tip.

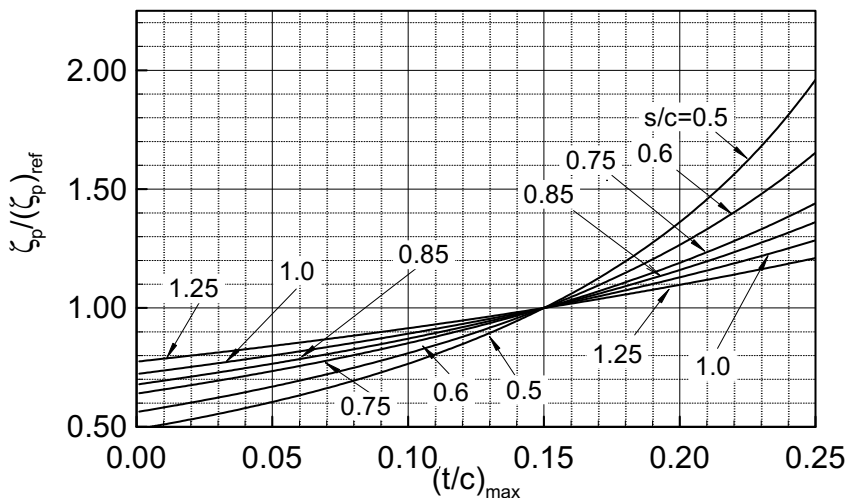


**Fig. 6.2:** Relative profile loss coefficient as a function of relative maximum thickness with  $s/c$  as the parameter.

## 6.2 Viscous Flow in Compressor Cascade

In order to calculate the total pressure losses within a compressor cascade caused by viscous effects, the boundary layer calculation method can be applied. Such investigations were performed by NACA (1940-1965), where a great number of compressor blades have been investigated systematically. The results of those investigations are still valid for compressor design calculations and are published in the NASA-Technical Note, NASA-SP-36 [6].

### 6.2.1 Calculation of Viscous Flows

The viscous flow through turbine and compressor cascades or through any other turbomachinery component is described by the Navier-Stokes equations. These equations are obtained if the shear stress term in equation of motion is replaced by the Stokes relation, where the shear stress tensor is directly proportional to the deformation tensor. The solution of these equations require considerable computational effort and CPU-time. An alternative method, which leads to satisfactory results, combines the classical boundary layer method with an inviscid flow calculation procedure that is applied to the *potential core*. The basic concept of this method states that the viscosity has a significant effect within a thin *boundary*

layer. Inside the boundary layer, the viscous flow causes drag forces that are associated with total pressure losses. Outside of the boundary layer, the viscosity effect might be neglected if the Reynolds number is high enough.

In the following section we present the basic features of a boundary layer flow essential for understanding its application to the compressor aerodynamic losses. In context of the turbomachinery flow physics the boundary layer is treated in more detail in Chapter 20.

### 6.2.2. Boundary Layer Thicknesses

Before discussing the boundary layer integral equation, we introduce the boundary layer quantities such as the *displacement thickness*,  $\delta_1$ , *momentum thickness*  $\delta_2$ , *energy dissipation thickness*  $\delta_3$  and *form parameters*. Assuming the flow is incompressible, Fig. 6.3 shows an example of boundary layer growth on a flat plate.

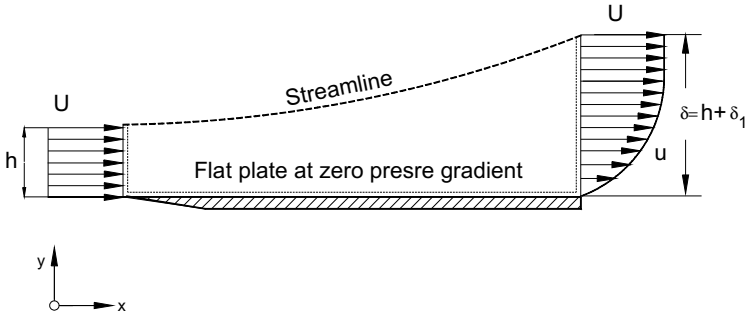


Fig. 6.3: Boundary layer development along a flat plate.

The displacement thickness is obtained by applying the continuity condition to the boundary layer flow:

$$\rho U h w = \rho w \int_0^{\delta} [(u - U) + U] dy = \rho w \left[ \int_0^{\delta} (u - U) dy + (h + \delta_1) U \right] \quad (6.3)$$

with  $\delta = h + \delta_1$  and  $U_1 = U_2 = U$  as the velocity at the edge of the boundary layer and  $w = 1$  as the width of the plate shown in Fig. 6.3. As a result, we obtain the boundary layer displacement thickness:

$$\delta_1 = \int_0^{\delta} \left( 1 - \frac{u}{U} \right) dy \quad (6.4)$$

The drag force in x-direction is obtained from:

$$D = \dot{m} U - \int_0^{\delta} u d\dot{m} \quad (6.5)$$

Using the continuity equation, the drag force becomes:

$$D = \rho w \int_0^{\delta} (U - u) u dy \quad (6.6)$$

We introduce the drag coefficient  $C_D$ :

$$C_D = \frac{D}{\frac{1}{2} \rho U^2 L w} = \frac{2}{L} \int_0^{\delta} \left(1 - \frac{u}{U}\right) \frac{u}{U} dy \quad (6.7)$$

with  $L$  and  $w=1$  as the length and the width of the plate, respectively. The integral in Eq. (6.7) is the *momentum deficiency thickness*  $\delta_2$ :

$$\delta_2 = \int_0^{\delta} \left(1 - \frac{u}{U}\right) \frac{u}{U} dy \quad (6.8)$$

and with Eq. (6.8) the drag coefficient yields:

$$C_D = \frac{2\delta_2}{L} \quad (6.9)$$

Thus, the drag coefficient  $C_D$  is directly proportional to the boundary layer momentum thickness  $\delta_2$ . In a similar manner, we find the *energy dissipation thickness*.

$$\delta_3 = \int_0^{\delta} \left(1 - \frac{u}{U}\right) \left(\frac{u}{U}\right)^2 dy \quad (6.10)$$

The energy dissipation thickness, especially defined for the compressor cascade, is not identical with the energy thickness in the external flow boundary layer calculation method. We further define the form parameter:

$$H_{12} = \frac{\delta_1}{\delta_2} \quad \text{and} \quad H_{32} = \frac{\delta_3}{\delta_2} \quad (6.11)$$

### 6.2.3 Boundary Layer Integral Equation

This Section presents the basic concept of boundary layer theory in the form of integral equation is presented. Detailed treatment of the boundary layer theory from

turbomachinery aerodynamics point of view is presented in Chapter 21.

We consider a two-dimensional incompressible viscous flow within the boundary layer of a flat plate as shown in Fig. 6.1. The equation of continuity is:

$$\frac{\partial u}{\partial x} + \frac{\partial v}{\partial y} = 0 \quad (6.12)$$

with  $u$  and  $v$  as the velocity components in  $x$ - and  $y$ -direction. The equations of momentum in  $x$ - and  $y$ -directions are:

$$\begin{aligned} \rho \left( u \frac{\partial u}{\partial x} + v \frac{\partial u}{\partial y} \right) &= - \frac{\partial p}{\partial x} + \mu \left( \frac{\partial^2 u}{\partial x^2} + \frac{\partial^2 u}{\partial y^2} \right) \\ \rho \left( u \frac{\partial v}{\partial x} + v \frac{\partial v}{\partial y} \right) &= - \frac{\partial p}{\partial y} + \mu \left( \frac{\partial^2 v}{\partial x^2} + \frac{\partial^2 v}{\partial y^2} \right) \end{aligned} \quad (6.13)$$

Based on systematic experimental investigations, Prandtl [7] deduced that if the Reynolds number is large enough, the shear layer must be very thin so that the following approximations can be applied:

$$\delta \ll L, \quad v \ll u \quad \text{and} \quad \frac{\partial}{\partial x} \ll \frac{\partial}{\partial y} \quad (6.14)$$

Using these approximations, we arrive at:

$$\frac{\partial p}{\partial y} \approx 0, \text{ this results in } p = p(x) \text{ and } \frac{\partial p}{\partial x} \equiv \frac{dp}{dx} \quad (6.15)$$

The change of static pressure in Eq. (6.15) can be obtained by applying the Bernoulli equation to the region outside the boundary layer. With  $U$  as the velocity outside the boundary layer (*potential flow velocity*) we obtain from Bernoulli equation:

$$\frac{\partial p}{\partial x} = -\rho U \frac{dU}{dx} \quad (6.16)$$

This requires that the distribution of  $U(x)$  outside the boundary layer be known. According to the previous assumptions, the following approximation can be made:

$$\frac{\partial^2 u}{\partial x^2} \ll \frac{\partial^2 u}{\partial y^2} \quad (6.17)$$

With the above approximations, the system of three Eqs. (6.12) and (6.13) is reduced to the following system of two boundary layer equations:



$$\frac{\partial u}{\partial x} + \frac{\partial v}{\partial y} = 0$$

$$u \frac{\partial u}{\partial x} + v \frac{\partial u}{\partial y} \approx U \frac{dU}{dx} + \frac{\mu}{\rho} \frac{\partial^2 u}{\partial y^2} \quad (6.18)$$

Introducing the shear stress  $\tau = \mu \frac{\partial u}{\partial y}$  the integration Eq. (6.18) leads to:

$$\frac{d\delta_2}{dx} + (2 + H_{12}) \frac{\delta_2}{U} \frac{dU}{dx} = \frac{\tau_w}{\rho U^2} = \frac{1}{2} C_f \quad (6.19)$$

This is the boundary layer equation developed by von Kármán [8]. It expresses the change of the momentum thickness  $\delta_2$  as a function of variable  $x$  and contains the form parameter  $H_{12}$  and the friction factor  $C_f$ , which can be obtained from experimental data. The shear stress diminishes if the velocity slope approaches negligible values  $\tau_w = \mu \frac{\partial u}{\partial y} \approx 0$  if  $\frac{\partial u}{\partial y} \rightarrow 0$ . To solve the differential equation

(6.19) for the momentum thickness  $\delta_2$ , relationships for the form parameter  $H_{12}$  and the friction coefficient  $C_f$  are needed. Furthermore, the streamwise pressure gradient, which is expressed in terms of  $dU/dx$ , must be known. As discussed in more detail in Chapter 21, Ludwig and Tillman [9] presented an empirical correlation for  $C_f$  with an acceptable accuracy.

#### 6.2.4 Application of Boundary Layer Theory to Compressor Blades

The objective of the following consideration is to calculate the compressor profile losses by applying the boundary layer theory. We assume that: 1) outside the boundary layer, the total pressure is constant, inside there is a total pressure loss; 2) the working fluid is incompressible ( $M < 0.3$ ); 3) outside the boundary layer at the exit, the static pressure and flow angles are constant. We define the profile loss coefficient as the total pressure loss due to the viscosity. With respect to the inlet kinetic energy it reads:

$$\zeta_P = \frac{\Delta p_o}{\frac{1}{2} \rho V_1^2} \quad (6.20)$$

with

$$\Delta p_o = \frac{1}{\dot{m}} \int_o^s (p_{o1} - p_{o2}) d\dot{m} \quad (6.21)$$

as the mass averaged total pressure loss.

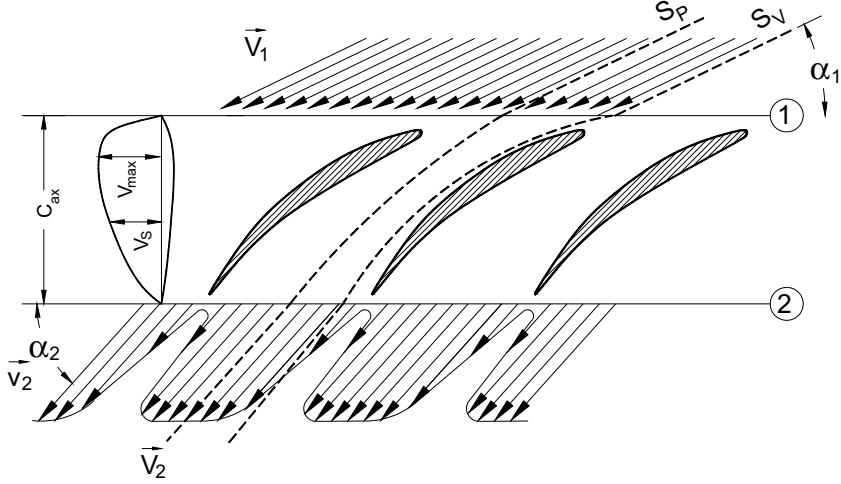


**Fig. 6.4:** Identification of total pressure losses due to the viscosity,  $S_P$  and  $S_V$  are streamlines within the potential core and the boundary layer,  $V_2$  and  $v_2$  are velocities outside and inside the boundary layer.

According to the above assumptions and Fig. 6.4, the total pressure outside the boundary layer,  $p_{o1}$ , is:

$$p_{o1} = p_{o2} = p_2 + \frac{1}{2} \rho V_2^2 \quad (6.22)$$

The static pressure  $p_2$  is constant within the boundary layer. Replacing the differential mass flow in Eq. (6.21)  $dm = \rho v_2 \sin \alpha_2 h ds$  with the cascade height  $h = l$ , the total pressure loss is obtained from:

$$\Delta p_0 = \frac{\int_o^s \frac{1}{2} \rho (V_2^2 - v_2^2) \rho v_2 \sin \alpha_2 ds}{\int_o^s \rho v_2 \sin \alpha_2 ds} \quad (6.23)$$

Using the following boundary layer quantities:

$$\delta_1, \delta_2, \delta_3, H_{12} = \frac{\delta_1}{\delta_2} \text{ and } H_{32} = \frac{\delta_3}{\delta_2} \quad (6.24)$$

where  $\delta_1 = \delta_{1S} + \delta_{1P}$ ,  $\delta_2 = \delta_{2S} + \delta_{2P}$ , with indices S and P referring to the suction and pressure side, respectively. Thus, the profile loss coefficient is re-written as:

$$\zeta_P = \sigma \left( \frac{\delta_2}{c} \right) \left( \frac{\sin^2 \alpha_1}{\sin^3 \alpha_2} \right) \left( \frac{1 + H_{32}}{1 - \frac{\delta_2}{c} \frac{\sigma H_{12}}{\sin \alpha_2}} \right) \quad (6.25)$$

For compressors with moderate flow deflection, the expression in the bracket is close to 2, thus, Eq. (6.25) can be approximated as:

$$\zeta_P = 2 \left( \frac{\delta_2}{c} \right) \left( \frac{\sigma}{\sin \alpha_2} \right) \left( \frac{\sin \alpha_1}{\sin \alpha_2} \right)^2 \quad (6.26)$$

The dimensionless momentum thickness  $\delta_2/c$  can be obtained either from the von Karman's boundary layer equation (6.19) or from experimental data. For design of compressor blading, it is more common to use experimental results. Comprehensive experimental investigations concerning the optimal design of compressor blading were performed by the National Advisory Committee for Aeronautics (NACA). NACA systematically investigated a number of cascade geometries, particularly the NACA-65 series published in [6].

In the following section we utilize the NACA correlations since they are still valid for low, intermediate and as high subsonic compressor blades. According to the NACA experimental observations, the velocity distribution on the blade suction surface is primarily responsible for the boundary layer development and consequently the velocity diffusion as shown in Fig. 6.5. Therefore, it is necessary to establish a relationship between the boundary layer momentum thickness and the velocity distribution on the suction surface. The velocity diffusion can be expressed in terms of diffusion ratio  $V_{\max}/V_2$ . Lieblein [10] introduced a functional relationship between the ratio  $V_{\max}/V_1$  and the circulation function  $G$ :

$$\frac{V_{\max}}{V_1} = C_1 f(G) + C_2 \quad (6.27)$$

where the circulation function is

$$G = \frac{\sin^2 \alpha_1}{\sigma} (\cot \alpha_2 - \cot \alpha_1) \quad (6.28)$$

which is directly related to the lift coefficient, Eq. (6.32) and further discussed in Chapter 16. Using the inlet and exit flow angles we set:

$$\frac{V_{\max}}{V_1} = C_1 \frac{\sin^2 \alpha_1}{\sigma} (\cot \alpha_2 - \cot \alpha_1) + C_2 \quad (6.29)$$

The constants  $C_1$  and  $C_2$  are evaluated from experiments. For NACA-65 and circular arc profiles their values are:  $C_1 = 0.61$ ,  $C_2 = 1.12$ . Using the diffusion ratio, Eq. (6.29), the *diffusion* factor is then calculated from:

$$D = \frac{V_{\max}}{V_2} = \left( \frac{V_{\max}}{V_1} \right) \left( \frac{V_1}{V_2} \right) \quad (6.30)$$

$$D = \frac{\sin \alpha_2}{\sin \alpha_1} \left[ 0.61 \frac{\sin^2 \alpha_1}{\sigma} (\cot \alpha_2 - \cot \alpha_1) + 1.12 \right]$$

Equation (6.30) is valid for the reference incidence angle  $i_{ref}$ . For incidence angles different from the design incidence angle, the diffusion ratio can be obtained from [11]:

$$D = \frac{\sin \alpha_2}{\sin \alpha_1} \left[ 0.746 (i - i_{ref}) + 0.65 (i - i_{ref})^2 + 0.61 \frac{\sin^2 \alpha_1}{\sigma} (\cot \alpha_2 - \cot \alpha_1) + 1.12 \right] \quad (6.31)$$

With  $D$  from Eq.(6.31) as an independent variable, the correlation for momentum thickness is obtained experimentally and is plotted in Fig. 6.5. Thus, the profile loss is obtained by inserting  $\delta_2/c$  from Fig. 6.5 into Eq.(6.26).

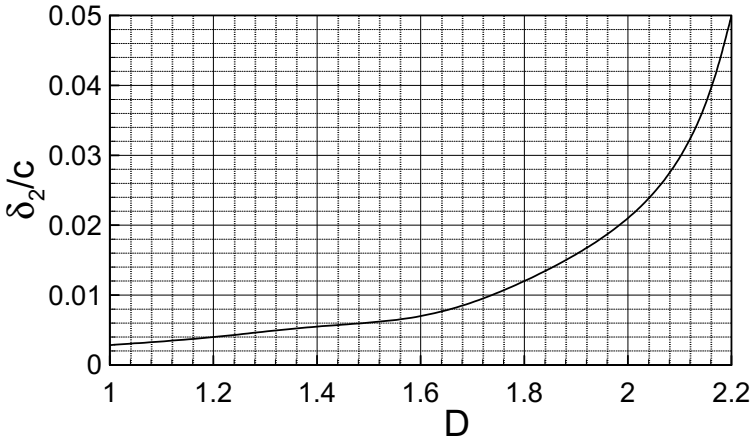


**Fig. 6.5:** Dimensionless momentum thickness as a function of diffusion factor.

### 6.2.5 Effect of Reynolds Number

As shown in Eq.(6.26), the total loss coefficient  $\zeta$  is directly proportional to the momentum thickness, which in turn is inversely proportional to the Reynolds number

$$\zeta \sim \delta_2 \sim \frac{1}{Re^m} \quad (6.32)$$

If the Reynolds number of the blading under consideration is different from the reference Reynolds number at which the experimental measurements have been carried out, the loss coefficient must be corrected by the following relation:

$$\frac{\zeta}{\zeta_{ref.}} = \left( \frac{Re_{ref.}}{Re} \right)^m, \quad \text{with } Re = \frac{cV_2}{\nu}, \quad m = -\frac{1}{5} = -0.2 \quad (6.33)$$

### 6.2.6 Stage Profile Losses

After determining the profile loss coefficients for stator and rotor blades, the stage profile loss coefficient  $Z_p$  can be obtained by two different calculation methods. The first method uses the loss coefficient for calculating the entropy difference across the blade row by applying Eq.(4.105). This locates the expansion or compression end points in an h-s-diagram. It enables the calculation of the static temperature and the total pressure at the end points and thus the row efficiency. The second method uses the stage loss coefficient as defined below:

$$Z_1 \equiv Z_p = \zeta'_p \left( \frac{V_i^2}{2l_m} \right) + \zeta''_p \left( \frac{W_{i+1}^2}{2l_m} \right) \quad (6.34)$$

with  $\zeta'_p$ ,  $\zeta''_p$  as the stator and rotor profile loss coefficients,  $l_m$  the specific stage mechanical energy, and  $i$  as the number of the reference plane, where  $\zeta_p$  has been obtained.

## 6.3 Trailing Edge Thickness Losses

Downstream of a stator or a rotor cascade, the trailing edge thickness causes an exit velocity deficit which produces a wake flow at the cascade trailing edge plane as shown in Fig. 6.6. Downstream of the cascade, at station 3 of Fig. 6.6, the non-uniform wake flow is assumed to become uniform because of the turbulent mixing. This mixing process causes additional total pressure losses that can be calculated by using the equations of continuity, momentum and energy. We start from the continuity equation for a blade height  $h=l$ :

$$\int_0^{s-d} \rho_2 V_2 \sin \alpha_2 dy = \rho_3 V_3 \sin \alpha_3 s \quad (6.35)$$

The momentum equation in y-direction reads:

$$\int_0^{s-d} \rho_2 V_2^2 \sin \alpha_2 \cos \alpha_2 dy = \rho_3 V_3^2 \sin \alpha_3 \cos \alpha_3 s \quad (6.36)$$

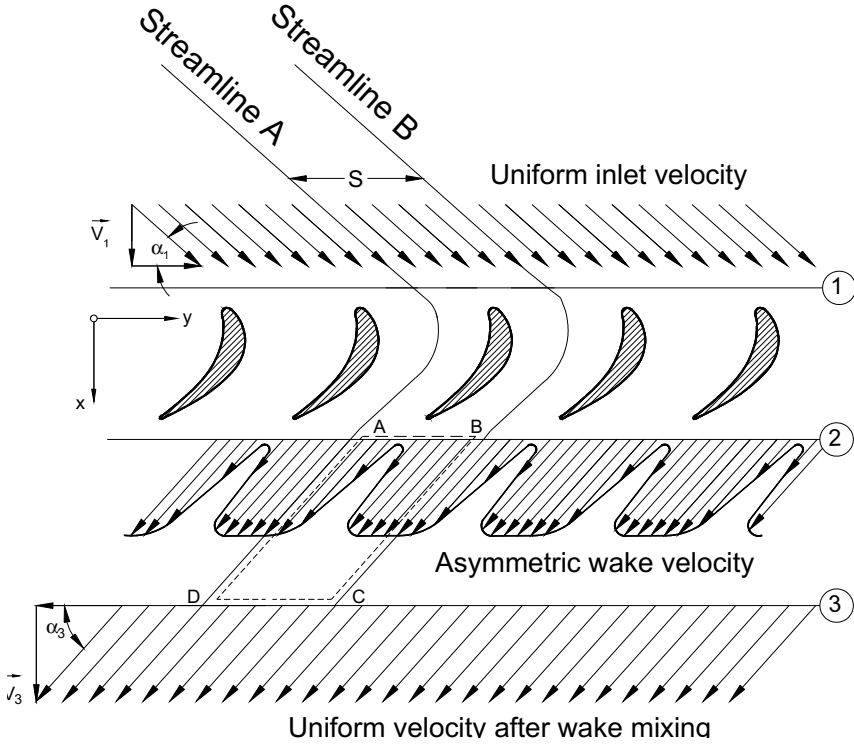


**Fig. 6.6:** Wake mixing downstream of a cascade with a finite trailing edge thickness.

and in x-direction

$$\int_0^{s-d} \rho_2 V_2^2 \sin^2 \alpha_2 dy + \int_0^s p_2(y) dy = \rho_3 V_3^2 \sin^2 \alpha_3 s + p_3 s \quad (6.37)$$

The energy equation yields:

$$\zeta = \frac{P_{o2} - P_{o3}}{\frac{1}{2} \rho V_3^2} \quad (6.38)$$

We introduce the boundary layer displacement and momentum thicknesses:

$$\delta_{1y} = \int_0^{s-d} \left( 1 - \frac{V_2}{V_{2o}} \right) dy, \quad \delta_{2y} = \int_0^{s-d} \frac{V_2}{V_{2o}} \left( 1 - \frac{V_2}{V_{2o}} \right) dy, \quad H_{12} = \frac{\delta_1}{\delta_2} \quad (6.39)$$

where  $\delta_{1y}$  and  $\delta_{2y}$  are displacement and momentum thicknesses in the  $y$ -direction. Furthermore, we introduce the following dimensionless variables with respect to the spacing:

$$D = \frac{d}{s} = \frac{b}{s \sin \alpha_2}, \quad \Delta_1 = \frac{\delta_{1y}}{s}, \quad \Delta_2 = \frac{\delta_{2y}}{s}$$

$$\delta_{1y} = \frac{\delta_{1S} + \delta_{1P}}{\sin \alpha_2}, \quad \text{and} \quad \delta_{2y} = \frac{\delta_{2S} + \delta_{2P}}{\sin \alpha_2} \quad (6.40)$$

with  $D$  as the dimensionless trailing edge thickness. Figure 6.7 shows the boundary layer thicknesses at the trailing edge.

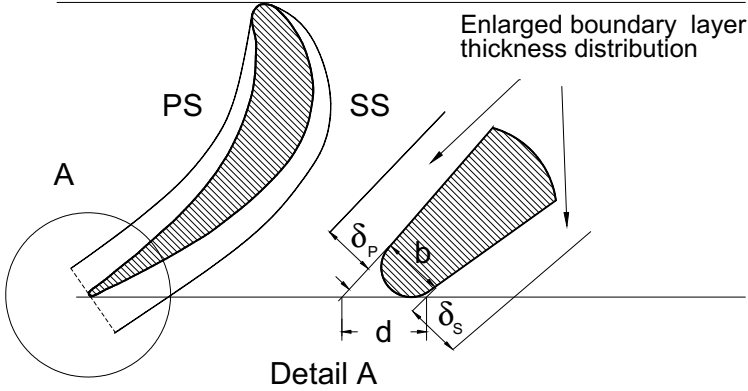


**Fig. 6.7:** Trailing edge geometry, boundary layer thickness distribution on suction and pressure surfaces.

In Eq. (6.40), the indices  $P$  and  $S$  refer to the pressure and suction side. Introducing relations in Eq. (6.40) into (6.35), the equation of continuity yields:

$$\frac{\rho_3 V_3}{\rho_2 V_{2o}} = \frac{\sin \alpha_2}{\sin \alpha_3} [1 - D - \Delta_1] \quad (6.41)$$

Dividing the momentum equation in  $y$ -direction, Eq. (6.36), by the constant velocity outside the boundary layer  $V_0$  and performing the following rearrangements:

$$\rho_2 \sin \alpha_2 \cos \alpha_2 \int_o^{s-d} \frac{V_2^2}{V_{2o}^2} dy = \rho_3 \sin \alpha_3 \cos \alpha_3 \frac{V_3^2}{V_{2o}^2} s$$

$$I = \int_o^{s-d} \left( \frac{V_2}{V_{2o}} \right)^2 dy = \int_o^{s-d} \left[ - \left( 1 - \frac{V_2}{V_{2o}} \right) + 1 - \frac{V_2}{V_{2o}} \left( 1 - \frac{V_2}{V_{2o}} \right) \right] dy$$

$$I = s - d - \delta_{1y} - \delta_{2y} \quad (6.42)$$

the momentum equation in y-direction becomes:

$$\frac{\rho_3 \sin \alpha_3 \cos \alpha_3}{\rho_2 \sin \alpha_2 \cos \alpha_2} \left( \frac{V_3}{V_{2o}} \right)^2 = 1 - D - \Delta_1 - \Delta_2 \quad (6.43)$$

For further treatment, Eq. (6.43) is rearranged as:

$$\left( \frac{\rho_3}{\rho_2} \right)^2 \left[ \frac{\rho_2 \sin \alpha_3 \cos \alpha_3}{\rho_3 \sin \alpha_2 \cos \alpha_2} \right] \left( \frac{V_3}{V_{2o}} \right)^2 = 1 - D - \Delta_1 - \Delta_2 \quad (6.44)$$

Dividing Eq. (6.44) by Eq. (6.41) results in:

$$\frac{\rho_2 \sin \alpha_2 \cos \alpha_3}{\rho_3 \cos \alpha_2 \sin \alpha_3} = \frac{1 - D - \Delta_1 - \Delta_2}{(1 - D - \Delta_1)^2} \quad (6.45)$$

Thus, the momentum equation in y-direction is simplified as:

$$\frac{\rho_2}{\rho_3} \cot \alpha_3 = \cot \alpha_2 \frac{1 - D - \Delta_1 - \Delta_2}{(1 - D - \Delta_1)^2} \quad (6.46)$$

For further treatment of the equation of momentum in x-direction:

$$\int_o^s p_2(y) dy - p_3 s = \rho_3 V_3^2 \sin \alpha_3^2 s - \int_o^{s-d} \rho_2 V_2^2 \sin \alpha_2^2 dy \quad (6.47)$$

we look at the first integral. At the trailing edge plane, the static pressure generally changes in the y-direction. However, we introduce an average  $\bar{p}_2$  that represents an integral average of the static pressure along the trailing edge area. Inserting the relationship for the integral term on the right-hand side of Eq.(6.47), we arrive at:



$$(\bar{p}_2 - p_3) = \rho_3 \sin^2 \alpha_3 V_3^2 - \rho_2 \sin^2 \alpha_2 V_{2o}^2 [1 - D - \Delta_1 - \Delta_2] \quad (6.48)$$

Finally, the dimensionless pressure difference reads:

$$\frac{\bar{p}_2 - p_3}{\frac{1}{2} \rho_3 V_3^2} = 2 \sin^2 \alpha_3 \left[ 1 - \frac{\rho_3}{\rho_2} \frac{1 - D - \Delta_1 - \Delta_2}{(1 - D - \Delta_1)^2} \right] \quad (6.49)$$

Thus, the total pressure loss coefficient is determined from:

$$\zeta = \frac{p_{o2} - p_{o3}}{\frac{1}{2} \rho_3 V_3^2} = \frac{p_2 - p_3}{\frac{1}{2} \rho_3 V_3^2} + \frac{\rho_2}{\rho_3} \left( \frac{V_{2o}}{V_3} \right)^2 - 1 \quad (6.50)$$

Now we introduce the following auxiliary functions:

$$\begin{aligned} G_1 &= 1 - D - \Delta_1 \\ G_2 &= 1 - D - \Delta_1 - \Delta_2 \\ \Delta_2 &= \Delta_1 / H \quad \text{and} \quad R = \frac{\rho_3}{\rho_2} \end{aligned} \quad (6.51)$$

with  $H = H_{12}$  as the form parameter. The total pressure loss coefficient is then:

$$\zeta = \frac{G_1^2 - 2RG_2 + R}{G_1^2} - \cos^2 \alpha_3 \left\{ \frac{2G_1^2 - 2G_2 + R}{G_1^2} - \frac{1}{R} \frac{G_1^2}{G_2^2} \right\} \quad (6.52)$$

For an incompressible flow, the density ratio can be set  $R = 1$  leading to:

$$\zeta = \frac{G_1^2 - 2G_2 + 1}{G_1^2} - \cos^2 \alpha_3 \left\{ \frac{2G_1^2 - 2G_2 + 1}{G_1^2} - \frac{G_1^2}{G_2^2} \right\} \quad (6.53)$$

This equation is plotted in Fig. 6.8 where the total pressure loss coefficient  $\zeta$  is plotted against the dimensionless trailing edge thickness  $D$ . As shown, the total pressure losses increase with increasing the trailing edge thickness. The figure also shows the effect of boundary layer thickness on the mixing process. The case  $\Delta_1 = 0.0$  represents the zero-boundary layer thickness. Increasing the boundary layer thickness results in higher mixing losses. To demonstrate the effect of the trailing edge thickness on the mixing losses, we define the mixing loss coefficient  $\zeta - \zeta_0$ , with  $\zeta_0$  as the loss coefficient at zero trailing edge thickness. The results, plotted in Fig. 6.9, show the mixing losses due to the trailing edge thickness only. Figures 6.8 and 6.9 display the trailing edge mixing loss coefficient with the relative boundary

layer displacement thickness as parameter. This parameter can easily be determined using the boundary layer calculation procedure as detailed in Chapter 21. To obtain a rapid solution, the von Karman integral method can be used.

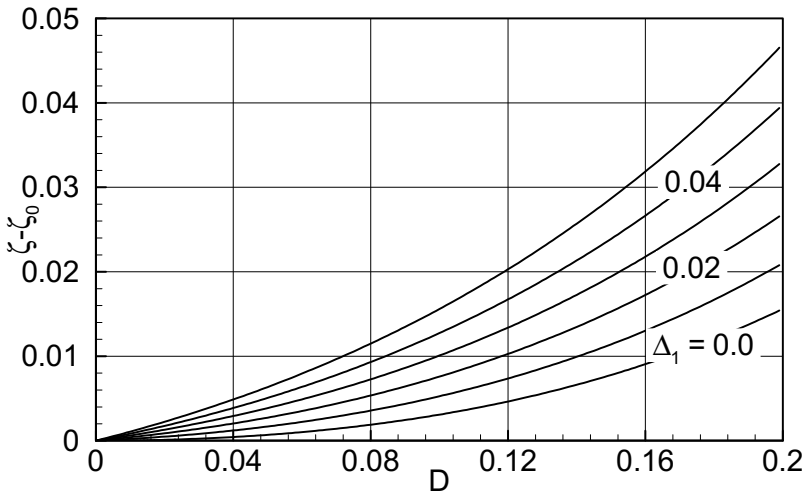


**Fig. 6.8:** Trailing edge mixing loss coefficient  $\zeta - \zeta_0$  as a function of dimensionless trailing edge thickness  $D$  with dimensionless boundary layer displacement thickness  $\Delta_1$  as a parameter.

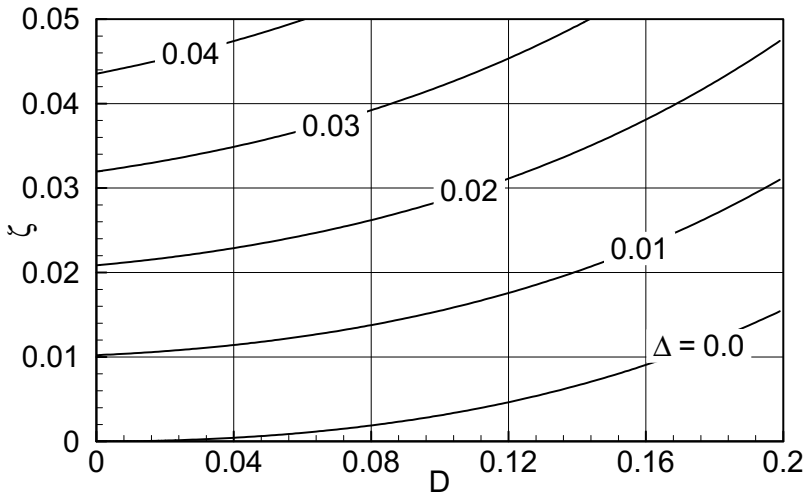


**Fig. 6.9:** Trailing edge loss coefficient  $\zeta$  as a function of dimensionless trailing edge thickness  $D$  with dimensionless boundary layer displacement thickness  $\Delta_1$  as a parameter.

It should be pointed out that calculating the trailing edge mixing loss is necessary whenever the profile loss coefficient is obtained by using a boundary layer

calculation. In case that the profile loss is estimated using experimental results, there is no need to calculate the trailing edge mixing losses since the latter are already included in experimentally determined loss correlations.

## 6.4 Losses Due to Secondary Flows

Secondary flow losses are induced by complex vortex systems within a turbomachinery stage. Among a variety of vortices inherent to a turbomachinery stage, tip clearance vortices, hub and tip endwall vortices are most instrumental in causing substantial losses. Figure 6.10 shows schematically an overview of the hub and tip clearance vortices.

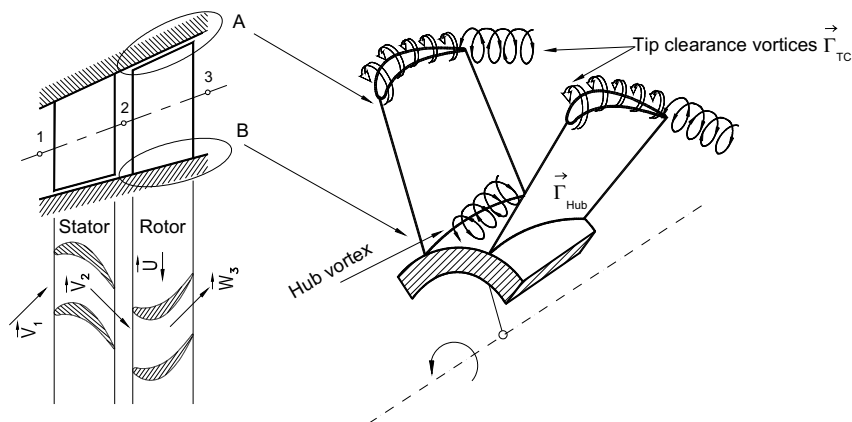


**Fig. 6.10:** Schematic explanation of secondary flows in a turbine stage.

**Tip Clearance Vortices:** These vortices are generated as the results of pressure differences at the blade tip. The fluid particles close to the blade tip have the tendency to move from the pressure surface to the suction surface and form a system of bound vortices, which at the blade trailing edge coalesce and form a free vortex system. The process of formation of the tip clearance bound and free vortices is illustrated in Fig. 6.11. As shown, the fluid particles move through the tip clearance  $\delta$  from the pressure side to the suction side. This movement triggers two mechanisms that contribute to efficiency and performance deterioration: 1) The tip clearance vortices induce drag forces and, thus, tip clearance secondary flow losses associated with an efficiency decrease of the turbo machinery stage. 2) The mass flow that escapes through the tip clearance does not contribute to the power generation thus causing a loss of turbine power. In case of a compressor, particularly the high pressure part, the existence of tip clearance causes a substantial reduction of the pressure. Details about this vortex system and how it is related to the induced velocity and drag force will be discussed in Section 6.4.1.

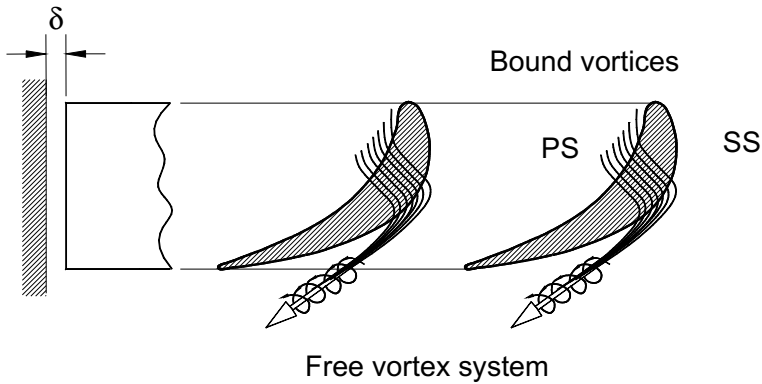


**Fig. 6.11:** Bound and free vortices caused by the tip clearance between the casing and the blade tip for an unshrouded turbine blade.

**Endwall Secondary Flow Vortices:** These vortices are formed as a result of the interaction between the low energetic endwall boundary layer and the governing pressure difference within the blade channel very close to the endwall. Details are shown in Fig. 6.12.

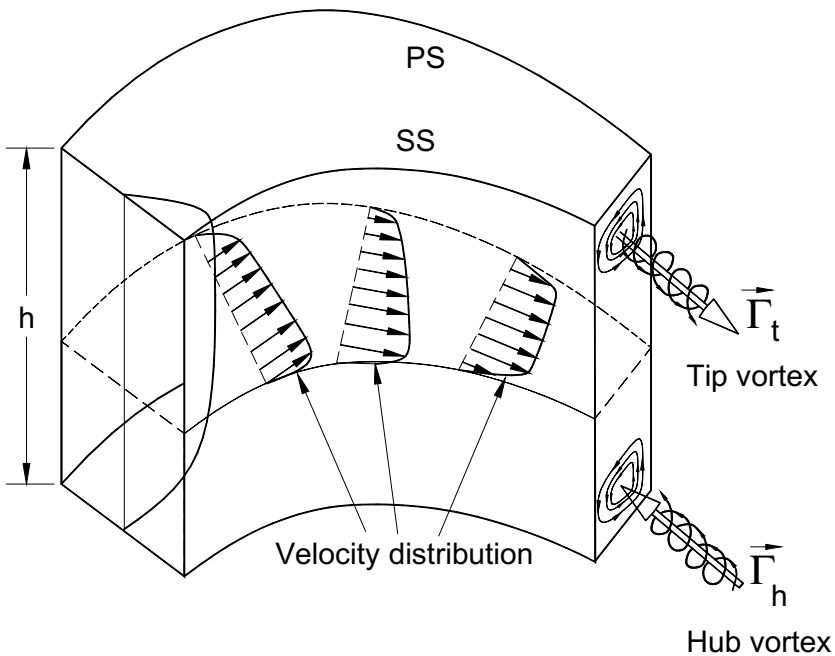


**Fig. 6.12:** Endwall secondary vortices at the hub and tip.

Within the blade channel, there is a static pressure difference between the suction and pressure surface. In the mid-section of the channel where the high Reynolds number flow is assumed to be quasi potential flow, there is an equilibrium condition between the forces due to the above pressure differences and the convective flow forces. Near the side walls (hub or casing) where the boundary layer velocity distribution is affected by the viscosity, the low energetic boundary layer is not able to maintain this equilibrium condition. As a result, the fluid particles in the boundary layers tend to move from the pressure side (concave) to the suction side and form, on blade hub and tip regions, systems of secondary vortices. This phenomenon is schematically sketched in Fig. 6.12. As seen, the circulation vectors of the two vortex systems have opposite directions. These vortices induce, according to the Bio-Savart law, a velocity field with the corresponding induced drag forces. These additional drag forces must be overcome by convective forces which result in an additional total pressure loss. For a better understanding, a brief summary of Bio-Savart law is presented below.

#### 6.4.1 Vortex Induced Velocity Field, Law of Bio -Savart, Preparatory

We consider now an isolated vortex filament with the strength  $\Gamma$  imbedded in an inviscid irrotational flow environment, as shown in Fig. 6.13.

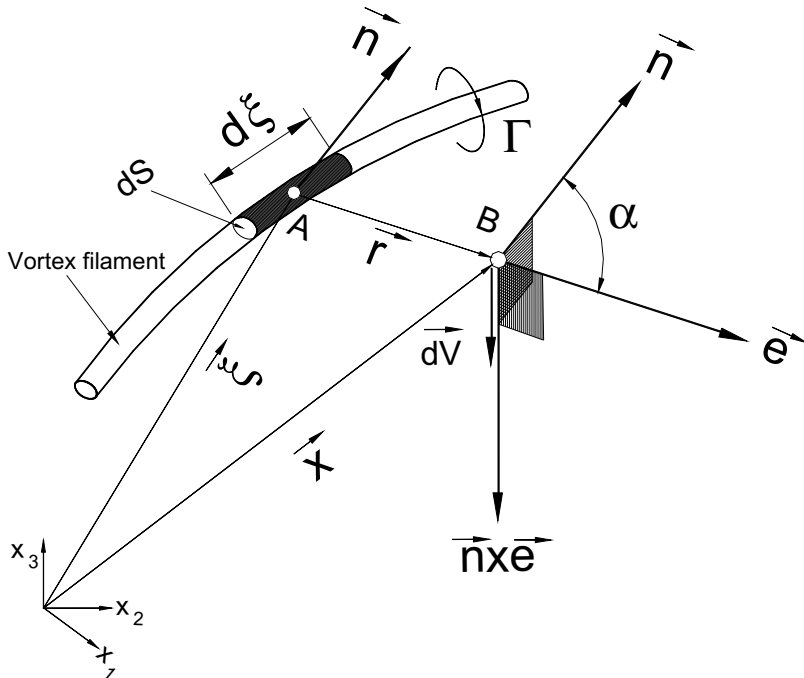


**Fig. 6.13** Velocity field induced by an isolated vortex filament.

A differential element  $d\xi$  of the vortex filament induces a differential velocity vector field  $d\mathbf{V}$  at the point B, which is in a distance  $r$  from Point A. The velocity vector  $d\mathbf{V}$

is perpendicular to the plane spanned by the normal unit vector  $\mathbf{n}$  and the unit vector  $\mathbf{e}$  in the  $r$ -direction. The unit vector  $\mathbf{n}$  is perpendicular to the infinitesimal cross section  $dS$ , whereas, the unit vector  $\mathbf{e}$  points from the center point of the element  $A$  to the position  $B$  where the velocity  $dV$  is being induced. The relationship describing the velocity field is analogous to the one discovered by Bio and Savart through electrodynamic experiments. The Bio-Savat law, its full derivation and its application to fluid mechanics, is discussed in details in [1]. In the following, we present the results essential for understanding the underlying basic physics of the Bio-Savart law.

We assume that the entire flow field is irrotational with the exception of the space occupied by the isolated vortex filament. Thus, the induced velocity field at  $B$  is obtained from:

$$\mathbf{V}_B = \frac{\Gamma}{4\pi} \int_{(L)} \frac{\mathbf{n} \times \mathbf{e}}{r^2} d\xi \quad (6.54)$$

Equation (6.54) is the Bio-Savart law for inviscid flow. Applying Eq. (6.54) to a straight vortex filament of infinite length and the strength  $\Gamma$  as shown in Fig. 6.14, the magnitude of the induced velocity is calculated from

$$V_B = \frac{\Gamma}{4\pi} \int_{-\infty}^{+\infty} \frac{\sin\alpha}{r^2} d\xi \quad (6.55)$$

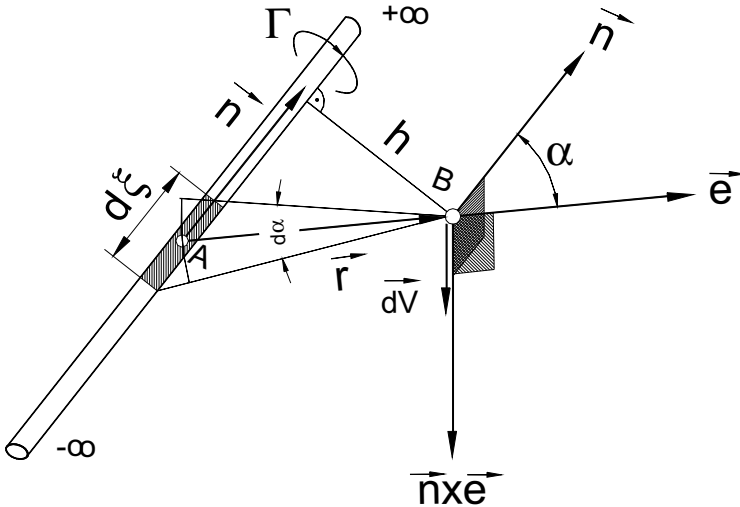


**Fig. 6.14** Induced velocity by a straight vortex filament with infinite length and strength  $\Gamma$ .

From Fig. 6.14, we find the following relationships

$$d\xi = \frac{r d\alpha}{\sin \alpha}, \quad r = \frac{h}{\sin \alpha} \quad (6.56)$$

Introducing Eq. (6.56) into (6.55) results in

$$V_B = \frac{\Gamma}{4\pi h} \int_0^\pi \sin \alpha \, d\alpha = -\frac{\Gamma}{4\pi h} \cos \alpha \Big|_0^\pi = \frac{\Gamma}{2\pi h} \quad (6.57)$$

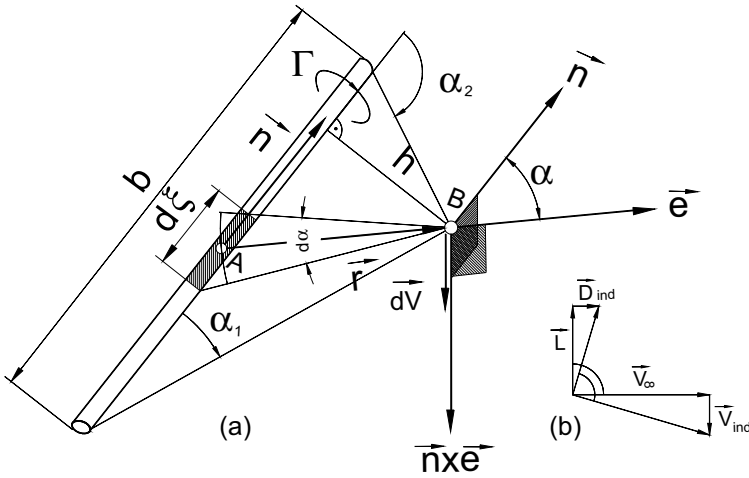


**Fig. 6.15:** Induced velocity field by a vortex of length  $b$  (a), Induced drag (b).

To calculate the velocity induced by a vortex filament of finite length  $b$ , the integration boundaries of Eq. (6.57) need to be replaced by  $\alpha_1$  and  $\alpha_2$ , shown in Fig. 6.15. The integration results in:

$$V_B = \frac{\Gamma}{4\pi h} \int_{\alpha_1}^{\alpha_2} \sin \alpha \, d\alpha = \frac{\Gamma}{4\pi h} (\cos \alpha_1 - \cos \alpha_2) \quad (6.58)$$

Setting  $\alpha_1 = 0$  and  $\alpha_2 = \pi/2$  for a semi-infinite vortex filament, we obtain the induced velocity:

$$V_B = \frac{\Gamma}{4\pi h} \quad (6.59)$$

Considering the drag/lift ratio  $D_{ind}/L = V_{ind}/V_\infty$  from Fig. 6.15(b), the induced drag force is calculated from:

$$D_{ind} = \int_{-b/2}^{b/2} \frac{V_{ind}}{V_\infty} dL = \int_{-b/2}^{b/2} \frac{V_{ind}}{V_\infty} V_\infty \Gamma(x) dx = \int_{-b/2}^{b/2} V_{ind} \Gamma(x) dx \quad (6.60)$$

with  $dL$  as an infinitesimal lift. For a single profile with an elliptic circulation distribution of  $\Gamma(x) = \Gamma_0 \sqrt{1 - (x/s)^2}$  over the span of  $b$  and  $s = b/2$ , Eq. (6.60) can be integrated analytically as given below

$$D_{ind} = \frac{2L^2}{\pi \rho V_\infty^2 b^2} \quad (6.61)$$

with the lift force  $L = (\pi/4)\rho b V_\infty \Gamma_0$ , the induced drag  $D_i = (\pi/8)\rho \Gamma_0^2$ , the induced velocity  $w_i(x) = \Gamma_0/2b$  and  $\Gamma_0$  as the maximum circulation in the middle of the airfoil. Equation (6.61) is the Prandtl equation for induced drag for a wing with an elliptical lift distribution. The induced drag coefficient is found by dividing Eq. (6.61) by  $\rho/2V_\infty^2 bc$

$$C_{D_{ind}} = \frac{C_L^2}{\pi} \frac{c}{b} \quad (6.62)$$

The total drag force acting on a wing of finite span with an arbitrary geometry is the sum of the viscous drag force and the induced drag force. To overcome the induced drag, additional mechanical energy must be provided externally. In contrast to the drag force caused by a boundary layer momentum deficit along the surface of the wing, the induced (inviscid) drag arises from a change of the flow direction due to the downward velocity field. The problematic of calculation of lift, drag, and other aerodynamic quantities is treated comprehensively in [1]. After the above preparatory introduction, we turn now to the application of the Bio-Savart law to secondary flow losses.

#### 6.4.2 Calculation of Tip Clearance Secondary Flow Losses

Consider now a turbine cascade that undergoes an inviscid flow. Since there is no viscosity effect within the flow field, the corresponding drag forces are zero. Instead, there is an induced drag force which is caused by the secondary flow field. For a wing with finite span and an elliptical lift distribution, Prandtl established a relationship between the induced drag force and the lift force. This relation can also be applied to the compressor or turbine with small aspect ratio where the secondary flow effects are dominant. For the turbine and compressor cascades, the induced drag forces cause a total pressure loss which is similar to the viscous pressure loss:

$$D_{\alpha in} = sh \Delta p_{os} = \frac{D_{in}}{\sin \alpha_\infty}, \text{ with } \Delta p_{os} = \frac{D_{in}}{\sin \alpha_\infty} \frac{1}{sh} \quad (6.63)$$



where,  $h$  represents the blade height,  $s$  the spacing and the subscripts  $s$  and  $in$  refer to secondary flow and induced quantities. Following Eq. (6.61) and using the cascade nomenclature, the induced drag may be set directly proportional to the quadrate of lift force:

$$D_{in} \sim \frac{F_i^2}{\frac{1}{2} \rho V_\infty^2 s h} \quad (6.64)$$

with  $F_i$  as the inviscid lift force. With the following definition of the total pressure loss coefficient due to the induced drag by the secondary flow

$$\zeta_s = \frac{\Delta p_{os}}{\frac{1}{2} \rho V_2^2} \quad (6.65)$$

and Eq. (6.63), we obtain:

$$\zeta_s = \frac{1}{\frac{1}{2} \rho V_2^2} \frac{D_{in}}{\sin \alpha_\infty} \frac{1}{s h} \quad (6.66)$$

Introducing Eq.(6.64) into (6.66) results in:

$$\zeta_s \sim \frac{F^2}{\left(\frac{\rho}{2}\right)^2 V_2^2 V_\infty^2 (s h)^2} \frac{1}{\sin \alpha_\infty} = \left(C_L \frac{c}{s}\right)^2 \frac{\sin \alpha_\infty}{\sin^2 \alpha_2}, \text{ with } C_L = \frac{F_i}{\frac{1}{2} \rho V_2^2 c h} \quad (6.67)$$

For an inviscid flow, as we saw in Chapter 5, the lift coefficient is given by:

$$C_L \frac{c}{s} = 2 \frac{\sin^2 \alpha_2}{\sin \alpha_\infty} (\cot \alpha_2 - \cot \alpha_1) \quad (6.68)$$

Incorporating Eq. (6.68) into (6.66), the total pressure loss coefficient due to the induced drag is expressed as:

$$\zeta_s \propto 4 (\cot \alpha_2 - \cot \alpha_1)^2 \frac{\sin^2 \alpha_2}{\sin \alpha_\infty} \quad (6.69)$$

for which we introduce the following *load function*

$$\Lambda = \left(C_L \frac{c}{s}\right)^2 \frac{\sin \alpha_\infty}{\sin^2 \alpha_2} = 4 \frac{\sin^2 \alpha_2}{\sin \alpha_\infty} (\cot \alpha_2 - \cot \alpha_1)^2 \quad (6.70)$$

with  $\alpha_\infty$  as

$$\cot\alpha_\infty = \frac{1}{2}(\cot\alpha_2 + \cot\alpha_1) \quad (6.71)$$

and considering Eq. (6.70), the proportionality relation (6.69) becomes

$$\zeta_s \propto \Lambda \quad (6.72)$$

The relation (6.72) shows that the secondary flow loss coefficient is linearly proportional to the load function Eq. (6.70). Experimental investigations by Berg [12] show that the secondary flow loss coefficient is also proportional to the dimensionless tip clearance:

$$\zeta_s \propto f\left(\frac{\delta - \delta_o}{c}\right) \quad (6.73)$$

where  $\delta$  is the actual tip clearance and  $\delta_o$  a fictive tip clearance at which the tip clearance loss becomes zero. Combining Eqs. (6.72) and (6.73) and introducing a constant  $K$  and an exponent  $m$ , Berg [12] arrived at the final equation that describes the loss coefficient due to the induced drag:

$$\zeta_s = K\Lambda\left(\frac{\delta - \delta_o}{c}\right)^m \quad (6.74)$$

with  $K = 0.169$  and  $m = 0.6$ . Thus, Eq. (6.74) is written for a stator blade without hub shroud:

$$\zeta'_{st} = 0.676(\cot\alpha_2 - \cot\alpha_1)^2 \frac{\sin^2\alpha_2}{\sin\alpha_\infty} \left[\frac{\delta - \delta_o}{c}\right]^m \quad (6.75)$$

and for rotor:

$$\zeta''_{st} = 0.676(\cot\beta_3 - \cot\beta_2)^2 \frac{\sin^2\beta_3}{\sin\beta_\infty} \left[\frac{\delta - \delta_o}{c}\right]^m \quad (6.76)$$

The tip and hub clearance flows have two different effects. First, they generate secondary flow vortices which induce additional drag forces and, second, in case of a turbine rotor they cause a mass flow defect which does not participate in power production. These two effects result in a decrease of the stage efficiency and also a decrease in overall efficiency of turbomachines. The secondary flow losses caused by the tip clearance and the endwall vortices particularly affect the efficiency of those stages with a small aspect ratios such as HP-blades.

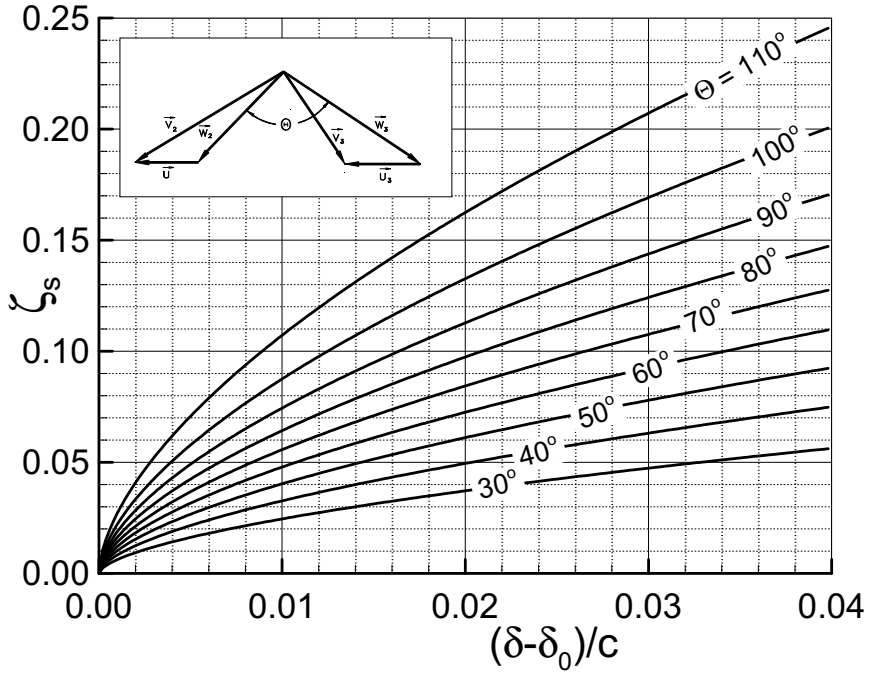


**Fig. 6.16:** Tip clearance total pressure loss coefficient as a function of dimensionless tip clearance with flow deflection  $\Theta$  as parameter.

Figure 6.16 shows the secondary flow loss coefficient  $\zeta_s$  as a function of dimensionless tip clearance  $\delta/c$  with the blade deflection  $\theta$  as the parameter. As shown, the total pressure loss coefficient increases as the tip clearance increases. Increasing the flow deflection causes the tip clearance loss to increase considerably. A blade with a higher flow deflection which is equivalent to higher load function  $\Lambda$  has a higher pressure difference between the suction and the pressure surface and, therefore, a stronger vortex system and consequently higher secondary flow losses compared to the one with lower flow deflection.

#### 6.4.3 Calculation of Endwall Secondary Flow Losses

As mentioned previously, at the hub and tip endwalls, vortices are formed as a result of the interaction between the low energetic endwall boundary layer and the governing pressure difference between the suction and pressure surfaces very close to the endwall. Details are shown in Fig. 6.16.

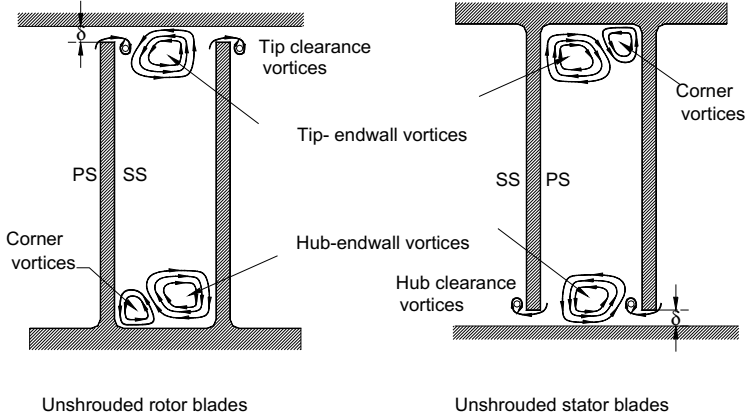


**Fig. 6.17:** Development of tip, hub and endwall vortices in rotor and stator blades channels.

In addition to the tip clearance vortices, at the tip of a rotor (Fig. 6.17 left) blade, endwall vortices are also present due to the pressure difference mentioned above. Similarly, at the hub of unshrouded stator blades (Fig. 6.17 right), clearance and endwall vortices are developed. The working principle of the endwall secondary flow vortices leading to induced drag forces and the subsequent total pressure loss is the same as the one by tip clearance vortices, as experimentally verified by Wolf [13] and further enhanced by Kirchberg and Pfeil [4]. Since the boundary layer development along the endwalls plays a significant role in generating the secondary vortices, it is obvious to include its momentum defect in a relationship that describes the endwall secondary flow loss coefficient. In order to account for the momentum deficit due to the boundary layer development, it is more appropriate to use the boundary layer momentum thickness  $\delta_2$  rather than the vague boundary layer thickness  $\delta$ . As a consequence, we may set the loss coefficient due to the secondary flow on the endwalls  $\zeta_{sw}$  as:

$$\zeta_{sw} = K \left( \frac{\delta_2}{h} \right) \left( C_L \frac{c}{s} \right)^2 \frac{\sin \alpha_\infty}{\sin^2 \alpha_2} \quad (6.77)$$

with  $h$  as the blade height. In addition to the endwall secondary flow losses, there is also a total pressure loss due to the wall friction caused by the fluid viscosity.

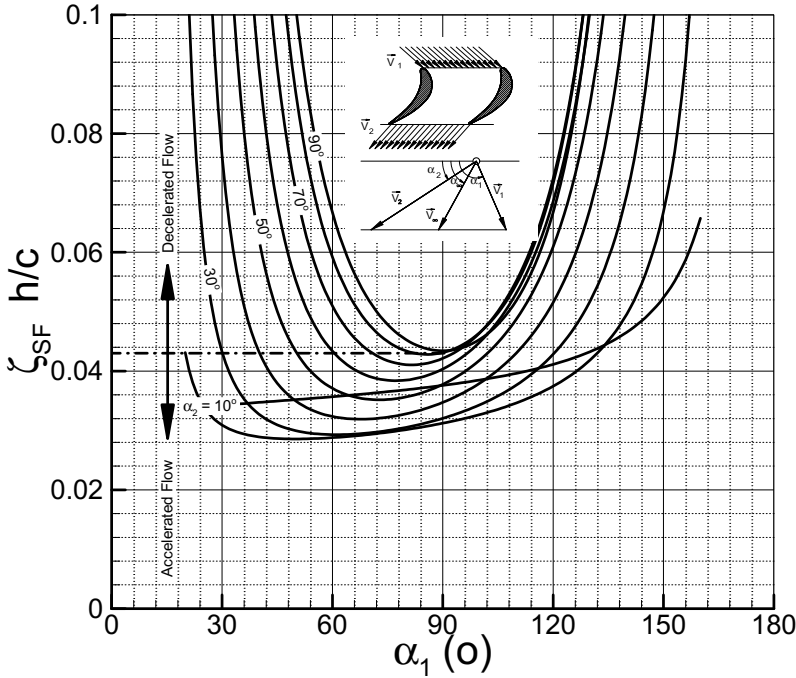


**Fig. 6.18:** Combined secondary and endwall friction loss coefficient as a function of  $\alpha_1$  with  $\alpha_2$  as parameter, recomplied from Kirchberg and Pfeil [4].

The loss coefficient due to the boundary layer development along the endwalls may be set linearly proportional to the boundary layer momentum thickness. Furthermore, since the effect of the endwall friction diminishes with increasing the blade height  $h$ , the loss coefficient may be set inversely proportional to  $h$ . The resulting relation is then multiplied with a constant to arrive at the following simple relationship for estimating the endwall friction coefficient:

$$\zeta_{fw} = K_1 \frac{\delta_2}{h} = K_1 \frac{\delta_2}{c} \frac{c}{h} \quad (6.78)$$

Assuming a fully turbulent boundary layer at the endwalls (this is of course a rough estimate) the momentum thickness can be estimated from the skin friction coefficient for a zero pressure gradient flat plate, Schlichting [14], as

$$c_{f_{FP}} = 2 \left( \frac{\delta_2}{c} \right)_{FP} = 0.074 Re_c^{-1/5}, \text{ with } Re_c = \frac{V_2 c}{\nu} \quad (6.79)$$

with  $\delta_2$  an  $c$  as the boundary layer momentum thickness and the blade chord, respectively. To account for the acceleration or deceleration within a turbine or a compressor cascade, the skin friction in Eq. (6.79) must be corrected first. This is done by multiplying  $c_{f_{FP}}$  from Eq. (6.79) with a velocity ratio as suggested by Kirchberg and Pfeil [4]:

$$c_f = c_{f_{FP}} f^{0.8}, \quad \frac{\delta_2}{c} = \left( \frac{\delta_2}{c} \right)_{FP} f^{0.8} \quad \text{with } f = 0.2 \sum_{n=0}^4 \left( \frac{V_1}{V_2} \right)^n \quad (6.80)$$

with  $V_1$  and  $V_2$  as the cascade inlet and exit velocities. In case of a rotor cascade, the absolute velocity must be replaced by the relative ones,  $W_2$  and  $W_3$ . Expressing the momentum thickness in Eq. (6.78) in terms of skin friction, Eq. (6.80), we obtain the friction loss coefficient for the two endwalls with the following relationship:

$$\zeta_{fw} \frac{h}{c} = 4K_1 \left( \frac{\delta_2}{c} \right) = 2K_1 c_f \quad (6.81)$$

Likewise, the boundary layer momentum thickness in Eq. (6.77) is expressed as:

$$\zeta_{sw} = 2c_f K_2 \frac{c}{h} \left( C_L \frac{c}{s} \right)^2 \frac{\sin \alpha_\infty}{\sin^2 \alpha_2} \quad (6.82)$$

With Eqs. (6.81) and (6.82), the total pressure loss coefficient due to the endwall friction and the secondary flow is determined from

$$\zeta_{sf} \frac{h}{c} = 2c_f \left[ K_1 + K_2 \left( C_L \frac{c}{s} \right)^2 \frac{\sin \alpha_\infty}{\sin^2 \alpha_2} \right] \quad (6.83)$$

with the coefficients  $K_1 = 4.65$  and  $K_2 = 0.675$  from experiments by Wolf [13]. Equation (6.83) is plotted in Fig. 6.18. It shows the combined secondary and friction loss coefficient as a function of the inlet flow angle  $\alpha_1$  with  $\alpha_2$  as a parameter. For accelerated flows through turbine cascades, the inlet flow angle is  $\alpha_1 > \alpha_2$ . The Dashed-dot line is the locus of all  $\alpha_1 = \alpha_2$ . This is an interesting special case where the flow undergoes no deflection, causing the contribution of the lift force in Eq. (6.83) to become zero. As a result, the wall friction is the only no-zero term in Eq. (6.83). For decelerated flows in compressor cascades, the inlet flow angle is  $\alpha_1 < \alpha_2$ . For a given exit flow angle  $\alpha_2$ , the loss coefficient remains close to its minimum as long as the  $\alpha_1 < 90^\circ$ . In this case, the cascade has a small flow deflection from inlet to exit. For  $\alpha_1 > 90^\circ$ , the deflection becomes large, leading to higher  $\zeta_{sf}$ -values. Once the combined secondary and friction coefficient are determined from (6.83), the corresponding stage loss coefficient is calculated from:

$$Z_{sf} = \zeta'_{sf} \frac{V_2^2}{2l} + \zeta''_{sf} \frac{W_3^2}{2l} \quad (6.84)$$

## 6.5 Flow Losses in Shrouded Blades

To reduce the clearance losses, shrouds with integrated labyrinth seals can be applied to the rotor tip and stator hub. This is a common practice in HP- and IP- steam turbine design. The purpose of the labyrinths is to reduce the pressure difference across each labyrinth, thus, reducing the clearance mass flow by dissipating the kinetic energy of the leakage mass flow through the clearance. Figure 6.19 shows a turbine stage with the labyrinth seals.

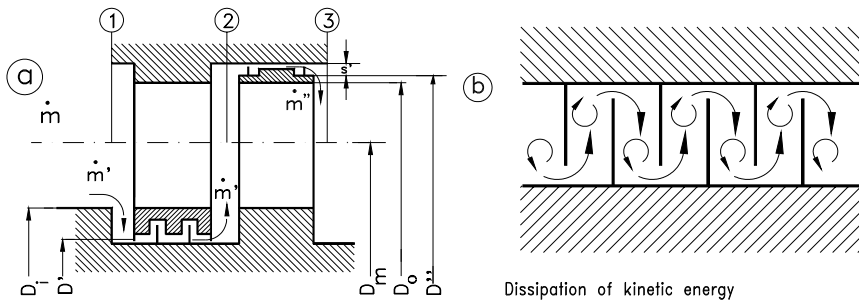


**Fig. 6.19:** a) A turbine stage with stator and rotor shrouds with labyrinth seals, b) Reduction of pressure across a labyrinth by means of dissipation of kinetic energy.

Since the shrouded blading has no tip clearances, there is no secondary flow vortices due to tip clearance, but there are still secondary flows which originate from the boundary layer development on hub and casing walls. Similar to the case treated in the previous section, the secondary flow loss as well as the endwall friction loss determine the flow loss situation close to the blade hub and tip. For their estimation, Eqs. (6.82) and (6.83) are used.

### 6.5.1 Losses Due to Leakage Flow in Shrouds

Consider a shrouded turbine stage, Fig. 6.20, upstream of the stator blade, the stage mass flow is  $\dot{m}$ . Immediately at the inlet of the stator, a fraction of this mass flow,  $\dot{m}'$ , penetrates into the stator labyrinth. In the axial gap, there is a mixing process between the remaining mass flow  $\dot{m} - \dot{m}'$  and the leakage flow  $\dot{m}'$  which is supposed to be completed immediately upstream of the rotor blading. After the mixing at station (2a), a small portion,  $\dot{m}''$ , flows through the rotor labyrinth and, therefore, does not contribute to power generation. Similar to the procedure used in [15], for the calculation of  $\dot{m}'$ ,  $\dot{m}''$  and their dependencies upon the pressure difference across the labyrinth tooth, the conservation laws discussed in Chapter 4 are used.

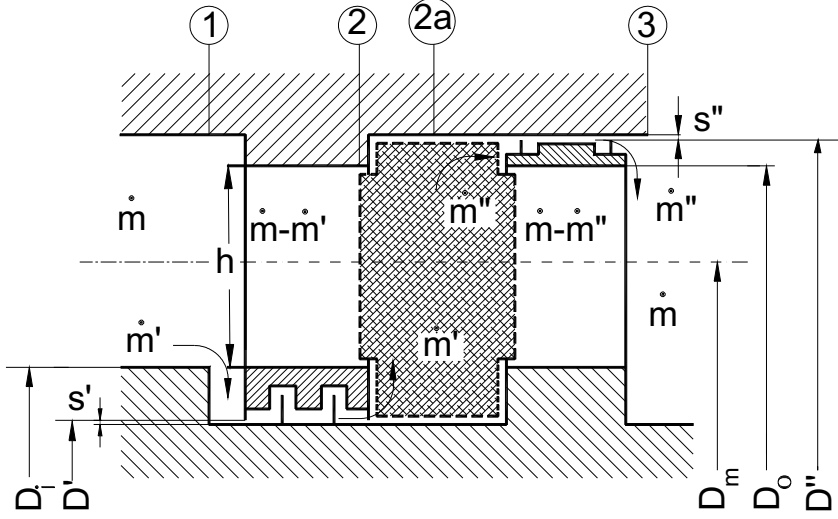


**Fig. 6.20:** Flow through a labyrinth seal with mixing process within the axial clearance. Quantities with “/” and “//” refer to stator and rotor, respectively.

At station 3, mixing of  $\dot{m}''$  and the remaining  $\dot{m} - \dot{m}''$  takes place. This mixing process is repeated for all stator and rotor rows and causes a total pressure loss that can be calculated by using the conservation equations. The continuity equation at station 2 in Fig. 6.20 yields:

$$(\dot{m} - \dot{m}') = \pi \rho D_m h V_{\alpha 2} \quad (6.85)$$

with  $\dot{m}'$  as the mass flow through the stator labyrinth. Assuming that at station 2a the mixing process has been completed, the mass flow is obtained from:

$$\dot{m} = \rho \pi D_m h V_{\alpha 2a} \quad (6.86)$$

Assuming an axisymmetric flow, the momentum equation in circumferential direction is:

$$(\dot{m} - \dot{m}') V_{u2} = \dot{m} V_{u2a} \quad (6.87)$$

and in axial direction

$$(\dot{m} - \dot{m}') V_{\alpha 2} + \pi D_m h p_2 = \dot{m} V_{\alpha 2a} + \pi D_m h p_{2a} \quad (6.88)$$

For the stator, the total pressure loss due to the mixing is then:



$$\Delta p_o' = p_{o2} - p_{o2a} = p_2 - p_{2a} + \frac{\rho}{2} V_2^2 - \frac{\rho}{2} V_{2a}^2 \quad (6.89)$$

Incorporating the above continuity and the momentum equations into Eq.(6.89), we find for the stator:

$$\Delta p_o' = \frac{2\dot{m}'}{\dot{m}} \frac{\rho}{2} V_2^2 \quad (6.90)$$

and for the rotor:

$$\Delta p_o'' = \frac{2\dot{m}''}{\dot{m}} \frac{\rho}{2} W_3^2 \quad (6.91)$$

where  $\dot{m}'$  and  $\dot{m}''$  represent the mass flows through the stator and rotor labyrinths. To find the mass flows  $\dot{m}'$  and  $\dot{m}''$  we consider the flow through a labyrinth seal which consists of  $n$  teeth, Fig. 6.21.

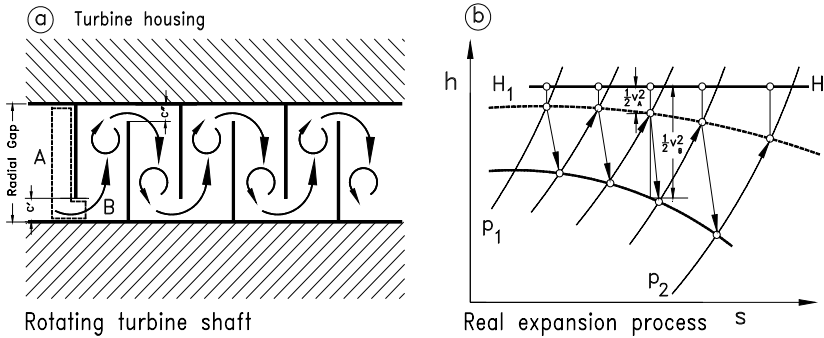


**Fig. 6.21:** Expansion and dissipation process through a labyrinth tooth and chamber. (a) Expansion from the labyrinth chamber with the area  $A_A$  through the tooth clearance  $c$  with the area  $A_B$  and the following dissipation in the labyrinth chamber. (b) Polytropic expansion, where the velocity inside the chamber is negligible compared with the tooth velocity.

We assume that the flow passing through the labyrinth clearance is isentropic. This assumption is not quite accurate as the real polytropic jet expansions in Fig. 6.21(b) obviously show. However, the entropy increase associated with the sharp expansion compared to the one due to the quasi-isobaric dissipation is so small that it can be neglected. This allows applying the Bernoulli equation to the expansion process inside the clearance:

$$\left( p + \frac{1}{2} \rho V^2 \right)_A = \left( p + \frac{1}{2} \rho V^2 \right)_B \quad (6.92)$$

where the subscript  $A$  refers to the cross sectional area within the labyrinth chamber

and  $B$  refers to the clearance area between the shaft and the labyrinth tooth. After entering the labyrinth chamber, its kinetic energy is isobarically dissipated as heat. Since the area  $a_B \ll a_A$ , the velocity  $V_B \gg V_A$ . Therefore  $V_A$  can be neglected compared to  $V_B$ . As a result, we get:

$$p_A - p_B = \Delta p = \frac{1}{2} \rho V_B^2 \quad (6.93)$$

since  $\dot{m}' = a_B \rho V_B$  we find:

$$V_B = \left( \frac{\dot{m}'}{a_B} \right) \frac{1}{\rho} \quad (6.94)$$

Introducing Eq. (6.94) into Eq. (6.93) yields:

$$\Delta p = \frac{1}{2\rho} \left( \frac{\dot{m}'}{a_B} \right)^2 \quad (6.95)$$

For better understanding, the pressure distribution along a labyrinth is shown in Fig. 6.21. For an equal pressure drop in each labyrinth, the pressure difference in a stator labyrinth can be expressed as:

$$\Delta p = \frac{p_1 - p_2}{n'} \quad (6.96)$$

where  $n'$  is the number of stator labyrinths. With Eq. (6.95), we find:

$$\frac{p_1 - p_2}{n'} = \frac{1}{2\rho} \left( \frac{\dot{m}'}{a_B} \right)^2 \quad (6.97)$$

Equation (6.97) delivers the mass flow fraction through the stator labyrinth as:

$$\dot{m}' = a_B \sqrt{\frac{2(p_1 - p_2)}{n'}} \rho \quad (6.98)$$

For an incompressible flow through the stator, the density is approximated as  $\rho_1 \approx \rho_2 = \rho$ . This approximation allows the introduction of the enthalpy difference:

$$(p_1 - p_2)v = h_1 - h_2 = \Delta h' \quad (6.99)$$

Inserting Eq. (6.99) into (6.98), the stator leakage mass flow is calculated as:

$$\dot{m}' = a_B \rho \sqrt{\frac{2\Delta h'}{n'}} \quad (6.100)$$

We introduce relative mass flows by using the main mass flow and the stage flow coefficient:

$$\dot{m} = A \rho V_{axl} = A \rho \phi U \quad (6.101)$$

The relative mass flow through the stator labyrinth is presented in terms of dimensionless stage parameters followed by the relative mass flow through the rotor labyrinth. The following step-by-step re-arrangement establishes relationships between the relative mass flow through the stator- and rotor-labyrinths and the stage parameters:

$$\begin{aligned} \frac{\dot{m}'}{\dot{m}} &= \frac{a_B}{A} \sqrt{\frac{2 \Delta h'}{n'}} \frac{1}{\phi} \frac{1}{U} \\ \frac{\dot{m}'}{\dot{m}} &= \frac{a_B}{A} \sqrt{\frac{2 \Delta h' \Delta h}{n' \Delta h}} \frac{1}{U^2} \frac{1}{\phi} \\ \frac{\dot{m}'}{\dot{m}} &= \frac{a_B}{A} \sqrt{\frac{2(1-r)\lambda}{n'\phi^2}} = \frac{\alpha' D' C'}{D_m h} \sqrt{\frac{2(1-r)\lambda}{n'\phi^2}} \end{aligned} \quad (6.102)$$

with the  $\Delta h \approx \Delta H$ , the clearance area  $a_B = \pi D' C' \alpha'$ , the blade cross section  $A = \pi D_m h$ , and the stator tooth clearance  $C'$  from Fig. 6.21. Similarly for the rotor labyrinth, we find:

$$\frac{\dot{m}''}{\dot{m}} = \frac{\alpha'' D'' C''}{D_m h} \sqrt{\frac{2r\lambda}{n''\phi^2}} \quad (6.103)$$

The values of the labyrinth flow contraction coefficients  $\alpha'$  and  $\alpha''$  depend strongly on the labyrinth shape. Typical values are 0.8-0.93. For a stage with the given  $\phi$ ,  $\lambda$ ,  $r$ , and labyrinth geometry, Figs. 6.22(a) and (b) exhibit the relative mass flows through stator- and rotor-labyrinths  $M_{Stator} = \dot{m}'/\dot{m}$  and  $M_{Rotor} = \dot{m}''/\dot{m}$  respectively with the degree of reaction  $r$  as parameter. For the stator, Fig. 6.22(a), the largest leakage occurs at  $r = 0$ . Increasing the degree of reaction leads to smaller relative mass flow through the labyrinths. This corresponds to the pressure difference across the stator labyrinths. For  $r = 0$ , the largest pressure difference occurs across the stator blade and, thus, stator labyrinths, while the pressure difference across the rotor is almost zero. Increasing the degree of reaction to  $r = 0.5$  reduces the pressure difference across the stator blades and, thus, the stator labyrinths to 50%, resulting in smaller relative mass flow through the stator labyrinths. The relative mass flow through the rotor labyrinths presented in Fig. 6.22(b), however, shows the opposite picture. Largest leakage flow occurs at  $r = 0.5$ , since it has the largest pressure difference across the rotor blading and, thus, the rotor labyrinths. Reducing the degree of reaction lowers the pressure difference across the rotor blading and, thus, the labyrinth causing the relative leakage mass flow to decrease. The stage loss coefficient due to mass flow loss is:

$$Z_{\dot{m}} = \frac{\Delta H \dot{m}''}{l \dot{m}} = \frac{\dot{m}''}{\dot{m}} \quad (6.104)$$

with the specific stage mechanical energy  $\Delta H = l_m$ .

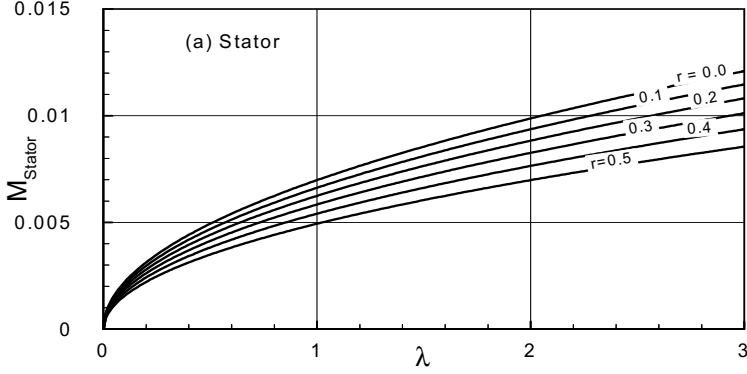


**Fig. 6.22:** (a) Relative mass flow  $M_{Stator} = \dot{m}''/\dot{m}$  through the stator as function of stage load coefficient  $\lambda$  with degree of reaction  $r$  as parameter with  $\phi = 1.0$ ,  $\alpha' = 0.9$ ,  $D'/D_m = 0.95$ ,  $D''/D_m = 1.05$ , and the clearance ratio  $c'/h = 0.01$ , see with  $c'$ ,  $c''$  from Fig. 6.21(a).

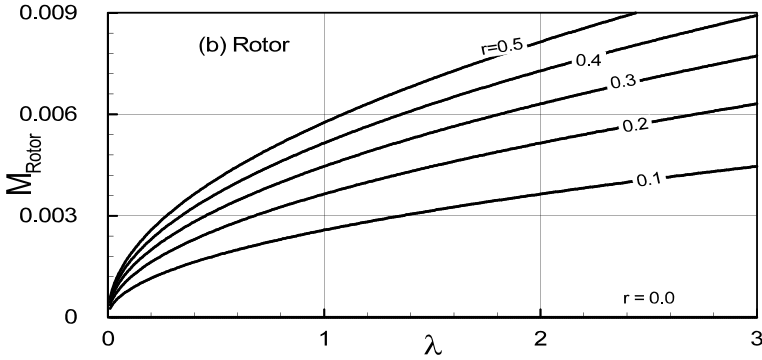


**Fig. 6.22:** (b) Relative mass flow  $M_{Rotor} = \dot{m}''/\dot{m}$  through the rotor-labyrinths as function of stage load coefficient  $\lambda$  with degree of reaction  $r$  as parameter with  $\phi = 1.0$ ,  $\alpha'' = 0.9$ ,  $D'/D_m = 0.95$ ,  $D''/D_m = 1.05$ , and  $c''/h = 0.01$ .

The stage clearance leakage loss is comprised of stator and rotor mixing losses with the mass flow ratios given by Eqs. (6.102) and (6.103) and rotor mass flow loss (6.104). It is summarized as  $Z_{LC} = Z_M + Z_{\dot{m}}$  and is detailed as:

$$Z_{LC} = \frac{\dot{m}'}{\dot{m}} \frac{\phi^2}{\lambda} \frac{1}{\sin^2 \alpha_2} + \frac{\dot{m}''}{\dot{m}} \frac{\phi^2}{\lambda} \frac{1}{\sin^2 \beta_3} + \frac{\dot{m}'''}{\dot{m}} \quad (6.105)$$

Equation (6.105) has been evaluated and is presented in Fig. 6.23 as a function of the degree of reaction  $r$  with the stage load coefficient  $\lambda$  as parameter. As seen, the lowest leakage loss is found at  $r = 0$ . Keeping the stage load coefficient  $\lambda$  constant and increasing the degree of reaction results in higher stage clearance leakage losses. Steeper increases are shown at higher  $\lambda$ -values.

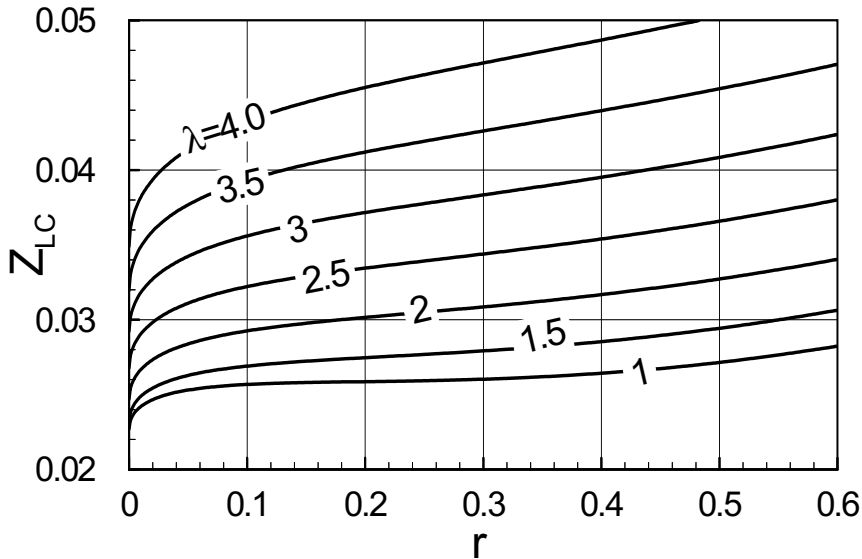


**Fig. 6.23:** Stage clearance leakage loss coefficient  $Z_{LC}$  for a shrouded stage as a function of degree of reaction with the stage load coefficient as parameter.

## 6.6 Exit Loss

The exit loss represents the total energy loss caused by the kinetic energy of the mass flow that exits the turbine or compressor component. For multi-stage turbomachines, it occurs only at the last stage. For a single stage machine, the exit loss has a significant influence on the overall drop of the stage efficiency. The exit loss coefficient  $Z_E$  is defined as the ratio of the exit kinetic energy with respect to specific mechanical energy of the stage:

$$Z_E = \frac{V_3^2}{2I} = \frac{V_3^2}{2\lambda U_3^2} \quad (6.106)$$

Expressing the exit velocity vector  $V_3$  in terms of axial velocity component and using the stage dimensionless parameter from Chapter 5, we get:

$$Z_E = \frac{\phi^2}{2\lambda \sin^2 \alpha_3} \quad (6.107)$$

Replacing the exit flow angle  $\alpha_3$  by the stage parameters from Chapter 5 yields:

$$Z_E = \frac{\phi^2 + \left(1 - \frac{\lambda}{2} - r\right)^2}{2\lambda} \quad (6.108)$$

The stage flow coefficient  $\phi$  can be expressed as a function of the stator exit flow angle  $\alpha_2$ , which is known as one of the stage design parameters.

$$\phi = \tan \alpha_2 \left[ 1 - r + \frac{\lambda}{2} \right] \quad (6.109)$$

Introducing Eq. (6.109) into Eq. (6.108), the result is:

$$Z_E = \frac{1}{2\lambda} \left[ \tan^2 \alpha_2 \left( 1 - r + \frac{\lambda}{2} \right)^2 + \left( 1 - \frac{\lambda}{2} - r \right)^2 \right] \quad (6.110)$$

Equation (6.110) shows the influence of the stage load coefficient  $\lambda$ , the stator exit flow angle  $\alpha_2$  and the degree of reaction  $r$  on the exit loss coefficient  $Z_E$ . The results are presented in Fig. 6.24. For each pair of stator exit flow angle  $\alpha_2$  and degree of reaction  $r$ , there is a minimum exit loss coefficient at a particular  $\lambda$ . Since the exit

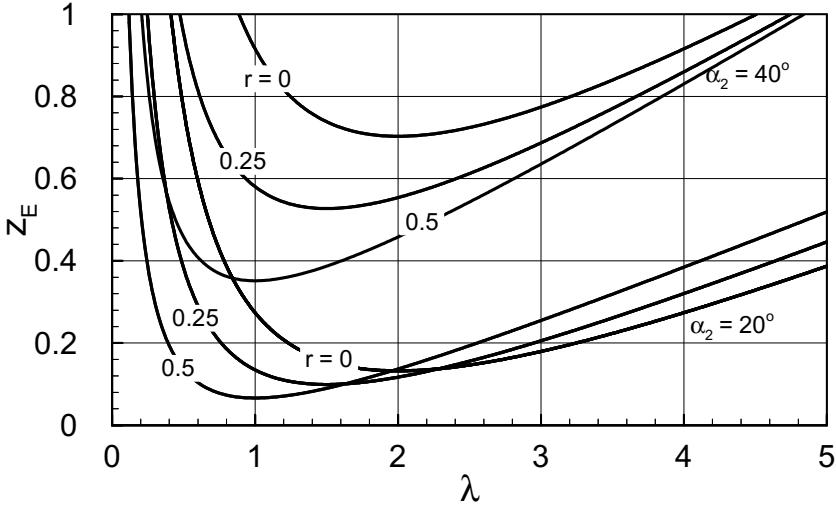


**Fig. 6.24:** Exit loss coefficient  $Z_E$  as a function of stage load coefficient  $\lambda$  with degree of reaction  $r$  as a parameter.

kinetic energy of the last stage in a multi-stage turbine does not contribute to

generation of shaft power, it must be kept as small as possible. For a stator exit flow angle of  $\alpha_2 = 20^\circ$ , a degree of reaction of  $r = 50\%$  yields a minimum at  $\lambda = 1$ . The rotor row with this stage characteristic has an absolute exit flow angle of  $\alpha_3 = 90^\circ$ .

## 6.7 Trailing Edge Ejection Mixing Losses of Gas Turbine Blades

Increasing the thermal efficiency of power or thrust generating gas turbine engines requires high turbine inlet temperatures. For conventional turbine blade materials, cooling of the front stages allows an increase of the turbine inlet temperature. The required cooling mass flow is injected partially or entirely through the trailing edge slots into the downstream axial gap where the cooling and main mass flows are mixed. The trailing edge ejection affects the flow regime downstream to the cooled blade, especially the losses associated with the mixing of the cooling mass flow and the main mass flow. The ejection velocity ratio, cooling mass flow ratio, slot-width ratio, and ejection angle affect the mixing losses and, therefore, the efficiency of cooled blades. Improper selection of these parameters results in higher mixing losses that reduce the efficiency of the cooled turbine stage. Experimental research work by Prust [16], [17] on a two-dimensional turbine stator cascade shows that the trailing edge ejection significantly affects the blade efficiency. Analytical and experimental investigations by Schobeiri [18], [19], and Schobeiri and Pappu [20] aim at identifying and optimizing the crucial design parameters to significantly reduce the aerodynamic losses that originate from trailing edge ejection mixing processes.

### 6.7.1 Calculation of Mixing Losses

Starting from the conservation laws presented in Chapter 4, relations are derived that accurately describe the influence of the above parameters on the flow field downstream of the cooled turbine blade. Figure 6.25 shows the stations upstream of the blade ①, immediately at the trailing edge plane ② at the mixing plane ③. The conservation laws are applied to the control volume ABCDA.

The continuity equation can be written as:

$$\int_0^{s-d} \rho_2 V_2 \sin \alpha_2 dy + \rho_c V_c \sin \alpha_c fd = \rho_3 V_3 \sin \alpha_3 s \quad (6.111)$$

The momentum equation in y-direction is:

$$\int_0^{s-d} \rho_2 V_2^2 \sin \alpha_2 \cos \alpha_2 dy + \rho_c V_c^2 \sin \alpha_c \cos \alpha_c fd = \rho_3 V_3^2 \sin \alpha_3 \cos \alpha_3 s \quad (6.112)$$

The momentum equation in x-direction is:

$$\int_0^{s-d} \rho_2 V_2^2 \sin^2 \alpha_2 dy + \rho_c V_c^2 \sin^2 \alpha_c fd + \int_0^s p_2(y) dy = \rho_3 V_3^2 \sin^2 \alpha_3 s + p_3 s \quad (6.113)$$

In Eqs.(6.111) through (6.113), the parameter  $f = s/b$  represents the ratio of slot width  $s$  and the trailing edge thickness  $b$ ;  $\alpha_2$  and  $\alpha_c$  are the exit flow angle and ejection angle, respectively, of the cooling mass flow;  $V_2$  and  $V_c$  are the blade exit velocity and mean ejection velocity;  $p_2(y)$  is the static pressure distribution along the spacing  $t$ . The angles  $\alpha_2$  and  $\alpha_c$  in Fig. 6.25 are assumed to be constant. Outside the trailing edge region, the static pressure  $p_2(y) = p_{20}$  can be assumed as constant. As shown by Sieverding [21], inside the trailing edge region,  $p_2$  has a nonlinear distribution whose average might differ from  $p_{20}$ . Since this pressure difference occurs only in a relatively small trailing edge region, its contribution compared with the other terms in Eq. (6.113), can be neglected. At the exit of the slot, the pressure  $p_2(y)$  is determined by

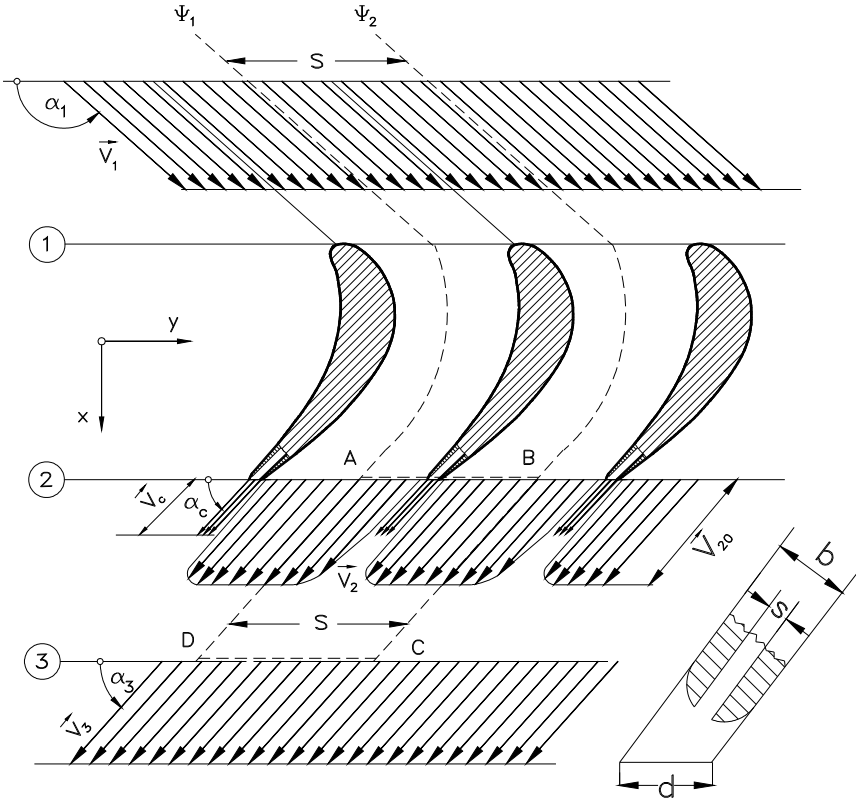


**Fig. 6.25:** Trailing edge ejection and mixing downstream of a cooled gas turbine blade.

the static pressure  $p_c$  of the cooling mass flow. By presuming  $p_c = p_{20}$  and considering the above facts, the static pressure can be approximated over the entire spacing by  $p_2 = p_{20}$ . For further treatment of Eqs.(6.111) through (6.113), the boundary layer parameters, namely displacement thickness, momentum thickness and the shape parameter, are introduced:



$$\delta_1 = \int_0^{s-d} \left( 1 - \frac{V_2}{V_{20}} \right) dy, \quad \delta_2 = \int_0^{s-d} \frac{V_2}{V_{20}} \left( 1 - \frac{V_2}{V_{20}} \right) dy \quad (6.114)$$

The dimensionless thicknesses are found by:

$$\begin{aligned} \Delta_1 &= \frac{\delta_1}{s} \text{ with } \delta_1 = \frac{\delta_{1S} + \delta_{1P}}{\sin \alpha_2} \\ \Delta_2 &= \frac{\delta_2}{s} \text{ with } \delta_2 = \frac{\delta_{2S} + \delta_{2P}}{\sin \alpha_2} \\ D &= \frac{b}{\sin \alpha_2} = \frac{d}{s} \end{aligned} \quad (6.115)$$

where the indices  $S$  and  $P$  refer to the suction and pressure surfaces. Introducing the dimensionless parameters (6.115) into the dimensionless versions of Eqs. (6.111) through (6.113), the continuity relation yields:

$$\frac{\rho_3}{\rho_2} \frac{V_3}{V_2} = \frac{\sin \alpha_2}{\sin \alpha_3} \left[ 1 - \Delta^* - D \left( 1 - \frac{\sin \alpha_c}{\sin \alpha_2} \mu \tau f \right) \right] \quad (6.116)$$

The momentum equation in y-direction is:

$$\frac{\rho_2}{\rho_3} \cot \alpha_3 = \cot \alpha_2 \left\{ \frac{1 - \Delta_1 - \Delta_2 - D \left( 1 - \frac{\sin 2\alpha_c}{\sin 2\alpha_2} \mu \tau f \right)}{\left[ 1 - \Delta_1 - D \left( 1 - \frac{\sin \alpha_c}{\sin \alpha_2} \mu \tau f \right) \right]^2} \right\} \quad (6.117)$$

The momentum equation in x-direction determines the static pressure difference:

$$\frac{P_{20} - P_3}{\frac{1}{2} \rho_3 V_3^2} = 2 \sin^2 \alpha_3 \left\{ 1 - \frac{\rho_3}{\rho_2} \frac{1 - \Delta^* - \Delta^{**} - D \left( 1 - \frac{\sin^2 \alpha_c}{\sin^2 \alpha_2} \mu^2 \tau f \right)}{\left[ 1 - \Delta^* - D \left( 1 - \frac{\sin \alpha_c}{\sin \alpha_2} \mu \tau f \right) \right]^2} \right\} \quad (6.118)$$

with:  $\mu = \frac{\bar{V}_c}{V_{20}}$ ,  $\tau = \frac{T_2}{T_c}$ ,  $R = \frac{\rho_3}{\rho_2}$  as velocity, temperature, and density ratio.

To define the energy dissipation due to the mixing process, it is necessary to consider not only the contribution of the main flow, but also the cooling mass flow. For this purpose, we combine the mechanical and thermal energy balances and arrive at a relationship that represents the change of total pressure within a system where an exchange of thermal and mechanical energy with the surroundings takes place (for detail see Chapter 12). For an adiabatic steady flow with no mechanical energy exchange, this equation is reduced to:

$$\nabla \cdot (\mathbf{VP}) = \frac{\kappa - 1}{\kappa} \nabla \cdot (\mathbf{V} \cdot \mathbf{T}) \quad (6.119)$$

where  $P \equiv p_0 = p + \frac{1}{2}\rho V^2$  is the total pressure,  $\mathbf{T}$  the shear stress tensor, and  $\kappa$  the ratio of the specific heats. Eq. (6.119) states that the rate of work done on fluid per unit volume by viscous forces causes a defect of total pressure work per unit volume. For an inviscid flow, Eq. (6.119) reduces to a Bernoulli equation. Integrating Eq. (6.119) over the control volume and converting the volume integrals into the surface integrals by means of Gauss' divergence theorem leads to:

$$\int_S (\mathbf{n} \cdot \mathbf{VP}) dS = \int_{S_{in}} (\mathbf{n} \cdot \mathbf{VP}) dS + \int_{S_{out}} (\mathbf{n} \cdot \mathbf{VP}) dS = \Delta \dot{E} \quad (6.120)$$

The second and third integral in Eq. (6.120) are carried out over the entire inlet and exit surfaces under consideration. Introducing the individual mass flows  $\dot{m}_c$ ,  $\dot{m}_2$  and substituting the inlet total pressure by the total pressure of the potential core at station 2, the total energy dissipation is obtained from:

$$\Delta \dot{E} = \dot{m}_2 \left( \frac{p_{20}}{\rho_2} + \frac{1}{2} V_{20}^2 \right) + \dot{m}_c \left( \frac{p_c}{\rho_c} + \frac{1}{2} V_c^2 \right) - \dot{m}_3 \left( \frac{p_3}{\rho_3} + \frac{1}{2} V_3^2 \right) \quad (6.121)$$

With respect to the exit kinetic energy, the loss coefficient is defined as:

$$\zeta = \frac{\Delta \dot{E}}{\frac{1}{2} \dot{m}_3 V_3^2} \quad (6.122)$$

Incorporating the mass flow ratios:

$$\begin{aligned} \frac{\dot{m}_2}{\dot{m}_3} &= \frac{1 - \Delta_1 - D}{1 - \Delta_1 - D \left( 1 - \frac{\sin \alpha_c}{\sin \alpha_2} \mu \tau f \right)} \\ \frac{\dot{m}_c}{\dot{m}_3} &= \frac{\sin \alpha_c \mu \tau f D}{\sin \alpha_2 \left[ 1 - \Delta_1 - D \left( 1 - \frac{\sin \alpha_c}{\sin \alpha_2} \mu \tau f \right) \right]} \end{aligned} \quad (6.123)$$

into Eq. (6.122), using Eqs. (6.116) through (6.118) and introducing the following auxiliary functions:

$$\begin{aligned}
 G_1 &= 1 - \Delta^* - D \left( 1 - \frac{\sin \alpha_c}{\sin \alpha_2} \mu \tau f \right) \\
 G_2 &= 1 - \Delta^* - \Delta^{**} - D \left[ \left( 1 - \frac{\sin^2 \alpha_c}{\sin^2 \alpha_2} \mu \tau f \right) \right] \\
 G_3 &= 1 - \Delta^* - D \left[ \left( 1 - \frac{\sin \alpha_c}{\sin \alpha_2} \mu^3 \tau f \right) \right] \\
 G_4 &= \frac{\sin \alpha_c \sin(\alpha_c - \alpha_2)}{\sin^2 \alpha_2 \cos \alpha_2} \mu^2 \tau f D
 \end{aligned} \tag{6.124}$$

The loss coefficient  $\zeta$  is completely described by:

$$\begin{aligned}
 \zeta &= \frac{G_1^3 - 2RG_1^2G_2 + R^2G_3}{G_1^3} \\
 &- \cos^2 \alpha_3 \left( \frac{2G_1^3 - 2RG_2G_1^2 + R^2G_3}{G_1^3} - \frac{G_1G_3}{(G_2 - G_4)^2} \right)
 \end{aligned} \tag{6.125}$$

where all the significant parameters determining the influence of trailing edge ejection are present. With this relation, it is possible to predict the energy dissipation due to the trailing edge thickness, the boundary layer thickness at the trailing edge, and the trailing edge ejection. In this connection, the contribution of the trailing edge ejection to the energy dissipation is of particular interest. For this purpose, a typical gas turbine cascade is considered where its geometry, exit flow angle  $\alpha_2$ , and the boundary layer parameters are known. To show the effect of trailing edge ejection, the loss coefficient  $\zeta$  is calculated from Eq. (6.125) as a function of cooling mass flow ratio  $\dot{m}_c/\dot{m}_2$ .

The loss coefficient  $\zeta$  includes the profile losses that are caused by viscosity effects. To eliminate this contribution, a cascade with the same flow conditions and boundary layer parameters, but with an infinitesimally thin trailing edge and no ejection is considered. This cascade has almost the same pressure distribution on the suction and pressure sides and also the same profile loss coefficient. The difference ( $\zeta - \zeta_0$ ) in this case illustrates the effect of trailing edge ejection for a given trailing edge thickness.

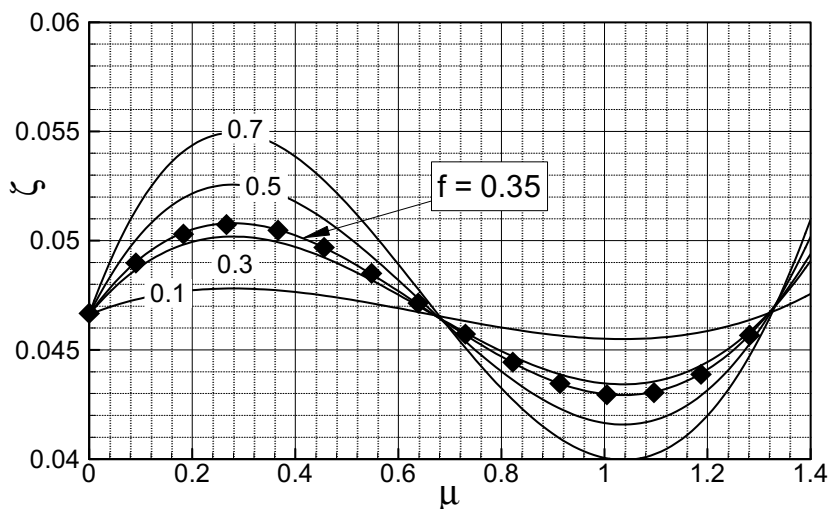
### 6.7.2 Trailing Edge Ejection Mixing Losses

Equation (6.125) includes three major ejection parameters that influence the mixing loss coefficient  $\zeta$ . These are the cooling velocity ratio  $\mu = \bar{V}_c/\bar{V}_2$ , the cooling mass flow ratio  $\dot{m}_c/\dot{m}_2$ , the slot-width ratio  $f = s/b$ , and the temperature ratio  $\tau = T_c/T_2$ . The effects of these parameters were theoretically investigated by Schobeiri [18], [19] and experimentally verified by Schobeiri and Pappu [20] for two different turbines, namely the Space Shuttle Main Engine (SSME) turbine and an industrial gas turbine. For both the cascades, the cooling mass flow ratio  $\dot{m}_c/\dot{m}_2$  was varied from 0.0 to 0.04 that corresponds to the cooling velocity ratio range of  $\mu = 0.0-1.40$ .

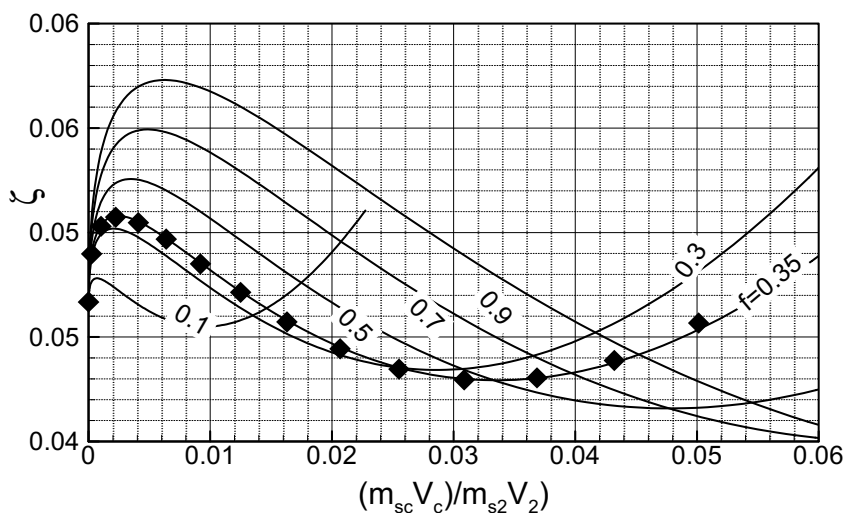
### 6.7.3 Effect of Ejection Velocity Ratio on Mixing Loss

Figure 6.26 shows the total pressure mixing loss coefficient as a function of the velocity ratio,  $\mu = \bar{V}_c/\bar{V}_2$ , with the non-dimensional slot-width ratio  $f$  as the parameter for the SSME blade. The symbols represent results from experimental measurements and the solid lines represent results from theoretical evaluations.

For no injection,  $\mu = 0.0$ , there is a pressure loss due to finite thickness of the trailing edge and also from the boundary layer development along the pressure and suction surfaces of the blade. With increasing the cooling jet velocities, the losses initially increase until a maximum is reached. Further increase in cooling jet velocities results in the decrease of  $\zeta$  to a minimum, and then increasing thereafter. For  $\mu < 0.7$ , the losses due to injection of cooling mass flow are higher than for the no injection case. This is caused by the low momentum of the cooling jet being unable to sustain the strong dissipative nature of the wake flow downstream of the trailing edge. So, the main mass flow entrains the cooling mass flow resulting in a complete dissipation of the energy of the jet. Therefore, higher mixing losses occur at low injection velocities until a maximum  $\zeta$  is reached, which occurs around  $\mu = 0.3$  beyond which  $\zeta$  begins to decrease. For injection velocity ratios  $\mu > 0.7$ , the momentum of a cooling jet is sufficient to overcome the wake flow without being dissipated completely. Owing to this phenomenon, a significant reduction in mixing losses is evident from Fig. 6.26. This reduction proceeds until  $\zeta$  reaches a minimum, which is around  $\mu = 1$ . Further increase of  $\mu$  above 1.1 increases the losses again for similar reasons explained earlier.



**Fig. 6.26:** Trailing edge mixing loss coefficient  $\zeta$  as a function of velocity ratio  $\mu$  with slot-width ratio  $f$  as a parameter for SSME blade, from [19] and [20]. Experiments shown as full squares.



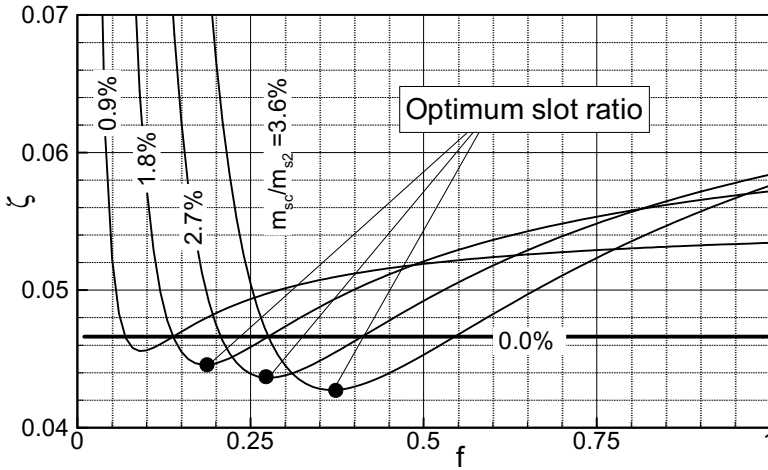
**Fig. 6.27:** Loss coefficient  $\zeta$  as a function of momentum ratio  $(\dot{m}_c \bar{V}_c)/(\dot{m}_2 V_2)$  with slot-width ratio  $f$  as parameter for SSME blades from [19] and [20].

Figure 6.27 shows the mixing loss coefficient  $\zeta$  as a function of cooling jet momentum ratio  $(\dot{m}_c \bar{V}_c)/(\dot{m}_2 V_2)$  with slot-width ratio  $f$  as the parameter for the Space Shuttle Main Engine turbine blade. Also, it is evident from this figure that for a given  $f$ , the mixing loss coefficient has a pronounced optimum. Taking into

consideration the wall thicknesses on each side of the slot at the trailing edge exit plane, the slot-width ratios of 0.3 to 0.35 seem to be a quite reasonable estimation for a cooled turbine with trailing edge ejection.

### 6.7.4 Optimum Mixing Losses

Of particular interest to the turbine blade aerodynamicists and designers is how small the slot-width ratio  $f$  should be for a given cooling mass flow which is dictated by the heat transfer requirements to meet the optimum conditions for  $\zeta$ . Figures 6.28 provides this crucial information. This figure shows the mixing loss coefficient  $\zeta$  as a function of slot-width ratio with the mass flow ratio  $\dot{m}_c/\dot{m}_2$  as the parameter. Optimum mixing loss can easily be found by choosing the appropriate slot-width



**Fig. 6.28:** Loss coefficient  $\zeta$  as a function of slot-width ratio  $f$  for SSME blade from [19] and [20].

## ratio. 6.8 Stage Total Loss Coefficient

After calculating the individual stage loss coefficients  $Z_i$ , the total stage coefficient is calculated as:

$$Z = \sum_{i=1}^n Z_i = Z_1 + Z_2 + \dots \quad (6.126)$$

where index  $i$  represents the individual stage losses, for example, profile losses, secondary losses, etc. We define the total isentropic stage loss coefficient  $Z_s$ :

$$Z_s = \frac{\Delta h_{loss}}{\Delta H_s} \quad (6.127)$$

where  $\Delta h_{loss}$  represents all the enthalpy losses due to the different loss mechanisms discussed in this chapter, and  $\Delta H_s$  the available stage isentropic enthalpy difference.

For the turbine stage, Eq. (6.127) is written as:

$$Z_s = \frac{\Delta h_{loss}}{l + \Delta h_{loss}} = \frac{Z}{Z + 1} \quad (6.128)$$

and for compressor stage:

$$Z_s = \frac{\Delta h_{loss}}{l - \Delta h_{loss}} = \frac{Z}{1 - Z} \quad (6.129)$$

The isentropic efficiency for turbine stage is defined as the ratio of actual total enthalpy difference, which is identical with stage mechanical energy and the isentropic stage total enthalpy difference. The isentropic stage efficiency in terms of  $Z_s$  is:

$$\eta_s = \frac{\Delta H}{\Delta H_s} = \frac{l}{\Delta H_s} = \frac{\Delta H_s - \Delta h_{loss}}{\Delta H_s} = 1 - Z_s \quad (6.130)$$

and in terms of  $Z$ :

$$\eta_s = \frac{\Delta H}{\Delta H_s} = \frac{l}{\Delta H_s} = \frac{l}{l + \Delta h_{loss}} = \frac{1}{1 + Z} \quad (6.131)$$

Equation (6.131) represents the isentropic turbine stage efficiency in terms of the actual total stage loss coefficient  $Z$ . Similar relations are derived for compressor stage in terms of  $Z_s$ :

$$\eta_s = \frac{\Delta H_s}{\Delta H} = \frac{\Delta H_s}{\Delta H} = \frac{\Delta H_s}{\Delta H_s + \Delta h_{loss}} = \frac{1}{1 + Z_s} \quad (6.132)$$

and in terms of  $Z$ :

$$\eta_s = \frac{\Delta H_s}{\Delta H} = \frac{\Delta H_s}{l} = \frac{l - \Delta h_{loss}}{l} = 1 - Z \quad (6.133)$$

## 6.9 Diffusers, Configurations, Pressure Recovery, Losses

Diffusers are attached to the exit of turbomachinery components such as compressors and turbines to partially convert the kinetic energy of the working medium into the potential energy. In the case of a power generation gas turbine with a subsonic exit Mach number, the diffuser back pressure is identical with the ambient pressure, thus, it cannot be increased. As a consequence, the diffuser reduces its inlet pressure below the ambient pressure to establish its design pressure ratio. Thus, installing a diffuser at the turbine exit causes the stage back pressure to drop. As a result, the specific total enthalpy difference of the turbine component will raise leading to an increased specific power at a higher efficiency. At the same time, the diffuser reduces the exit

kinetic energy which is associated with a decrease in the exit loss of the engine. In steam turbine power plants, the diffuser attached to the last stage of the low pressure turbine has a back pressure which is dictated by the condenser pressure. The condenser pressure, however, is determined by the environmental temperature (river temperature, cooling tower air temperature), thus, is considered constant. In the case of a compressor with a predefined exit pressure, the installation of a diffuser leads to a decrease of specific mechanical energy input to the compressor. The thermodynamic working principles of a diffuser installed at the exit of a turbine and a compressor component is shown in Fig. 6.29.

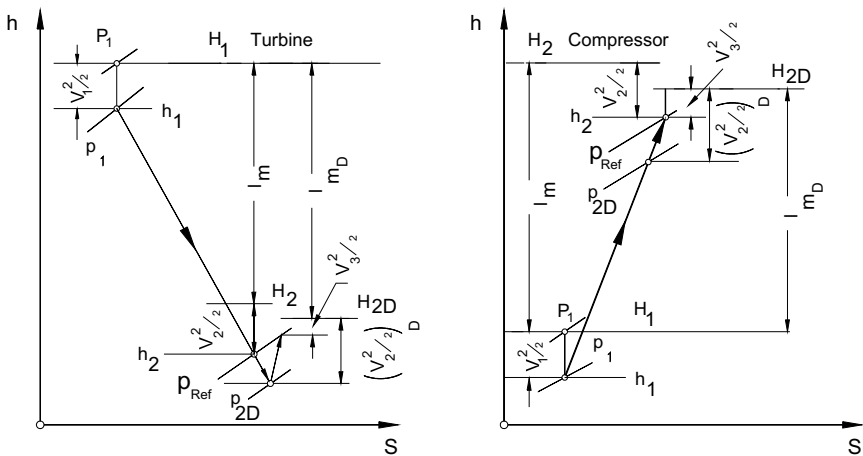


**Fig. 6.29:** Interaction of diffuser-thermodynamics with the a turbine component (left) and a compressor component (right). Quantities with subscript D refer to the cases with diffuser.

As seen, the reference pressure  $p_{\text{ref}}$  in case of a gas turbine or a steam turbine is identical with the ambient pressure and the condenser pressure, respectively. In the case of a compressor, it represents the desired compressor exit pressure.

### 6.9.1 Diffuser Configurations

To effectively convert the kinetic energy of the exiting fluid into potential energy, axial, radial and mixed flow diffusers are used. The choice of a particular diffuser configuration primary depends on the design constraints dictated by the compressor or turbine sizes and their exit geometries. For gas turbine applications, axial flow diffusers are used that may have different geometries. As shown in Fig. 6.30(a,b), they may have outer conical casings and conical shaped or constant diameter center bodies. Multi-channel short diffusers may also be used to allow larger opening angles to avoid flow separation. While the short diffusers allow a more compact design, the additional surfaces pertaining to the separators increase the friction losses causing a decrease in diffuser efficiency. For steam turbines, based on specific design requirements, axial as well as radial diffusers are applied, Fig. 6.31.



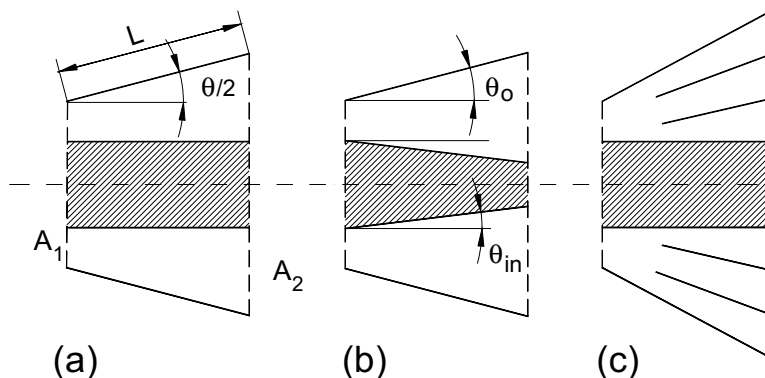


Fig. 6.30: Different diffuser configurations for axial turbines: (a) Diffuser with constant inner diameter, (b) with variable inner and outer diameter, (c) a multi-channel diffuser.

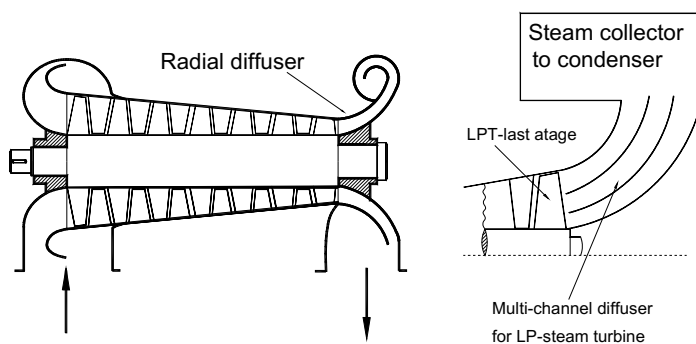


Fig. 6.31: Radial diffuser configurations for axial compressors and low pressure steam turbines.

For industrial compressors, radial diffusers are usually applied that facilitate an effective kinetic energy conversion from the compressor exit to the collector, as shown in Fig. 6.31. Diffusers of radial compressors may be either vaneless or have vanes based on the absolute exit flow angle from the rotor blades.

### 6.9.2 Diffuser Pressure Recovery

Performing an optimum conversion of the exiting kinetic energy from the last stage of a compressor or a turbine component into potential energy requires adequate composition of the following diffuser parameters: (a) area ratio, (b) length/height ratio ( $L/h$ ), (c) diffuser angle  $\theta$ , which is directly related to the axial length ratio ( $L_{ax}/L$ ), (d) inlet swirl parameter, (e) inlet turbulence intensity, (g) Re-number and (f) Mach

number. In addition, the boundary layer thickness at the inlet as well as blockage factors play a substantial role in separation-free operation of diffusers.

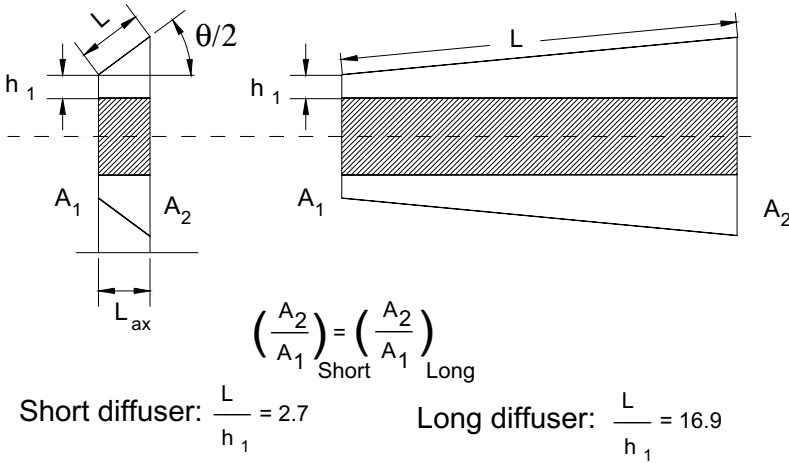


**Fig. 6.32:** A short and a long diffuser with the same area ratio but different opening angles.

As Fig.6.32 indicates, two diffusers may be designed with the same area ratio but have two different axial lengths. While the long diffuser has a smaller opening angle that makes it less susceptible to flow separation, the short one has the advantage of performing the energy conversion within a much shorter length resulting in a significantly reduced axial length of a turbomachine. A short diffuser, if designed properly, can produce the same or even higher degree of pressure recovery than a long one. Therefore, the objective of an appropriate diffuser design is to achieve a near-optimum pressure recovery at an acceptably short axial length (opening angle  $\theta$ ). An optimum pressure recovery can be achieved if the diffuser operates close to the separation point. At this point, the wall shear stress is  $\tau_w = \partial u / \partial y \approx 0$  causing a reduction of total pressure loss coefficient  $\zeta$ , thus, an increase in pressure recovery.

Earlier classical research work by Kline, et. al.[22] was conducted on straight walled diffusers to expedite the basic design parameters. Sovran and Klomp [23] conducted a systematic experimental research to determine the optimum geometries for diffusers with rectangular, conical and annular cross-sections. From a multitude of experiments working diagrams were generated that allow extracting pressure recovery values for given area ratios and length/inlet height ratio  $L/h$ .

Averaging the flow quantities at the inlet and exit, the total pressure balance at any arbitrary position in x-direction reads:

$$\bar{p}_1 - \bar{p}_x = \frac{\rho}{2} (\bar{v}_x^2 - \bar{v}_1^2) + \zeta \frac{\rho}{2} \bar{v}_1^2 \quad (6.134)$$

Since the loss coefficient  $\zeta$  is directly related to the wall shear stress, for an

incompressible flow and  $\tau_w \rightarrow 0$ , Eq.(6.134) with approaches the Bernoulli equation leading to a maximum pressure recovery. Considering the averaged quantities in Eq.(6.134), we define the pressure *recovery factor*:

$$c_{PR} = \frac{\frac{1}{x_x} \int_{b_x} p_x db - \frac{1}{b_1} \int_{b_1} p_1 db}{\frac{1}{b_1} \int_{b_1} q_1 db} \quad (6.135)$$

In Eq.(6.135)  $c_{pR}$  exhibits the real pressure recovery factor,  $q_1 = \rho \bar{V}_1^2/2$ ,  $b_1$  and  $b_x$  the width at station 1 and  $x$ , respectively as shown in Fig. 6.33.

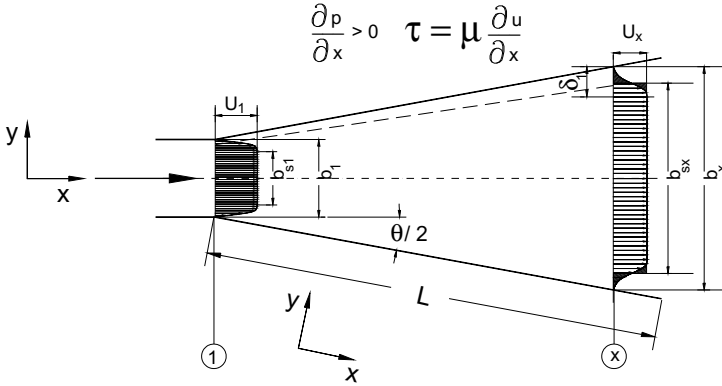


**Fig. 6.33:** Schematics of velocity and boundary layer distributions.

As Eq. (6.135) indicates, the calculation of  $c_{pR}$  requires the knowledge of the entire distribution of  $p_1$  and  $p_x$  over the width. Applying the Prandtl assumption that the pressure on the wall and within the boundary is determined by the pressure outside the boundary layer, Eq.(6.135) can be simplified as:

$$c_{PR} = \frac{P_x - P_1}{\bar{q}_1} \quad (6.136)$$

with  $p_1$  and  $p_x$  as the wall static pressures. Equation (6.136) can be applied for diffuser performance assessment as long as the boundary layer is fully attached. In case of a flow separation, the boundary layer thickness becomes large and the above Prandtl assumption loses its validity. Therefore, a different recovery factor needs to be defined that accounts for adverse changes of the boundary layer including separation. A physically similar criterion that also considers the adverse effects of boundary growth in case of flow separation is the *conversion coefficient*  $\lambda$  defined as:

$$\lambda = \frac{U_1^2 - U_x^2}{U_1^2} \quad (6.137)$$

with  $U_1$  and  $U_x$  as the velocities outside the boundary layer, as shown in Fig. 6.33. Equation (6.137) indicates that increasing the boundary layer thickness as a result of an adverse pressure gradient caused by a large  $\theta$ , reduces the size of the core flow, thus, increases its velocity and reduces  $\lambda$ . Increasing  $\theta$  beyond its limit leads to a massive flow separation. In this case, the fluid exits the diffuser as a jet with a velocity

$U_x \approx U_1$  and  $\lambda = 0$ . The flow separation produces a strongly vortical unsteady flow regime that occupies a major portion of the diffuser volume, Fig. 6.34. The exiting jet may oscillate between the walls or be attached to one of the side walls, as shown in Fig. 6.34.

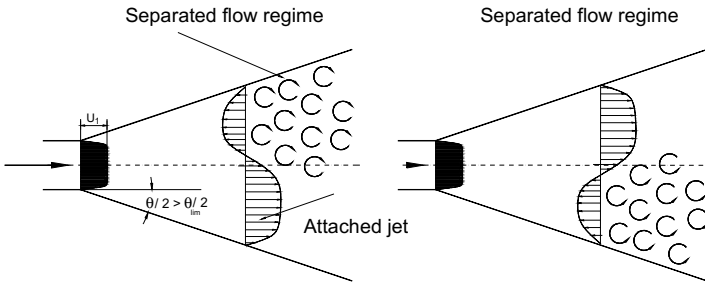


**Fig. 6.34:** Unsteady exiting jet oscillating between the two side walls for  $\theta > \theta_{\text{lim}}$ .

### 6.9.3 Design of Short Diffusers

While the specific net power of gas turbines continuously increase, making them more compact, their exit diffusers still occupy a substantial volume. To reduce the volume, short diffusers may be designed that fulfill the following criteria: (a) the diffuser contour should be configured such that its boundary layer is less susceptible to separation, (b) measures should be taken to prevent/suppress the boundary layer separation by influencing the inlet flow condition of a short diffuser within which the boundary would separate. The above issues were addressed in an experimental and theoretical study by Schobeiri [24].

In case (a), a systematic conformal transformation was conducted, where the geometry of diffusers with straight, concave and convex walls were described, Fig. 6.35. To calculate the degree of susceptibility with regard to flow separation, in [25], a laminar flow was assumed which is more sensitive to separation than the turbulent one. For the above geometries, the Navier Stokes equations were transformed into the respective body fitted orthogonal coordinate systems and the corresponding solutions for different diffuser geometries were found. Given the same area ratio and the inlet flow condition for all three geometries (convex, straight, concave), the concave walled

diffuser showed to be less sensitive to the flow separation as shown in Fig.6.35.

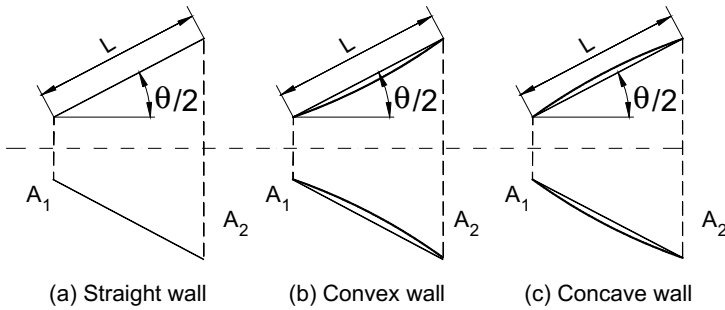


**Fig. 6.35:** Optimization of the diffuser contour: (a) reference configuration flow close to separation  $\theta = \theta_{\text{lim}}$ , (b) convex wall: flow already separated, (c)concave wall: separation delayed.

In case (b) the boundary layer separation is prevented by generating vortices to control the flow separation as reported in [25]. Experimental investigations were performed by varying the opening angle  $\Theta$  at three different diffuser length ratios  $l/w = 4, 6, 8$ , Fig.6.36.

Straight walled diffuser with vortex generator edge (VGE)

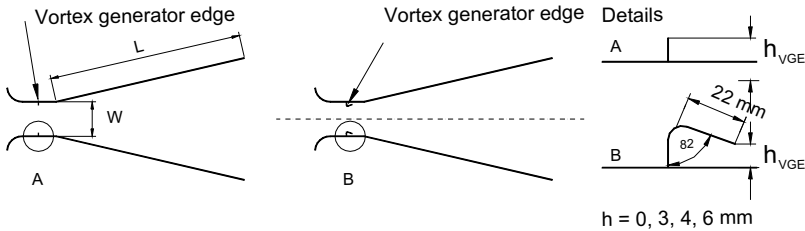


**Fig. 6.36:** Straight walled diffuser with vortex generator (VGE) to avoid early flow separation.

To suppress or delay the boundary layer separation, a system of two vortex filaments were generated by two vortex generator edges (VGE) installed upstream of the diffuser inlet. Two types of VGE were applied, Fig. 6.36 A and B. The first VGE had a straight edge, whose immersion height was varying from 0.0 to 6.0 mm. The second VGE had a nozzle shape with an optimized angle of  $82^\circ$  and an immersion of 6.0 mm. The flow visualization, Fig. 6.37, shows the generation of a strong vortex filament by a VGE. This vortex generates downstream of the edge an induced velocity field that is described by the Bio-Sawart law, which we discussed in Section 6.4.1. Referring to Section 6.4.1, Fig. 6.15 schematically shows the working principle of the Bio-Sawart law in context of diffuser flow stability. As seen, an infinitesimal section of a vortex filament  $d\vec{\zeta}$  with the vortex strength  $\vec{\Gamma}$  induces at a distance  $\vec{r}$  a velocity field  $d\vec{v}$  which is perpendicular to the plane described by the normal unit vector  $\vec{n}$  at the unit vector of the distance  $\vec{r}$ .



**Fig. 6.37:** Visualization of a straight vortex filament by a VGE.

Integrating over the entire vortex length determines the induced velocity that adds a component to the flow velocity pushing the fluid particle to the diffuser wall thereby suppressing the onset of a separation. Besides the stabilizing effect through the induced velocity component, the presence of VGEs contributes to energizing the boundary layer by increasing the turbulence intensity, thereby increasing the exchange of lateral momentum with the boundary layer fluid.

The effect of VGEs on conversion coefficient  $\lambda$  is shown in Fig. 6.38 for a diffuser with  $l/w = 6$  for four different VGE-configurations, A,B,C and D. In Diagram A, where the VGE-height  $h = 0$ , the conversion factor  $\lambda$  for  $\theta = 0$ , has a decreasing tendency which is equivalent to accelerating the flow within the diffuser because of the blockage due to the boundary layer development. Increasing  $\theta$  causes an increase in  $\lambda$ . Up to  $\theta/2 = 5^\circ$ , the entire diffuser operates separation free. Further increasing  $\theta$  leads to separation. Introducing straight VGEs of height, 3mm and 4 mm respectively (Fig. 6.38 B and C), allows larger opening angles at higher  $\lambda$ . A substantial increase in  $\lambda$  is obtained by introducing a VGE with the height of 6 mm and an angle of  $82^\circ$  as shown in 6.38B. It should be emphasized that application of VGEs is associated with a total pressure loss. However, the pressure gain compensates for this loss [25].

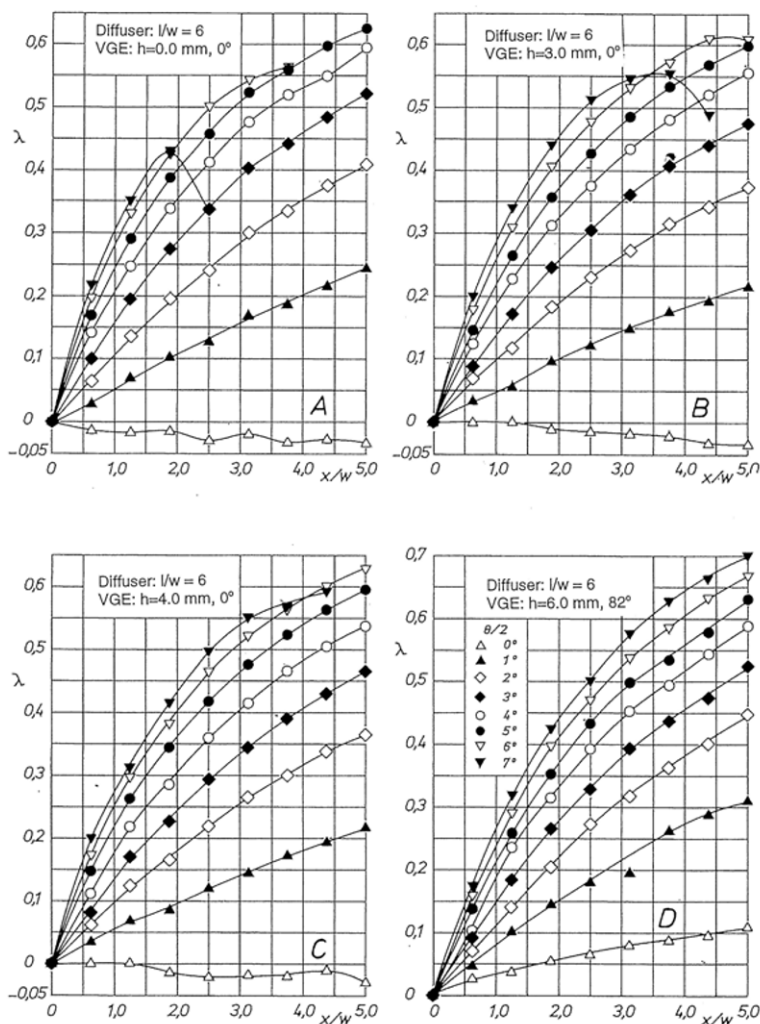


**Fig. 6.38:** Effect of Vortex generator edge on diffuser conversion coefficient from [25].

#### 6.9.4 Some Guidelines for Designing High Efficiency Diffusers

Diffusers may improve the efficiency of gas turbines, steam turbines, compressors and turbochargers by up to 4 % if designed properly. As mentioned above, the axial length ratio and the area ratio are the major parameters defining the conversion coefficient  $\lambda$ . Equally important is taking into consideration the distribution of the velocity and angle of the mass flow exiting the last stage of the turbomachinery component. Here, particular attention must be paid to designing multi-channel diffusers with struts and positioning the latter in such a way that they are not exposed to adverse flow incidence. The following steps may help designing a diffuser that

operates at a high  $\lambda$  with adequate efficiency:

- 1) First, accurately determine the distribution of flow velocity and angle at the exit of the last stage. This can be done using the streamline curvature method for stage aerodynamic design and is treated in Chapter 10. Using commercial CFD-packages may help in qualitatively estimating these distributions. For details refer to Chapter 20.
- 2) Consider a plane diffuser with a total limiting angle  $\theta_{\text{lim}}$  of  $12^\circ$  to  $16^\circ$ , and a given length ratio as the reference diffuser.
- 3) For the diffuser to be designed, convert the area ratio and the axial length ratio such that they correspond to the opening angle and the area ratio of the reference plane diffuser in step (2).
- 4) If a multi-channel design is used, each single channel should be treated individually as an independent diffuser following step (3). Also important is the design and the radial distribution of the struts to ensure incidence free flow.

## References

1. Schobeiri, M.T., 2010, "Fluid Mechanics for Engineers, A Graduate Text Book," ISBN 978-3-642-11593-6, e-ISBN 978-3-642-11594-3 2010 Springer-Verlag Berlin, Heidelberg.
2. Traupel, W., "Thermische Turbomaschinen," Bd.I, 1977, Springer-Verlag Berlin Heidelberg New York.
3. Pfeil, H., 1968, "Verlustbeiwerte von optimal ausgelegten Beschaufelungsgittern," *Energie und Technik* 20, Jahrgang 1968, Heft 1, L.A. Leipzig Verlag Düsseldorf.
4. Kirchberg, G., Pfeil, H., 1971, "Einfluß der Stufenkenngrößen auf die Auslegung von HD-Turbinen," *Zeitschrift Konstruktion*, 23, Jahrgang (1971), Heft 6.
5. Speidel, L., 1954, "Einfluß der Oberflächenrauigkeit auf die Strömungsverluste in ebenen Schaufelgittern," *Zeitschrift Forschung auf dem Gebiete des Ingenieurwesens*, Band 20, Heft 5.
6. NASA SP-36 NASA Report, 1965.
7. Prandtl, L., 1938, "Zur Berechnung von Grenzschichten," *ZAMM* 18, 77-82.
8. von Kármán, Th., 1921, "Über laminare und turbulente Reibung," *ZAMM*, 1, 233-253, (1921).
9. Ludwig, H., and Tillman, W., 1949, "Untersuchungen über die Wand-schubspannung in turbulenten Reibungsschichten," *Ingenieur Archiv* 17, 288-299, Summary and translation in NACA-TM- 12185 (1950).
10. Lieblein, S., Schwenk, F., Broderick, R.L., 1953, "Diffusions factor for estimating losses and limiting blade loadings in axial flow compressor blade elements," *NACA RM E53D01* June 1953.
11. Schobeiri, M.T., 1998, "A New Shock Loss Model for Transonic and Supersonic Axial Compressors With Curved Blades," *AIAA, Journal of Propulsion and Power*, Vol. 14, No. 4, pp. 470-478.



12. Berg, H., 1973 "Untersuchungen über den Einfluß der Leistungszahl auf Verluste in Axialturbinen," Dissertation, Technische Hochschule Darmstadt, D 16.
13. Wolf, H., 1960, "Die Randverluste in geraden Schaufelgittern," Dissertation, Technische Universität Dresden.
14. Schichting, H., 1979, "Boundary Layer Theory," McGraw Hill Series, ISBN 0-07-055334-3.
15. Pfeil, H., 1971, "Zur Frage der Spaltverluste in labyrinthgedichteten Hochdruckstufen von Dampfturbinen," Zeitschrift Konstruktion, 23 Heft 4, Seite 140-142.
16. Prust, H., 1974, "Cold-air study of the effect on turbine stator blade aerodynamic performance of coolant ejection from various trailing-edge slot geometries," NASA-Reports I: TMX 3000.
17. Prust, H., 1975, "Cold-air study of the effect on turbine stator blade aerodynamic performance of coolant ejection from various trailing-edge slot geometries," NASA-Reports II: TMX 3190.
18. Schobeiri, T., 1985, "Einfluß der Hinterkantenausblasung auf die hinter den gekühlten Schaufeln entstehenden Mischungsverluste," *Forschung im Ingenieurwesen*, Bd.51 Nr.1, pp.25-28.
19. Schobeiri, M.T., 1989, "Optimum Trailing Edge Ejection for Cooled Gas Turbine Blades," ASME Transaction, *Journal of Turbo machinery*, Vol. 111, No. 4, pp.510-514, October 1989.
20. Schobeiri, M.T. and Pappu, K., 1999, "Optimization of Trailing Edge Ejection Mixing Losses Downstream of Cooled Turbine Blades: A theoretical and Experimental Study," ASME Transactions, *Journal of Fluids Engineering*, 1999, Vol. 121, pp. 118-125
21. Sieverding, C.H., 1982, "The Influence of Trailing Edge Ejection on the Base Pressure in Transonic Cascade," ASME Paper: 82-GT-50.
22. Kline, S.J., Abbot, D., Fox, R., 1959, "Optimum design of straight-wall diffusers," ASME, *Journal of Basic Engineering*, Vol. 81, S. 321-331.
23. Sovran, G., Klomp, E.D., 1967, "Experimentally determined optimum geometries for rectilinear diffusers with rectangular, conical and annular cross-section," *Fluid Dynamics of Internal Flow*, Elsevier Publishing Co..
24. Schobeiri, M.T., 1979, "Theoretische und experimentelle Untersuchungen laminarer und turbulenter Strömungen in Diffusoren," Dissertation, Technische Universität Darmstadt, D16.

## 7 Efficiency of Multi-Stage Turbomachines

In Chapter 6, we derived the equations for calculation of different losses that occur within a stage of a turbomachine. As shown, the sum of those losses determines the stage efficiency which shows the capability of energy conversion within the stage. The stage efficiency, however, is not fully identical with the efficiency of the entire turbomachine. In a multi-stage turbomachine, the expansion or compression process within individual stages causes an entropy production which is associated with a temperature increase. For an expansion process, this temperature increase leads to a heat recovery and for a compression process, it is associated with a reheat ash shown in Fig.7.1. As a consequence, the turbine efficiency is higher and the compressor efficiency lower than the stage efficiency. The objective of this chapter is to describe this phenomenon by means of classical thermodynamic relations. The approach is adopted by many authors, among others, Traupel [1] and Vavra [2].

### 7.1 Polytropic Efficiency

For an infinitesimal expansion and compression, shown in Fig. 7.1, we define the *small polytropic efficiency*:

$$\eta_p = \frac{dh}{dh_s} \text{ (expansion)}, \quad \eta_p = \frac{dh_s}{dh} \text{ (compression)}, \quad dh = c_p dT, \quad dh_s = c_p dT_s \quad (7.1)$$

For an infinitesimal expansion,  $c_p$  can be considered as constant:

$$\eta_p = \frac{(T + dT) - T}{T + dT_s - T} = \frac{\frac{T + dT}{T} - 1}{\frac{T + dT_s}{T} - 1} \quad (7.2)$$

For a polytropic process it generally holds  $pv^n = \text{const.}$  Inserting Eq. (7.2) into Eq. (7.1):

$$\eta_p = \frac{dh}{dh_s} = \frac{\left( \frac{p + dp}{p} \right)^{\frac{n-1}{n}} - 1}{\left( \frac{p + dp}{p} \right)^{\frac{k-1}{k}} - 1} \quad (7.3)$$

After expanding the expressions in the parentheses in Eq. (7.3):

$$\left( \frac{p + dp}{p} \right)^{\frac{n-1}{n}} \quad \text{and} \quad \left( \frac{p + dp}{p} \right)^{\frac{\kappa-1}{\kappa}} \quad (7.4)$$

and neglecting the higher order terms, we find:

$$\left( 1 + \frac{dp}{p} \right)^{\frac{n-1}{n}} \approx 1 + \left( \frac{n-1}{n} \right) \frac{dp}{p} \quad (7.5)$$

Now, we introduce Eq. (7.5) into (7.3) and obtain the small polytropic efficiency:

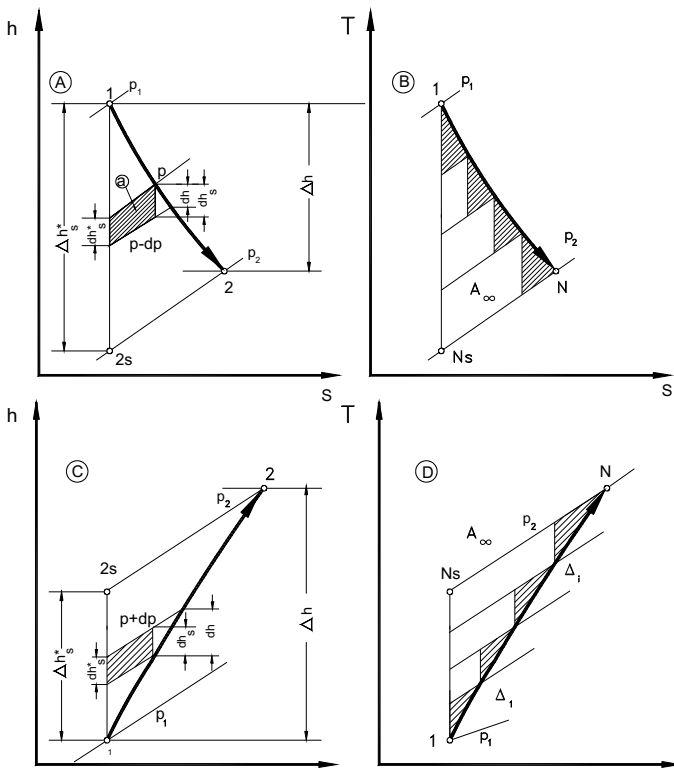


**Fig. 7.1:** A) Heat recovery in a turbine with  $N_{\text{stage}} = \infty$ , B) Heat recovery in a turbine with  $N_{\text{stage}} = 4$ , C) Reheat process in a compressor with  $N_{\text{stage}} = \infty$ , D) Reheat process in a compressor with  $N_{\text{stage}} = 4$ .

$$\eta_p = \frac{dh}{dh_s} = \frac{1 + \frac{dp}{p} \frac{n-1}{n} - 1}{1 + \frac{dp}{p} \frac{\kappa-1}{\kappa} - 1} \quad (7.6)$$

For the expansion process, Eq. (7.6) reduces to:

$$\eta_p = \left( \frac{\kappa}{\kappa - 1} \right) \left( \frac{n - 1}{n} \right) \quad (7.7)$$

likewise for a compression process we find:

$$\eta_p = \left( \frac{n}{n - 1} \right) \left( \frac{\kappa - 1}{\kappa} \right) \quad (7.8)$$

with  $n$  as the polytropic and  $\kappa$  as isentropic exponents. Equations (7.7) and (7.8) express the direct relation between the polytropic efficiency  $\eta_p$  and the polytropic exponent  $n$  for *infinitesimally small* expansion and compression, where  $n$  and  $\kappa$  are considered constant. In a multi-stage environment, both exponents change from the start of expansion or compression to the end. As a result, Eqs. (7.7) and (7.8) are not valid for finite expansion or compression processes. However, if the end points of these processes are known, averaged polytropic efficiency for multi-stage compression and expansion can be found. For a process with known beginning and end points, we may use the polytropic relation:

$$p_1 v_1^{\bar{n}} = p_2 v_2^{\bar{n}} \quad (7.9)$$

and the following enthalpy relation:

$$h = \frac{\bar{\kappa}}{\bar{\kappa} - 1} p v \quad (7.10)$$

where  $\bar{n}$  and  $\bar{\kappa}$  are the averaged polytropic and isentropic exponents. From Eq. (7.9), we find:

$$\bar{n} = \frac{\ln \frac{p_2}{p_1}}{\ln \frac{v_1}{v_2}} \quad (7.11)$$

Inserting Eq. (7.11) into Eqs. (7.7) and (7.8), we find

$$\overline{\eta}_{pC} = \frac{\overline{\kappa} - 1}{\overline{\kappa}} \frac{\ln \frac{p_2}{p_1}}{\ln \frac{T_2}{T_1}}, \quad \overline{\eta}_{pT} = \frac{\overline{\kappa}}{\overline{\kappa} - 1} \frac{\ln \frac{T_2}{T_1}}{\ln \frac{p_2}{p_1}} \quad (7.12)$$

As mentioned previously, calculating the above polytropic efficiencies require the knowledge of the process end points, which are at the beginning of a design process, unknown, but can be determined after the individual losses are calculated. The averaged isentropic exponent in Eq. (7.12) is calculated from:

$$\overline{c_p} = \frac{h_2 - h_1}{T_2 - T_1}, \quad \frac{\overline{c_p}}{\overline{c_v}} = \overline{\kappa}, \quad \text{and} \quad \overline{c_p} - \overline{c_v} = R \quad (7.13)$$

## 7.2 Isentropic Turbine Efficiency, Recovery Factor

Assuming the turbine has an infinite number of stages, we start from an infinitesimal expansion to define the isentropic stage efficiency, Fig. 7.1:

$$\eta_s = \frac{dh}{dh_{s'}} \Rightarrow dh = \eta_s dh_{s'} \quad (7.14)$$

Using the definitions in Eq. (7.1), we find the enthalpy differential:

$$dh = \eta_p dh_s \quad (7.15)$$

As shown in Fig. 7.1, for an infinitesimally small cycle with the area  $a$ , the isentropic enthalpy differentials are interrelated by the first law as:  $dh_s = dh_{s'} + a$ . Using Eq. (7.15), we arrive at:

$$dh = \eta_p (dh_{s'} + a) \quad (7.16)$$

Integration of Eq. (7.15) and (7.16) yields:

$$\Delta h = \overline{\eta}_s \Delta h_{s'} \quad (7.17)$$

and:

$$\Delta h = \overline{\eta}_p \Delta h_s = \overline{\eta}_p (\Delta h_{s'} + A_\infty) \quad (7.18)$$

with  $A_\infty$  as the area 122'1, and  $\overline{\eta}_s$  and  $\overline{\eta}_p$  as the mean isentropic turbine and mean

polytropic efficiencies. Equating (7.17) and (7.18) results in:

$$\bar{\eta}_s = \bar{\eta}_p \frac{(\Delta h_{s'} + A_\infty)}{\Delta h_{s'}} = \bar{\eta}_p \left[ 1 + \frac{A_\infty}{\Delta h_{s'}} \right] \quad (7.19)$$

We introduce the heat recovery factor for a turbine with the stage number  $N = \infty$ :

$$1 + f_{\infty T} = 1 + \frac{A_\infty}{\Delta h_{s'}} \quad (7.20)$$

With this definition, Eq. (7.19) becomes:

$$\bar{\eta}_s = \bar{\eta}_p (1 + f_{\infty T}) \quad (7.21)$$

To find the recovery factor, we divide Eq. (7.17) by (7.18):

$$\frac{\bar{\eta}_s}{\bar{\eta}_p} = \frac{\Delta h_s}{\Delta h_{s'}} = \frac{\int_{p_2}^{p_1} v dp}{\int_{p_2}^{p_1} v_s dp} = 1 + f_{\infty T} \quad (7.22)$$

The integral in the numerator must be performed along the polytropic expansion, whereas the integral expression in the denominator must be performed along the isentropic expansion. We insert in Eq. (7.22) for the specific volume, the relationship for polytropic and isentropic processes:

$$v_s = v_1 \left( \frac{p_1}{p} \right)^{\frac{1}{\kappa}}, \quad v = v_1 \left( \frac{p_1}{p} \right)^{\frac{1}{n}} \quad (7.23)$$

and arrive at:

$$1 + f_{\infty T} = \frac{\frac{\bar{n}}{\bar{n} - 1}}{\frac{\bar{\kappa}}{\bar{\kappa} - 1}} \left( \frac{1 - \left[ \frac{p_2}{p_1} \right]^{\frac{\bar{n} - 1}{\bar{n}}}}{1 - \left[ \frac{p_2}{p_1} \right]^{\frac{\bar{\kappa} - 1}{\bar{\kappa}}}} \right) \quad (7.24)$$

The polytropic exponent  $\bar{n}$  in Eq. (7.23) can be expressed in terms of  $\bar{\kappa}$  and  $\eta_p$  using Eq. (7.8). With this modification, the recovery factor is obtained from:

$$1 + f_{\infty T} = \frac{1}{\eta_p} \frac{\left( 1 - \left[ \frac{p_2}{p_1} \right]^{\frac{\bar{\kappa} - 1}{\bar{\kappa}} \frac{1}{\eta_p}} \right)}{\left( 1 - \left[ \frac{p_2}{p_1} \right]^{\frac{\bar{\kappa} - 1}{\bar{\kappa}}} \right)} \quad (7.25)$$

For a multi-stage turbine with N stages, Fig. 7.1B, the following geometrical approximations may be made:

$$A_N = A_{\infty} - \sum_{i=0}^N \Delta_i \quad (7.26)$$

$$\Delta_i \approx \Delta_{i+1} \approx \Delta_m$$

with  $\Delta_m$  as the area that represents an average of all triangular areas  $\Delta_i$ . With this approximation, we obtain  $A_N = A_{\infty} - N\Delta_m$  and define the ratio:

$$f_T = \frac{A_N}{\Delta h_s} = \frac{A_{\infty}}{\Delta h_s} \left( 1 - \frac{N\Delta_m}{A_{\infty}} \right) \quad (7.27)$$

Since  $A_{\infty}$  and  $\Delta_m$  are similar, we may approximate

$$\Delta_m \approx \frac{A_{\infty}}{N^2} \quad (7.28)$$

As a result, Eq. (7.27) reduces to:

$$f_T = f_{\infty T} \left( 1 - \frac{NA_{\infty}}{N^2 A_{\infty}} \right) = f_{\infty T} \left( 1 - \frac{1}{N} \right) \quad (7.29)$$

Using the same procedure that has lead to Eq. (7.22) for a turbine component with a finite number of stages, we find:

$$\overline{\eta}_s = \overline{\eta}_p (1 + f_T) \quad (7.30)$$

Since  $f_T$  is  $> 0$ , the turbine isentropic efficiency is greater than the polytropic efficiency. This is a consequence of stage entropy production that results in heat recovery. For a turbine component with a pressure ratio  $\pi_T = p_2/p_1$ , the recovery factor  $f_{\omega_T}$  is plotted in Fig. 7.2, where the averaged turbine polytropic efficiency  $\overline{\eta}_p$  is varied from 0.7 to 0.95. As seen, the lowest efficiency of  $\overline{\eta}_p = 0.7$  causes the highest dissipation that leads to a high recovery factor. Increasing the polytropic efficiency to  $\overline{\eta}_p = 0.95$  causes a much less dissipative expansion. As a result, the heat recovery for the turbine with  $\overline{\eta}_p = 0.95$  is much lower than the previous one with  $\overline{\eta}_p = 0.7$ .

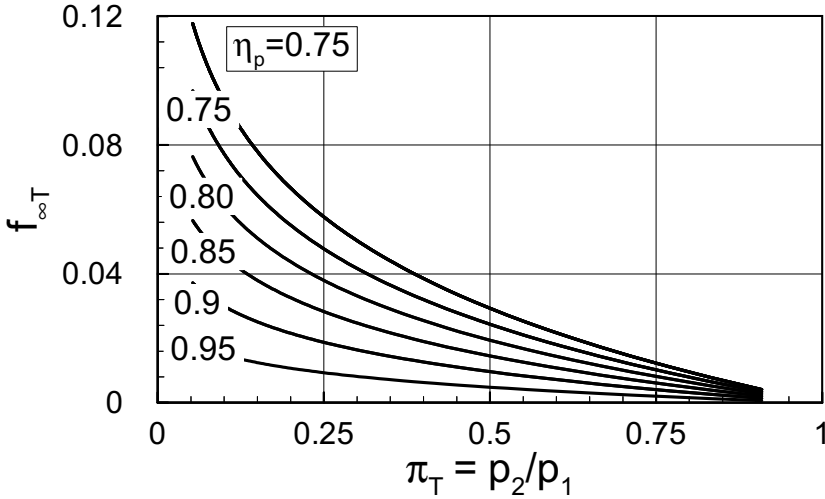


Fig. 7.2: Recovery factor of a multi-stage turbine for  $\kappa = 1.4$ .

### 7.3 Compressor Efficiency, Reheat Factor

To obtain the reheat factor for a multi-stage compressor, we apply a similar procedure as outlined in Section 7.2. The isentropic efficiency of an infinitely small compression, shown in Fig. 7.1, is defined as:

$$\eta_s = \frac{dh_{s'}}{dh} \quad , \quad dh = \frac{dh_{s'}}{\eta_s} \quad (7.31)$$



Polytropic efficiency is:

$$\eta_p = \frac{dh_s}{dh} \quad , \quad dh = \frac{dh_s}{\eta_p} \quad (7.32)$$

For a compressor with an infinite number of stages, the mean isentropic efficiency is:

$$\overline{\eta}_s = \overline{\eta}_p \frac{1}{1 + f_{\infty C}} \quad (7.33)$$

where the expression  $1 + f_{\infty C}$  is the reheat factor and the subscript C refers to a compressor. The reheat factor is obtained from:

$$1 + f_{\infty C} = \overline{\eta}_p \frac{\left( \frac{p_2}{p_1} \right)^{\frac{1}{\eta_p} \frac{\bar{\kappa} - 1}{\bar{\kappa}}} - 1}{\left( \frac{p_2}{p_1} \right)^{\frac{\bar{\kappa} - 1}{\bar{\kappa}}} - 1} \quad (7.34)$$

For a multi-stage high pressure compressor component with a pressure ratio  $\pi_C = p_2/p_1$ , the reheat factor  $f_{\infty C}$  is plotted in Fig. 7.3 where the averaged compressor polytropic efficiency  $\overline{\eta}_p$  is varied from 0.7 to 0.95. Similar to the turbine component discussed in Section 9.2, the lowest efficiency of  $\overline{\eta}_p = 0.7$  causes the highest dissipation that leads to a high reheat factor. Increasing the polytropic efficiency to  $\overline{\eta}_p = 0.95$  causes much less dissipation. As a result, the reheat for the compressor with  $\overline{\eta}_p = 0.95$  is much lower than the previous one with  $\overline{\eta}_p = 0.7$ . Using the same procedure discussed in the previous section, we find the following relationship between  $f_C$  and  $f_{\infty C}$  for a multi-stage compressor with N stages:

$$f_C = f_{\infty C} \left( \frac{N - 1}{N} \right) = f_{\infty C} \left( 1 - \frac{1}{N} \right) \quad (7.35)$$

Once the reheat factor for a compressor with an infinite number of stages  $f_{\infty C}$  is determined, the reheat factor of a compressor with a finite number of stages is calculated using Eq.(7.35).

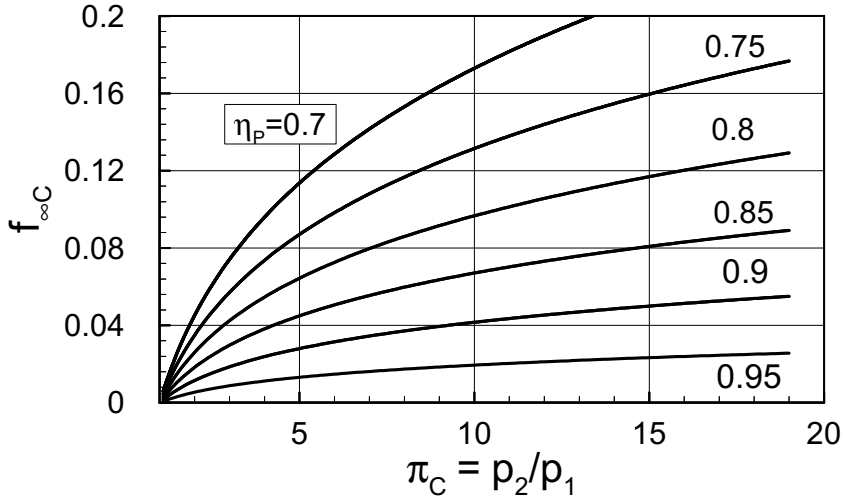
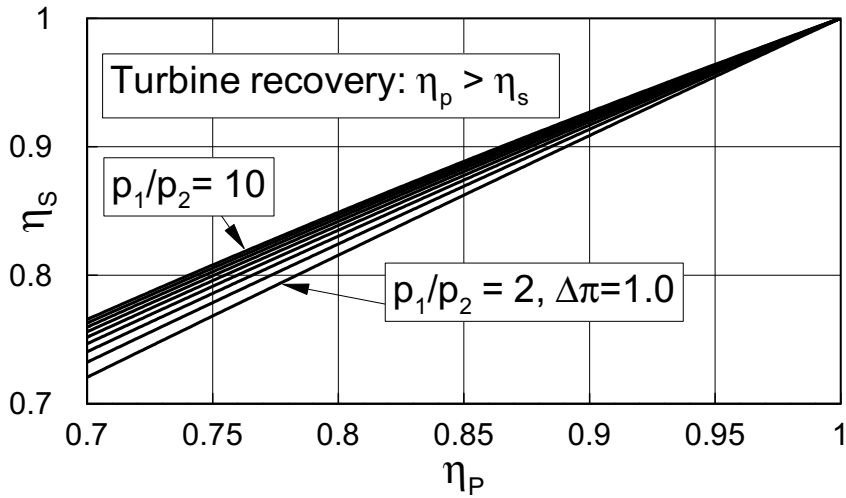


Fig. 7.3: Reheat factor of a multistage compressor for  $\kappa = 1.4$ .

#### 7.4 Polytropic versus Isentropic Efficiency

As shown in Eqs. (7.18) and (7.34), the polytropic efficiency accounts for the energy dissipation within a turbine and a compressor component. Furthermore, the polytropic efficiency can be used to compare turbine or compressor components that are operating under different initial conditions or have different working media. In these cases, both polytropic and isentropic efficiencies change. However, the rate of change for polytropic efficiency is much smaller than that of an isentropic one. It is indeed possible for two compressor or turbine components to have the same polytropic efficiency if certain similarity conditions are met. This is not the case for isentropic efficiency. Therefore, the isentropic efficiency is not appropriate for comparison purposes. Another major advantage of polytropic efficiency is the use of row-efficiencies to calculate the row-by-row expansion or compression process. Calculating the polytropic efficiency, however, requires the knowledge of expansion or compression end points which are generally unknown at the stage of design. The isentropic efficiency, on the other hand, exhibits a simple and practical tool, since the isentropic enthalpy difference is calculated from the inlet and exit conditions at constant entropy. As we saw in this chapter, these two efficiencies are related to each other. Figure 7.4 exhibits, for a multi-stage turbine component, the dependency of the isentropic efficiency upon the polytropic efficiency with the pressure ratio  $\pi_T = p_1/p_2$  as the parameter. As shown in Fig. 7.4, the isentropic efficiency is always greater than the polytropic one. The difference diminishes by increasing the polytropic efficiency, which reflects a reduction in dissipation. Figure 7.5 exhibits an opposite tendency for a multi-stage compression process. In this case, the polytropic efficiency is always greater than the isentropic one.



**Fig. 7.4:** Turbine isentropic efficiency as a function of polytropic efficiency with turbine pressure ratio  $\pi_T = p_1/p_2$  as parameter for  $\kappa = 1.4$

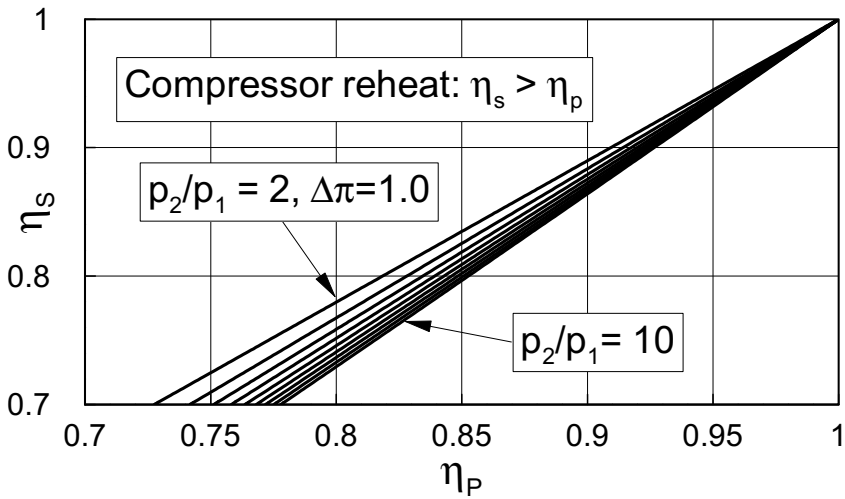


**Fig. 7.5:** Compressor isentropic efficiency as a function of polytropic efficiency with compressor pressure ratio  $\pi_C = p_2/p_1$  as parameter for  $\kappa = 1.4$ .

---

## References

- 7.1 Traupel, W., Thermische Turbomaschinen, Bd.I, 1977, Springer-Verlag Berlin Heidelberg New York.
- 7.2 Vavra, M.H., 1960, Aero-Thermodynamics and Flow in Turbomachines, John Wiley & Sons, Inc.

## 8 Incidence and Deviation

Up to this point, the relationships developed for a turbomachinery stage have been strictly correct for given velocity diagrams with known inlet and exit flow angles. We assumed that the flow is fully congruent with the blade profile. This assumption implies that the inlet and exit flow angles coincide with the camber angles at the leading and trailing edges. Based on the operation condition and the design philosophy, there might be a difference between the camber and flow angle at the leading edge, which is called the incidence angle. The difference between the blade camber angle and the flow angle at the exit is termed the deviation angle. Since the incidence and deviation affect the required total flow deflection, the velocity diagram changes. If this change is not predicted accurately, the stage operates under a condition not identical with the optimum operation condition for which the stage is designed. This situation affects the efficiency and performance of the stage and thus the entire turbomachine. In order to prevent this, the total flow deflection must be accurately predicted. The compressor and the turbine flows react differently to a change of incidence. For instance, a slight change of incidence causes a partial flow separation on the compressor blade suction surface that can trigger a rotating stall; a turbine blade is less sensitive even to greater incidence change. To obtain the incidence and deviation angle for compressor and turbine blades, we use two different calculation methods. The first method deals with the application of conformal transformation to cascade flows with low deflection as in compressor blades. The second method concerns the calculation of deviation in high loaded cascades as in turbine blades.

### 8.1 Cascade with Low Flow Deflection

#### 8.1.1 Conformal Transformation

Conformal transformation is one of the areas in classical complex analysis. Its application to fluid dynamics and cascade aerodynamics can be found, among others, in [1], [2], and [3]. Weinig [4] applied the conformal transformation method to turbomachinery blading and developed a simple procedure for calculating the exit flow angle of cascades with low flow deflection such as compressor cascades. Further treatment of cascade aerodynamics using method of conformal transformation by Weinig is found in [5], [6], [7], and [8].

Starting from the simplest case, consider the physical plane where a cascade consisting of identical straight-line profiles is located (Fig. 8.1).

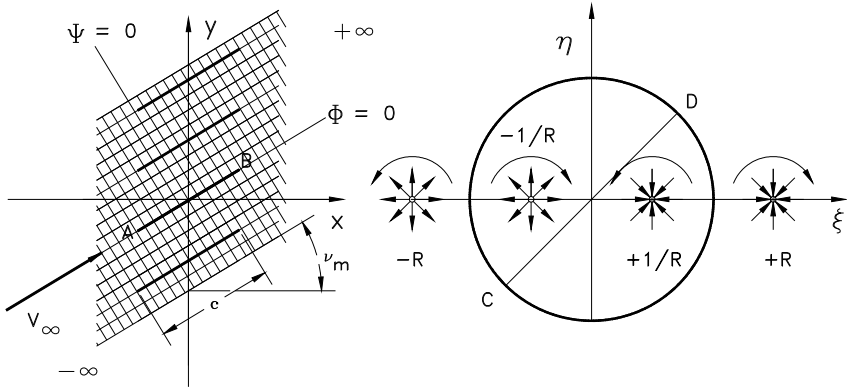


**Fig. 8.1:** Conformal transformation of a straight cascade. The cascade in  $z$ -plane is mapped onto the unit circle in  $\zeta$ -plane.

The profiles are staggered at an angle  $\nu_m$  and have a spacing  $s$ . The flow is parallel to the cascade profiles. In other words, the profiles themselves are stream lines. Furthermore, assume that the flow originates from  $-\infty$  and flows to  $+\infty$ . Since the flow from one cascade strip to another remains the same, it is sufficient to map only one of the profiles into the complex plane  $\zeta$  on the unit circle. This unit circle exhibits one Riemann's sheet in the complex plane. The  $\zeta$ -plane consists of an infinite number of Riemann's sheets, which correspond to the number of straight-line profiles within the cascade. The origin and end of the flow field, located  $\pm \infty$  in  $z$ -plane, must be mapped onto the real axis of  $\zeta$ -plane at  $\pm R$  (Fig.8.1). The complex potential in  $z$ -plane may be written as:

$$X(z) = \Phi + i\Psi \quad (8.1)$$

where  $\Phi$  and  $\Psi$  are the potential and stream functions. The function  $X(z)$  is holomorphic if it is on the closed curve ABA continuous and differentiable, in other words, it must be an analytic function with the derivative

$$\frac{dX(z)}{dz} = \frac{\partial \Phi}{\partial x} + i \frac{\partial \Psi}{\partial x} \quad (8.2)$$

that satisfies the Cauchy-Riemann's condition:

$$\frac{\partial \Phi}{\partial x} = \frac{\partial \Psi}{\partial y} \equiv u, \quad \frac{\partial \Phi}{\partial y} = - \frac{\partial \Psi}{\partial x} \equiv v \quad (8.3)$$

Inserting Eqs. (8.3) into Eq. (8.2), we find

$$\frac{dX(z)}{dz} = u - iv \quad (8.4)$$

If the velocity in z-plane is  $V_\infty$  its components in x- and y-directions are:

$$u = V_\infty \cos \gamma_m ; \quad v = V_\infty \sin \gamma_m \quad (8.5)$$

Introducing Eq. (8.5) into (8.4) yields:

$$\frac{dX(z)}{dz} = V_\infty (\cos \gamma_m - i \sin \gamma_m) = V_\infty e^{-i\gamma_m} \quad (8.6)$$

The integration of Eq. (8.6) leads to :

$$X(z) = z V_\infty e^{-i\gamma_m} \quad \text{where } z = r e^{i\theta} \quad \text{or } X(z) = V_\infty r e^{i(\theta - \gamma_m)} \quad (8.7)$$

which is:

$$X(z) = V_\infty r [\cos(\theta - \gamma_m) + i \sin(\theta - \gamma_m)] \quad (8.8)$$

Comparing Eq. (8.8) with (8.1) delivers:

$$\begin{aligned} \Phi &= V_\infty r \cos(\theta - \gamma_m) \\ \Psi &= V_\infty r \sin(\theta - \gamma_m) \end{aligned} \quad (8.9)$$

with  $\Phi$  in Eq. (8.9) as the complex velocity potential (potential function) and  $\Psi$  the stream function. Moving from one profile to another, as shown in Fig. 8.1, the potential and stream functions experience the following changes:

$$\text{at } r = 0, \quad \Phi = \Phi_0 = 0, \text{ and } \Psi = \Psi_0 = 0$$

$$\text{at } r = s, \quad \Phi = \Phi_1 = V_\infty s \cos(\pi/2 - \gamma_m) = V_\infty s \sin \gamma_m$$

$$\text{and } \Psi = \Psi_1 = V_\infty s \sin(\pi/2 - \gamma_m) = V_\infty s \cos \gamma_m$$

Using Eq. (8.9), the potential difference can be expressed as:

$$\Delta \Phi = \Phi_1 - \Phi_o = V_\infty s \sin \nu_m \quad (8.10)$$

and the stream function difference is:

$$\Delta \Psi = \Psi_1 - \Psi_o = V_\infty s \cos \nu_m \quad (8.11)$$

The stream function difference, Eq. (8.11), represents the volume flow through a strip of the cascade with spacing  $s$  and height  $h=1$ . This volume flow originates from a source at  $z = -\infty$  and has a source strength  $Q$  with  $Q = \Delta \Psi = V_\infty s \cos \nu_m$ . To generate such  $\Delta \Psi$  and  $\Delta \Phi$  in  $z$ -plane, the corresponding conformal transformation in  $\zeta$ -plane at  $-R$  must contain a source and a vortex with the strengths  $Q$  and  $\Gamma$ . Similarly at  $+R$ , a sink and a vortex with the strengths  $-Q$  and  $-\Gamma$  must be placed that correspond to the station  $+\infty$  in  $z$ -plane. Thus, a system of sources, sinks, and vortices is arranged on the real  $\zeta$ -axis outside (exterior) the unit circle. This system fulfills the boundary condition at  $+\infty$  and also  $\pm R$ , but the most important requirement that the unit circle must itself be a streamline, is not fulfilled. This problem can be solved simply by reflecting the singularities onto the unit circle. The locations of the reflected singularities are then  $\pm 1/R$  inside (interior) the unit circle. The next step is to find the corresponding transformation function in  $\zeta$ -plane.

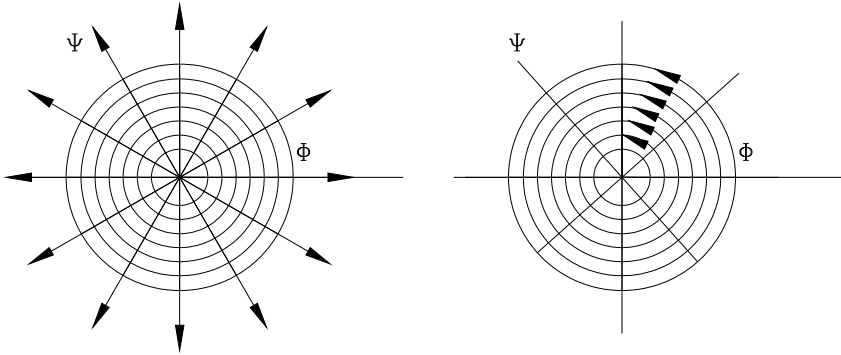


**Fig. 8.2:** Singularities source and circulation distribution with stream function  $\Psi$  and potential function  $\Phi$ .

The complex potential for a source located at  $\zeta = 0$  and has a strength  $Q$  is (Fig. 8.2):

$$X = \phi + i\Psi \equiv \frac{Q}{2\pi} \ln \zeta \quad (8.12)$$



In Eq. (8.12) the complex function  $\zeta$  is:

$$\zeta = \xi + i\eta \text{ and since}$$

$$\xi = r\cos\theta, \quad \eta = r\sin\theta, \quad e^{i\theta} = \cos\theta + i\sin\theta \quad (8.13)$$

$$\zeta = r(\cos\theta + i\sin\theta) = re^{i\theta}$$

Introducing Eq. (8.13) into (8.12) and decomposing the result into its real and imaginary parts  $\Phi, \Psi$  respectively, we find

$$X = \Phi + i\Psi = \frac{Q}{2\pi} \ln(re^{i\theta}) = \frac{Q}{2\pi} (\ln r + i\theta) \quad (8.14)$$

$$\Phi = \frac{Q}{2\pi} \ln r, \quad \Psi = \frac{Q}{2\pi} \theta$$

with the radius in Eq.(8.14) as

$$r = \sqrt{\xi^2 + \eta^2}, \quad \theta = \arctg \frac{\eta}{\xi} \quad (8.15)$$

By moving around the center of the source along a closed curve,  $\theta$  in Eq. (8.15) will change from 0 to  $2\pi$  and as a result, the change of stream function is:

$$\Delta\Psi = \frac{Q}{2\pi} 2\pi = Q = V_\infty s \cos\alpha_m \quad (8.16)$$

which corresponds to the source strength. For a source located at  $\zeta = R$ , the complex potential is:

$$X = \frac{Q}{2\pi} \ln(\zeta - R) \quad (8.17)$$

where for sources  $Q > 0$  and for sinks  $Q < 0$ . The potential lines of source, at  $\zeta = 0$  are concentric circles, Fig. 8.2. The vortex flow can be established by generating stream lines from these concentric circles, inserting  $Q = i\Gamma$  in Eq. (8.14):

$$X = \frac{i\Gamma}{2\pi} \ln \zeta = \frac{i\Gamma}{2\pi} (\ln r + i\theta) \quad (8.18)$$

The variables in the parentheses of Eq. (8.18) are expressed in terms of

$$\Phi = -\frac{\Gamma}{2\pi} \theta, \quad \Psi = \frac{\Gamma}{2\pi} \ln r \quad (8.19)$$

Using  $\Phi$  and  $\Psi$  as the potential and stream function from Eq. (8.19), the velocity can be obtained from Eq. (8.20)

$$V = -\frac{d\Phi}{ds} = -\frac{\Gamma}{2\pi} \frac{1}{r} \quad (8.20)$$

where the differential arc length  $ds = r d\theta$ . By moving around the vortex center from  $\theta = 0$  to  $2\pi$ , the potential difference is  $\Delta\Phi = \Gamma = V_\infty s \sin \nu_m$ , where  $\Gamma$  is the circulation. For a vortex located at  $\zeta = R$ , the complex potential is:

$$X = \frac{i\Gamma}{2\pi} \ln(\zeta - R) \quad (8.21)$$

If the source is located at an arbitrary point  $\zeta_o$ , Eq. (8.21) can be written as:

$$X = \frac{Q}{2\pi} \ln(\zeta - \zeta_o) \quad (8.22)$$

For a vortex flow, Eq. (8.22) yields:

$$X = \frac{i\Gamma}{2\pi} \ln(\zeta - \zeta_o) \quad (8.23)$$

The required complex potential consists of sinks, sources and vortices located at  $\pm R$  and  $\pm 1/R$  which we summarize as  $X(\zeta) = \sum X(\zeta)_{\text{sources}} + \sum X(\zeta)_{\text{sinks}} + \sum X(\zeta)_{\text{vortices}}$  is given as

$$\begin{aligned} X(\zeta) = & \frac{s}{2\pi} \cos \nu_m \ln(\zeta + R) + \frac{s}{2\pi} \cos \nu_m \ln\left(\zeta + \frac{1}{R}\right) - \\ & - \frac{is}{2\pi} \sin \nu_m \ln(\zeta + R) + \frac{is}{2\pi} \sin \nu_m \ln\left(\zeta + \frac{1}{R}\right) - \\ & - \frac{s}{2\pi} \cos \nu_m \ln(\zeta - R) - \frac{s}{2\pi} \cos \nu_m \ln\left(\zeta - \frac{1}{R}\right) + \\ & + \frac{is}{2\pi} \sin \nu_m \ln(\zeta - R) - \frac{is}{2\pi} \sin \nu_m \ln\left(\zeta - \frac{1}{R}\right) \end{aligned} \quad (8.24)$$

Rearranging Eq. (8.24):

$$X(\zeta) = \frac{s}{2\pi} \left\{ e^{-iv_m \ln \frac{R + \zeta}{R - \zeta}} + e^{iv_m \ln \frac{\zeta + \frac{1}{R}}{\zeta - \frac{1}{R}}} \right\} \quad (8.25)$$

Setting  $|V_\infty| = 1$  and equating Eq. (8.7) and (8.25) yields:

$$X(Z) = X(\zeta) \quad (8.26)$$

resulting in:

$$z = \frac{s}{2\pi} \left\{ \ln \frac{R + \zeta}{R - \zeta} + e^{2iv_m \ln \frac{\zeta + \frac{1}{R}}{\zeta - \frac{1}{R}}} \right\} \quad (8.27)$$

With Eq. (8.27), the transformation function is completely defined. As shown, the complex potential  $X(\zeta)$  fulfills the streamline requirement on the unit circle. The contributions of all the singularities outside (exterior) the circle are exactly equal to the contributions of the singularities inside (interior) the circle. The complex potential on the unit circle that characterizes the equilibrium state between the singularities is expressed as:

$$X(\zeta_c) = \frac{s}{\pi} e^{iv_m \ln \frac{\zeta_c + \frac{1}{R}}{\zeta_c - \frac{1}{R}}} \quad (8.28)$$

where the subscript  $c$  in Eq. (8.28) refers to unit circle contour with  $\zeta_c = 1.e^{i\alpha}$ . Decomposing Eq. (8.28) into its real and imaginary parts, the real part is :

$$\Phi_c = \frac{s}{2\pi} \left\{ \cos v_m \ln \frac{R^2 + 2R \cos \alpha + 1}{R^2 - 2R \cos \alpha + 1} + 2 \sin v_m \arctan \left[ \frac{2R \sin \alpha}{R^2 - 1} \right] \right\} \quad (8.29)$$

The velocity distribution on the unit circle can be obtained by differentiating Eq. (8.29) around the circle:

$$V = \frac{d\Phi_c}{rd\alpha} \quad \text{where } r = 1 \quad (8.30)$$

The stagnation points on the unit circle requires that in Eq. (8.30) the velocity vanishes,  $V = 0$ . This requirement leads to:

$$tg\alpha_s = \frac{R^2 - 1}{R^2 + 1} tg v_m \quad (8.31)$$

In Eq. (8.31)  $\alpha_s$  is the first stagnation angle. To find the potential difference between the stagnation points  $\alpha_s$  and  $\alpha_s + \pi$ , the angle  $\alpha$  in Eq. (8.29) is replaced successively by  $\alpha_s$  and  $\alpha_s + \pi$ . In  $\zeta$ -plane:

$$\Delta\Phi_{CD} = \Phi_C - \Phi_D = \Phi_{\alpha_s} - \Phi_{(\alpha_s + \pi)} \quad (8.32)$$

In  $z$ -plane:

$$\begin{aligned} \Phi_A &= V_\infty \frac{c}{2} \cos(\theta_A - v_m) = V_\infty \frac{c}{2}, \quad \text{since } \theta_A = v_m \\ \Phi_B &= V_\infty \frac{c}{2} \cos(\theta_E - v_m) = -V_\infty \frac{c}{2}, \quad \text{since } \theta_E = v_m + \pi \end{aligned} \quad (8.33)$$

As a result, we obtain the potential difference from Eq. (8.33):

$$\Delta\Phi_{AB} = \Phi_A - \Phi_B = V_\infty c = c, \quad \text{where } V_\infty = 1 \quad (8.34)$$

Equating the potential differences in  $\zeta$ - and  $z$ -plane from Eq. (8.32) and (8.34) yields:

$$\Delta\Phi_{CD}(\zeta) = \Delta\Phi_{AB}(z) \quad (8.35)$$

and with Eq. (8.29) we have:

$$\frac{c}{s} = \frac{1}{\pi} \left\{ \cos v_m \ln \frac{R^2 + 2R \cos \alpha + 1}{R^2 - 2R \cos \alpha + 1} + 2 \sin v_m \arctg \left[ \frac{2R \sin \alpha}{R^2 - 1} \right] \right\} \quad (8.36)$$

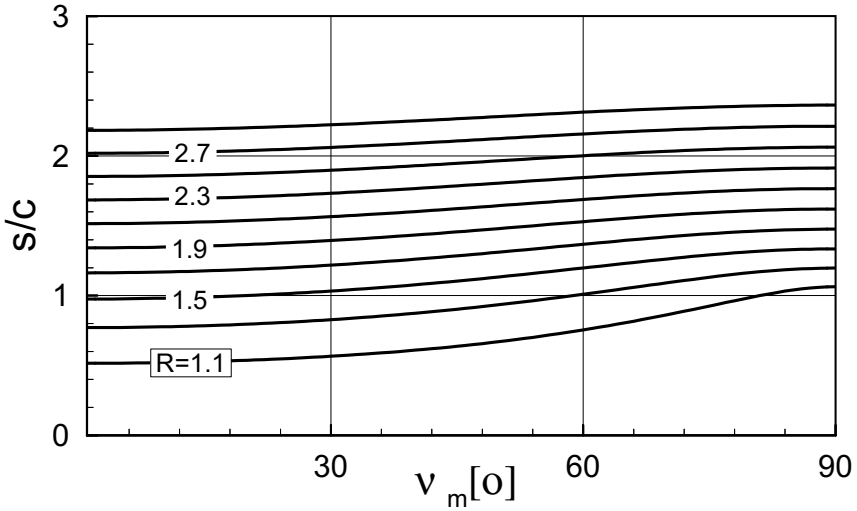


**Fig. 8.3:** Spacing/chord ratio  $s/c$  as a function of the cascade stagger angle  $v_m$  with the mapping parameter  $R$  as parameter.

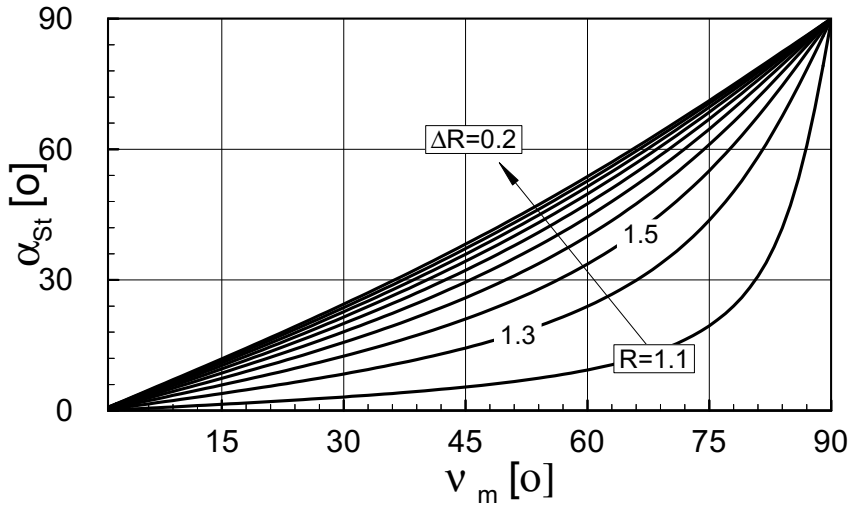


**Fig. 8.4:** Stagnation angle  $\alpha_{st}$  as a function of the cascade stagger angle  $v_m$  with the mapping parameter  $R$  as parameter.

The cascade parameter  $v_m$  and  $c/s$  from Eq. (8.36) that belong to  $z$ -plane correspond

to the  $\alpha_s$  and  $R$  in  $\zeta$ -plane. Equations (8.31) and (8.36) can be computed easily. The result of such a computation is shown in Figs. 8.3 and 8.4. As Fig. 8.3 shows, to each given pair of  $s/c$  and  $v_m$  only one value is allocated to the transformation parameter  $R$ . Taking this parameter and the stagger angle  $v_m$ , the stagnation angle  $\alpha_{st}$  is determined from Fig. 8.4. With the aid of Eqs. (8.24) to (8.36), it is possible to calculate exactly the potential flow through cascades that consist of straight-line profiles. Since the turbomachinery blading has always curved camber lines, the derived conformal transformation methods must be extended to the profiles with curved camber lines. Since the compressor blade profiles have usually low deflection, their camber line can be approximated by a circular arc. In the following section, we replace the straight-line cascade by circular arc one.

### 8.1.2 Flow Through an Infinitely Thin Circular Arc Cascade

Consider a potential flow through a cascade consisting of a number of circular arcs. The potential flow condition requires that the contour of the circular arc follow the stream lines. This requirement implies that the flow direction must be identical to the contour direction  $v$  of the circular arc profiles under consideration. To simplify the problem, replace the circular arc cascade by a straight cascade, EA, with prescribed flow directions that correspond to the contour direction  $v$  as shown in Fig. 8.5.

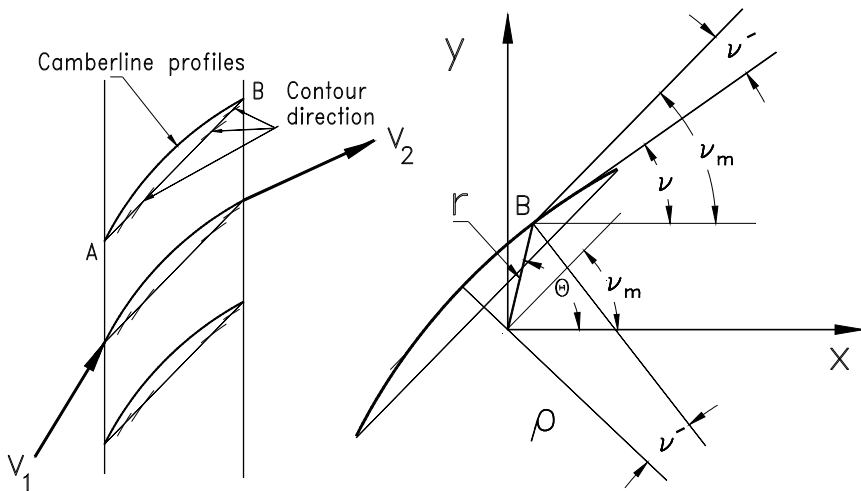


**Fig. 8.5:** Prescribed velocity directions on straight line cascade

To establish the corresponding analytical relations, we start from the conformal transformation relations derived in the previous section and extend them to an infinitely thin cascade with variable direction. For the cascade with the prescribed

direction  $\mathbf{v}$ , the complex potential, Eq (8.7) is rewritten as:

$$X(z) = zVe^{-i\mathbf{v}} \quad (8.37)$$

with  $V$  as contour velocity and  $\mathbf{v}$  its direction. Differentiating Eq. (8.37), its logarithm yields:

$$\ln \left[ \frac{dX(z)}{dz} \right] = \ln V - i\mathbf{v} \quad (8.38)$$

Since  $X(z)$  in Eq. (8.38) is an analytic function, its derivative and the logarithm of its derivative must be analytic functions also. It follows that:

$$\bar{X}(z) = \bar{\Phi} + i\bar{\Psi} \quad (8.39)$$

where

$$\bar{X}(z) = \ln \left[ \frac{dX(z)}{dz} \right], \quad \bar{\Phi} = \ln V, \quad \text{and} \quad \bar{\Psi} = -\mathbf{v} \quad (8.40)$$

Similar to Eq. (8.9), the velocity potential from Eq. (8.40) at an arbitrary point B, shown in Fig. 8.5 can be found:

$$\Phi = Vr \cos(\Theta - \mathbf{v}_m) \quad (8.41)$$

The position vector  $\mathbf{r}$  in Eq. (8.41) shown in Fig. 8.5 is obtained from

$$\mathbf{r} \approx \frac{\rho \mathbf{v}'}{\cos(\Theta - \mathbf{v}_m)} \quad \text{with} \quad \mathbf{v}' = \frac{\Phi}{V\rho}, \quad \text{and} \quad \mathbf{v}' = \mathbf{v}_m - \mathbf{v} \quad (8.42)$$

Considering Eqs. (8.39) and (8.42), we find :

$$\bar{\Psi} = \frac{\Phi}{V\rho} - \mathbf{v}_m \quad (8.43)$$

Equation (8.43) states that the stream function  $\bar{\Psi}$  which according to Eq. (8.39) exhibits the flow direction, is up to the additive constant  $\mathbf{v}_m$  proportional to the potential function  $\bar{\Phi}$ . It follows that the complex potential  $\bar{X}(z)$  is also up to an additive constant directory proportional to  $\bar{\Phi}$  resulting in:

$$\bar{X}(z) = \bar{\Phi} + i\bar{\Psi} = i \left[ \frac{\Phi}{V\rho} - \mathbf{v}_m \right] + \ln V = \frac{i\Phi}{V\rho} + (\ln V - i\mathbf{v}_m) \quad (8.44)$$

for  $V = 1$  and  $(\ln V - i\mathbf{v}_m) = \text{const.} = C$ , Eq. (8.44) is reduced to

$$\bar{X}(z) = \frac{i\Phi}{V\rho} + C \quad (8.45)$$

The new complex potential  $\bar{X}(z) \sim \Phi(z)$  is now mapped into the  $\zeta$ -plane. The potential  $\Phi$  represents in  $\zeta$ -plane vortices, which are located at  $\pm R$  and reflected on the unit circle  $\pm 1/R$ . Since on the unit circle, the contribution of the vortices outside the circle is exactly equal to the contribution of those vortices located inside the circle, the new complex potential Eq. (8.45) can be written as:

$$\bar{X}(\zeta) = \frac{i}{\rho} \frac{s}{\pi} e^{i\mathbf{v}_m} \ln \frac{\zeta + \frac{1}{R}}{\zeta - \frac{1}{R}} \quad (8.46)$$

The imaginary part of Eq. (8.46) corresponds to the imaginary part of Eq. (8.39) that contains the angle  $\mathbf{v}$ . After decomposition of Eq. (8.46), we find:

$$\text{Im} \{ \bar{X}(\zeta) \} = \frac{s}{\rho \pi} \cos \mathbf{v}_m \ln \frac{\zeta + \frac{1}{R}}{\zeta - \frac{1}{R}} \quad (8.47)$$

Along the unit circle we set in Eq. (8.47)  $\zeta = 1$  and replace the left-hand side of (8.47) by Eq. (8.45) and consider Eq. (8.42) that contains  $\mathbf{v}'$ , we find

$$\left. \begin{matrix} \mathbf{v}'_1 \\ \mathbf{v}'_2 \end{matrix} \right\} = \mp \frac{s}{\pi \rho} \cos \mathbf{v}_m \ln \frac{R^2 - 1}{R^2 + 1} \quad (8.48)$$

In Eq. (8.48) we replace  $\mathbf{v}' = \mathbf{v}_m - \mathbf{v}$  from Eq. (8.42) and arrive at

$$\left. \begin{matrix} \mathbf{v}_1 \\ \mathbf{v}_2 \end{matrix} \right\} = \mathbf{v}_m \mp \frac{1}{\pi} \left( \frac{s}{c} \frac{c}{\rho} \right) \cos \mathbf{v}_m \ln \frac{R^2 - 1}{R^2 + 1} \quad (8.49)$$



For a circular arc, the chord-curvature radius ratio  $c/\rho$  in Eq. (8.49) can be approximated by the flow deflection  $c/\rho \approx \theta$ . As a result, Eq. (8.49) is modified as

$$\left. \begin{matrix} v_1 \\ v_2 \end{matrix} \right\} = v_m \pm \frac{\theta}{\pi} \frac{s}{c} \cos v_m \ln \frac{R^2 + 1}{R^2 - 1} \quad (8.50)$$

For the second term on the right-hand side of Eq. (8.50), we now introduce the following auxiliary function:

$$\frac{\mu}{2} = \frac{1}{\pi} \frac{s}{c} \cos v_m \ln \frac{R^2 + 1}{R^2 - 1} \quad (8.51)$$

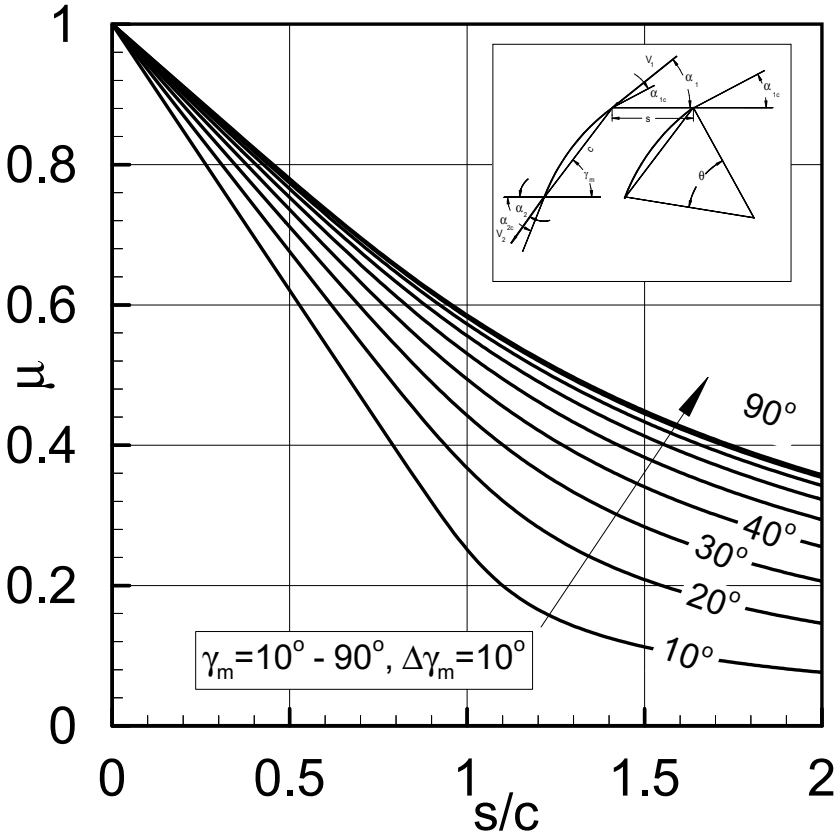


Fig. 8.6: Weinig  $\mu$ -factor as a function of  $s/c$  with  $\gamma_m$  as parameter.

For a straight cascade with the given cascade solidity ( $c/s$ ) and stagger angle  $\nu_m$ , the transformation parameter  $R$  in Eq. (8.51) is completely defined by Eqs. (8.31) and (8.36). Thus, in the auxiliary function, Eq. (8.51),  $\mu$  is uniquely determined. Figure 8.6 exhibits the values for  $\mu$  as a function of space/chord ratio with the cascade stagger angle  $\nu_m$  as a parameter. Using  $\alpha_2$ , and  $\gamma_m$  instead of  $\nu_1$ ,  $\nu_2$ , and  $\nu_m$  for a profile, the result for a compressor cascade or decelerated flow is:

$$\alpha_2 = \alpha_1 + \mu\Theta - A \left( \alpha_1 - \gamma_m + \frac{\Theta\mu}{2} \right) \quad (8.52)$$

and for accelerated flow:

$$\alpha_2 = \alpha_1 - \mu\Theta - A \left( \alpha_1 - \gamma_m - \frac{\Theta\mu}{2} \right) \quad (8.53)$$

Factor  $A$  is a correction factor that was introduced by Traupel [6] and accounts for a non-zero incidence. It depends on the cascade parameter  $s/c$  and the stagger angle  $\gamma_m$  as is shown in Fig.8.7.

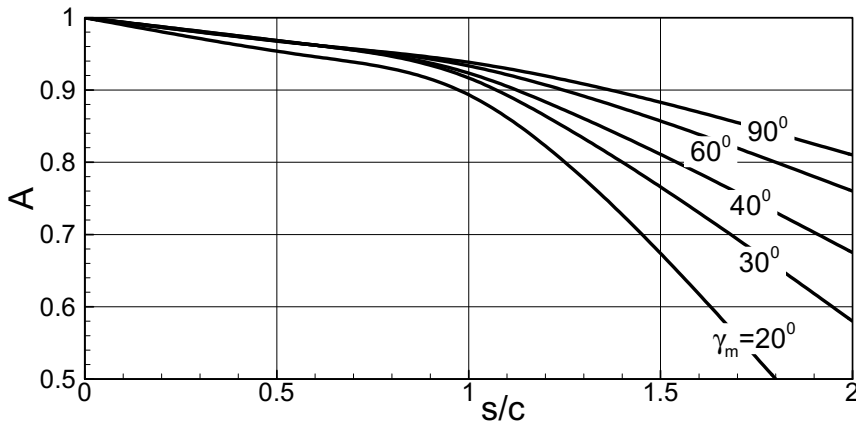


**Fig. 8.7:** Correction factor  $A$  as a function of  $s/c$  with  $\gamma_m$  as parameter.

For  $A = 1$ , we have :

$$\alpha_2 = \gamma_m \pm \frac{\mu\Theta}{2} \quad (8.54)$$

with (+) and (-) signs for compressor and turbine cascade, respectively. For an infinitely thin blade, the exit flow angle is identical to the camber angle  $\alpha_{2c}$  since  $\mu = 1$ . It is calculated from:

$$\alpha_{2c} = \gamma_m \pm \frac{\Theta}{2} \quad (8.55)$$

The deviation angle  $\delta\alpha_2$  is obtained as follows:

$$\delta\alpha_2 = \alpha_{2c} - \alpha_2 = (\gamma_m - \alpha_1)(1 - A) + \Theta \left[ \frac{1}{2} - \mu \left( 1 - \frac{A}{2} \right) \right] \quad (8.56)$$

with  $\alpha_{2c}$  as the exit camber angle, the correction factor  $A$  from Fig. 8.7, and  $\mu$  from Fig. 8.5. Once the deviation angle is calculated from Eq. (8.56), the exit flow angle  $\alpha_2$  is calculated as the difference  $\alpha_2 = \alpha_{2c} - \delta\alpha_2$ .

**Table 8.1:** Cascade parameters

$\gamma_m$	c/s	$A_\alpha$	$A_t$	$\gamma_m$	c/s	$A_\alpha$	$A_t$
30	0.5	1.096	-0.084	45	0.5	0.982	-0.076
	1.0	1.130	-0.351		1.0	0.814	-0.211
	1.5	0.849	-0.448		1.5	0.602	-0.245
	2.0	0.663	-0.443		2.0	0.451	-0.233
30	0.5	1.052	-0.17	45	0.5	0.942	-0.154
	1.0	0.948	-0.399		1.0	0.720	-0.242
	1.5	0.657	-0.368		1.5	0.506	-0.222
	2.0	0.489	-0.310		2.0	0.367	-0.182
60	0.5	0.901	-0.056	75	0.5	0.845	-0.027
	1.0	0.672	-0.115		1.0	0.605	-0.056
	1.5	0.484	-0.135		1.5	0.430	-0.060
	2.0	0.365	-0.128		2.0	0.327	-0.060
60	0.5	0.872	-0.125	75	0.5	0.830	-0.090
	1.0	0.620	-0.145		1.0	0.581	-0.088
	1.5	0.434	-0.133		0.5	0.408	-0.069
	2.0	0.321	-0.109		2.0	0.307	-0.055

A purely empirical correlation for deviation angle known as the Carter's rule is:

$$\delta\alpha_2 = \frac{\Theta}{4\sqrt{\sigma}} \quad (8.57)$$

with  $\Theta$  as the difference between the inlet and exit camber angles. Carter [9] modified the correlation for compressor cascades as  $\delta\alpha_2 = m(\Theta/\sigma)$  with  $m$  as an empirical function of stagger angle.

### 8.1.3 Thickness Correction

For a profile with finite thickness  $t$ , the stagger angle is corrected by:

$$\gamma_{mt} = \gamma_m + \Delta_\gamma \quad \text{where} \quad \Delta_\gamma = 57.3 \frac{|A_t|}{A_\alpha} \frac{t}{c} \quad (8.58)$$

with  $A_t$  and  $A_\alpha$  from Table 8.1. For compressor cascades, the range of thickness/chord ratio is  $t/c = 0.1-0.15$ .

### 8.1.4 Optimum Incidence

To obtain the optimum incidence angle  $i_{opt}$  for an arbitrary blade thickness, Johnsen and Bullock [10] introduced an empirical correlation that relates the optimum incidence angle  $i_{opt}$  to the incidence angle  $i_{10}$  of a NACA-type blade, Fig. 8.8, with the maximum thickness  $t/s=0.1$ .

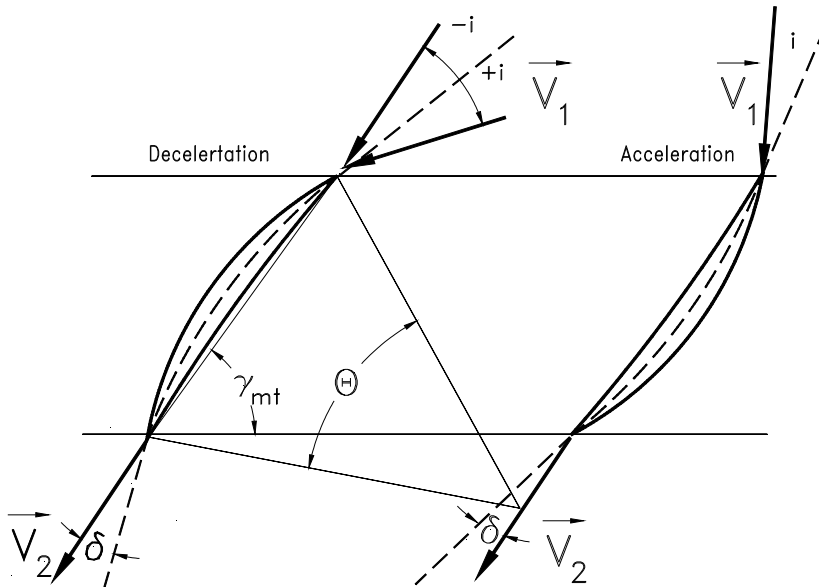
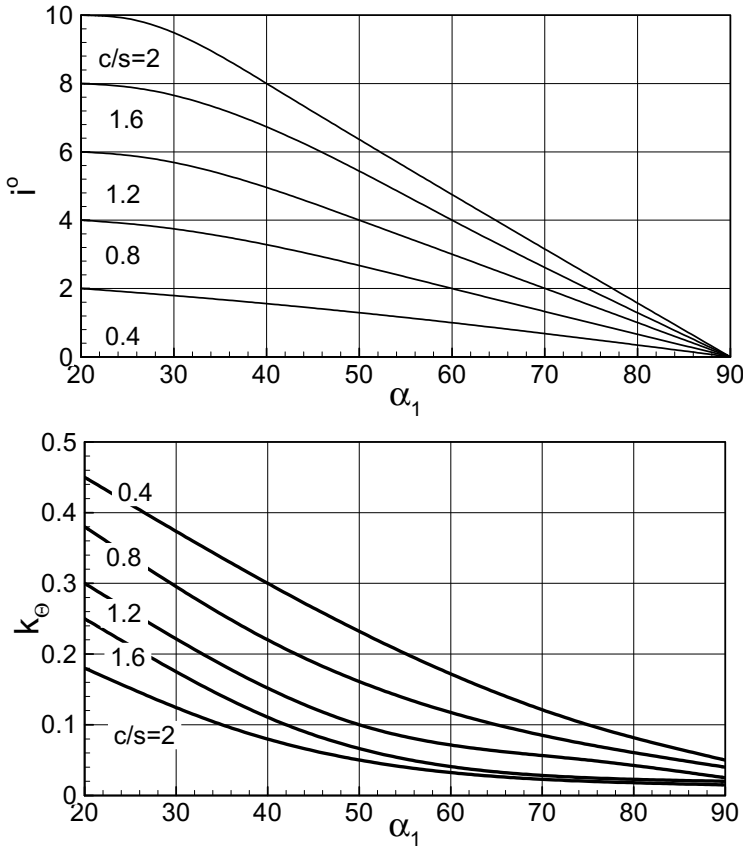


Fig. 8.8: Incidence and deviation for a DCA-profile.

Taking  $i_{10}$  from Fig. 8.9,  $i_{opt}$  can be estimated from:

$$i_{opt} = K_p K_{th} i_{10} - K_\theta \Theta \quad (8.59)$$

where  $i_{10}$  is the optimum incidence for a profile with  $t/c = 0.1$ . The coefficients  $K_p$  and  $K_{th}$  account for the profile type and profile thickness. For DCA and NACA profile types, the following empirical values  $K_p = 0.7$  for NACA profiles and  $K_p = 1.0$  for DCA profiles are suggested. Figure 8.9 shows the variation of  $i_{10}$  and  $n$  with the inlet flow angle  $\alpha_1$ . Figure 10 shows the thickness factor  $K_{th}$  as a function of thickness-chord ratio  $t/c$ .



**Fig. 8.9:** Coefficients  $i_0$  and  $K_\theta$  as functions of inlet flow angle  $\alpha_1$  with  $c/s$  as parameter

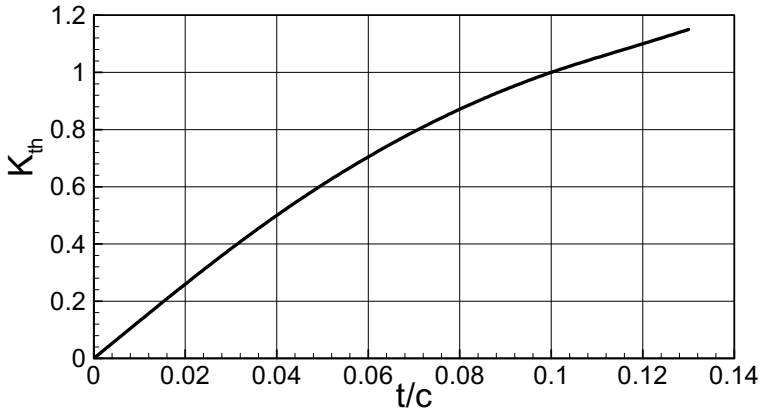


**Fig. 8.10:** Coefficients  $K_{th}$  as a function of the relative thickness

### 8.1.5 Effect of Compressibility

For intermediate to high subsonic inlet flow with  $M = 0.6 - 0.8$ , the incidence and the deviation angle are affected by the compressibility. The deviation angle of a compressible flow may be related to the deviation angle of an incompressible flow by using the following correlation proposed by Wennerström [11]:

$$\delta_{com} = K_C \delta_{inc} \quad (8.60)$$

with  $K_C$  as the compressibility function from Fig. 8.11.

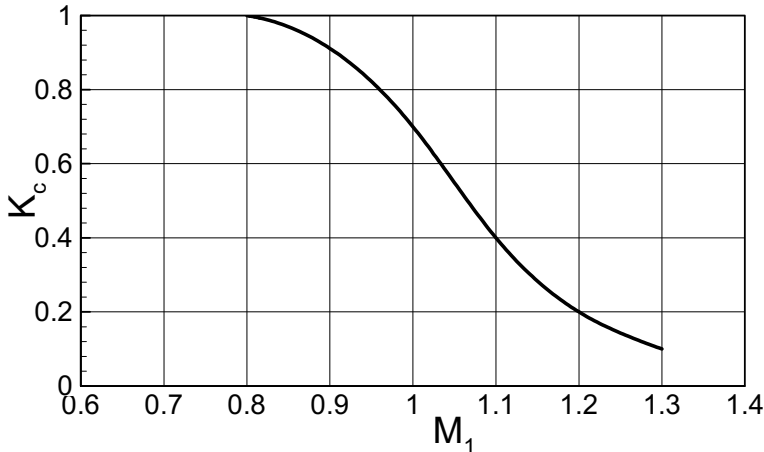


**Fig. 8.11:** Influence of mach number on deviation factor  $K_C$

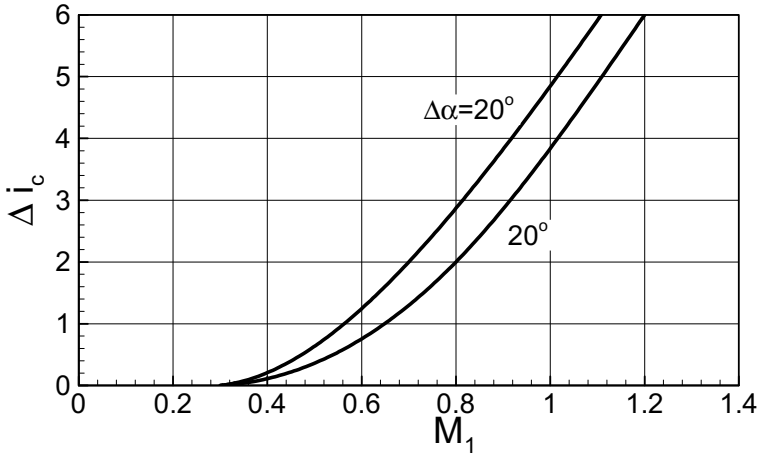


**Fig. 8.12:** Influence of Mach number on optimum incidence factors  $\Delta i_c$

The compressibility effect causes an increase in incidence angle, which can be corrected using the empirical correlation suggested in [6] and [11]:

$$i_{opt}(M_1) = i_{opt}(0) + \Delta i_c \quad (8.61)$$

with  $i_{opt}(0)$  from Eq. (8.59) and  $\Delta i_c$  from Fig. 8.12.

## 8.2 Deviation for High Flow Deflection

The accelerated flow through the turbine blades generally undergoes higher deflection than the decelerated flow through the compressor blades. The major parameter affecting the behavior of an accelerated flow with respect to the change of inlet flow direction is the Mach number, which determines the cascade flow geometry. If the flow has a low subsonic Mach number, such as in high pressure or intermediate pressure steam turbines, then the flow behavior is affected by the change of incidence if the blade profile has a small leading edge thickness. This fact enables the application of relatively thicker profiles that are less sensitive to changes of the inlet flow direction. In the rear stages of a low pressure steam turbine or a modern gas turbine, however, the inlet flow in the tip region is high subsonic that requires relatively thin profiles. Fig. 8.13 depicts the blade sections at the hub and the tip of a typical gas turbine rotor blade.

Since the flow at the hub is low subsonic with high deflection, a thick profile with a relatively large leading edge radius is applied, Fig. 8.13. Its corresponding

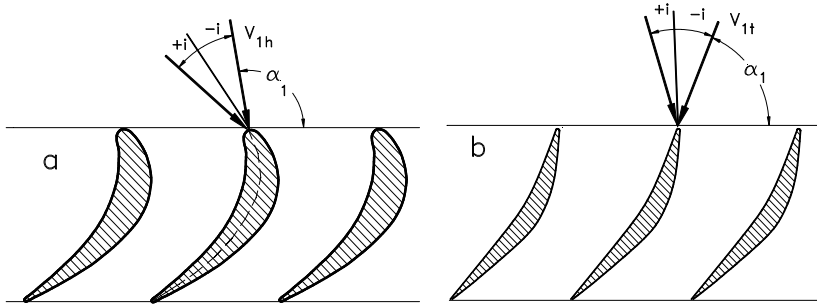


**Fig. 8.13:** Hub (a) and tip (b) section of a turbine blade

profile loss coefficient is plotted in Fig. (8.14) against the inlet flow angle.

Starting from the optimum flow angle  $\alpha_{1opt}$ , Fig. 8.14, curve (a) shows that the loss coefficient is not affected by the change of the inlet flow angle within an incidence range of  $-15^\circ < i < +15^\circ$ . Thus the change of incidence for a high deflected turbine cascade with a relatively large leading edge diameter that operates at a low subsonic mach number does not significantly increase the profile loss at moderate off-design operation conditions. The situation changes drastically towards the tip where the blade profile is subjected to a high subsonic even transonic inlet flow condition. For the profile at the tip section, Fig. 8.14b, the loss coefficient in Fig. 8.14, curve b changes considerably if the inlet flow direction departs from the design point. As seen in Fig. 8.14b, the flow has a comparatively low deflection, so that the calculation procedure derived in Chapter 8.1 can be applied. Based on the above facts for an accelerated flow, only the changes of deviation angles need to be considered.

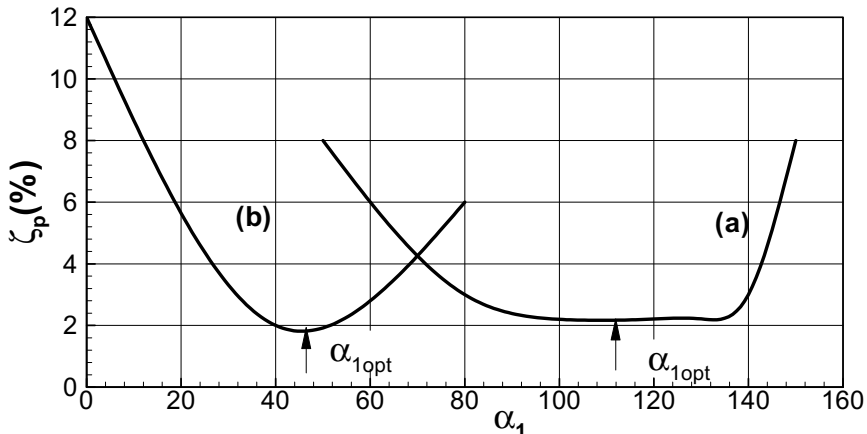


**Fig. 8.14:** Profile loss coefficient as a function of inlet flow angle for (a) hub section and (b) tip section



Since a high deflected turbine cascade cannot be approximated by a straight-line cascade, the conformal transformation method discussed in Chapter 8.1 can not be used for the calculation of exit flow angle. Based on conservation laws, Traupel [6] derived the following simple method that allows an accurate prediction of the deviation angle for cascades with high flow deflection.

### 8.2.1 Calculation of Exit Flow Angle

Consider the pressure distribution on the suction and pressure surface of a turbine

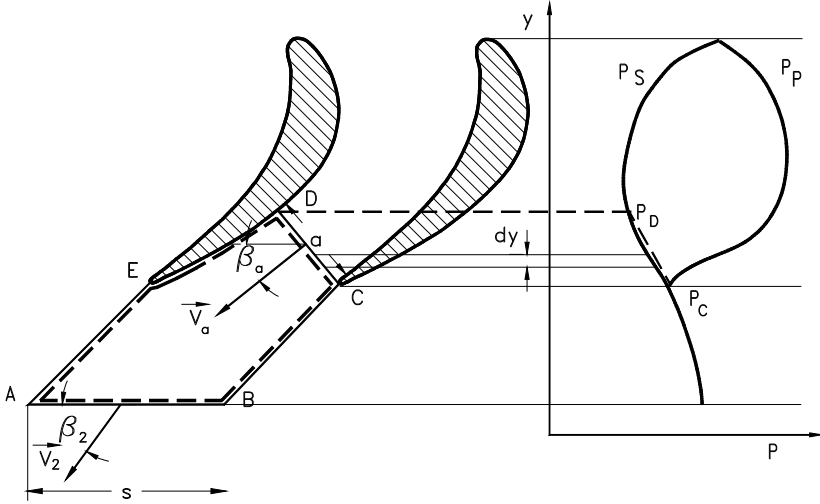


**Fig.8.15:** On the estimation of pressure momentum along the throat  $CD$  and the suction surface blade portion  $DE$  by Traupel method [6]

cascade shown in Fig. 8.15.

The pressure difference:

$$\Delta F_y = h_a \int_C^D p dy - h_2 \int_E^D p dy \approx 0 \quad (8.62)$$

With the approximation described by Eq. (8.62), the momentum balance in circumferential direction yields:

$$V_2 \cos \beta_2 = V_a \cos \beta_a \quad (8.63)$$

From the continuity equation we find:

$$sh_2\rho_2V_2\sin\beta_2 = ah_a\rho_aV_a \quad (8.64)$$

where  $h_2$  and  $h_a$  in Eq. (8.64) are the blade heights at stations 2 and  $a$ . For an isentropic flow, Eqs. (8.63) and (8.64) are written as:

$$\sin\beta_2 = \frac{ah_a\rho_a\cos\beta_2}{sh_2\rho_s\cos\beta_a} = \frac{ah_a\cos\beta_2}{sh_2\cos\beta_a} \left[ \frac{p_a}{p_2} \right]^{\frac{1}{k}} \quad (8.65)$$

Further, we assume an isentropic expansion process between  $a$  and 2 and calculate the isentropic enthalpy difference:

$$\frac{V_a^2 - V_2^2}{2} = [\Delta h_s]_a^2 = h_2 \left[ 1 - \left( \frac{p_a}{p_2} \right)^{\frac{\kappa - 1}{\kappa}} \right] - 1 \quad (8.66)$$

introducing the exit Mach number  $M_2 = V_2/c_2$  and the static enthalpy  $h_2 = c_2^2/(\kappa - 1)$  with  $c$  as the speed of sound at the exit, Eq. (8.66) becomes:

$$\frac{V_a^2}{V_2^2} = \frac{2}{M_2^2(\kappa - 1)} \left[ 1 - \left( \frac{p_a}{p_2} \right)^{\frac{\kappa - 1}{\kappa}} \right] - 1 \quad (8.67)$$

Introducing Eq. (8.63) into (8.67):

$$\frac{\cos^2\beta_2}{\cos^2\beta_a} = \frac{2}{M_2^2(\kappa - 1)} \left[ 1 - \left( \frac{p_a}{p_2} \right)^{\frac{\kappa - 1}{\kappa}} \right] - 1 \quad (8.68)$$

The solution of Eq. (8.68) for pressure ratio is:

$$\frac{p_a}{p_2} = \left[ 1 - M_2^2 \left( \frac{\kappa - 1}{\kappa} \right) \left( \frac{\cos^2\beta_2}{\cos^2\beta_a} - 1 \right) \right]^{\frac{\kappa}{\kappa - 1}} \quad (8.69)$$

Incorporating Eq. (8.69) into (8.65):

$$\operatorname{tg} \beta_2 = \frac{a}{s} \frac{h_a}{h_2} \frac{1}{\cos \beta_a} \left\{ 1 - M_2^2 \left( \frac{\kappa - 1}{2} \right) \left[ \frac{\cos^2 \beta_2}{\cos^2 \beta_a} - 1 \right] \right\}^{\frac{1}{\kappa - 1}} \quad (8.70)$$

For a Mach number approaching unity and a constant blade height  $h_2 = h_a$ , the exit flow angle  $\beta_2$  approaches  $\beta_a$ , which leads to

$$\operatorname{tg} \beta_2 = \frac{a}{s} \frac{1}{\cos \beta_2} \quad (8.71)$$

$$\sin \beta_2 = \frac{a}{s}$$

For incompressible flow,  $\delta_2$  can be obtained from:

$$\sin \beta_2 = \frac{a}{s} \frac{\cos \beta_2}{\cos \beta_a} \quad \text{or:} \quad \operatorname{tg} \beta_2 = \frac{a}{s} \frac{1}{\cos \beta_a} \quad (8.72)$$

where the exit flow angle  $\beta_2$  is:

$$\beta_2 = \arctg \left[ \frac{a}{s} \frac{1}{\cos \beta_a} \right] \quad (8.73)$$

The deviation is obtained from the difference

$$\delta_2 = \beta_{2c} - \beta_2 \quad (8.74)$$

with  $\beta_{2c}$  as the camber angle at the trailing edge.

## References

- 1 Gostelow, J.P., 1984, "Cascade Aerodynamics," Pergamon Press.
- 2 Scholz, N., 1965, "Aerodynamik der Schaufelgitter," Brwon-Verlag, Karlsruhe.
- 3 Betz, A., 1948, "Konforme Abbildung," Berlin, Göttingen, Springer-Verlag.
- 4 Weinig, F., 1935, "Die Strömung um die Schaufeln von Turbomaschinen," Leipzig, Barth-Verlag.
- 5 Eckert, B., Schnell, E., 1961, "Axial-und Radialkompressoren," 2. Auflage, Berlin, Göttingen, Heidelberg, Springer-Verlag.

- 6 Traupel, W., "Thermische Turbomaschinen," Bd.I, 1977, Springer-Verlag Berlin.
- 7 Lakschminarayana, B., 1995, "Fluid Dynamics and Heat Transfer of Turbomachinery," John Wiley and Sons, Inc.
- 8 Cumpsty, N. A., 1989, "Compressor Aerodynamics," Longman Group, New York.
- 9 Carter, A.D. , 1950, "The Low Speed Performance of Related Airfoils in Cascades, Aeronautical Research Council.
- 10 Johnsen, I. A, Bullock, R., O., 1965: "Aerodynamic Design of Axial Flow Compressors, "NASA SP 36.
- 11 Wennerström, A., 1965, "Simplified design Theory of highly loaded axial Compressor Rotors and Experimental Study of two Transonic Examples," Diss. ETH-Zürich.

## 9 Blade Design

Flow deflection in turbomachines is established by stator and rotor blades with prescribed geometry that includes inlet and exit *camber angles*, *stagger angle*, *camberline*, and *thickness distribution*. The blade geometry is adjusted to the stage velocity diagram which is designed for specific turbine or compressor flow applications. Simple blade design methods are available in the open literature (see References). More sophisticated and high efficiency blade designs developed by engine manufacturers are generally not available to the public. An earlier theoretical approach by Joukowsky [1] uses the method of conformal transformation to obtain cambered profiles that can generate lift force. The mathematical limitations of the conformal transformation do not allow modifications of a cambered profile to produce the desired pressure distribution required by a turbine or a compressor blade design. In the following, a simple method is presented that is equally applicable for designing compressor and turbine blades. The method is based on (a) constructing the blade *camberline* and (b) superimposing a predefined *base profile* on the camberline. With regard to generating a base profile, the conformal transformation can be used to produce useful profiles for superposition purposes. A brief description of the Joukowsky transformation explains the methodology of symmetric and a-symmetric (Cambered) profiles. The transformation uses the complex analysis which is a powerful tool to deal with the potential theory in general and the potential flow in particular. It is found in almost every fluid mechanics textbook that has a chapter dealing with potential flow. While they all share the same underlying mathematics, the style of describing the subject to engineering students differ. A very compact and precise description of this subject matter is found in an excellent textbook by Spurk [2].

### 9.1 Conformal Transformation, Basics

Before treating the Joukowsky transformation, a brief description of the method is given below. We consider the mapping of a circular cylinder from the  $z$ -plane onto the  $\zeta$ -plane, Fig.9.1. Using a mapping function, the region outside the cylinder in the  $z$ -plane is mapped onto the region outside another cylinder in the  $\zeta$ -plane. Let  $P$  and  $Q$  be the corresponding points in the  $z$ - and  $\zeta$ -planes respectively. The potential at the point  $P$  is

$$F(z) = \Phi + i\Psi \quad (9.1)$$

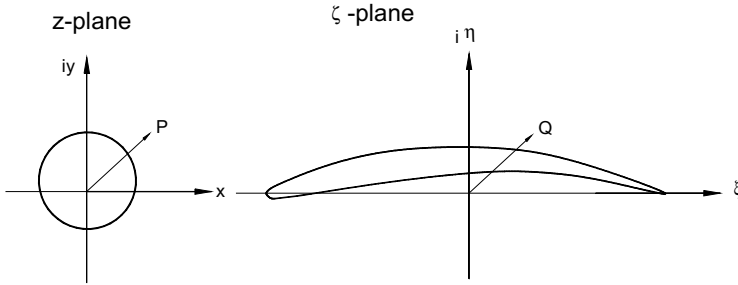


**Fig. 9.1:** Conformal transformation of a circular cylinder onto an airfoil.

The point  $Q$  has the same potential, and we obtain it by insertion of the mapping function

$$F(z) = F(z(\zeta)) = F(\zeta) \quad (9.2)$$

Taking the first derivative of Eq. (9.2) with respect to  $\zeta$ , we obtain the complex conjugate velocity  $\bar{V}_\zeta$  in the  $\zeta$  plane from

$$\bar{V}_\zeta(\zeta) = \frac{dF}{d\zeta}. \quad (9.3)$$

Considering  $z$  to be a parameter, we calculate the value of the potential at the point  $z$ . Using the transformation function  $\zeta = f(z)$ , we determine the value of  $\zeta$  which corresponds to  $z$ . At this point  $\zeta$ , the potential then has the same value as at the point  $z$ . To determine the velocity in the  $\zeta$  plane, we form

$$\frac{dF}{d\zeta} = \frac{dF}{dz} \frac{dz}{d\zeta} = \frac{dF}{dz} \left( \frac{d\zeta}{dz} \right)^{-1} \quad (9.4)$$

after introducing Eq. (9.3) into (9.4) and considering  $\bar{V}_z(z) = dF/dz$ , Eq. (9.4) is rearranged as

$$\bar{V}_\zeta(\zeta) = \bar{V}_z(z) \left( \frac{d\zeta}{dz} \right)^{-1} \quad (9.5)$$

Equation (9.5) expresses the relationship between the velocity in  $\zeta$ -plane and the one in  $z$ -plane. Thus, to compute the velocity at a point in the  $\zeta$ - plane, we divide the velocity at the corresponding point in the  $z$ -plane by  $d\zeta/dz$ . The derivative  $dF/d\zeta$

exists at all points where  $d\zeta/dz \neq 0$ . At singular points with  $d\zeta/dz = 0$ , the complex conjugate velocity in the  $\zeta$  plane  $\overline{V}_\zeta(\zeta) = dF/d\zeta$  becomes infinite if it is not equal to zero at the corresponding point in the  $z$ -plane.

### 9.1.1 Joukowski Transformation

The conformal transformation method introduced by Joukowski allows mapping an unknown flow past a cylindrical airfoil to a known flow past a circular cylinder. Using the method of conformal transformation, we can obtain the direct solution of the flow past a cylinder of an arbitrary cross section. Although numerical methods of solution of the direct problem have now superseded the method of conformal mapping, it has still retained its fundamental importance. In what follows, we shall examine several flow cases using the *Joukowski* transformation function:

$$\zeta = f(z) = z + \frac{a^2}{z}, \text{ with } z = re^{i\theta}, \quad \zeta = \xi + i\eta \quad (9.6)$$

### 9.1.2 Circle-Flat Plate Transformation

Decomposing Eq. (9.6) into its real and imaginary parts, we obtain:

$$\xi = \left(r + \frac{a^2}{r}\right)\cos\theta, \quad \eta = \left(r - \frac{a^2}{r}\right)\sin\theta \quad (9.7)$$

The function  $f(z)$  maps a circle with radius  $r = a$  in the  $z$ -plane onto a “slit” in the  $\zeta$  plane. Equation (9.7) delivers the coordinates:

$$\xi = 2a \cos \theta, \quad \eta = 0 \quad (9.8)$$

with  $\xi$  as a real independent variable in the  $\zeta$ -plane. As the point  $P$  with the angle  $\theta$  moves in  $z$ -plane from  $0$  to  $2\pi$ , Fig. 9.2, its image  $p'$  moves from  $+2a$  to  $-2a$  in the  $\zeta$ -plane with the complex potential  $F(z)$ . The potential  $F(z)$  is:

$$F(z) = V_\infty \left( z + \frac{R^2}{z} \right) \quad (9.9)$$

Setting  $R = a$ , the Joukowski transformation function directly provides the

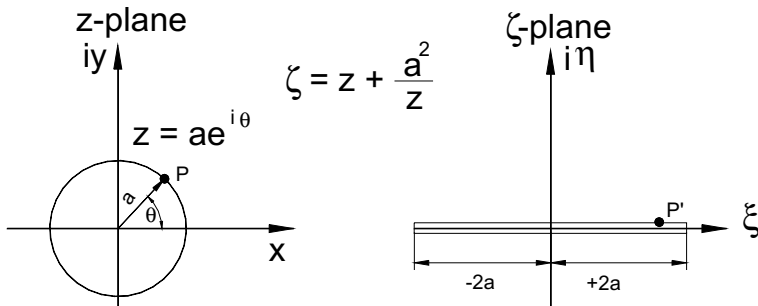


**Fig. 9.2** Transformation of a circle onto a slit (straight line section).

potential in the  $\zeta$ -plane as

$$F(\zeta) = V_{\infty} \zeta \quad (9.10)$$

### 9.1.3 Circle-Ellipse Transformation

For this transformation, the circle center is still at the origin of the  $z$ -plane. Now, if we map a circle with radius  $b$  which is smaller or larger than the mapping constant  $a$ , we obtain an ellipse. Replacing  $r$  by  $b$  ( $b \neq a$ ), Eq. (9.7) becomes

$$\xi = \left(b + \frac{a^2}{b}\right) \cos \Theta, \quad \eta = \left(b - \frac{a^2}{b}\right) \sin \Theta \quad (9.11)$$

Eliminating  $\Theta$  from Eq. (9.11), we find:

$$\cos^2 \Theta = \left( \frac{\xi}{b + a^2/b} \right)^2, \quad \sin^2 \Theta = \left( \frac{\eta}{b - a^2/b} \right)^2 \quad (9.12)$$

and with  $\sin^2 \Theta + \cos^2 \Theta = 1$ , we obtain the equation of ellipse as:

$$\left( \frac{\xi}{b + a^2/b} \right)^2 + \left( \frac{\eta}{b - a^2/b} \right)^2 = 1 \quad (9.13)$$

Equation (9.13) describes an ellipse, plotted in Fig. 9.3, with the major and minor axes which are given as the denominators in Eq. (9.13). In Fig. 9.3,  $b > a$ , however any ellipse may be constructed by varying the ratio  $b/a$ .



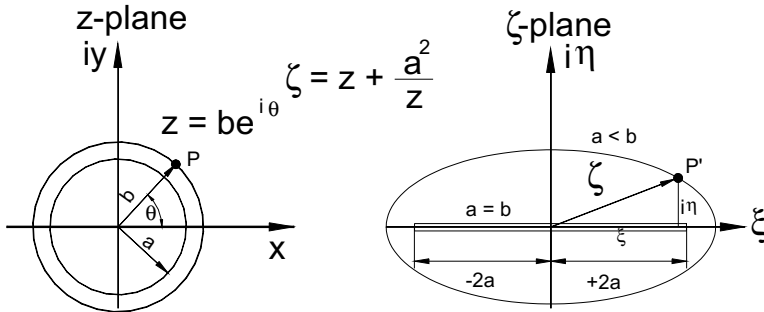


Fig. 9.3 Conformal transformation of a circle to an ellipse.

#### 9.1.4 Circle-Symmetric Airfoil Transformation

A set of symmetrical airfoils can be constructed by shifting the center of the circle with the radius  $b$  by  $\Delta x$  along the  $x$ -axis on the  $z$ -plane as shown in Fig. 9.4.

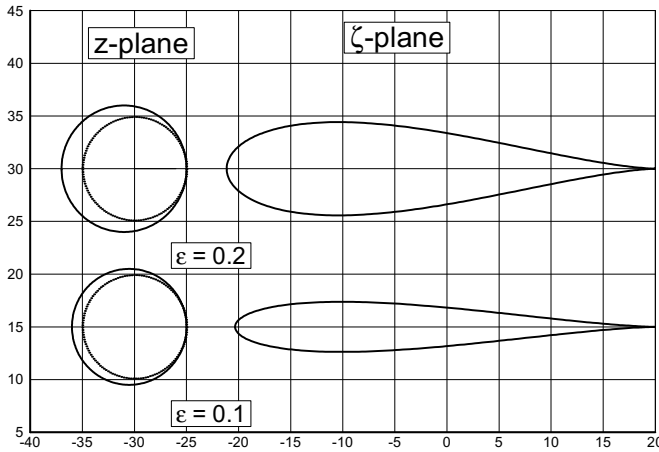


Fig. 9.4 Transformation of a circle into a symmetric airfoil.

An eccentricity  $\epsilon = e/a$  with  $e = \Delta x$  is defined that determines the thickness of the airfoil. The radius of the circle is determined by:

$$b = (1 + \epsilon)a \quad (9.14)$$

Thus, the magnitude of the eccentricity defines the slenderness of the airfoil. For  $\epsilon = 0$ , the circle is mapped into a slit, as seen in Fig. 9.3. Due to zero flow deflection, the symmetrical airfoils at zero-angle of attack do not generate circulation and,

therefore, no lift. Similar profiles can be used as *base profiles* in compressor and turbine blade design to be superimposed on the *camberline*. Since these profiles have a sharp trailing edge (zero thickness), they cannot be used in practical applications because of stress concentration at the trailing edge. This can be avoided by placing a certain radius at the trailing edge as shown in Fig. 9.5.



**Fig. 9.5:** Symmetric profile constructed by conformal transformation, (a) with sharp trailing edge, (b) same profile with trailing edge radius.

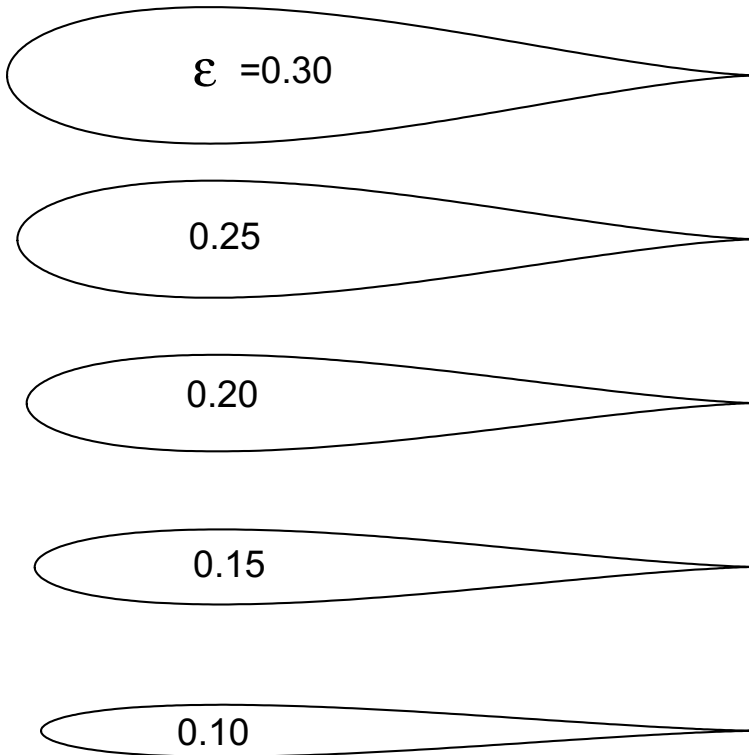


**Fig. 9.6:** Example of a systematic generation of base profiles varying the eccentricity  $\epsilon$ .

Figure 9.6 exhibits a systematic generation of base profiles by varying the

eccentricity  $\varepsilon$ . Turbine blades that are exposed to a frequent off-design operation condition have generally a larger leading edge radius than those that operate almost in design point. In this case,  $\varepsilon > 0.15$  may be chosen. A FORTRAN program is presented in the Appendix that calculates the symmetric profiles shown in Fig. 9.6

### 9.1.5 Circle-Cambered Airfoil Transformation

To generate airfoils that produce circulation and, therefore, lift, the profile must be cambered. In this case, the circle with the radius  $b$  is displaced horizontally as well as vertically relative to the origin of the circle with the radius  $a$ . To generate a systematic set of profiles, we need to know how the circle  $b$  is to be displaced relative to the origin of the circle  $a$ . Only three parameters define the shape of the cambered profiles. These are: (a) Eccentricity  $e$ , angle  $\alpha$ , and the intersection angle  $\beta$ . With these three parameters, the displacements in  $x$ - and  $y$ -directions as well as the radius of the circle  $b$  to be mapped onto the  $\zeta$ -plane are calculated using the following relations from Fig.9.7.

$$a = \overline{OB}, \quad b = \overline{AB} = a \cos \gamma + e \cos(\beta/2)$$

$$\gamma = \arcsin\left(\frac{e}{a} \sin \beta/2\right) = \arcsin(\varepsilon \sin \beta/2)$$

$$b/a = \cos \gamma + \varepsilon \cos(\beta/2)$$

$$\overline{OC} = a \sin \gamma = e \sin(\beta/2)$$

$$\varepsilon = e/a$$

$$\Delta x = \overline{OD} = e \cos(\alpha + \beta/2)$$

$$\Delta y = \overline{DA} = e \sin(\alpha + \beta/2)$$

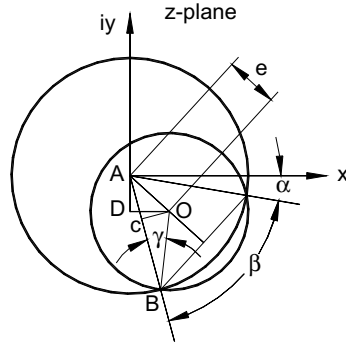


**Fig. 9.7** Construction of cambered airfoils.

Figure 9.7 shows a family of profiles generated by varying the above parameters. Starting with a small eccentricity of  $\varepsilon = 10\%$ , we set  $\beta = 0^\circ$  and vary the angle  $\alpha$  from  $-10^\circ$  to  $-30^\circ$ . The resulting configuration indicates that the two circles have tangents at the angle  $\alpha$ . At this small eccentricity, slender profiles are generated that resemble low subsonic compressor blade profiles. Increasing the magnitude of  $\alpha$  results in an increase of the profile cambers. If the angle  $\beta$  is different from zero, then the two circles intersect each other, as shown in Fig.9.7. This is also shown in Fig. 9.8 with  $\varepsilon = 0.2$ ,  $\beta = 60^\circ$  and  $\alpha$  varied from  $-10^\circ$  to  $-30^\circ$ .

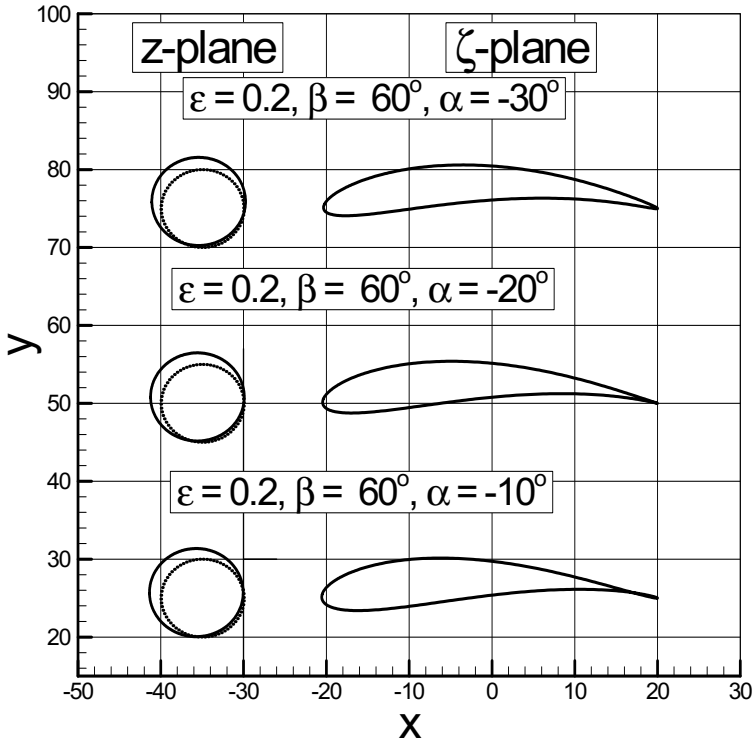


Fig. 9.8: Cambered profiles constructed by conformal transformation.

For  $\epsilon > 0.2$ , the resulting profiles resemble turbine profiles, however, they cannot be used in practice because the resulting cascade channel does not yield a continuous acceleration.

## 9.2 Compressor Blade Design

The major parameter for determining the shape of a compressor blade is the Mach number. For low-subsonic to intermediate-subsonic Mach range ( $M_1 = 0.1$  to  $0.6$ ), NACA-65 profiles [3] give a relatively high pressure at a reasonably high efficiency. For intermediate Mach numbers, *double circular arc* (DCA) and *multi-circular arc* (MCA) profiles may be used. Surface pressure measurements by Cumpsty [4] show that at an inlet Mach number of  $M_1 = 0.6$  at the design incidence, the NACA-65 and DCA profiles have comparable pressure distributions. However, due to a sharp leading edge, the DCA-profiles may have higher profile losses than the NACA-65 series when operating at off-design conditions. For high subsonic Mach range ( $M_1 > 0.6$ ), DCA or MCA profiles are used. Controlled diffusion profiles CD are used

for transonic Mach ranges in order to reduce the shock losses. Supersonic compressors require s-shaped blades with sharp leading edges to avoid the shock detachment.

### 9.2.1 Low Subsonic Compressor Blade Design

In Chapter 5.2, it was shown that for an inviscid flow, the lift force can be expressed as:

$$\mathbf{F} = \rho \mathbf{V}_\infty \times \mathbf{\Gamma}, \quad \text{where} \quad \mathbf{\Gamma} = \oint \mathbf{V} \cdot d\mathbf{c} \quad (9.15)$$

This relation shows that the lift force can exist if there is circulation around the airfoil. As we saw, the circulation was directly related to the flow deflection from the cascade inlet to the exit, which is shown in Fig. 9.9.

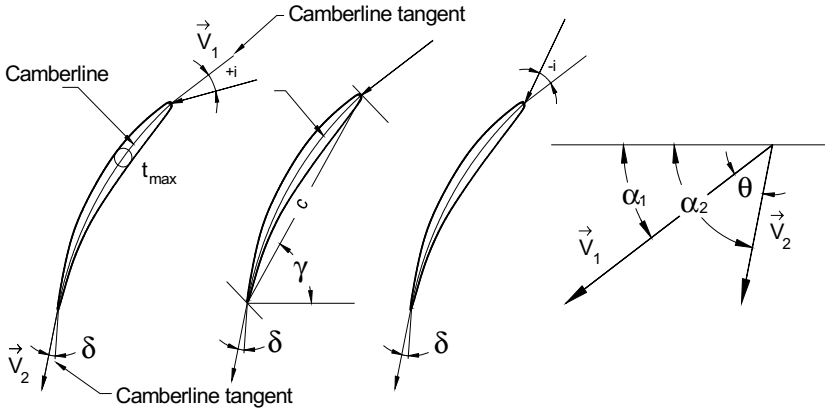


**Fig. 9.9:** Compressor cascade nomenclature,  $c$  = chord length,  $t_{\max}$  = maximum thickness,  $\gamma$  = cascade stagger angle,  $\Theta$  = cascade flow deflection angle,  $i$  = flow incidence angle,  $\delta$  = flow deviation angle. For  $i > 0$  the actual deflection  $\Theta > \Theta_{\text{design}}$ .

For an incidence free ( $i = 0$ ) flow, the velocity vector at the inlet is tangent to the camberline. Likewise, for a deviation free ( $\delta = 0$ ) exit flow, the velocity vector is tangent to the camberline at the cascade exit, as seen in Fig. 9.9. Once the compressor stage velocity diagram is constructed, the deflection angle  $\theta$  and, thus, the circulation  $\Gamma$  is known. The problem now is to find the corresponding blade profile for a given circulation. For a compressor blade which generally has a small flow deflection, the circulation  $\Gamma$  can be thought of as the sum of infinitesimal vortices with the intensity  $d\Gamma$ . If we distribute the vortices along the blade chord and consider the specific circulation at an arbitrary point  $x$  to be:

$$\gamma(x) = \frac{d\Gamma}{dx} \quad (9.16)$$

the integrating Eq. (9.16) yields:

$$\Gamma = \int_0^c \gamma(x) dx \quad (9.17)$$

The vortex  $d\Gamma$ , located at the point  $\zeta$ , induces a velocity at an arbitrary point  $x$ , that can be calculated from Bio-Sawart's law. Figure 9.10 shows the distribution of discrete vortices along the chord (left) and their induced velocity (right).

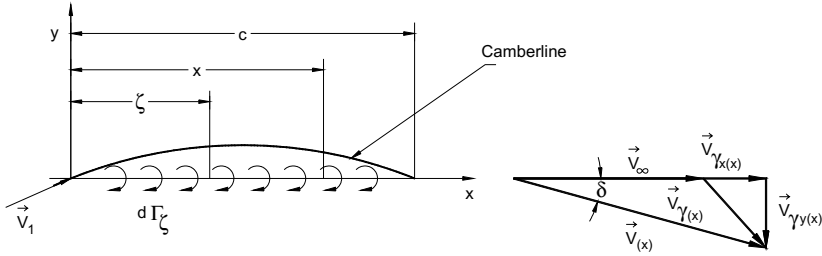


**Fig. 9.10:** Vortex distribution along the blade chord and induced velocity.

An induced velocity in  $y$ -direction is:

$$dV_{\gamma y}(x) = - \frac{d\Gamma_{\zeta}}{2\pi(x - \zeta)} \quad (9.18)$$

and in the  $x$ -direction:

$$V_{\gamma x}(x) = \pm \frac{\gamma(x)}{2}, \quad (- \text{ sign for } x > \zeta) \quad (9.19)$$

The integration of Eq. (9.19) gives the total velocity induced at  $x$  by the vortices distributed at  $\zeta$ :

$$V_{\gamma y}(x) = - \frac{1}{2\pi} \int_0^c \frac{\gamma(\zeta) d\zeta}{(x - \zeta)} \quad (9.20)$$

The induced velocity for the incidence angle  $i = \theta$  is shown in Fig. 9.9. Superimposing the induced velocity  $V_{\gamma}(x)$  on  $V_I$ , we get the contour velocity  $V(x)$  around

the profile. Since the direction of this velocity must be identical with the slope of the camberline,

$$\tan \delta = \frac{dy(x)}{dx} = \frac{V_{\gamma y}(x)}{V_1 + V_{\gamma x}(x)} \quad (9.21)$$

and since the induced velocity component  $V_{\gamma x}(x) \ll V_1$ , it follows that

$$\frac{dy(x)}{dx} = \frac{V_{\gamma y}(x)}{V_1} \quad (9.22)$$

Introducing Eq. (9.18) into (9.22):

$$\frac{dy(x)}{dx} = - \frac{1}{2\pi V_1} \int_0^c \frac{\gamma(\zeta) d\zeta}{x - \zeta} \text{ for } i = 0 \quad (9.23)$$

and for considering a small incidence angle  $i$ , we find:

$$i + \frac{dy(x)}{dx} = - \frac{1}{2\pi V_1} \int_0^c \frac{\gamma(\zeta) d\zeta}{x - \zeta} \quad (9.24)$$

Now, we introduce the lift coefficient for the camberline and label it with the superscript \*:

$$C_L^* = \frac{F^*}{\frac{\rho}{2} V_1^2 c} = \frac{\rho \Gamma V_1}{\frac{\rho}{2} V_1^2} = \frac{2\Gamma}{V_1 c} \quad (9.25)$$

We assume that the lift force induced by a discrete vortex is linearly proportional to the blade lift. This uniform lift distribution assumption results in:

$$\frac{d\Gamma_\zeta}{d\zeta} = \frac{\Gamma}{c} \quad (9.26)$$

and so:

$$\frac{d\Gamma_\zeta}{d\zeta} = \gamma(\zeta) = \frac{C_L^*}{2} V_1 \quad (9.27)$$

Inserting Eq. (9.27) into (9.24) and setting for  $i = 0$ :

$$\frac{dy(x)}{dx} = \frac{C_L^*}{4\pi} \int_0^c \frac{d\zeta}{x - \zeta} \quad (9.28)$$

The first integration of Eq. (9.28) yields:

$$\frac{dy(x)}{dx} = \frac{C_L^*}{4\pi} \ln \left( \frac{1 - \frac{x}{c}}{\frac{x}{c}} \right) \quad (9.29)$$

The second integration determines the coordinate for the camberline:

$$\frac{y(x)}{c} = -\frac{C_L^*}{4\pi} \left[ \left( 1 - \frac{x}{c} \right) \ln \left( 1 - \frac{x}{c} \right) + \frac{x}{c} \ln \left( \frac{x}{c} \right) \right] \quad (9.30)$$

This is the equation of the camberline for the NACA-compressor blades. The maximum camber is at  $x/c = 0.5$

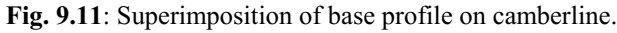
$$\frac{y_{\max}}{c} = \frac{C_L^*}{4\pi} \ln 2 \quad (9.31)$$

**Superimposing the Base Profile:** With Eq. (9.30), we are able to design the compressor blade camberline at a particular position where the lift coefficient is already calculated. To construct the profile, we need a base profile to superimpose on the camber. The base profile is given for NACA-65 series. For a profile with chord  $c$  the camberline coordinates are:

$$\begin{aligned} x_c &= \frac{x}{c} c \\ y_c &= \frac{y}{c} c \end{aligned} \quad (9.32)$$

where the subscript  $c$  represents the camberline. The next step is to superimpose the base profile either from Section 9.1.4 or from Table 9.1 on the camber.




$$\frac{t}{c} = \left( \frac{t}{c} \right)_{ref} \frac{\left( \frac{t}{c} \right)_{\max}}{\left( \frac{t}{c} \right)_{\max ref}} \quad (9.33)$$
$$\left. \begin{aligned} x &= x_c - \left(\frac{t}{2}\right) \sin \vartheta \\ y &= y_c + \left(\frac{t}{2}\right) \cos \vartheta \end{aligned} \right\} \quad (9.34)$$

and for the pressure side, where  $\bar{c}_p = t/2$ :

$$\left. \begin{aligned} x &= x_c + \left( \frac{t}{2} \right) \sin \vartheta \\ y &= y_c - \left( \frac{t}{2} \right) \cos \vartheta \end{aligned} \right\} \quad (9.35)$$

The angle  $\vartheta$  is calculated from Eq. (9.29):

$$\frac{dy(x)}{dx} = \tan \vartheta = \frac{C_L^*}{4\pi} \ln \left( \frac{1 - \frac{x_c}{c}}{\frac{x_c}{c}} \right) \quad (9.36)$$

In addition to the base profiles listed in Section 9.1.4, a NACA-base profile for subsonic compressors and a base profile for subsonic turbines used in industrial practice as well as in research are listed in Table 1 and 2 with the nomenclature shown in Fig. 9.12. The maximum thickness for compressors is around  $t_{\max}/c = 10\%$ , whereas for turbines it may vary from 15% to 18%.

**Table 9.1:** Thickness distribution of a NACA-65 compressor base profile.

$\xi$	0.00	0.50	0.75	1.25	2.5	5.0	7.5	10	15
$f(\xi)$	0.00	0.772	0.932	1.690	1.574	2.177	2.641	3.040	3.666
$\xi$	20	25	30	35	40	45	50	55	60
$f(\xi)$	4.143	4.503	4.760	4.924	4.996	4.963	4.812	4.530	4.146
$\xi$	65	70	75	80	85	90	95	100	
$f(\xi)$	3.682	3.156	2.584	1.987	1.385	0.810	0.306	0	

**Table 9.2:** Thickness distribution of a turbine base profile.

$\xi$	0.00	5.0	10.00	15.00	20.00	25.00	30.00	35.00	40.00
$f(\xi)$	0.00	8.40	11.11	13.00	14.40	14.90	15.00	14.40	13.50
$\xi$	45.00	50.00	55.00	60.00	65.00	70.00	75.00	85.00	90.00
$f(\xi)$	12.40	11.20	10.10	8.90	7.70	6.70	5.70	3.80	3.00
$\xi$	95.00	100.0	$r_L/c = 0.030$ $r_T/c = 0.009$		$t_{\max}/c = 0.15$				
$f(\xi)$	2.10	0.00							

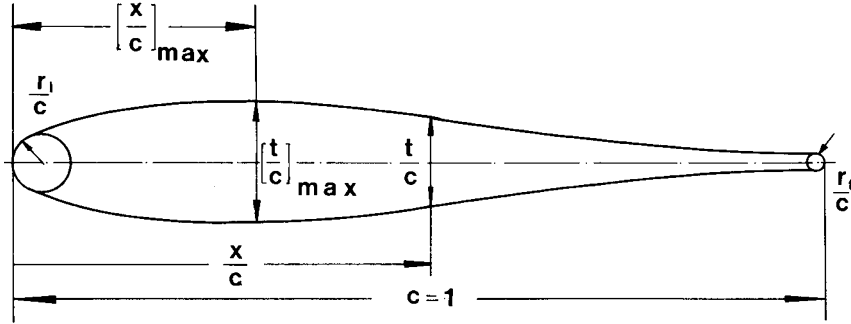


**Fig. 9.12:** Schematic of a base profile to be superimposed on camberline,  $\xi = x/c$ ,  $t/c = f(\xi)$ .

It should be noted that the base profiles with lower eccentricity shown in Fig. 9.6 may also be used for subsonic compressor design.

#### **Summary, simple compressor blade design steps:**

1. Calculate  $C_L^*$  from velocity diagram using Eq. (9.25)
2. To find  $(y/c)$ , calculate  $y(x)/c$  from Eq. (9.30)
3. Calculate  $\bar{V}$  from Eqs. (9.25) and (9.36).
4. If  $(t/c)_{\max}$  is different from  $(t/c)_{\max \text{ ref.}}$ , then introduce new  $(t/c)_{\max}$  into Eq. (9.33) and use the data for the reference base profile.
5. With the actual  $t$ , calculate the suction surface coordinates from Eq. (9.34) and the pressure surface coordinates from Eq. (9.35)
6. Smooth the profile and make sure, there is no discontinuity and no waviness on the surface. This is done by taking the first derivative of the surface function. Any CAD system has the capability to do this task.

The above procedure is equally valid for the turbine profile design also.

### **9.2.2 Compressors Blades for High Subsonic Mach Number**

Double circular arc (DCA) and multi-circular arc (MCA) profiles are used particularly for compressors operating at intermediate and high subsonic inlet Mach numbers ( $M > 0.6$ ). Considering a particular cross section through a compressor cascade as shown in Fig. 9.13, the suction and pressure surfaces of a DCA-profile consist of two circular arcs. The suction and pressure surfaces of MCA-profiles however, may consist of several circular arcs. The arc must have the same slopes at the joints to avoid surface discontinuities. This can be assured by plotting the first surface derivative.

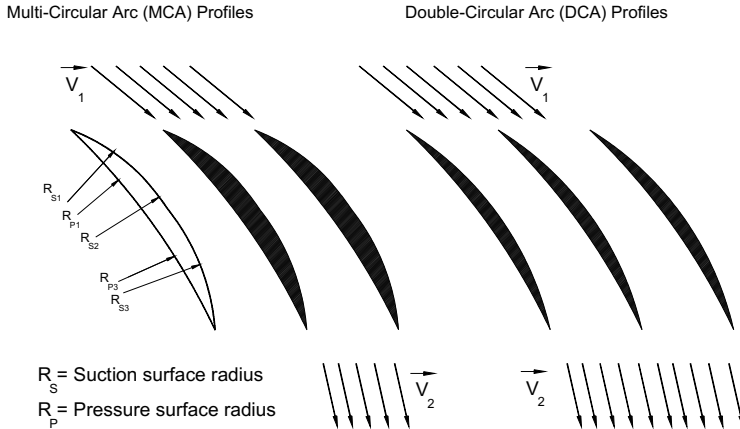


**Fig. 9.13:** DCA and MCA Profiles for high subsonic Mach number applications.

The following criteria dictate the selection of a particular profile for high subsonic compression application:

- 1) The inlet Mach number
- 2) Incidence tolerance with regard to the profile losses
- 3) Pressure distribution determining the lift coefficient
- 4) Drag forces determining the blade profile loss

(1) and (4) can be combined to arrive at the optimum lift/drag ratio, which we have treated in Chapter 5.

### 9.2.3 Transonic, Supersonic Compressor Blades

For compressors operating at transonic and supersonic Mach numbers, blade design efforts are concentrated at keeping the shock losses at a minimum level. In doing so, it is important to accurately determine the shock angle. This topic is extensively discussed in Chapter 15. Figure 9.14 shows a supersonic compressor cascade with an inlet Mach number  $M_\infty > 1$ . The incoming supersonic flow impinges on the sharp leading edge and forms a weak oblique shock, followed by an expansion fan. Passing through the shock front, the Mach number, although smaller, remains supersonic. Expansion waves are formed along the suction surface (convex side) of the blade from the leading edge  $L$  to the point  $e$  where the subsequent Mach wave at point  $e$  intersects the adjacent blade leading edge.

Regarding the transonic compressors, the research efforts resulted in the design of *controlled diffusion blades* that almost eliminate shock losses [5], [6] and [7].

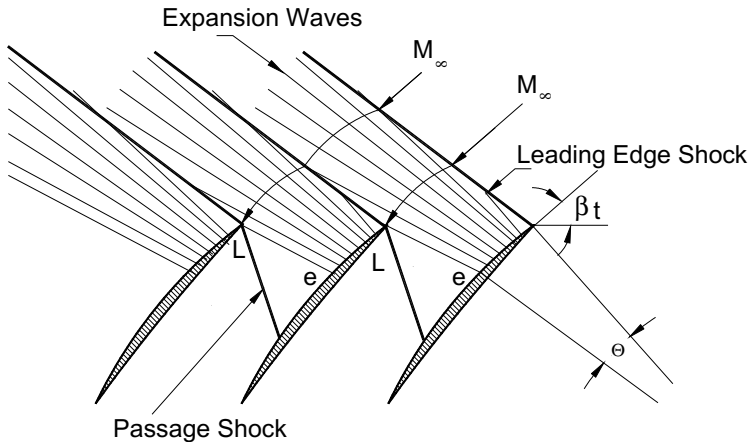


**Fig. 9.14:** Schematic of a supersonic compressor cascade the supersonic inlet mach number, expansion wave and passage shocks.

For compressors operating in the supersonic Mach range, the so called S-profiles with sharp leading edges are used. The pressure and suction surfaces consist of multi-circular arcs with very small curvatures (large radii). Particular attention must be paid to the shock losses, as discussed in Chapters 6 and [8]. The flow decelerates within the convergent part by a system of oblique shock waves followed by a normal shock. Further deceleration is achieved by diffusion within the divergent part. As seen, these profiles have a slightly convergent inlet tangent to a throat which is followed by a slightly divergent channel.

### 9.3 Turbine Blade Design

Different turbine blade designs are discussed in literature among others, [9], [10], [11], [12], and [13]. Given the stage velocity diagram with the flow velocity vectors and angles, the corresponding blade profiles are constructed such that the flow angles at the inlet and exit are realized. This includes the incorporation of the design incidence and deviation into the design process as discussed in Chapter 8. Figure 9.15 schematically shows the velocity diagram and the corresponding stator and rotor blades. Analogous to Section 9.2, the task here is designing the camberline on which a base profile will be superimposed. The camberline can be constructed from the inlet and exit flow angles under consideration of the incidence and deviation discussed in Chapter 8. This can be done graphically or numerically. Both methods are discussed in the following Section.

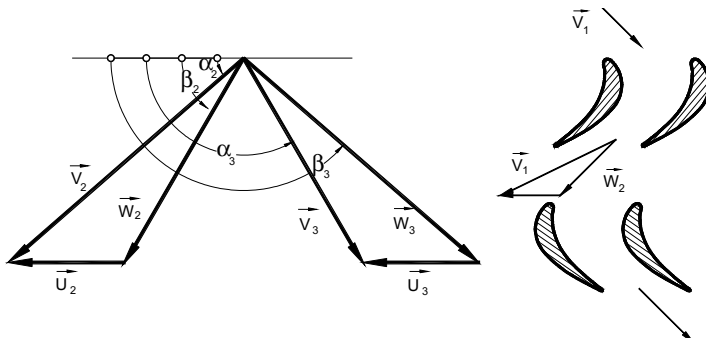


**Fig. 9.15:** Allocation of a set of stator and rotor blades to a given velocity diagram.

### 9.3.1 Steps for Designing the Camberline

**Step 1a:** This step determines the stagger angle  $\gamma$  graphically. Given the inlet and the exit velocity vectors  $V_1$ ,  $V_2$  with the flow angle  $\alpha_1$ ,  $\alpha_2$  for a stator blade and  $\beta_1$ ,  $\beta_2$  for the rotor blade, first the stagger angle  $\gamma$  must be determined. For this purpose, the location of the maximum thickness  $(t/c)_{\max}$  of the base profile  $(x/c)_{\max}$  is an appropriate guideline for determining  $\gamma$ . As an example, we choose an axial chord of  $c_{ax} = c \sin \gamma = a$  as shown in Fig. 9.16 and assume the position of  $(x/c)_{\max} = c$  and draw a line parallel to the cascade front. Then we intersect the continuation of the inlet velocity vector with that line. At the point of intersection we draw a line parallel to the exit velocity vector and find immediately the stagger angle  $\gamma$  as shown in Fig. 9.16.

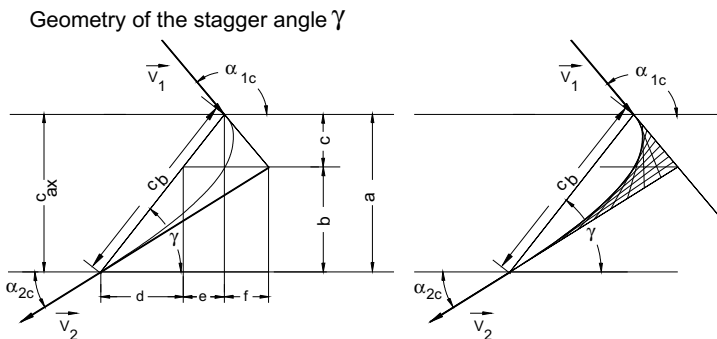


**Fig. 9.16:** Geometry for calculating the stagger angle.

**Step 1b:** This steps determined the stagger angle computationally. With the geometry

from Fig. 9.16, the stagger angle can be computed as follows. Using the flow angles tangent to the camber leading edge and trailing edge  $\alpha_{1c}$ ,  $\alpha_{2c}$  for the stator row and  $\beta_{2c}$ ,  $\beta_{3c}$  for the rotor row along with the axial chord  $a$ , the distance of the maximum camber from the leading edge  $c$  and the trailing edge  $b$  with  $b = a - c$ , the stagger angle is calculated as:

$$\tan \gamma = \frac{a}{\frac{a-c}{\tan \alpha_2} - \frac{c}{\tan (\pi - \alpha_1)}} \quad (9.37)$$

In Eq. (9.37) the distances  $a$ , and  $c$  are dimensional parameters. They can be non-dimensionalized by dividing the nominator and denominator in (9.37) by  $a$  and defining the ratio  $c/a$  as the fraction of the axial cord  $F = c/a$  to arrive at:

$$\tan \gamma = \frac{1}{\frac{1-F}{\tan \alpha_2} - \frac{F}{\tan (\pi - \alpha_1)}} \quad (9.38)$$

from which the stagger angle  $\gamma$  is calculated immediately.

**Step II:** Prepares the geometry detailed in Figs.9.17, 918 for constructing the camberline. Given the chord length  $c$  and the stagger angle  $\gamma$  from the previous step, the tangents to the leading- and trailing-edge of the camberline to be determined are

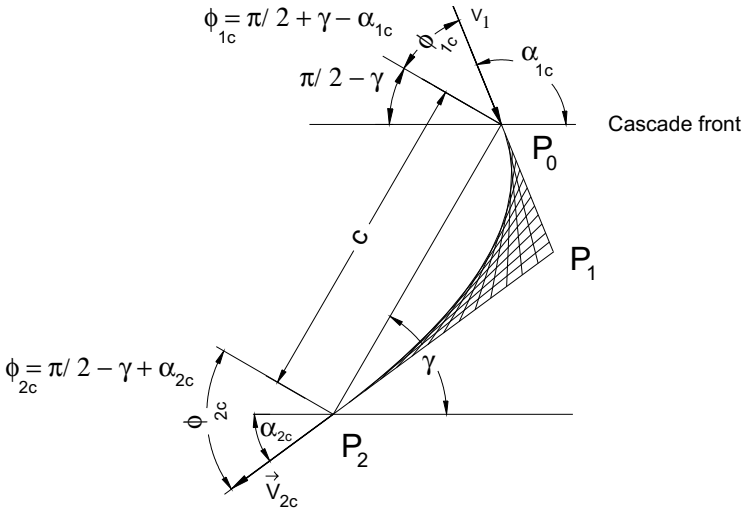


**Fig. 9.17:** Camber angle definitions:  $\alpha_{1c}$ ,  $\alpha_{2c}$  are camber angles at the cascade inlet and exit,  $\phi_{1c}$ ,  $\phi_{2c}$  are auxiliary angle required for camberline construction.

constructed by the inlet and exit metal angles as shown in Fig. 9.17. The latter is found from the stage velocity diagram under consideration of incidence and deviation angles, detailed in Chapter 8, leading to camber angle  $\alpha_{1c}$  and  $\alpha_{2c}$ . The tangents intersect each other at the point  $P_1$  and are subdivided into  $n-1$  equal distances as shown in Fig. 9.18. Starting with the first point 1 at the leading edge (LE) tangent, a line is drawn to intersect the trailing edge (TE) tangent at point  $n$ . The following lines start at the second point on the LE-tangent and intersects the TE-tangent at  $n-1$  and so on. The envelope of the inner region of the connecting lines is the camberline.

**Step III:** Prepares the camberline for the superposition of the base profile on camber line. This step requires turning the chord  $c$  counter clockwise by an angle of  $180^\circ - \gamma$  making the axial chord the reference line. It is important to keep the entire angle configuration as detailed in Figs. 9.17 and 9.18, while turning the cascade. Superimposing the base profile on the camberline as shown in Fig. 9.19 delivers the turbine profile.

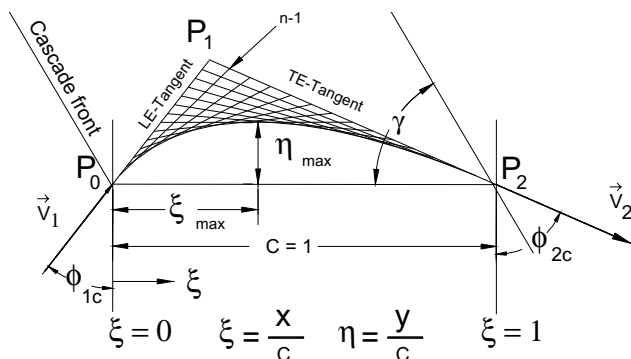


**Fig. 9.18:** Figure is turned counter clockwise by an angle of  $180^\circ - \gamma$ .

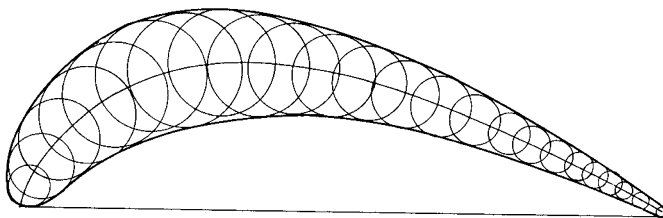


**Fig. 9.19:** Superposition of the base profile on the camber



### 9.3.2 Camberline Coordinates Using Bèzier Function

A similar camberline is constructed using Bèzier polynomial presented, among others, in [14]. The general Bèzier polynomial of degree  $n$  is given as:

$$\mathbf{B}(t) = \sum_{i=0}^n \binom{n}{i} (1-t)^{n-i} t^i \mathbf{P}_i \quad (9.39)$$

with  $\mathbf{P}_i$  as the given points in Fig. 9.19,  $t \in [0,1]$  the curve parameter, and  $\mathbf{B}(t)$  the position vector of the Bèzier curve at the curve parameter  $t$ . For the purpose of designing the camberline, a quadratic Bèzier curve is quite appropriate for a conventional turbine blade design. It reads:

$$\mathbf{B}(t) = (1-t)^2 \mathbf{P}_0 + 2(1-t)t \mathbf{P}_1 + t^2 \mathbf{P}_2 \quad (9.40)$$

Before re-writing the Bèzier formulation in terms of our nomenclature, we resort to Fig. 9.18, where the camber and Bèzier quantities are shown. Thus, Eq. (9.40) reads

$$B_{\xi}(\xi) = (1-\xi)^2 \mathbf{P}_{0_{\xi}} + 2(1-\xi)\xi \mathbf{P}_{1_{\xi}} + \xi^2 \mathbf{P}_{2_{\xi}} \quad (9.41)$$

$$B_{\eta}(\xi) = (1-\xi)^2 \mathbf{P}_{0_{\eta}} + 2(1-\xi)\xi \mathbf{P}_{1_{\eta}} + \xi^2 \mathbf{P}_{2_{\eta}}$$

Considering the nomenclature in Fig. 9.18, the boundary conditions are:

$$\text{For } P_0: \quad \xi = 0: \quad P_{0_{\xi}} = 0, \quad P_{0_{\eta}} = 0$$

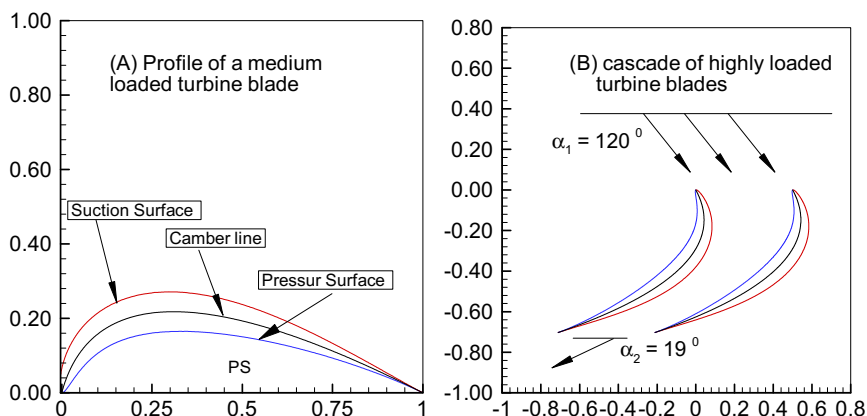
$$\text{For } P_1: \quad P_{1_{\xi}} = \frac{1}{1 + \frac{\cot \phi_{1c}}{\cot \phi_{2c}}}, \quad P_{1_{\eta}} = \frac{\cot \phi_{1c}}{1 + \frac{\cot \phi_{1c}}{\cot \phi_{2c}}} \quad (9.42)$$

$$\text{For } P_2: \quad \xi = 1: \quad P_{2_{\xi}} = 1, \quad P_{2_{\eta}} = 0$$

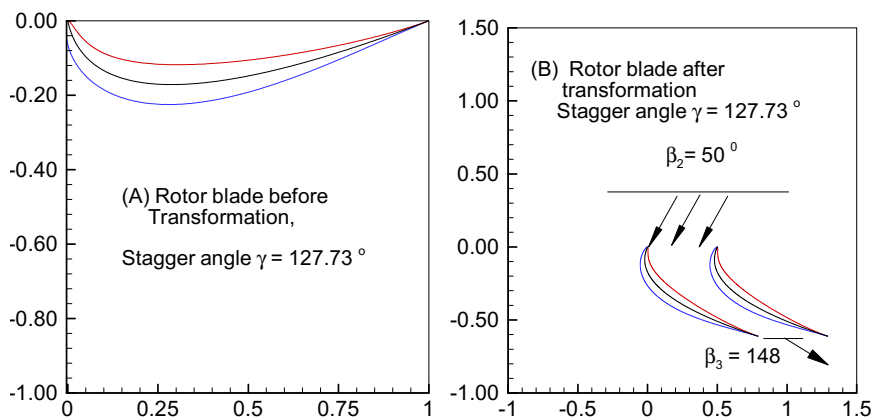
With Eqs. (9.41) and (9.42), the coordinates of the camberline are calculated by varying the dimensionless variable  $\xi$  from 0 to 1. A smooth camberline is obtained by introducing a small increment of  $\xi = 0.01$  or less.

Figure 9.20 shows the construction of a turbine blade profile for the stator row using  $\alpha_{1c}$ ,  $\alpha_{2c}$ , the stagger angle from Eq.(9.38) and the Bèzier function. For designing the rotor blade the relative rotor angles,  $\beta_{2c}$ ,  $\beta_{3c}$  along with the stagger angle equation (9.38) are used. In both cases, coordinate transformations facilitate rotation of the blades into correct positions as shown in Fig. 9.20 and 9.21 for stator and rotor blades respectively.

As seen the blades have very sharp trailing edges. This is the result of superimposing



**Fig. 9.20:** Generation of a turbine stator blade profile using Bezier function for construction of camber, stagger angle  $\gamma = 45^\circ$ .



**Fig. 9.21:** Generation of a turbine rotor blade profile using Bezier function for construction of camber.

the base profile, which was obtained from the conformal transformation with zero trailing edge thickness. Blades with sharp trailing edges are subject to high stress concentration. An excessive stress concentration leads to cracks that propagates from the blade hub to tip resulting in mechanical failure of the blade. To avoided the high level of stresses concentration, a circle with a radius of 0.5-1.2 mm (based on the blade chord length) may be drawn tangent to the suction and pressure surfaces of the blade trailing edge. This can be done before superimposing the base profile.

### 9.3.3 Alternative Calculation Method

Although a Bèzier curve provides a reasonable solution for camberline design, the position of the maximum thickness ( $\xi_{\max}$ ,  $\eta_{\max}$ ) may or may not be accurate. In this case, the following simpler method offers an appropriate alternative. The camberline can be described by a polynomial:

$$\eta = \sum_{v=0}^n a_v \xi^v \quad (9.43)$$

The coefficients  $a_v$  are obtained from the following boundary conditions:

$$\text{At } \xi = \frac{x}{c} = 0 \Rightarrow \eta = 0, \text{ and } \frac{d\eta}{d\xi} = \tan(\pi/2 - \phi_{1c}) \quad \text{BC1}$$

$$\text{At } \xi = \frac{x}{c} = 1 \Rightarrow \eta = 0, \text{ and } \frac{d\eta}{d\xi} = \tan(\pi/2 - \phi_{2c}) \quad \text{BC2}$$

$$\text{BC3}$$

$$\text{At } \xi = \xi_{\max} \Rightarrow \frac{\partial \eta}{\partial \xi} = 0$$

where  $\xi_{\max}$  and  $\eta_{\max}$  are given. With the boundary conditions BC1 to BC3, five coefficients can be determined. The corresponding polynomial is of fourth order:

$$\eta = \sum_{v=0}^4 a_v \xi^v \quad (9.44)$$

or

$$\eta = a_0 + a_1 \xi + a_2 \xi^2 + a_3 \xi^3 + a_4 \xi^4 \quad (9.45)$$

From BC1, it follows immediately that  $a_0 = 0$ . It is important to ensure that there is no discontinuity on the profile surfaces. For this purpose, the final profile should be smoothed mathematically. For a highly deflected turbine cascade, the application of the above procedure may result in an inflection point. To prevent this, the camberline may be subdivided into two or more lower degree polynomials that tangent each other at the same slope. It should be pointed out that, for subsonic turbine blades with  $r > 0.0\%$ , the area between two adjacent blades must continuously converge, enabling the flow to accelerate continuously. For zero-degree reaction, the blade channel area must be constant throughout. Once the cambrline is constructed, a turbine base profile is superimposed and the profile is generated, Fig.9.19.

In applying the methods discussed above, blade profiles can be designed for different flow deflections. Moderate flow deflection blades are used in steam turbine design to keep the profile losses as low as possible. In contrast, the gas turbine engines, particularly the aircraft engines, use high deflection blades to reduce the

number of stages thus, keep the weight/thrust ratio as low as possible.

## 9.4 Assessment of Blades Aerodynamic Quality

The objective of a turbine stator or rotor blade design is to accomplish a certain flow deflection that is required to produce a prescribed amount of power per stage. Given the inlet and the exit flow angles resulting in a given flow deflection, an infinite number of blades with different shapes can be constructed that realize the above flow deflection. These blades, however, will have different boundary layer distributions on suction and pressure surfaces and, thus, different profile loss coefficients. Among the numerous possible designs, only one has the lowest loss coefficient, i.e., the optimum efficiency at the design operating point only. Figure 9.22 shows the pressure distribution along the suction and pressure surfaces of a high efficiency turbine blade at the design point. This blade type is sensitive to incidence changes caused by off-design operation.

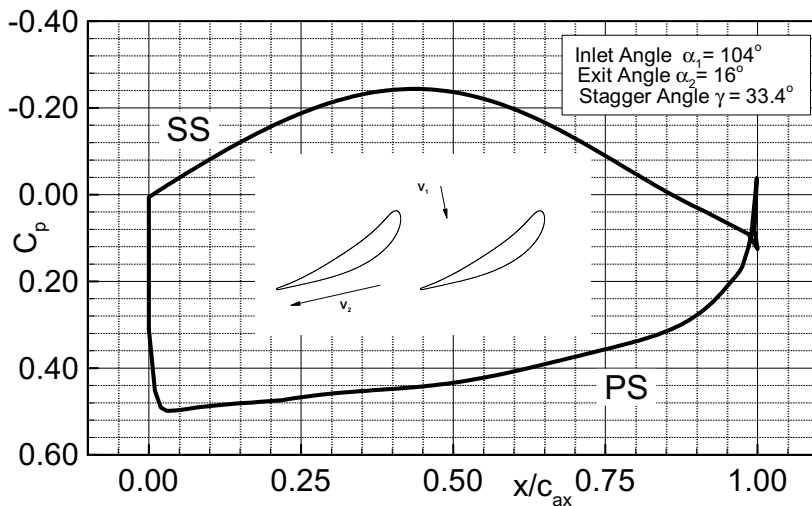


**Fig. 9.22:** Pressure distribution along the suction and pressure surfaces of a high efficiency turbine blade, *TPFL-Class Project 209*.

A change in operation condition results in a change of incidence angle and an increase in profile losses. Thus, the operation condition of a turbine plays a crucial role in designing the blade. If the mass flow or the pressure ratio of a turbine component undergo frequent changes, the blades must be designed in such a way that their profile losses do not experience significant increases. Parameters determining the efficiency and performance behavior of a turbine as a result of the boundary layer development on the suction and pressure surface are, among others, Reynolds number, Mach

number, pressure gradient, turbulence intensity and unsteady inlet flow conditions. Of the above parameters, the blade geometry defines the pressure gradient which is, in the first place, responsible for the boundary layer development, separation and re-attachment. Since the pressure distribution is determined by the geometry and vice versa, the question arises as to how the blade geometry should be configured in order to establish a desired pressure distribution. This question has been the subject of numerous papers dealing with the *inverse blade design*, particularly for subcritical and supercritical compressor cascades [15], [16], and [17]. In context of this Chapter, we treat the question of the pressure distribution versus geometry from a simple physical point of view to establish a few criteria as a guideline for turbine blade design. The following example should demonstrate what criteria should be used in order to design a turbine blade that operates at a wide range of incidence changes without a substantial decrease of its efficiency:

- (1) With exception of the leading edge portion, the pressure gradient on the pressure and suction surfaces should not experience sign changes over a range of 60% to 70% of the blade axial chord.
- (2) Over the above range, the pressure gradient should be close to zero. This means that flow on both surfaces neither accelerates nor decelerates.
- (3) Over the rest of 30% to 40% of the blade surface, the flow should strongly accelerate.

Applying the criteria (1) through (3) associated with a moderately thick leading edge radius provides a turbine blade that is insensitive to adverse off-design operation conditions at a relatively high efficiency, Fig. 9.22.

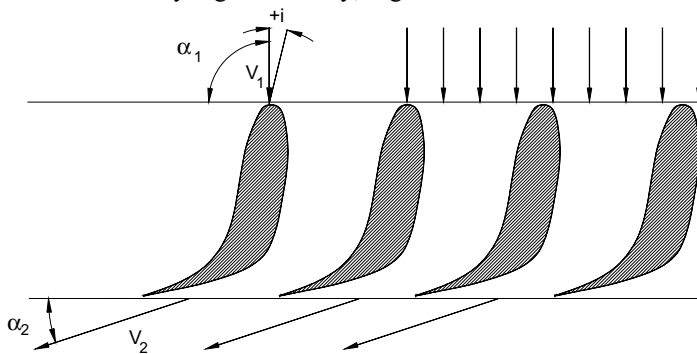


**Fig. 9.22:** A turbine cascade that fulfils the criteria (1) through (3).

Figure 9.23 shows the numerical calculation of the pressure coefficient versus the dimensionless axial chord. As seen, with exception of the leading edge portion the pressure distributions do not change over a wide range of incidence from  $-15^\circ$  to  $+21^\circ$ . This numerical result is verified experimentally and presented in Figs. 9.24.

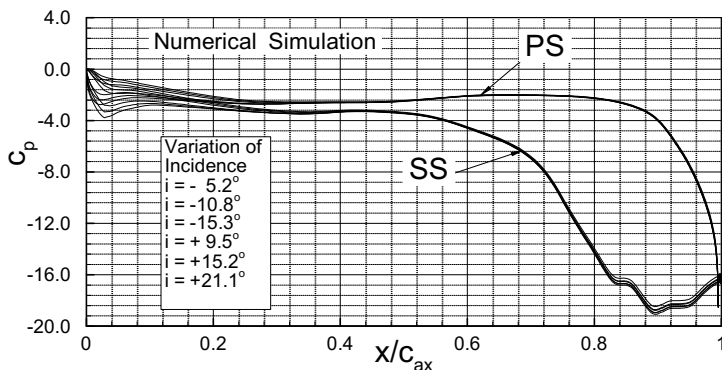


**Fig. 9.23:** Pressure distribution as a function of dimensionless axial chord with the incidence angle as parameter, TPFL-design.

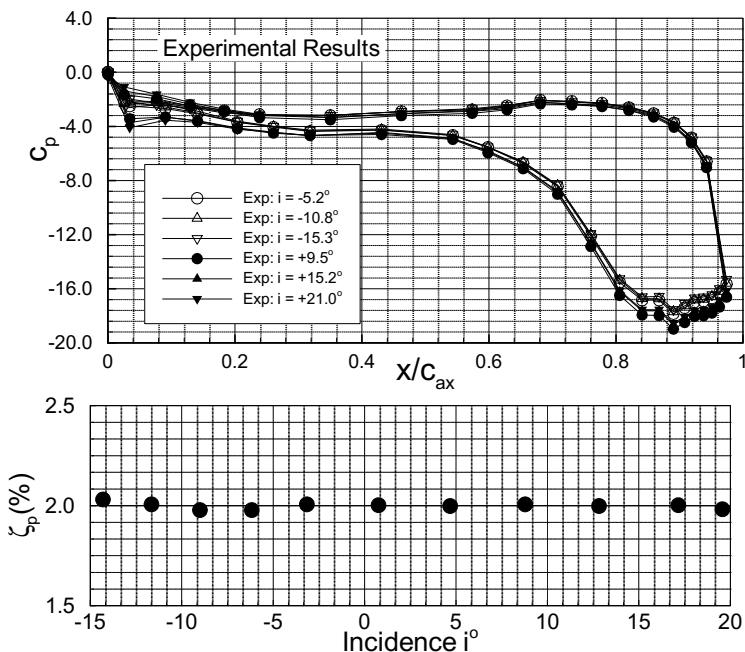


**Fig. 9.24:** Experimental pressure distribution as a function of dimensionless surface, total pressure loss coefficient as a function of incidence angle, TPFL experimental verification of the design shown in Fig. 9.23.

Figure 9.24 shows the experimental verification of the numerical results presented in Fig. 9.23. It also shows the profile loss coefficient  $\zeta_p$  as a function of the incidence angle. Here as in Fig. 9. 23, the pressure distributions do not change over a wide range of incidences from  $-15^\circ$  to  $+21^\circ$ . The results are in reasonable agreement with the numerical results, resulting in an approximate constant loss coefficient of 2%.

## References

1. Joukowsky, N.E., 1918, "Vortex Theory of Screw Propeller," I-IV, I-III, The forth paper published in the Transactions of the Office for Aerodynamic Calculations and Essays of the Superior Technical School of Moscow 1918 (in Russian). Also published in Gauthier-Villars et Cie. (eds). *Théorie Tourbillonnaire de l'Hélice Propulsive*, Quatrième Mémoire. 123–146: Paris, 1929 (in French).
2. Spurk, J.H., 1997, "Fluid Mechanics," ISBN 3-540-61651-9, Springer Verlag Berlin Heidelberg New York.
3. NASA SP-36 NASA Report, 1965.
4. Cumpsty, N.A., 1989, "Compressor Aerodynamics," Longman Group, New York.
5. Hobson, D.E., 1979, "Shock Free Transonic Flow in Turbomachinery cascade," Ph.D-thesis, Cambridge University Report CUED/A Turbo/65.
6. Schmidt, J.F., et al., 1984, "Redesign and Cascade tests of a Supercritical Controlled Diffusion stator Blade Section," AIAA Paper 84-1207.
7. Lakschminarayana, B., 1995, "Fluid Dynamics and Heat Transfer of Turbomachinery," John Wiley and Sons, Inc.
8. Schobeiri, M.T., 1998, "A New Shock Loss Model for Transonic and Supersonic Axial Compressors With Curved Blades," *AIAA, Journal of Propulsion and Power*, Vol. 14, No. 4, pp. 470-478.
9. Teufelberger, A., "Choice of an optimum blade profile for steam turbines," *Rev. Brown Boveri*, 1976, (2), 126-128.
10. Kobayashi, K., Honjo, M., Tashiro, H. and Nagayama, T., "Verification of flow pattern for three-dimensional-designed blades," ImechE paper C423/015, 1991.
11. Jansen, M. and Ulm, W., "Modern blade design for improving steam turbine efficiency," *VDI Ber.*, 1995, 1185.
12. Emunds, R., Jennions, I.K., Bohn, D. and Gier, J., "The computation of adjacent blade-row effects in a 1.5 stage axial flow turbine," ASME paper 97-GT-81, Orlando, Florida, June 1997.
13. Dunavant, J.C. and Erwin, J.R., 1956, "Investigation of a Related Series of Turbine-blade Profiles in Cascade," NACA TN-3802, 1956.
14. Gerald, F., 1997, "Curves and Surfaces for Computer-aided Geometric Design," (4th Ed.), Elsevier Science & Technology Books, Isbn 9780- 12249054 5.
15. Bauer, F., Garabedian, P. and Korn., D., 1977, "Supercritical Wing Sections III," Springer-Verlag, New York.

16. Dang, T., Damle, S., and Qiu, X., 2000, "Euler-Based Inverse Method for Turbomachine Blades: Part II—Three Dimensions," *AIAA Journal*, 38, no. 11.
17. Medd, A.J., 2002, "Enhanced Inverse Design Code and Development of Design Strategies for Transonic Compressor Blading," Ph.D. dissertation, Department of Mechanical Engineering, Syracuse University.



## 10 Radial Equilibrium

In Chapter 4, we briefly described a simple radial equilibrium condition necessary to determine the radial distribution of the stage parameters such as,  $\phi$ ,  $\lambda$ ,  $r$ ,  $\alpha_i$ , and  $\beta_i$ . Assuming an axisymmetric flow with constant meridional velocity and total pressure distributions, we arrived at free vortex flow as a simple radial equilibrium condition with  $rv_u = \text{const}$ . In practice, from an aerodynamics design point of view, a constant meridional velocity component or constant total pressure may not be desirable. As an example, consider the flow field close to the hub or tip of a stage where secondary flow vortices predominate. As discussed in Chapter 4, these secondary vortices induce drag forces leading to secondary flow losses which reduce the efficiency of the stage. To reduce the secondary flow losses, specific measures can be taken that are not compatible with the simple radial equilibrium condition. In this case, the simple radial equilibrium method needs to be replaced by a general one. Wu [1] proposed a general theory for calculating the three-dimensional flow in turbomachines. He introduced two sets of surfaces: Blade to blade surfaces called  $S_{li}$  and hub-to-tip surfaces labeled with  $S_{2j}$ . Utilizing  $S_{li}$  and  $S_{2j}$  surfaces, Wu [1] proposed an iterative method to solve the three-dimensional inviscid flow field in turbomachinery stages. Coupling both surfaces, however, is associated with computational instabilities that gives rise to replacing the technique by complete Euler or Navier-Stokes solver, [2]. A computationally more stable method for solving the flow field is the streamline curvature technique. This method is widely used in turbomachinery industry and is the essential tool for generating the basic design structure necessary to start with CFD application. The streamline curvature method can be used for design, off-design, and analysis. Vavra [3] presented the theoretical structure for inviscid axisymmetric flow in turbomachines that can be used to derive the streamline curvature equations. A thorough review of the streamline curvature method can be found in a recent book by Schobeiri, [4] Novak and Hearsey [5], Wilkinson [6], and Lakshminarayana [2]. Wennerstrom [7] presented a concise description of this technique which is given in this section in its original form. Rapid calculation procedures used in the turbomachinery industry determining the distribution of flow properties within the turbomachinery assume steady adiabatic flow and axial symmetry. The more sophisticated of these procedures include calculation stations within blade rows as well as the more easily treated stations at the blading, leading and trailing edges. The assumption of axial symmetry in the bladed

region implies an infinite number of blades. The blade forces acting between the blades and the fluid are taken into consideration by body force terms in equation of motion. The streamlines are not straight lines as could be supposed. They usually have certain curvatures that are maintained if the forces exerted on the fluid particle are in an equilibrium state described by the equilibrium equation. This equation includes various derivatives in the meridional plane and is solved in this plane along the computing stations which are normal to the average meridional flow direction. The equilibrium equation in its complete form cannot be solved analytically, therefore, numerical calculation methods are necessary. For the application of the equilibrium equation to the stage flow with streamline curvature, Hearsey [8] developed a comprehensive computer program which is successfully used in the turbomachinery industry for design of advanced compressors and turbines. Since the treatment of the corresponding numerical method for the solution of this equation is given in [7], this chapter discusses the basic physical description of the calculation method. As a result, the streamline curvature method can be used as a design tool and for the post design analysis. An advanced compressor design is presented followed by a brief discussion of special cases.

### 10.1 Derivation of Equilibrium Equation

The starting point for this derivation is the formulation of the equations of motion for an axisymmetric flow in intrinsic coordinates fixed in space along streamlines as shown in Fig.10.1.

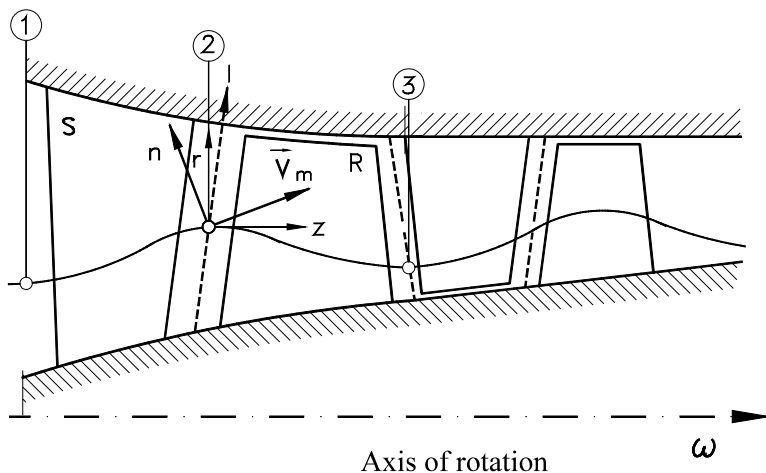


**Fig. 10.1:** Flow through axial compressor, streamline, directions are:  $n$  = normal,  $m$  = meridional,  $r$  = radial,  $z$  = axial, and  $l$  = computing station

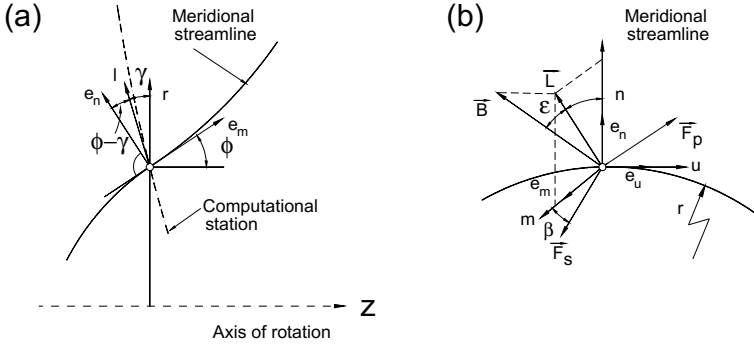


**Fig. 10. 2:** (a) Coordinate directions in the meridional plane, (b) orientation of vectors with respect to  $m, u, n$  orthogonal coordinate system, redrawn from [6].

The momentum equation is in meridional direction:

$$V_m \frac{\partial V_m}{\partial m} - \frac{V_u^2}{r} \sin \phi = - \frac{1}{\rho} \frac{\partial p}{\partial m} + F_m \quad (10.1)$$

in stream surface normal direction:

$$\frac{V_m^2}{r_c} - \frac{V_u^2}{r} \cos \phi = - \frac{1}{\rho} \frac{\partial p}{\partial n} + F_n \quad (10.2)$$

and in circumferential direction:

$$\frac{V_m}{r} \frac{\partial(rV_u)}{\partial m} = F_u \quad (10.3)$$

with  $F_m$ ,  $F_n$  and  $F_u$  as the components of a field force in meridional, normal and circumferential directions. This field force is thought of as the real blade force that causes the flow to deflect from the leading edge to trailing edge of a turbine or a compressor. The thermodynamic equations required are the energy equations for steady adiabatic flow:

$$H = h + \frac{V^2}{2} \quad (10.4)$$

and the Clausius entropy relation:

$$\frac{1}{\rho} dp = dh - Tds \quad (10.5)$$

Since, in intrinsic coordinates there is no velocity component in the  $n$ -direction (by definition),

$$V^2 = V_m^2 + V_u^2 \quad (10.6)$$

Equations (10.4), (10.5), and (10.6) are combined to give:

$$\frac{1}{\rho} dp = dH - Tds - V_m dV_m - V_u dV_u \quad (10.7)$$

Since the computation station lies in the space between the stator and the rotor, usually not normal to the meridional stream surface, the derivatives must be defined with respect to the  $l$ -direction along a computing station, Fig.10.2:

$$\frac{d}{dl} = \frac{dn}{dl} \frac{\partial}{\partial n} + \frac{dm}{dl} \frac{\partial}{\partial m} = \cos(\phi - \gamma) \frac{\partial}{\partial n} + \sin(\phi - \gamma) \frac{\partial}{\partial m} \quad (10.8)$$

Rearranging Eq.(10.8) to eliminate the derivatives with respect to the normal direction:

$$\frac{\partial}{\partial n} = \sec(\phi - \gamma) \frac{d}{dl} - \tan(\phi - \gamma) \frac{\partial}{\partial m} \quad (10.9)$$

Introducing Eq.(10.7) into Eq.(10.1) and (10.2), eliminating derivatives with respect to  $n$  with Eq.(10.9), the resulting equations are combined to eliminate

$$\frac{\partial H}{\partial m} - T \frac{\partial s}{\partial m} \quad (10.10)$$

The equation obtained after algebraic rearrangement and trigonometric substitution is:

$$V_m \frac{dV_m}{dl} = \sin(\phi - \gamma) V_m \frac{\partial V_m}{\partial m} + \cos(\phi - \gamma) \frac{V_m^2}{r_c} - \frac{V_u}{r} \frac{d(rV_u)}{dl} + \frac{dH}{dl} - T \frac{ds}{dl} - \sin(\phi - \gamma) F_m - \cos(\phi - \gamma) F_n \quad (10.11)$$

In some cases, it is more convenient to work in a similar system of coordinates which is stationary with respect to a rotating blade row. As shown in Chapter 4, Eq.(10.11) is easily transformed into the rotating frame of reference by introducing the substitution:

$$V_u = W_u + \omega r \quad (10.12)$$

for the circumferential velocity component. The corresponding relative total enthalpy<sup>1</sup>  $H_r$  from Eq. (4.3) is:

$$H_r = h + \frac{W^2}{2} - \frac{U^2}{2} \quad (10.13)$$

Combining Eqs. (10.12), and (10.13) leads to:

$$H = H_r + \omega r(W_u + \omega r) \quad (10.14)$$

Introducing Eqs.(10.12) and (10.14) into Eq. (10.11), the corresponding radial equilibrium equation is:

$$V_m \frac{dV_m}{dl} = \sin(\phi - \gamma) V_m \frac{\partial V_m}{\partial m} + \cos(\phi - \gamma) \frac{V_m^2}{r_c} - \frac{W_u}{r} \frac{d(rW_u)}{dl} +$$

$$\frac{dH_r}{dl} - T \frac{ds}{dl} - 2\omega W_u \cos\gamma - \sin(\phi - \gamma) F_m - \cos(\phi - \gamma) F_n \quad (10.15)$$

Equations (10.11) and (10.15) represent the radial equilibrium condition. The points of principal interest in this derivation are associated with the treatment of the body forces,  $F_m$  and  $F_n$ . Note that the complete body force field contains a third component  $F_u$  which is orthogonal to the other two mutually orthogonal components  $F_m$  and  $F_n$  and can be directly calculated from Eq. (10.3). The remainder of this derivation is aimed at obtaining expressions for  $F_m$  and  $F_n$  which relate to geometric properties of the blading. Combining Eqs.(10.1) and (10.7) gives:

$$T \frac{\partial s}{\partial m} = \frac{\partial H}{\partial m} - \frac{V_u^2}{r} \sin\phi - V_u \frac{\partial V_u}{\partial m} - F_m \quad (10.16)$$

---

<sup>1</sup> Wennerstrom [6] calls this quantity rothalpy which was introduced by Wu [1], who termed the sum of the static enthalpy and the kinetic energy of the relative flow  $h_R = h + W^2/2$  as the relative total enthalpy (see also Lakshminarayana [2]). In a rotating frame of reference, the expression  $h_R$  changes along a streamline that varies in radial direction. In contrast, the relative total enthalpy given by Eq. (10.13) derived in [4], Chapter 3, remains constant and is generally valid within a rotating frame of reference, where the streamlines may change in radial direction (see also Vavra [3]).

or

$$T \frac{\partial s}{\partial m} = \frac{\partial H}{\partial m} - \frac{V_u}{r} \frac{\partial(rV_u)}{\partial m} - F_m \quad (10.17)$$

Equation (10.3) and the thermodynamic definition of work (applied to a turbomachine) may be combined to give

$$\frac{\partial H}{\partial m} = \frac{U}{r} \frac{\partial(rV_u)}{\partial m} \quad (10.18)$$

a differential form of the Euler equation of turbomachinery. Combining Equations (10.17) and (10.18), noting from the velocity triangle that

$$\tan \beta = \frac{W_u}{V_m} \quad (10.19)$$

and introducing Equation (10.3) again leads to

$$F_m = -F_u \tan \beta - T \frac{\partial s}{\partial m} \quad (10.20)$$

Equation (10.20) is sufficient to solve Eqs. (10.11) or (10.15) for some bladeless cases but, in order to solve the equations within a bladed region, more information is required concerning the direction and nature of the force components. For this purpose, it is convenient to resort to vector analysis to relate the various force components and coordinate directions. Fig. 10.2b illustrates the vectors described in the following discussion. The variables  $m$ ,  $u$ ,  $n$  are the principal orthogonal axes of a right handed, streamline coordinate system. In this system,  $F_s$  is the body force vector acting to oppose motion of the fluid; i.e. the body force which produces an irreversible increase in entropy. It lies in the  $m$ - $u$  plane and at the angle  $\beta$  (relative flow angle) from the meridional direction. The vector  $L$  is coincident with the  $l$ -direction and lies in the  $n$ - $m$  plane at the angle  $(\phi - \gamma)$  from the  $n$ -direction. The vector  $B$  is tangent to the mean blade surface and lies in the  $l$ - $u$  plane at an angle  $\epsilon$  from the  $l$ -direction. Planes such as the  $m$ - $u$  plane and  $l$ - $u$  plane are understood as planes tangent to the curved surface, described by the respective coordinates at the point in question. The equation of the unit vector in  $F_s$ -direction is:

$$\frac{\mathbf{F}_s}{F_s} = \cos \beta \mathbf{e}_m + \sin \beta \mathbf{e}_u + (0) \mathbf{e}_n \quad (10.21)$$

and the equation of the unit vector  $B$  is

$$\mathbf{B} = \cos \epsilon \sin(\phi - \gamma) \mathbf{e}_m - \sin \epsilon \mathbf{e}_u + \cos \epsilon \cos(\phi - \gamma) \mathbf{e}_n \quad (10.22)$$

The force due to a pressure difference across a blade acts in a direction normal to both vectors  $F_s$  and  $B$ , which together define the local plane of the mean blade surface at a point. Therefore, the pressure force vector can be defined by the cross product of  $F_s$  and  $B$ . Since  $F_s$  and  $B$  are usually not perpendicular but at an angle  $(\pi/2 - (\phi - \gamma))$  to one another, the product of these vectors differs from a unit vector by  $\cos(\phi - \gamma)$ . Therefore to obtain a unit vector for the force due to pressure across a blade and because  $F_p$  must be in the positive direction of rotation, this is written

$$\frac{F_p}{F_p} = \frac{1}{\cos(\phi - \gamma)} \left( \frac{B \times F}{F_s} \right)$$

$$\frac{F_p}{F_p} = -\sin\beta \cos\epsilon e_m + \cos\beta \cos\epsilon e_u + \left( \frac{\cos\beta \sin\epsilon}{\cos(\phi - \gamma)} + \sin\beta \cos\epsilon \tan(\phi - \gamma) \right) e_n \quad (10.23)$$

From Fig. 10.2b, note that  $F_m$  is composed of the m-components of  $F_s$  and  $F_p$ . Consequently, from Eqs. (10.21) and (10.23) we obtain:

$$F_m = F_s \cos\beta - F_p \sin\beta \cos\epsilon \quad (10.24)$$

Similarly,  $F_u$  and  $F_n$  are composed respectively of the u and n components of  $F_s$  and  $F_p$

$$F_u = F_s \sin\beta + F_p \cos\beta \cos\epsilon \quad (10.25)$$

$$F_n = F_p [\cos\beta \sin\epsilon \sec(\phi - \gamma) + \sin\beta \cos\epsilon \tan(\phi - \gamma)] \quad (10.26)$$

Since the orthogonal components of the force field have been defined in terms of components acting along and perpendicular to the relative flow direction, it is possible to solve for these two components. By inserting Eqs. (10.24) and (10.25) into Eq. (10.20) and simplifying, one obtains:

$$F_s = -\cos\beta T \frac{\partial s}{\partial m} \quad (10.27)$$

Subsequently, Eqs. (10.25) and (10.27) can be combined to give

$$F_p = \frac{F_u}{\cos\beta \cos\epsilon} + \frac{\sin\beta}{\cos\epsilon} T \frac{\partial s}{\partial m} \quad (10.28)$$

If Eqs. (10.27) and (10.28) are now inserted into Eqs. (10.24) and (10.26), the body forces appropriate to the intrinsic coordinate system are defined in terms of

parameters readily calculated. The most useful form of the radial equilibrium equation is the form in relative system, Equation (10.15), since it becomes identical to Eq. (10.11) in the absolute system when the angular velocity of the coordinates is set equal to zero. Combining Eq. (10.24), (10.26), (10.27) and (10.28) into Eq. (10.15) puts the radial equilibrium equation in the form:

$$V_m \frac{dV_m}{dl} = \sin(\phi - \gamma) V_m \frac{\partial V_m}{\partial m} + \cos(\phi - \gamma) \frac{V_m^2}{r_c} - \frac{W_u}{r} \frac{d(rW_u)}{dl} + \frac{dH_r}{dl} - T \frac{ds}{dl} - 2\omega W_u \cos\gamma - \tan\epsilon F_u + [\sin(\phi - \gamma)\cos^2\beta - \tan\epsilon \sin\beta \cos\beta] T \frac{\partial s}{\partial m} \quad (10.29)$$

The force  $F_u$  can be obtained from Eq. (10.3) or from

$$F_u = \frac{V_m}{r} \frac{\partial(rW_u)}{\partial m} + 2\omega V_m \sin\phi \quad (10.30)$$

applicable to the relative system. If working in a relative system with specified flow angle, it is convenient to employ Eq. (10.19) to eliminate  $W_u$ . The result of this substitution, included in a combined form of Eq. (10.29) and (10.30), is

$$V_m \frac{dV_m}{dl} = \cos^2\beta \left[ (\sin(\phi - \gamma) - \tan\epsilon \tan\beta) V_m \frac{\partial V_m}{\partial m} + \cos(\phi - \gamma) \frac{V_m^2}{r_c} \right. \\ \left. \cos^2\beta \left[ V_m^2 \frac{\tan\beta}{r} \frac{d(r\tan\beta)}{dl} - 2\omega V_m (\tan\epsilon \sin\phi + \tan\beta \cos\gamma) \right] + \right. \\ \left. \cos^2\beta \left[ (\sin(\phi - \gamma)\cos^2\beta - \tan\epsilon \sin\beta \cos\beta) T \frac{\partial s}{\partial m} \right] + \right. \\ \left. \cos^2\beta \left[ \frac{dH_r}{dl} - T \frac{ds}{dl} - V_m^2 \frac{\tan\epsilon}{r} \frac{\partial(r\tan\beta)}{\partial m} \right] \right] \quad (10.31)$$

The form of the radial equilibrium equation most appropriate for a particular calculation depends on a number of factors. The most important of these are the nature of the numerical scheme for analysis and the choice of parameters to be specified. This derivation was guided by the intent to apply the results to a streamline curvature type of computing procedure wherein the meridional velocity was the primary variable for which solutions were sought. In this type of procedure, the radial



equilibrium equation is solved along each computing station for an assumed set of streamlines. The streamlines are then refined and this process repeated until a satisfactory degree of convergence is attained. This calculation method is used successfully in the turbomachinery industry for design of advanced compressors and turbines.

Before discussing applications in bladed regions of a turbomachine, consider applications involving bladefree spaces. The body force due to a pressure difference across a blade was defined by the vector  $F_p$  in Eq. (10.23). In a bladefree space, this component is zero. The remaining body force,  $F_s$ , associated with the entropy increase, was defined by Eq. (10.26). Hence, Eqs. (10.24), (10.25) and (10.26) describing the three orthogonal body forces of the intrinsic coordinate system reduces to

$$F_m = - \cos^2\beta T \frac{\partial s}{\partial m} \quad (10.32)$$

$$F_u = - \sin\beta \cos\beta T \frac{\partial s}{\partial m} \quad (10.33)$$

$$F_n = 0 \quad (10.34)$$

In addition, all terms involving the blade lean angle,  $\epsilon$ , drop out of the radial equilibrium equation. Equation (10.29) then reduces to:

$$\begin{aligned} V_m \frac{dV_m}{dl} = & \sin(\phi - \gamma) V_m \frac{\partial V_m}{\partial m} + \cos(\phi - \gamma) \frac{V_m^2}{r_c} - \\ & - \frac{W_u}{r} \frac{d(rW_u)}{dl} + \frac{dH_r}{dl} - T \frac{ds}{dl} - 2\omega W_u \cos\gamma + \\ & + \sin(\phi - \gamma) \cos^2\beta T \frac{\partial s}{\partial m} \end{aligned} \quad (10.35)$$

It is interesting to note that, according to Eq. (10.32) and (10.33) in a swirling flow, an entropy rise in the direction of flow always leads to body force terms both in — and  $u$ -directions. This is obvious for the vaneless diffuser and a centrifugal machine where most of the entropy rise occurs from wall friction. It is much less obvious for an axial turbomachine of high aspect ratio where annulus wall friction may be negligibly small in relation to losses due to wake mixing. However, it appears that a change in angular momentum occurs in both cases if the entropy is assumed to be

increasing in the flow direction.

Considering bladed regions, the choice of parameters specified initially generally falls into one of two categories. The first involves cases where total temperature or circumferential velocity component is specified. Practically, these variables are for all practical purposes interchangeable, being simply related through Eq. (10.18). The most convenient solution for these cases is usually obtained in the stationary frame of reference using Eq. (10.29) with  $\omega = 0$ ,  $W_u = V_u$ , and  $H_r = H$ . During each calculation pass, the only variables in Eq. (10.29) are usually  $V_m$  and  $\beta$ , since all the other parameters distributed along the  $l$ -direction are either input data or upgraded between passes. The second important category of calculation within the bladed region involves specified relative flow angles. For this purpose, it is most expedient to work in a relative frame of reference, specifying  $\omega$  within the rotors and zero elsewhere. The most convenient radial equilibrium equation is Eq. (10.31). In this instance, the only variable in Eq. (10.31) during a calculation pass is  $V_m$  and all other variations in  $l$ -direction are either input data or upgraded only between calculation passes.

## 10.2 Application of Streamline Curvature Method

Utilizing the equations derived in section 10.1, Hearsey [7] developed a computational tool that can be used for design and analysis of turbomachines. This section summarizes the computational aspects of the streamline curvature technique by Hearsey [7].

As discussed in the previous section, the streamline curvature method offers a flexible method of determining a Euler solution of the axisymmetric flow through a turbomachine. The computational grid comprises the streamlines, as seen in a meridional view of the flow path, and quasi-normals that are strategically located in the flow, Figs. 10.1. Several stations are generally placed in the inlet duct upstream of the turbomachine proper, and several more are generally placed downstream. Within the turbomachine, the minimum number of quasi-normals, or "stations", is simply one between each adjacent pair of blade-rows, which would then represent both outlet conditions from the previous row and inlet conditions to the next. A better choice is one at each edge of each blade-row. For some calculations, additional stations are added within the blade-rows. This is a relatively coarse grid (compared with that used for CFD computations), making for calculations that typically take just seconds to complete (when run on a typical year-2003 PC).

By virtue of being an axisymmetric, Euler solution, the basic method is inherently incapable of predicting entropy rises, that is pressure losses and efficiency. This is handled by invoking a cascade performance prediction scheme to estimate losses and, in some situations, discharge flow angles from blading. Complicated boundary layers form on the flow path inner and outer walls of turbomachinery, causing "blockage" and participating in secondary flows. Especially for multi-stage axial compressors, a good estimate of blockage is required in order to correctly

predict stage matching.

The equation system that is broadly used caters to two situations: when the variation of absolute tangential velocity component along a computing station is known, and when the relative flow angle distribution is known. The former generally arises in "design" calculations, and the latter in "analysis" or performance prediction, cases. Thus, the streamline curvature procedure may be used for design calculations, off-design performance predictions and test-data analysis. This versatility, combined with the speed of solution, makes the method a work-horse tool. Many designs can be accomplished using only the streamline curvature method, and while some CFD computations are now offering design capability, even then a good candidate design is generally required as a starting point.

Although the Euler equations are the basis of the method, properly accounting for the change in entropy that is super-imposed from station to station, that is, in the streamline direction, requires some care. This was highlighted in Horlock [9] in which several previously-published equation systems were examined and found to be missing what is usually a small term.

For the case where tangential velocities are known, the appropriate equation is Eq. (10.29). When relative flow angles are known, Eq. (10.31) is used. In conjunction with one of these equations, the continuity equation and the energy equation are required. Fluid properties are also required; these are best computed in a discreet sub-program to allow for easy replacement. The continuity equation takes the form:

$$\dot{m} = \int_{r_h}^{r_t} V_m \rho \cos(\phi - \gamma) 2\pi r dl \quad (10.36)$$

The rate of change of flow with meridional velocity will also be required. This is given by:

$$\frac{d\dot{m}}{dV_m} = \int_{r_h}^{r_t} (1 - M_m^2) \frac{d\dot{m}}{V_m} \quad (10.37)$$

when tangential velocity component is specified, or:

$$\frac{d\dot{m}}{dV_m} = \int_{r_h}^{r_t} \left[ 1 - M_{m,rel}^2 \left( 1 + \frac{\zeta \kappa p/P_{rel}}{1 + \zeta(1 - p/P_{rel})} \right) \right] \frac{d\dot{m}}{V_m} \quad (10.38)$$

when relative flow angle is given. The loss coefficient  $\zeta$  included in Eq. (10.38) is the total pressure loss coefficient normalized by *exit* dynamic pressure. If not used, it is set zero in Eq. (10.38). The Euler equation of turbomachinery relates total enthalpy change to angular momentum change:

$$\Delta H = H_3 - H_2 = \omega(r_3 V_{u3} - r_2 V_{u2}) \quad (10.39)$$

### 10.2.1 Step-by-step solution procedure

Given these equations, a step-by-step procedure to obtain a solution is as follows:

- (1) An initial estimate of the streamline pattern is made. An obvious choice is to divide the flow path into equal areas at each station. Slightly more uniform (final) streamline spacing may be achieved by dividing the inlet (or some other) station into equal increments and then using the resulting area fractions to guide the remaining estimates.
- (2) Initial estimates of the streamwise gradients that occur in Eqs. (10.29) and (10.31) are made. These are all second-order terms and zero is the usual first estimate.
- (3) The streamline slopes and curvatures are computed at all mesh points (although, alternatively, this can be done station-by-station as the calculation proceeds). Curvatures are normally set to zero for the first and last stations.
- (4) At the first station, the user is required to specify the variation of total enthalpy, entropy and angular momentum or flow angle along the station. Enthalpy and entropy are typically implied by total pressure and temperature in the users input data. The fluids package can then be used to obtain enthalpy and entropy on each streamline.
- (5) A first estimate of the meridional velocity on one streamline is made from the inlet flow and the first station area. It is recommended that the mid-streamline value be defined. High accuracy is not required (this will not be required after the first pass).
- (6) Depending upon whether angular momentum or flow angle was given in the input data, Eq. (10.29) or (10.31) is integrated from the mid-streamline to the inner wall, and from the mid-streamline to the outer wall. This yields a meridional velocity distribution that is consistent with the momentum equation, the assumed streamline characteristics and the estimated mid-line velocity estimate. Although this is not likely to occur at Station 1, extreme values can lead to negative velocities, or values greater than the speed of sound. Provisions must be made for such occurrence.
- (7) Equations (10.36) and (10.37) or (10.38) are integrated across all streamlines to yield the achieved flow and its rate of change with meridional velocity.
- (8) The sign of the flow gradient indicates on which branch of the continuity equation the current velocity profile lies, a positive value indicating the subsonic branch, and a negative value, the supersonic branch. If tangential velocity is specified, only the subsonic branch is valid for a streamline

curvature solution, but if flow angle is specified, the user must specify which branch is required; both are potentially valid. (The criterion for a valid solution is actually that the meridional velocities be less than the speed of sound. Thus, if zero or small flow angles are specified, the supersonic solution will not be valid). If the profile lies on the correct branch and the achieved flow is within the desired tolerance of the specified flow, control passes to Step 9. Otherwise, a new estimate of the mid-line meridional velocity is required. If the profile lies on the wrong branch, a semi-arbitrary change in the mid-line meridional velocity estimate is made and control returns to Step 6 (subject to some limit on the permitted number of iterations). Otherwise, the mid-line meridional velocity is re-estimated using:

$$V_{m_{new}} = V_{m_{old}} + \frac{(\dot{m}_{specified} - \dot{m}_{achieved})}{\frac{d\dot{m}}{dV_m}} \quad (10.40)$$

and again, control returns to Step 6 (subject to some limit on the permitted number of iterations). Several potential difficulties exist when applying Eq. (10.40). The gradient  $d\dot{m}/dV_m$  becomes ever smaller as the junction between the two branches of the continuity equation is approached. Thus, very large changes in  $V_m$ -mid may be calculated (although usually not at Station 1, but this same procedure will be used at stations). Some logic should therefore be employed to ensure that the result of applying Eq. (10.39) is plausible.

- (9) The process moves on to the next station. Although Station 2 will usually be in an inlet duct, a general description applicable to all stations after the first will be given.
- (10) If the station follows a blade-free space, total enthalpy, entropy and angular momentum are convected along streamlines from the previous station (these may have to be computed following a solution at the previous station if Eq. (10.29) or (10.31) in rotating coordinates was used). Equation (10.29) will be applied whenever absolute angular momentum is given or implied by the user input data. Equation (10.39) will usually be used to determine total enthalpy from angular momentum or vice versa. Entropy is determined from the efficiency or pressure loss however expressed. In some cases, for example when a total pressure loss coefficient relative to the exit dynamic pressure is given, entropy can only be estimated because the loss depends upon the as-yet unknown velocity distribution. Then, an initial estimate of meridional velocities on all streamlines is required; this can be made by assuming the values determined at the previous station. Note that this is done on the first pass through all stations only. There are numerous possible combinations of data. Total temperature, total enthalpy, total temperature or enthalpy change from the previous station, total pressure or pressure ratio from the previous

station are some of the possibilities. In conjunction with these, various efficiencies or loss coefficients may be prescribed. For test data analysis, and following a rotor, total temperature and total pressure will be the inputs. A significant amount of programming logic is required to navigate the choices. Equation (10.31) will be applied when relative flow angle is given or implied. A design calculation might specify flow angle rather than angular momentum at a stator discharge station, where test data will normally be total pressure and flow angle. (If total temperature is also measured, there is a choice to be made between convecting the temperatures from the leading edge station or abandoning them and imposing the newly measured values. Some care would then be required with the overall thermodynamics of the calculation). Relative flow angle will be implied by any off-design performance calculation when blade geometry is the input data. This will require the estimation of losses and discharge flow angles by a cascade performance prediction scheme. Depending upon the scheme selected, the losses and/or flow angles may be dependent upon the as-yet unknown meridional velocities, leading only to estimates. Equation (10.29) or (10.31) is integrated, as was done in Step 6. If any of the data required for Eq. (10.29) or (10.31) could only be estimated, an iterative loop should be performed to obtain a meridional velocity distribution that is consistent with the performance modeling, although once a few overall passes have been performed, any discrepancy should become very small.

- (11) The continuity equation is applied as in Steps 7 and 8, with control passing back to Step 10 until the specified flow is achieved (or all permitted iterations have been performed). The stream function on each streamline will be required later.
- (12) Control passes repeatedly back to Step 9 until the last station has been processed.
- (13) The overall convergence of the calculation is checked, unless this point has been reached at the completion of the first pass. The following two criteria should be applied:
  - (a) The stream functions along each streamline should be constant, and
  - (b) The meridional velocities computed at each mesh point should not change from one pass to the next.

If convergence has been achieved, the desired output data may be generated (tolerances are discussed below). If convergence has not been achieved, and subject to a maximum permitted number of passes, control is passed to Step 14.

- (14) The estimated streamline pattern for the entire machine may now be updated, the intent being to have the stream functions established at Station 1

maintained throughout. A simple interpolation of the streamline coordinates at each computing station using the Station 1 stream functions, provides the new, raw streamline coordinates. In order to ensure a stable, convergent procedure, a relaxation factor must be applied to the coordinate changes that the interpolation provides. This is discussed further below.

- (15) All streamwise gradients are updated.
- (16) Control passes back to Step 3, to start another pass.
- (17) The relaxation factor required when relocating the streamlines is:

$$RF = \frac{1}{1 + \frac{A}{6} \left( \frac{h}{\Delta m} \right)^2} \quad (10.41)$$

where  $h/\Delta m$  is the ratio of the station length to the meridional distance to the closest adjacent station,  $A = (1 - M_m^2)$  if tangential velocity component is given, and  $A = \cos^2 \beta (1 - M_m^2)$  if relative flow angle is given. Occasionally, the constant shown as 6 in Eq.(10.41) needs to be set to 4. Typically, this occurs when many stations are placed relatively close together, for example, when multiple stations are placed within blade-rows. Although not supported by theory, it seems reasonable to limit the Mach numbers to maximum values of perhaps 0.7. These equations are based on Wilkinson [10].

Nested iterative calculations are involved in the solution procedure, and appropriate tolerances to judge convergence of each loop are needed. A master tolerance should be defined by the input data, and this can be used for the outermost loop, that is, the streamline location and meridional velocity convergence check. For normal engineering purposes, a tolerance of 1 or 2 parts in  $10^4$  is adequate and easily obtained. If the results are to be used in a gradient-based optimization scheme, it may be necessary to reduce the master tolerance to 1 part in  $10^7$  or less.

Tolerances should be reduced by a factor of 5 or 10 for each successive nesting level. Several additional calculations can be integrated in the above procedure. Bleed flows can be modeled by arranging that, at the first station, the desired bleed flows be contained within the outermost streamtubes. One or more streamlines are then removed at appropriate stations along the flow path. Overall pressure ratio can be specified for off-design calculations by estimating the corresponding flow and then refining the estimate as the solution proceeds. Logic is required to handle the various failure situations that may occur, for example, choking of the machine when the estimated flow is too large. Loss models may be incorporated so that when a converged solution is achieved, it includes losses consistent with the derived flow both for design and off-design calculations. During design calculations, blade

geometry may also be simultaneously generated.

A major shortcoming of the basic streamline curvature method lies in its use of the Euler equations: no transfer of momentum or heat occurs in the transverse direction. This is in contrast to both real flows and CFD solutions of the Navier-Stokes equations. The result is that, realistic span-wise variations of losses cannot be specified through multi-stage machines because extreme profiles of properties typically develop. This can be largely overcome by superimposing a "mixing" calculation upon the basic streamline curvature calculation. While there is evidence that some of the transverse effects, such as radial wake movement in axial compressors, are not random (Adkins and Smith [11]), a simple turbulent mixing calculation, as suggested in Gallimore [12], seems to capture most important effects. With this addition to the flow-model, off-design calculations can be performed that include realistic span-wise variations of losses which result in realistic profiles of properties.

A momentum equation of somewhat different form to Eq. (10.29) and (10.31) is shown in Smith [13]. Here, the gradient of meridional velocity in the meridional direction is eliminated through use of the continuity equation and streamline characteristics. This is aesthetically pleasing (at least) as it removes a streamwise gradient from those that must be updated from pass to pass. Further, for cases with few stations, such as when there are stations at blade-row edges only, intuitively it seems that the local streamwise velocity gradient might be better estimated from the streamline pattern than from velocities at points beyond a blade-row. In a case with many stations within all blade-rows, the differences should be very small. As presented, Smith's equation is less useful because it is framed in the radial rather than an arbitrary direction.

### 10.3 Compressor Examples

In this section, some representative examples of the use of a streamline curvature program are shown. A design is pursued that aims to meet the targets defined by the NASA UEET project for a four-stage aero-engine HP-compressor with an overall pressure ratio of 12:1.

The first calculations use the compressor preliminary design (CPD) procedure that is included in the program. In this mode of operation, streamline slope and curvature are assumed zero, and the blade forces acting in the station-wise direction are ignored. Radial stations are placed at each blade-row edge so that a greatly simplified form of the momentum equation applies. These simplifications are made in order to stabilize and speed the solution. An optimizer package is used to derive the design of maximum efficiency that meets various constraints that the designer specifies. Figure 10.3 shows the resulting variation of design-point efficiency with first rotor tip speed. The optimum corrected tip of 589 m/sec results from the over-ambitious project goals. For the purposes of this rather academic exercise, a tip speed of 548 m/sec was selected as a possible compromise between mechanical and aerodynamic considerations. Figure 10.4 is the corresponding flow-path.



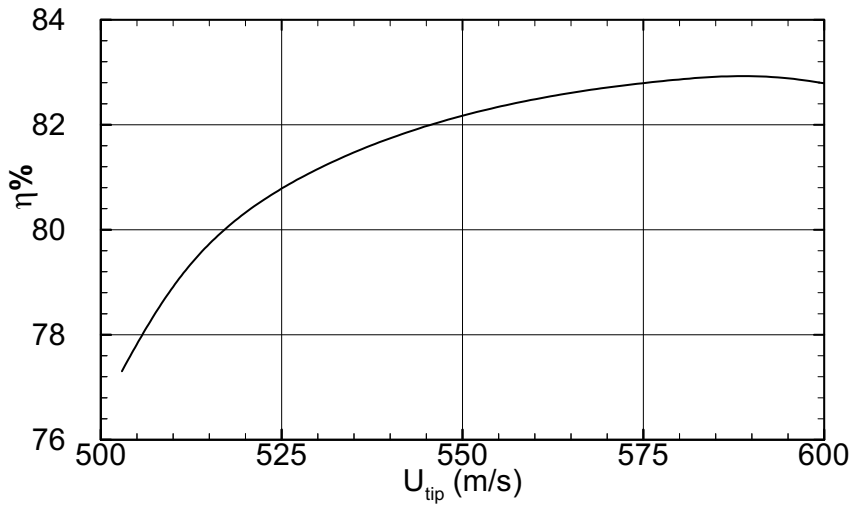
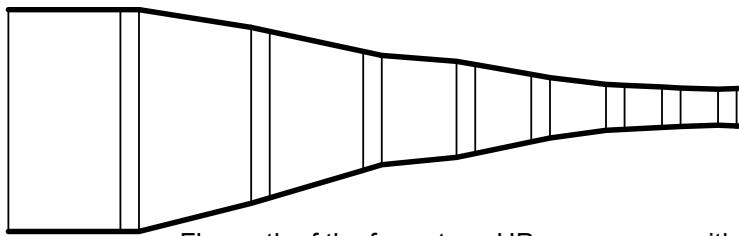


**Fig. 10. 3:** Efficiency versus tip speed for NASA -UEET four stage compressor with pressure ratio 12:1



Flowpath of the four-stage HP-compressor with pressure ratio 12:1. first iteration

**Fig. 10. 4:** Preliminary flow path of NASA-UEET for stage compressor.

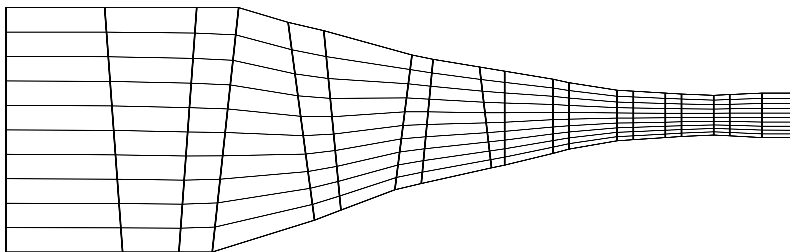


**Fig. 10. 5:** Second iteration flow path of NASA UEET four-stage HP-compressor with pressure ratio 12:1

The next calculation made is a "first detail design". As for the CPD, total pressure is specified at rotor exits and tangential velocity component is specified at stator exits. Whereas for the CPD, losses are estimated based solely on flow angles and Mach numbers, in the detail, design blading, albeit generic, is derived by the design procedure. The flow model simplifications that were used for the CPD are removed. Figure 10.5 shows the computed streamline pattern. The first detail design assumed generic blading (DCA profiles), but with a first rotor tip Mach number approaching 1.5, a more sophisticated design is required. This is accomplished by adding stations within the blade-rows, and then distributing the effects of the blade-rows amongst the station-to-station intervals.

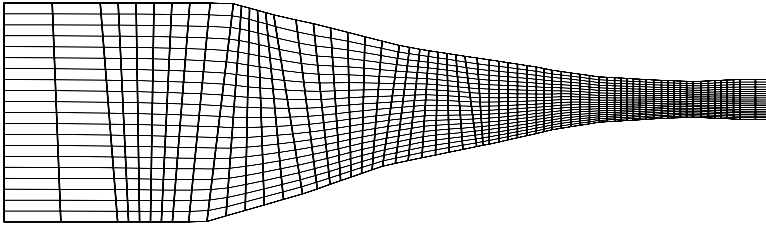


**Fig. 10. 6:** Refined final flow path of NASA UEET four-stage HP-compressor with pressure ration 12:1

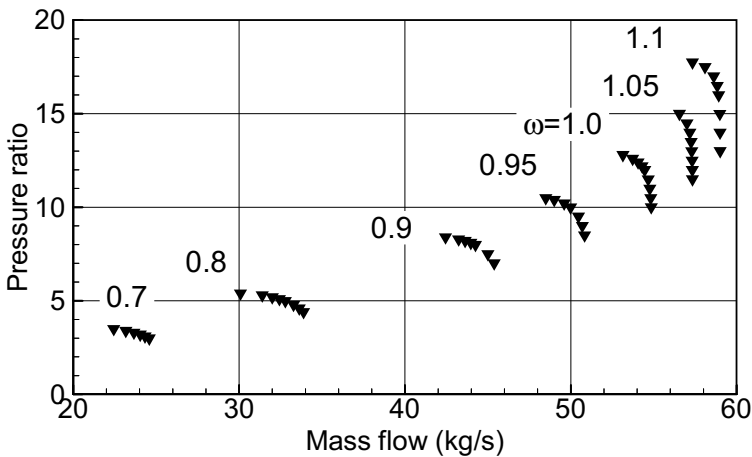


**Fig. 10. 7:** Performance map of NASA UEET four-stage HP-compressor

Figure 10.6 shows the streamline pattern that is computed. Given the blading specification that the calculation created, an off-design calculation can now be performed; Figure 10.7 shows the resulting performance map.



**Fig. 10.8:** Solid model of two adjacent blades.

Figure 10.8 shows a solid-model of two adjacent blades looking from downstream. The procedure described may be used to produce a final design, although nowadays it will generally be used to create a "first candidate" for further analysis using CFD.

## 10.4 Turbine Example, Compound Lean Design

The streamline curvature method has been most heavily used in turbine design and analysis. The area of turbine applications covers the HP-, IP- and LP-parts of steam turbines, power generation gas turbines and aircraft jet engines. In case of IP- and LP-turbine design, the radial equilibrium condition is achieved based on a prescribed variation of the absolute tangential velocity component along a computing station. The computational results allow designing highly three-dimensional blades that follow the calculated flow angles using the streamline curvature method. Once the design process is completed and the relative angle distribution is known, off-design calculation can be performed on a routine basis using the streamline curvature method. The condition for an accurate off-design performance prediction is the implementation of appropriate loss calculation models, as we discussed in Chapter 6.

In contrast to IP- and LP-turbines, HP-turbines have relatively small aspect ratios that cause the hub and tip secondary flow zones come closer occupying a major portion of the blade height. The secondary flow zones caused by a system of hub and

tip vortices induce drag forces resulting in an increase of secondary flow losses that account for almost 40-50% of the entire stage total pressure loss. The most efficient methods of reducing the secondary flow zones in HP-turbines is utilizing the *compound lean blade* design by varying the lean angle. In recent years, engine manufacturers extensively use leaned blades for new turbines as well as for retrofitting the existing HP-turbines. The application of compound lean design to both stator and rotor blades has been proven as an effective measure of secondary flow control. Using the streamline curvature method, optimizing the lean angle, and placing appropriate turbine profiles from hub to tip, the HP-turbine blades are designed with stage efficiencies that are more than 1.5% higher than those with cylindrical blades. The efficacy of the 3-D leaned design in suppressing the secondary flow is demonstrated in efficiency and performance studies on a three-stage HP-turbine by Schobeiri and his co-workers, among others [14] and [15]. A subsequent comparative study, [16], using cylindrical blades with identical blade height, hub and tip diameter, and inlet conditions, revealed a significant efficiency improvement of more than  $\Delta \eta \approx 2\%$  for the rotor with 3-D compound lean blades compared to the one with cylindrical blades. Abhari and his co-workers [17] performed similar investigations on two bladings. They reported that the compound-lean blading has a clear performance advantage of 1% to 1.5% in cascade efficiency over the cylindrical blading. While a combined stator-rotor blade lean has proven to bring efficiency improvement, the stator-row only lean does not seem to have a noticeable efficiency improvement effect, as reported among others in [18]. Before discussing some recent experimental and numerical results, we present in the following the basics of blade lean nomenclature.

#### 10.4.1 Blade Lean Geometry

Figure 10.9 shows three sets of stator blades with different lean configurations: (a) exhibits conventional cylindrical blades which have been traditionally used in HP-turbines, (b) shows a blade set with constant lean blades, and (c) a blade set with a symmetric lean configuration also called compound lean. The compound lean blade is characterized by a circumferential displacement of the profiles from hub to tip that results in blade surface bow. As Fig. 10.19 (top) shows, the pressure surface has a convex bow, while the suction surface bow is concave. The corresponding lean distribution at the trailing edge is shown in Fig. 10.19 (bottom). The compound lean blade may have a symmetric lean angle distribution with  $+\epsilon$  at the hub and  $-\epsilon$  at the tip. It may also have an asymmetric  $\epsilon$ -distribution with  $+\epsilon_1$  at the hub and  $-\epsilon_2$  at the tip, Fig. 10.19 bottom (c) and (d). The compound mean may also be confined to the hub and tip regions only, as shown in Fig. 10.19(e).

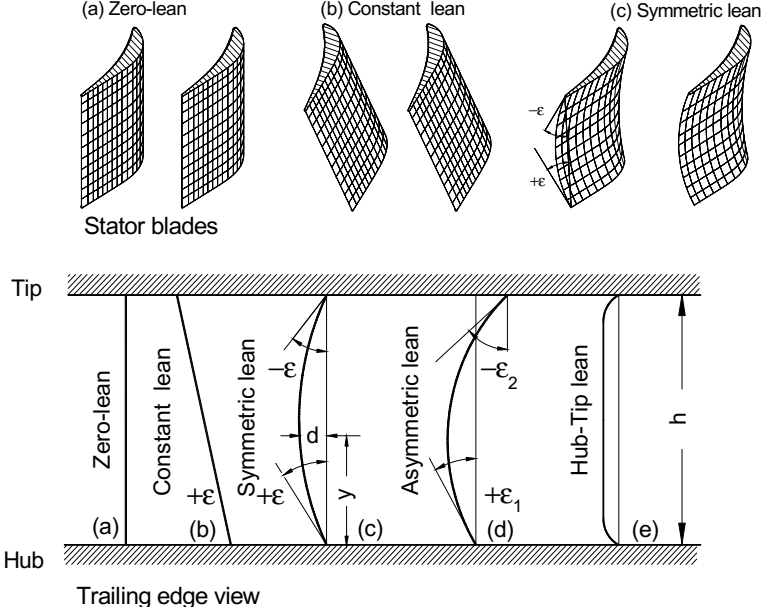


Fig. 10. 9: Blades with different lean geometry.

#### 10.4.2 Calculation of Compound Lean Angle Distribution

The general case of an asymmetric compound lean is shown in Fig. 10.9 (d), the dimensionless circumferential displacement distribution (bow)  $\delta = d/h$  can be expressed in terms of a second order polynomial as a function of the dimensionless height  $\eta = y/h$  as:

$$\delta = a_0 + a_1 \eta + a_2 \eta^2 \quad (10.42)$$

Using the following boundary conditions:

$$\begin{aligned} \eta = 0 &\Rightarrow \delta = 0, \quad \eta = 0 \Rightarrow \frac{d\delta}{d\eta} = \tan \varepsilon_1, \\ \eta = 1 &\Rightarrow \frac{d\delta}{d\eta} = \tan (-\varepsilon_2) \end{aligned} \quad (10.43)$$

we find the coefficients:

$$a_0 = 0, \quad a_1 = \tan \varepsilon_1, \quad a_2 = -\frac{1}{2}(\tan \varepsilon_1 + \tan \varepsilon_2) \quad (10.44)$$

and Eq. (10.42) becomes:

$$\delta = \tan \varepsilon_1 \eta - \frac{1}{2}(\tan \varepsilon_1 + \tan \varepsilon_2) \eta^2 \quad (10.45)$$

The position of the maximum bow can be calculated from

$$\eta_{\max} = \frac{\tan \varepsilon_1}{\tan \varepsilon_1 + \tan \varepsilon_2}, \quad \delta_{\max} = \frac{1}{2} \left( \frac{\tan^2 \varepsilon_1}{\tan \varepsilon_1 + \tan \varepsilon_2} \right) \quad (10.46)$$

Figure 10.10 shows the dimensionless circumferential displacement  $\delta$  (bow) as a function of dimensionless variable  $\eta$  for three different  $\varepsilon_1$ -values with  $\varepsilon_2$  as a parameter.

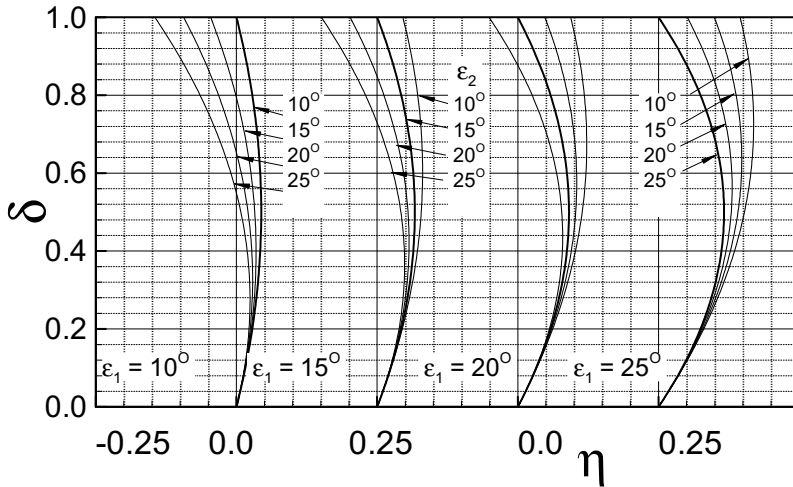
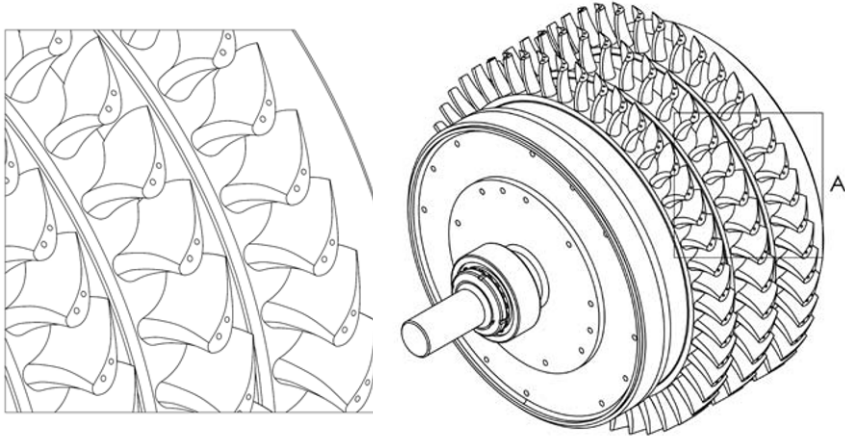


**Fig. 10.10:** Dimensionless bow  $\delta$  as a function of dimensionless blade height  $\eta$  for constant lean angles  $\varepsilon_1$  with  $\varepsilon_2$  as parameter. Note: The abscissa is displaced by 0.25.

Keeping  $\varepsilon_1$  at a time constant and varying  $\varepsilon_2$  from  $10^\circ$  to  $25^\circ$  changes the bow curvature. As shown, for  $|\varepsilon_2| = |\varepsilon_1|$  the bow is symmetric. For  $|\varepsilon_2| > |\varepsilon_1|$  the bow increases progressively, whereas for  $|\varepsilon_2| < |\varepsilon_1|$ , it decreases. In an actual design process, these two angles serve as design parameters in addition to the stage parameters we discussed in Chapter 4. An optimization process with the efficiency as the target can be used in conjunction with the streamline curvature method to achieve the optimum efficiency.

### 10.4.3 Example: Three-Stage Turbine Design

Using the streamline curvature method, multi-stage HP-, IP-, and LP turbines can be optimally designed. As an example, a three-stage HP-research turbine with 3-D compound lean blades is presented in Fig. 10.11 with the specifications in Table 1.



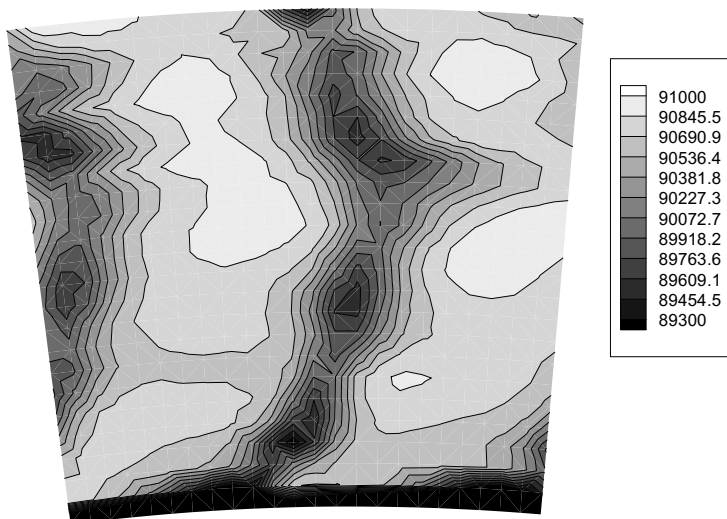
**Fig. 10.11:** A three-stage high efficiency HP-research turbine with 3-D compound lean blades with enlarged details A, TPFL.

Table 1 : Turbine research facility data

Item	Specification	Item	Specification
Stage number	$N = 3$	Mass flow	$\dot{m}_s = 3.728 \text{ kg/s}$
Tip diameter	$D_t = 685.8 \text{ mm}$	Speed range	$n = 1800\text{-}2800 \text{ rpm}$
Hub diameter	$D_h = 558.8 \text{ mm}$	Inlet pressure	$p_{in} = 101.356 \text{ kPa}$
Blade height	$H_b = 63.5 \text{ mm}$	Exit pressure	$p_{ex} = 71.708 \text{ kPa}$
Blade number	Stator row 1 = 58	Stator row 2 = 52	Stator row 3 = 56
Blade number.	Rotor row 1 = 46	Rotor row 2 = 40	Rotor row 3 = 44

As seen in Fig. 10.11, the blades have an asymmetric lean with  $|\epsilon_2| < |\epsilon_1|$ .

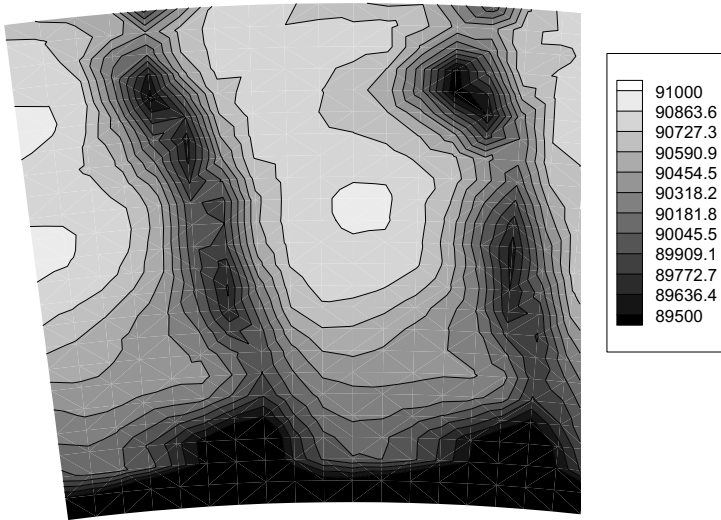
The effectiveness of the compound lean in reducing the secondary flow zone is illustrated in Fig. 10.12. It shows the total pressure contour upstream of the second stator for both rotors.



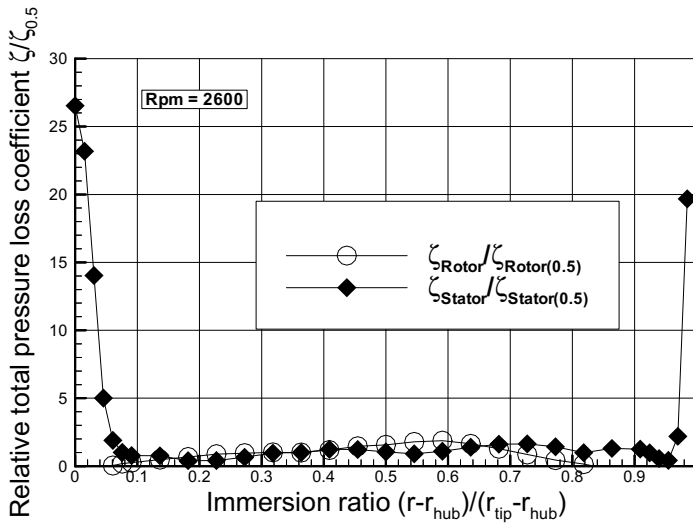
**Fig. 10.12:** Total pressure contours upstream of the second stator ring, rotor with compound lean, rotational speed 2600 rpm, TPFL.

Figure 10.12 shows the distribution of the total pressure upstream of the second stator (downstream of the first rotor row). The secondary flow zones are expressed by decreasing the contour level in Fig. 10.12 (dark zones). The wakes generated by the preceding rotor blade cause a reduction of the total pressure. For comparison purposes, the total pressure distribution downstream of the second stator pertaining to a second rotor with identical blade counts and boundary conditions but with cylindrical blades is shown in Fig. 10.13. As seen, major total pressure reduction at the hub exists for the cylindrical blade. The comparison of these two blade types shows that a substantial reduction of total pressure loss is achieved by the compound lean design of stator and the rotor blades. The dimensionless loss coefficient in Fig. 10.14, shows that the typical large region of secondary flow that is present in cylindrical blades has been diminished by the compound lean design.





**Fig. 10.13:** Total pressure contours upstream of the second stator rings for rotor with cylindrical blades, rotational speed 2600 rpm.



**Fig. 10.14:** Radial distribution of the relative total pressure loss coefficients for stator and rotor row for a TPFL-rotor with compound lean stator and rotor blades,

## 10.5 Special Cases

The radial equilibrium calculation method derived in section 10.3 was applied to design compressor stages using numerical procedures. The method is also applicable to turbine stages as we saw in the previous section. For few special cases, analytical solutions can be found. For this purpose, simplifications are necessary to obtain analytical solutions.

### 10.5.1 Free Vortex Flow

The flow under consideration is assumed to fulfill the conditions: isentropic:  $\nabla s = 0$ , isoenergetic:  $\nabla H = 0$ , and constant meridional velocity,  $dV_m = 0$ . With these conditions and the assumption that the streamlines have no curvature, (cylindrical stream surfaces), Eq. (10.11) reduces for a bladeless channel, where  $F_m = F_n = 0$ , and  $(\Phi - \gamma) = 0$ , to:

$$d(rV_u) = 0, \quad rV_u = \text{const.} \quad (10.47)$$

Eq.(10.47) is the radial equilibrium equation for a free vortex flow, called Beltrami free vortex flow. Figure 10.15 shows the radial pressure distribution within an annular channel for different circumferential Mach number.

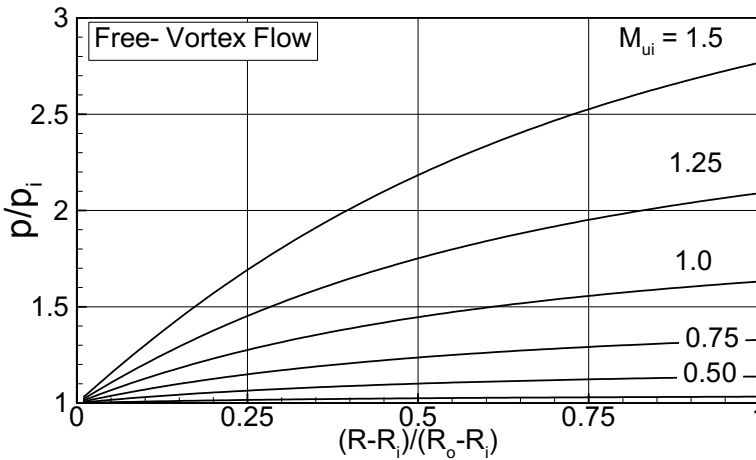


**Fig. 10.15:** Radial pressure distribution of a free-vortex flow with the hub circumferential Mach number  $M_u$  as parameter.

### 10.5.2 Forced vortex flow

This type of flow is assumed to satisfy the following conditions: isentropic,  $\bar{V}_s = 0$  isoenergetic,  $\nabla H = 0$ , and circumferential velocity is proportional to the radius:  $V_u \propto r$  or  $V_u = K r$ , where  $K$  is a constant. With these conditions and the assumption that the streamlines have no curvature, (cylindrical stream surface), Eq. (10.11) reduces for a bladeless channel, where  $F_m = F_n = 0$ , and  $(\phi - \gamma) = 0$ , to:

$$V_m \frac{dV_m}{dr} = - \frac{K r d(K r^2)}{r dr} = -2K^2 r dr \quad (10.48)$$

Integration of Eq. (10.48) gives:

$$V_m^2 = 2K^2(r_i^2 - r^2) + V_{mi}^2 \quad (10.49)$$

The constant  $K$  is:

$$K = \frac{V_u}{r} = \frac{V_{ui}}{r_i} \quad (10.50)$$

Using the angle definition in Fig. 10.3 where  $\beta$  is replaced by  $\alpha$  and  $V_{ui} = V_{mi} \tan \alpha_i$  and introducing Eq.(10.50) into (10.49) gives:

$$\left[ \frac{V_m}{V_{mi}} \right]^2 = 1 - 2 \tan^2 \alpha_i \left[ \left( \frac{r}{r_i} \right)^2 - 1 \right] \quad (10.51)$$

Figure 10.16 shows the radial distribution of pressure .

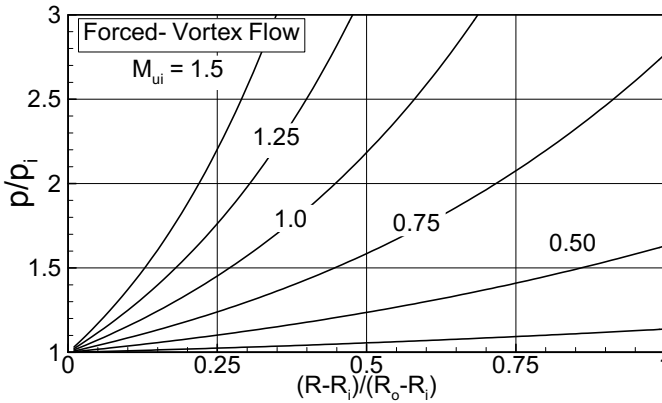


**Fig. 10.16:** Pressure distribution of a forced-vortex flow with the hub circumferential Mach number  $M_{ui}$  as parameter.

### 10.5.3 Flow with constant flow angle

The flow under consideration is assumed to fulfill the conditions: isentropic,  $\nabla s = 0$  isoennergetic,  $\nabla H = 0$ , and constant inlet flow angle,  $d\alpha_1 = 0$ . With these conditions and the assumption that the streamlines have no curvature, (cylindrical stream surface), Eq. (10.11) then reduces for a bladeless channel, where  $F_m = F_n = 0$ , and  $(\phi - \gamma) = 0$ , to:

$$V_m \frac{dV_m}{dr} = - \frac{V_u}{r} \frac{d(rV_u)}{dr} \quad (10.52)$$

Since

$$V_u = V_m \tan \alpha_1 \quad (10.53)$$

introducing Eq.(10.52) into (10.53) leads to:

$$\frac{dV_m}{V_m} = - \sin^2 \alpha_1 \frac{dr}{r} \quad (10.54)$$

Integrating Eq.(10.54) gives:

$$\frac{V_m}{V_{mi}} = \left( \frac{r_i}{r} \right)^{\sin^2 \alpha_1} \quad (10.55)$$

Figure 10.17 depicts the axial velocity ratio as a function of the radius ratio with  $\alpha_1$  as parameter.

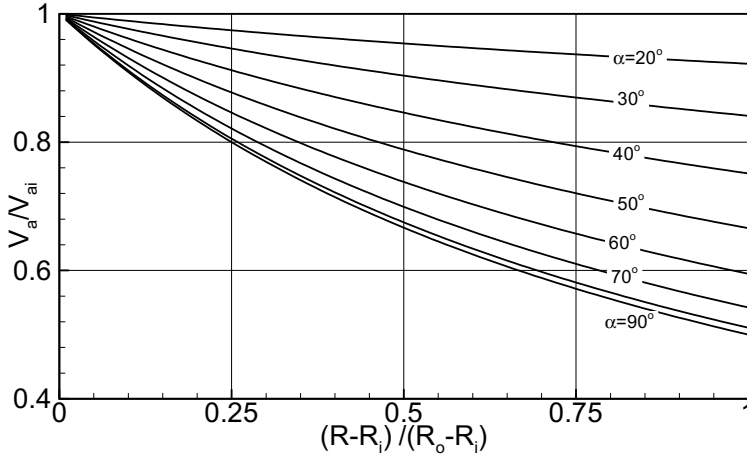


**Fig. 10.17:** Axial velocity ratio as a function of dimensionless blade height with the inlet angle as parameter.

## References

1. Wu, Chung-Hua, 1952, "A general Theory of Three-Dimensional Flow in Subsonic and Supersonic Turbomachines of Axial-, Radial, and mixed-Flow Types," NACA technical Note 2604, Washington, D.C., January 1952.
2. Lakshminarayana, B., 1996, "Fluid Dynamics and Heat Transfer of Turbomachinery," John Wiley & Sons.
3. Vavra, M.H., 1960, "Aero-Thermodynamics and Flow in Turbomachines," John Wiley & Sons, Inc.
4. Schobeiri, M.T., 2012 "Turbomachinery Flow Physics and Dynamic Performance, Second Edition, Springer-Verlag.
5. Novak, R.A., and Hearsey, R.M., "A Nearly Three Dimensional Intra blade Computing System for Turbomachinery, Part I & II," *Journal of Fluid Engineering*, Vol 99, pp. 154-166.
6. Wilkinson, D.H., 1972, "Calculation of Blade-to-Blade Flow in Turbomachine by Streamline Curvature," British ARC R&M 3704.
7. Wennerstrom, A.J., 1974, "On the Treatment of body Forces in the radial Equilibrium Equation of Turbomachinery," Traupel-Festschrift, Juris-Verlag, Zürich.
8. Hearsey, R.M., 2003, "Computer Program HT 0300 version 2.0," Hearsey technology, Bellevue, Washington .
9. Horlock, J.H., 1971, "On Entropy Production in Adiabatic Flow in Turbomachines," *ASME Journal of Basic Engineering*, pp. 587-593.
10. Wilkinson, D.H., 1969, Stability, Convergence and Accuracy of 2-Dimensional Streamline Curvature Methods Using Quasi-Orthogonals, Proceedings of the Institution of Mechanical Engineers, Volume 184, 1979-1970.
11. Adkins, G.G., Smith L.H., 1982, "Spanwise Mixing in Axial-Flow Turbomachines," *ASME Journal of Engineering for Gas Turbines and Power*, Vol. 104, pp. 97-110.
12. Gallimore, S.J., 1986, "Spanwise mixing in Multistage Axial Flow Compressors: Part II – Throughflow Calculations Including Mixing," *ASME Journal of Turbomachinery*, Vol. 108, pp. 10-16.
13. Smith, L.H. Jr., 1966, "The Radial-Equilibrium Equation of Turbomachinery," *ASME Journal of Engineering for Power*, January, 1966, pp. 1-12.
14. Schobeiri, M.T., Gilarranz, J., and Johansen, E., "Final Report on: Efficiency, Performance, and Interstage Flow Field Measurement of Siemens-Westinghouse HP-Turbine Blade Series 9600 and 5600," September, 1999.
15. Schobeiri M.T., Gillaranz, J.L., and Johansen E.S., 2000, "Aerodynamic and Performance Studies of a Three Stage High Pressure Research Turbine with 3-D Blades, Design Point and Off-Design Experimental Investigations," Proceedings of ASME Turbo Expo 2000, 2000-GT-484.
16. Schobeiri, M.T., Suryanarayanan, A., Jerman, C., and Neuenschwander, T., 2004, "A Comparative Aerodynamic and performance study of a three-stage high pressure turbine with 3-D bowed blades and cylindrical blades,"

- Proceedings of ASME Turbo Expo 2004 Power of Land Air and Sea, June 14 - 17, 2004, Vienna, Austria, paper GT2004-53650.
17. Treiber, M., Abhari, R.S., and Sell, M., 2002, "Flow Physics and Vortex Evolution in Annular Turbine Cascades," ASME, GT-2002-30540, Proceedings of ASME TURBO EXPO 2002, June 3-6, 2002, Amsterdam, The Netherlands.
  18. Rosic, B. and Xu, L., 2008, " Blade Lean and Shroud Leakage Flows in Low Aspect Ratio Turbines," Proceedings of ASME Turbo Expo 2008: Power for Land, Sea and Air, June 9-13, 2008, Berlin, Germany, GT2008-50565

## 11 Nonlinear Dynamic Simulation of Turbomachinery Components and Systems

The following chapters deal with the nonlinear transient simulation of turbomachinery systems. Power generation steam and gas turbine engines, combined cycle systems, aero gas turbine engines ranging from single spool engines to multi-spool high pressure core engines with an afterburner for supersonic flights, rocket propulsion systems and compression systems for transport of natural gas with a network of pipeline systems are a few examples of systems that heavily involve turbomachinery components.

Considering a power generation gas turbine engine as a turbomachinery system that is designed for steady state operation, its behavior during routine startups, shot downs, and operational load changes significantly deviates from the steady state design point. Aero gas turbine engines have to cover a relatively broad operational envelope that includes takeoff, low and high altitude operation conditions, as well as landing. During these operations, the components are in a continuous dynamic interaction with each other, where the aero-thermodynamic as well as the mechanical load conditions undergo temporal changes. As an example, the acceleration/deceleration process causes a dynamic mismatch between the turbine and compressor power resulting in temporal change of the shaft speed.

In the above cases, the turbomachinery systems are subjected to the operating modes that are specific to the system operation. Besides these foreseeable events, there are unforeseeable operation scenarios that are not accounted for when designing the system. System failures, such as, blade loss during a routine operation, loss of cooling mass flow through the cooled turbine blades, adverse operation conditions that force the compressor component to surge, and failure of the control system, are a few examples of adverse operational conditions. In all of these operations, the system experiences adverse changes in total fluid and the thermodynamic process leading to greater aerodynamic, thermal and mechanical stress conditions.

The trend in the development of gas turbine technology during the past decades shows a continuous increase in efficiency, performance, and specific load capacities. This trend is inherently associated with increased aerodynamic, thermal, and mechanical stresses. Under this circumstance, each component operates in the vicinity of its aerodynamic, thermal and mechanical stress limits. Adverse operational conditions that cause a component to operate beyond its limits can cause structural damages as a result of increased aerodynamic, thermal, and structural stresses. To prevent this, the total response of the system, including aerodynamic, thermal, and mechanical responses must be known in the stage of design and development of new

turbomachinery systems.

This chapter describes the physical basis for the non-linear dynamic simulation of gas turbine components and systems. A brief explanation of the numerical method for solution is followed by detailed dynamic simulation of several components described in the following chapters.

## 11.1 Theoretical Background

Dynamic behavior of turbomachinery components and systems can generally be described by conservation laws of fluid mechanics and thermodynamics ([1], [2], [3], [4]). The fluid dynamic process that takes place within an inertial system is, as a rule, unsteady. The steady state, a special case, always originates from an unsteady condition during which the temporal changes in the process parameters have largely come to a standstill. Considering this fact, the conservation laws of fluid dynamics and thermodynamics must be rearranged such that temporal changes of thermo-fluid dynamic quantities are expressed in terms of spatial changes. A summary of relevant equations are found in [5]. For an unsteady flow, the conservation of mass derived in [5], Chapter 3, Eq. (3.4), is called upon:

$$\frac{\partial \rho}{\partial t} = -\nabla \cdot (\rho \mathbf{V}) \quad (11.1)$$

Equation (11.1) expresses the *temporal change* of the density in terms of *spatial change* of the specific mass flow. Neglecting the gravitational force, the Cauchy equation of motion in [5] Eq.(3.22) was derived as:

$$\frac{\partial \mathbf{V}}{\partial t} + \mathbf{V} \cdot \nabla \mathbf{V} = \frac{1}{\rho} \nabla \cdot \mathbf{\Pi} \quad (11.2)$$

We rearrange Eq. (11.2) to include the density in the temporal and spatial derivatives by implementing the continuity equation [5], Eq.(3.4)

$$\frac{\partial(\rho \mathbf{V})}{\partial t} + \nabla \cdot (\rho \mathbf{V} \mathbf{V}) = \nabla \cdot \mathbf{\Pi} \quad (11.3)$$

where the stress tensor  $\mathbf{\Pi}$  can be decomposed into the pressure and shear stress tensor as follows:

$$\mathbf{\Pi} = \mathbf{Ip} + \mathbf{T} \quad (11.4)$$

with  $\mathbf{Ip}$  as the normal stress and  $\mathbf{T}$  as the shear stress tensor. Inserting Eq. (11.4) into



(11.3) results in

$$\frac{\partial(\rho \mathbf{V})}{\partial t} + \nabla \cdot (\rho \mathbf{V} \mathbf{V}) = -\nabla p + \nabla \cdot \mathbf{T} \quad (11.5)$$

Equation (11.5) directly relates the temporal changes of the specific mass flow to the spatial changes of the velocity, pressure, and shear stresses. For the complete description of the unsteady flow process, the total energy equation that includes mechanical and thermal energy balance is needed. Referring to [5], Eq. (3.58) and neglecting the gravitational contribution, we find for mechanical energy that:

$$\rho \frac{D}{Dt} \left( \frac{V^2}{2} \right) = -\mathbf{V} \cdot \nabla p + \nabla \cdot (\mathbf{T} \cdot \mathbf{V}) - \mathbf{T} : \mathbf{D} \quad (11.6)$$

Equation (11.6) exhibits the mechanical energy balance in differential form. The first term on the right-hand side represents the mechanical energy contribution due to the pressure gradient. The second term is the contribution of the shear stress work. The third term represents the production of the irreversible mechanical energy due to the shear stress. It dissipates as heat and increases the internal energy of the system. Before rearranging Eq. (11.6) and performing the material differentiation, we revert to the thermal energy balance, [5], Eq. (3.66),

$$\rho \frac{Du}{Dt} = -\nabla \cdot \dot{\mathbf{q}} - p \nabla \cdot \mathbf{V} + \mathbf{T} : \mathbf{D} \quad (11.7)$$

The combination of the mechanical and thermal energy balances, Eq. (11.6) and (11.7), results in:

$$\rho \frac{D}{Dt} \left( u + \frac{V^2}{2} \right) = -\nabla \cdot \dot{\mathbf{q}} + \nabla \cdot (\mathbf{\Pi} \cdot \mathbf{V}) \quad (11.8)$$

Since all components of a turbomachinery system are considered open systems, it is appropriate to use enthalpy  $h$  rather than internal energy  $u$ . The state properties  $h$  and  $u$  can be expressed as a function of other state properties such as  $T$ ,  $v$ ,  $p$  etc.

$$u = u(T, v), \quad du = \left( \frac{\partial u}{\partial T} \right)_v dT + \left( \frac{\partial u}{\partial v} \right)_T dv \quad (11.9)$$

$$h = h(T, p), \quad dh = \left( \frac{\partial h}{\partial T} \right)_p dT + \left( \frac{\partial h}{\partial p} \right)_T dp \quad (11.10)$$

where  $T$  and  $h$  are the absolute static temperature and enthalpy. With the definitions:

$$c_v = \left( \frac{\partial u}{\partial T} \right)_v, \quad c_p = \left( \frac{\partial h}{\partial T} \right)_p \quad (11.11)$$

and the application of the first law, the following relation between  $c_p$  and  $c_v$  is established:

$$c_p = c_v + \left[ \left( \frac{\partial u}{\partial v} \right)_T + p \right] \left( \frac{\partial v}{\partial T} \right)_p \quad (11.12)$$

For the open cycle gas turbines and also jet engines with moderate pressure ratios, the working fluids air and combustion gases behave practically like ideal gases whose internal energy is only a function of temperature and not volume. This circumstance considerably simplifies the interconnection of different thermodynamic properties if the equation of state of ideal gases is considered:

$$pv = RT \quad (11.13)$$

Introducing the Gibbs's enthalpy function:

$$h = u + pv \quad (11.14)$$

the differentiation gives:

$$dh = \frac{\kappa}{\kappa - 1} d(pv) \text{ and } dh = \kappa du \quad (11.15)$$

with

$$c_p - c_v = R \quad \text{and} \quad \frac{c_p}{c_v} = \kappa \quad (11.16)$$

As a consequence, for ideal gases, the result of this operation leads to:

$$\left( \frac{\partial v}{\partial T} \right)_p = \frac{R}{p} \quad (11.17)$$

Thus, the state properties,  $u$  and  $h$ , as well as the specific heat capacities  $c_p$ , and  $c_v$  and their ratio  $\kappa$  are solely functions of temperature. This is also valid for combustion gases with approximately ideal behavior. For combustion gases, there is a parametric dependency of the above stated properties and the fuel-air ratio. After this preparation, Eq. (11.7) can be written in terms of  $h$  and  $p$ :

$$\rho \frac{Dh}{Dt} = -\nabla \cdot \dot{\mathbf{q}} + \frac{Dp}{Dt} + \mathbf{T}:\mathbf{D} \quad (11.18)$$

with Eq. (11.15) and considering the continuity equation (11.54), the substantial change of the static pressure is:

$$\frac{Dp}{Dt} = \frac{\kappa - 1}{\kappa} \rho \frac{Dh}{Dt} - p \nabla \cdot \mathbf{V} \quad (11.19)$$

Introducing Eq. (11.19) into (11.18):

$$\frac{\rho}{\kappa} \frac{Dh}{Dt} = -\nabla \dot{\mathbf{q}} - p \nabla \cdot \mathbf{V} + \mathbf{T}:\mathbf{D} \quad (11.20)$$

The combination of thermal energy equation (11.20) and mechanical energy equation (11.6) leads to:

$$\begin{aligned} \frac{\partial H}{\partial t} = & -k \mathbf{V} \cdot \nabla H - (\kappa - 1) \left( \frac{1}{\rho} \nabla \cdot (\rho \mathbf{V})(H + K) + \frac{\mathbf{V} \cdot \partial(\rho \mathbf{V})}{\rho \partial t} \right) \\ & + \left( -\frac{\kappa \nabla \cdot \dot{\mathbf{q}}}{\rho} + \frac{\kappa}{\rho} \nabla \cdot (\mathbf{V} \cdot \mathbf{T}) \right) \end{aligned} \quad (11.21)$$

with  $H = h + V^2/2$  as the total enthalpy and  $K = V^2/2$  the kinetic energy. Equation (11.21) can also be obtained by introducing the relationship between the pressure and enthalpy into Eq.(11.21). The total enthalpy can be expressed in terms of total temperature:

$$\begin{aligned} c_p \frac{\partial T_0}{\partial t} = & -k \mathbf{V} \cdot \nabla (c_p T_0) - (\kappa - 1) \left( \frac{1}{\rho} \nabla \cdot (\rho \mathbf{V})(c_p T_0 + K) + \frac{\mathbf{V} \cdot \partial(\rho \mathbf{V})}{\rho \partial t} \right) \\ & + \left( -\frac{\kappa \nabla \cdot \dot{\mathbf{q}}}{\rho} + \frac{\kappa}{\rho} \nabla \cdot (\mathbf{V} \cdot \mathbf{T}) \right) \end{aligned} \quad (11.22)$$

Finally, the total energy equation in terms of total pressure can be established by inserting Eqs. (11.14) and (11.16) into Eq. (11.8):

$$\begin{aligned} \frac{\partial P}{\partial t} = & -\kappa \nabla \cdot (\mathbf{V}P) + (\kappa - 1)[-\nabla \cdot (\dot{\mathbf{q}}) + \nabla \cdot (\mathbf{V} \cdot \mathbf{T})] \\ & - (\kappa - 2) \left[ \frac{\partial (\rho K)}{\partial t} + \nabla \cdot (\rho K \mathbf{V}) \right] + \rho \mathbf{g} \cdot \mathbf{V} \end{aligned} \quad (11.23)$$

where  $P = p + \rho V^2/2$  is the total pressure. Equations (11.21), (11.22) and (11.23) express the same physical principles, namely the law of conservation of energy in two different forms. In physical terms, they are fully equivalent and mathematically convertible to each other. As shown in the following chapters, one or the other of these equations is called upon in conjunction with the other laws to deal with various dynamic problems. For example, in dealing with an unsteady exchange of energy and impulse, it is useful to apply the differential equation for total temperature. If the principal goal of a problem is the determination of the unsteady changes in pressure, the total pressure differential equation should be used. A summary of the working equations is given in Table 11.1.

**Table 11.1:** Summary of thermo-fluid dynamic equations.

Equations In terms of substantial derivatives $D/Dt$	Eq. No.
Continuity $\frac{D\rho}{Dt} = -\rho \nabla \cdot \mathbf{V}$	(11.1)
Motion $\rho \frac{D\mathbf{V}}{Dt} = \nabla \cdot \mathbf{T} + \rho \mathbf{g}$	(11.2)
Mechanical Energy $\rho \frac{D}{Dt} \left( \frac{V^2}{2} \right) = -\mathbf{V} \cdot \nabla p + \nabla \cdot (\mathbf{T} \cdot \mathbf{V}) - \mathbf{T} : \mathbf{D} + \rho \mathbf{V} \cdot \mathbf{g}$	(11.6)

**Table 11.1:** Summary of thermo-fluid dynamic equations (continued).

Equations in terms of substantial and local derivatives $D/Dt$ , $\partial/\partial t$	Eq. No.
Equation of thermal energy in terms of $u$ $\rho \frac{Du}{Dt} = -\nabla \cdot \dot{\mathbf{q}} - p \nabla \cdot \mathbf{V} + \mathbf{T} : \mathbf{D}$	(11.7)
Equation of thermal energy in terms of $h$ for ideal gas $\rho \frac{Dh}{Dt} = -\nabla \cdot \dot{\mathbf{q}} + \frac{Dp}{Dt} + \mathbf{T} : \mathbf{D}$	(11.18)
Equation of total enthalpy $\rho \frac{DH}{Dt} = \rho \frac{D}{Dt} \left( h + \frac{V^2}{2} \right) = \frac{\partial p}{\partial t} + -\nabla \cdot \dot{\mathbf{q}} + \nabla \cdot (\mathbf{T} \cdot \mathbf{V}) + \rho \mathbf{V} \cdot \mathbf{g}$	(11.21)
Equation of thermal energy in terms of $c_v$ and $T$ for ideal gas $\rho c_v \frac{DT}{Dt} = -\nabla \cdot \dot{\mathbf{q}} - p \nabla \cdot \mathbf{V} + \mathbf{T} : \mathbf{D}$	(11.7)
Equation of thermal energy in terms of $c_p$ and $T$ for ideal gas $\rho c_p \frac{DT}{Dt} = -\nabla \cdot \dot{\mathbf{q}} + \frac{Dp}{Dt} + \mathbf{T} : \mathbf{D}$	(11.7)
Equation of continuity $\frac{\partial \rho}{\partial t} = -\nabla \cdot (\rho \mathbf{V})$	(11.1)
Equation of motion in terms of total stress tensor $\frac{\partial(\rho \mathbf{V})}{\partial t} + \nabla \cdot (\rho \mathbf{V} \mathbf{V}) = \nabla \cdot \mathbf{\Pi}$	(11.2)
Equation of motion, stress tensor decomposed $\frac{\partial(\rho \mathbf{V})}{\partial t} + \nabla \cdot (\rho \mathbf{V} \mathbf{V}) = -\nabla p + \nabla \cdot \mathbf{T}$	(11.5)
Equation of mechanical energy including $\rho$ $\frac{\partial(\rho K)}{\partial t} = -\nabla \cdot (\rho K \mathbf{V}) - \mathbf{V} \cdot \nabla p + \nabla \cdot (\mathbf{T} \cdot \mathbf{V}) + \rho \mathbf{V} \cdot \mathbf{g}$	(11.6)
Equation of thermal energy in terms of $u$ for ideal gas $\frac{\partial(\rho u)}{\partial t} = -\nabla \cdot (\rho u \mathbf{V}) - \nabla \cdot \dot{\mathbf{q}} - p \nabla \cdot \mathbf{V} + \mathbf{T} : \nabla \mathbf{V}$	(11.7) Re- arranged

**Table 11.1:** Summary of thermo-fluid dynamic equations (continued).

Equations in terms of local derivatives $\partial/\partial t$	Eq. No.
Equation of thermal energy in terms of $h$ for ideal gas $\frac{\partial(\rho h)}{\partial t} = -\nabla \cdot (\rho h \mathbf{V}) - \nabla \cdot \dot{\mathbf{q}} + \frac{Dp}{Dt} + \mathbf{T} : \nabla \mathbf{V}$	(11.7) Rearranged
Equation of thermal energy in terms of $c_v$ and $T$ $\frac{\partial(\rho c_v T)}{\partial t} = -\nabla \cdot (\rho u \mathbf{V}) - \nabla \cdot \dot{\mathbf{q}} - p \nabla \cdot \mathbf{V} + \mathbf{T} : \nabla \mathbf{V}$	(11.7) Re-arranged
Equation of thermal energy in terms of static $h$ for ideal gases $\frac{\partial(\rho c_p T)}{\partial t} = -\nabla \cdot (\rho h \mathbf{V}) - \nabla \cdot \dot{\mathbf{q}} + \frac{Dp}{Dt} + \mathbf{T} : \nabla \mathbf{V}$	(11.7) Re-arranged
Energy equation in terms of total enthalpy $\begin{aligned} \frac{\partial H}{\partial t} = & -k \mathbf{V} \cdot \nabla H - (\kappa - 1) \left( \frac{1}{\rho} \nabla \cdot (\rho \mathbf{V})(H + K) + \frac{\mathbf{V} \cdot \partial(\rho \mathbf{V})}{\rho \partial t} \right) \\ & + \left( -\frac{\kappa \nabla \cdot \mathbf{q}}{\rho} + \frac{\kappa}{\rho} \nabla \cdot (\mathbf{V} \cdot \mathbf{T}) \right) \end{aligned}$	(11.21)
Energy equation in terms of total temperature $\begin{aligned} c_p \frac{\partial T_0}{\partial t} = & -k \mathbf{V} \cdot \nabla (c_p T_0) - (\kappa - 1) \left( \frac{1}{\rho} \nabla \cdot (\rho \mathbf{V})(c_p T_0 + K) + \frac{\mathbf{V} \cdot \partial(\rho \mathbf{V})}{\rho \partial t} \right) \\ & - \left( \frac{\kappa \nabla \cdot \dot{\mathbf{q}}}{\rho} - \frac{\kappa}{\rho} \nabla \cdot (\mathbf{V} \cdot \mathbf{T}) \right) \end{aligned}$	(11.22)
Energy equation in terms of total pressure $\begin{aligned} \frac{\partial P}{\partial t} = & -k \nabla \cdot (\mathbf{V} P) - (\kappa - 1) [\nabla \cdot \dot{\mathbf{q}} + \nabla \cdot (\mathbf{V} \cdot \mathbf{T})] \\ & - (\kappa - 2) \left[ \frac{\partial(\rho K)}{\partial t} + \nabla \cdot (\rho K \mathbf{V}) \right] \end{aligned}$	(11.23)

## 11.2 Preparation for Numerical Treatment

The thermo-fluid dynamic equations discussed above constitute the theoretical basis describing the dynamic process that takes place within a turbomachinery component during a transient operation. A four-dimensional time space treatment that involves the Navier solution is, at least for the time being, out of reach. For simulation of dynamic behavior of a turbomachine that consists of many components, it is not primarily important to calculate the unsteady three-dimensional flow processes in great detail. However, it is critical to accurately predict the response of each individual component as a result of dynamic operation conditions. A one-dimensional time dependent calculation procedure provides sufficiently accurate results. In the following, the conservation equations are presented in index notation. For the one-dimensional time dependent treatment, the basic equations are prepared first by setting the index  $i = 1$  in Eqs. (11.24-11.27).

## 11.3 One-Dimensional Approximation

The thermo-fluid dynamic equations discussed above constitute the theoretical basis describing the dynamic process that takes place within a turbomachinery component during a transient operation. A four-dimensional time space treatment that involves the Navier solution is, at least for the time being, out of reach. For simulation of the dynamic behavior of a turbomachine that consists of many components, it is not primarily important to calculate the unsteady three-dimensional flow processes in great detail. However, it is critical to accurately predict the response of each individual component as a result of dynamic operation conditions. A one-dimensional time dependent calculation procedure provides sufficiently accurate results. For this purpose, firstly, the basic equations are prepared for the one-dimensional treatment.

### 11.3.1 Time Dependent Equation of Continuity

In Cartesian coordinate system the continuity equation (11.1) is:

$$\frac{\partial \rho}{\partial t} = - \frac{\partial}{\partial x_i} (\rho V_i) \quad (11.24)$$

Equation (11.24), after setting  $\rho V_1 = \dot{m}/S$ , becomes:

$$\frac{\partial \rho}{\partial t} = - \frac{\partial}{\partial x_1} \left( \frac{\dot{m}}{S} \right) \quad (11.25)$$

with  $x_1 \equiv x$  as the length in streamwise direction and  $S = S(x)$  the cross sectional area of the component under investigation. Equation (11.25) expresses the fact that the temporal change of the density is determined from the spatial change of the

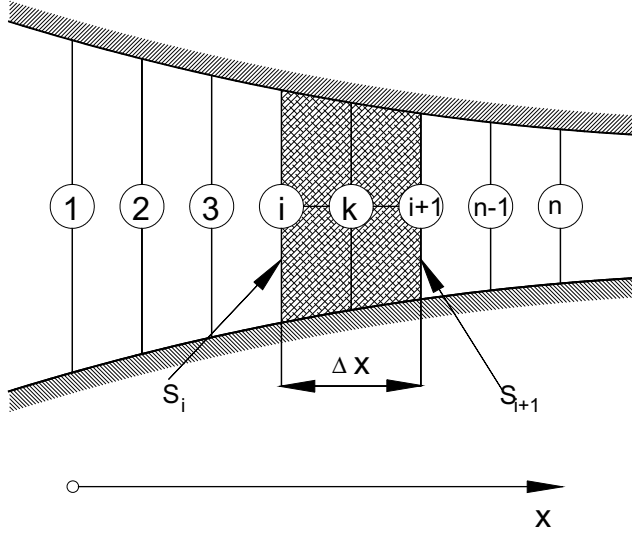


**Fig. 11.1:** Discretization of an arbitrary flow path with variable cross section  $S = S(x)$ .

specific mass flow within a component. The partial differential Eq. (11.25) can be approximated as an ordinary differential equation by means of conversion into a difference equation. The ordinary differential equation can then be solved numerically with the prescribed initial and boundary conditions. For this purpose, the flow field is equidistantly divided into a number of discrete zones with prescribed length,  $\Delta X$ , inlet and exit cross sections  $S_i$  and  $S_{i+1}$  as Fig. 11.1 shows. The quantities pertaining to the inlet and exit cross sections represent averages over the inlet and exit heights. For the annular nozzles and diffusers the quantities are thought of as averages taken in circumferential as well as radial direction. Using the nomenclature in Fig. 11.1, Eq. (11.25) is approximated as:

$$\frac{\partial \rho_k}{\partial t} = - \frac{1}{\Delta x} \left( \frac{\dot{m}_{i+1}}{S_{i+1}} - \frac{\dot{m}_i}{S_i} \right) \quad (11.26)$$

with  $\dot{m}_i$  and  $\dot{m}_{i+1}$  as the mass flows at stations  $i$  and  $i+1$  with the corresponding cross sections. For a constant cross section, Eq.(11.26) reduces to:

$$\frac{\partial \rho_k}{\partial t} = - \frac{1}{\Delta x S} (\dot{m}_{i+1} - \dot{m}_i) = - \frac{1}{\Delta V} (\dot{m}_{i+1} - \dot{m}_i) \quad (11.27)$$



with  $\Delta V = \Delta x S$  as the volume of the element  $k$  enclosed between the surfaces  $i$  and  $i+1$ . The index  $k$  refers to the position at  $\Delta x/2$ , Fig. 11.1

### 11.3.2 Time Dependent Equation of Motion

The index notation of the momentum equation (11.5) is:

$$\frac{\partial(\rho V_i)}{\partial t} = -\frac{\partial}{\partial x_j}(\rho V_i V_j) - \frac{\partial p}{\partial x_i} + \frac{\partial T_{ij}}{\partial x_j} \quad (11.28)$$

In the divergence of the shear stress tensor in Eq. (11.28),  $\nabla \cdot \mathbf{T} = e_i \partial T_{ij} / \partial x_j$  represents the shear force acting on the surface of the component. For a one-dimensional flow, the only non-zero term is  $\partial \tau_{21} / \partial x_2$ . It can be related to the wall shear stress  $\tau_w$  which is a function of the friction coefficient  $c_f$ .

$$\tau_w = c_f \frac{\rho}{2} V^2 \quad (11.29)$$

In the near of the wall, the change of the shear stress can be approximated as the difference between the wall shear stress  $\tau_w$  and the shear stress at the edge of the boundary layer, which can be set as  $\tau_e \approx 0$

$$\left( \frac{\partial \tau_{12}}{\partial x_2} \right)_{x_2=0} = \frac{\tau_e - \tau_w}{\Delta x_2} = - \frac{\tau_w}{\Delta x_2} \quad (11.30)$$

The distance in  $\Delta x_2$  can be replaced by a characteristic length such as the hydraulic diameter  $D_h$ . Expressing the wall shear stress in Eq. (11.30) by the skin friction coefficient

$$\left( \frac{\partial \tau_{12}}{\partial x_2} \right)_{x_2=0} = -c_f \frac{\rho}{D_h} \frac{V^2}{2} = -c_f \frac{\dot{m}^2}{2 D_h \rho S^2} \quad (11.31)$$

and inserting Eq. (11.31) into the one-dimensional version of Eq. (11.28), we obtain

$$\frac{\partial \dot{m}}{\partial t} = - \frac{\partial}{\partial x_1} (\dot{m} V_1 + p S) + (\dot{m} V_1 + p S) \frac{1}{S} \frac{\partial S}{\partial x_1} - c_f \frac{\dot{m}^2}{2 D_h \rho S} \quad (11.32)$$

Equation (11.32) relates the temporal change of the mass flow to the spatial change of the velocity, pressure and shear stress momentums. As we will see in the following sections, mass flow transients can be accurately determined using Eq. (11.32). Using the nomenclature from Fig. 11.1, we approximate Eq. (11.32) as:

$$\begin{aligned} \frac{\partial \dot{m}_k}{\partial t} = & -\frac{1}{\Delta x} (\dot{m}_{i+1} V_{i+1} - \dot{m}_i V_i + p_{i+1} S_{i+1} - p_i S_i) \\ & + \left( \frac{\dot{m}_k V_k + P_k S_k}{S_k} \right) \left( \frac{S_{i+1} - S_i}{\Delta x} \right) - c_f \frac{m_k^2}{2 D_{h_k} \rho_k S_k} \end{aligned} \quad (11.33)$$

For a constant cross section, Eq. (11.33) is modified as:

$$\frac{\partial \dot{m}_k}{\partial t} = -\frac{1}{\Delta x} [\dot{m}_{i+1} V_{i+1} - \dot{m}_i V_i + (p_{i+1} - p_i) S] - c_f \frac{m_k^2}{2 D_{h_k} \rho_k S_k} \quad (11.34)$$

### 11.3.3 Time Dependent Equation of Total Energy

The energy equation in (11.21), in terms of total enthalpy, is written in index notation

$$\begin{aligned} \frac{\partial H}{\partial t} = & -k V_i \frac{\partial H}{\partial x_i} - \frac{\kappa - 1}{\rho} \left[ (H + K) \frac{\partial(\rho V_i)}{\partial x_i} + \frac{V_i \cdot \partial(\rho V_i)}{\partial t} \right] \\ & - \frac{\kappa}{\rho} \left[ \frac{\partial \dot{q}_i}{\partial x_i} - \frac{\partial(V_j T_{ij})}{\partial x_i} \right] \end{aligned} \quad (11.35)$$

expressing the total enthalpy, Eqs. (11.35), in terms of total temperature results in:

$$\begin{aligned} \frac{\partial(c_p T_0)}{\partial t} = & -k V_i \frac{\partial(c_p T_0)}{\partial x_i} - \frac{\kappa - 1}{\rho} \left[ (c_p T_0 + K) \frac{\partial(\rho V_i)}{\partial x_i} + \frac{V_i \cdot \partial(\rho V_i)}{\partial t} \right] \\ & - \frac{\kappa}{\rho} \left[ \frac{\partial \dot{q}_i}{\partial x_i} - \frac{\partial(V_j T_{ij})}{\partial x_i} \right] \end{aligned} \quad (11.36)$$

For calculating the total pressure, the equation of total energy is written in terms of total pressure already derived as Eq. (11.23), which is presented for the Cartesian coordinate system as:

$$\begin{aligned} \frac{\partial P}{\partial t} = & -\kappa \frac{\partial}{\partial x_i} (P V_i) - (\kappa - 1) \left( \frac{\partial \dot{q}_i}{\partial x_i} - \frac{\partial}{\partial x_i} (V_j T_{ij}) \right) \\ & - (\kappa - 2) \left( \frac{\partial (\rho K V_i)}{\partial x_i} + \frac{\partial (\rho K)}{\partial t} \right) \end{aligned} \quad (11.37)$$

Before treating the energy equation, the shear stress work needs to be evaluated:

$$\nabla \cdot (\mathbf{T} \cdot \mathbf{V}) = \delta_{ij} \delta_{km} \frac{\partial (\tau_{jk} V_m)}{\partial x_i} = \frac{\partial (\tau_{ij} V_j)}{\partial x_i} \quad (11.38)$$

For a two-dimensional flow, Eq. (11.38) gives

$$\nabla \cdot (\mathbf{T} \cdot \mathbf{V}) = \frac{\partial (\tau_{ij} V_j)}{\partial x_i} = \frac{\partial (\tau_{11} V_1 + \tau_{12} V_2)}{\partial x_1} + \frac{\partial (\tau_{21} V_1 + \tau_{22} V_2)}{\partial x_2} \quad (11.39)$$

Assuming a one-dimensional flow with  $V_2 = 0$ , the contribution of the shear stress work Eq. (11.39) is reduced to

$$\nabla \cdot (\mathbf{T} \cdot \mathbf{V}) = \frac{\partial (\tau_{11} V_1)}{\partial x_1} \approx \frac{(\tau_{11 \text{inlet}} V_{\text{inlet}} - \tau_{11 \text{exit}} V_{\text{exit}})}{\Delta x_1} \quad (11.40)$$

The differences in  $\tau_{11}$  at the inlet and exit of the component under simulation stem from velocity deformation at the inlet and exit. Its contribution, however, compared to the enthalpy terms in the energy equation, is negligibly small. Thus, the one-dimensional approximation of total energy equation (11.35) in terms of total enthalpy reads:

$$\frac{\partial H}{\partial t} = -\frac{\kappa \dot{m}}{\rho S} \frac{\partial H}{\partial x_1} - \frac{\kappa - 1}{\rho} \left[ (H + K) \frac{\partial}{\partial x_1} \left( \frac{\dot{m}}{S} \right) + \frac{1}{2\rho S^2} \frac{\partial \dot{m}^2}{\partial t} \right] - \frac{\kappa}{\rho} \frac{\partial}{\partial t} \quad (11.41)$$

For a steady state case without changes of specific mass  $\dot{m}/S$ , Eq. (11.41) leads to:

$$\frac{\partial H}{\partial x_1} = - \frac{S}{\dot{m}} \frac{\partial \dot{q}_i}{\partial x_i} \quad (11.42)$$

Assuming a constant cross section and mass flow, Eq. (11.42) gives

$$\frac{\partial H}{\partial x_1} = - \frac{\partial}{\partial x_1} \left( \frac{S \dot{q}_i}{\dot{m}} \right) \quad (11.43)$$

Integrating Eq. (11.43) in a streamwise direction results in:

$$H_{out} - H_{in} = - \left( \frac{S}{\dot{m}} \right) \Delta \dot{q} \quad (11.44)$$

for Eq. (11.44) to be compatible with the energy equation, a modified version of Eq. (4.75) is presented.

$$H_{Out} - H_{In} = q + w_{Shaft} \quad (11.45)$$

Equating (11.44) and (11.45) in the absence of a specific shaft power, the following relation between the heat flux vector and the heat added or rejected from the element must hold:

$$q = - \left( \frac{S}{\dot{m}} \right) \Delta \dot{q} \quad (11.46)$$

From (11.46), it immediately follows that

$$\Delta \dot{q} = - \frac{q \dot{m}}{S} = - \frac{\dot{Q}}{S} \quad (11.47)$$

where  $\dot{Q}$  is the thermal energy flow added to or rejected from the component. In the presence of shaft power, the specific heat in Eq. (11.47) may be replaced by the sum of the specific heat and specific shaft power:

$$\Delta \dot{q} = - \frac{\dot{m}q + \dot{m}l_m}{S} = - \left( \frac{\dot{Q} + L}{S} \right) \quad (11.48)$$

Equation (11.48) in differential form in terms of  $\dot{Q}$  and  $L$  is

$$\frac{\partial \dot{q}}{\partial x} = - \frac{\partial}{\partial x} \left( \frac{\dot{m}q + \dot{m}l_m}{S} \right) = - \frac{\partial}{\partial x} \left( \frac{\dot{Q} + L}{S} \right) \quad (11.49)$$

With Eq. (11.49), we find:

$$\begin{aligned} \frac{\partial H}{\partial t} = & - \frac{\kappa \dot{m}}{\rho S} \frac{\partial H}{\partial x_1} - \frac{\kappa - 1}{\rho} \left[ (H + K) \frac{\partial}{\partial x_1} \left( \frac{\dot{m}}{S} \right) + \frac{1}{2\rho S^2} \frac{\partial \dot{m}^2}{\partial t} \right] \\ & - \frac{\kappa}{\rho} \frac{\partial}{\partial x} \left( \frac{\dot{Q} + L}{S} \right) \end{aligned} \quad (11.50)$$

Using the nomenclature in Fig. 11.1, Eq. (11.50) is written as:

$$\begin{aligned} \frac{\partial H}{\partial t} = & -\kappa_k \frac{\dot{m}_k}{\rho_k S_k} \left( \frac{H_{i+1} - H_i}{\Delta x} \right) - \\ & - \left( \frac{\kappa - 1}{\rho} \right)_k \left[ \left( \frac{H_k + K_k}{\Delta x} \right) \left( \frac{\dot{m}_{i+1}}{S_{i+1}} - \frac{\dot{m}_i}{S_i} \right) + \frac{\dot{m}_k}{\rho_k S_k^2} \frac{\partial \dot{m}_{i+1}}{\partial t} \right] - \\ & - \frac{\kappa_k}{\rho_k} \left( \frac{\Delta \dot{Q} + \Delta L}{\Delta V} \right) \end{aligned} \quad (11.51)$$

In terms of total temperature, Eq. (11.51) is rearranged as:

$$\begin{aligned}
\frac{\partial c_p T_0}{\partial t} = & -\kappa_k \frac{\dot{m}_k}{\rho_k S_k} \left( \frac{c_p T_{0_{i+1}} - c_p T_{0_i}}{\Delta x} \right) - \\
& - \left( \frac{\kappa - 1}{\rho} \right)_k \left[ \left( \frac{c_p T_{0_k} + K_k}{\Delta x} \right) \left( \frac{\dot{m}_{i+1}}{S_{i+1}} - \frac{\dot{m}_i}{S_i} \right) + \frac{\dot{m}_k}{\rho_k S_k^2} \frac{\partial \dot{m}_{i+1}}{\partial t} \right] - (11.52) \\
& - \frac{\kappa_k}{\rho_k} \left( \frac{\Delta \dot{Q} + \Delta L}{\Delta V} \right)
\end{aligned}$$

In terms of total pressure, Eq. (11.37) is:

$$\begin{aligned}
\frac{\partial P}{\partial t} = & -\kappa \frac{\partial}{\partial x_1} (P V_1) - (\kappa - 1) \left( \frac{\partial \dot{q}_1}{\partial x_1} - \frac{\partial}{\partial x_1} (V_j T_{1j}) \right) \\
& - (\kappa - 2) \left( \frac{\partial (\rho K V_1)}{\partial x_1} + \frac{\partial (\rho K)}{\partial t} \right)
\end{aligned} \quad (11.53)$$

which is approximated as:

$$\begin{aligned}
\frac{\partial P_k}{\partial t} = & -\frac{\kappa_k}{\Delta x} \left( \frac{\dot{m}_{i+1} p_{i+1}}{\rho_{i+1} S_{i+1}} - \frac{\dot{m}_i p_i}{\rho_i S_i} \right) - (\kappa_k - 1) \left( \frac{\dot{m}_k q_k}{\Delta V} + c_{f_k} \frac{\dot{m}_{i+1} \dot{m}_i}{2 D_{h_{i+1}} S_{i+1} \rho} \right. \\
& - (\kappa_k - 2) \frac{\dot{m}_k}{\rho_k S_k^2} \left( \frac{1}{2} \frac{\dot{m}_k}{\rho_k} \frac{1}{\Delta x} \left( \frac{\dot{m}_{i+1}}{S_{i+1}} - \frac{\dot{m}_i}{S_i} \right) + \frac{\partial \dot{m}_{i+1}}{\partial t} \right) \\
& \left. - \frac{(\kappa_k - 2)}{2 \Delta x} \left( \frac{\dot{m}_{i+1}^3}{\rho_{i+1}^2 S_{i+1}^3} - \frac{\dot{m}_i^3}{\rho_i^2 S_i^3} \right) \right)
\end{aligned} \quad (11.54)$$

with:

$$\rho_k = \frac{1}{R} \left( \frac{p_{i+1} + p_i}{T_{i+1} + T_i} \right), \quad c_{p_k} = \frac{H_{i+1} - H_i}{T_{i+1}^* - T_i^*}, \quad \kappa_k = \frac{c_{p_k}}{c_{p_k} - R} \quad (11.55)$$

## 11.4 Numerical Treatment

The above partial differential equations can be reduced to a system of ordinary differential equations by a one-dimensional approximation. The simulation of a complete gas turbine system is accomplished by combining individual components that have been modeled mathematically. The result is a system of ordinary differential equations that can be dealt with numerically. For weak transients, Runge-Kutta or Predictor-Corrector procedures may be used for the solution. When strong transient processes are simulated, the time constants of the differential equation system can differ significantly so that difficulties must be expected with stability and convergence with the integration methods. An implicit method avoids this problem. The system of ordinary differential equations generated in a mathematical simulation can be represented by:

$$\frac{d\mathbf{X}}{dt} = \mathbf{G}(\mathbf{X}, t) \quad (11.56)$$

with  $\mathbf{X}$  as the state vector sought. If the state vector  $\mathbf{X}$  is known at the time  $t$ , it can be approximated as follows for the time  $t+dt$  by the trapezoidal rule:

$$\mathbf{X}_{t+\Delta t} = \mathbf{X}_t + \frac{1}{2}\Delta t(\mathbf{G}_{t+\Delta t} + \mathbf{G}_t) \quad (11.57)$$

Because the vector  $\mathbf{X}$  and the function  $\mathbf{G}$  are known at the time  $t$ , i.e.,  $\mathbf{X}_t$  and  $\mathbf{G}_t$  are known, Eq. (11.57) can be expressed as:

$$\mathbf{X}_{t+\Delta t} - \mathbf{X}_t - \frac{1}{2}\Delta t(\mathbf{G}_{t+\Delta t} + \mathbf{G}_t) = \mathbf{F}(\mathbf{X}_{t+\Delta t}) \quad (11.58)$$

As a rule, the function  $\mathbf{F}$  is non-linear. It can be used to determine  $\mathbf{X}_{t+dt}$  by iteration when  $\mathbf{X}_t$  is known. The iteration process is concluded for the time  $t+dt$  when the convergence criterion

$$\frac{\mathbf{X}_t^{(k+1)} - \mathbf{X}_t^{(k)}}{\mathbf{X}_t^{(k+1)}} < \epsilon \quad (11.59)$$

is fulfilled. If the maximum number of iterations,  $k = k_{\max}$ , is reached without fulfilling the convergence criterion, the time interval  $\Delta t$  is halved, and the process of iteration is repeated until the criterion of convergence is met. This integration process, based on the implicit one-step method described by Liniger and Willoughby [6] is reliable for the solution of stiff differential equations. The computer time required depends, first, on the number of components in the system and, second, on the nature

of the transient processes. If the transients are very strong, the computer time can be 10 times greater than the real time because of the halving of the time interval. For weak transients, this ratio is less than 1.

## References

1. Schobeiri, M.T., 1985, "Aero-Thermodynamics of Unsteady Flows in Gas Turbine Systems," Brown Boveri Company, Gas Turbine Division Baden Switzerland, BBC-TCG-51.
2. Schobeiri, T., 1985b, "COTRAN, the Computer Code for Simulation of Unsteady Behavior of Gas Turbines," Brown Boveri Company, Gas Turbine Division Baden Switzerland, BBC-TCG-53.
3. Schobeiri, T., 1986: "A General Computational Method for Simulation and Prediction of Transient Behavior of Gas Turbines," ASME-86-GT-180.
4. Schobeiri, M.T., Abouelkheir, M., Lippke, C., 1994, "GETRAN: A Generic, Modularly Structured Computer Code for Simulation of Dynamic Behavior of Aero-and Power Generation Gas Turbine Engines," an honor paper, ASME Transactions, *Journal of Gas Turbine and Power*, Vol. 1, pp. 483-494.
5. Schobeiri, M.,T., 2012, "Turbomachinery Flow Physics and Dynamic Performance," ISBN 978-3-642-2467-6, Springer Heidelberg, New York.
6. Liniger, W., Willoughby, R., 1970, "Efficient integration methods for stiff systems of ordinary differential equations," SIAM. Numerical Analysis Vol. 7, No. 1.



## 12 Generic Modeling of Turbomachinery Components and Systems

A turbomachinery *system* such as a power generation gas turbine engine, a thrust generation aero-engine, rocket propulsion, or a small turbocharger, consist of several *sub-systems* that we call *components* ([1],[2],[3],[4]). Each component is an autonomous entity with a defined function within the system. Inlet nozzles, exit diffusers, combustion chambers, compressors, and turbines are a few component examples. A component may consist of several *sub-components*. A turbine or a compressor stage exhibits such a sub-component. The numerical models of components are called *modules*.

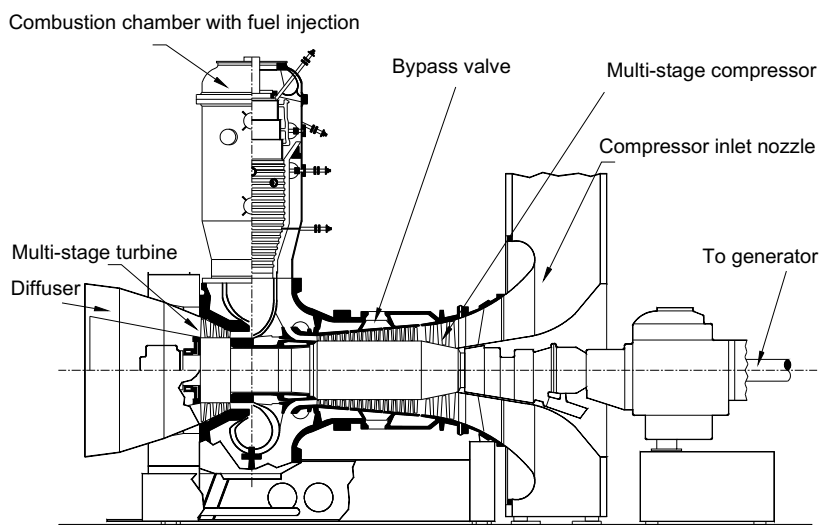


**Fig. 12.1:** Single-spool power generation gas turbine engine, BBC-GT-9 with major components.

The gas turbine engine shown in Fig. 12.1 composed of an inlet nozzle, a multistage compressor component with cooling air extraction and bypass systems. The cooling air extraction provides cooling mass flow for the shaft, the high pressure turbine, and the mixing air for reducing the combustion chamber exit temperature. The bypass system prevents the compressor from getting into a rotating stall and surge during the startup and shutdown procedures (see Chapter 15). To reduce the compressor exit flow velocity and thus the kinetic energy, the remaining compressor mass flow passes through a diffuser before entering the combustion chamber. In the following combustion chamber component, fuel is added to establish the required turbine inlet

temperature. The following multistage turbine component placed on the same shaft as the compressor, drives the compressor and the generator. The configuration of the compressor and the turbine components placed on the same shaft is called a *spool*. As seen in Fig. 12.1, the spool shaft is coupled with the generator shaft, which converts the net turbine power into electrical power.

Figure 12.2 illustrates a decomposition of a *twin-spool* engine into its major components. It consists of (1) a *high pressure-spool*, the so-called gas generator that encompasses the multistage high pressure compressor (HP-compressor), combustion chamber component, and the high pressure turbine (HP-turbine) component, (2) a *low pressure-spool* shaft connects the low pressure compressor with the low pressure turbine component, (3) the combustion chamber, (4) an inlet diffuser and exit nozzle. The two spools are connected aerodynamically. The mass flow, with high kinetic energy exiting from the last stage of the HP-turbine stage, impinges on the first stator of the LP-turbine, and is further expanded within the LP-component and the following thrust nozzle, that provides the required kinetic energy for thrust generation. Besides the major components shown in Fig. 12.1 and 12.2, there are several other components such as pipes that serve the transport of mass flow from compressor to turbine for cooling purposes, valves with the operation ramp defined by the control system, control systems, lubrication systems, bearings, electric motors for power supply, etc.

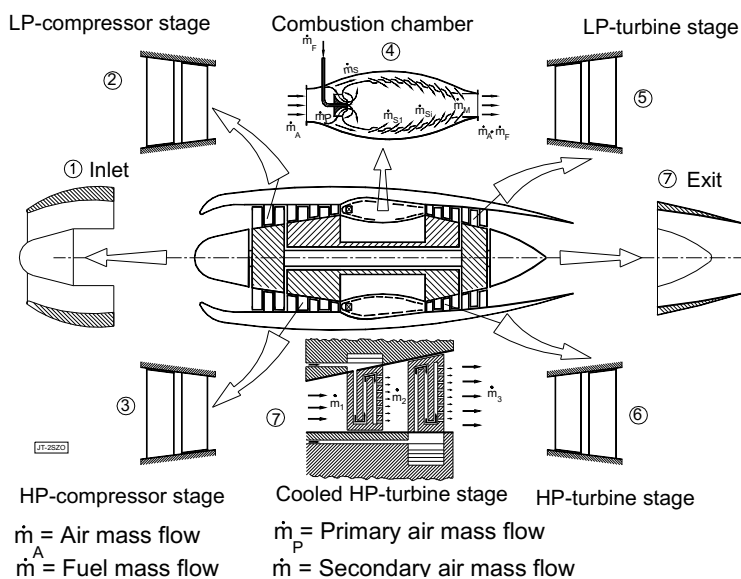


**Fig. 12.2** A twin-spool aero-gas turbine with its major components.

## 12.1 Generic Component, Modular Configuration

These components shown in Fig. 12.1 and 12.2 are common to a small or large gas turbine engine regardless if it is a power generation engine, a thrust generation, or an engine that serves as a turbocharger. They can be modeled as modules to assemble a complete system ranging from a single spool power generation gas turbine to the most complicated of rocket propulsion systems. The components can be categorized into three groups according to their functions. The representatives of each of these groups are described below.

### 12.1.1 Plenum the Coupling Module

Before describing in detail the individual component modeling in Chapters 13 to 18, we first mathematically describe the module *plenum* that connects the components in a turbomachine. The plenum is the coupling module between two or more successive components, Fig. 12.3. Its primary function is to couple the dynamic information of entering and exiting components. The volume of the plenum is the sum of half of all volumes of the components that enter and exit the plenum. The inlet components transfer information about mass flow  $\dot{m}_i$ , total pressure  $P$ , total temperature  $T_0$ , fuel/air  $f$  ratio, and water/air ratio  $w$  to the plenum. After entering the plenum, a mixing process takes place, where the aforementioned quantities reach their equilibrium values. These values are the same for all outlet components exiting the plenum. Each component represented by a module is uniquely defined by its name, inlet and outlet plenum.

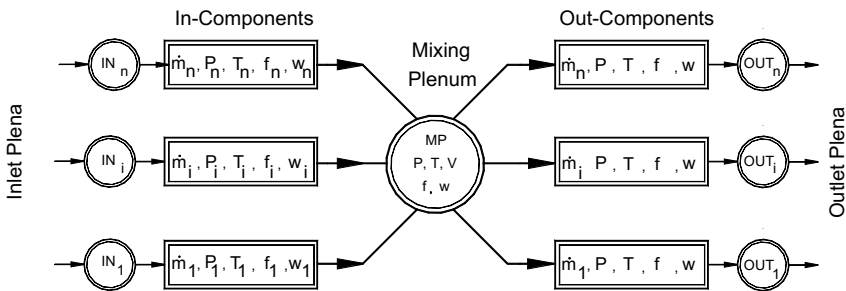


**Fig. 12.3:** Plenum as the coupling module between components.

The enthalpy, temperature and pressure transients are obtained from Eq. (12.21) and (12.23) neglecting, however, the contribution of the kinetic energy and time change in mass flow relative to other terms. The enthalpy equation (12.21)

$$\frac{\partial H}{\partial t} = -\kappa \mathbf{V} \cdot \nabla H - (\kappa - 1) \frac{H}{\rho} \nabla \cdot (\rho \mathbf{V}) \quad (12.1)$$

applying the chain rule of differentiation to Eq. (12.1), we arrive at:

$$\frac{\partial H}{\partial t} = -\frac{\kappa}{\rho} \nabla \cdot (\rho \mathbf{V} H) + \frac{H}{\rho} \nabla \cdot (\rho \mathbf{V}) \quad (12.2)$$

Equation (12.2) can be expressed in terms of total temperature by replacing the total enthalpy with  $H = c_p T_o$  as follows:

$$\frac{\partial c_p T_o}{\partial t} = -\frac{\kappa}{\rho} \nabla \cdot (\rho \mathbf{V} c_p T_o) + \frac{c_p T_o}{\rho} \nabla \cdot (\rho \mathbf{V}) \quad (12.3)$$

The total pressure equation (11.23) applied to the plenum, where no heat is added and the terms that include temporal and spatial changes of the kinetic energy as well as the friction compared to the enthalpy terms are neglected is written as:

$$\frac{\partial P}{\partial t} = -\kappa \nabla \cdot (\mathbf{V} P) \quad (12.4)$$

The index notation of Eq. (12.3) is:

$$\frac{\partial c_p T_o}{\partial t} = -\frac{k}{\rho} \frac{\partial (\rho V_i c_p T_o)}{\partial x_i} + \frac{1}{\rho} \left( c_p T_o \frac{\partial (\rho V_i)}{\partial x_i} \right) \quad (12.5)$$

For a one-dimensional time dependent flow the approximation of Eq. (12.5) leads to:

$$\frac{\partial c_p T_o}{\partial t} = -\frac{k}{\rho} \frac{\partial (\rho V_1 c_p T_o)}{\partial x_1} + \frac{1}{\rho} \left( c_p T_o \frac{\partial (\rho V_1)}{\partial x_1} \right) \quad (12.6)$$

Implementing the mass flow in Eq. (12.6) results in

$$\frac{\partial c_p T_o}{\partial t} = -\frac{k}{\rho S} \frac{\partial (\dot{m} c_p T_o)}{\partial x_1} + \frac{c_p T_o}{\rho S} \frac{\partial \dot{m}}{\partial x_1} \quad (12.7)$$

Approximating the differentials by differences, Eq. (12.7) reads:

$$\frac{\partial c_p T_o}{\partial t} = -\frac{k}{\rho S \Delta x_1} [(\dot{m} c_p T_o)_{out} - (\dot{m} c_p T_o)_{in}] + \frac{c_p T_o}{\rho S \Delta x_1} (\dot{m}_{out} - \dot{m}_{in}) \quad (12.8)$$

In Eq. (12.8) the quantities with subscript *in* and *out* refer to inlet and outlet, respectively. In case that the plenum has *m* inlet and *n* exit components, Eq. (12.8)

is be written as:

$$\frac{\partial T_o}{\partial t} = \frac{RT_{pl}}{V_{pl}P_{pl}} \left[ \sum_{i=1}^m \dot{m}_{I_i} \left( \kappa \frac{c_{pI_i}}{c_p} T_{oI_i} - T_{pl} \right) - (\kappa - 1) \sum_{j=1}^n \dot{m}_{O_j} T_{pl} \right] \quad (12.9)$$

In Eq. (12.9) the quantities  $T_o = T_{pl}$ ,  $P_{pl}$  and  $V_{pl} = S\Delta x$  refer to the plenum total temperature, total pressure and the volume, respectively. As Fig. 12.3 shows, the mass flow pertaining to the components that enter the plenum may contain certain amount of combustion products and water vapor specified by the fuel/air ratio  $f$  and water /air ratio  $w$ , respectively. This information is already included in the corresponding specific heats  $c_{pI_i}$  and the gas constants of the individual components.

Once these mass flows are mixed in the plenum, the resulting  $f$  and  $w$  of the exiting mass flows are different from entering ones. This is accounted for by the exiting specific heat  $c_p = c_{ppl}$ . Similar procedure is applied to obtain the plenum pressure using Eq.(12.4) with the index notation:

$$\frac{\partial P}{\partial t} = -k \frac{\partial (V_i P)}{\partial x_i} = -k \frac{\partial \left( \frac{\dot{m} P}{\rho} \right)}{S} = -\frac{kR}{S} \frac{\partial (\dot{m} T_o)}{\partial x_i} \quad (12.10)$$

Resulting in:

$$\frac{\partial P}{\partial t} = \frac{\kappa R}{V_{pl}} \left( \sum_{i=1}^n \dot{m}_{I_i} T_{oI_i} - \sum_{j=1}^m \dot{m}_{O_j} T_{pl} \right) \quad (12.11)$$

With Eqs. (12.9) and (12.11) the temperature and pressure information of the plenum as the connecting module is completely defined. As seen from Eq. (12.11), the plenum pressure includes the plenum temperature. The implicit method of integration described in Section 11.4 utilizes the initial values for the quantities in Eqs. (12.9) and (12.11) and performs the iteration until the convergence criterium has been satisfied.

### 12.1.2 Group1 Modules: Inlet, Exhaust, Pipe

Group 1 includes those components in which no transfer of thermal energy with the surrounding environment takes place. Their function consists, among other things, of transporting the mass, accelerating the mass flow through the nozzle, and reducing the kinetic energy through a diffuser. Figure 12.4 exhibits the physical as well as the modular representation of the component's nozzle, pipe, and diffuser. Each module

is surrounded by an inlet and an outlet plenum. These plena serve as the coupling element between two or more modules. Detailed physical and mathematical modeling of these modules are presented in Chapter 13.

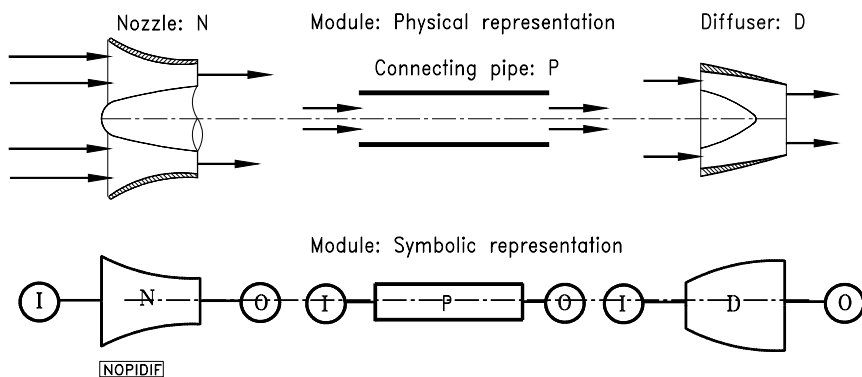


**Fig. 12.4:** Component and modular representation of inlet nozzle N, connecting pipe P, and Diffuser D

### 12.1.3 Group 2: Heat Exchangers, Combustion Chamber, After- Burners

Group 2 includes those components within which the processes of thermal energy exchange or heat generation take place. Heat exchangers are encountered in different forms such as recuperators, regenerators, inter-coolers, and after-coolers. Combustion chambers and afterburners share the same function. They convert the chemical energy of the fuel into thermal energy. As an example, Fig. 12.5 shows the component and modular representation of a recuperator and an inter-cooler. Recuperators are used to improve the thermal efficiency of small power generation gas turbines. While hot gas from the exhaust system enters the low pressure side (hot side) of the recuperator, compressor air enters the high pressure side (cold side). By passing over a number of contact surfaces, the hot side of the recuperator transfers thermal energy to the compressor air that passes through the recuperator cold side. After exiting the recuperator air side, preheated air enters the following combustion chamber.

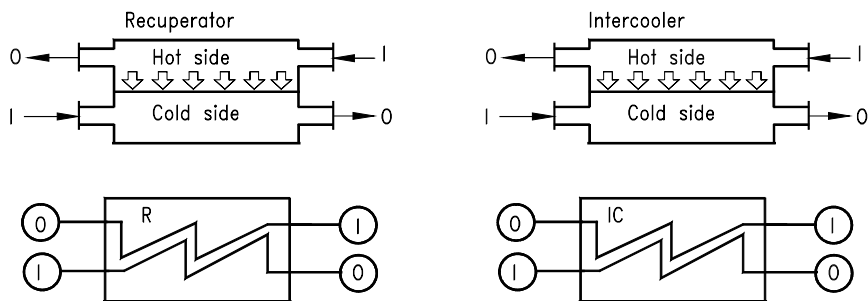


**Fig. 12.5:** Component and modular representations of a recuperator and an intercooler with the inlet and exit plena

The component combustion chamber is exhibited in Fig. 12.6. It generally consists of a primary combustion zone, a secondary zone, and a mixing zone. The primary zone, surrounded by  $n$  rows of ceramic segments, separates the primary combustion zone from the secondary zone and protects the combustion chamber casing from

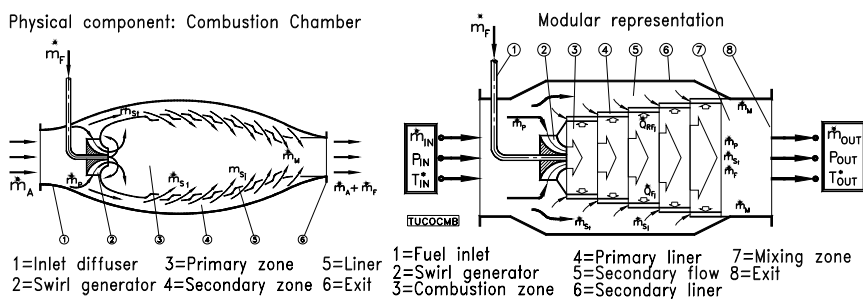


**Fig. 12.6:** Component and modular representation of a typical combustion chamber.

being exposed to high temperature radiation. The actual process of combustion occurs in the primary zone. The mixing in of the secondary air passing through mixing nozzles and holes reduces the gas temperature in the mixing zone to an acceptable level for the gas turbine that follows. The rows of segments in the combustion zone are subjected to a severe thermal loading due to direct flame radiation. Film and convective cooling on both the air and the gas sides cools these segments. The air mass flows required to cool these hot segments flow through finned cooling channels, thereby contributing to the convection cooling of the segments on the air side. The cooling air mass flow exiting from the  $j^{th}$  segment row, effects a film cooling process on the gas side within the boundary layer in the next row of segments. At the end of that process, the cooling air mass flow is mixed with the primary air mass flow, thus,

reducing the exit temperature.

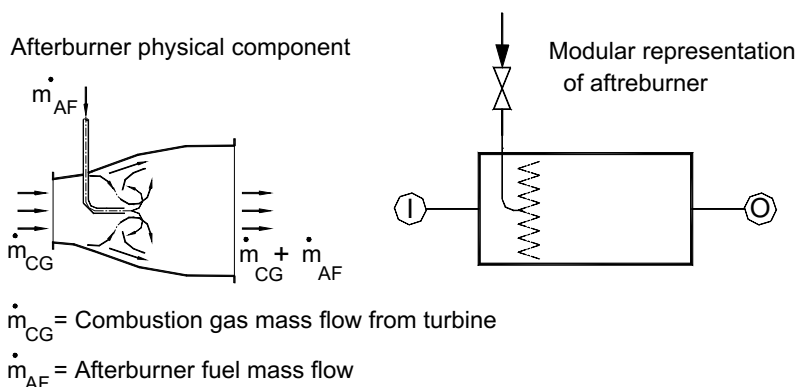


**Fig. 12.7:** Component and modular representation of a typical afterburner.

The afterburner (AF) component is applied to supersonic aero-engines that require supersonic exit velocities. Figure 12.7 exhibits a typical afterburner component with its modular representation. After leaving the low pressure turbine component, fuel is added to the mass flow inside the afterburner component causing an increase in temperature. The combustion gas is accelerated from subsonic to supersonic in a Laval nozzle that follows the afterburner. From combustion process point of view the principle function of the afterburner component and its modular simulation is very similar to the one discussed for combustion chambers.

### 12.1.4 Group 3: Adiabatic Compressor and Turbine Components

This group includes components within which an exchange of mechanical energy (shaft power) with the surroundings takes place. The representatives of this group are compressors and turbines. Figure 12.8 (a) and (b) show a compressor and a turbine stage with the velocity diagrams and the modular representations. The modules represent one stage within a multi-stage environment. The stages are decomposed into a stator and a rotor row that are connected by the corresponding plena. The row-by-row adiabatic compression and expansion processes are described by the conservation laws in conjunction with the known stage characteristics as discussed in Chapter 4. These components are comprehensively treated in Chapters 15 and 16.



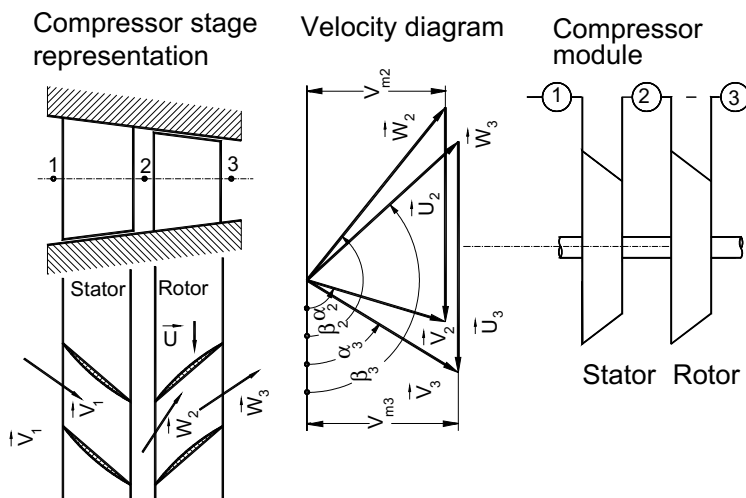


**Fig. 12.8(a):** Representation of an adiabatic compressor stage, module. The stage is decomposed into two rows that are connected via plenum No. 2.

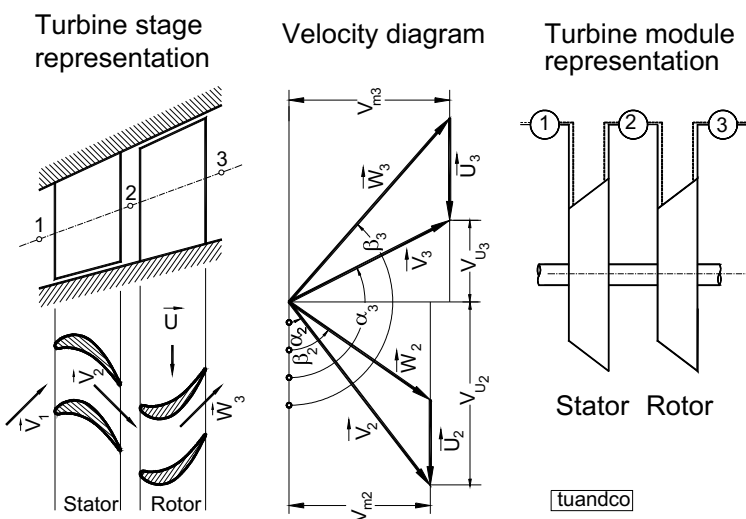


**Fig. 12.8(b):** Representation of an adiabatic turbine stage, module.

### 12.1.5 Group 4: Diabatic Turbine and Compressor Components

Unlike the adiabatic turbine and compressor components discussed in Section 12.1.4, this group includes turbine and compressor components within which not only the exchange of mechanical energy (in terms of shaft power) with the surroundings takes place, but also thermal energy exchange with the working fluid occurs. This group encompasses cooled turbines and compressors as well as those that are not cooled. Figure 12.9 shows a cooled turbine stage with the corresponding modular representation. It is considered a special module that is usually utilized in the first three rows of the high pressure part of gas turbine engines. Its modular representation shows the decomposition of the stage into its stator and rotor row that are separated by the corresponding plenum 2.

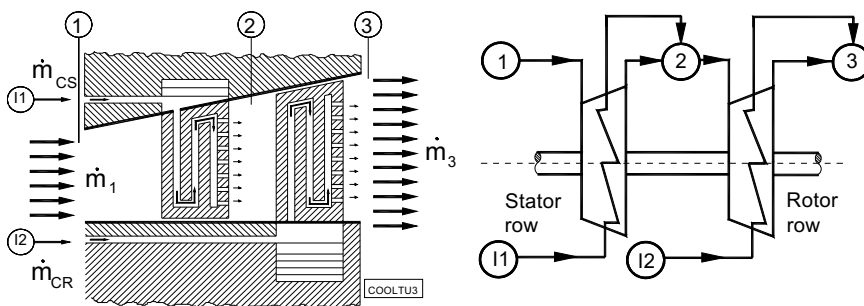


**Fig. 12.9:** Schematic of a cooled turbine stage and its modular representation .

As Fig. 12.9 shows, a fraction of the air mass flow,  $\dot{m}_{CS}$ , extracted from the HP-compressor is diverted into the first stator row and enters the cooling channels that might have several pin-fins and rib turbulators. Heat is transferred from the blade surface to the cooling air which may exit through several film cooling holes, slots at the trailing edge, and other holes. After exiting the blade surface, the cooling mass flow joins the turbine main mass flow. The same procedure may repeat in the subsequent rotor and stator rows as shown in Fig. 12.9. The module representation in Fig. 12.9 reflects the cooling and mixing procedure in the turbine stage. The main mass flow, with certain fuel/air and humidity/air ratios enters the upstream station 1 that corresponds to plenum (1) and expands through the stator row. The cooling mass flow from plenum (11), with certain water/air ratios but zero fuel/air ratios, passes through the cooling channel and mixes with the mainstream combustion gas in plenum (2). The mixing process changes the fuel/air and humidity/air ratios, which is precisely calculated. Similar heat transfer and mixing processes occur within the rotor row with rotor cooling mass flow  $\dot{m}_{CR}$  that enters the plenum at (12). The non-linear dynamic behavior of the cooled turbine stage represented by the above module, is described by three differential equations for the gas side, three differential equations

for the cooling air side, and one differential equation for the turbine material heat conduction as the closure condition. The same number of differential equations are generated for the rotor row. A diabatic expansion is not necessarily limited to the cooled turbine component. Uncooled blades are also subjected to diabatic processes whenever there is a temperature difference between the working medium and the turbine blade material. In steady state operations, which is specific to power generation gas turbine systems, there is a temperature equilibrium between the combustion gas and the blade material. Changing the engine load condition disrupts this equilibrium leading to a temperature difference between the turbine mass flow and the blade material. In the case of load addition, opening the fuel valve causes an instantaneous gas temperature increase. Since the blade metal temperature response significantly lags behind the response of the gas temperature, heat is transferred from the gas to the turbine material. Reducing the load by closing the fuel valve causes a portion of the thermal energy stored in the turbine blade material to be transferred to the working medium, causing a reduction of the turbine blade metal temperature. In case of aero-gas turbine engines, where acceleration and deceleration is the routine operational procedure, the turbine operates under diabatic conditions. A similar diabatic process is encountered in uncooled compressor components. However, the temperature differences are significantly lower.

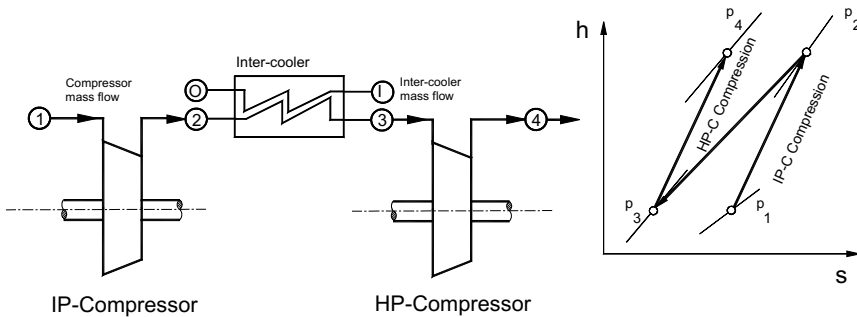


**Fig. 12.10:** Modular configuration of an intermediate pressure compressor, inter-cooler and a high pressure compressor,  $h$ - $s$  diagram of inter-cooling process.

The same cooling and simulation principle can be applied to compressor stages. However, it is a common practice for compressor trains consisting of several compressor components, and a high pressure ratio to intercool the mass flow. The process of intercooling serves to substantially reduce the temperature of the working medium. Figure 12.10 shows the modular configuration of an intermediate pressure compressor (IP-C), an intercooler (IC), and a high pressure compressor (HP-C). The  $h$ - $s$  diagram shows the two-stage compression process with intercooling.

After the compression in IP-C, the working medium is intercooled to the initial temperature and is compressed in HP-C to arrive at the final pressure. Usually, the intercooling process is applied to industrial processes, where compression ratios

above  $\pi > 30$  are required. For higher compression ratios, it is necessary to apply more than one intercooler. In this case the compression-cooling process is repeated. It should be noted that compressing to high pressure ratios without intercooling results in a substantial efficiency drop. Intercooling is also applied to Compressed Air Energy Storage plants (CAES, see Chapter 18), where the working medium air is compressed to pressure levels close to 70 bar and is stored in underground caverns. The high pressure air allows operating the CAES-gas turbine to operate during the period of high electric power consumption demand.

### 12.1.6 Group 5: Control System, Valves, Shaft, Sensors

This group of modules consists of shafts, sensors, control systems, and fuel and load schedule generators, shown in Fig. 12.11.

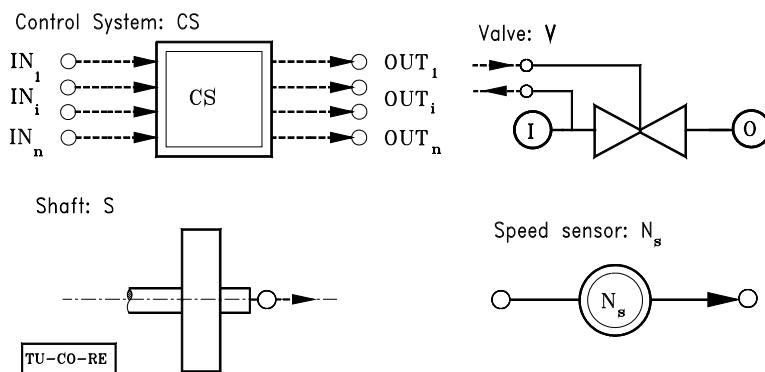


**Fig. 12.11:** Schematics of the modules: control system, valve, shaft, and sensor.

The control system is a major module that controls the entire engine. Input information may contain rotor speed transferred by the speed sensors, turbine inlet temperature, pressure, and compressor inlet and exit pressures and temperatures. This information may trigger closing or opening of the fuel valves and several bypass valves, and can perform other control functions, such as the adjustment of compressor stator blades to perform active surge protection.

## 12.2 System Configuration, Nonlinear Dynamic Simulation

From the conceptual dynamic simulation point of view, the previous survey has led to the practical conclusion that any arbitrary aircraft or power generation gas turbine engine and its derivatives, regardless of configuration, i.e., number of spools and components, can be generically simulated by arranging the modules according to the

engine of interest. The nonlinear dynamic simulation method discussed in this and the next following chapters, is based on this modular configuration concept, and is a generic, modularly structured computational procedure that simulates the transient behavior of individual components, gas turbine engines, and their derivatives. The modules are identified by their names, spool numbers, and the inlet and outlet plena.

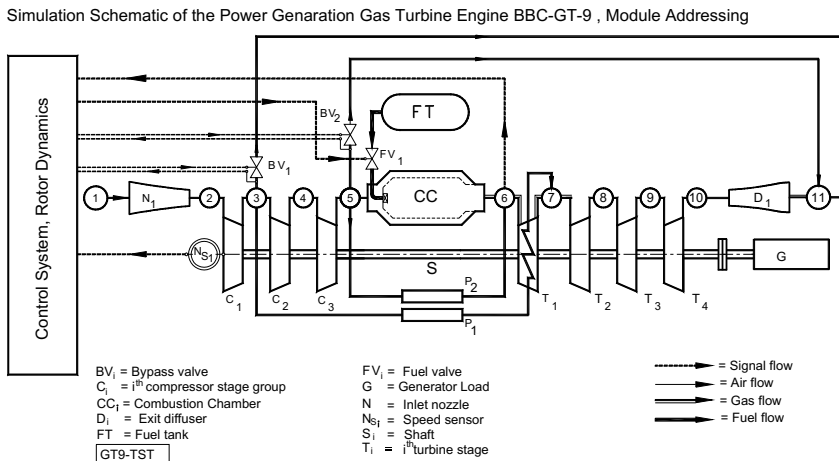


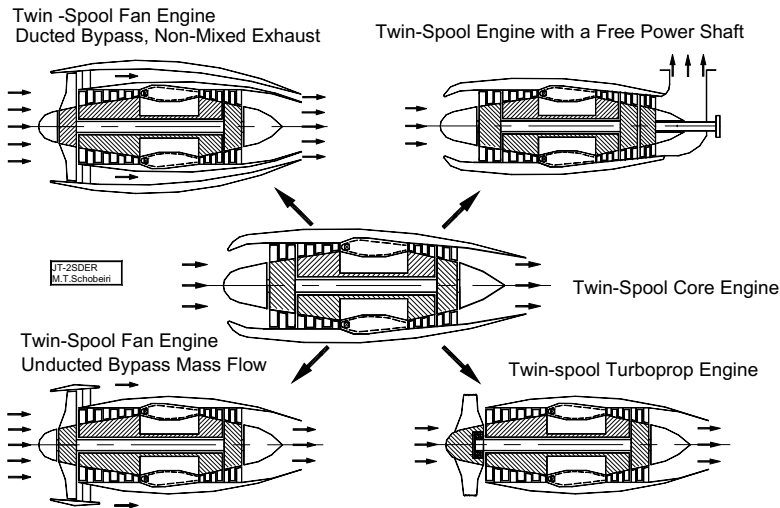
Fig. 12.12: Modular configuration of the gas turbine presented in Fig.12.1.

This information is vital for automatically generating the system of differential equations that represent individual modules. Modules are then combined into a complete system that correspond to the system configuration. Each module is physically described by the conservation laws of thermo-fluid mechanics, which result in a system of nonlinear partial differential or algebraic equations. Since an engine consists of a number of components, its modular arrangement leads to a system containing a number of sets of equations. The above concept can be systematically applied to any aircraft or power generation gas turbine engine. The modular concept allows the choice of generating a wide variety of simulation cases from single spool, power generation engines to twin, and multi spool thrust or combined thrust-power generation engines. The following three examples explain the modular design and simulation capability. To simulate the gas turbine engine shown in Fig. 12.1, first a modular representation is constructed for the purpose of the module addressing and plena assignments. Figure 12.12 represents the schematic simulation scheme for this engine. The first plenum numbered 1, is open to the atmosphere, and is the entrance to the engine. The entrance to the compressor is represented by an inlet nozzle  $N_1$ . The compression system is divided into three compressors, the low pressure compressor stage group,  $C_1$ , which is assigned plenum 2 as the inlet plenum and plenum 3 as the exit plenum, the intermediate pressure stage

group, C2, and the high pressure stage group, C3. Upon exiting the first compressor, a portion of the flow is removed via the second pipe of the engine system, P2, and is assigned plenum 3 as its inlet plenum, and plenum 7 as its exit plenum. The temperature of the flow at this point is relatively low and the second pipe mass flow serves for the turbine blade internal cooling. A portion of the flow is removed upon exiting the high pressure compressor, C3, via the second pipe, P2, and is transferred to the turbine inlet without passing through the combustion chamber. Fuel is injected into the combustion chamber at a rate which is given in the input data. The combustion gas then exits the combustion chamber, is mixed with the exiting flow from the third pipe, P2, for the purpose of temperature control, and enters the turbine which resides between plena 6 and 10. The exit diffuser, D1, leads to plenum 11 which is also open to the atmosphere.

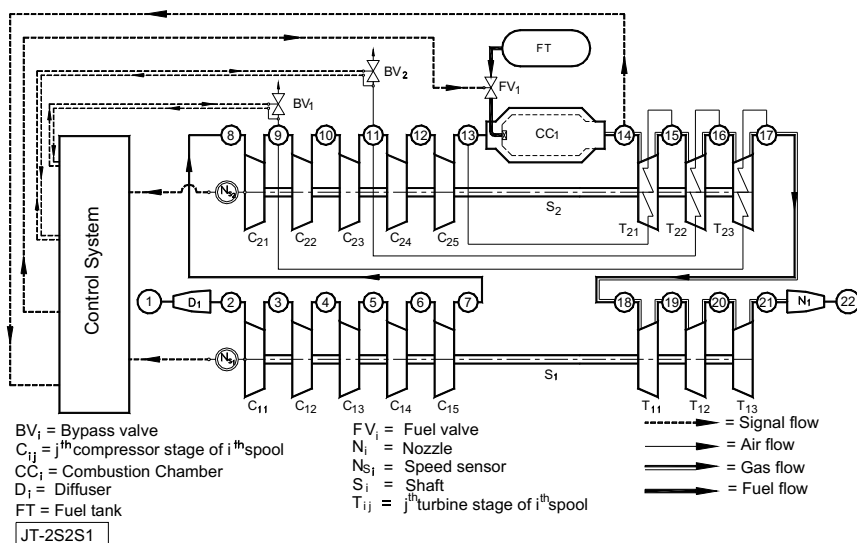
The control system input variables are the rotational speed of the shaft and the turbine inlet temperature. Output from the control system is the opening and closing of the fuel valve to control fuel flow into the combustion chamber (Fig.12.12). Each component corresponds to a simulation module consisting of a main routine and several subroutines, which determine the complete thermo-fluid dynamic profile of the component during the transient.

Figure 12.13 schematically exhibits a twin spool aircraft engine with its derivatives. The base engine (middle) is modified to construct a ducted bypass engine, where the exit jets are not mixed (top left) and an unducted bypass engine (bottom left). The same base engine also serves to design a power generation and a turboprop engine. While in the case of the power generation example a third shaft has



**Fig. 12.13:** A twin spool base engine (middle) with different derivatives been added, in the turboprop example, the low pressure turbine drives the propeller.

Figure 12.13 presents an appropriate example of a generic, modularly structured, component and system modeling. The schematic of the base engine is shown in Fig. 12.14. Two shafts are defined as S1 and S2. The flow passes through the engine in the following manner: first its velocity is reduced and its pressure is increased in the inlet diffuser (D1) which is between plena 1 and 2. The low pressure compressor group (C11 - C15) will then further increase the flow pressure. Next, the high pressure compressor group (C21 - C25), which resides on the second shaft, S2, further raises the pressure. Fuel is injected into the combustion chamber (CC1), which is located between plena 13 and 14, thus, raising its temperature. High pressure and temperature gas is expanded through the HP-turbine group (T21 - T23) which is resided on the second shaft (S2) that drives the HP-compressor. Due to high thermal loading on the blades, the HP-turbine requires cooling. The combustion gas further expands through the LP-turbine group (T11 - T13) that drives the LP-compressor before it is exhausted into the atmosphere through the exit nozzle (N1), which is between plena 21 and 22.



**Fig. 12.14:** Modular configuration of the twin spool core engine of Fig.12.12.

As shown in Fig. 12.14, signal flow from each module to the control system is represented by dashed lines, air flow is represented by single lines, gas flow is represented by the double lines, and fuel flow is represented by thick single lines.

An example of a modular composition of a helicopter gas turbine engine charged with a wave rotor is shown in Fig. 12.15. Compared to a single spool engine, Fig.12.15 reveals two new features: (1) a wave rotor super charger component is installed between the compressor and the combustion chamber that further increases

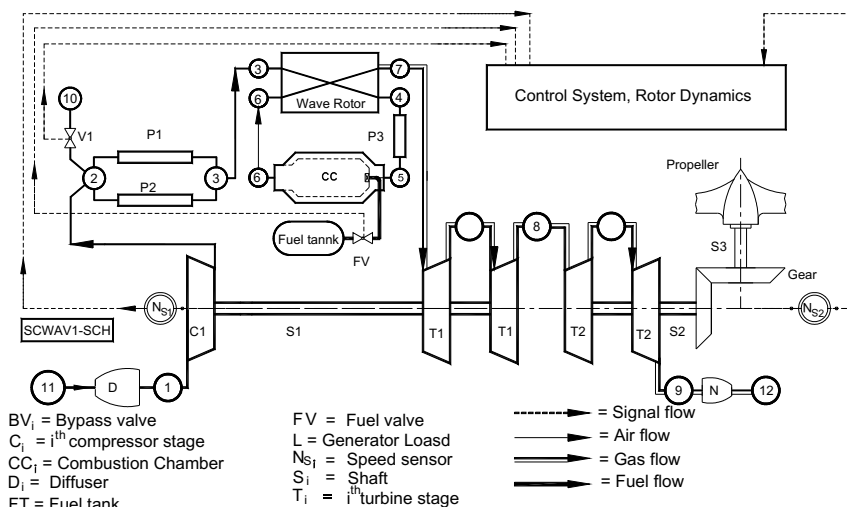


**Fig. 12.15:** Modular configuration of a helicopter gas turbine engine supercharged by a wave rotor.

the compression ratio leading to higher thermal efficiency, and (2) a propeller is driven by the spool shaft, whose rotational speed is reduced by a gear transmission.

### 12.3 Configuration of Systems of Non-linear Partial Differential Equations

Each component of the above modular system configuration is completely described by a set of partial differential equations and algebraic equations. These modules are connected via plena that are described by two differential equations. Thus, the modular system configuration consists of a set of differential equation systems. The solution of these equations depend on the initial and boundary conditions that trigger the nonlinear dynamic event. This and other related issues will be comprehensively discussed in the following chapters.

### References

1. Schobeiri, M. T., Abouelkheir, M., Lippke, C., 1994, "GETRAN: A Generic, Modularly Structured Computer Code for Simulation of Dynamic Behavior of Aero-and Power Generation Gas Turbine Engines," an honor paper, ASME Transactions, *Journal of Gas Turbine and Power*, Vol. 1, pp. 483-494.
2. Schobeiri T., 1986: "A General Computational Method for Simulation and Prediction of Transient Behavior of Gas Turbines." ASME-86-GT-180.



3. Schobeiri M. T., 1985 "Aero-Thermodynamics of Unsteady Flows in Gas Turbine Systems." Brown Boveri Company, Gas Turbine Division Baden Switzerland, BBC-TCG-51.
4. Schobeiri M.T., 1985b "COTRAN, the Computer Code for Simulation of Unsteady Behavior of Gas Turbines." Brown Boveri Company, Gas Turbine Division Baden Switzerland, BBC-TCG-53-Technical Report.

## 13 Modeling of Inlet, Exhaust, and Pipe Systems

### 13.1 Unified Modular Treatment

This chapter deals with the numerical modeling of the components pertaining to group 1 discussed in section 13.1.1. The components pertaining to this category are the connecting pipes, inlet and exhaust systems, as shown in Fig. 13.1.

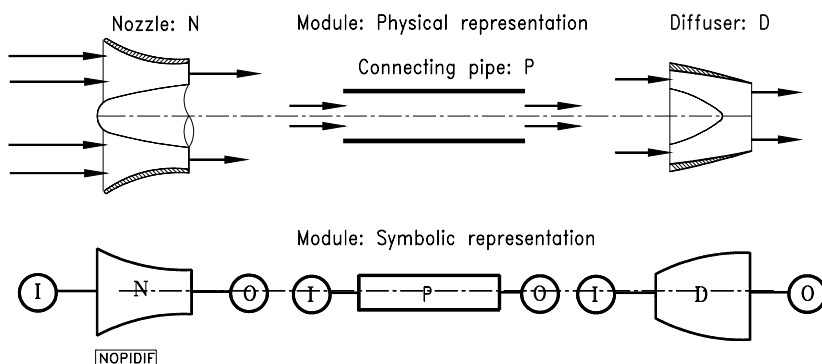


**Fig. 13.1:** Component and modular representation of inlet nozzle N, connecting pipe P, and Diffuser D

The function of this group consists, among other things, of the transportation of mass flow, and of converting the kinetic energy into potential energy and vice versa. Their geometry differs only in the sign of the gradient of the cross section in streamwise direction  $\partial S / \partial x$ . For  $\partial S / \partial x < 0$ , flow is accelerated for subsonic and decelerated for supersonic Mach numbers. On the other hand, for  $\partial S / \partial x > 0$ , the flow is decelerated for subsonic and accelerated for supersonic Mach numbers.

### 13.2 Physical and Mathematical Modeling of Modules

For modeling ducts with the varying cross sections, we apply the conservation laws derived in Chapter 11 ([1], [2], [3], [4]). The temporal change of the density at position  $k$ , shown in Fig. 13.2, is determined from Eq. (11.26) as is given below:

$$\frac{\partial \rho_k}{\partial t} = -\frac{1}{\Delta x} \left( \frac{\dot{m}_{i+1}}{S_{i+1}} - \frac{\dot{m}_i}{S_i} \right) \quad (13.1)$$

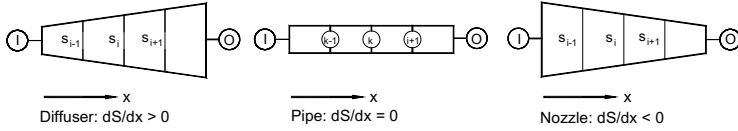


**Fig. 13.2:** Modeling the components diffuser  $\partial S/\partial x > 0$ , pipe  $\partial S/\partial x = 0$  and nozzle  $\partial S/\partial x < 0$

The mass flows  $\dot{m}_i$  and  $\dot{m}_{i+1}$  at stations  $i$  and  $i+1$  are determined in conjunction with the momentum equation (11.33):

$$\begin{aligned} \frac{\partial \dot{m}_k}{\partial t} = & -\frac{1}{\Delta x} \left( \dot{m}_{i+1} V_{i+1} - \dot{m}_i V_i + p_{i+1} S_{i+1} - p_i S_i \right) \\ & + \left( \frac{\dot{m}_k V_k + P_k S_k}{S_k} \right) \left( \frac{S_{i+1} - S_i}{\Delta x} \right) - c_f \frac{\dot{m}_k^2}{2 D_{h_k} \rho_k S_k} \end{aligned} \quad (13.2)$$

The energy equation in terms of total pressure Eq. (11.54) in the absence of heat addition is modified as follows:

$$\begin{aligned} \frac{\partial P_k}{\partial t} = & -\frac{\kappa_k}{\Delta x} \left( \frac{\dot{m}_{i+1} P_{i+1}}{\rho_{i+1} S_{i+1}} - \frac{\dot{m}_i P_i}{\rho_i S_i} \right) - (\kappa_k - 1) \left( \frac{\dot{m}_k q_k}{\Delta V} + c_{f_k} \frac{\dot{m}_{i+1} \dot{m}_k^2}{2 D_{h_{i+1}} S_{i+1} \rho_i^2} \right. \\ & \left. - (\kappa_k - 2) \frac{\dot{m}_k}{\rho_k S_k^2} \left[ \frac{1}{2} \frac{\dot{m}_k}{\rho_k} \frac{1}{\Delta x} \left( \frac{\dot{m}_{i+1}}{S_{i+1}} - \frac{\dot{m}_i}{S_i} \right) + \frac{\partial \dot{m}_{i+1}}{\partial t} \right] \right. \\ & \left. - \frac{(\kappa_k - 2)}{2 \Delta x} \left( \frac{\dot{m}_{i+1}^3}{\rho_{i+1}^2 S_{i+1}^3} - \frac{\dot{m}_i^3}{\rho_i^2 S_i^3} \right) \right) \end{aligned} \quad (13.3)$$

For a constant cross-section, the equation of continuity (13.1) and motion (13.2) are written respectively as:

$$\frac{\partial \rho}{\partial t} = - \frac{1}{\Delta x S} \left( \dot{m}_{i+1} - \dot{m}_i \right) \quad (13.4)$$

$$\frac{\partial \dot{m}_k}{\partial t} = - \frac{1}{\Delta x} \left[ \frac{\dot{m}_{i+1}^2}{\rho_{i+1} S} - \frac{\dot{m}_i^2}{\rho_i S} + S \left( P_{i+1} - P_i \right) \right] - c_f \frac{\dot{m}_k^2}{2 \rho_k S D_h} \quad (13.5)$$

Similarly, the equation of energy in terms of total pressure is simplified to:

$$\begin{aligned} \frac{\partial P_k}{\partial t} = & - \frac{\kappa_k}{\Delta x S} \left( \frac{\dot{m}_{i+1} P_{i+1}}{\rho_{i+1}} - \frac{\dot{m}_i P_i}{\rho_i} \right) - (\kappa_k - 1) \left( \frac{\dot{m}_k q_k}{\Delta V} + c_{fk} \frac{\dot{m}_{i+1} \dot{m}_k^2}{2 D_{h_{i+1}} \rho_k^2 S^3} \right) \\ & - (\kappa_k - 2) \frac{\dot{m}_k}{\rho_k S^2} \left[ \frac{1}{2} \frac{\dot{m}_k}{\rho_k} \frac{1}{\Delta x S} (\dot{m}_{i+1} - \dot{m}_i) + \frac{\partial \dot{m}_{i+1}}{\partial t} \right] \\ & - \frac{(\kappa_k - 2)}{2 \Delta x S^3} \left( \frac{\dot{m}_{i+1}^3}{\rho_{i+1}^2} - \frac{\dot{m}_i^3}{\rho_i^2} \right) \end{aligned} \quad (13.6)$$

Equations (13.4), (13.5), and (13.6) describe the transient process of a compressible flow within a tube with a constant cross section. For an incompressible flow Eq. (13.5) can be reduced to a simple differential equation:

$$\frac{\partial \dot{m}}{\partial t} = \frac{R}{L S} \left( \frac{T_1}{P_1} - \frac{T_n}{P_n} \right) + \frac{S}{L} (P_1 - P_n) - c_f \frac{\dot{m}^2}{\rho S D_h} \quad (13.7)$$

The friction coefficient  $c_f$  can be determined from the known steady-state condition, where the temporal changes of the mass flow are set equal to zero. The indices  $l$  and  $n$  refer to the first and last station of the component. The solution of Eqs. (13.1) - ?, and (13.4) - (13.7) can be performed using the implicit integration method discussed later. However, considerable calculation speed is reached if the component under investigation is subdivided into several subsections that are connected to each other via plena. In this case, for each discrete section, the mass flow can be considered as spatially independent, which leads to further simplification of the above equations.

### 13.3 Example: Dynamic behavior of a Shock Tube

Simulation of a high frequency compression-expansion process within a shock tube

is an appropriate example to demonstrate the nonlinear dynamic behavior of the above components. The shock-expansion process within shock tubes has been the subject of classical gas dynamics for many decades ([5], [6], [7],[8]). With the introduction of fast response surface mounted sensors, shock tubes have gained practical relevance for calibrating the high frequency response pressure and temperature probes. In classical gas dynamics, shock-expansion process are treated using the method of characteristics. Results of studies presented in [9] show substantial disagreement between calculations using method of characteristics and experiments. In this and the subsequent chapters, we simulate the dynamic behavior of each individual component using the simulation code GETRAN [2]. In GETRAN, the system of non-linear differential equations is solved using the implicit solution method described in Chapter 12.

The shock tube under investigation has a length of  $L=1\text{m}$  and a constant diameter  $D=0.5\text{m}$ . The tube is divided into two equal length compartments separated by a membrane. The left compartment has a pressure of  $p_L = 100\text{bar}$ , while the right one has a pressure of  $p_R = 50\text{bar}$ . Both compartments are under the same temperature of  $T_L = T_R = 400\text{K}$ . The working medium is dry air, whose thermodynamic properties, specific heat capacities, absolute viscosity, and other substance quantities change during the process and are calculated using a gas table integrated in GETRAN. The pressure ratio of 2 to 1 is greater than the critical pressure ratio and allows a shock propagation with the speed of sound. Two equivalent schemes can be used to predict the compression-expansion process through the tube. These are shown in Fig. 13.3. In schematic (a), each half of the tube is subdivided into 10 equal pieces. The corresponding coupling plane 1 though 11, and thus, the left half of the tube are under pressure of 100 bar, while the right half with the plenums 12 through 21 are under the pressure of 50 bar.

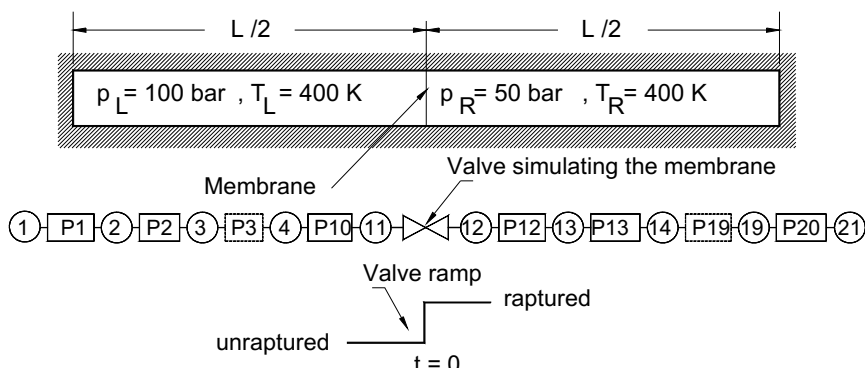


**Fig. 13.3:** Simulation schematics for a shock tube: the physical tube (top), and the simulation schematics (a) and (b).

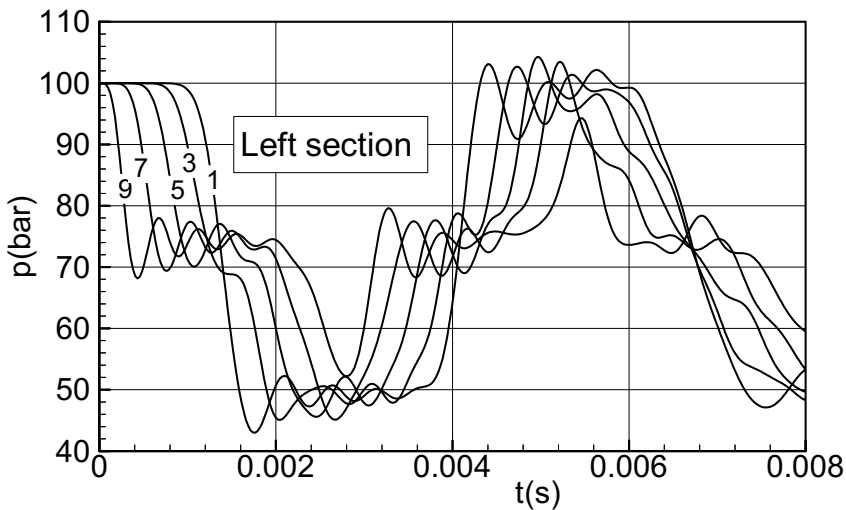
The membrane is modeled by a throttle system with a ramp that indicates the cross sectional area shown underneath the throttle. The sudden rupture of the membrane is

modeled by a sudden jump of the ramp. The schematic (b) offers a simpler alternative. Here, as in case (a), the tube is subdivided into 20 pieces that are connected via plenums 1 to 21.

### 13.3.1 Shock Tube Dynamic Behavior

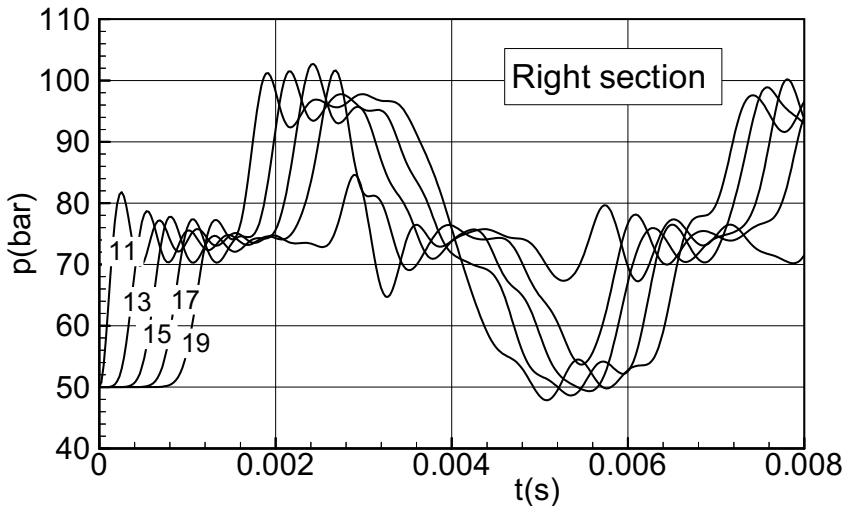
**Pressure Transients:** The process of expansion and compression is initiated by suddenly rupturing the membrane. At time  $t = 0$ , the membrane is ruptured which causes strong pressure, temperatures, and thus, mass flow transients. Since the dynamic process is primarily determined by pressure, temperature, and mass flow transients, only a few representative results are discussed as shown in Figs. 13.4 through 13.9.

Figure 13.4 shows the pressure transients within the left sections 1 to 9. As curve 9 shows, the section of the tube that is close to the membrane reacts with a steep expansion wave. On the other hand, the pressure within the pipe section ahead of the shock, Fig. 13.5, curve 11, increases as the shock passes through the section. Oscillatory behavior is noted as the shock strength diminishes. The pipe sections that are farther away from the membrane, represented by curves 7, 5, 3, and 1 on the left and curves 13, 15, 17, and 19 on the right section, follow the pressure transient with certain time lags. Once the wave fronts have reached the end wall of the tube, they are reflected as compression waves. The aperiodic compression-expansion process is associated with a propagation speed which corresponds to the speed of sound. The expansion and compression waves cause the air, which was initially at rest, to



**Fig. 13.4:** Pressure transients within the shock tube. Left section includes all tube sections initially under high pressure of 100 bar, while the right section include those initially at 50 bar

perform an aperiodic oscillatory motion. Since the viscosity and the surface roughness effects are accounted for by introducing a friction coefficient, the transient process is of dissipative nature. This pressure rise is followed by a damped oscillating wave that hits the opposite wall and reflects back with an initially increased pressure followed by a damped oscillation



**Fig. 13.5:** Pressure transients within the shock tube. Right section includes all tube sections initially under high pressure of 50 bar, while the left section includes those initially at 100 bar

**Temperature Transients:** Figure 13.6 shows the temperature transients within the left sections 1 to 9. As curve 9 shows, the section of the tube that is close to the membrane reacts with a steep temperature decrease. The pipe sections that are farther away from the membrane, represented by curves 7, 5, 3, and 1 on the left and curves 13, 15, 17, and 19 on the right section, follow the temperature transient with certain time lags. Once the shock waves have reached the end wall of the tube, they are reflected as compression waves where the temperature experience a continuous increase.

Slightly different temperature transient behavior of the right sections are revealed in Fig. 13.7. Compared to the temperature transients of the left sections, the right sections temperature transients seem to be inconsistent. However, a closer look at the pressure transients explains the physics underlying the temperature transients. For this purpose we consider the pressure transient curve 11, in Fig. 13.5. The location of this pressure transient is in the vicinity of the membrane's right side with the pressure of 50 bar. Sudden rupture of the membrane simulated by a sudden ramp (Fig. 13.2) has caused a steep pressure rise from 50 bar to slightly above 80 bar.

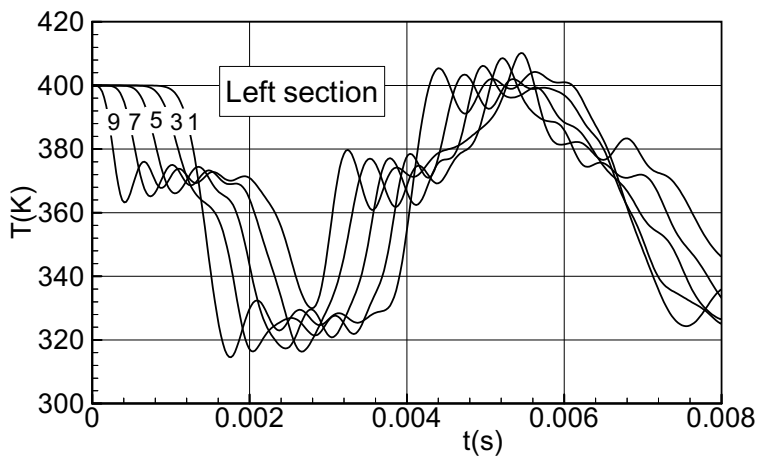


**Fig. 13.6:** Temperature transients within the left sections of the tube. Left and right sections includes all tube sections initially under temperature of 400 K

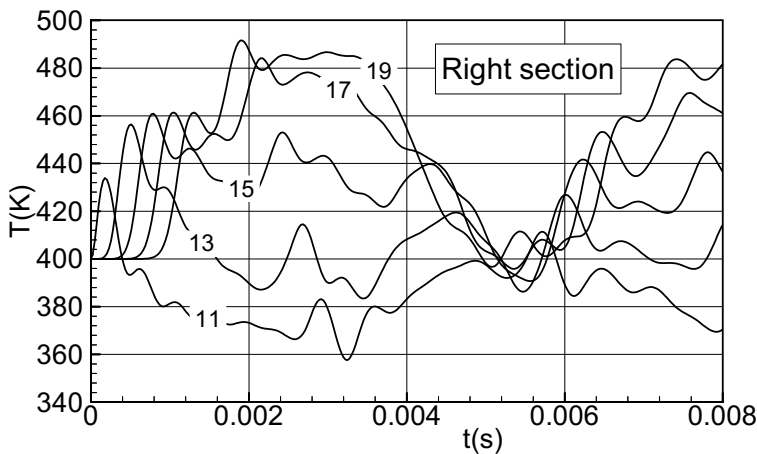


**Fig. 13.7:** Temperature transients within the right sections of the tube. Left and right sections includes all tube sections initially under temperature of 400 K



The pattern of the pressure transients is reflected in temperature distribution, where the pressure rise causes a temperature increase and vice versa. The temperature transients at downstream locations 12 to 20 follow the same trend.

**Mass flow Transients:** Figures 13.8 and 13.9 show the mass flow transients within the left and the right section of the tube. The steep negative pressure gradient causes

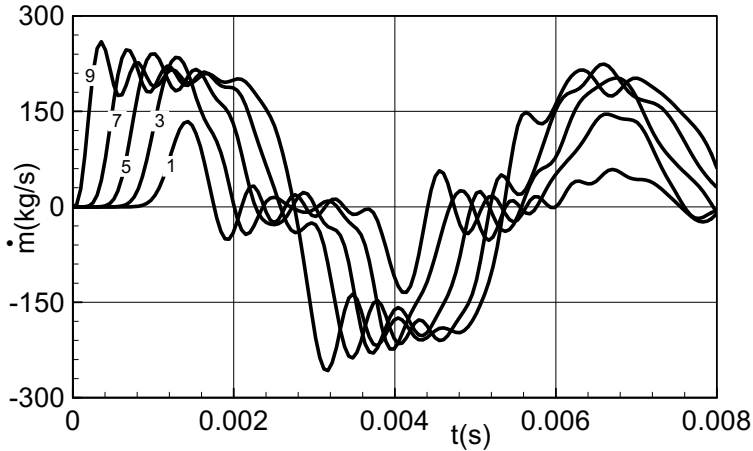


**Fig. 13.8:** Mass flow transients within left section of shock tube.

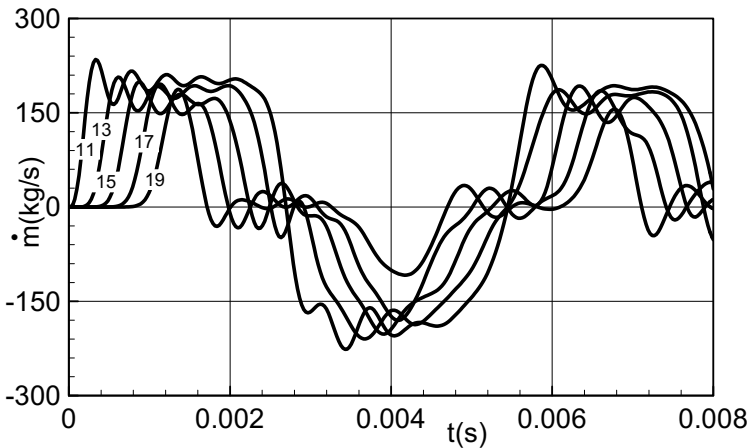


**Fig. 13.9:** Mass flow transients within the shock tube. The right section include all tube sections initially under high pressure of 50 bar, while the left section include those initially at 100 bar.

the mass contained within the tube to perform aperiodic oscillatory motions. During the expansion process, curve 1, mass flows in the positive  $x$ -direction. It continues to stay positive as long as the pressure in individual sections are above their minimum. This means that the shock front has not reached the right wall yet. Once the shock front hits the right wall, it is reflected initiating a compression process that causes the mass flows in the negative  $x$ -direction. Figures 13.8 through 13.9 clearly show the dissipative nature of the compression and expansion process that results in diminishing the wave amplitudes and damping the frequency. The degree of damping depends on the magnitude of the friction coefficient  $c_f$  that includes the Re-number and surface roughness effects. For a sufficiently long computational time, the oscillations of pressure, temperature, and mass flow will decay. For  $c_f = 0$ , the aperiodic oscillating motion persists with no decay.

## References

1. Schobeiri T., 1986: "A General Computational Method for Simulation and Prediction of Transient Behavior of Gas Turbines," ASME-86-GT-180.
2. Schobeiri, M. T., Abouelkheir, M., Lippke, C., 1994, "GETRAN: A Generic, Modularly Structured Computer Code for Simulation of Dynamic Behavior of Aero-and Power Generation Gas Turbine Engines," an honor paper, ASME Transactions, *Journal of Gas Turbine and Power*, Vol. 1, pp. 483-494.
3. Schobeiri, M. T., Attia, M, Lippke, C., 1994, "Nonlinear Dynamic Simulation of Single and Multi-spool Core Engines, Part I: Theoretical Method," *AIAA, Journal of Propulsion and Power*, Volume 10, Number 6, pp. 855-862, 1994.
4. Schobeiri, M. T., Attia, M, Lippke, C., 1994, "Nonlinear Dynamic Simulation of Single and Multi-spool Core Engines, Part II: Modeling and Simulation Cases," *AIAA Journal of Propulsion and Power*, Volume 10, Number 6, pp. 863-867, 1994.
5. Prandtl, L., Oswatisch, K., Wiegand, K., 1984, "Führer durch die Strömungslehre," 8. Auflage, Branschweig, Vieweg Verlag.
6. Shapiro, A.H., 1954, "The Dynamics and Thermodynamics of Compressible Fluid Flow," Vol. I, Ronald Press Company, New York, 1954.
7. Spurk, J, 1997, "Fluid mechanics," Springer-Verlag, Berlin, Heidelberg, New York.
8. Becker, E., 1969, "Gasdynamik, Stuttgart, Teubner Studienbücher Mechanik, Leitfaden der angewandten Mathematik und Mechanik.
9. Kentfield, J. A. C., 1993, "Nonsteady, One-Dimensional, Internal, Compressible Flows, Theory and Applications," Oxford University Press.

## 14 Modeling of Recuperators, Combustion Chambers, Afterburners

This category of components includes recuperators, preheaters, regenerators, intercoolers, and aftercoolers, Fig. 14.1. Within these components the process of heat exchange occurs between the high and low temperature sides. The working principle of these components is the same ([1], [2], [3]). However, different working media are involved in the heat transfer process. More recently recuperators are applied to small and medium size gas turbine engines to improve their thermal efficiency. The exhaust thermal energy is used to warm up the compressor exit air before it enters the combustion chamber. A typical recuperator consists of a low pressure hot side flow path, a high pressure cold side flow path, and the wall that separates the two flow paths. A variety of design concepts are used to maximize the heat exchange between the hot and the cold side by improving the heat transfer coefficients. A cold side flow path may consist of a number of tubes with turbulators, fin pins, and other features that enhance the heat transfer coefficient. Based on the individual recuperator design concept, hot gas impinges on the tube surface in cross flow or counter flow directions. The working media entering and exiting the recuperator is generally combustion gas that exits the diffuser (hot side) and air that exits the compressor (cold side).

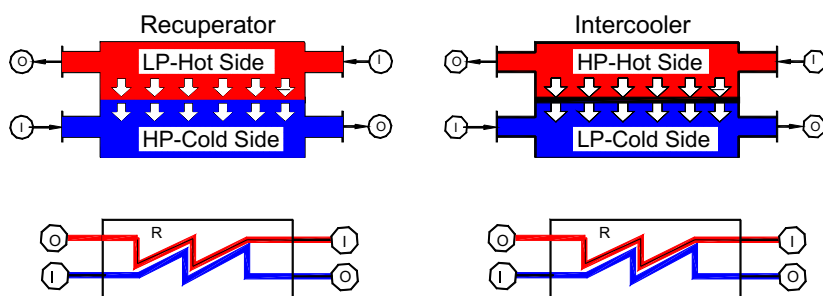


**Fig. 14.1:** Schematics of a recuperator and an intercooler and their modular representation, recuperator heat exchange between low pressure hot combustion gas from exhaust and high pressure cold air from compressor.

Intercooler is applied for intercooling the compressor mass flow before it enters the next stage of compression. In contrast to recuperators, the working medium on the intercooler hot side is air that exits the intermediate pressure compressor before entering the high pressure compressor. On the low pressure side, the working medium

is water that removes the heat from the compressed air before entering the high pressure compressor for further compression. Aftercooler is used to aftercool the high pressure working medium for storage purposes in order to reduce the specific volume, thereby increasing the amount of stored air mass. This procedure is used, among other things, in compressed air storage facilities. Figure 14.1 shows schematics of a recuperator and an intercooler and their modular representation.

### 14.1 Modeling Recuperators

Within this component, the heat exchange occurs between the high temperature low pressure combustion gas, and low temperature high pressure air. A schematic representation of a counter flow heat exchanger is given in Fig. 14.2. As shown, the heat exchange zone between the inlet, and exit plena on the hot, and cold sides is divided into  $(n-1)$  sections. The flow direction as well as the direction of the heat flow is shown in Fig. 14.2.

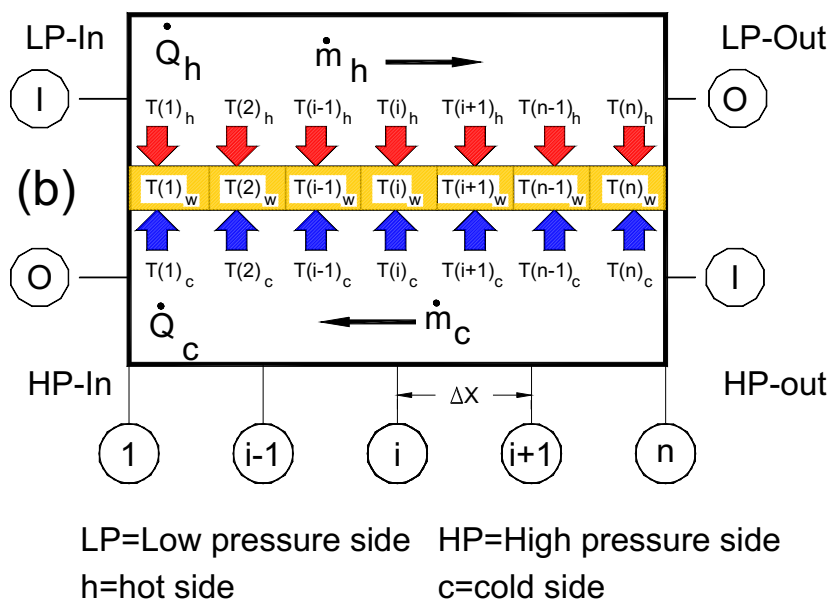


**Fig. 14.2:** A segment of a heat exchanger with heat transfer, temperature distribution, inlet and outlet plane.

Since both the cold and hot gas streams have low subsonic velocities, they can be considered as incompressible, resulting in  $Dp/Dt = 0$ . For the sake of unifying treatment, we adopt the positive sign for heat transfer whenever heat is added to the

wall. Furthermore, no cross section changes occur, so that  $\nabla S = 0$ . These specifications lead to a significant simplification of Eq. (12.33) and (12.52) that described the mass flow and temperature transients on the hot side.

### 14.1.1 Recuperator Hot Side Transients

Starting from the equation of motion, the above simplifications lead to the following relations that describe the mass flow and temperature transients on the hot side. The mass flow dynamics is obtained by rearranging Eq. (12.34):

$$\frac{\partial \dot{m}_h}{\partial t} = \frac{R_h}{L_h} \frac{\dot{m}_h^2}{S_h} \left( \frac{T_{h1}}{P_{h1}} - \frac{T_{hn}}{P_{hn}} \right) + \frac{S_h}{L_h} (P_{h1} - P_{hn}) - c_{fh} \frac{\dot{m}_h^2}{2 \rho_{hn} S_h D_{hn}} \quad (14.1)$$

The temperature transients are calculated by rearranging Eq. (12.52) as follows:

$$\begin{aligned} \frac{\partial T_{o,h,i+1}}{\partial t} = & \frac{-\kappa_{hk}}{c_{p,h,i+1} \rho_{hk} \Delta V_h} \left[ \dot{m}_h (c_{p,h,i} T_{o,h,i} - c_{p,h,i+1} T_{o,h,i+1}) - \dot{Q}_{hk} \right] \\ & - \left( \frac{\kappa_{hk} - 1}{c_{p,h,i+1}} \right) \frac{\dot{m}_h}{\rho_{hk}^2 S_h^2} \frac{\partial \dot{m}_h}{\partial t} \end{aligned} \quad (14.2)$$

The quantities in Eq. (14.2) with the subscript k refer to the averages as in Eq. (12.55).

### 14.1.2 Recuperator Cold Side Transients

The dynamic behavior of the recuperator cold side is determined by the equations of motion and energy, adopting the same simplification as for the flow on the hot side. The mass flow transient is calculated by rearranging Eq. (12.34) for the cold side as:

$$\frac{\partial \dot{m}_c}{\partial t} = \frac{R_c}{L_c} \frac{\dot{m}_c^2}{S_c} \left( \frac{T_{c1}}{P_{c1}} - \frac{T_{cn}}{P_{cn}} \right) + \frac{S_c}{L_c} (P_{c1} - P_{cn}) - c_{fc} \frac{\dot{m}_c^2}{2 \rho_{cn} S_c D_{cn}} \quad (14.3)$$

The temperature transients are calculated by rearranging from Eq. (12.52) as:

$$\frac{\partial T_{o,c,i+1}}{\partial t} = \frac{-\kappa_{ck}}{c_{p,c,i+1} \rho_{ck} \Delta V_h} \left[ \dot{m}_h (c_{p,c,i} T_{o,c,i} - c_{p,c,i+1} T_{o,c,i+1}) - \dot{Q}_{ck} \right] - \left( \frac{\kappa_{ck} - 1}{c_{p,c,i+1}} \right) \frac{\dot{m}_c}{\rho_{ck}^2 S_c^2} \frac{\partial \dot{m}_c}{\partial t} \quad (14.4)$$

The subscripts  $h$  and  $c$  in Eqs. (14.1), (14.2), (14.3), and (14.4) refer to the *hot* and *cold* sides, respectively. The subscripts  $i, i+1$  refer to computational stations in Fig. 14.2. The quantities with the subscript  $k$  are averaged between  $i$  and  $i+1$ . Equations (14.1), (14.2), (14.3), and (14.4) describe the mass flow transients as well as the temperature transients within volume elements of the width  $\Delta x$ . The thermal energy flow portions  $\dot{Q}_{hk}$  and  $\dot{Q}_{ck}$  assume positive (heat addition) or negative signs (heat rejection) based on the direction of the heat flow that pertains to the individual volume elements. They are calculated using the heat transfer coefficient and the temperature difference:

$$\dot{Q}_c = \bar{\alpha}_c A_c \Delta \bar{T}_c, \quad \dot{Q}_h = \bar{\alpha}_h A_h \Delta \bar{T}_h \quad (14.5)$$

In Eq. (14.5),  $\bar{\alpha}_c, \bar{\alpha}_h$  are the averaged heat transfer coefficients,  $\Delta \bar{T}_c, \Delta \bar{T}_h$  the mean temperature and  $A_c, A_h$  the contact surfaces on the cold and hot sides, respectively. The mean temperatures are:

$$\Delta \bar{T}_h = \bar{T}_{S_h} - \bar{T}_{\infty_h}, \quad \Delta \bar{T}_c = \bar{T}_{S_c} - \bar{T}_{\infty_c} \quad (14.6)$$

The subscripts  $S$  and  $\infty$  in Eq. (14.6) refer to the *surface temperature* and the temperature outside the boundary layer, respectively.

### 14.1.3 Coupling Condition Hot, Cold Side

The coupling condition between the cold and hot side is provided by the material temperature differential equation:

$$\frac{dT_w}{dt} = \frac{1}{\rho_w c_w \Delta v_w} (\dot{Q}_c + \dot{Q}_h) \quad (14.7)$$

where the  $\dot{Q}_c$  and  $\dot{Q}_{hc}$  assume negative values if the heat is rejected. For the special steady state case, Eq. (14.7) is reduced to:

$$\dot{Q}_c + \dot{Q}_h = 0 \quad (14.8)$$

### 14.1.4 Recuperator Heat Transfer Coefficient

The heat transfer coefficients on both sides are determined by using Nusselt based correlations:

$$Nu = 0.023 Re^{0.8} Pr^{0.4} \quad (14.9)$$

Kays and London [4] give a summary of empirical correlations for heat exchangers with different geometries. A more detailed explanation of the heat transfer process within different exchangers is found in Hausen [5]. The  $Re$ -number in Eq. (14.9), which must be individually determined for each side, is determined using the individual mass flow and hydraulic diameter

$$Re = \frac{VD_{hyd}}{\nu} = \frac{\dot{m} D_{hyd}}{S\mu} \quad (14.10)$$

With Eq. (14.9) and (14.10), the Stanton number can be calculated that determines the heat transfer coefficient:

$$St = \frac{Nu}{RePr} = \frac{\alpha}{\rho c_p V} \quad (14.11)$$

From Eq. (14.11), the individual heat transfer coefficient  $\alpha$  is calculated as:

$$\alpha = St \rho c_p V = \frac{St c_p \dot{m}}{S} \quad (14.12)$$

with  $c_p$  as the specific heat at constant pressure and  $S$  the cross section. To account for the thermal resistance on the cold and hot side of the recuperator, the surface temperatures in Eqs. (14.5) and (14.6) must be replaced by the wall mean temperature. This is done by introducing the combined thermal resistance into Eq. (14.5)

$$\dot{Q}_c = \frac{A_c(\bar{T}_{S_c} - \bar{T}_{\infty_c})}{R_{w_c} + \frac{1}{\alpha_c}}, \quad \dot{Q}_h = \frac{A_h(\bar{T}_{S_h} - \bar{T}_{\infty_h})}{R_{w_h} + \frac{1}{\alpha_h}} \quad (14.13)$$

In most of the recuperators' high pressure sides, the working medium passes through a number of tubes. It is appropriate to approximate the thermal resistance  $R_{w_c}$  and  $R_{w_h}$  by an equivalent cylindrical pipe resistance. For determining the material temperature transients, Eq. (14.13) is inserted into (14.7). With the above equations and the following boundary conditions (14.14)

$$\begin{array}{llll}
 P_{hl} = P_{lh} & P_{hm} = P_{Oh} & T_{o,hl} = T_{o,lh} & T_{o,hm} = T_{o,Oh} \\
 P_{cl} = P_{Oc} & P_{cn} = P_{lc} & T_{o,cl} = T_{o,Oc} & T_{o,cn} = T_{o,lc}
 \end{array} \quad (14.14)$$

the transient behavior of the recuperator is completely described.

## 14.2 Modeling Combustion Chambers

A generic representation of three different types of combustion chambers used in aero- and power generation gas turbine engines is given in Fig. 14.3.

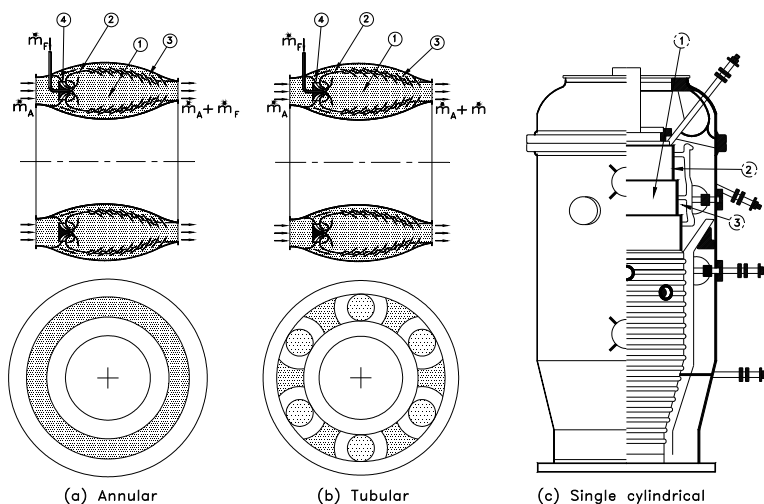


**Fig. 14.3:** Three different types of combustion chambers utilized in aircraft and power generation gas turbines. (a) Annular type, (b) tubular type, (c) heavy duty, single cylindrical power generation (BBC)

Key design features of gas turbine combustion chambers are given in [6]. While the annular (a) and tubular type (b) combustion chambers are encountered in both aircraft and power generation gas turbines, the single cylindrical silo type (c) is utilized only in power generation gas turbine engines. All three types, regardless of their size and application fields, share the following features: (1) Primary combustion zone, (2) secondary air zone for protecting the combustion chamber casing against excessive flame radiation temperature, (3) mixing zone, where the hot gas and the rest of the secondary air are mixed, and (4) the fuel/air inlet nozzle. Since these features are common to the above, and almost all other types of combustion chambers, a generic module can be designed that entails the above features. Figure 14.4 exhibits such a generic module. Figure 14.4 is a modular representation of a gas turbine component.



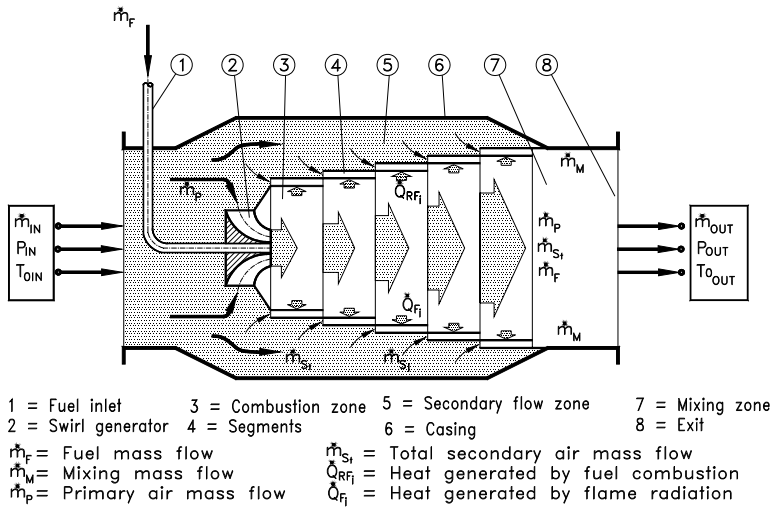


**Fig. 14.4:** Generic modular representation of a combustion chamber

It consists of a primary combustion zone, or primary zone, surrounded by  $n$  rows of segments, the secondary air zone, and the mixing zone. The actual combustion process occurs in the primary zone. The secondary air zone separates the hot primary combustion zone from the combustion chamber casing. The rows of segments in the combustion zone are subjected to a severe thermal loading due to direct flame radiation. Film and/or convection cooling on both the air and the gas sides cools these segments. The air required to cool the hot segments flows through finned cooling channels, thereby contributing to the convection cooling of the segments on the air side. The cooling air flow exiting from the  $j^{th}$  segment row affects the film cooling process on the gas side within the boundary layer in the next row of segments. At the end of that process, the cooling air mass flow is mixed completely with the primary air mass flow. The mass flow relationships prevailing in the primary, the cooling, and the mixing zones are substituted into the energy equation, already formulated. Their effect is significant, particularly in the case of energy balance, because they determine temperature distribution in the individual combustion chamber stations. For that reason, we first determine the mass flow relationships and then deal with the energy balance.

### 14.2.1. Mass Flow Transients

The combustion chamber mass flow is divided into primary mass flow, secondary (cooling) mass flow, and mixing mass flow, as shown in Fig. 14.4.

$$\dot{m}_P = \mu_P \dot{m}, \quad \dot{m}_S = \mu_S \dot{m}, \quad \dot{m}_M = \mu_M \dot{m}, \quad \text{with } \mu_P + \mu_S + \mu_M = 1 \quad (14.15)$$

In Eq. (14.15),  $\mu_P$ ,  $\mu_S$ , and  $\mu_M$  denote the primary, secondary, and mixing mass flow ratios, respectively. If the primary zone consists of  $n$  rows of segments, the cooling mass flow for the  $j^{\text{th}}$  row of segments is:

$$\dot{m}_{S_j} = \mu_j \dot{m}_S = \mu_j \mu_S \dot{m} \quad (14.16)$$

Considering the fuel/air ratio,  $\mu_F = \dot{m}_F / \dot{m}$ , the mass flow within the  $j^{\text{th}}$  row of the segments is:

$$\dot{m}_j = \sigma_j \dot{m}, \quad \sigma_j = \mu_F + \mu_P + \mu_S \sum_{v=1}^j \mu_v \quad (14.17)$$

To determine the transient behavior of a combustion chamber that has already been designed, it is necessary to start from the given ratios  $\mu_P$ ,  $\mu_S$ ,  $\mu_M$ , and  $\sigma_j$ . For a new design, it is possible to vary these ratios until the desired solution is attained that fulfils the required material temperature conditions dictated by the local heat transfer. The mass flow in the combustion chamber is obtained as the solution of the modified version of Eq. (12.34):

$$\begin{aligned} \frac{\partial \dot{m}}{\partial t} = & \frac{R \dot{m}^2 (1 + \mu_F)^2}{L_c S} \left[ \left( \frac{T}{P} \right)_I - \left( \frac{T}{P} \right)_O \right] + \\ & + \frac{S}{L_c x} \left( \frac{p_I - p_O}{1 + \mu_F} \right) - c_f \frac{\dot{m}^2 (1 + \mu_F)^2}{2 \rho S D_h} \end{aligned} \quad (14.18)$$

In Eq. (14.18), the subscripts  $I$  and  $O$  stand for the inlet and outlet plena, respectively. The volume of the combustion chamber is replaced here with an equivalent volume, which is the product of a constant cross section  $S$  and the characteristic length  $L_c$ . Thus, the pressures and temperatures in Eq. (14.18) represent the inlet and outlet quantities, which must be known at the design point.

### 14.2.2. Temperature Transients

To determine the temperature transients for gas within the primary combustion zone and air within the secondary zone, we start from Eq. (12.52). Considering air, fuel, and eventually, water as the main combustion constituents, Eq. (12.52) needs to be rearranged as follows:

$$\begin{aligned}
\frac{\partial T_{o_{i+1}}}{\partial t} = & \frac{1}{V \rho_{i+1} c_{p_{i+1}}} \left\{ \sum_{k=1}^K \dot{m}_{i,k} \left[ \kappa_{i+1} (c_{p_i} T_{o_i})_k - c_{p_{i+1}} T_{o_{i+1}} \right] \right\} \\
& + \frac{1}{V \rho_{i+1} c_{p_{i+1}}} \left[ (1 - \kappa_{i+1}) \dot{m}_{i+1} c_{p_{i+1}} T_{o_{i+1}} - \kappa_{i+1} \dot{Q}_G \right] \\
& - \left( \frac{1 - \kappa_{i+1}}{c_{p_{i+1}}} \right) \left( \frac{\dot{m}}{\rho^2 S^2} \right)_{i+1} \frac{\partial \dot{m}_{i+1}}{\partial t}
\end{aligned} \quad (14.19)$$

with  $\dot{Q}_G = V \Delta \dot{Q}$  as the gas side heat flow. The index  $i$  refers to the computation station in question. The mixing components are identified with the sequential index  $k$ , the upper summation limit for which  $K$  represents the number of constituents involved in a mixing and combustion process. The mixing components at the inlet station are the cooling air from secondary zone, the combustion air, and the fuel. For the cooling zone, Eq. (12.52) yields:

$$\frac{\partial T_{o_{i+1}}}{\partial t} = \frac{\kappa}{V \rho c_p} \left[ \dot{m} c_p (T_{o_i} - T_{o_{i+1}}) - \dot{Q}_A \right] + \frac{1 - \kappa}{c_p} \left( \frac{\dot{m}}{\rho^2 S^2} \right) \frac{\partial \dot{m}}{\partial t} \quad (14.20)$$

with  $\dot{Q}_A = V \Delta \dot{Q}$  as the air side heat flow. The temperature distribution within the segment material can be determined as follows using the heat conductance equation:

$$\frac{\partial \bar{T}_w}{\partial t} = \frac{1}{\rho_w c_w v_w} [\dot{Q}_h + \dot{Q}_c] \quad (14.21)$$

with  $\dot{Q}_h$  and  $\dot{Q}_c$  as the heat flows supplied and carried from the combustion chamber segment, respectively. For the primary zone surrounded by a row of segments,  $\dot{Q}_G$  is made up of the fuel heat,  $\dot{Q}_F$ , the flame radiation heat,  $\dot{Q}_{RF}$ , and the convection heat,  $\dot{Q}_{CG}$ , on the gas (or hot) side:

$$\dot{Q}_G = \dot{Q}_F + \dot{Q}_{RF} + \dot{Q}_{CG} \quad (14.22)$$

radiation is reduced to an acceptable level by an intensive film cooling on the gas side and convective heat removal on the air side. The segments are therefore subjected to the following thermal loading on the gas side (or hot side):

$$\dot{Q}_h = \dot{Q}_{RF} + \dot{Q}_{Fi} \quad (14.23)$$

with  $\dot{Q}_{Fi}$  standing for the amount of heat carried off by the film cooling. The heat flow carried off on the air side (cold side),  $\dot{Q}_c$ , consists of a convection and a

radiation component. The latter is due to the difference in temperature between the cold air enclosure liner and the hot surface of the fins. As a result we find:

$$\dot{Q}_A \equiv \dot{Q}_c = \dot{Q}_{CA} + \dot{Q}_{RA} \quad (14.24)$$

For the film cooling:

$$\dot{Q}_{Fi} = \bar{\alpha}_{Fi} S_G (\bar{T}_{Fi} - \bar{T}_w) \quad (14.25)$$

with  $\bar{\alpha}_{Fi}$  as the average heat transfer coefficient and  $\bar{T}_{Fi}$  the average film temperature. The convective heat removal on the air side is obtained from:

$$\dot{Q}_{CA} = \bar{\alpha}_A S_A (\bar{T}_w - \bar{T}_A) \quad (14.26)$$

The calculation of the radiation heat flows  $\dot{Q}_{RA}$  and  $\dot{Q}_{RF}$  is explained in the following section.

### 14.2.3 Combustion Chamber Heat Transfer

Heat transfer processes in combustion chambers involve several mechanisms. To distinguish these mechanisms, we consider a section of the heavy duty combustion chamber shown in Fig. 14.3 with the corresponding generic module Fig. 14.4. Different heat transfer mechanisms are shown in Fig. 14.5.

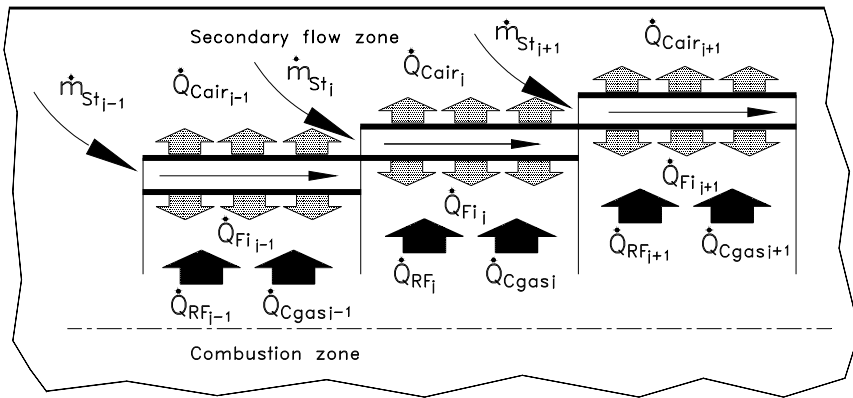


**Fig. 14.5:** Details of heat transfer radiation, conduction, and convection heat transfer along a generic segment of a gas turbine combustion chamber.

Considering the combustion zone on the hot (or gas side) of a segment that separates the primary combustion zone from the secondary flow zone, as shown in Fig. 14.5, the following heat transfer types are distinguished: (1)  $\dot{Q}_{RF,i}$  is added by the flame radiation (2)  $\dot{Q}_{Cgas,i}$ , is added to the segments by convection, (3)  $\dot{Q}_{Fi,i}$  is removed from the gas side by film jets, (4)  $\dot{Q}_{Cair,i}$  is removed from the segment on the air side (cold side) by convection, and (5) the conduction through the segment

wall couples the heat transfer portions on both sides of the segment. Convective and conductive heat transfer types are discussed in Section 14.1. For the jet film cooling heat transfer, correlations by Juhasz and Marek [7] can be used. On the primary combustion side, the flame radiation is, by far, the major contributor to the radiation heat transfer. There is also radiation on the secondary air side between the segment material, enclosed secondary air, and the casing. However, its contribution compared to the flame radiation is negligibly small. The basis for the radiative heat transfer is the Planck's [8] spectral distribution of radiation for an ideal radiating body, called *black body* given as:

$$E_{\lambda,b}(T) = \frac{C_1}{\lambda^5 \left( \exp(C_2/\lambda T) - 1 \right)} \quad (W/m^2 \mu m) \quad (14.27)$$

In Eq. (14.27),  $E_{\lambda,b}(T)$  is the spectral emissive power of a black body as a function of wave length and temperature of the emitting surface,  $\lambda$  is the wave length in microns (or meters),  $T$  the absolute temperature of the body, and the subscript  $b$  stands for black ideal body. The constants are  $C_1 = 3.742 \times 10^8 W \mu m^4/m^2$  and  $C_2 = 1.439 \times 10^4 \mu m K$ . Equation (14.27) is derived for an emitting surface in a vacuum, where the index of refraction is unity. This index is defined as the ratio of velocity of light in a vacuum to the velocity of light in a non-vacuum environment. The spectral distribution described by Eq. (14.27) is plotted in Fig. 14.6 with body temperature as a parameter. Equation (14.27) describes the radiation power for each given wave length  $\lambda = c/v$  with  $c$  as the speed of light and  $v$  wave frequency. For combustion chamber application, it is necessary to find the total energy emitted by the body. This can be found by integrating Eq. (14.27):

$$E_b(T) = \int_0^\infty E_{\lambda,b}(T) d\lambda = \sigma T^4 \quad (14.28)$$

with  $\sigma$  as the Stefan-Boltzmann constant. Equation (14.28) can be applied to two or more bodies that are in radiative interaction. Consider the simplest case of two parallel black surfaces that are at different temperatures. The net rate of heat transfer between these two surfaces is:

$$\dot{Q} = \sigma (T_1^4 A_1 - T_2^4 A_2) \quad (14.29)$$

For radiative heat transfer, the flame shape may be approximated as a cylinder.

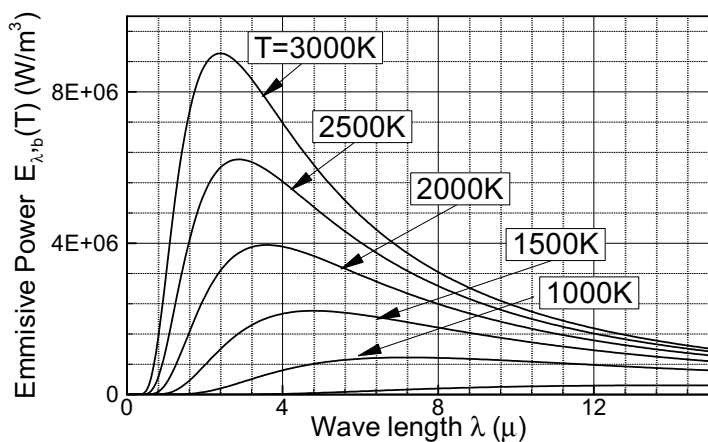


**Fig. 14.6:** Spectral emissive power as a function of wave length with body temperature as parameter described by Planck's Eq. (14.27).

### 14.3 Example: Startup and Shutdown of a Combustion Chamber-Preheater System

The example deals with the startup and shutdown process of a generic system consisting of a combustion chamber, a pipe and a preheater as shown in Fig. 14.7.

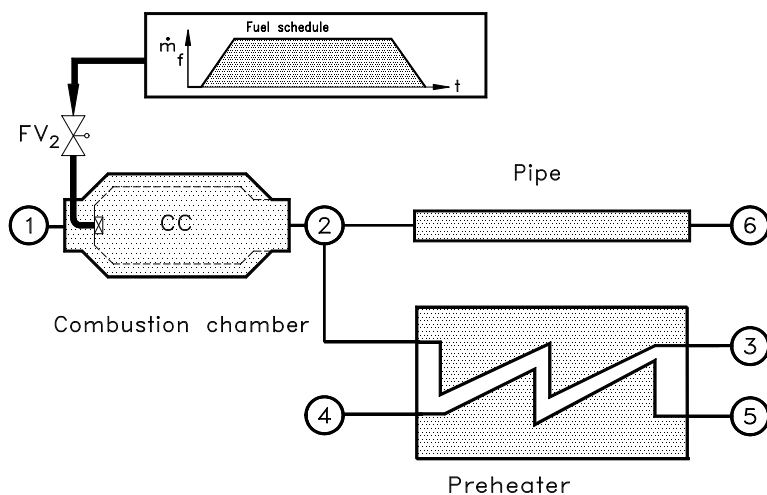


**Fig. 14.7:** A system consisting of a combustion chamber, a preheater and a pipe.

These components are parts of a Compressed Air Energy Storage (CAES) plant discussed in Chapter 18, Section 18.5.1.1. The combustion chamber is connected to plenum (1), which operates at a constant pressure and temperature. Constant air flow enters the combustion chamber which is connected to plenum (2). A major portion of the combustion gas passes through a pipe and exits the system at plenum (6). A minor portion of the combustion gas enters the hot side of the preheater and leaves it at plenum (3). The cold side of the preheater continuously receives cold air at constant pressure and room temperature from plenum (4) and exits the cold side preheater at plenum (5). The fuel valve is programmed to provide the combustion chamber with the fuel schedule  $\dot{m} = \dot{m}(t)$ . The fuel schedule shows the startup, normal operation and the combustion chamber shutdown, Fig. 14.8.

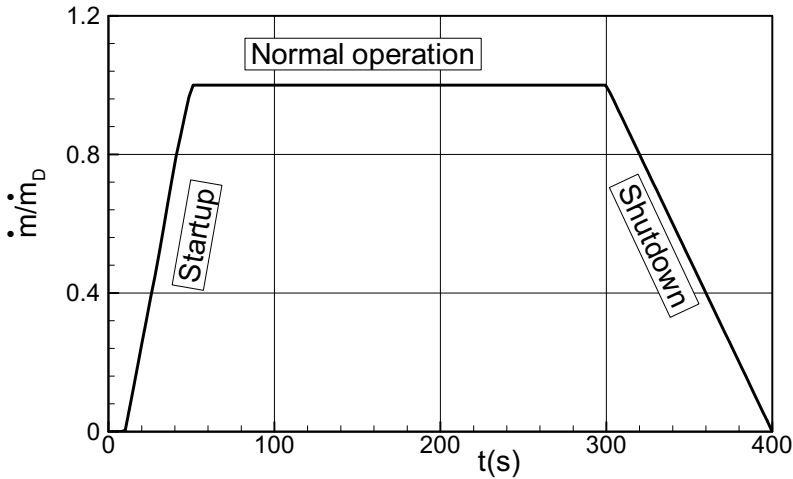


**Fig. 14.8:** Combustion chamber fuel schedule: Startup, design operation, shutdown, calculated by GETRAN.

Similar to the cases discussed previously, each component of the above system represented by the corresponding module is described by a system of differential equations. Prescribing the following boundary conditions:

$$\begin{aligned} P_1 &= \text{const.} & P_3 &= \text{const.} & P_4 &= \text{const.} & P_5 &= \text{const.} & P_6 &= \text{const.} \\ T_{01} &= \text{const.} & T_{03} &= \text{const.} & T_{04} &= \text{const.} & T_{05} &= \text{const.} & T_{06} &= \text{const.} \end{aligned} \quad (14.30)$$

the systems of the corresponding differential equations can be solved using an appropriate solver for stiff differential equations [1], [2].

**Combustion Chamber Startup:** Using the boundary conditions (14.30), we first simulate a cold start of the combustion chamber followed by its design point operation and the subsequent shutdown. This process is controlled by the fuel

schedule shown in Fig. 14.8 with  $\dot{m}$  and  $\dot{m}_D$  as the actual and the design point fuel mass flow, respectively. Starting from a cold combustion chamber and preheater, cold air flows through the entire system for about 10 seconds. At  $t = 10$  s, the fuel valve starts to open adding fuel continuously until the design fuel mass flow has been reached. During the fuel addition, the temperature of the entire system starts to rise. The combustion chamber gas temperature, Fig. 14.9, reacts to this event with a corresponding increase.

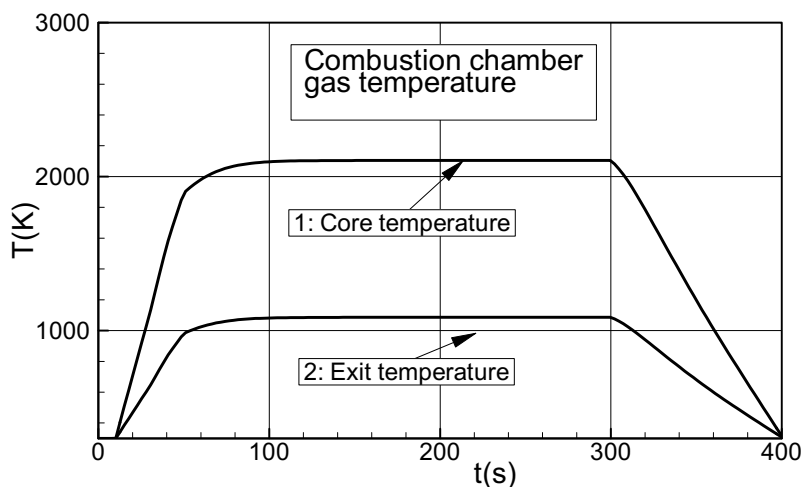


**Fig. 14.9:** Combustion chamber gas temperature, startup, design operation, shutdown, calculated by GETRAN.

Curve 1 exhibits the temperature of the core flow within the primary combustion zone. Mixing with the secondary air significantly reduces the gas temperature to the exit temperature level of slightly above 1100 K, curve 2.

**Preheater Temperature Transient:** The combustion gas enters the hot side of the preheater and increases its temperature as seen in Fig. 14.10.

Curves 1 represents the gas temperature at the rear portion of the preheater. Heat is transferred from the hot combustion gas to the cold side air of the preheater by means of convection and conduction through the preheater metal raising its temperature. The metal temperature transient is shown in Fig. 14.10, curve 2. The heat transferred from the preheater metal to its air side causes the cold side air temperature to rise as seen in Fig. 14.10, curve 3.



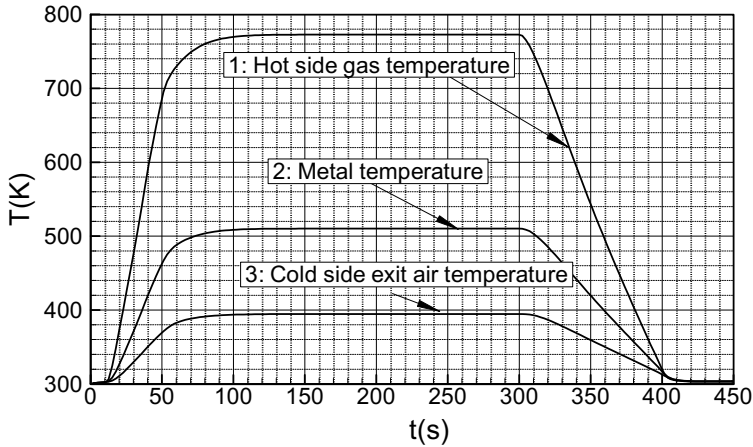


**Fig. 14.10:** Gas, metal and air temperature transients at the exit portion of the preheater.

Accurate prediction of the design and off-design dynamic behavior of the components discussed in this chapter requires the implementation of appropriate heat transfer coefficients. For design purposes, useful correlations can be found, among others in [4] and [5]. The heat transfer coefficient ( $\alpha$ ) utilized for dynamic calculations in conjunction with the skin friction coefficient are expected to deliver the desired temperature and pressure distributions within these components. Is this not the case,  $\alpha$  can be calculated using steady state condition, where the temporal changes of plena temperature in Eq. (14.19) and (14.20) are set equal to zero. As a results, the amount of the heat transfered and thus the heat transfer coefficient are accurately calculated. This allows a correction of the heat transfer coefficient initially used for dynamic calculation.

## 14.4 Modeling of Afterburners

This component, from a modeling point of view, exhibits a simplified version of the combustion chamber discussed in the previous section. This component, and its modular representation is shown in Fig. 14.11. The modeling of this component follows the same procedure as the combustion chamber. However, because of the absence of secondary flow, the mass flow ratios  $\mu_p$ ,  $\mu_s$ , and  $\mu_M$  have the following values:  $\mu_p = 1$ ,  $\mu_s = 0$ , and  $\mu_M = 0$ .

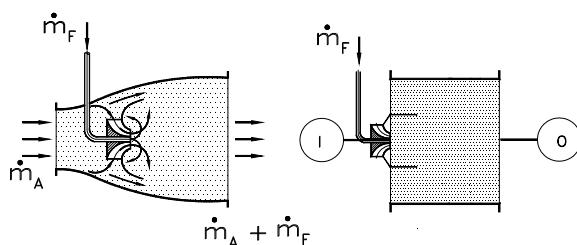


Fig. 14.11: Schematic of an afterburner module

## References

1. Schobeiri T., 1986; "A General Computational Method for Simulation and Prediction of Transient Behavior of Gas Turbines," ASME-86-GT-180.
2. Schobeiri, M. T., Abouelkheir, M., Lippke, C., 1994, "GETRAN: A Generic, Modularly Structured Computer Code for Simulation of Dynamic Behavior of Aero-and Power Generation Gas Turbine Engines," an honor paper, ASME Transactions, *Journal of Gas Turbine and Power*, Vol. 1, pp. 483-494.
3. Schobeiri, M. T., Attia, M, Lippke, C., 1994, "Nonlinear Dynamic Simulation of Single and Multi-spool Core Engines, Part I, II: Theoretical Method, Simulation Cases " *AIAA, Journal of Propulsion and Power*, Volume 10, Number 6, pp. 855-867, 1994.
4. Kays, W.M, London, A. L., 1984, "Compact Heat Exchangers," McGraw-Hill Book Company, third Edition.
5. Hansen, H., 1976, "Wärmeübertragung im Gegenstrom, Gleichstrom und Kreuzstrom, 2. Auflage, ISBN 3854080755286 Springer-Verlag, Berlin Heidelberg New York.
6. Lefebvre, AS.H., 1983, "Gas Turbine Combustion," Hemisphere Publishing Corporation.
7. Marek, C. J., and Huhasz, A. J., 1974, "Simultaneous Film and Convection Cooling of a Plate inserted in the Exhaust Stream of a Gas Turbine Combustor, NASA TND-7689.
8. Planck, M., 1959, " Theory of Heat Radiation," Dover Publication, Inc, New York.

## 15 Modeling the Compressor Component, Design and Off-Design

As mentioned in Chapter 1, the function of a compressor is to increase the total pressure of the working fluid. According to the conservation law of energy, this total pressure increase requires external energy input, which must be added to the system in the form of mechanical energy. The compressor rotor blades exert forces on the working medium thereby increasing its total pressure. Based on efficiency and performance requirements, three types of compressor designs are applied. These are axial flow compressors, radial or centrifugal compressors, and mixed flow compressors. Axial flow compressors are characterized by a negligible change of the radius along the streamlines in axial direction. As a result, the contribution of the circumferential kinetic energy difference  $(U_3^2 - U_2^2)/2$  to the pressure buildup is marginal. In contrast, the above difference is substantial for a radial compressor stage, where it significantly contributes to increasing the total pressure as discussed in Chapter 4.

During the compression process, the fluid particles are subjected to a positive pressure gradient environment that may cause the boundary layer along the compressor blade surface to separate. To avoid separation, the flow deflection across each stage and thus the stage pressure ratio is kept within certain limits discussed in the following section. Compared to an axial stage, a centrifugal compressor stage can achieve pressure ratios of  $\pi_{rad} > 4$  and above at relatively moderate flow deflections. However, geometry, mass flow, efficiency and material constraints place limitations on utilizing radial compressors for large power generation gas turbines and aircraft engines applications. Radial compressors designed for high stage pressure ratios and mass flows comparable to those of axial compressors require substantially larger exit diameters. This can be considered an acceptable solution for industrial applications, but is not a practical solution for implementing into gas turbine engines. In addition, for gas turbine applications, high compressor efficiencies are required to achieve acceptable thermal efficiencies. While the efficiencies of advanced axial compressors have already exceeded 91.5% range, those of advanced centrifugal compressors are still below 90%. Power generation gas turbine engines of 10 MW and above as well as medium and large aircraft engines use axial compressor design. Small gas turbines, turbochargers for small and large Diesel engines have radial impellers that generate high pressure ratios as mentioned above. Compact engines for turboprop applications may have a combination of both. In this case a relatively high efficiency multi-stage axial compressor is followed by a lower efficiency centrifugal compressor to achieve the required engine pressure ratio at smaller stage numbers.

Further stage pressure buildup is achieved by increasing the inlet relative Mach

number  $M_{2rel.} = W_2/c_2$ . In case of subsonic axial flow compressors with  $M_{2rel.} < 1$ , the compression process is primarily established by *diffusion* and *flow deflection*. However, in the case of supersonic relative Mach number  $M_{2rel.} > 1$  that occupies the entire compressor blade height from hub to tip, the formation of oblique shock waves followed by normal shocks as discussed in this chapter contributes to a major pressure increase. However, the increase of stage pressure ratio as a result of compression shocks is associated with additional shock losses that reduce the stage efficiency. To achieve a higher stage pressure ratio at an acceptable loss level, the compressor stage can be designed as *transonic compressor stage*. In this case, the relative Mach number at the hub is subsonic and at the tip supersonic, with transonic Mach range in between. Transonic compressor stage design is applied to the first compressor stage with a relatively low aspect ratio of high performance gas turbine engines.

In this chapter, we first investigate several loss mechanisms and correlations that are specific to compressor component. Using these correlations, first the basic concept for a row-by-row adiabatic calculation method is presented that accurately predicts the design and off-design behavior of single and multi-stage compressors. With the aid of this method, efficiency and performance maps are easily generated. The chapter is then enhanced to calculate the diabatic compression process where the blade rows exchange thermal energy with the working medium and vice versa. The above methods provide three different options for dynamically simulating the compressor component. The first option is to utilize the steady state compressor performance maps associated with dynamic coupling. The second option considers the row-by-row adiabatic calculation. Finally, the third option uses the diabatic compression process. Examples are presented.

## 15.1 Compressor Losses

In Chapter 5 we attempted to provide the basic physics of different loss mechanisms for accelerating and decelerating cascades from a unifying point of view. This section deals with particular loss mechanisms encountered in compressors. Because of its significance to aircraft gas turbine engines, manufacturers and research centers have been focusing their attention on developing compressor components with higher efficiency. To predict the compressor stage efficiency accurately, compressor designers often use loss correlations that reflect different loss mechanisms within the compressor stage flow field. In the early fifties, Lieblein and his co-workers [1], [2], [3], [4] and [5] conducted fundamental research in compressor cascade and stage aerodynamics. Their research work, NASA-Report SP-36 [6], is a guideline for compressor designers. Miller and Hartmann [7], Miller et al. [8], and Schwenk et al. [9] initiated their fundamental research on transonic compressors where they primarily investigated the shock losses. Gostelow et al. [10], Gostelow [11], Saylor and Smith [12], Saylor and Gostelow [13], Gostelow and Krabacher [14], Krabacher and Gostelow [15] and [16] focused their experimental research on single-stage high Mach number compressor stages. Their comprehensive experimental research

includes the performance evaluation of several rotors. et al. [17] performed similar investigations on single-stage high Mach number compressor stages. Koch and Smith [18] presented a method for calculating the design point efficiency potential of a multi-stage compressor. Schobeiri [19] investigated the individual loss mechanisms that occur in an advanced compressor stage. He developed a new shock loss model, introduced a modified diffusion factor and re-evaluated the relevant experimental data published by NASA. Recent investigations by König et al. [20] investigate the loss and deviation angles for transonic blading.

The total pressure losses encountered in an advanced compressor stage are: (1a) The blade primary losses generated by the wall shear stress, which is proportional to the local velocity deformation. Since the blade mid-section is not affected by the secondary flow that originates from the hub and casing, the primary losses are dominant. (1b) The trailing edge mixing losses are due to the thickness of the trailing edge and the boundary layer thicknesses on the suction and pressure surfaces that causes wake defect, mixing, and thus additional entropy increase. From an experimental point of view, these two losses are not separable since the total pressure measurements occur at a certain distance downstream of the trailing edge plane and inherently include the wake total pressure defect. The combination of these two losses is frequently called profile loss. (2) Shock losses are encountered in compressor stages with high transonic to supersonic inlet relative flow conditions. Based on an angle incidence and the shock position, these losses may generate considerable entropy increase that result in significant deterioration of the stage efficiency. The shock losses are approximately of the same order of magnitude as the profile losses. (3) Secondary losses due to the end wall boundary layer development and blade tip clearances. (4) Secondary flow losses are also present for compressor blades with shrouds. A comprehensive treatment of compressor losses is found in Schobeiri [19], [21], [22], [23] and Schobeiri and Attia [24].

This chapter focuses on three issues: (1) A new modified diffusion factor that describes the blade loading for the rectilinear and annular cascades, as well as for the entire compressor stage. This new diffusion factor, which includes the compressibility effects, allows the loss parameters to be systematically correlated with the diffusion factor. (2) A new shock loss model is presented that overcomes the weakness of the existing loss models described by Levine [25], Balzer [26] and Swan [27]. (3) The existing published data are re-evaluated and detailed correlations are presented. In conjunction with the loss calculation, it should be mentioned that the currently available commercial numerical codes such as the Reynolds Averaged Navier-Stokes (RANS) code are capable of calculating the total pressure losses and thus the efficiency of a compressor stage and thus the entire compressor. The use of RANS-solvers for predicting the losses and thus the efficiency is associated with (a) a substantial amount of computational time, and (b) certain discrepancies between the numerical results and the results of compressor efficiency and performance tests. This circumstance is the reason, why the use of loss correlations in compressor design process is indispensable.

### 15.1.1 Profile Losses

Lieblein and Roudebush [3] derived the expression for profile loss coefficient as a function of cascade geometry, flow angles, and the boundary layer parameters shown in Eq. (15.1):

$$\zeta_P = \sigma \left( \frac{\delta_2}{c} \right) \left( \frac{\sin \beta_1}{\sin \beta_2} \right)^2 \left( \frac{1 + H_{32}}{\left( 1 - \frac{\delta_2}{c} \sigma H_{12} \right)^3} \right) \quad (15.1)$$

with the form factor  $H_{32} = f(H_{12})$ . Among the boundary layer parameters in Eq. (15.1), the momentum thickness  $\delta_2$  is of primary importance. It gives a direct relationship between the separation point and the free-stream velocity gradient (or pressure gradient) shown in the following von Kàrmàn integral equation for incompressible flow:

$$\frac{\tau_w}{\rho V^2} = \frac{d\delta_2}{dx} + (2 + H_{12}) \frac{\delta_2}{V} \frac{dV}{dx} \quad (15.2)$$

with  $\tau_w$  as the wall shear stress and  $H_{12}$  the form parameter. For a highly loaded compressor blade, flow separation may occur, where the velocity profile starts to separate at the profile inflection point. Consequently, the wall shear stress at that point vanishes and Eq. (15.2) reduces to:

$$\frac{d\delta_2}{dx} = - (2 + H_{12}) \frac{\delta_2}{V} \frac{dV}{dx} \quad (15.3)$$

Equation (15.3) shows a direct relation between the blade velocity gradient and the momentum thickness. As an appropriate measure for the velocity gradient, Lieblein et al. [1] introduced the equivalent diffusion factor:

$$D_{eq} = \frac{V_{\max}}{V_2} = \frac{V_1}{V_2} \frac{V_{\max}}{V_1} \quad (15.4)$$

with  $V_{\max}$  as the maximum velocity on the suction surface shown in Fig.15.1. This velocity ratio, which changes by changing the flow deflection given by the velocity triangle, properly reflects the blade loading situation. However, it requires the knowledge of the maximum velocity at different flow deflections, which is not always given. From a compressor designer point of view, relating the blade loading

to the actual velocity triangle is most appropriate.

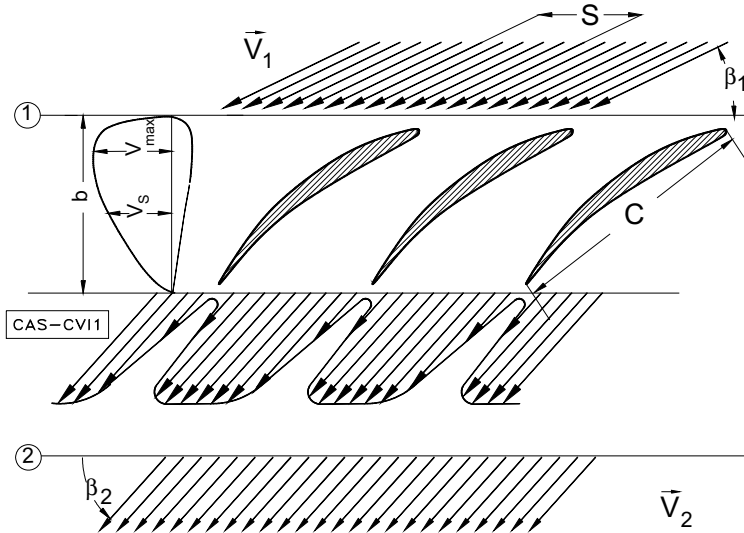


Fig.15.1: Schematic representation of a compressor cascade flow.

### 15.1.2 Diffusion Factor

Using Fig. 15.1, we introduce the dimensionless parameters  $\eta = V_s/V_1$ ,  $\xi = x/b$  and approximate the dimensionless velocity distribution  $\eta$  by a polynomial

$$\eta = \sum_{n=0}^N a_n \xi^n = a_0 + a_1 \xi + a_2 \xi^2 + \dots + a_N \xi^N \quad (15.5)$$

The Taylor expansion in the near of  $\xi_{\max}$  results in:

$$\eta = \eta_{\max} + \frac{d\eta}{d\xi} \Delta\xi + \frac{1}{2} \frac{d^2\eta}{d\xi^2} \Delta\xi^2 + \dots \quad (15.6)$$

with  $\Delta\xi = \xi - \xi_{\max}$ . Neglecting the higher order terms, Eq. (15.6) can reduce to:

$$\eta = \eta_{\max} + \left( \frac{d\eta}{d\xi} \right)_{\xi_{\max}} (\xi - \xi_{\max}) \quad (15.7)$$

The velocity slope is found from Eq. (15.5):

$$\left( \frac{d\eta}{d\xi} \right)_{\xi_{\max}} = a_1 + 2a_2 \xi_{\max} \quad (15.8)$$

Incorporating Eq. (15.8) into Eq. (15.7) results in:

$$\eta = \eta_{\max} + C_1 \xi + C_2 \quad (15.9)$$

with the constants:  $C_1 = a_1 + 2a_2 \xi_{\max}$  and  $C_2 = -C_1 \xi_{\max}$ . The circumferential component of the force acting on the blade in Fig.15.1 is calculated by integrating the pressure distribution along the blade suction and pressure surfaces using the Bernoulli equation:

$$T = T_P - T_S = \int_0^b (p_P - p_S) dx = \frac{1}{2} \rho \int_0^b (V_S^2 - V_P^2) dx \quad (15.10)$$

Since only the contribution of the suction surface is considered for estimating the diffusion factor, the second term in the integrand may be set equal to zero. Incorporating Eq. (15.9) into Eq. (15.10) results in:

$$\frac{T}{\frac{1}{2} \rho V_1^2 b} = \eta_{\max}^2 + (C_1 + 2C_2) \eta_{\max} + \frac{1}{3} C_1^2 + C_1 C_2 + C_2^2 \quad (15.11)$$

The force component  $T$  can also be calculated using the momentum equation in the circumferential direction:

$$T = s \rho V_m (V_{u1} - V_{u2}) \quad (15.12)$$

with  $s$  and  $\rho$  as the blade spacing and the flow density,  $V_m$  and  $V_u$  as the meridional and circumferential velocity components. Inserting the velocity components defined in Fig.15.1 into Eq. (15.12), it becomes:

$$\frac{T}{\frac{1}{2} \rho V_1^2 b} = 2 \frac{s}{b} \sin^2 \beta_1 (\cot \beta_1 - \cot \beta_2) \quad (15.13)$$

Equating Eq. (15.11) and (15.13) results in the following relationship:

$$\eta_{\max}^2 + D_1 \eta_{\max} + D_3 = 0 \quad (15.14)$$



with the coefficients  $D_i$  as:

$$\begin{aligned} D_1 &= C_1 + 2 C_2 \\ D_2 &= C_1 C_2 + C_2^2 + \frac{1}{3} C_1^2 \\ D_3 &= D_2 - \frac{2s}{b} \sin^2 \beta_1 (\cot \beta_1 - \cot \beta_2) \end{aligned} \quad (15.15)$$

The solution of Eq. (15.14) after neglecting the higher order terms in  $D_3$  yields:

$$\eta_{\max} = \frac{V_{\max}}{V_1} = K_1 \left[ \frac{\sin^2 \beta_1}{\sigma} (\cot \beta_1 - \cot \beta_2) \right] + K_2 = K_1 G + K_2 \quad (15.16)$$

Equation (15.16) exhibits a special case of Eq. (15.14) and gives an explicit relationship between the maximum velocity  $V_{\max}$  and the cascade *circulation function*

$G = \frac{\sin^2 \beta_1}{\sigma} (\cot \beta_1 - \cot \beta_2)$  in the bracket. Using the NACA-65(A10) series and the

circular arc blade C.4, for the optimum flow condition that causes a minimum loss denoted by (\*), the constants in Eq. (15.16) are experimentally determined by Lieblein [5] as  $K_1 = 0.6$  and  $K_2 = 1.12$ :

$$\eta_{\max}^* = \left( \frac{V_{\max}}{V_1} \right)^* = K_1 G^* + K_2 = 1.12 + 0.6 \frac{\sin^2 \beta_1}{\sigma} (\cot \beta_1 - \cot \beta_2) \quad (15.17)$$

Equation (15.17) is generally valid for any arbitrary inlet flow angle including the off-design incidence angles, Fig.15.2 . However, the compressor designer prefers to

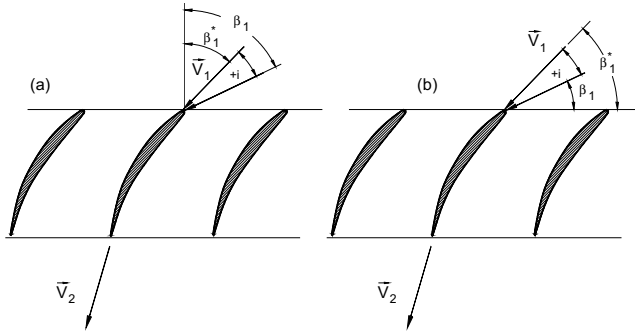


**Fig.15.2:** Positive incidence angle: (a) definition by Lieblein [4], (b) based on the unified velocity diagram angle definition in this book.

relate the off-design  $\eta_{\max} = V_{\max}/V_1$  to the design point  $\eta_{\max}^*$ . For this purpose, Lieblein [4] introduced an empirical correlation for  $\eta_{\max}$  for positive incidence angles  $i = \beta - \beta^*$  as defined in Fig.15.2:

$$\eta_{\max} = \left( \frac{V_{\max}}{V_1} \right) = 1.12 + 0.61 G^* + a (\beta_1 - \beta_1^*)^{1.42} \quad (15.18)$$

where  $a = 0.0117$  for the NACA 65(A10) and  $a = 0.0070$  for the C.4 circular arc blades. Equation (15.18) accurately estimates the maximum velocity ratio for a positive incidence. However, it cannot be used for negative incidence angles because of the rational exponent of the argument  $i = \beta_1 - \beta_1^*$ . To eliminate this deficiency, we replace Eq. (15.18) with the following polynomial:

$$\eta_{\max} = \eta_{\max}^* + \sum_{n=1}^N a_n (\beta_1 - \beta_1^*)^n \quad (15.19)$$

and neglect the terms with  $n > 2$ , Eq. (15.19) becomes:

$$\eta_{\max} = \left( \frac{V_{\max}}{V_1} \right) = \left( \frac{V_{\max}}{V_1} \right)^* + a_1 (\beta_1 - \beta_1^*) + a_2 (\beta_1 - \beta_1^*)^2 \quad (15.20)$$

Re-evaluating the experimental results obtained by Lieblein [4], Fig.15.3, leads to

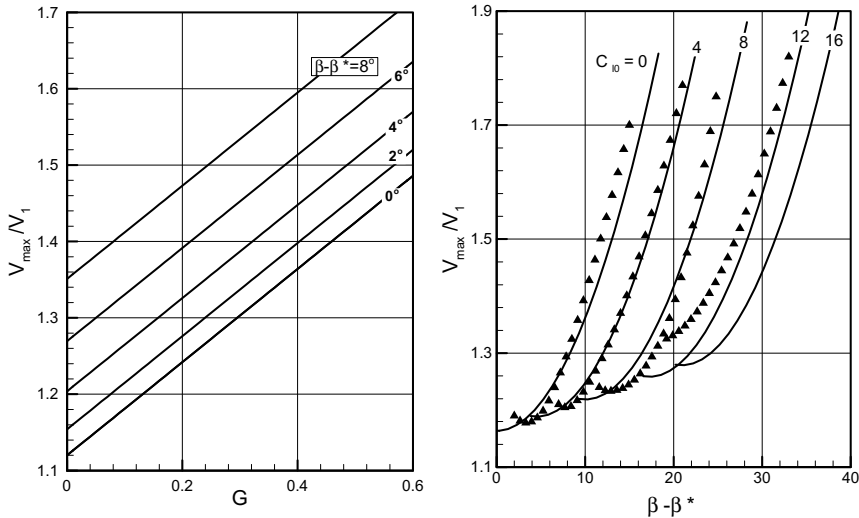


**Fig. 15.3:** Velocity ratio (left) as a function of the circulation function  $G$  with the incidence angle  $i = \beta_1 - \beta_1^*$  as parameter, and (right) as a function of incidence angle  $i = \beta_1 - \beta_1^*$  with lift coefficient  $C_{l0}$  as parameter, experiments represented by symbols taken from Lieblein.

leads to  $a_1 = 0.746$  and  $a_2 = 6.5$ . Equation (15.20) enables the calculation of the velocity ratio and thus the diffusion factor for any off-design operation range. shows the results of Eq. (15.20), where the velocity ratio is plotted against the circulation function  $G$  with the incidence angle  $i = \beta_1 - \beta_1^*$  as a parameter. Compared with the Lieblein's correlation Eq. (15.18), the new correlation Eq. (15.20) yields more accurate results. This statement is also true for Fig.15.3, where the maximum velocity ratio is plotted versus the incidence angle with the lift coefficient  $C_{l0}$  as parameter.

### 15.1.3 Generalized Maximum Velocity Ratio for Stator and Rotor

Lieblein's correlations for the maximum velocity ratio and their experimental verifications were based exclusively on the two-dimensional incompressible cascade flow situation. Significant effects such as compressibility and three-dimensionality were not considered. Furthermore, changes of axial velocity component and streamline curvature, which are always present in a modern compressor, were ignored. Finally, the effect of rotational motion on circulation was disregarded. This section includes the above-mentioned effects in the maximum velocity ratio by employing a generalized circulation concept that leads to a modified diffusion factor. Starting from the Kutta-Joukowski's lift equation (lift force/unit span) with  $\rho_\infty$ ,  $V_\infty$  as the free stream density, velocity, and  $\Gamma$  as the circulation,

$$A = \rho_\infty V_\infty \times \Gamma \quad (15.21)$$

the circulation for an annular compressor cascade is shown in Fig.15.4.

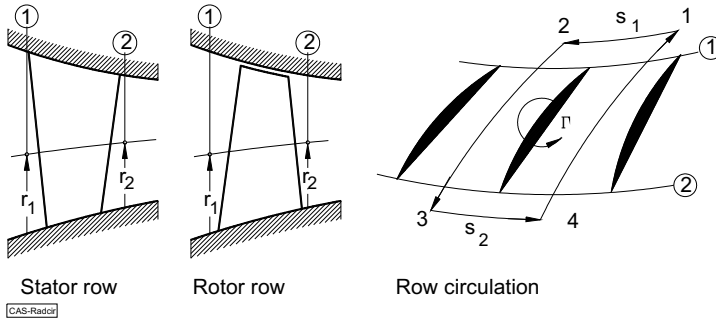


**Fig.15.4:** Unified station definition to circulate the compressor row circulation.

Using the definition in Fig.15.4, the circulation is expressed as:

$$\Gamma = \oint \vec{V} \cdot d\vec{s} \equiv \Gamma_{12} + \Gamma_{23} + \Gamma_{34} + \Gamma_{41} = V_{u1} s_1 - V_{u2} s_2 \quad (15.22)$$

where  $V_{u1}$  and  $V_{u2}$  represent the circumferential velocity components at the inlet and exit and  $\Gamma_{23} = -\Gamma_{41}$ . For a rectilinear cascade with constant height or a stator cascade with constant radius cylindrical streamlines, the spacings are equal at the inlet and exit,  $s_1 = s_2 = s$ . For a stator cascade with conical streamlines as discussed in Chapter 5, different spacings at the inlet and exit are present that relate to each other by the radius of the streamline curvature,  $s_1 = \Delta \theta r_1$  and  $s_2 = \Delta \theta r_2$ . As shown in Fig. 15.4, the stator and the rotor row have identical station numbers as opposed to the ones defined in Chapter 4. Also for both rows the generic angle  $\beta$  is used. As we see below, this convention allows developing unified equations for diffusion factor that can be applied to stator row as well as to rotor row by inserting the absolute and relative flow angles defined in Chapter 4. Using the following velocity ratios:

$$\phi = \frac{V_{m2}}{U_2}, \quad v = \frac{U_1}{U_2} = \frac{r_1}{r_2} = \frac{s_1}{s_2}, \quad \mu = \frac{V_{m1}}{V_{m2}} = \frac{W_{m1}}{W_{m2}} \quad (15.23)$$

and defining the specific circulation function  $\gamma$ , we obtain the following relations for the stator  $\gamma_S$  and rotor  $\gamma_R$ :

$$\gamma_S = \frac{A_S}{\rho_\infty V_\infty V_{m1} s_1} = \left( V_{u1} - V_{u2} \frac{r_2}{r_1} \right) \frac{1}{V_{m1}} = \cot \beta_1 - \frac{1}{v \mu} \cot \beta_2 \quad (15.24)$$

With  $\beta_1, \beta_2$  as the generic stator inlet and exit flow angles. Replacing in Eq. (15.22) the circumferential components of the absolute velocities by the relative one and the rotational velocities at the same streamline, we have for the rotor row:

$$\begin{aligned} \gamma_R &= -\frac{U_1}{V_{m1}} + \frac{W_{u1}}{V_{m1}} + \frac{r_2}{r_1} \frac{U_2}{V_{m1}} - \frac{r_2}{r_1} \frac{W_{u2}}{V_{m1}} \\ \gamma_R &= \frac{1}{v \phi \mu} (1 - v^2) + \cot \beta_1 - \frac{1}{v \mu} \cot \beta_2 \end{aligned} \quad (15.25)$$

With  $\beta_1, \beta_2$  as the generic rotor inlet and exit flow angles. The ratios in the first equation of (15.25) are replaced by the corresponding dimensionless stage parameters and flow angles. Equation (15.25) exhibits a generalized relation for the specific circulation function. As seen, to calculate the circulation, the absolute velocity components  $V_{u1}$  and  $V_{u2}$  are utilized and refer to the absolute circulation rather than the relative one. Using (15.25), we obtain the circulation function for the stator and rotor as:

$$\begin{aligned}
 G_S &= \frac{\sin^2 \beta_1}{\sigma} \gamma_S = \frac{\sin^2 \beta_1}{\sigma} \left( \cot \beta_1 - \frac{1}{\mu v} \cot \beta_2 \right) \\
 G_R &= \frac{\sin^2 \beta_1}{\sigma} \gamma_R = \frac{\sin^2 \beta_1}{\sigma} \left( \frac{1}{\mu v \phi} (1 - v^2) + \cot \beta_1 - \frac{1}{\mu v} \cot \beta_2 \right)
 \end{aligned} \quad (15.26)$$

As seen, the first equation in ? is obtained by setting in the second equation  $U \rightarrow 0$  leading  $\phi \rightarrow \infty$ . With Eqs. ?, the maximum velocity ratio at the optimum point for stator (S), and rotor (R) are calculated from:

$$\left( \frac{V_{\max}}{V_1} \right)_{S,R}^* = 1.2 + 0.6 G_{S,R} \quad (15.27)$$

Correspondingly, we obtain the off-design maximum velocity ratio by using Eq. (15.20):

$$\left( \frac{V_{\max}}{V_1} \right)_{S,R} = 1.12 + 0.6 G_{S,R} + 0.746 (\beta_1 - \beta_1^*) + 6.5 (\beta_1 - \beta_1^*)^2 \quad (15.28)$$

In Eqs. (15.27) and (15.28), the individual quantities denoted by the subscripts  $S$ , and  $R$  pertain to the stator and rotor row, respectively. Thus, the Lieblein's equivalent diffusion factor defined in Eq. (15.4) becomes:

$$\begin{aligned}
 D_{eq} &= \frac{V_{\max}}{V_2} = \mu \frac{\sin \beta_2}{\sin \beta_1} \left( \frac{V_{\max}}{V_1} \right) \\
 D_{eq} &= \mu \frac{\sin \beta_2}{\sin \beta_1} \left[ 1.12 + 0.6 G_{C,S,R}^* + 0.746 (\beta_1 - \beta_1^*) + 6.5 (\beta_1 - \beta_1^*)^2 \right]
 \end{aligned} \quad (15.29)$$

#### 15.1.4 Compressibility Effect

To consider the effect of compressibility on the maximum velocity ratio and thus on the diffusion factor, we modify the specific circulation function for the simplest case, namely a linear cascade, by introducing the inlet density  $\rho_1$ :

$$\gamma_{C_c} = \frac{A_c}{\rho_1 V_{\infty} V_{m1} s} = \frac{\rho_{\infty}}{\rho_1} (V_{u1} - V_{u2}) \frac{1}{V_{m1}} \quad (15.30)$$

The second subscript  $c$  refers to the compressible flow. The freestream density  $\rho_\infty$  can be expressed in terms of the density at the inlet  $\rho_1$  and a finite increase  $\Delta\rho$ :  $\rho_\infty = \rho_1 + \Delta\rho$ . This assumption is an acceptable approximation for the flow outside the boundary layer, where the flow is assumed as a potential flow. With this assumption, the Euler equation combined with the speed of sound may be applied:

$$VdV = -C^2 \frac{d\rho}{\rho} \quad (15.31)$$

with  $C$  as the speed of sound. For small changes, the flow quantities can be related to the quantities at the inlet:

$$\begin{aligned} V &= V_1 + \Delta V; & C &= C_1 + \Delta C \\ \rho &= \rho_1 + \Delta\rho; & d\rho &\approx \Delta\rho \end{aligned} \quad (15.32)$$

We introduce the above relations into Eq. (15.31) and approximate the differentials by differences and neglect the higher order terms. After some rearranging we obtain the density changes by:

$$\frac{\Delta\rho}{\rho_1} = -M_1^2 \left( \frac{V_2}{V_1} \right) \left( \frac{V_2}{V_1} - 1 \right) \quad (15.33)$$

Introducing Eq. (15.33) into the relation  $\rho_\infty = \rho_1 + \Delta\rho$  results in:

$$\frac{\rho_\infty}{\rho_1} = \left[ 1 - M_1^2 \left( \frac{\sin\beta_1}{\sin\beta_2} \right) \left( \frac{\sin\beta_1}{\sin\beta_2} - 1 \right) \right] \quad (15.34)$$

Implementing Eq. (15.34) into Eq. (15.30) obtains the specific circulation functions for linear cascade and stators with cylindrical streamlines:

$$\gamma_{c_c} = \left[ 1 - M_1^2 \left( \frac{\sin\beta_1}{\sin\beta_2} \right) \left( \frac{\sin\beta_1}{\sin\beta_2} - 1 \right) \right] [\cot\beta_1 - \cot\beta_2] \quad (15.35)$$

The expression in the above bracket reflects the Mach number effect on the specific circulation function. Accounting for the compressibility effects and using the same procedure applied above, the generalized circulation function for the rotor is obtained by:

$$\gamma_{R_c} = \left[ 1 - M_1^2 \left( \frac{1}{\mu} \frac{\sin \beta_1}{\sin \beta_2} \right) \left( \frac{1}{\mu} \frac{\sin \beta_1}{\sin \beta_2} - 1 \right) \right] \times \left[ \frac{1}{\mu v \phi} (1 - v^2) + \cot \beta_1 - \frac{1}{\mu v} \cot \beta_2 \right] \quad (15.36)$$

As seen from Eqs. (15.35) and (15.36) and comparing them with Eqs. (15.24) and (15.26), the specific circulation of compressible and incompressible flows are related to each other by the density ratio and thus the Mach number. Considering the simplest case, namely the linear cascade described by Eq. (15.35), because of the compression process with  $V_2 < V_1$ , the bracket representing the compressibility effect is always greater than unity. With Eq. (15.35), the circulation functions for stator and rotor considering the compressibility effect are:

$$(G_{C,S,R})_c = \frac{\sin^2 \beta_1}{\sigma} (\gamma_{S,R})_c \quad (15.37)$$

Using Eq. (15.37) for optimum conditions, the velocity ratio for compressible flow is obtained from:

$$\left( \frac{V_{\max}}{V_1} \right)_{(S,R)_c} = a_1 (\beta_1 - \beta_1^*) + a_2 (\beta_1 - \beta_1^*)^2 + b_1 + b_2 G_{(S,R)_c}^* \quad (15.38)$$

Introducing Eq. (15.38) into the relationship for the equivalent diffusion factor for the rotor as a generalized case, reads:

$$D_{eq} = \left\{ a_1 (\beta_1 - \beta_1^*) + a_2 (\beta_1 - \beta_1^*)^2 + b_1 + b_2 \frac{\sin^2 \beta_1}{\sigma} \left[ \frac{1}{\mu v \phi} (1 - v^2) + \cot \beta_1 - \frac{1}{\mu v} \cot \beta_2 \right] \times \left[ 1 - \frac{1}{\mu} \frac{\sin \beta_1^*}{\sin \beta_2} M_1^2 \left( \frac{1}{\mu} \frac{\sin \beta_1^*}{\sin \beta_2} - 1 \right) \right] \right\} \frac{\sin \beta_2}{\sin \beta_1} \mu \quad (15.39)$$

The angles used in the above equations correspond to those defined in Fig.15.1 and Fig.15.5. Equations (15.38) and (15.39) show the direct relationship between the maximum velocity ratio and the specific circulation function. Equation (15.39) inherently includes the compressibility effect and the actual and optimum flow angles. An alternative diffusion factor, which was first proposed by Smith [28], is:

$$D = 1 - \frac{W_2}{W_1} + \frac{1}{\sigma} \frac{r_2 V_{u2} - r_1 V_{u1}}{(r_1 + r_2) W_1} \quad (15.40)$$

This relation has been accepted and widely used by compressor aerodynamicists. It includes the effect of the rotation in its third term.

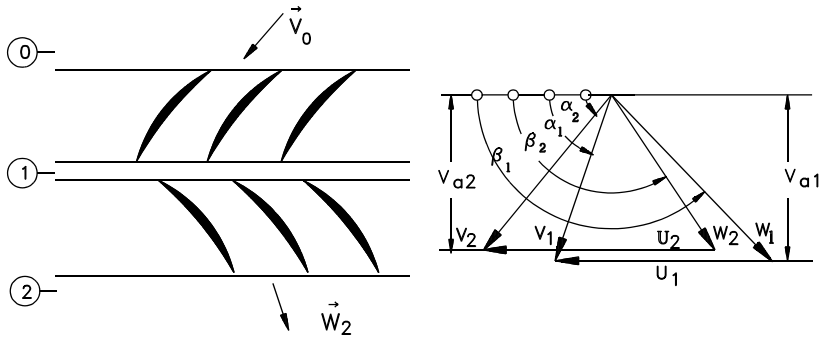


**Fig.15.5** Velocity triangle, angle definition for a compressor stage.

Using the angle definition in Fig.15.5 and the dimensionless parameters previously defined, the re-arrangement of Eq. (15.40) results in:

$$D = 1 - \frac{1}{\mu} \frac{\sin\beta_1}{\sin\beta_2} + \frac{v \sin\beta_1}{\sigma(v+1)} \left[ \frac{1}{\mu v \phi} (1 - v^2) - \cot\beta_1 + \frac{1}{\mu v} \cot\beta_2 \right] \quad (15.41)$$

The crucial part of this equation is the expression in the bracket, which is identical to the specific circulation function in Eqs.(15.26). Introducing the compressibility effect results in a modified version of Eq. (15.41):

$$D_m = 1 - \frac{1}{\mu} \frac{\sin\beta_1}{\sin\beta_2} + \frac{v \sin\beta_1}{\sigma(v+1)} \left[ \frac{1}{\mu v \phi} (1 - v^2) - \cot\beta_1 + \frac{1}{\mu v} \cot\beta_2 \right] x \quad (15.42)$$

$$x \left[ 1 - \frac{1}{\mu} \frac{\sin\beta_1}{\sin\beta_2} M_1^2 \left( \frac{1}{\mu} \frac{\sin\beta_1}{\sin\beta_2} - 1 \right) \right]$$

The diffusion factors presented above are used to establish correlations for the compressor total pressure losses. The theoretical background and the above discussion showed a direct correlation between the profile losses and the boundary layer quantities, particularly the boundary layer momentum thickness. Investigations by NACA, summarized in NASA SP-36 [6] and briefly reviewed in this chapter, showed that measuring the total pressure losses can experimentally determine the



momentum thickness. Further investigations presented in [10], [11], [14], [29], [30] and [31] deal with the spanwise distribution of the total pressure and the total pressure loss coefficient. For the aerodynamic design of a single-stage compressor, et al. [31] presented correlations between the profile loss parameter and the diffusion factor using the experimental data by Sulam et al. [32]. The loss correlations by Monsarrat et al. [31] are frequently used as a guideline for designing compressor stages with the profile similar to that described in [30]. Although the experimental data revealed certain systematic tendencies, no attempt was made to develop a correlation to describe the loss situation in a systematic manner. These facts gave impetus to consider the above experimental data in the present analysis.

### 15.1.5 Shock Losses

Several studies have discussed experimental and theoretical shock loss investigations. As indicated previously, Miller and Hartmann [7], Miller et al. [8], and Schwenk et al. [9] initiated their fundamental research on transonic compressors where they investigated shock losses. Schwenk et al. [9] considered a normal shock in the entrance region of the cascade using a Prandtl-Meyer expansion. Levine [33], Balzer [34], and Swan [35] made efforts to calculate shock losses by estimating the shock position. Their proposed methods, particularly, Levine's [33] and Swan's [35] found their application in compressor design. Similar to Schwenk et al. [9], the methods by Levine, Balzer and Swan include the assumption of a normal shock. While Levine and Swan considered the acceleration on the suction surface by using the continuity and Prandtl-Meyer expansion, Balzer disregarded the expansion completely and used the continuity requirement. The deficiencies in the existing methods can be summarized as: a) They cannot accurately calculate the shock position, which is a prerequisite for accurately predicting the shock losses. b) The Mach number calculated by the Prandtl-Meyer expansion on the suction surface does not represent the shock Mach number along the channel width. Swan partially corrected this deficiency by building an average Mach number. c) The description of the physical process is not complete: the Prandtl-Meyer expansion combined with the continuity requirement is not sufficient to describe the physics. The above deficiencies gave impetus to generate the following new shock loss model, [36]. For the development of this model we assume the passage shock as an oblique shock, whose position changes according to the operating point and may include normal shock as a special case. Furthermore, we assume that the blading has a sufficiently sharp leading edge, where the shocks are attached at least at the design point with no detached bow waves expected. Fig.15.6 shows the shock situation with the inlet flow angle  $\beta_i$ , the metal angle  $\beta_l$  (camber angle), and the incidence angle  $i$ . To determine the shock position we use the continuity equation, the Prandtl-Meyer expansion, and the momentum equation. For the control volume in Fig.15.6, the continuity requirement for a uniform flow is:



where  $v$  is determined from the Prandtl-Meyer expansion law:

$$v = \left( \frac{\kappa + 1}{\kappa - 1} \right)^{\frac{1}{2}} \tan^{-1} \left[ \frac{\kappa - 1}{\kappa + 1} (M^2 - 1) \right]^{\frac{1}{2}} - \tan^{-1} (M^2 - 1)^{\frac{1}{2}} \quad (15.47)$$

The momentum equation in circumferential direction is given by:

$$\int_{S_1} V_1 \cos \beta_1 d\dot{m}_1 - \int_{S_s} V_s \cos \beta_s d\dot{m}_s - \int_{S_s} p_s \cos(\beta_s - \delta) dS_s - \int_{S_w} p_w \cos \alpha_w dS_w = 0 \quad (15.48)$$

with  $S_1$  as the inlet surface,  $S_s$  the shock surface characterized by AB,  $S_w$  the portion of the blade suction surface denoted by BC and  $\alpha_w$  the variable angle between the normal unit vector  $\mathbf{n}_w$  and the circumferential direction (Fig.15.6). As Fig.15.6 shows, because of the cascade periodicity, the pressure at the point A is identical to the pressure at point C. Furthermore, point B on the suction surface represents the common end point for both distances, AB and CB. This means that the pressure distributions along AB and CB have exactly the same beginning and ending values, but may have different distributions between the points AB and CB. Assuming that the pressure integrals along the shock front AB and the blade contour portion CB are approximately equal, their projections in circumferential direction may cancel each other simplifying Eq.(15.48) as:

$$\frac{V_1}{V_s} = \frac{\cos \beta_s}{\cos \beta_1} = \frac{M_1}{M_s} \left( \frac{1 + \frac{\kappa - 1}{2} M_s^2}{1 + \frac{\kappa - 1}{2} M_1^2} \right)^{\frac{1}{2}} \quad (15.49)$$

Finally, we arrive at a geometric closure condition that uses the mean stream line, which is assumed to be identical to the mean camber line of the blade with the radius  $R$  as shown in Fig.15.7. From Fig.15.7, it follows immediately that

$$R [\cos \beta_t - \cos (\beta_t + \theta)] = \frac{S_s}{2} \sin \gamma \quad (15.50)$$

and

$$R [-\sin \beta_t + \sin (\beta_t + \theta)] = \frac{S_s}{2} \cos \gamma + \frac{S_1}{2} \quad (15.51)$$

The shock angle is determined from:

$$\tan \gamma = \frac{\cos \beta_t - \cos(\beta_t + \theta)}{-\sin \beta_t + \sin(\beta_t + \theta) - \frac{1}{2} \frac{S_1}{R}} \quad (15.52)$$

Considering the above procedure, the continuity equation yields:

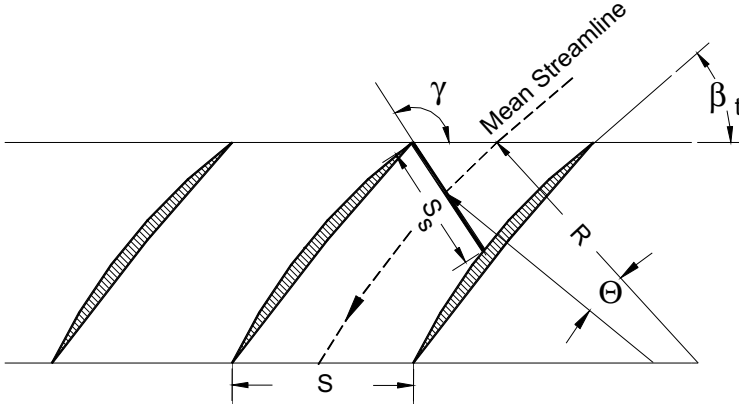


Fig.15.7: Introduction of mean streamline with curvature radius.

$$\frac{h_1}{h_s} \frac{\sin(\beta_t + i) \sin \gamma}{2 \frac{R}{S_1} [\cos \beta_t - \cos(\beta_t + \theta)] \sin(\gamma - \beta_s)} = \frac{M_s}{M_1} \left( \frac{1 + \frac{\kappa - 1}{2} M_1^2}{1 + \frac{\kappa - 1}{2} M_s^2} \right)^{\frac{1}{2} \frac{\kappa + 1}{\kappa - 1}} \quad (15.53)$$

With Eqs. (15.45), (15.46), (15.49), and (15.53), we have a system of four equations that easily calculates the four unknowns, namely:  $\delta$ ,  $\beta_s$ ,  $\gamma$ , and  $M_s$ . The shock loss is:

$$\zeta_s = \frac{P_b - P_a}{P_b} \quad (15.54)$$

$$\zeta_s = 1 - \left[ \frac{(\kappa + 1) M_s^2 \cos^2 \delta}{2 + (\kappa - 1) M_s^2 \cos^2 \delta} \right]^{\frac{\kappa}{\kappa - 1}} \left[ 1 + \frac{2\kappa}{\kappa + 1} (M_s^2 \cos^2 \delta - 1) \right]^{\frac{-1}{\kappa - 1}}$$

where  $P_b$  and  $P_a$  represent the total pressure before and after the shock. For  $\beta_t = 30^\circ$  and the incidence angle  $i = 0^\circ$ , the above equation system is used to calculate the shock Mach number, the expansion angle  $\theta$ , the shock position  $\gamma$ , the total pressure ratio, and the shock losses. Fig.15.8 shows the shock Mach number as a function of spacing ratio  $S/R$  with the inlet Mach number  $M_1$  as the parameter. This figure shows

that increasing the spacing ratio cause the shock Mach number to continuously increase and approach an asymptotic value. These results are similar to those presented by Levine [37]. However, the values are slightly different because of the simplifying assumptions by Levine. Keeping the inlet Mach number constant, the increase of spacing ratio leads to higher expansion angle  $\theta$  as shown in Fig.15.9. However, increasing the inlet Mach number at a constant spacing ratio  $S/R$  leads to a smaller expansion angle.

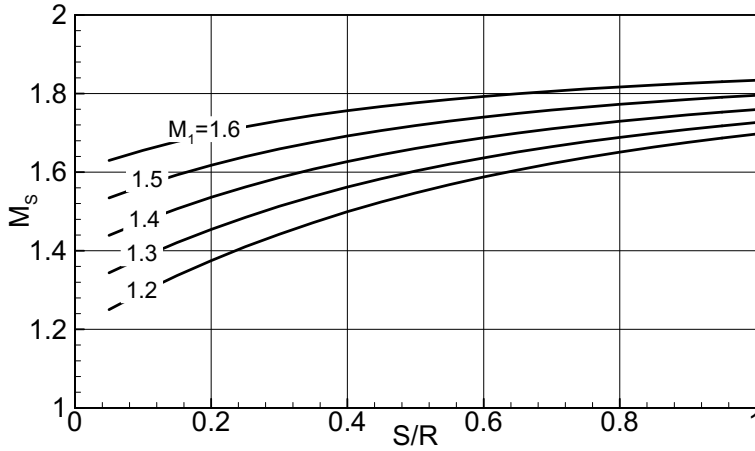


**Fig.15.8** Shock Mach number as a function of the spacing ratio  $S/R$  with the inlet Mach number  $M_1$  as parameter with  $\beta_t = 30^\circ$ , and the incidence angle  $i = 0^\circ$

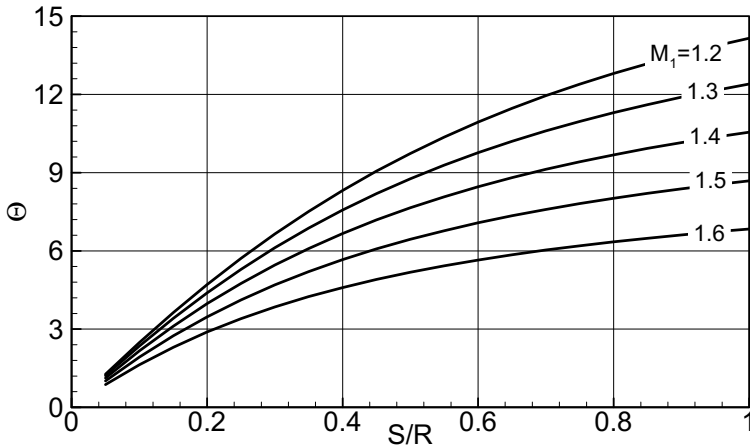


**Fig.15.9** Expansion angle  $\Theta$  as a function of  $S/R$  with inlet Mach number  $M_1$  as parameter with  $\beta_2 = 30^\circ$  and incidence angle  $i = 0^\circ$

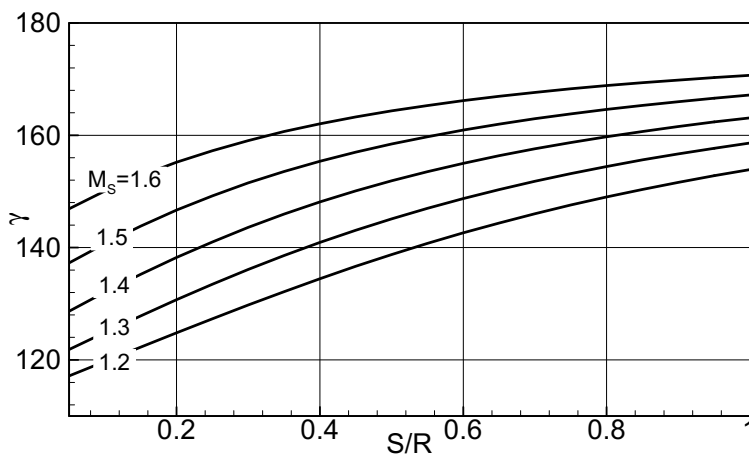


**Fig.15.10** Shock angle  $\gamma$  as a function of  $S/R$  with shock Mach number as parameter.

The same tendency can be read from the charts by Levine. For an inlet Mach number  $M_i = 1.2$  and  $S/R = 0.5$ , the Levine's method gives an expansion angle  $\theta = 8^\circ$ , while the method presented in here calculates  $\theta = 9.7^\circ$ . Fig.15.10 shows the shock angle  $\gamma$  as a function of spacing ratio  $S/R$ . This figure shows the significant effect of the inlet Mach number on the shock position. Once the shock angle is calculated at the design point, it may undergo changes during an off-design operation. The off-design operation places a limitation on the shock angle range as Fig.15.11 illustrates. Beginning with a design point speed line characterized by  $\omega_d$ , Fig.15.11a, the

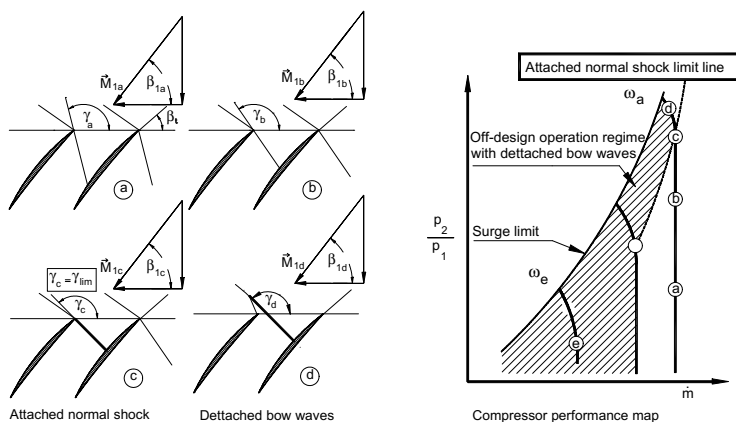


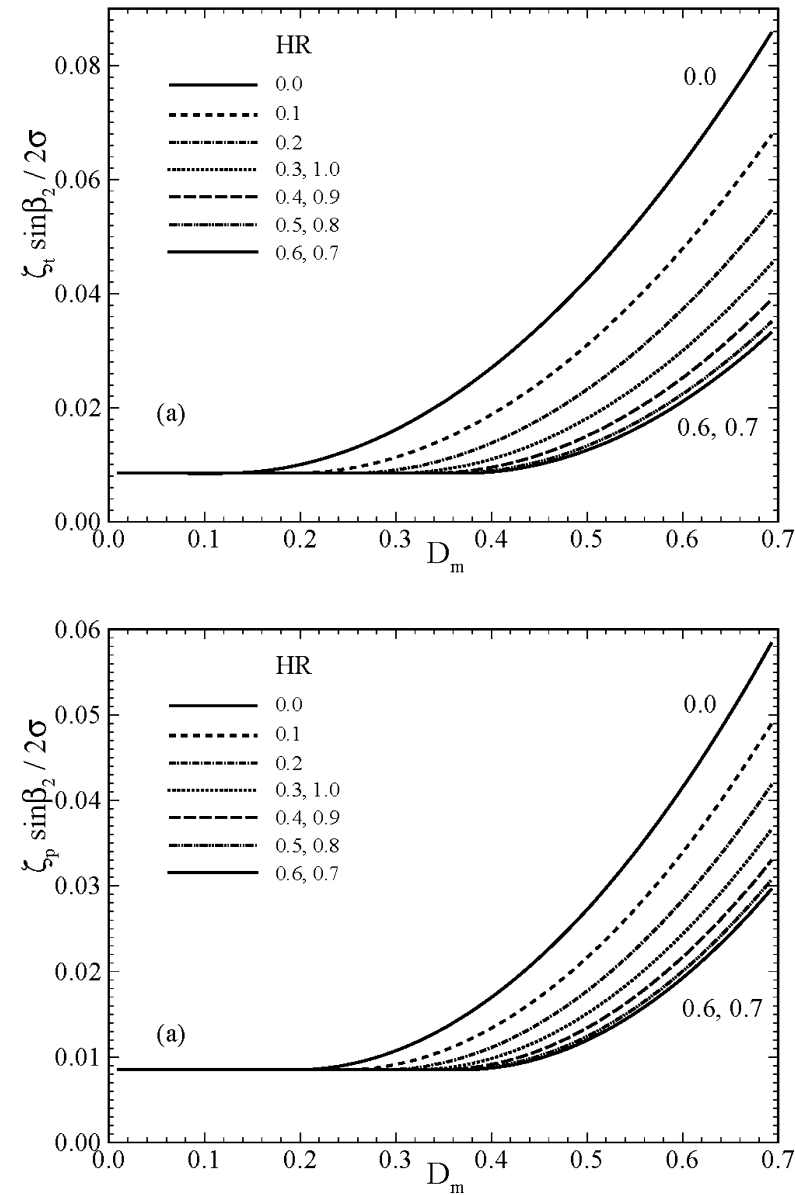
**Fig.15.11:** Effect of shock angle  $\gamma$  change described in Fig.15.8 on compressor performance at 4 different operation conditions (a) through (d), map .

operating point (a) is given by the inlet Mach number  $M_1$  with a uniquely allocated inlet flow angle  $\beta_1$  that satisfies the *unique shock angle criterion*. Increasing the back pressure from the design point back pressure to a higher level (b) causes the shock angle  $\gamma$  to increase ( $\gamma_b > \gamma_a$ ). Thus the end point of the passage shock moves toward the cascade entrance. By further increasing the back pressure from (b) to (c), a normal shock is established, which is still attached. The corresponding shock angle  $\gamma$  can be set equal to  $\gamma_{lim} \equiv \gamma_a$ . This particular shock angle that we call *unique shock angle* corresponds to an inlet flow angle which is frequently referred to as the *unique incidence angle*. Increasing the back pressure and thus decreasing the mass flow beyond this point, causes the shock to detach from the leading edge, as shown in Fig.15.11d. Reducing the rotational speed changes the incidence and may lead to further moving the shock from the leading edge as shown in Fig.15.11d. These operating points are plotted schematically in a compressor performance map shown in Fig.15.11(right).

To establish the loss correlations, the existing available experimental data were re-evaluated, particularly those in Gostelow et al. [10] and Krabacher and Gostelow [15] and [15] which used four single-stage compressors with multi-circular-arc profiles. A detailed description of the compressor facility and the stages are found in their reports. The data analysis used the following information: (1) the total pressure losses as a function of diffusion factor in the spanwise direction, (2) inlet, exit, and incidence angles, (3) Mach numbers, (4) velocities, and (5) geometry. To consider the compressibility effect discussed previously, the modified diffusion factor  $D_m$  was obtained using the information from Gostelow's report mentioned previously.

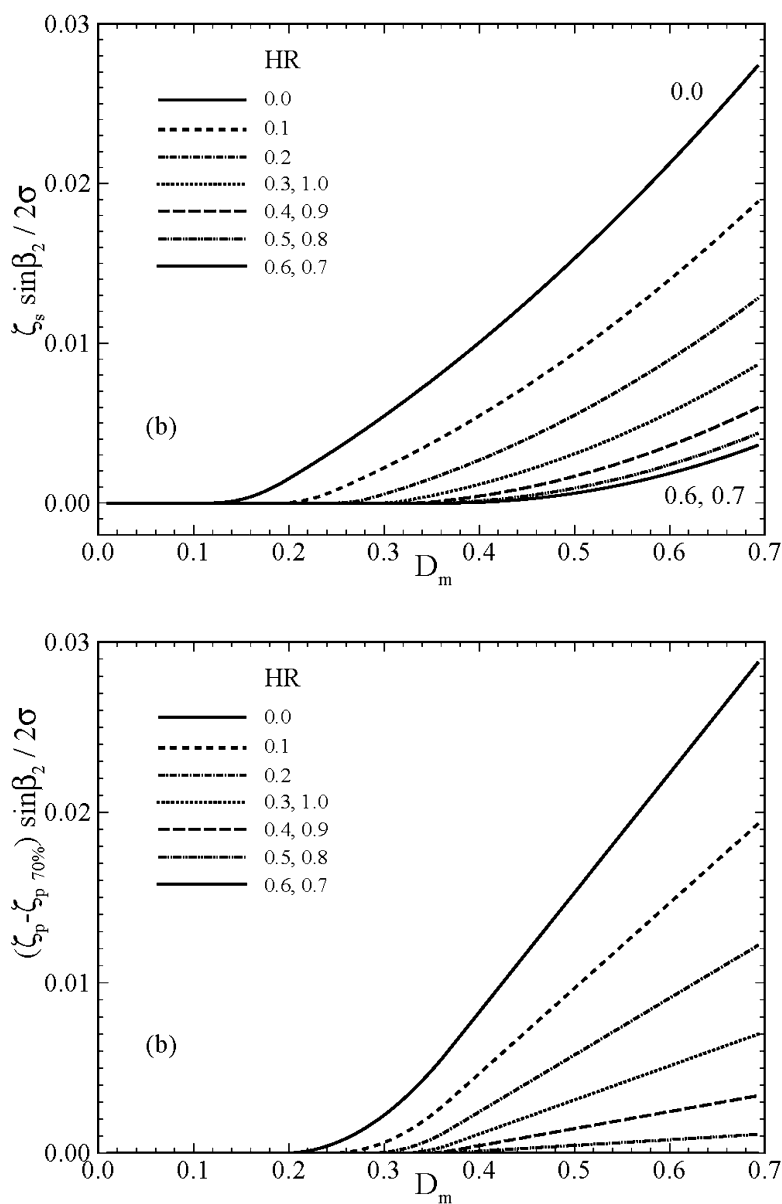
Figures 15.12 and 15.13 show the results. Starting from the tip with an immersion ratio of  $H_R = (R_t - R)/(R_t - R_h) = 0$ , Fig.15.12 (top) shows the total loss parameter as a function of the modified diffusion factor. As shown, the highest total pressure loss that consists of shock loss, profile loss, and secondary flow loss is encountered at the tip region, with shock and secondary flow losses as the predominant losses. Subtracting the shock loss coefficients from the total loss coefficients provides the loss coefficients that contain the primary and the secondary flow effects. The resulting loss coefficients are plotted in Fig.15.13 (bottom) and are approximately 30% smaller than the total pressure loss coefficient.

Figure 15.13 (top) exhibits the shock losses as a function of modified diffusion factor with the immersion ratio as a parameter. Highest shock losses occur at the tip region, with the relative Mach number above unity and decrease toward the hub. The fact that the sum of primary and secondary flow losses exhibit a minimum range of  $H_{Rmin} = 0.5 - 0.7$ , where the secondary flow effects diminish, enables the compressor designer to estimate the secondary flow losses. This is done by subtracting the losses at  $H_{Rmin}$  from the loss distribution at different spanwise locations. As a result, these losses include the effect of the secondary flows associated with wall boundary layer development and clearance vortices. Figure 15.13 (bottom) shows the distribution of the secondary loss parameter as a function of the modified diffusion factor. It exhibits a linear dependency of the secondary loss parameter as a function of the modified diffusion factor with the immersion ratio as



**Fig.15.12:** Total loss parameter (top) and profile loss parameter(bottom) as a function of modified diffusion factor





**Fig.15.13:** Shock loss (top) and difference in profile loss parameter with respect to the minimum profile loss parameter (bottom) as a function of the modified diffusion factor with the immersion ratio as parameter.

a parameter. Since the diffusion factor is directly related to the lift force and thus to the lift coefficient ( $C_L c/s$ ) as a linear function, one may conclude that the secondary flow losses are linearly proportional to ( $C_L c/s$ ). This is in agreement with the measurements by Grieb et al. [38] and in contrast to the correlation proposed earlier by Carter [39] that includes the term  $(C_L c/s)^2$  and is adopted by many other researchers.

A similar dependency for  $H_r = 50, 70$  and  $90\%$ , where the smallest losses are encountered at  $H_r = 60 - 70$ . Moving further toward the hub at  $H_r = 90\%$ , the total pressure losses experience a continuous increase attributed to higher friction losses and the secondary flow caused by the secondary vortices at the hub. A comparison of the loss parameters plotted in Fig. 15.13 (top) shows that the total pressure losses in the tip region ( $H_r = 10\%$ ) are much higher than those in the hub region ( $H_r = 90\%$ ). The higher losses at the tip are due to an increased secondary flow effect that is attributed to the tip clearance vortices.

### 15.1.6 Correlations for Boundary Layer Momentum Thickness

As shown, the profile loss coefficient and the boundary layer momentum thickness are interrelated by:

$$\zeta_P = \sigma \left( \frac{\delta_2}{c} \right) \left( \frac{\sin \beta_1}{\sin \beta_2} \right)^2 F(H_{12}, H_{32}, \delta_2, \sigma, c) \quad (15.55)$$

The momentum thickness in Eq. (15.55) is the projection of the suction surface and pressure surface momentum thicknesses given by:

$$\delta_2 \sin \beta_2 \equiv \delta_{2SP} = \delta_{2S} + \delta_{2P} \quad (15.56)$$

where the subscripts  $S$  and  $P$  refer to the suction and pressure surface, respectively, and the function  $F$  is given by:

$$F = \frac{1 + H_{32}}{\left( 1 - \frac{\delta_2}{c} \sigma H_{12} \right)^3} \quad (15.57)$$

with  $H_{12}, H_{32}$  as the displacement and energy form factors,  $\delta_2$  as the boundary layer momentum thickness,  $\sigma$  as the solidity, and  $c$  as the blade chord. In the literature (see also Hirsch [40] and Swan [41]), the function  $F$  is frequently approximated as a constant with the value  $F = 2$ . For a realistic velocity distribution, Schobeiri [19] showed that the value of  $F$  may differ from 2. To arrive at a better estimation for  $F$ , the boundary layer velocity profile is approximated by several simple functions such as a linear function, a power law, a sine function, and an exponential function. A

close examination of the results and their comparison with the experiments showed that the velocity approximation by a power function yields better results. However, the exponential approximation would be more appropriate for those profiles that are close to separation. Using the law function approximation, we arrive at:

$$H_{32} = \frac{H_{12} + 1}{3H_{12} - 1} \quad (15.58)$$

Introducing Eq. (15.58) into Eq. (15.57) and the results into Eq. (15.55) leads to:

$$\zeta_P = \sigma \left( \frac{\delta_2}{c} \right) \left( \frac{\sin\beta_1}{\sin\beta_2} \right)^2 \left[ \frac{\frac{4H_{12}}{3H_{12} - 1}}{\left( 1 - \frac{\delta_2}{c} \sigma H_{12} \right)^3} \right] \quad (15.59)$$

With Eq. (15.59) and (15.57), the momentum thickness is determined from:

$$\frac{\delta_2}{c} = \frac{\zeta_P \sin\beta_2}{\sigma} \left( \frac{\sin\beta_2}{\sin\beta_1} \right)^2 \frac{1}{F} \quad (15.60)$$

Using the profile losses as previously discussed, the correlation for the momentum thickness as a function of modified equivalent diffusion factor are plotted in Fig. 15.13 with the immersion ratio as a parameter. The highest value for the momentum thickness is encountered in the vicinity of the tip that includes the viscosity effects as well as the secondary flow effects. Similar to the profile losses, the momentum thickness continuously decreases by moving toward the blade mid-section up to  $H_r = 0.6$ . It assumes a minimum at  $H_r = 0.7$ . At this radius, the secondary flow effect apparently diminishes completely so that the momentum thickness corresponds to the one generated by the blade surface friction only. For immersion ratios greater than  $H_r = 0.7$ , the momentum thickness starts increasing again, which indicates the strong effect of the secondary flow.

### 15.1.7 Influence of Different Parameters on Profile Losses

The correlations presented above are based on experimental results performed on typical high performance compressors with specific flow characteristics and blade geometries similar to those discussed previously. These correlations may be applied to other compressors with similar geometries but different flow conditions by considering the effect of the following individual parameters.

**15.1.7.1 Mach Number Effect:** Estimating the Mach number effect requires calculating the critical Mach number. When the Mach number reaches unity locally in a compressor cascade, the corresponding inlet Mach number is said to have reached its critical value. Jansen and Moffat [42] made the assumptions that below

the critical Mach number, the total pressure losses and the turning angle are essentially constant. The pressure losses increase rapidly beyond this value. Using the gas dynamics relations, Jansen and Moffat [42] determined the local critical Mach number by the following implicit relation:

$$\left(\frac{V_{\max}}{V_1}\right)^2 - 1 = \frac{1 - \left(\frac{2}{k+1} + \frac{k-1}{k+1} M_{1cr}^2\right)^{\frac{k}{k-1}}}{-1 + \left(1 + \frac{k-1}{2} M_{1cr}^2\right)^{\frac{k}{k-1}}} \quad (15.61)$$

To estimate the critical Mach number directly, Davis [43] suggested the following explicit relation:

$$M_{1cr} = 2.925 - 2.948 \left(\frac{V_{\max}}{V_1}\right) + 1.17 \left(\frac{V_{\max}}{V_1}\right)^2 - 0.1614 \left(\frac{V_{\max}}{V_1}\right)^3 \quad (15.62)$$

As seen in Part I, the velocity ratio  $V_{\max}/V_1$  is directly related to the circulation function and thus the diffusion factor. With the critical Mach number from Eq. (15.7) or (15.8), the profile loss coefficient can be corrected as:

$$\zeta_{pcor} = \zeta_p \left[ A(M_1 - M_{1cr}) + 1.0 \right] \quad (15.63)$$

with  $A = 1.8$ - $2.0$  (see Moffat [42] and Davis [43]). For DCA-profiles, Dettmering and Grahl [44] found that Eq. (15.9) underestimates the correction and suggested the following modified approximation:

$$\zeta_{pcor} = \zeta_p \left\{ 14.0 \left[ M_1 - (M_{1cr} - 0.4)^3 \right] + 1.0 \right\} \quad (15.64)$$

**15.1.7.2 Reynolds number effect:** This effect is only at lower Reynolds number ranges of practical significance. For high performance compressors, the Reynolds number is high enough so that its changes do not affect the profile losses. The following profile loss correction is suggested for Reynolds number ranges  $Re < 2.5 \times 10^5$ :

$$\zeta_{pcor} = \zeta_p \left( \frac{Re}{Re_{cor}} \right)^{0.2} \quad (15.65)$$

**15.1.7.3 Blade thickness effect:** To consider the effect of the thickness ratio  $t/c$ , the boundary layer momentum thickness may be corrected using the correlation by

Fottner [45].

$$\left( \frac{\delta_2}{c} \right)_{cor} = \frac{\delta_2}{c} \left( 6.6 \frac{t}{c} + 0.34 \right) \quad (15.66)$$

## 15.2 Compressor Design and Off-Design Performance

The prerequisite for simulating the dynamic behavior of a compressor is a detailed knowledge of the design point properties as well as the overall performance characteristics. Three levels of simulation are discussed. The *first level* deals with steady state performance maps. It provides global information about the design and off-design efficiency and performance behavior of a compressor. It does not contain any detailed information about the individual stage parameters such as stage flow, load coefficients, degree of reaction, absolute and relative flow angles. However, this information is necessary to construct the compressor performance map. The map can be generated either by a stage-by-stage or by a row-by-row compression calculation procedure, which treats the compression procedure fully adiabatic, neglecting the heat transfer to/from the blade material. The following row-by-row adiabatic compression calculation method, which provides the basis for the *second level* simulation will be followed by the diabatic compression process that is necessary for the *third level* comprehensive dynamic simulation.

### 15.2.1 Stage-by-stage and Row-by-Row Adiabatic Compression Process

The stage-by-stage and row-by-row methods for calculating the compression process within a multi-stage compressor, Fig.15.14, presented in this chapter are equally applicable to axial and radial turbines and compressors, as discussed in Chapter 6. These methods are based on a one-dimensional calculation of the compression or expansion process using a set of dimensionless stage or row characteristics. These characteristics, along with loss correlations discussed in Section 15.1 describe the design and off-design behavior of the compressor or turbine component under consideration. In the following we discuss and evaluate both methods. The equation derived for the stage-by-stage calculation method follows the nomenclature in Fig.15.14.

**15.2.1.1 Stage-by-stage calculation of compression process:** The performance behavior of the compressor stage is completely described by the stage characteristics. The meridional view, blade configuration, compression diagram and velocity diagram of a typical compressor are shown in Fig.15.14. For stage-by-stage analysis, we resort

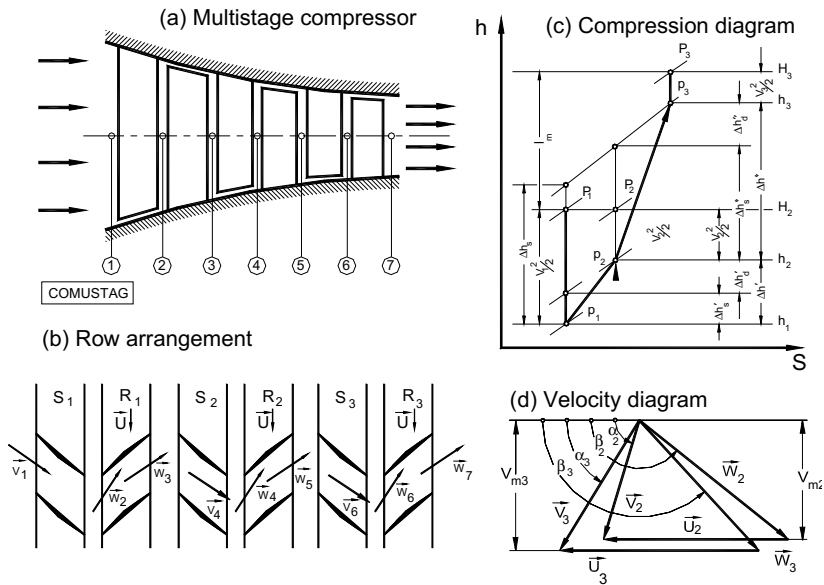


Fig.15.14: Multi-stage compressor (a) flow path, (b) row-by-row arrangement, (c) compression diagram, (d) velocity diagram.

to the following dimensionless variables introduced in Chapter 5 in conjunction with the stage-by-stage arrangement, Fig.15.14a and b, compression diagram, Fig.15.14c and velocity diagram in Fig.15.14d.

$$\mu = \frac{V_{m2}}{V_{m3}}, \quad v = \frac{U_2}{U_3}, \quad \phi = \frac{V_{m3}}{U_3}, \quad \lambda = \frac{1_m}{U_3^2}, \quad r = \frac{\Delta h''}{\Delta h'' + \Delta h'} \quad (15.67)$$

As shown in Chapter 4, these dimensionless variables were incorporated into the conservation equations of mass, momentum, moment of momentum, and energy leading to the following relations (5.50) to (5.53):

$$\cot \alpha_2 - \cot \beta_2 = \frac{v}{\mu \phi} \quad (15.68)$$

$$\cot \alpha_3 - \cot \beta_3 = \frac{1}{\phi} \quad (15.69)$$

$$\lambda = \phi(\mu v \cot \alpha_2 - \cot \alpha_3) - 1 \quad (15.70)$$

$$r = \frac{1}{2} \frac{\mu^2 \phi^2 \cot^2 \alpha_2 (v^2 - 1) - 2 \mu v \phi \lambda \cot \alpha_2 + \lambda^2 + 2 \lambda - \phi(\mu^2 - 1)}{\lambda} \quad (15.71)$$

Using the above set of stage characteristics in conjunction with the stage loss coefficients discussed in Chapter 6, the compression process is accurately calculated. This process, however, requires a few assumptions and several iterations. The four equations (15.68) to (15.71) contain nine unknowns. The following quantities are assumed to be known: (1) the compressor mass flow, (2) the compressor pressure ratio, (3) the type of blades, their exit flow angles  $\alpha_2$  and  $\beta_3$  for each individual stage, and their configuration in terms of degree of reaction. Further, we may assume the absolute inlet flow angle of the first stage and the exit flow angle of the last stage to be  $90^\circ$ . With these assumptions, all nine stage characteristics are estimated in the first iteration step, which usually does not deliver the required compression pressure ratio and exit enthalpy. The process of iteration is continued until the enthalpy and pressure convergence have been reached. This stage-by-stage compression calculation method delivers accurate results, however, it requires some experience in guessing the initial values for unknown characteristics. As an alternative, the row-by-row calculation is discussed in more detail in the following section. It is computationally more efficient and does not require a lot of iterations.

**15.2.1.2 Row-by-row adiabatic compression:** As discussed in Chapter 4, the compression process within stator and rotor row, shown in Fig.15.15, is summarized as:

$$\begin{aligned} \Delta h' &= h_1 - h_2 = \frac{1}{2} (V_2^2 - V_1^2) \\ \Delta h'_s &= h_1 - h_{2s} = \frac{1}{2} (V_{2s}^2 - V_1^2) \\ \Delta h'' &= h_2 - h_3 = \frac{1}{2} (W_3^2 - W_2^2 + U_2^2 - U_3^2) \\ \Delta h''_s &= h_2 - h_{3s} = \frac{1}{2} (W_{3s}^2 - W_2^2 + U_2^2 - U_3^2) \end{aligned} \quad (15.72)$$

The quantities in Eq. (15.72), the decomposition of a compressor stage in its stator and rotor rows, and the compression diagram are presented in Fig.15.15. In Eq. (15.72) and in the following sections, all quantities with superscripts “/” and “//” refer to stator and rotor rows, respectively. For the stator row, the compression diagram shows the details of an adiabatic compression, where the absolute total enthalpy remains constant. The following rotor row with the corresponding compression diagram exhibits the details of energy balance in relative frame of reference with constant relative total enthalpy.

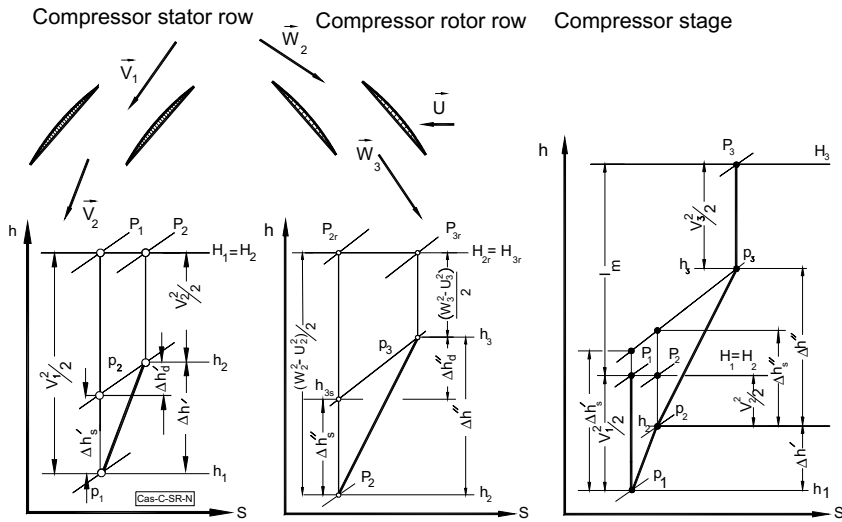


**Fig.15.15:** Stator, rotor, stage compression diagrams. P: total pressure, p: static pressure, “/”, “//” mark stator and rotor, respectively.

The compression diagram for the entire stage exhibits a composite picture of energy balance within stator and rotor row. Introducing the efficiency definition for the stator and rotor row, respectively:

$$\eta' = \frac{\Delta h_s'}{\Delta h'} \quad , \quad \eta'' = \frac{\Delta h_s''}{\Delta h''} \quad (15.73)$$

Incorporating Eq. (15.73) into Eqs. (15.72), the isentropic enthalpy difference for stator and rotor row, respectively, is expressed by:

$$\begin{aligned} \Delta h_s' &= \frac{\eta'}{2} (V_2^2 - V_3^2) \\ \Delta h_s'' &= \frac{\eta''}{2} (W_3^2 - V_2^2 + 2V_{u2}U_2 - U_3^2) \end{aligned} \quad (15.74)$$

The expression for the dimensionless isentropic enthalpy difference is obtained by dividing Eqs. (15.74) by the circumferential kinetic energy at the exit of the stage. The dimensionless isentropic enthalpy difference is written in terms of the stage parameters of Eq. (15.67) as:



$$\begin{aligned}\chi' &= \frac{\Delta h'_s}{U_3^2} = \frac{\eta'}{2} \left( \frac{\phi^2}{\sin^2 \alpha_2} \frac{\mu^2}{\sin^2 \beta_3} - \frac{\phi^2}{\sin^2 \beta_3} - 2\phi \cot \beta_3 - 1 \right) \\ \chi'' &= \frac{\Delta h''_s}{U_3^2} = \frac{\eta''}{2} \left( \frac{\phi^2}{\sin^2 \beta_3} - \frac{\mu^2 \phi^2}{\sin^2 \alpha_2} + 2\phi \mu \cot \alpha_2 - 1 \right)\end{aligned}\quad (15.75)$$

Further analysis of Eqs. (15.75) shows that knowledge of the entire stage parameter is necessary to determine the row isentropic enthalpy difference, which is similar to the stage-by-stage procedure discussed in the previous section, and requires many iterations. To avoid the iterative procedure, we subdivide the stage specific polytropic mechanical energy  $l$ , as well as the isentropic mechanical energy  $l_s$ , into two virtual contributions  $l'$  and  $l''$  that we allocate to stator and rotor row as shown in Fig.15.15. This step does not imply that the stator row is performing shaft power, which would violate the energy balance. It merely provides a smooth transition from stator row to rotor row when calculating the compression process. With this re-arrangement, we arrive at the contributions allocated to the stator and rotor rows as:

$$\begin{aligned}l' &= \frac{1}{2} V_2^2 - \frac{1}{2} W_2^2 \\ l'' &= \frac{1}{2} (W_3^2 - U_3^2 + U_2^2 - V_3^2)\end{aligned}\quad (15.76)$$

Similarly we find:

$$\begin{aligned}l'_s &= \frac{1}{2} V_{2s}^2 - \frac{1}{2} W_2^2 \\ l''_s &= \frac{1}{2} (W_{3s}^2 - U_3^2 + U_2^2 - V_3^2)\end{aligned}\quad (15.77)$$

As seen, the sum of stator and rotor contributions leads to the stage specific mechanical energy. Using the polytropic specific mechanical energy expressions given in Eqs. (15.77) and dividing them by the circumferential kinetic energy at the exit of the individual row, the dimensionless row polytropic load coefficients for stator and rotor are:

$$\begin{aligned}\lambda' &= \frac{l'}{U_2^2} = \phi' \cot \alpha_2 - \frac{1}{2} \\ \lambda'' &= \frac{l''}{U_3^2} = -\phi'' \cot \beta_3 - 1 + \frac{v^2}{2}\end{aligned}\quad (15.78)$$

where,  $\phi' = V_{\alpha 2} / U_2$ , and  $\phi'' = V_{\alpha 3} / U_3$ . Combining Eqs. (15.78) with the efficiency definition for the stator and rotor rows, Eq. (15.73), the following expressions for the efficiency are obtained:

$$\eta' = \frac{2l'_s - 2l' + V_2^2 - V_1^2}{V_2^2 - V_1^2} \quad (15.79)$$

$$\eta'' = \frac{2l''_s - 2l'' + W_3^2 - W_2^2}{W_3^2 - W_2^2}$$

The isentropic row load coefficient  $\psi$  is defined as the dimensionless isentropic specific mechanical energy for the row. Implementing the efficiency expressions from Eqs. (15.79), the isentropic row load coefficients for the stator and rotor rows are obtained:

$$\psi' = \frac{l'_s}{U_2^2} = \lambda' + \frac{\phi^2}{2} \left( \frac{1}{\sin^2 \alpha_2} - \frac{1}{\mu^2 \sin^2 \alpha_3} \right) (\eta' - 1) \quad (15.80)$$

$$\psi'' = \frac{l''_s}{U_3^2} = \lambda'' + \frac{\phi^2}{2} \left( \frac{1}{\sin^2 \beta_3} - \frac{\mu^2}{\sin^2 \beta_2} \right) (\eta'' - 1) \quad (15.81)$$

All the information necessary to pursue the compression process on the h-s diagram is now available to predict the compressor behavior with sufficient accuracy and reliability. Given the pressure and temperature at the inlet, the remaining thermodynamic properties are calculated using the property tables of the working medium that can be implemented as a subroutine within the calculation procedure. The row flow coefficients  $\phi'$   $\phi''$  are calculated from the continuity equation:

$$\phi = \frac{V_{ax}}{U} = \frac{\dot{m}}{\rho A U} = \frac{\dot{m}}{\rho A \omega R} \quad (15.82)$$

Given the exit stator and rotor blade angle  $\alpha_2, \beta_3$  as input data necessary to describe the geometry and the above flow coefficient, we determine the flow angles  $\alpha_3, \beta_2$  for the stator and rotor rows, respectively:

$$\beta_2 = \tan^{-1} \frac{\phi'}{\phi' \cot \alpha_2 - 1} \quad (15.83)$$

$$\alpha_3 = \tan^{-1} \frac{\phi''}{\phi'' \cot \beta_3 + 1}$$

The incidence and deviation angles are calculated according to the procedure described in Chapter 8. Upon determining all the angles involved in the velocity

diagram, the velocities and their components are completely known. The velocity triangle at the exit of the row is calculated and the flow behavior is completely described by the velocity diagram. The flow coefficient  $\phi'$ ,  $\phi''$ , and the flow angles  $\alpha_3, \beta_2, \alpha_2, \beta_3$  are essential parameters to determine the polytropic and isentropic enthalpy differences between the inlet and exit of the row. The amount of mechanical energy consumed by the flow to increase its total pressure is represented by the polytropic load coefficients,  $\lambda'$ ,  $\lambda''$ , and the isentropic load coefficients  $\psi'$ ,  $\psi''$  as presented above. Finally, from the energy balance relationships, the complete compression process for the stage is determined by the following set of equations:

$$\begin{aligned} h_2 &= h_1 - l' - \frac{1}{2} (W_2^2 - V_1^2) \\ h_3 &= h_2 - l'' - \frac{1}{2} (V_3^2 - W_2^2) \end{aligned} \quad (15.84)$$

$$\begin{aligned} h_{2s} &= h_1 - l'_s - \frac{1}{2} (W_2^2 - V_1^2) \\ h_{3s} &= h_2 - l''_s - \frac{1}{2} (V_3^2 - W_2^2) \end{aligned} \quad (15.85)$$

the above procedure can be easily repeated for all the stages of the compressor in question. However, it should be pointed out that the above analysis is completely dependent on an accurate and reliable method for determining the off-design efficiency. This is the subject of the next section.

**15.2.1.3 Off-design efficiency calculation:** The off-design efficiency calculation is based on the analysis of the diffusion factor. The modified diffusion factor, Eq. (15.44), includes compressibility effects and, therefore, is capable of handling highly compressible flow such as in transonic compressors. To apply the diffusion factor definition to stators and rotors on an individual basis, separate expressions were derived in terms of known stage and row quantities. The expression for the stator row given is:

$$\begin{aligned} D'_m &= 1 - \frac{\sin\alpha_1}{\mu\sin\alpha_2} + \frac{v\sin\alpha_1}{\sigma(v+1)} \left( \cot\alpha_1 - \frac{\cot\alpha_2}{\mu v} \right) \times \\ &\quad \left[ 1 - M_1^2 \left( \frac{\sin\alpha_1}{\mu\sin\alpha_2} \right) \left( \frac{\sin\alpha_1}{\mu\sin\alpha_2} - 1 \right) \right] \end{aligned} \quad (15.86)$$

and for the rotor row:

$$D_m'' = 1 - \frac{\sin\beta_2}{\mu\sin\beta_3} + \frac{\nu\sin\beta_2}{\sigma(\nu+1)} \left( \frac{1-\nu^2}{\mu\nu\phi''} - \cot\beta_2 + \frac{\cot\beta_3}{\mu\nu} \right) \times$$

$$\left[ 1 - M_2^2 \left( \frac{\sin\beta_2}{\mu\sin\beta_3} \right) \left( \frac{\sin\beta_2}{\mu\sin\beta_3} - 1 \right) \right] \quad (15.87)$$

The parameters  $\mu$ ,  $\nu$ , and  $\sigma$  in Eqs. (15.86) and (15.88) pertain to the individual row under consideration. Using the above modified diffusion factor, the total loss parameter can be taken as a function of modified diffusion factor with the immersion ratio defined in Fig.15.16 as a parameter.

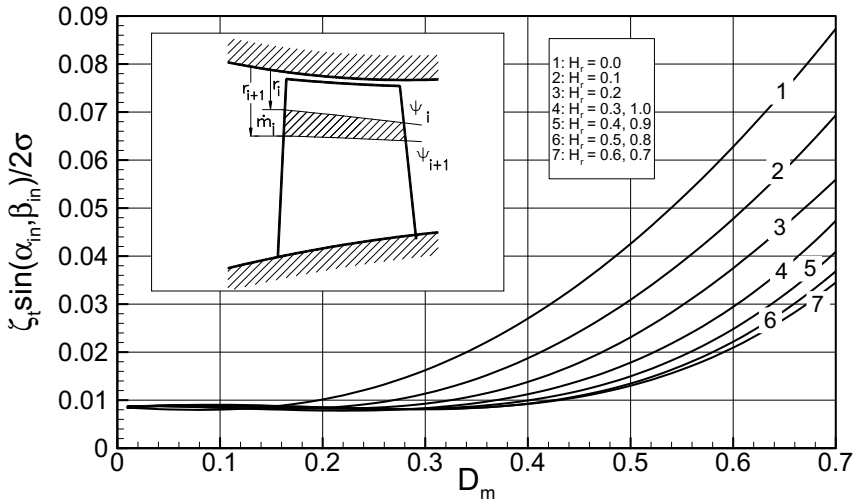


**Fig.15.16** Total loss parameter as a function of modified diffusion factor with immersion ratio as parameter from Schobeiri [21].

As shown, a set of curves representing the blade total loss parameter  $\zeta_t \sin(\alpha_{in}, \beta_{in}) / 2\sigma$  is plotted, with  $\alpha_{in}, \beta_{in}$  as the inlet flow angle of stator or rotor row and  $\sigma$  as the blade solidity ratio. These curves may be presented in the form of polynomials to be implemented into a calculation procedure. The highest loss is encountered close to the tip at an immersion ratio of  $H_r = 0.0$ , where secondary flow and tip clearance losses predominate the loss picture. These losses decrease as the immersion ratio approaches the blade mid height. However, for this particular compressor blade, the lowest loss is located around  $H_r = 0.6 - 0.7$ . Approaching the hub, the secondary losses dominate the losses leading to higher total loss parameter. It should be pointed out that, the loss parameter presented in Fig.15.16 represents only the loss situation for a particular compressor, whose efficiency and performance are calculated and presented in this section. As indicated previously, the

generation of compressor efficiency performance maps requires knowledge of the individual losses of the stator and rotor rows. The loss parameter curves of Fig. 15.16 are not symmetric and, therefore, must be applied to the blade in a manner compatible with their distribution over the blade spanwise direction. For this purpose, we apply energy balance to the blade, which results in:

$$\sum_{j=1}^n \dot{m}_j \left( \frac{\Delta h_{sj}}{\eta_j} \right) = \dot{m} \left( \frac{\Delta h_s}{\eta} \right) \quad (15.88)$$

where the index  $j$  refers to the blade spanwise positions from tip to hub. The efficiency is defined in terms of the row loss coefficient  $Z$ , introduced in Chapter 6, which is a function of  $\zeta_i$  and may be written for the stator and rotor, respectively:

$$Z'_t = \frac{\zeta'_t V_1^2}{2 l'}, \quad Z''_t = \frac{\zeta''_t W_2^2}{2 l''} \quad (15.89)$$

Using Eq. (15.89), the row efficiency can be expressed as:

$$\eta' = 1 - Z'_t, \quad \eta'' = 1 - Z''_t \quad (15.90)$$

Eq. (15.90), coupled with the total loss definition, can be reduced to:

$$Z_t = \frac{1}{\Delta h_s A_t} \left( \sum_{j=1}^n \Delta h_{sj} A_j Z_j \right) \quad (15.91)$$

Equation (15.91) is an integral representation of the loss distribution in the spanwise direction.

An alternative calculation method for calculating the efficiency is using the entropy change as a result of a row-by-row compression process. The design and off-design efficiency is then determined as an outcome of the loss calculation which reduces the number of iterations involved. Applying Eq. (4.103) to the stator row, the entropy change is directly related results in:

$$s_2 - s_1 = R \ln \left( \frac{P_{01}}{P_{02}} \right) \quad (15.92)$$

With the given initial entropy  $s_1$  and total pressure  $P_{01}$ , the row exit entropy is calculated by using the row loss coefficient. For the stator row it is expressed by:

$$\zeta' = \frac{P_{01} - P_{02}}{\frac{1}{2} \rho_1 V_1^2} = \frac{P_{01}}{\frac{1}{2} \rho_1 V_1^2} \cdot \left[ 1 - \left( \frac{P_{02}}{P_{01}} \right) \right] \quad (15.93)$$

Substituting Eq. (15.93) into (15.92) after some rearrangement, we obtain the entropy at the exit of the row:

$$s_2 = s_1 - R \ln \left[ 1 - \frac{\zeta' \rho_1 V_1^2}{2 P_{o1}} \right] \quad (15.94)$$

With the exit entropy and the corresponding enthalpy, the stator row exit thermodynamic condition is fully determined. The following rotor row is treated similarly considering the relative frame of reference. The entropy increase is related to the change of the relative total pressure which is expressed in the following relation:

$$s_3 - s_2 = R \ln \left( \frac{P_{o2r}}{P_{o3r}} \right) \quad (15.95)$$

Similar to the stator, with the given initial entropy  $s_1$  and relative total pressure  $P_{o1r}$ , the row exit entropy is calculated by using the rotor row loss coefficient. For the rotor row it is expressed by:

$$\zeta' = \frac{P_{o2r} - P_{o3r}}{\frac{1}{2} \rho_2 W_2^2} = \frac{P_{o2r}}{\frac{1}{2} \rho_2 W_2^2} \cdot \left[ 1 - \left( \frac{P_{o3r}}{P_{o2r}} \right) \right] \quad (15.96)$$

Substituting Eq. (15.89) into (15.88), we obtain

$$s_3 = s_2 - R \ln \left[ 1 - \frac{\zeta'' \rho_2 W_2^2}{2 P_{o2r1}} \right] \quad (15.97)$$

With the exit entropy and the corresponding enthalpy, the rotor row exit thermodynamic condition is fully determined. The row-by-row calculation is continued until the compression process for the entire compressor is completed.

### 15.3 Generation of Steady State Performance Map

Using the row-by-row calculation method described above, the compression process for design and off-design operation conditions can be accurately calculated. As a result, the calculation procedure provides efficiency and performance maps for single-stage axial, radial, and multi-stage axial compressors. The prerequisite for an accurate efficiency and performance prediction is the knowledge of the compressor blade's loss behavior. Given the geometry of a nine-stage subsonic axial compressor, steady state calculations are performed by varying the rotational speed and the compressor mass flow. Figures 15.17 and Fig.15.18 exhibit the performance and efficiency behavior of a 3-stage subsonic compressor at its design and off-design operating points. The rotational speed is non-dimensionalized by the design angular

velocity. Figure 15.17 shows the compressor pressure ratio versus the non-dimensionalized mass flow ratio. Starting with the design speed ratio of  $\omega/\omega_D = 1$ , we first reduce the mass flow.

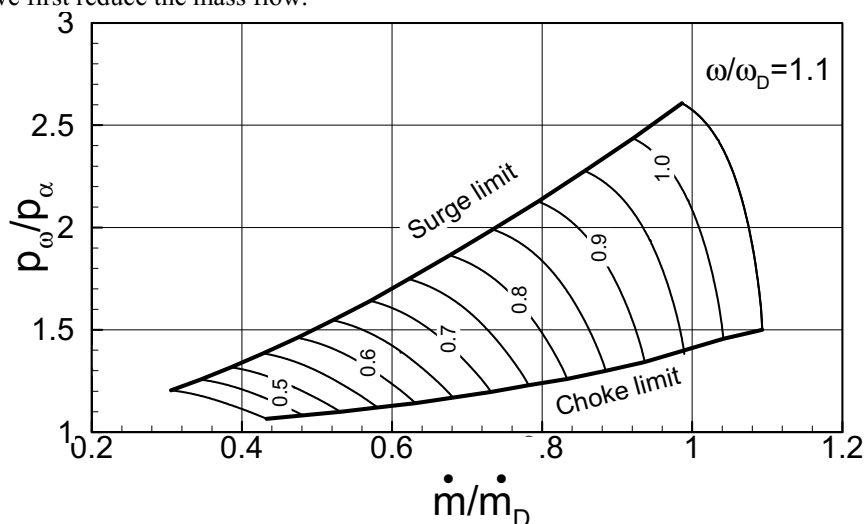


**Fig.15.17:** Compressor pressure ratio as a function of relative mass flow with relative angular velocity as parameter.

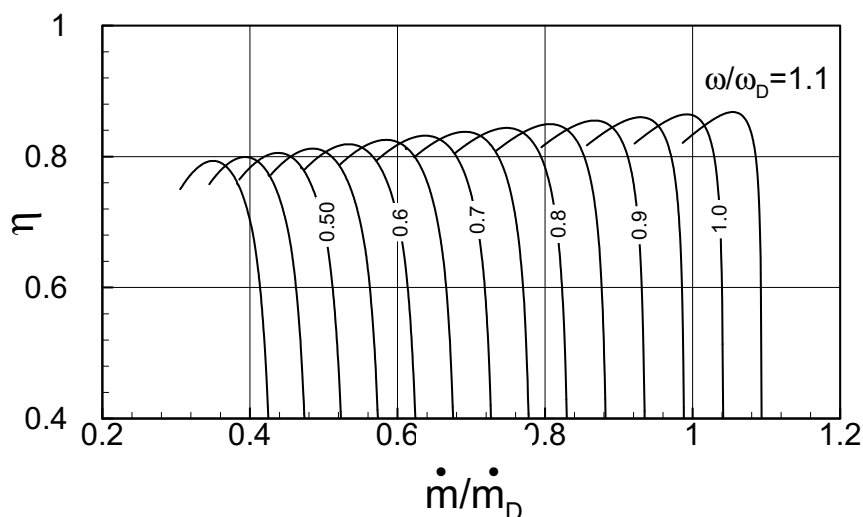


**Fig.15.18:** Efficiency as a function of relative mass flow with relative angular velocity as parameter.

This in turn changes the stage velocity diagrams, and thus, the incidence angle of

blades resulting in higher flow deflection, greater stage load coefficient, and therefore, higher pressure ratio. The mass flow reduction may be caused by specific operation conditions such as closing a valve of a compression system or increasing the compressor back pressure of a gas turbine system. For the case that mass flow at a constant speed is further reduced, a subsequent increase in inlet flow incidence will cause a *partial or total flow separation* resulting in a compressor *surge*. On the other hand, if at a constant rotational speed the compressor back pressure is reduced, the incidence angle assumes negative values causing the axial velocity component to increase. Further reducing the back pressure results in higher velocity that may approach the speed of sound. In this case, the compressor operates in a state of *choke*. Thus, the operational envelope of the compressor is bounded by a *surge limit* and a *choke limit* plotted in Fig.15.17 and Fig.15.19.

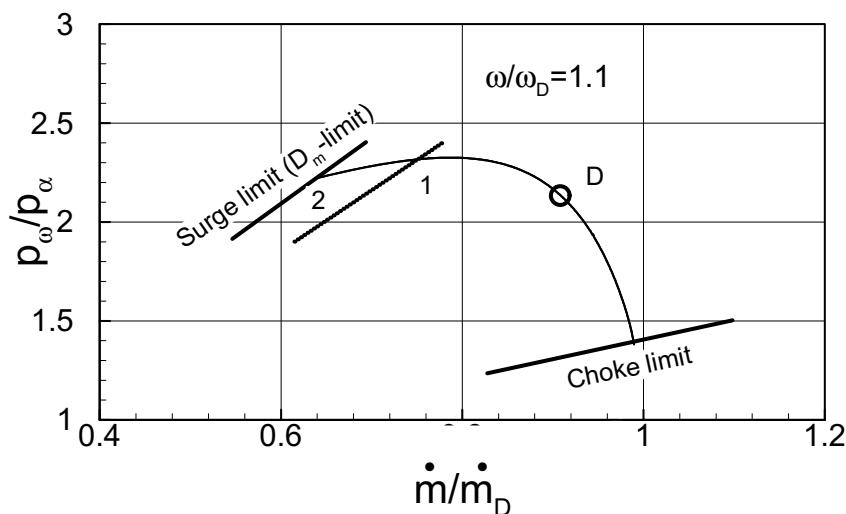


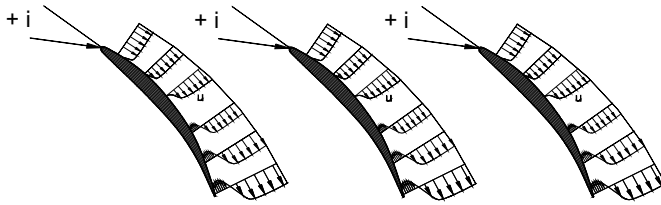
**Fig.15.19:**Construction of surge and choke limits, point D refers to design point, point 2 corresponds to the maximum diffusion factor, 1-2 precautionary surge margin set by compressor designer.

### 15.3.1 Inception of Rotating Stall

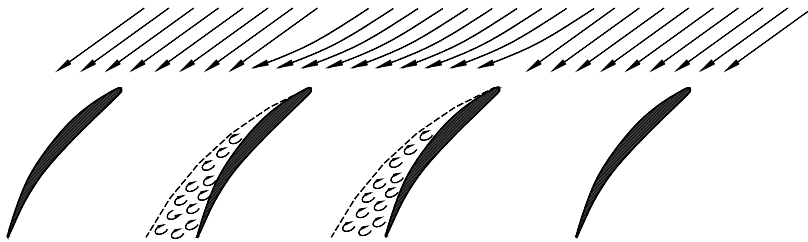
Details of the performance map is shown in Fig.15.20. After passing through the design point *D*, by further decreasing the compressor mass flow rate, the pressure ratio first reaches a maximum followed by a continuous decrease. Further decreasing the mass flow may trigger a sequence of events, sketched in Fig.15.20. First, a boundary layer separation inception may occur at a few blades, as sketched in Fig.15.20(a). While the channel of these blades are occupied by low energetic stall cells, the rest of the blades operate at normal flow condition, however, at a different incidence angle, as shown in Fig.15.20(b). Since the stall cells have blocked a



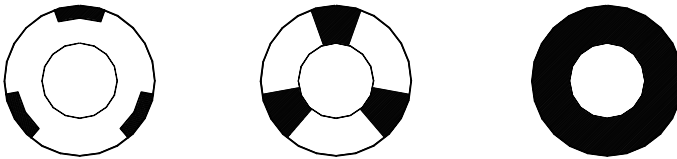
portion of the cross sectional area, a redistribution of the mass flow in circumferential direction occurs, leading to a redistribution of the incidence angles. Based on the separation extent, the cells may partially occupy the tip and hub region, as well as the entire blade channels from hub to tip, as shown in c).



a) Inception of stall cells, boundary layer separation.  
due to an increase of positive incidence angle



b) Manifestation of stall cell, deflection of velocity  
direction caused by stall cells



c) Growth of stall cells to surge

**Fig.15.20:** Inception of rotating stall and surge.

If these stall cells are located within rotor blades, they rotate with the corresponding frequency causing the compressor to *operate in rotating stall* mode. This operating mode is characterized by temporal fluctuations of the mass flow. Further reducing the mass flow may lead to a complete breakdown of the compressor operation that is called compressor *surge*. In this case, the compressor mass flow periodically oscillates between positive and negative. In conjunction with the combustion chamber, the compressor surge may suck hot gas and eject it in a counter flow

direction. To prevent the compressor from getting into surge operation, the compressor designer places a *surge limit* on the performance map. This limit may be experimentally determined or empirically estimated by setting certain flow deflection limits, diffusion factor limits, or even boundary layer separation criterion. For the performance map presented in Fig. 15.19, we set the diffusion factor to  $D_m = 0.65$  as the limiting criterion for the beginning of a rotating stall. This is shown in Fig. 15.20 as the surge limit that intersects the pressure curve at point 2. The compressor aerodynamicist wishes to have certain margins to this limit, and may construct a second surge limit. This is illustrated in Fig. 15.19, where the diffusion factor limit was set at  $D_m = 0.45$ , point 1.

### 15.3.2 Degeneration of Rotating Stall into Surge

The surge process is graphically explained in Fig. 15.21, where an axial compressor is connected to an air storage tank. The compressor is driven by an electric motor that operates at a constant frequency. At the time  $t = 0$ , where the tank is assumed to be completely empty, the compressor starts pressurizing the tank Fig. 15.21 (A). The process of pressurization continues until the tank pressure is equal to the compressor exit design pressure. Further compressor operation causes the blade incidence angles to become greater than the design incidence angle resulting in an adverse increase of the compressor stage flow deflection. As a consequence, the compressor exit pressure and thus the storage pressure will raise, causing first a rotating stall followed by a stable surge with a reversed flow direction as indicated in Fig. 15.21(B) if operation continues.

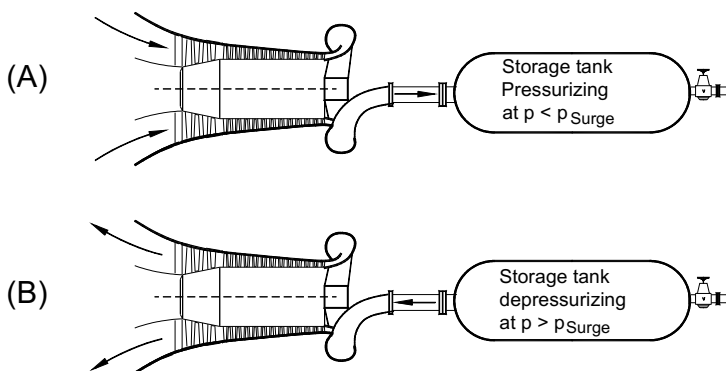


**Fig.15.21:** Explaining the phenomenon of compressor surge.

The details of the surge process is qualitatively shown in Fig. 15.22(a) with the pressure performance curves, the surge and the choke limits. Starting from an arbitrary point *D* below the design point, the compressor continuously sucks air from the environment pumps it into the storage and raises the storage pressure approaching

the design point pressure  $DP$ . During this process the blades boundary layer is fully attached Fig.15.22(b) and the compressor operates in normal compression mode. Passing through the design point and approaching the surge limit at point  $A$ , a few blades may experience rotating stall with partial separation on the blade suction surface, Fig.15.22(c). As the compressor operation continues the flow deflections increase, the number of the blades that operate in rotating stall mode increases and the storage pressure exceeds the compressor surge limit. At this point a flow reversal takes place and the mass flow jumps from positive to negative causing the tank to depressurize. Since the compressor blades are subject to a reversed flow, they function as an energy dissipator that might has a characteristic qualitatively shown as the curve  $BC$  Fig.15.22(a). Once the tank's pressure is substantially lowered below the compressor design point  $DP$ , for instance  $D$ , the compressor resumes its normal operation. If the compression process continues at the same rotational speed, the surge process will repeat itself leading to a hysteresis pattern. This non-linear dynamic operation causes the blades to be subjected to severe periodic forces that may result in a complete de-blading of the compressor rows if immediate actions are not taken.

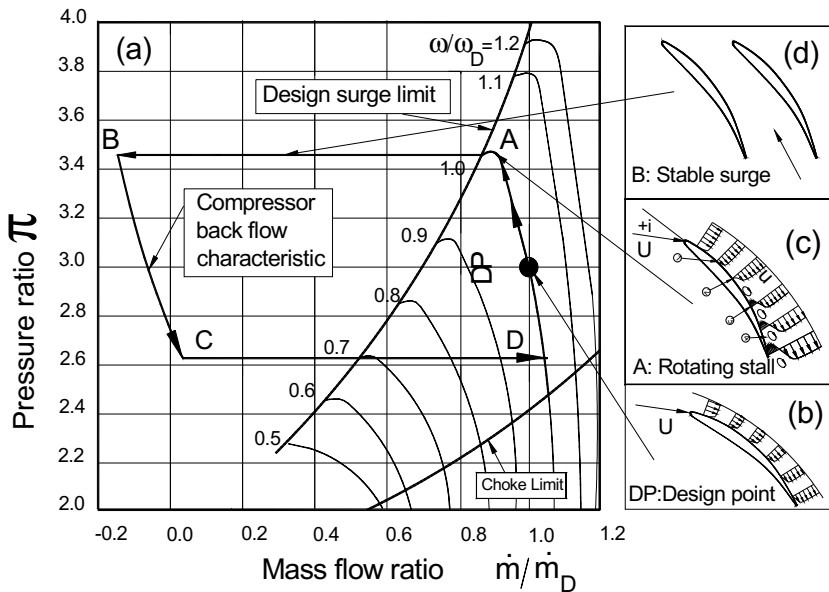


Fig.15.22: Dynamic operation of a compressor.

## 15.4 Compressor Modeling Levels

Three levels of compressor modeling are presented in this section. The first level utilizes the steady performance map. The second level uses the row-by-row adiabatic compression process, and the third level employs a diabatic row-by-row calculation

method. The first level exhibits the global performance behavior of a compression system under dynamic operation condition. The second level delivers a detailed calculation of the adiabatic compression process under any dynamic operation condition. In addition to the information provided by the second level model, the third level provides detailed information about the blade temperature and the effect of the heat transfer on an operation envelope that includes the performance, surge, and choke limits.

### 15.4.1 Module Level 1: Using Performance Maps

The efficiency and performance maps generated in section 15.2.3 can be used for a first level compressor simulation. This simulation level obviously does not provide details regarding the dynamic events within compressor stages. However, it is capable of globally reflecting the state of the compressor during a dynamic event. The global compressor module is modeled mathematically by a set of algebraic equations. It receives the dynamic information from the inlet plenum, performs off-design calculations, and transfers the results to the exit plenum. This arrangement allows a quasi dynamic simulation of the compressor component. The set of algebraic equations determines the off-design values of the mass flow rate  $\dot{m}$ , total temperature  $T_o$ , power consumption  $P_C$ , efficiency and the volume flow rate  $\dot{V}$  as functions of the efficiency, pressure ratio, inlet temperature, and angular velocity  $\omega$ , as follows:

$$\begin{aligned}
 P_C &= \dot{m} \bar{c}_p (T_{oO} - T_{oI}) \\
 T_{oD} &= T_{oD}(\pi, \eta, T_{oI}, \omega) \\
 \dot{m} &= \dot{m}(\pi, \eta, T_{oI}, \omega) \\
 \dot{V} &= \dot{V}(\pi, T_{oI}, \omega) \\
 P_C &= P_C(\pi, \eta, T_{oI}, \omega)
 \end{aligned} \tag{15.98}$$

To account for the effect of temperature on the results obtained from the performance map, we introduce a non-dimensional *relative* volume flow rate,  $\dot{V}_R$

$$\dot{V}_R = \frac{\dot{V}}{\dot{V}_D} \sqrt{\frac{T_D}{T}} \tag{15.99}$$

a relative rotational speed,

$$\omega_R = \frac{\omega}{\omega_D} \sqrt{\frac{T_D}{T}} \tag{15.100}$$

and a relative pressure ratio

$$\pi_R = \frac{\pi}{\pi_D} - 1 \quad (15.101)$$

where, the subscript  $R$  and  $D$  refer to relative and design point values, respectively. By introducing the above non-dimensionalized parameters into Eqs. (15.98), we obtain two functional relations for the efficiency and the volume flow rate:

$$\eta = \eta (\pi_R, \omega_R) \quad (15.102)$$

$$\dot{V}_R = \dot{V}_R (\pi_R, \omega_R) \quad (15.103)$$

As seen from Eqs. (15.102) and (15.103), the number of the parameters has reduced by one, resulting in simpler relationships that can be expressed in terms of two-dimensional polynomials as functions of  $\pi_R$ , and  $\omega_R$  as given below:

$$\dot{V}_R = \Pi_R \cdot A \cdot \Omega = \Pi_i A_{ij} \Omega_j \quad (15.104)$$

$$\eta = \Pi_R \cdot C \cdot \Omega = \Pi_i C_{ij} \Omega_j \quad (15.105)$$

with  $\Pi_i = \pi_R^{i-1}$  and  $\Omega_j = \omega_R^{j-1}$ . The matrices  $(A) = A_{ij}$ , and  $(C) = C_{ij}$  represent the coefficients of the two dimensional polynomial describing the behavior of the volume flow rate and efficiency, respectively, as functions of the given pressure ratio and angular velocity. Considering the non-dimensionalized Eqs. (15.103)-(15.105), the first element of the matrices  $A$  and  $C$  are determined by the map as  $A_{11} = \dot{V}_{RD}$  and  $C_{11} = \eta_D$ . Expanding Eqs. (15.104) and (15.105) we find the relative volume flow rate  $\dot{V}_R$  as:

$$\begin{aligned} \dot{V}_R = & \Pi_1 A_{11} \Omega_1 + \Pi_1 A_{12} \Omega_2 + \dots + \Pi_1 A_{1n} \Omega_n \\ & + \Pi_2 A_{21} \Omega_1 + \Pi_2 A_{22} \Omega_2 + \dots + \Pi_2 A_{2n} \Omega_n \\ & + \Pi_m A_{m1} \Omega_1 + \Pi_m A_{m2} \Omega_2 + \dots + \Pi_m A_{mn} \Omega_n \end{aligned} \quad (15.106)$$

and the efficiency

$$\begin{aligned} \eta = & \Pi_1 C_{11} \Omega_1 + \Pi_1 C_{12} \Omega_2 + \dots + \Pi_1 C_{1n} \Omega_n \\ & + \Pi_2 A_{21} \Omega_1 + \Pi_2 C_{22} \Omega_2 + \dots + \Pi_2 C_{2n} \Omega_n \\ & + \Pi_m A_{m1} \Omega_1 + \Pi_m C_{m2} \Omega_m + \dots + \Pi_m C_{mn} \Omega_n \end{aligned} \quad (15.107)$$

The elements are

$$\begin{aligned} \Pi_1 &= \pi_R, \Pi_2 = \pi_R^j, \Pi_3 = \pi_R^2, \Pi_i = \pi_R^{i-1} \\ \Omega_1 &= \omega_R, \Omega_2 = \omega_R^j, \Omega_3 = \omega_R^2, \Omega_j = \omega_R^{j-1} \end{aligned} \quad (15.108)$$

Using Eqs.(15.106) to (15.108), the off-design mass flow,

$$\dot{m} = \rho \dot{V} \quad (15.109)$$

the total exit temperature

$$T_{oO} = T_{oI} \pi^{\frac{\kappa-1}{\kappa}} \frac{1}{\eta} \quad (15.110)$$

and the power consumption  $P_C$

$$P_C = \dot{m} \bar{c}_p (T_{oO} - T_{oI}) \quad (15.111)$$

are calculated with  $\dot{V}$  as the volume flow rate,  $T_{oI}$  the inlet stagnation temperature,  $T_{oO}$  the exit stagnation temperature,  $\bar{c}_p$  the average specific heat at constant pressure, and  $\eta$  as the compressor efficiency.

**15.4.1.1 Quasi dynamic modeling using performance maps:** The compressor components are modeled quasi-dynamically using a steady state performance maps. The compressors are operating between two plena as Fig. 15.23 reveals. For a compressor with up to three-stages, a single performance map is sufficient to calculate the global transient behavior of the compressor. However, if the compressor

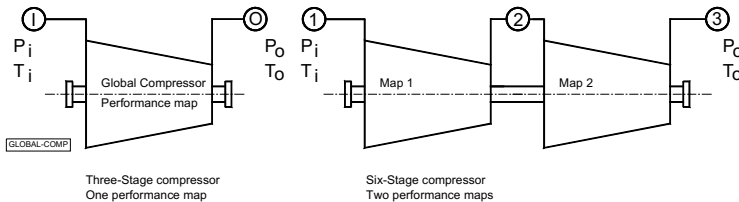


**Fig.15.23:** Modeling the dynamic performance of a multi-stage compressor using (a) one performance map, (b) two or more maps.

has more than three stages, two or more performance maps may be necessary to satisfactorily predict the transient behavior of the compressor. The steady performance map is obviously not able to handle transient events. However, if it is placed between two plena that continuously feed the steady map with unsteady data, it may deliver reasonable dynamic results. The inlet plenum transfers the time dependent pressure and temperature to the global map which calculates the compressor performance and transfers the information to the outlet plenum. For this purpose, the following system of differential and algebraic equation are used: (1) The inlet and outlet plena are described by Eq. (13.9) and (13.11). For the sake of completeness, these equations are listed below:

$$\frac{\partial T_0}{\partial t} = \frac{1}{\rho V} \left[ \sum_{i=1}^n \dot{m}_{I_i} \left( \kappa \frac{c_{pI_i}}{c_p} T_{0I_i} - T_0 \right) - (\kappa - 1) \sum_{j=1}^m \dot{m}_{O_j} T_0 \right] \quad (15.112)$$

$$\frac{\partial P}{\partial t} = \frac{\kappa R}{V} \left[ \sum_{i=1}^n \dot{m}_{I_i} \frac{c_{pI_i}}{c_p} T_{0I_i} - \sum_{j=1}^m \dot{m}_{O_j} T_0 \right] \quad (15.113)$$

with Eqs. (15.112) and (15.113) and the performance map described by algebraic equations (15.106), (15.107), (15.109), (15.110) and (15.111), we are now able to quasi-dynamically model the compressor component.

**15.4.1.2 Simulation Example:** As an example, the global dynamic performance of a three-stage compressor is quantitatively investigated. The compressor, Fig.15.24, running at a constant rotational speed is connected to a large air storage facility similar to the one presented in Fig.15.21. It continuously pumps air into the storage.

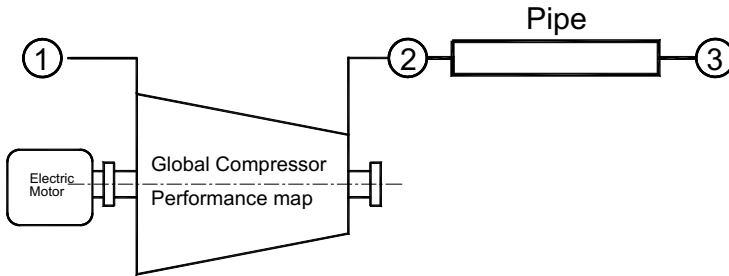


**Fig.15.24:** Simulation schematics using a compressor performance map.

The system, schematically shown in Fig.15.24, consists of an electric motor drive, a

three-stage compressor with the performance maps shown in Fig.15.17 and Fig.15.18 and a pipe that connects the compressor exit with the storage. Air is sucked from the environment at a constant pressure and temperature which is modeled by plenum 1. The storage is represented by plenum 3.

Starting from an absolute storage pressure of one atmosphere, air is pumped raising the pressure. Approaching the surge limit at point *A*, Fig.15.25, the compressor operation experiences an instantaneous breakdown that causes the mass flow to reverse the direction, point *B*.

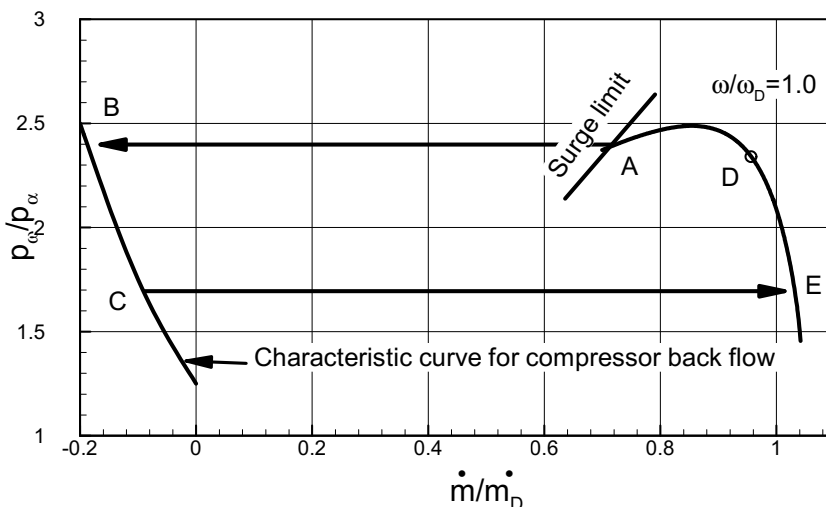


**Fig.15.25:** Compression, surge, and recovery plotted in performance map

At this point the compressor functions as an energy dissipater with the characteristic curve *BC* shown in Fig. 15.25. The air storage system starts rapidly to depressurize to arrive at point *C*, which is below the compressor design point *D*. This depressurization causes the compressor to return to its normal compression mode. The mass flow jumps to the right side, passes through the design point *D*, reaches the surge limit and repeats the surge cycle, while the electric motor continues to drive the compressor. It should be pointed out that the characteristic curve for the compressor back flow is not a part of the performance map that can be accurately predicted. It is merely an approximation that assumes the compressor channel as an annular pipe filled with blades that are exposed to a reverse flow. The blades function as obstacles that dissipate the mechanical energy of the rotating shaft without being able to convert it into potential energy. Figure 15.26 reflects the details of the surge cycle that includes discharging from *A* to *B* and filling from *B* to *E*.



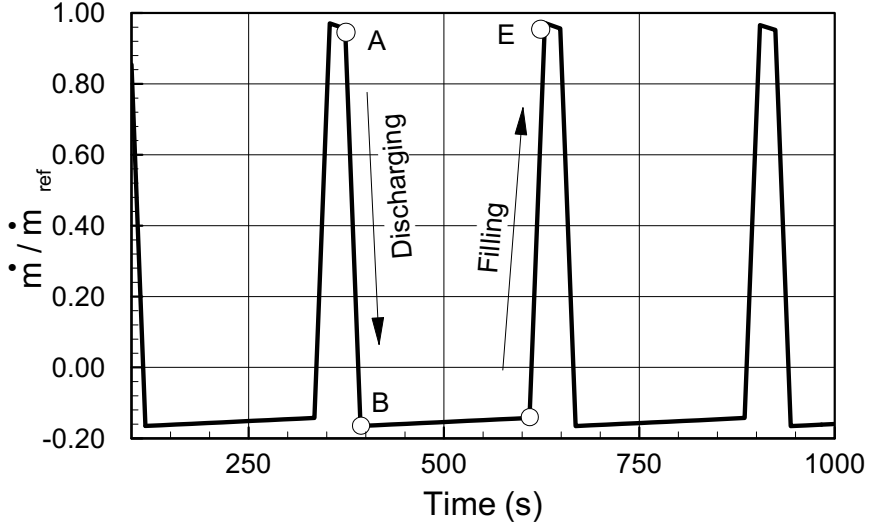


Fig.15.26: Quantitative details of surge cycle

#### 15.4.2 Module Level 2: Row-by-Row Adiabatic Calculation Procedure

This compressor module provides detailed information about the compressor behavior during dynamic events. Two methods can be used for describing this module. The first method utilizes the time dependent conservation laws for continuity, momentum, and energy Eqs. (14. 26), (14.33), and (14.51) derived in Chapter 14. For adiabatic stage compression calculation, Eq. (14.51) is reduced to:

$$\begin{aligned} \frac{\partial H}{\partial t} = & -\kappa_k \frac{\dot{m}_k}{\rho_k S_k} \left( \frac{H_{i+1} - H_i}{\Delta x} \right) + \frac{\kappa_k}{\rho_k} \left( \frac{\dot{L}}{\Delta V} \right) \\ & - \left( \frac{\kappa - 1}{\rho_k} \right)_k \left[ \left( \frac{H_k + K_k}{\Delta x} \right) \left( \frac{\dot{m}_{i+1}}{S_{i+1}} - \frac{\dot{m}_i}{S_i} \right) + \frac{\dot{m}_k}{\rho_k S_k^2} \frac{\partial \dot{m}_{i+1}}{\partial t} \right] \end{aligned} \quad (15.114)$$

The stage power  $\dot{L}$  in Eq. (15.114) is directly related to the specific stage mechanical energy  $\dot{L} = \dot{m} l_m$  with  $l_m = \lambda U_3^2$ . For a row-by-row dynamic calculation, Eq. (15.114) may be decomposed using the row-parameters discussed in section 15.2.1.2. This method allows a detailed, dynamic calculation of row properties. The second method is based on the row-by-row adiabatic calculation procedure outlined in section 15.2.1.2 under utilization of plena Eqs.(15.112) and (15.113) for dynamic coupling. Three alternative coupling configurations for a two-stage compressor are shown in Fig. 15.27. In configuration (a) each row has an inlet and an exit plenum, whereas in (b) each stage is enclosed by an exit and an inlet plenum. In (c) the entire

compressor is placed between an inlet and an exit plenum. This configuration provides satisfactory results for small size compressors such as those of a helicopter gas turbine as shown in Fig 15.27. To accurately account for the volume dynamics of a multi-stage compressor, it is more appropriate to decompose the compressor into several stage groups, where each group may consist of two to three stages that have configuration (b).

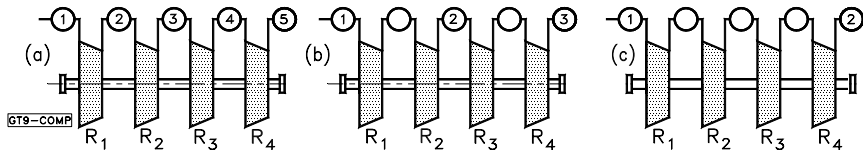


**Fig.15.27:** Row-by-row plena configuration, (a) each row enclosed by two plena, (b) each stage enclosed by two plena, (c) the entire compressor enclosed by two plena.

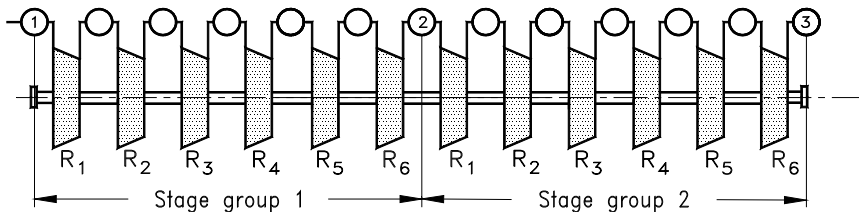


**Fig.15.28:** Decomposition of a six stage compressor into two three-stage groups. Each group is enclosed by two plena.

### 15.4.3 Active Surge Prevention by Adjusting the Stator Blades

The row-by-row calculation procedure not only provides a detailed information about the compression process of individual rows and the entire compressor, but it also enables an active control of compressor instability and surge by adjusting the stagger angles of the stator rows. It is probably the most effective active aerodynamic control mechanism. The configuration of a multi-stage compressor with adjustable stator blade rows is shown schematically in Fig. 25.29. As shown in Fig. 25.29.(a) and Fig. 25.29.(b), the stagger angle of each individual stator row  $\gamma_{si}$  can be changed according to a  $\gamma$ -scheme controlled by a multi-variable control system with the row exit pressure as one of its input variables. The effect of the adjustment on the stage velocity diagram is shown in Fig. 15.30. Figure 15.30(a) exhibits the velocity diagram pertaining to the stator row in its design stagger position under an adverse operation condition which is associated with an increase in compressor pressure ratio. This pressure ratio, however, is established by a deflection angle  $\theta$  that may cause a boundary layer separation on stator and rotor blades thus, leading to an inception of rotating stall and surge condition. To prevent this, the stagger angle  $\gamma$  is adjusted resulting in a reduced  $\theta$  as Fig. 15.30(b) shows.

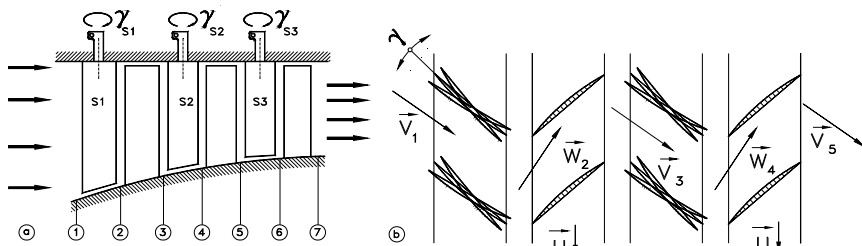


**Fig.15.29:** (a) Multistage compressor with adjustable stator blades, (b) Stagger angle adjustment.

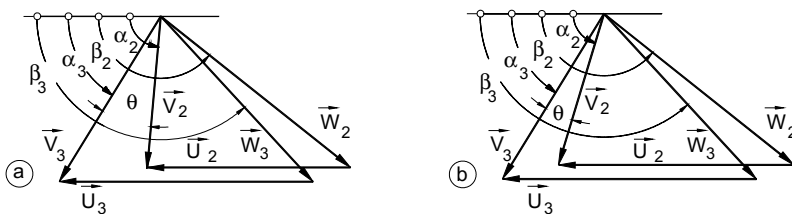


**Fig.15.30(a):** Velocity diagram with increased flow deflection  $\theta$  as a result of adverse dynamic operation, (b) adjusted stator blades causing a reduction in flow deflection  $\theta$ , thus preventing rotating stall and surge.

### 15.4.4 Module Level 3: Row-by-Row Diabatic Compression

During startup, shutdown, load change, or any other transient operation, there is a temperature difference between the compressor blade, hub, casing, discs, and the compressor working medium. This temperature difference causes a heat transfer from the working medium to the blade material and vice versa. In case of high pressure compressor trains utilized in the industry, the working medium exiting the IP-compressor passes through an inter-cooler, thus substantially reducing its temperature before entering the HP-compressor. Moreover, the trend in the development of future generation of high performance gas turbine engines point toward higher pressure ratios that inherently result in higher temperature requiring cooling of rear stages. In these cases, the compression process is no longer adiabatic, it is termed *diabatic compression*. Figure 15.31 displays a diabatic compressor stage with the corresponding instantaneous velocity diagram during a transient event, where heat from a working medium at a higher temperature is transferred to stator and rotor blade material, thus, increasing the blade temperature. The total heat added to the stage is the sum of the heat transferred to the stator and to the rotor. Heat transfers from a working medium to the compressor structure and thus, blading, hub and casing

occurs when the compressor is required to increase the higher pressure ratio. Heat rejection from the blading occurs when the compressor is relaxed. The process of heat transfer described in this section automatically captures both directions of heat transfer.

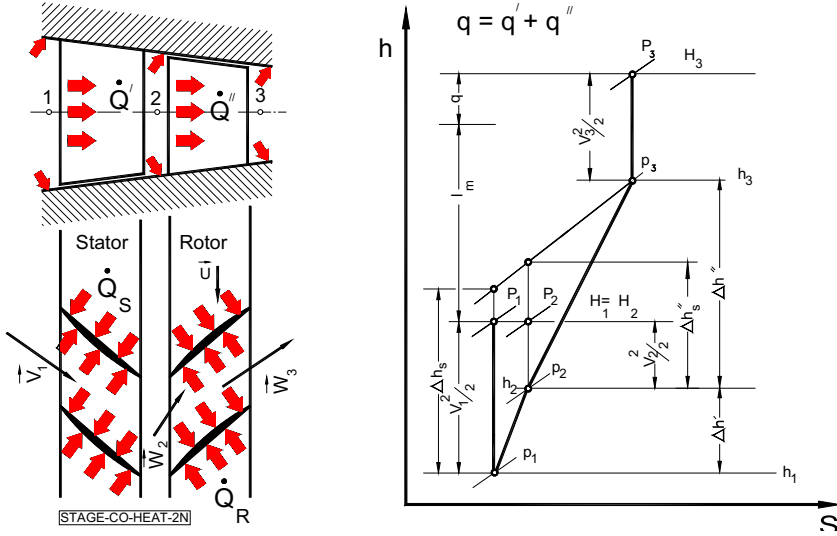


Fig.15.31: Diabatic compression process, h-s-diagram.

**15.4.4.1 Description of diabatic compressor module:** This compressor module provides a detailed information about the compressor behavior during a transient operation that causes heat transferred to/from the blade during the operation. Similar to the adiabatic case discussed in Section 15.4.2, two methods can be used for describing this module. The first method utilizes the time dependent conservation laws for continuity, momentum, and energy Eqs. (11. 26), (11.33), and (11.51) derived in Chapter 11. For diabatic stage compression calculation, Eq. (11.51) is:

$$\frac{\partial H}{\partial t} = -\kappa_k \frac{\dot{m}_k}{\rho_k S_k} \left( \frac{H_{i+1} - H_i}{\Delta x} \right) - \left( \frac{\kappa - 1}{\rho k} \right)_k \times$$

$$\left[ \left( \frac{H_k + K_k}{\Delta x} \right) \left( \frac{\dot{m}_{i+1}}{S_{i+1}} - \frac{\dot{m}_i}{S_i} \right) + \frac{\dot{m}_k}{\rho_k S_k^2} \frac{\partial \dot{m}_{i+1}}{\partial t} \right] + \frac{\kappa_k}{\rho_k} \left( \frac{\dot{Q} + \dot{L}}{\Delta V} \right) \quad (15.115)$$

The stage power  $\dot{L}$  in Eq. (15.115) is directly related to the specific stage mechanical energy  $\dot{L} = \dot{m}l_m$  with  $l_m = \lambda U_3^2$ . The heat transferred to the blades is  $\dot{Q} = \dot{m}q$  with  $q$  as the specific heat (kJ/kg) added/rejected to/from the stage. Based on the sign convention in Chapter 4, for compressors the sign the power input  $\dot{L}$  automatically assumes a positive sign. However the sign of  $\dot{Q}$  may be positive or negative based on transient operation discussed below. For steady state case with a constant mass flow, Eq. (15.115) immediately yields the conservation of energy  $q + l_m = H_3 - H_1$ . Thus, the equation of energy is rearranged as:

$$\begin{aligned} \frac{\partial H}{\partial t} = & -\kappa_k \frac{\dot{m}_k}{\rho_k} \left( \frac{H_{i+1} - H_i}{\Delta V} \right) + \frac{\kappa_k \dot{m}_k}{\rho_k} \left( \frac{q + l_m}{\Delta V} \right) \\ & - \left( \frac{\kappa - 1}{\rho_k} \right)_k \left[ \left( \frac{H_k + K_k}{\Delta x} \right) \left( \frac{\dot{m}_{i+1}}{S_{i+1}} - \frac{\dot{m}_i}{S_i} \right) + \frac{\dot{m}_k}{\rho_k S_k^2} \frac{\partial \dot{m}_{i+1}}{\partial t} \right] \end{aligned} \quad (15.116)$$

Equation. (15.116) together with equations of continuity and momentum, and the additional information about the heat transfer coefficient, describes the dynamic behavior of the diabatic compressor stage. For a row-by-row analysis it can be decomposed into two equations that describe the individual stator and rotor rows. For stator row  $q_s = q'$ , we find:

$$\begin{aligned} \frac{\partial c_{p_{i+1}} T_{0_{i+1}}}{\partial t} = & -\kappa_k \frac{\dot{m}_k}{\rho_k} \left( \frac{c_{p_{i+1}} T_{0_{i+1}} - c_{p_i} T_{0_i}}{\Delta V} \right) + \frac{\kappa_k \dot{m}_k}{\rho_k} \left( \frac{q'}{\Delta V} \right) \\ & - \left( \frac{\kappa - 1}{\rho_k} \right)_k \left[ \left( \frac{c_{p_k} T_{0_k} + K_k}{\Delta x} \right) \left( \frac{\dot{m}_{i+1}}{S_{i+1}} - \frac{\dot{m}_i}{S_i} \right) + \frac{\dot{m}_k}{\rho_k S_k^2} \frac{\partial \dot{m}_{i+1}}{\partial t} \right] \end{aligned} \quad (15.117)$$

For the rotor row, because  $l_R = l_m$  and  $q_R = q''$ , we find:

$$\begin{aligned} \frac{\partial c_{p_{i+1}} T_{0_{i+1}}}{\partial t} = & -\kappa_k \frac{\dot{m}_k}{\rho_k} \left( \frac{c_{p_{i+1}} T_{0_{i+1}} - c_{p_i} T_{0_i}}{\Delta V} \right) + \frac{\kappa_k \dot{m}_k}{\rho_k} \left( \frac{q'' + l_m}{\Delta V} \right) \\ & - \left( \frac{\kappa - 1}{\rho_k} \right)_k \left[ \left( \frac{c_{p_k} T_{0_k} + K_k}{\Delta x} \right) \left( \frac{\dot{m}_{i+1}}{S_{i+1}} - \frac{\dot{m}_i}{S_i} \right) + \frac{\dot{m}_k}{\rho_k S_k^2} \frac{\partial \dot{m}_{i+1}}{\partial t} \right] \end{aligned} \quad (15.118)$$

with  $l_m$  as the stage specific mechanical energy. To completely describe the diabatic compression process with stator and rotor rows, heat transfer equations as well as blade material temperature equations must be added to the set of equations (15.117),

(15.118), Eqs. (12. 26), and (12.33). The terms in the brackets in Equations (15.117) and (15.118) are of second order, therefore, may be neglected. As a result we obtain for stator:

$$\begin{aligned} \frac{\partial c_{p_{i+1}} T_{0_{i+1}}}{\partial t} = & -\frac{\kappa_k}{\rho_k \Delta V} \left( \dot{m}_k c_{p_{i+1}} T_{0_{i+1}} - \dot{m}_k c_{p_i} T_{0_i} + \dot{Q}'' \right) \\ & - \left( \frac{\kappa - 1}{\rho_k} \right)_k \frac{\dot{m}_k}{\rho_k S_k^2} \frac{\partial \dot{m}_{i+1}}{\partial t} \end{aligned} \quad (15.119)$$

and for the rotor row

$$\begin{aligned} \frac{\partial c_{p_{i+1}} T_{0_{i+1}}}{\partial t} = & -\frac{\kappa_k}{\rho_k \Delta V} \left( \dot{m}_k c_{p_{i+1}} T_{0_{i+1}} - \dot{m}_k c_{p_i} T_{0_i} + \dot{L} + \dot{Q}'' \right) \\ & - \left( \frac{\kappa - 1}{\rho_k} \right)_k \frac{\dot{m}_k}{\rho_k S_k^2} \frac{\partial \dot{m}_{i+1}}{\partial t} \end{aligned} \quad (15.120)$$

with  $\Delta V$  as net volume of the row space occupied by the working medium. The heat added to or rejected from the working medium in Equations (15.119) and (15.120) is transferred to the stator and rotor blade material. The heat transfer aspect is treated in the subsequent section.

**15.4.4.2 Heat transfer closure equations:** Utilizing the stator blades as an example, details of heat transfer mechanism are shown in Fig.15.32. As shown, during the cold start of power generation gas turbine engines or the acceleration phase of aircraft engines the temperature of the working medium quickly reaches its polytropic compression temperature, while the blade material temperature lags behind, Fig.15.32(a). The temperature difference  $\Delta \bar{T} = \bar{T}_{gas} - \bar{T}_{wall}$  causes a heat flow  $\dot{Q}$  from the working medium (air) into the blade material. During the deceleration and shutdown process, Fig.15.32(b), heat is transferred from the blade material to the working medium. For the sake of completeness, we may assume that the compressor blades are cooled internally. For gas turbine engines in general, this assumption is, at this stage of compressor development, merely a hypothetical one. Its realization requires a high pressure ratio far above the one that is present in the current gas turbine engines. For the future generation of high performance gas turbine with sequential combustion such the one discussed in Chapter 16, for the sake of *Carnitization* of the gas turbine process, pressure ratios above 40 are necessary that may require compressor blade cooling. In this case, the compressor working medium

transfers certain amounts of thermal energy flow or heat flow  $\dot{Q}$  to the compressor blades.

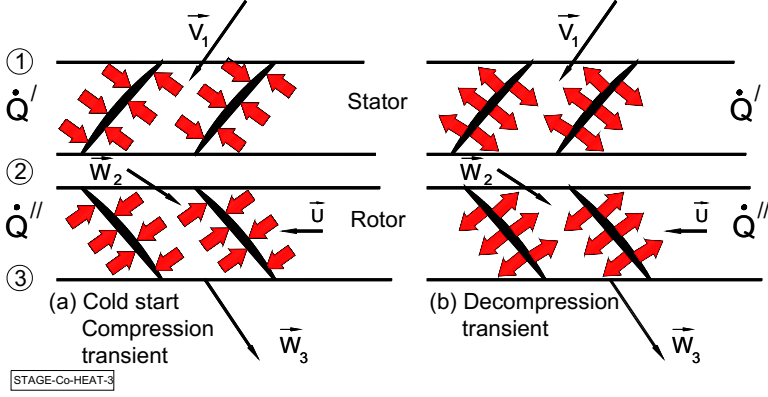


Fig.15.32: (a) Heat transferred from hot compressor working medium to cold compressor blades, (b) heat transferred from blade hot blade material to compressor working medium.

To maintain a desired blade temperature, the cooling mass flow through the blade internal channels have to remove the heat flow from the blade. The transferred thermal energies flows on hot and cold sides are:

$$\begin{aligned}\dot{Q}_h &= \bar{\alpha}_h A_h (\bar{T}_h - \bar{T}_w) \\ \dot{Q}_c &= \bar{\alpha}_c A_c (\bar{T}_w - \bar{T}_c)\end{aligned}\quad (15.121)$$

In Eq. (15.121)  $\bar{\alpha}_h$  and  $\bar{\alpha}_c$  are the averaged heat transfer coefficients for the blade external hot side and internal cooling channels. Furthermore,  $\bar{T}_c$ ,  $\bar{T}_h$ , and  $\bar{T}_w$  are the mean temperatures of coolant flow, compressor working medium, wall temperature and  $A_h$ ,  $A_c$  are the contact surfaces on blade hot and cold side, respectively. The coupling condition between the cold and the hot side is provided by the material temperature differential equation:

$$\frac{dT_w}{dt} = \frac{1}{\rho_w c_w \Delta V_w} (\dot{Q}_c + \dot{Q}_h) \quad (15.122)$$

The heat flow  $\dot{Q}_h$  in Eq. (15.122) may assume positive or negative values, whereas  $\dot{Q}_c$  is always negative, since heat is rejected. For the case of no cooling  $\dot{Q}_c$  is zero. In case of a dynamic temperature equilibrium, where the blade temperature change approaches zero, Eq. (15.122) is reduced to:

$$\dot{Q}_c + \dot{Q}_h = 0 \quad (15.123)$$

To calculate  $\dot{Q}_h$  and  $\dot{Q}_c$  for inserting into Eq. (15.122), we use the Nusselt number correlation as a result of dimensional analysis:

$$Nu = \frac{\bar{\alpha}c}{k} = f(Re, Pr, Ti, Str, Rs, Ar) \quad (15.124)$$

with  $\bar{\alpha}$  as the averaged heat transfer coefficient,  $c$  the blade chord length and  $k$  the thermal conductivity. Major parameters affecting the compressor or turbine blade heat transfer are Reynold's number  $Re$ , Prandtl number  $Pr$ , Strouhal number  $Str$ , turbulence intensity  $Ti$ , surface roughness  $R$ , and acceleration ratio  $Ar$  :

$$Re = \frac{V_\infty c}{\nu}, Pr = \frac{c_p \mu}{k}, Ti = \frac{\sqrt{v^2}}{V_\infty}, Str = \frac{f_w c}{V_\infty}, R = \frac{h_R}{c}, Ar = \frac{V_2}{V_1} \quad (15.125)$$

The dimensionless parameters in Eq. (15.125) contain a group of flow quantities and geometric parameters that are relevant for heat transfer calculations. Besides the  $Re$ - and  $Pr$ - number, the turbulence intensity which is the magnitude of the fluctuation velocity divided by the blade mean velocity  $V_\infty$  is a major parameter in heat transfer enhancement. Likewise, the Strouhal number that contains the wake passing frequency, the blade chord and the blade mean velocity plays a similar role. Despite tremendous amounts of publications that deal with the heat transfer issues in turbomachinery, no correlation can be found that incorporates all the above parameters. Therefore, we resort to simple correlations such as the one given below:

$$Nu = \frac{\bar{\alpha}c}{k} = C_1 Re^m Pr^n \quad (15.126)$$

The coefficient  $C_1$  as well as the exponents  $m$  and  $n$  in Eq. (15.126) depend upon the type of flow, the surface roughness, and the heat transfer direction. For turbulent flow, empirical correlations by Dittus-Boelter were found to be adequate.

Surge

## References

1. Lieblein, S., Schwenk, F., Broderick, R.L., Diffusions factor for estimating losses and limiting blade loadings in axial flow compressor blade elements, *NACA RME53D01* June 1953.
2. Lieblein, S., Review of high performance axial flow compressor blade element theory, *NACA RME 53L22* April 1954.
3. Lieblein, S., Roudebush, W. H., Theoretical loss relations for low speed two dimensional cascade flow *NACA Technical Note 3662* March 1956.
4. Lieblein, S., Analysis of experimental low-speed loss and stall characteristics of



- two-dimensional compressor blade cascades, NACA RM E57A28 March 1957.
5. Lieblein, S., Loss and stall analysis of compressor cascades, *ASME Journal of Basic Engineering*, Sept. 1959.
  6. NASA SP-36 NASA Report, 1965.
  7. Miller, G.R., Hartmann, M.J., Experimental shock configuration and shock losses in a transonic compressor rotor at design point NACA RM E58A14b, June 1958.
  8. Miller, G.R., Lewis, G.W., Hartman, M.J., Shock losses in transonic compressor blade rows *ASME Journal for Engineering and Power* July 1961, pp. 235-241.
  9. Schwenk, F.C., Lewis, G.W., Hartmann, M.J., A preliminary analysis of the magnitude of shock losses in transonic compressors NACA RM #57A30 March 1957.
  10. Gostelow, J.P., Krabacher, K.W., Smith, L.H., Performance comparisons of the high Mach number compressor rotor blading NASA Washington 1968, NASA CR-1256.
  11. Gostelow, J.P., Design performance evaluation of four transonic compressor rotors, *ASME Journal for Engineering and Power*, January 1971.
  12. Seylor, D.R., Smith, L.H., Single stage experimental evaluation of high Mach number compressor rotor blading, Part I, Design of rotor blading. NASA CR-54581, GE R66fpd321P, 1967.
  13. Seylor, D.R., Gostelow, J.P., Single stage experimental evaluation of high Mach number compressor rotor blading, Part II, Performance of rotor 1B. NASA CR-54582, GE R67fpd236, 1967.
  14. Gostelow, J.P., Krabacher, K.W., Single stage experimental evaluation of high Mach number compressor rotor blading, Part III, Performance of rotor 2E. NASA CR-54583, 1967.
  15. Krabacher, K.W., Gostelow, J.P., Single stage experimental evaluation of high Mach number compressor rotor blading, Part IV, Performance of Rotor 2D. NASA CR-54584, 1967.
  16. Krabacher, K.W., Gostelow, J.P., Single stage experimental evaluation of high Mach number compressor rotor blading, Part V, Performance of Rotor 2B. NASA CR-54585, 1967.
  17. N.T., Keenan, M.J., Tramm, P.C., Design report, Single stage evaluation of high Mach number compressor stages, NASA CR-72562 PWA-3546, July 1969.
  18. Koch, C.C., Smith, L.H., Loss sources and magnitudes in axial-flow compressors, *ASME Journal of Engineering and Power*, January 5, Vol. 98, NO. 3, pp. 411-424, July 1976.
  19. Schobeiri, M.T., Verlustkorrelationen für transsonische Kompressoren, *BBC-Studie*, TN-78/20, 1987.
  20. König, W.M., Hennecke, D.K., Fottner, L., Improved Blade Profile Loss and Deviation Angle Models for Advanced Transonic Compressor Bladings: Part I-A Model for Subsonic Flow, ASME Paper, No. 94-GT-335.
  21. Schobeiri, M. T., 1998, "A New Shock Loss Model for Transonic and Supersonic Axial Compressors With Curved Blades," *AIAA, Journal of Propulsion and*

- Power*, Vol. 14, No. 4, pp. 470-478.
22. Schobeiri, M. T., 1997, "Advanced Compressor Loss Correlations, Part I: Theoretical Aspects," *International Journal of Rotating Machinery*, 1997, Vol. 3, pp. 163-177.
  23. Schobeiri, M. T., 1997, "Advanced Compressor Loss Correlations, Part II: Experimental Verifications," *International Journal of Rotating Machinery*, 1997, Vol. 3, pp. 179-187.
  24. Schobeiri, M.T, Attia, M. 2003, "Active Aerodynamic Control of Multi-stage Axial Compressor Instability and Surge by Dynamically Adjusting the Stator Blades," *AIAA-Journal of Propulsion and Power*, Vol. 19, No. 2, pp 312-317.
  25. Levine, Ph., Two-dimensional inlet conditions for a supersonic compressor with curved blades, *Journal of Applied Mechanics*, Vol. 24, No. 2, June 1957.
  26. Balzer, R.L., A method for predicting compressor cascade total pressure losses when the inlet relative Mach number is greater than unity, *ASME Paper 70-GT-57*.
  27. Swan, W.C., A practical method of predicting transonic compressor performance, *ASME Journal for Engineering and Power*, Vol. 83, pp. 322-330, July 1961.
  28. Smith, L.H., Private communication with the author and the GE-Design Information Memorandum 1954: A Note on The NACA Diffusion Factor, 1995.
  29. Seylor, D.R., Smith, L.H., Single stage experimental evaluation of high Mach number compressor rotor blading, Part I, Design of rotor blading. *NASA CR-54581, GE R66fpd321P*, 1967.
  30. Seylor, D.R., Gostelow, J.P., Single stage experimental evaluation of high Mach number compressor rotor blading, Part II, Performance of rotor 1B. *NASA CR-54582, GE R67fpd236*, 1967.
  31. N.T., Keenan, M.J., Tramm, P.C., Design report, Single stage evaluation of high Mach number compressor stages, *NASA CR-72562 PWA-3546*, July 1969.
  32. Sulam, D.H., Keenan, M.J., Flynn, J.T., 1970. Single stage evaluation of highly loaded high Mach number compressor stages. II Data and performance of a multi-circular arc rotor. *NASA CR-72694 PWA*
  33. Levine, Ph., Two-dimensional inlet conditions for a supersonic compressor with curved blades, *Journal of Applied Mechanics*, Vol. 24, No. 2, June 1957.
  34. Balzer, R.L., A method for predicting compressor cascade total pressure losses when the inlet relative Mach number is greater than unity, *ASME Paper 70-GT-57*.
  35. Swan, W.C., A practical method of predicting transonic compressor performance, *ASME Journal for Engineering and Power*, Vol. 83, pp. 322-330, July 1961.
  36. Schobeiri, M. T., 1998, "A New Shock Loss Model for Transonic and Supersonic Axial Compressors With Curved Blades," *AIAA, Journal of Propulsion and Power*, Vol. 14, No. 4, pp. 470-478.
  37. Levine, Ph., Two-dimensional inlet conditions for a supersonic compressor with curved blades, *Journal of Applied Mechanics*, Vol. 24, No. 2, June 1957.

38. Grieb, H., Schill, G., Gumucio, R., 1975. A semi-empirical method for the determination of multistage axial compressor efficiency. *ASME-Paper 75-GT-11*.
39. Carter, A.D.S., 1948. Three-Dimensional flow theories for axial compressors and turbines, *Proceedings of the Institution of Mechanical Engineers*, Vol. 159, p. 255.
40. Hirsch, Ch., 1978. Axial compressor performance prediction, survey of deviation and loss correlations *AGARD PEP Working Group 12*.
41. Swan, W.C., A practical method of predicting transonic compressor performance, *ASME Journal for Engineering and Power*, Vol. 83, pp. 322-330, July 1961.
42. Jansen, W., Moffat, W.C., 1967. The off-design analysis of axial flow compressors ASME, *Journal of Eng for Power*, pp. 453-462.
43. Davis, W. R., 1971. A computer program for the analysis and design of turbomachinery, *Carleton University Report No. ME/A*.
44. Dettmering, W., Grahl, K., 1971. Machzahleinfluß auf Verdichter charakteristik, *ZFW* 19.
45. Fottner, L., 1979. Answer to questionnaire on compressor loss and deviation angle correlations, AGARD-PEP, 1979. Working Group 12.

## 16 Turbine Aerodynamic Design and Off-design Performance

The turbine component is the power generator in a gas turbine system. As briefly discussed in Chapter 12, within a turbine component, an exchange of mechanical energy (shaft work) with the surroundings takes place. In contrast to compressors, the total energy of the working medium is partially converted into shaft work, thus supplying necessary power to drive the compressor component, compensate for the bearing losses and provide the net power for driving the generator.

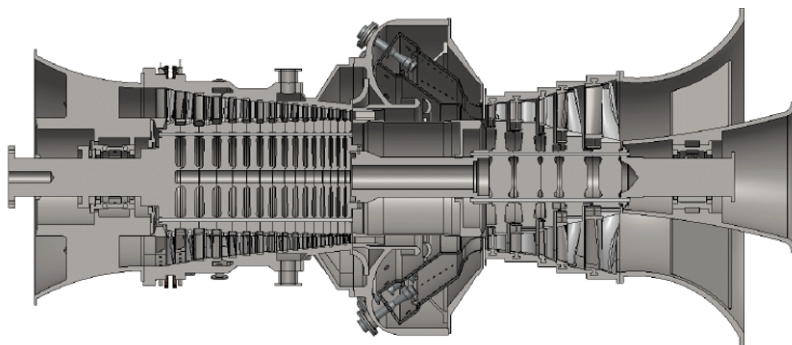


**Fig. 16.1:** Cross section of a gas turbine with its five-stage turbine component.

Figure 16.1 shows the cross section of a conventional gas turbine with a five-stage turbine component. The stator and the rotor blades are of fully 3-D design to account for secondary flow at the hub and tip. Unlike the *based load power* generation steam turbines, where the turbine consists of a high pressure (HP), an intermediate pressure (IP) and a low pressure (LP) unit, each of which may have over ten stages, the turbine component of a gas turbine has only four to five stages. As shown in Fig. 16.1 the first stage has a relatively short blade height. In traditional HP-steam turbine design, the blades were of 2-D cylindrical design. In gas turbine design, however, all blades are designed fully 3-D to reduce the stage total pressure losses as much as possible. The main purpose of using 3-D design is to reduce the secondary flow losses as discussed in Chapter 6. A difference in design configuration is shown in Figs. 16.2 and 16.3.



**Fig. 16.2** Turbine rotor with cylindrical blades

Figure 16.2 exhibits a three-stage research turbine rotor with cylindrical blades (constant profile shape and stagger angle) from hub to tip. The blades are designed to have a minimum profile loss at the mid-section. The cylindrical configuration causes the flow angle to change from hub to tip resulting in higher profile losses and consequently lower efficiencies. The low aspect ratio also causes relatively high secondary flow losses at the hub and tip sections that originate from the secondary flow, as extensively discussed in Chapter 6. Stacking different profiles from hub to tip improves the efficiency only marginally, but it does not counteract the secondary flow cause and effect. As a result, in the past, most of HP-turbines used a cylindrical blade design, accepting higher losses. In recent years, however, the streamline curvature method discussed in Chapter 10 in conjunction with the computational fluid dynamics (CFD) are used to design high efficiency HP-turbine blades. This technology has made it possible to design HP-units with efficiencies close to 94% by using 3-D bowed blades (also called compound lean), where the pressure surface is bowed in a convex shape as shown in Fig. 16.3, [1].

Before discussing the effect of 3-D blade design on efficiency and performance of turbine components, we present the necessary aero-thermodynamic tool for a 1-D turbine design, which is a prerequisite for any 3-D design process. Regarding the turbine component modeling for dynamic simulation, similar to the compressor component we discussed in Chapter 15, we present three simulation levels. First, we treat the fundamental aspects of 1-D adiabatic design, followed by a section that deals

with generation of global turbine performance characteristics. Three dynamic simulation levels using simple performance characteristics, row-by-row adiabatic, and row-by-row diabatic dynamic performance simulation, concludes the chapter.



**Fig. 16.3:** Rotor with a 3-D compound lean of the TPFL- research turbine.

## **16.1 Stage-by-Stage and Row-by-Row Adiabatic Design and Off-Design Performance**

The unifying treatment of the design calculation procedure outlined in Chapter 15 for compressors is now extended to the turbine component. Stage-by-stage and row-by-row methods for calculating the expansion process within a multi-stage turbine component are presented. The performance behavior of a single- or multi-stage turbine component is completely described by the individual stage characteristics in conjunction with the total pressure losses that we extensively discussed in Chapter 5. The meridional view, the blade row configuration, the expansion and the velocity diagram of a typical multi-stage turbine, are shown in Fig. 16.4. Similar to Chapter 15, using the variables in Fig. 16.4(c) and (d), the following dimensionless parameters are defined:

$$\phi = \frac{V_{\alpha 3}}{U_3}, \mu = \frac{V_{\alpha 2}}{V_{\alpha 3}}, v = \frac{U_2}{U_3}, r = \frac{\Delta h''}{\Delta h'' + \Delta h'},$$

$$\lambda = \frac{\Delta h}{U_3^2} = \frac{l_m}{U_3^2} = \frac{U_2 V_{u2} + U_3 V_{u3}}{U_3^2}, R = \frac{\rho_2}{\rho_3} = \frac{b_3 D_3}{b_2 \mu D_2} \quad (16.1)$$

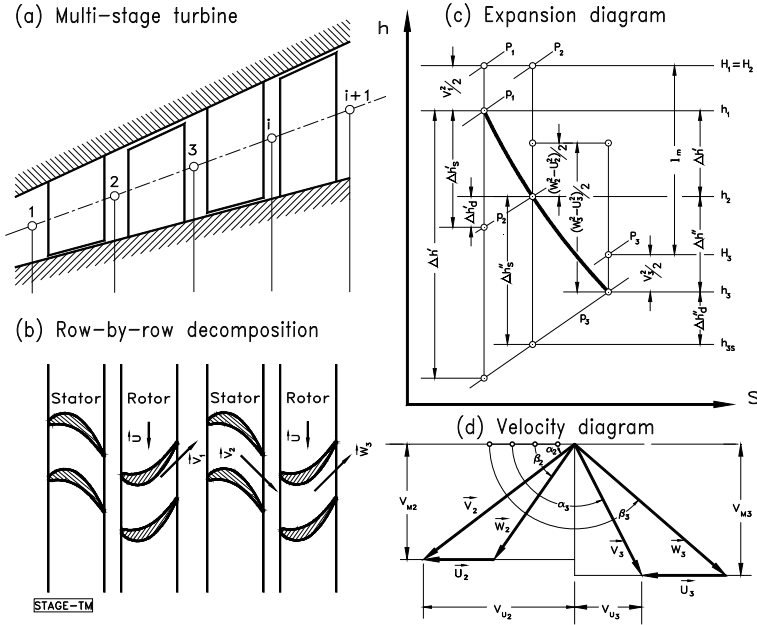


**Fig. 16.4** Meridional view, blade row configuration, expansion and velocity diagram of a typical multi-stage turbine

The dimensionless parameters from Eq. (16.1) are used to treat the following stage-by-stage as well as row-by-row design and off-design analysis.

### 16.1.1 Stage-by-Stage Calculation of Expansion Process

Using the characteristics defined in (16.1) in conjunction with the stage efficiency discussed in Chapter 6, the expansion is accurately calculated from:

$$\begin{aligned}
\cot\alpha_2 - \cot\beta_2 &= \frac{v}{\mu\phi} \\
\cot\alpha_3 - \cot\beta_3 &= \frac{1}{\phi} \\
\lambda &= \phi(\mu v \cot\alpha_2 - \cot\alpha_3) - 1 \\
r &= \frac{1}{2} \frac{\mu^2 \phi^2 \cot^2 \alpha_2 (v^2 - 1) - 2\mu v \phi \lambda \cot\alpha_2 + \lambda^2 + 2\lambda - \phi(\mu^2 - 1)}{\lambda}
\end{aligned} \tag{16.2}$$

As we saw in Chapters 4 and 15, the four equations in (16.2) contain nine unknowns. The following quantities are assumed to be known: (1) the turbine mass flow, (2) the turbine pressure ratio, (3) the type of blades, and (4) their exit metal angles,  $\alpha_{2m}$  and  $\beta_{3m}$ , for each individual stage and their configuration in terms of degree of reaction. Further, we may assume the absolute inlet flow angle of the first stage and the exit flow angle of the last stage to be  $90^\circ$ . With these assumptions, all nine stage characteristics are estimated in the first iteration step, which usually does not deliver the required turbine power at the given conditions (pressure ratio, mass flow, inlet or exit enthalpy). The process of iteration is continued until the enthalpy and mass flow convergence has been reached. This stage-by-stage expansion calculation method delivers accurate results, however, it requires some experience in guessing the initial values for unknown characteristics. In the following row-by-row calculation, we will discuss in more detail how it is computationally more efficient and does not require a lot of iterations.

### 16.1.2 Row-by-Row Adiabatic Expansion

As discussed in Chapter 4, the expansion process within stator and rotor row shown in Fig. 16.5 is summarized as:

$$\begin{aligned}
\Delta h' &= h_1 - h_2 = \frac{1}{2} (V_2^2 - V_1^2) \\
\Delta h_s' &= h_1 - h_{2s} = \frac{1}{2} (V_{2s}^2 - V_1^2) \\
\Delta h'' &= h_2 - h_3 = \frac{1}{2} (W_3^2 - W_2^2 + U_2^2 - U_3^2) \\
\Delta h_s'' &= h_2 - h_{3s} = \frac{1}{2} (W_{3s}^2 - W_2^2 + U_2^2 - U_3^2)
\end{aligned} \tag{16.3}$$

The quantities in Eqs. (16.3), the decomposition of the turbine stage in its stator and



rotor rows, and the expansion diagram are presented in Fig. 16.5. The quantities with superscripts “/” and “//” in Fig. 16.5, refer to stator and rotor rows, respectively. For the stator row, the expansion diagram shows the details of an adiabatic expansion where the absolute total enthalpy remains constant. The following rotor row with the corresponding expansion diagram exhibits the details of energy balance in a relative frame of reference with constant relative total enthalpy. The expansion diagram for the entire stage exhibits a composite picture of energy balance within the stator and rotor row. We introduce the following efficiency definition for the stator and rotor row:

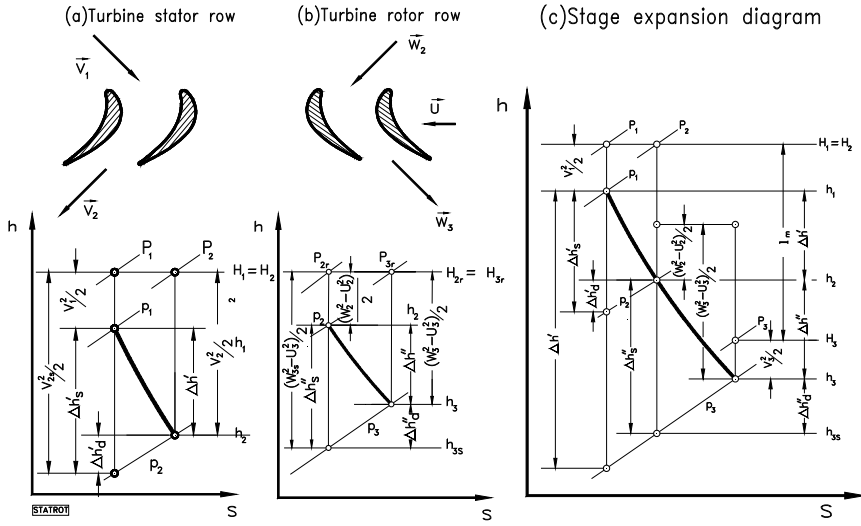


**Fig. 16.5:** Energy transfer in turbine stator row, turbine rotor row, and turbine stage

$$\eta' = \frac{\Delta h'}{\Delta h'_s} = \frac{V_2^2 - V_1^2}{V_{2s}^2 - V_1^2}, \quad (16.4)$$

$$\eta'' = \frac{\Delta h''}{\Delta h''_s} = \frac{W_3^2 - W_2^2 + U_2^2 - U_3^2}{W_{3s}^2 - W_2^2 + U_2^2 - U_3^2}$$

For the sake of completeness, the rotor efficiency definition in Eq. (16.4) includes the difference of circumferential kinetic energies  $U_2^2 - U_3^2$  in denominator and numerator. However, this difference may be neglected without causing any noticeable error. The choice of efficiency definition varies throughout the literature (see Traupel [2], Vavra

[3], NASA [4]). Engine aerodynamicists and researchers frequently prefer to use their own efficiency definition that may serve their design purpose. Regardless how the efficiency is defined, it must be kept consistently throughout the calculation procedure. We chose definition (16.4) which is consistent with the one defined in Chapter 15. Incorporating Eq.(16.4) into Eqs.(16.3), the isentropic enthalpy difference for stator and rotor row, respectively, is expressed by:

$$\Delta h'_s = \frac{1}{2\eta'} (V_2^2 - V_1^2) \quad (16.5)$$

$$\Delta h''_s = \frac{1}{2\eta''} (\mathcal{W}_{3s}^2 - \mathcal{W}_2^2 + U_2^2 - U_3^2)$$

Introducing the dimensionless isentropic enthalpy differences by dividing Eqs. (16.5) by the circumferential kinetic energy at the exit of the turbine stage and incorporating the stage parameters Eqs. (16.2), the dimensionless row parameters are developed as follows:

$$\chi' = \frac{1}{2\eta'} \left[ \phi \left( \frac{\mu^2}{\sin^2 \alpha_2} - \frac{1}{\sin^2 \beta_3} \right) - 2 \phi \cot \beta_3 - 1 \right] \quad (16.6)$$

$$\chi'' = \frac{1}{2\eta''} \left[ \phi^2 \left( \frac{\mu^2}{\sin^2 \beta_3} - \frac{1}{\sin^2 \alpha_2} \right) + 2 \mu v \phi \cot \alpha_2 - 1 \right] \quad (16.7)$$

Equations (16.6) and (16.7) represent the dimensionless isentropic enthalpy differences for the expansion through stator and rotor row, respectively. As the above equations indicate, the calculation of each row necessitates the knowledge of entire stage parameters which requires few iterations. Similar to the compression process outlined in Chapter 15, to substantially reduce the number of iterations, we subdivide the stage specific polytropic mechanical energy  $l_m$ , as well as the isentropic mechanical energy  $l_{ms}$ , into two virtual contributions  $l_m = l' + l''$  and  $l_{ms} = l'_s + l''_s$  that we allocate to stator and rotor row. This step does not imply that the stator row is performing shaft power which would violate the energy balance. It merely provides a smooth transition from stator row to rotor row when calculating the compression and expansion processes. With this re-arrangement, we arrive at the contributions allocated to the stator and rotor rows as:

$$\begin{aligned} l' &= \frac{1}{2} V_2^2 - \frac{1}{2} \mathcal{W}_2^2 \\ l'' &= \frac{1}{2} (\mathcal{W}_3^2 - U_3^2 + U_2^2 - V_3^2) \end{aligned} \quad (16.8)$$

Similarly we find the isentropic parts:

$$\begin{aligned} l'_s &= \frac{1}{2} V_{2s}^2 - \frac{1}{2} W_2^2 \\ l''_s &= \frac{1}{2} (W_{3s}^2 - U_3^2 + U_2^2 - V_3^2) \end{aligned} \quad (16.9)$$

As seen, the sum of stator and rotor contributions leads to the stage specific mechanical energy. Using the polytropic specific mechanical energy expressions given in Eqs.(16.8) and dividing them by the circumferential kinetic energy at the exit of the individual row, the dimensionless row polytropic load coefficients for stator and rotor are:

$$\begin{aligned} \lambda' &= \frac{l'}{U_2^2} = \phi' \cot \alpha_2 - \frac{1}{2} \\ \lambda'' &= \frac{l''}{U_3^2} = -\phi'' \cot \beta_3 - 1 + \frac{v^2}{2} \end{aligned} \quad (16.10)$$

with stator and rotor flow coefficient  $\phi' = V_{\alpha 2} / U_2$ , and  $\phi'' = V_{\alpha 3} / U_3$ . Combining Eqs.(16.10) with the efficiency definition for the stator and rotor rows, Eq.(16.4), the following expressions for the efficiency are obtained:

$$\begin{aligned} \eta' &= \frac{V_2^2 - V_1^2}{2l'_s - 2l' + V_2^2 - V_1^2} \\ \eta'' &= \frac{W_3^2 - W_2^2}{2l''_s - 2l'' + W_3^2 - W_2^2} \end{aligned} \quad (16.11)$$

The isentropic row load coefficient  $\psi$  is defined as the dimensionless isentropic specific mechanical energy for the row. Implementing the efficiency expressions from Eqs. (16.11), the isentropic row load coefficients for the stator and rotor rows are obtained:

$$\psi' = \frac{l'_s}{U_2^2} = \lambda' + \frac{\phi'^2}{2} \left( \frac{1}{\sin^2 \alpha_2} - \frac{1}{\mu^2 \sin^2 \alpha_3} \right) \left( \frac{1}{\eta'} - 1 \right) \quad (16.12)$$

$$\psi'' = \frac{l''_s}{U_3^2} = \lambda'' + \frac{\phi''^2}{2} \left( \frac{1}{\sin^2 \beta_3} - \frac{\mu^2}{\sin^2 \beta_2} \right) \left( \frac{1}{\eta''} - 1 \right) \quad (16.13)$$

Similar to compressor component treated in Chapter 15, all the information necessary to pursue the expansion process on the h-s diagram is now available to predict the turbine performance behavior at the design point. Likewise, the off-design operation can be predicted accurately providing that a reliable off-design efficiency calculation method exists. Such a method will be presented in the next section.

Given the pressure and temperature at the inlet, the density can be calculated from the equation of state, as well as the enthalpy and entropy of the gas at the inlet. Utilizing the gas tables, the first point on the h-s diagram can be determined easily. The row flow coefficients ( $\phi'$ ) and ( $\phi''$ ) are calculated using the continuity equation:

$$\phi = \frac{V_{ax}}{U} = \frac{\dot{m}}{\rho AU} = \frac{\dot{m}}{\rho A \omega R} \quad (16.14)$$

Given the stator and rotor exit metal angles  $\alpha_{2m}$ ,  $\beta_{3m}$  as the input data necessary to describe the geometry, the flow angles  $\alpha_2$ ,  $\beta_3$  are calculated using deviation angles outlined in Chapter 8. The remaining flow angles  $\beta_2$ ,  $\alpha_3$  are determined by using the flow coefficient from Eq. (16.14):

$$\beta_2 = \tan^{-1} \left( \frac{W_{ax2}}{W_{u2}} \right) = \tan^{-1} \left( \frac{V_{ax2}}{W_{u2}} \right) \quad (16.15)$$

From the velocity diagram of Fig. 16.4, we introduce the relationship:

$$W_{u2} = V_{u2} - U_2 \quad (16.16)$$

Implementing Eq. (16.16) into (16.15) and introducing the stator flow coefficient  $\phi'$ , we obtain the expression:

$$\beta_2 = \tan^{-1} \left( \frac{\phi'}{\phi' \cot \alpha_2 - 1} \right) \quad (16.17)$$

Similarly for the rotor:

$$\alpha_3 = \tan^{-1} \left( \frac{\phi''}{\phi'' \cot \beta_3 + 1} \right) \quad (16.18)$$

Upon the determination of all the angles involved in the velocity diagram, the velocities and their components are fully described. The flow coefficients,  $\phi'$  and  $\phi''$ , and the flow angles  $\alpha_2$ ,  $\beta_2$ ,  $\alpha_3$ ,  $\beta_3$  are necessary tools to determine the polytropic

and isentropic enthalpy differences between the inlet and exit of the row. The amount of work produced by the flow is fully represented by the load coefficients  $\lambda$  and  $\psi$ , as presented in the previous sections. Finally, from the energy balance relationships presented above, the complete expansion process for the turbine stage is determined as follows:

$$\begin{aligned} h_2 &= h_1 - l' - \frac{1}{2} (W_2^2 - V_1^2) \\ h_{2s} &= h_1 - l'_s - \frac{1}{2} (W_2^2 - V_1^2) \\ h_3 &= h_2 - l'' - \frac{1}{2} (V_3^2 - W_2^2) \\ h_{3s} &= h_2 - l''_s - \frac{1}{2} (V_3^2 - W_2^2) \end{aligned} \quad (16.19)$$

The above procedure can easily be repeated for all the rows and stages of the turbine under consideration.

### 16.1.3 Off-Design Efficiency Calculation

Accurate prediction of the turbine cascade off-design efficiency is essential for calculating performance behavior of a turbine stage and component. For multi-stage axial flow turbines, the primary loss coefficient is the major contributor to the overall stage efficiency. Numerous correlations are given in the literature for off-design efficiency calculation procedure, where the off-design primary loss coefficient is related to its design point value (see Kroon and Tobias [5], Kochendorfer and Nettles [6]). In a comprehensive and systematic study, Bammert and Zehner [7] and Zehner [8] investigated the off-design behavior of single- and multi-stage turbines with different blade geometry. Based on the experimental results, Zehner [7] established the following relationship for the off-design primary loss coefficient:

$$1 - \zeta_p = (1 - \zeta_p^*) e^{[-a(\Delta\Theta)^b]} \quad (16.20)$$

with

$$\Delta\Theta = \frac{\theta_i - \theta_i^*}{180 - \theta_i^*}, \quad \Delta\Theta_s = \frac{\alpha_i - \alpha_i^*}{180 - \alpha_i^*}, \quad \Delta\Theta_R = \frac{\beta_i - \beta_i^*}{180 - \beta_i^*} \quad (16.21)$$

where  $\theta_i$ ,  $\theta_i^*$  represent the stator/rotor inlet flow angle  $\alpha_1$ ,  $\beta_2$  at the off-design point and  $\alpha_1^*$ ,  $\beta_2^*$  at the design point respectively. The coefficients  $a$ ,  $b$  are functions of the cascade characteristic described by Zehner [7]. Once the off-design primary loss coefficient has been calculated, the row efficiency is calculated by considering

the other individual losses such as secondary and clearance losses (see Chapter 6, Schobeiri [9], Zehner [7]):

$$\eta = 1 - \sum \zeta_i \quad (16.22)$$

with  $\zeta_i$  as the individual loss coefficient such as primary, trailing edge, secondary, and shock losses. Equations (16.20) and (16.21) explicitly relate the primary loss coefficient of the off-design operation to the design point. A similar relation does not exist for the rest of the losses. This is partially due to the complexity of the secondary flow phenomena. An alternative off-design efficiency correlation presented in [10] directly relates the off-design efficiency to the design efficiency as follows:

$$\eta' = \eta^{*'} (1 - e^{c'}) \quad , \quad \eta'' = \eta^{*''} (1 - e^{c''}) \quad (16.23)$$

where, the exponent  $c$  is expressed for the stator, and rotor as:

$$c' = A' \left( \frac{\alpha_1}{\alpha_1^*} \right)^{B'} \quad , \quad c'' = A'' \left( \frac{\beta_2}{\beta_2^*} \right)^{B''} \quad (16.24)$$

The coefficients  $A'$ ,  $A''$ ,  $B'$ ,  $B''$  may, among other things, depend on the Re-number, Mach number, and blade geometry. For a particular set of turbine blade profiles, N-8000, developed by Brown Boveri & Cie, the following coefficients were found:

$$\begin{aligned} A' &= 0.075 \alpha_2 - 7.8460 \quad , \quad A'' = 0.075 (180 - \beta_3) - 7.8460 \\ B' &= 0.029 \alpha_2 + 0.6107 \quad , \quad B'' = 0.029 (180 - \beta_3) + 0.6107 \end{aligned} \quad (16.25)$$

where, the angles are in degrees and the angle directions follow the convention in Fig. 16.4. Equations (16.23), (16.24), and (16.25) satisfactorily relate the off-design efficiency of typical turbine blades to the design point efficiency.

With the procedure described above, it is possible to accurately predict the off-design efficiency of a turbine stage provided that the given off-design mass flow permits a normal turbine operation. However, if the mass flow has been reduced to such an extent that the turbine stage is no longer able to produce mechanical energy, the efficiency has to be redefined in such a way that it reflects the dissipative nature of the energy conversion. To evaluate the degree of dissipation, the following loss coefficients and efficiencies are introduced:

$$\zeta' = \frac{\Delta h_D'}{V_1'^2/2}, \quad \zeta'' = \frac{\Delta h_D''}{W_2''^2/2} \quad (16.26)$$

$$\eta' = 1 - \zeta', \quad \eta'' = 1 - \zeta'' \quad (16.27)$$

with  $\Delta h_D' = h_2 - h_{2s}$  and  $\Delta h_D'' = h_3 - h_{3s}$  from Fig. 16.4c. For the extreme off-design cases, the relationships between the stage parameters based on the normal turbine stage operation as previously described, are no longer valid. In the following section, a method is presented that predicts accurately the off-design behavior of a turbine stage for extreme low mass flows.

### 16.1.4 Behavior Under Extreme Low Mass Flows

During the shutdown process of a steam turbine or a compressed air storage gas turbine, the mass flow and the turbine power continuously decrease. By approaching a certain mass flow  $\dot{m}_{L=0}$  at which the turbine ceases to produce power, the rear stages of a multi-stage turbine are not able to produce mechanical energy and act as an energy dissipater, Fig 16.6. As a result, the kinetic energy of the rotating shaft dissipates into heat, resulting in excessive temperature and entropy rise.

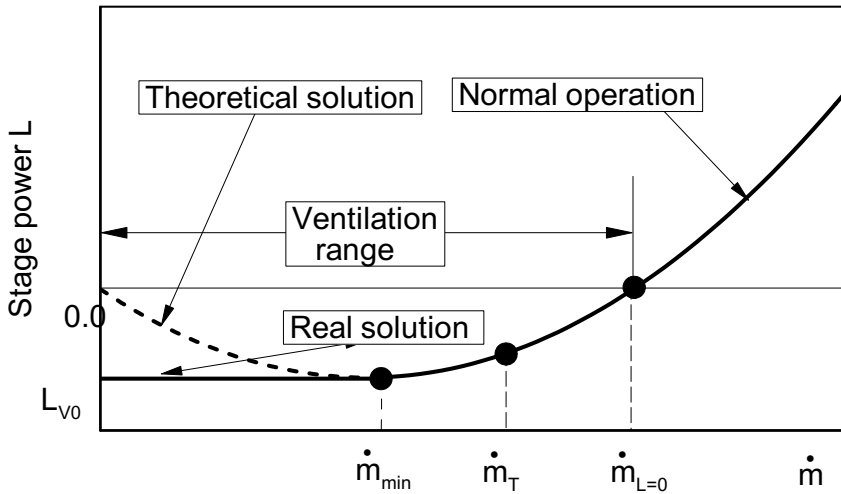


**Fig. 16.6:** Turbine performance behavior under low mass flow conditions

For  $\dot{m} < \dot{m}_{L=0}$  the turbine starts to *ventilate* (wind milling) and is no longer able to remove the heat. In order to prevent the turbine blades and structure from damages caused by excessive temperature development, cooling mass flow must be injected into the flow path to remove the heat. Figure 16.6 shows the detail of the ventilation process. The ventilation process cannot be captured by the method used for predicting the design and normal off-design behavior discussed above. In the following section

we present a method discussed in [12] and [13] that accurately predicts the dissipation process.

Consider a turbine stage operating under normal condition. The stage power determined by a second order polynomial in  $\dot{m}$  is:

$$\dot{L} = \dot{m} \lambda U_3^2 = \dot{m} \left[ \phi (\mu v \cot \alpha_2 - \cot \beta_3) - 1 \right] U_3^2 \quad (16.28)$$

The stage flow coefficient  $\phi$  in Eq. (16.28) is expressed in terms of the stage mass flow rate as follows:

$$\phi = \frac{V_{ax3}}{U_3} = \frac{\dot{m}}{\pi D_{m3} h_{b3} \rho_3 U_3} = \frac{\dot{m}}{\xi} \quad (16.29)$$

where,  $\xi$  is the mass flow parameter defined as:

$$\xi = \pi D_{m3} h_{b3} \rho_3 U_3 \quad (16.30)$$

with  $D_{m3}$ ,  $h_{b3}$  as the mean radius and the blade height at the exit of the stage. Substituting Eqs. (16.29) and (16.30) into (16.28), the power expression is then re-written:

$$\dot{L} = \frac{\dot{m}^2}{\xi} (\mu v \cot \alpha_2 - \cot \beta_3) U_3^2 - \dot{m} U_3^2 \quad (16.31)$$

Equation (16.31) accurately represents the stage power behavior under normal operating conditions. However, for  $\dot{m} < \dot{m}_{\min}$ , it leads to the erroneous theoretical solution as a dashed curve shown in Fig. 16.6. For ventilation condition, a different expression for the stage power is written that accurately describes the ventilation branch as a second order polynomial:

$$\dot{L}_v = C_1 \dot{m}^2 + C_2 \dot{m} + C_3 \quad (16.32)$$

The constant  $C_3$  is found immediately by setting in Eq. (16.32)  $\dot{m} = 0$ . This results in  $C_3 = \dot{L}_{vo}$  as seen from Fig. 16.6. For the calculation of the ventilation power at zero mass flow,  $\dot{L}_{vo}$ , Traupel [2] suggests:

$$\dot{L}_{vo} = C \pi D_{m3} h_{b3} \rho_3 U_3^3 \quad (16.33)$$



where the constant  $C$  is obtained from the experiment. Since this constant changes with the blade geometry, it seems more appropriate to replace it by a blade geometry functional  $g(G)$  with  $G$  as a geometry parameter:

$$\dot{L}_v = g(G) \xi U^2 \quad (16.34)$$

Zehner [7] proposed for  $G$  the following relationship that accounts for the blade geometry:

$$G = \frac{f}{s} (\theta \gamma)^{\frac{1}{2}} \quad (16.35)$$

with  $s$  as the blade spacing,  $\theta$  the total flow deflection,  $\gamma$  the stagger angle and  $f$  the maximum camber height shown in Fig. 16.7.

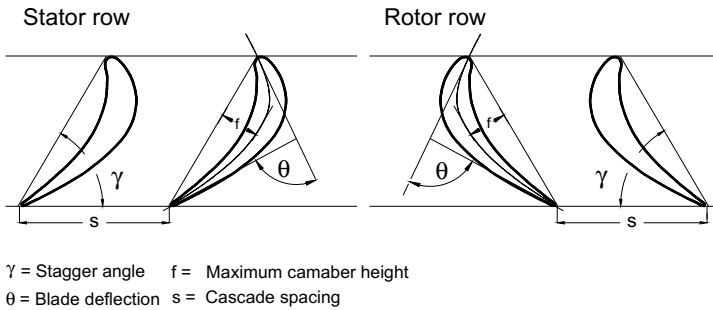


**Fig. 16.7:** Blade nomenclature for defining the geometry parameter  $\gamma$ .

For the functional  $g(G)$  we set:

$$g(G) = C_G G^2 \quad (16.36)$$

with  $C_G = 0.97121$ . To determine the constant  $C_2$  in Eq.(16.32), we assume that the maximum power consumption occurs at zero mass flow rate. This assumption leads to the conclusion that  $C_2 = 0$ . The constant  $C_1$  in Eq.(16.32) is calculated from the requirement that  $\dot{L}_v$  must follow the continuous course of  $L$  given by Eq. (16.31) with the same value, and slope at a common tangent point at  $\dot{m}_T$  shown in Fig. 16.6. Equating (16.31) and (16.32) and their respective derivatives at the common tangent point given in the following Eq. (16.37).

$$(\dot{L})_{\dot{m}_T} = (\dot{L}_v)_{\dot{m}_T}, \quad \left( \frac{\partial \dot{L}}{\partial \dot{m}} \right)_{\dot{m}_T} = \left( \frac{\partial \dot{L}_v}{\partial \dot{m}} \right)_{\dot{m}_T} \quad (16.37)$$

As a result, Eqs. (16.37) determine the mass flow at the tangent point  $\dot{m}_T$ :

$$\dot{m}_T = \frac{\xi}{2 \left( \mu v \cot \alpha_2 - \cot \beta_3 - \frac{\xi C_1}{v U_3^2} \right)} \quad (16.38)$$

and:

$$C_1 = \frac{U_3^2}{\xi''} \left( \mu v \cot \alpha_2 - \cot \beta_3 - \frac{\xi U_3^2}{4 \dot{L}_{vo}} \right) \quad (16.39)$$

Finally, an expression for the stage power during the ventilation is found as:

$$\dot{L}_v = \frac{\dot{m}^2 U_3^4}{4 \dot{L}_{vo}} \left( 4g(G) \frac{v^3}{\mu} (\mu v \cot \alpha_2 - \cot \beta_3) - 1 \right) - \dot{L}_{vo} \quad (16.40)$$

Equation (16.40) describes the performance behavior of a turbine stage during the ventilation operation. It can be decomposed into portions that are allocated to stator and rotor row, as discussed previously.

### 16.1.5 Example: Steady Design and Off-Design Behavior of a Multi-Stage Turbine

The row-by-row expansion calculation discussed above provides information relevant for performance and efficiency prediction during design and off-design operation. It also supplies essential information related to reliability aspects of the design that includes thermal and mechanical stress analysis of blade rows. This analysis requires accurate information about the temperature and pressure distributions along the expansion path. Considering these aspects, the method discussed above is applied to a multi-stage turbine, where its design and off-design performance is calculated and the results are compared with the measurement. As an appropriate application example, a seven-stage research turbine is chosen, whose geometry, design, and off-design performance behavior were extensively studied and well documented in [7], [8], and [14]. For this turbine, three different off-design points are calculated and compared with the measurement. The corresponding mass flow and speed ratios are given as  $\mu = \dot{m}/\dot{m}_D = 0.13, 0.38, 0.83$  and  $\omega/\omega_D = 1$ . Figure 16.8 exhibits the dimensionless temperature distribution along the expansion path at different stations

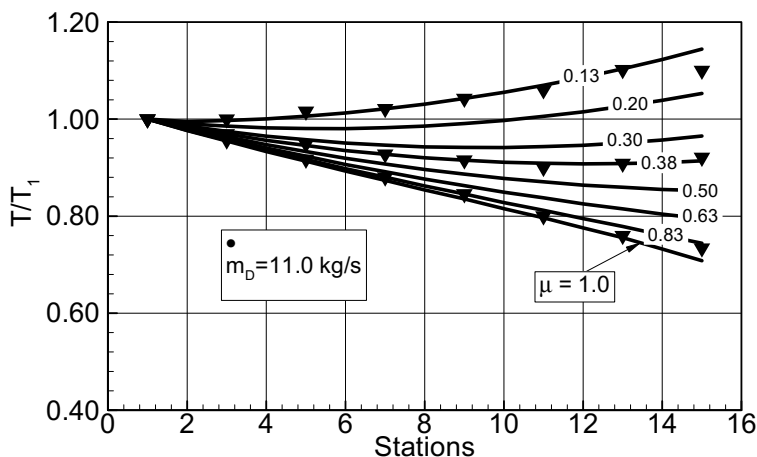


**Fig. 16.8** Temperature distribution in a seven stage turbine for design and off-design mass flow rates, experiments denoted by ▼ from [7]

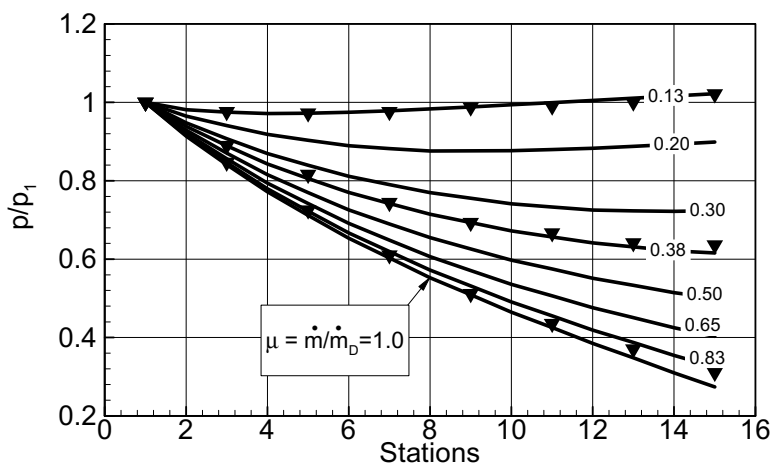


**Fig. 16.9:** Pressure distribution in a seven stage turbine for design and off-design mass flow rates, experiments denoted by ▼ from [7]

with the mass flow ratio as the parameter. As shown, the temperature increases occur at the rear stages for mass flow ratios less than 0.4, indicating the beginning of a dissipation process associated with entropy and temperature increases. Decreasing the mass flow ratio results in strong dissipation with corresponding temperature rise. A

similar tendency is displayed by the pressure distribution in Fig. 16.9. As shown, the reduction of the turbine mass flow ratio to 0.13 leads to a considerable distortion of the stage velocity diagram and flow deflection that is associated with dissipation of mechanical energy resulting in pressure increase along the flow path. Figure 16.8 also includes complementary calculations for  $\mu = \dot{m}/\dot{m}_D = 0.20, 0.30, 0.50, 1.00$ .

## 16.2 Off-Design Calculation Using Global Turbine Characteristics Method

This method introduced by Stodola [11] and Traupel [2] replaces the turbine component by a nozzle that can be described by a set of algebraic equations. Horlock [12], Pfeil [13], and Schobeiri [14] derived differential equations for predicting the off-design behavior of multi-stage turbines. These methods require the knowledge of efficiency behavior of the turbine during off-design operation. The method suggested by Stodola [11] exhibits a simple method for calculating the mass flow. However, it does not provide any details relative to the expansion process. The off-design mass flow is determined from the following expression:

$$\dot{m} = \dot{m}^* \frac{P_I}{P_I^*} \left( \frac{T_I^*}{T_I} \right)^{\frac{1}{2}} \left( \frac{1 - (\pi)^{\frac{n+1}{n}}}{1 - (\pi^*)^{\frac{n+1}{n}}} \right)^{\frac{1}{2}} \quad (16.41)$$

where  $\pi$  is the turbine pressure ratio defined as  $\pi = P_{outlet}/P_{inlet}$ , and  $n$  as the polytropic exponent given by the expression:

$$n = \frac{\kappa}{\kappa - \eta (\kappa - 1)} \quad (16.42)$$

with  $\kappa = c_p/c_v$  as the isentropic exponent. Accurate determination of the off-design performance behavior of a multi-stage turbine using the global characteristics method requires accurate calculation of the efficiency. This can be done utilizing the above row-by-row calculation procedure, where the dimensionless velocity parameter  $v$ , as defined below, is varied:

$$v = \frac{U}{\sqrt{2 \Delta h_s}} \quad (16.43)$$

In Eq. (16.43),  $U$  is the circumferential velocity and  $\Delta h_s$  is the isentropic enthalpy difference of the turbine component. Once the efficiency versus  $v$  is obtained, the relative efficiency  $\eta/\eta^*$  can be plotted versus the relative velocity parameter  $v/v^*$ ,

where the superscript “\*” refers to the design point. Figure 16.10 qualitatively shows the relative efficiency versus relative velocity parameter. The circumferential velocity  $U$  in Eq.(16.43) may be calculated using an average mean radius for the entire turbine. The characteristic curve of  $\eta/\eta^*$  depends on the type of turbine blade geometry and the stage characteristics. Once it is calculated for a particular turbine, it can be expressed as a polynomial such that:

$$\frac{\eta}{\eta^*} = \sum_{n=1}^N a_n \left( \frac{v}{v^*} \right)^n \quad (16.44)$$

The coefficients  $a_n$  are determined by a least square fit or the data calculated from the steady state row-by-row procedure. The turbine exit temperature may then be determined by the expression:

$$T_o = T_I \pi^{\left( \frac{\kappa-1}{\kappa} \eta \right)} \quad (16.45)$$

and finally, the net power production is calculated by:

$$\dot{L} = \dot{m} \bar{c}_p \Delta T, \quad \dot{L}_{net} = \dot{L} \eta_{mech} \quad (16.46)$$

where  $\Delta T$  is the total temperature difference expressed by  $\Delta T = T_I - T_o$ , and  $\eta_{mech}$  is the mechanical efficiency, and accounts for bearing friction losses.

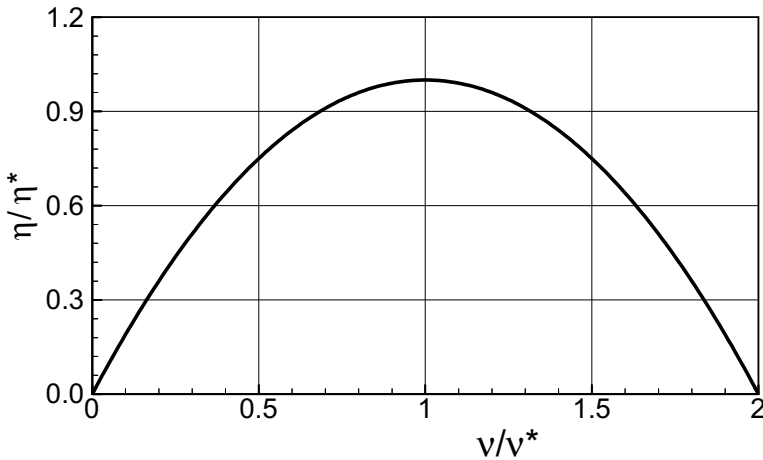


**Fig. 16.10:** relative efficiency as a function of relative velocity parameter

## 16.3 Modeling the Turbine Module for Dynamic Performance Simulation

Three levels of turbine modeling are presented in this section. The first level utilizes the steady performance characteristics discussed in Section 16.2. It exhibits the global performance behavior of a turbine component under dynamic operation conditions. The second level uses the row-by-row adiabatic expansion process and delivers a detailed calculation of the adiabatic expansion process under any dynamic operation condition. In addition to the information provided by the second level model, the third level provides detailed information about the blade temperature under the effect of the different cooling procedures.

### 16.3.1 Module Level 1: Using Turbine Performance Characteristics

The efficiency and performance characteristic generated in Section 16.2 can be used for a first level turbine simulation. This simulation level obviously does not provide details regarding the aerodynamic events within turbine stages. However, it is capable of globally estimating the thermodynamic state of the turbine component during a dynamic event. In contrast to the compressor module, the global turbine module does not have a performance map that defines surge limits for each individual rotational speed. This is due to the accelerating nature of the flow through the turbine expansion path. Although local flow separation may occur on turbine blade surfaces, particularly on the suction surface of low pressure turbine blades, a total flow separation and reversal under normal operating conditions will never occur. However, strong flow separation may occur at extremely low mass flows far below the normal operating range. The global turbine module is modeled mathematically by a set of algebraic equations. It receives dynamic information from the inlet plenum, performs off-design calculations, and transfers the results to the exit plenum. This arrangement allows a quasi dynamic simulation of the turbine component. The set of algebraic equations (16.41) to (16.46) determine the off-design values of the efficiency, the mass flow rate,  $\dot{m}$ , the total temperature,  $T_o$ , and the power consumption .

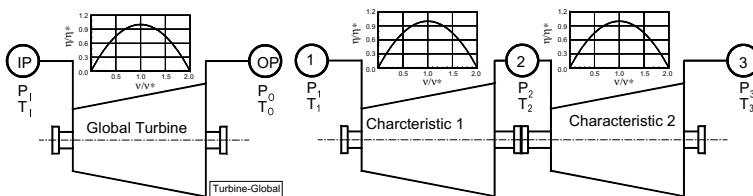


**Fig. 16.11:** Global simulation of a multi-stage turbine using one turbine characteristic (left) and two characteristics (right)

Figure 16.11 shows a turbine component using a steady state performance

characteristic enclosed within two plena. For a turbine with up to three stages, a single performance characteristic is sufficient to calculate the global transient behavior of the turbine. However, if the turbine has more than three stages, two or more performance characteristics may be necessary to satisfactorily predict the transient behavior of the turbine. The steady performance characteristic is obviously not able to handle transient events. However, if it is placed between two plena that continuously feed the steady map with unsteady data, it may deliver reasonable dynamic results. The inlet plenum transfers the time dependent pressure and temperature to the global map which calculates the turbine performance and transfers the information to the outlet plenum. For this purpose, the following system of differential equations and the algebraic equations (16.41) to (16.46) are used. The inlet and outlet plena are described by Eq. (13.9) and (13.11). For the sake of completeness, these equations are listed below:

$$\frac{\partial T_0}{\partial t} = \frac{1}{\rho V} \left[ \sum_{i=1}^n \dot{m}_{I_i} \left( \kappa \frac{c_{pI_i}}{c_p} T_{0I_i} - T_0 \right) - (\kappa - 1) \sum_{j=1}^m \dot{m}_{O_j} T_0 \right] \quad (16.47)$$

$$\frac{\partial P}{\partial t} = \frac{\kappa R}{V} \left[ \sum_{i=1}^n \dot{m}_{I_i} \frac{c_{pI_i}}{c_p} T_{0I_i} - \sum_{j=1}^m \dot{m}_{O_j} T_0 \right] \quad (16.48)$$

with Eqs.(16.47), (16.48), and the performance characteristic described by algebraic equations (16.41) to (16.46), we are now able to quasi-dynamically model the turbine component.

### 16.3.2 Module Level 2: Row-by-Row Adiabatic Expansion Calculation

This turbine module provides detailed information about the compressor behavior during dynamic events. Two methods can be used for describing this module. The first method utilizes the time dependent conservation laws for continuity, momentum, and energy Eqs. (12.26), (12.33), and (12.51) derived in Chapter 11. For adiabatic stage expansion calculation, Eq. (12.51) is reduced to:

$$\begin{aligned} \frac{\partial H}{\partial t} = & -\kappa_k \frac{\dot{m}_k}{\rho_k S_k} \left( \frac{H_{i+1} - H_i}{\Delta x} \right) + \frac{\kappa_k}{\rho_k} \left( \frac{\dot{L}}{\Delta V} \right) - \\ & - \left( \frac{\kappa - 1}{\rho k} \right)_k \left[ \left( \frac{H_k + K_k}{\Delta x} \right) \left( \frac{\dot{m}_{i+1}}{S_{i+1}} - \frac{\dot{m}_i}{S_i} \right) + \frac{\dot{m}_k}{\rho_k S_k^2} \frac{\partial \dot{m}_{i+1}}{\partial t} \right] \end{aligned} \quad (16.49)$$

The stage power  $L$  in Eq. (16.49) is directly related to the specific stage mechanical energy  $\dot{L} = \dot{m} l_m$  with  $l_m = \lambda U_3^2$ . Similar to the compressor module discussed in

Chapter 15 for row-by-row dynamic calculation of a turbine component, Eq. (16.49) may be decomposed using the row parameters discussed in Section 16.1. This method allows detailed dynamic calculation of the row properties.

The second method is based on the row-by-row adiabatic calculation procedure outlined in Section 16.1 under utilization of plena Eqs. (16.47) and (16.48) for dynamic coupling. Three alternative coupling configurations for a two-stage turbine are shown in Fig. 16.12. In Configuration (a), each row has an inlet and exit plenum, whereas in (b) each stage is bounded by an exit and inlet plenum. In (c) the entire turbine is placed between an inlet and exit plenum. This configuration provides satisfactory results for gas turbine engines where stage number does not exceed 4. It also can be applied to high pressure steam turbine units, where the volume dynamic is not substantial. However, to accurately account for the volume dynamics of an intermediate or low pressure turbine unit, it is more appropriate to decompose the turbine into several stage groups, where each group may consist of two to three stages that have Configuration (b).

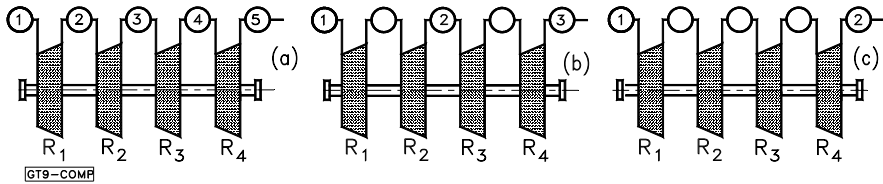


**Fig. 16.12:** Row-plena configuration, (a) each row is placed between two plane, (b) each stage is placed between two plena, (c) the entire turbine is placed between two plena.

### 16.3.3 Module Level 3: Row-by-Row Diabatic Expansion

During startup, shutdown, load change, or other transient operation of gas turbine engines, the turbine component experiences adverse temperature changes between the turbine blade material, rotor hub, casing, discs, and the combustion gas. This temperature change causes a heat transfer from the working medium to the blade material and vice versa. In addition, the first three rows of gas turbine engines require cooling. In these cases, the expansion process is no longer adiabatic. Figure 16.13 displays a cooled (diabatic) turbine stage, where heat is removed from the stator and rotor blade material by the stator and rotor cooling mass flows  $\dot{m}_{cS} = \dot{m}_4$  and  $\dot{m}_{cR} = \dot{m}_5$ . Gas turbine manufacturers use internal, external, or the combination of both cooling schemes. During the past three decades, numerous papers have been published that discuss different cooling aspects such as internal, external and film cooling aspects. Annually countless papers dealing with all heat transfer aspects are presented at international conferences in general and ASME conferences in particular.



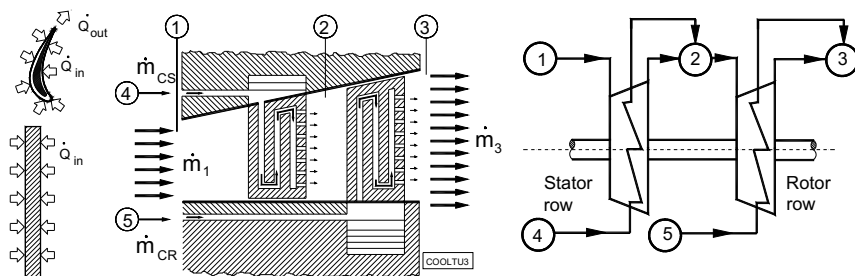


**Fig. 16.13:** Cooled module component (left) and simulation schematic (right).

The original contributions are published in the *ASME Journal of Turbomachinery*, the *ASME Journal of Heat Transfer* and other journals. Most of the experimental papers deal with measurement of the heat transfer coefficient around turbine blades installed in stationary cascades. There are only a few that deal with heat transfer in rotating turbine. Because of the significance of heat transfer in rotating turbine, this issue will be treated in later in this book. In conjunction with the modeling, we generically use the major cooling techniques. A high efficiency gas turbine engine with advanced cooling technology requires a total cooling mass flow of  $\dot{m}_c = 3\% - 6\%$  extracted from the compressor air to cool the front turbine rows. This amount is distributed among the rows that require cooling. Air is extracted from different compressor locations and is injected into the stator and rotor blades. The cooling mass flow at the compressor extraction point has a slightly higher pressure than the pressure at the injection points of the turbine. The mass flow extraction from the compressor causes a decrease of the engine thermal efficiency. However, the thermal efficiency gained by higher turbine inlet temperature offsets the loss caused by the extraction.

In case of internally cooled blades, the cooling air mass flow  $\dot{m}_{cS}$  and  $\dot{m}_{cR}$  passes through different channels that have internal turbulators and pin fins for enhancing the heat transfer as schematically shown in Fig. 16.13. The cooling mass flow  $\dot{m}_{cS}$  and  $\dot{m}_{cR}$  may eject at the blade trailing edge or at the blade tip to join the primary mass flow. The trailing edge ejection loss and its optimization were discussed in Chapter 6. As seen, the optimization of the ejection slot geometry minimized the ejection losses.

In case of an external cooling that includes, among others, shower head, full coverage film cooling, and transpiration cooling, the cooling mass flow passes through different blade cooling plena and ejects through a number of holes that are arranged on the blade surface with certain spacings and angles. The purpose of external cooling is to build a thin “cool” buffer layer distributed on the blade surface to prevent hot gas from directly transferring heat to the blade material. Because of discrete spacings of holes, a uniform distribution of cooling air is not possible. This leads to a mixing of the cooling mass flow and the primary hot gas. To circumvent this deficiency, a

transpiration cooling technique can be used. The cooling passes through uniformly porous material that builds a uniformly distributed protective cool air shield on the blade surface. Although transpiration cooling is the most efficient cooling technique, it has not reached the state of maturity to be implemented into gas turbines.

For turbine blades without internal or external cooling, heat exchange between the blade material and the primary hot gas occurs during off-design operations. Heat transfer from hot gas to turbine blade and structure occurs when the turbine component undergoes a transient power increase by adding fuel in the combustion chamber. On the other hand, heat is rejected from blades, when a transient operation triggers throttling of fuel to reduce the turbine power. As shown in an  $h$ - $s$  diagram in Fig. 16.14, the total heat added to the stage is the sum of the heat transferred to the stator and to the rotor  $q = q' + q''$ . These partial heat contributions may originate from blade cooling, Fig. 16.14(a), or from transient operation of uncooled blades.

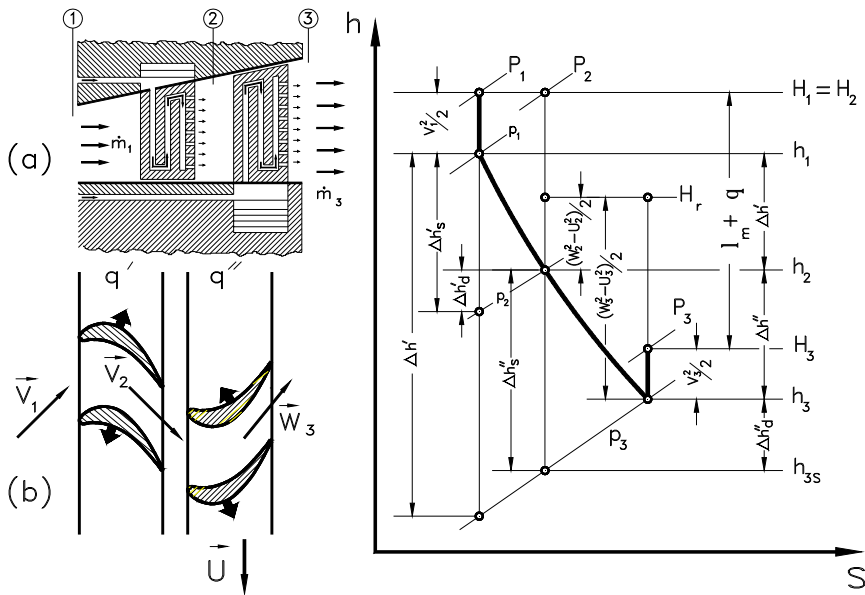


Fig. 16.14: Cooled turbine component with expansion diagram

**16.3.3.1 Description of diabatic turbine module, first method:** This turbine module provides detailed information about the turbine behavior during dynamic operations and the heat transferred to/from the blade during a transient event. Similar to the adiabatic turbine case discussed in Section 16.3.2, two methods can be used for describing this module. The first method utilizes the time dependent conservation laws for continuity, momentum, and energy, Eqs. (11.26), (11.33), and (11.51),

derived in Chapter 11. For diabatic turbine stage calculation, Eq. (11.51) is re-written:

$$\begin{aligned} \frac{\partial H}{\partial t} = & -\kappa_k \frac{\dot{m}_k}{\rho_k S_k} \left( \frac{H_{i+1} - H_i}{\Delta x} \right) \\ & - \left( \frac{\kappa - 1}{\rho k} \right)_k \left[ \left( \frac{H_k + K_k}{\Delta x} \right) \left( \frac{\dot{m}_{i+1}}{S_{i+1}} - \frac{\dot{m}_i}{S_i} \right) + \frac{\dot{m}_k}{\rho_k S_k^2} \frac{\partial \dot{m}_{i+1}}{\partial t} \right] \\ & + \frac{\kappa_k}{\rho_k} \left( \frac{\dot{Q} + \dot{L}}{\Delta V} \right) \end{aligned} \quad (16.50)$$

The stage power  $\dot{L}$  in Eq.(16.50) is directly related to the specific stage mechanical energy  $\dot{L} = \dot{m} l_m$  with  $l_m = \lambda U_3^2$ . The heat added to (+) or rejected from(-) the stage is  $\dot{Q} = \dot{m} q$  with  $q$  as the specific heat (heat per unit mass kJ/kg) transferred to/from the stage. For a steady state case with a constant mass flow, Eq.(16.50) immediately yields the conservation of energy  $q + l_m = H_{out} - H_{in}$ . Thus, the equation of energy is rearranged as:

$$\begin{aligned} \frac{\partial H}{\partial t} = & -\kappa_k \frac{\dot{m}_k}{\rho_k} \left( \frac{H_{i+1} - H_i}{\Delta V} \right) \\ & - \left( \frac{\kappa - 1}{\rho k} \right)_k \left[ \left( \frac{H_k + K_k}{\Delta x} \right) \left( \frac{\dot{m}_{i+1}}{S_{i+1}} - \frac{\dot{m}_i}{S_i} \right) + \frac{\dot{m}_k}{\rho_k S_k^2} \frac{\partial \dot{m}_{i+1}}{\partial t} \right] \\ & + \frac{\kappa_k \dot{m}_k}{\rho_k} \left( \frac{q + l_m}{\Delta V} \right) \end{aligned} \quad (16.51)$$

Equation (16.51) together with equations of continuity, momentum, and additional information about the heat transfer coefficient, describes the dynamic behavior of the diabatic turbine stage. For a row-by-row analysis it can be decomposed into two equations that describe the individual stator and rotor rows. For stator row, because  $l_s = 0$ , and  $q \equiv q_s = q'$ , we find:

$$\begin{aligned} \frac{\partial c_{p_{i+1}} T_{0_{i+1}}}{\partial t} = & -\kappa_k \frac{\dot{m}_k}{\rho_k} \left( \frac{c_{p_{i+1}} T_{0_{i+1}} - c_{p_{i+1}} T_{0_i}}{\Delta V} \right) + \frac{\kappa_k \dot{m}_k}{\rho_k} \left( \frac{q'}{\Delta V} \right) \\ & - \left( \frac{\kappa - 1}{\rho k} \right)_k \left[ \left( \frac{c_{p_k} T_{0_k} + K_k}{\Delta x} \right) \left( \frac{\dot{m}_{i+1}}{S_{i+1}} - \frac{\dot{m}_i}{S_i} \right) + \frac{\dot{m}_k}{\rho_k S_k^2} \frac{\partial \dot{m}_{i+1}}{\partial t} \right] \end{aligned} \quad (16.52)$$

For the rotor row, because  $l_R = l_m$  and  $q \equiv q_R = q''$ , we find:

$$\begin{aligned} \frac{\partial c_{p_{i+1}} T_{0_{i+1}}}{\partial t} = & -\kappa_k \frac{\dot{m}_k}{\rho_k} \left( \frac{c_{p_{i+1}} T_{0_{i+1}} - c_{p_i} T_{0_i}}{\Delta V} \right) + \frac{\kappa_k \dot{m}_k}{\rho_k} \left( \frac{q'' + l_m}{\Delta V} \right) \\ & - \left( \frac{\kappa - 1}{\rho k} \right)_k \left[ \left( \frac{c_{p_k} T_{0_k} + K_k}{\Delta x} \right) \left( \frac{\dot{m}_{i+1}}{S_{i+1}} - \frac{\dot{m}_i}{S_i} \right) + \frac{\dot{m}_k}{\rho_k S_k^2} \frac{\partial \dot{m}_{i+1}}{\partial t} \right] \end{aligned} \quad (16.53)$$

with  $l_m$  as the stage mechanical energy. To completely describe the diabatic expansion process within stator and rotor rows, heat transfer equations as well as blade material temperature equations must be added to the set of Eqs. (16.52), (16.53), (12.26), and (12.33). The terms in the brackets in Eqs. (16.52) and (16.53) are of second order significance, therefore may be neglected. As a result we obtain for stator:

$$\begin{aligned} \frac{\partial c_{p_{i+1}} T_{0_{i+1}}}{\partial t} = & -\frac{\kappa_k}{\rho_k \Delta V} \left( \dot{m}_k c_{p_{i+1}} T_{0_{i+1}} - \dot{m}_k c_{p_i} T_{0_i} + \dot{Q}' \right) \\ & - \left( \frac{\kappa - 1}{\rho k} \right)_k \frac{\dot{m}_k}{\rho_k S_k^2} \frac{\partial \dot{m}_{i+1}}{\partial t} \end{aligned} \quad (16.54)$$

and for the rotor row,

$$\begin{aligned} \frac{\partial c_{p_{i+1}} T_{0_{i+1}}}{\partial t} = & -\frac{\kappa_k}{\rho_k \Delta V} \left( \dot{m}_k c_{p_{i+1}} T_{0_{i+1}} - \dot{m}_k c_{p_i} T_{0_i} + \dot{L} + \dot{Q}'' \right) \\ & - \left( \frac{\kappa - 1}{\rho k} \right)_k \frac{\dot{m}_k}{\rho_k S_k^2} \frac{\partial \dot{m}_{i+1}}{\partial t} \end{aligned} \quad (16.55)$$

with  $\Delta V$  as net volume of the row space occupied by the working medium. The heat added to or rejected from the working medium in Equations (16.54) and (16.55) is transferred to the stator and rotor blade material. The heat transfer aspect is treated in the subsequent section.

**16.3.3.2 Description of diabatic turbine module, second method:** The second method is an enhanced diabatic calculation procedure that is based on the row-by-row calculation method outlined in Section 16.1. In this case, the thermal energy supplied to the system is included in the governing equations. The new equation set is combined with the plena Eqs. (16.47) and (16.48) for dynamic coupling. The amount

of heat supplied to the stage is expressed in stage mechanical energy balance, Eq.(5.8):

$$l_m + q = \frac{1}{2} \left[ (v_2^2 - v_3^2) + (w_3^2 - w_2^2) + (U_2^2 - U_3^2) \right] \quad (16.56)$$

with  $q$  as the specific heat (heat per unit mass kJ/kg) added to or rejected from the stage. As in Eq. (16.8), to substantially reduce the number of iterations, we decompose the stage specific polytropic mechanical energy  $l_m$ , as well as the specific isentropic mechanical energy  $l_{ms}$ , into two virtual contributions  $l_m = l' + l''$  and  $l_{ms} = l'_s + l''_s$  that we allocate to stator and rotor row. This decomposition results in a modified version of Eqs.(16.8) and (16.9). Thus, we arrive at the thermal and mechanical energy contributions allocated to the stator and rotor rows as:

$$\begin{aligned} l' + q' &= \frac{1}{2} v_2^2 - \frac{1}{2} w_2^2 \\ l'' + q'' &= \frac{1}{2} (w_3^2 - U_3^2 + U_2^2 - v_3^2) \end{aligned} \quad (16.57)$$

Similarly we find the isentropic parts:

$$\begin{aligned} l'_s + q' &= \frac{1}{2} (v_{2s}^2 - w_2^2) \\ l''_s + q'' &= \frac{1}{2} (w_{3s}^2 - U_3^2 + U_2^2 - v_3^2) \end{aligned} \quad (16.58)$$

Similar to the polytropic specific mechanical energy expressions given in Eqs. (16.8), we divide Eqs. (16.57) and (16.58) by the circumferential kinetic energy at the exit of the individual row. The dimensionless row polytropic load coefficients for stator and rotor with heat transfer are:

$$\begin{aligned} \lambda' &= \frac{l'}{U_2^2} = \phi' \cot \alpha_2 - \frac{1}{2} - \epsilon' \\ \lambda'' &= \frac{l''}{U_3^2} = -\phi'' \cot \beta_3 - 1 + \frac{v^2}{2} - \epsilon'' \end{aligned} \quad (16.59)$$

with the dimensionless parameters  $\epsilon' = q'/U_2^2$  and  $\epsilon'' = q''/U_3^2$ . The rotor row parameters in Eq. (16.59) have the same definition as those in Section 16.1.2. For the row-by-row diabatic calculation, the row load coefficients in Eqs. (16.8) must be replaced by (16.59).

**16.3.3.3 Heat transfer closure equations:** The heat transfer mechanism for cooled and uncooled blades are shown schematically in Fig. 15.15. Considering cooled turbine blades, the hot gas transfers certain amounts of thermal energy flow or heat flow  $\dot{Q}_h$  to the stator ( $\dot{Q}_h \equiv \dot{Q}_h'$ ), and rotor ( $\dot{Q}_h \equiv \dot{Q}_h''$ ). To maintain a desired blade temperature, the cooling mass flow through the blade internal channels has to

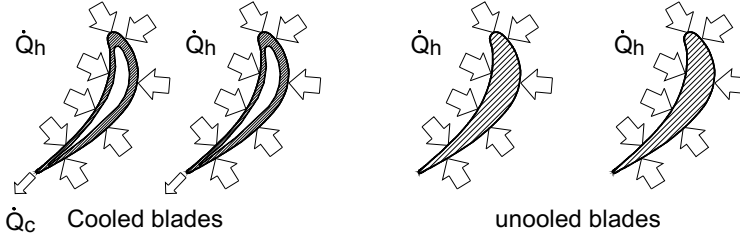


**Fig. 16.15:** Heat flow is transferred from turbine working medium to turbine blades  $\dot{Q}_h$ , the amount of  $\dot{Q}_c$  is removed by the cooling medium.

remove the heat flow  $\dot{Q}_c$  from the blade. The transferred thermal energies on hot and cold sides are:

$$\begin{aligned}\dot{Q}_h &= \bar{\alpha}_h A_h (\bar{T}_h - \bar{T}_w) \\ \dot{Q}_c &= \bar{\alpha}_c A_c (\bar{T}_w - \bar{T}_c)\end{aligned}\quad (16.60)$$

In Eq. (16.60),  $\bar{\alpha}_c, \bar{\alpha}_h$  are the averaged heat transfer coefficients for cold side (internal cooling channels) and the hot side (external flow path through the blade row),  $\bar{T}_c, \bar{T}_h$ , and  $\bar{T}_w$  are the mean temperatures of coolant flow, row working medium, row wall temperature, and  $A_c, A_h$  are the contact surfaces on the cold and hot side, respectively. The coupling condition between the cold and the hot side is provided by the material temperature differential equation:

$$\frac{dT_w}{dt} = \frac{1}{\rho_w c_w \Delta V_w} (\dot{Q}_c + \dot{Q}_h) \quad (16.61)$$

the heat flow  $\dot{Q}_h$  in Eq. (16.61) may assume positive or negative values, whereas  $\dot{Q}_c = \dot{m}_c q_c$  is always negative, since heat is rejected. For the case of no cooling,  $\dot{Q}_c$  is zero. In case of a dynamic temperature equilibrium where the blade temperature change approaches zero, Eq. (16.61) is reduced to:

$$\dot{Q}_c + \dot{Q}_h = 0 \quad (16.62)$$

To calculate  $\dot{Q}_h$  and  $\dot{Q}_c$  for inserting into Eq. (16.61), we use the Nusselt number correlation, Eq.(16.127), as discussed in Chapter 15. For blades without cooling, generic Nusselt number correlations from Chapter 6 can be used. For determination of heat transfer coefficients for particular cooling schemes, Han et al. [15] offers a comprehensive source.

## References

1. Schobeiri, M.T., Gilarranz, J.L and Johansen, E.S., 2000, "Aerodynamic and Performance Studies of a Three-Stage High Pressure Research Turbine with 3-D-Blades, Design Point and Off-Design Experimental Investigations," ASME-paper: 2000-GT-484.
2. Traupel, W., 1977, "Thermische Turbomaschinen," 3. Auflage, Springer-Verlag.
3. Vavra, M.H., 1960, "Aero-Thermodynamics and Flow in Turbomachines," John Wiley & Sons, Inc.
4. NASA SP-290, 1975, "Turbine Design and Application," Volume 2
5. Kroon, R.P., Tobiasz, H.J., 1971, "Off-Design Performance of Multistage Turbines," Trans. ASME, *Journal of Eng. Power* 93, pp. 21-27.
6. Kochendorfer, F.D., Nettles, J.C., 1948, "An Analytical Method Estimating Turbine Performance," NACA Report 930.
7. Bammert, K., Zehner, P., 1980, "Measurement of the Four-Quadrant Characteristics on a Multistage Turbine," Trans. ASME, *Journal of Eng. Power*, 102, No. 2.
8. Zehner, P., 1980, "Vier-Quadranten Charakteristiken mehrstufiger axialer Turbinen," *VDI-Forsch. -Bericht. VDI-2, Reihe 6, Nr. 75*.
9. Schobeiri, T., 1990, "Thermo-Fluid Dynamic Design Study of Single and Double Inflow Radial and Single-Stage Axial Steam Turbines for Open-Cycle Ocean Thermal Energy Conversion, Net Power Producing Experiment Facility," ASME Transaction, *Journal of Energy Resources*, Vol. 112, pp. 41-50.
10. Schobeiri, M. T., Abouelkheir, M., 1992, "A Row-by-Row Off-Design Performance Calculation Method for Turbines," *AIAA, Journal of propulsion and Power*, Vol. 8, Number 4, July-August 1992, pp. 823-826
11. Stodola, A., 1924, "Dampf- und Gasturbinen," 6. Auflage, Springer-Verlag, Berlin.
12. Horlock, J.H., 1973, "Axial Flow Turbines," Robert E. Krieger Publishing Company.
13. Pfeil, H., 1975, "Zur Frage des Betriebesverhaltens von Turbinen," *VDI-Zeitschrift, Forschung im Ingenieurwesen*, Bd. 41, Nr. 2, Ppg, 33-36.
14. Schobeiri, M.T., 1987, "Eine einfache Näherungsmethode zur Berechnung des Betriebsverhaltens von Turbinen," *VDI-Zeitschrift, Forschung im Ingenieurwesen* Bd. 53, Nr. 1, pp-33-36.

## 17 Gas Turbine Design, Preliminary Considerations

The objective of this chapter is to introduce novice engineers and students of turbomachinery design course to the fundamentals of gas turbine design.

In previous chapters detailed instructions were presented for designing the components of a gas turbine. For each component the conservation laws were formulated for time dependent unsteady operation with steady operation as the special case, where all unsteady terms within an equation were set to zero. Once the components are described by sets of partial and algebraic equations, they can be put together to configure a gas turbine system. This chapter provides the necessary basics for integrating the components to arrive at a gas turbine system. Mathematically, the system will consist of many systems of partial differential and algebraic equations, whose solutions require boundary conditions. Once the system of partial and algebraic equation is established, it will have infinite number of solutions. If we wish to simulate the gas turbine behavior under a particular dynamic situation, we have to formulate the boundary condition correspondingly. This solution is the unique one amongst the infinite number of solutions mentioned above. The following examples should clarify this further: An aircraft is in a landing position and is approaching an airport. It encounters a large number of birds that are flying on the same altitude but in opposite direction. The engine ingests several large size birds. This case exhibit an adverse dynamic operation that may affect the components of the engine and damage its integrity. Another example: A compressed air energy storage gas turbine drives a generator, which is connected to a grid. A sudden accident disconnects the generator from the grid. The fuel control system and the shutdown valves have certain time lags to act on the event. During this short period of time, high pressure air from the storage flows into the combustion chambers where fuel is still added generating the same amount of thermal energy as before the accident. The full turbine power acts on the shaft, which is no longer connected to the grid. As a result the rotational speed of the shaft starts accelerating surpasses the allowable speed limit, causing a partial or total de-blading of the turbine unit. The behavior of the gas turbines subjected to these or and any other adverse dynamic operations cannot be predicted by steady state calculation. In this chapter we discuss first how a gas turbine system can be composed of several components that we discussed earlier. In the following chapter we present case studies dealing with the dynamic simulation of several gas turbine engines.

Gas turbine engines are integral parts of today's power generation. They are used as a standalone power generators, as the topping unit of a combined cycle (CC) and in cogeneration heat and power (CHP) plants. As a power generator unit of compressed air energy storage (CAES) plants, the gas turbine generates power at high efficiency during the period of high electric energy demand. The design concept and the manufacture of a gas turbine correspond to the technological capability of the



individual original engine manufacturer (OEM). To compete in the global market, the OEMs and the utility companies are forced to improve the thermal efficiency of their gas turbines, to reduce the fossil fuel consumption and the output of CO<sub>2</sub> emissions. As we saw in the previous chapters, the single most important parameter to increase the thermal efficiency of conventional gas turbines is the turbine inlet temperature (TIT). This, however requires massive cooling of the components downstream of the compressor such as the combustion chamber and the turbine. Focusing on TIT increase requires incorporating advanced *thermal barrier coating* (TBC) and high effectiveness film cooling technologies as reported, among others in [1], [2] and [3]. Particular attention must be paid to the design of internal cooling flow passages and positioning of film cooling holes and their compound angles for external blade cooling. Appropriate design of the cooled blades requires full understanding of aerodynamic behavior of the internal flow and its impact on the heat transfer behavior of the blades. There are numerous cases, where an inappropriate design has led to non-uniform thermal stress conditions causing the inception of micro cracks and their propagation. Once the cracks are detected the engine must be shutdown and the unit must be taken off the grid. It is well known that this event is associated with a substantial loss of revenue for the utility company.

Continuous efficiency improvement of gas turbine components are also an integral part of research and development (R&D) activity of gas turbine OEMs. The component efficiency improvement, although necessary, do not substantially enhance the thermal efficiency of the engine and compared to the impact of TIT-increase, their contribution to the thermal efficiency enhancement is of secondary relevance.

## 17.1 Gas Turbine Preliminary Design Procedure

As we saw in Chapter 1 and 2, a gas turbine may consist of a single or multiple shafts. The conventional power generation gas turbine consists of a multi-stage compressor unit, a combustion chamber and a multi-stage turbine. The compressor is connected with the turbine via the shaft. Each shaft may incorporate a single compressor unit that consists of low pressure, intermediate pressure and high pressure parts (LPC, IPC, HPC). An aircraft engine or a power generation derivative thereof may consist of multiple shafts. In a multiple shaft configuration, each compressor part is directly connected with the corresponding turbine part via the respective shaft. The shafts rotating with different frequencies are connected with each other aerodynamically. Each compressor generates its own pressure ratio,  $\pi_{LP}$ ,  $\pi_{IP}$ ,  $\pi_{HP}$  with the total pressure ratio of  $\pi_{total} = \pi_{LPC} \pi_{IPC} \pi_{HPC}$ . The combustion chamber follows the compressor units. Based on the technological capability and design philosophy, the OEMs may incorporate can-combustors, annular-combustors or

sequential combustion introduced by ABB<sup>1</sup>. The fuel flexibility is one of the boundary conditions that determines the design configuration of the combustion chambers. Based on the level of TIT, for a typical four stage turbine unit, the stator and rotor rows of the first three stages may be cooled. This requires special design of stator and rotor blades with internal and external cooling. In what follows, we focus of the major gas turbine components namely the compressor, combustion chamber and turbine. Before starting, we look at the thermodynamic process and show, how the TIT defines the rest of gas turbine design.

## 17.2 Gas Turbine Cycle

Generating the diagram of thermal efficiency vs. pressure ratio is the first step towards an optimum design of a gas turbine. Given the TIT, the designer determines the compressor pressure ratio that corresponds to the optimum thermal efficiency  $\eta_{th}$ . As an example, Fig. 17.1 shows  $\eta_{th}$  as a function of compressor pressure ratio  $\pi_c$  with the TIT as a parameter.

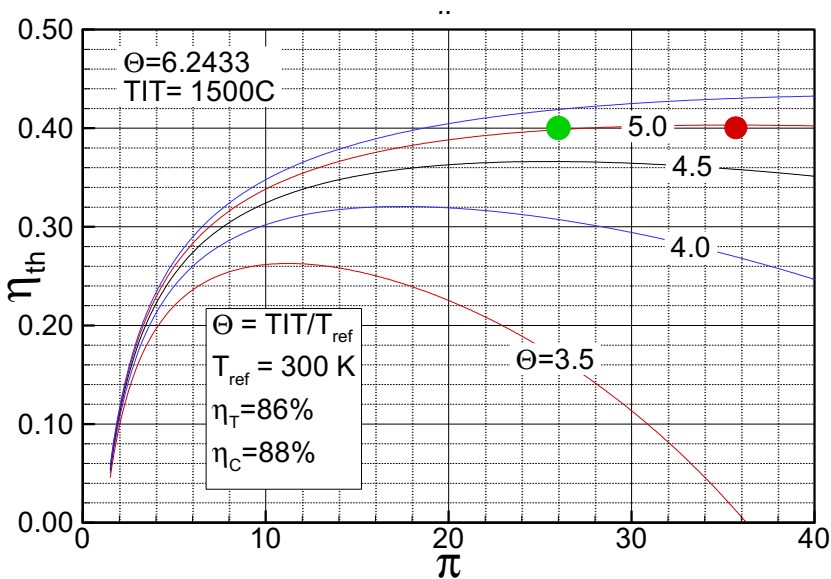


**Fig.17.1:** Thermal efficiency as a function of pressure ratio with TIT as parameter

1) ABB is the 1988 merger of ASEA of Sweden and Switzerland's BBC, formerly known as Brown Boveri & Cie. In 2000 Alstom acquired 50% of ABB shares and the name changed to ALSTOM. In 2015 GE bought ALSTOM.

As seen, the optimum pressure ratio that corresponds to a  $TIT=1500.0C$  is only slightly above 40%. This optimum efficiency is achieved at a pressure ratio close to  $\pi_c = 36$ . Almost the same efficiency, however, can be reached with a pressure ratio close to  $\pi_c = 26$ . As detailed in Chapter 2, if reaching the optimum pressure ratio is not associated with a noticeable thermal efficiency increase ( $\Delta\eta_{th} > 0.5\%$ ), then it is recommended to choose a lower pressure ratio but with an efficiency close to the optimum one. Figure 17.1 justifies this recommendation. It shows that the optimum pressure ratio of  $\pi_{opt} = 26$  (red circle) has almost the same  $\eta_{th}$  as the one with  $\pi_{opt} = 36$ . These two pressure ratios are shown in Fig. 17.1 as the optimum pressure ratio of  $\pi_{opt} = 36$  and the actual pressure ratio  $\pi_{act} = 26$ . To provide the difference of  $\Delta\pi = \pi_{opt} - \pi_{act} = 10$ ., at least 2 stages must be added to the compressor. As a consequence, the blade heights of the rear stages become shorter causing higher secondary flow losses thus reducing the compressor stage and unit efficiencies.

### 17.3 Compressor Design, Boundary Conditions, Design Process

Once the *actual pressure ratio* is determined, the compressor design process can start using the following given quantities:

- Compressor mass flow  $\dot{m}$
- Compressor pressure ratio  $\pi_{act}$
- Compressor inlet temperature  $T_{inlet}$
- Compressor rotational frequency  $n$
- Relative humidity of local air, this goes into the calculation of humid air properties.

#### 17.3.1 Design Process

To execute the design process, we first use a row-by-row meanline design method detailed in Chapter 15. This process is an iterative one that may take only a few second of computation. In the following the design process is explained through a step-by-step approach:

##### Step 1: Determine the Compressor Flow Path, Blade Height Distribution

Before starting with the iterative design process, the compressor flow path in terms of hub and tip diameter distribution needs to be determined, from which the distribution of the blade heights is calculated. From previous section we know the following quantities:

- ▶ the inlet and exit pressures or the compressor pressure ratio  $\pi_c$ ,
- ▶ the compressor mass flow,
- ▶ we may assume the flow coefficient in the range of  $\phi = 0.4$  to  $0.8$ .

- we also may assume a constant hub diameter.

With the above quantities, the application of continuity equation determines the blade height at the inlet and exit. For the power generation gas turbines, the blade height should not go below 80 mm, since shorter blade height causes substantial secondary flow losses. Note that this is only the first approximation.

In determining the distribution of the blade height, the choice of the hub diameter or mean diameter is crucial for the compressor design. For power generation gas turbines with welded rotor cylinder such as those manufactured by Alstom, a constant hub diameter constitutes a standard design process, Fig. 17.2.

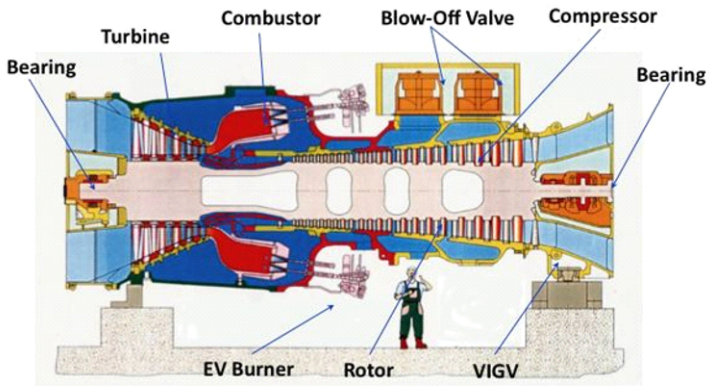


**Fig.17.2:** Constant hub diameter for a conventional power generation gas turbine, GT-13E, Alstom.

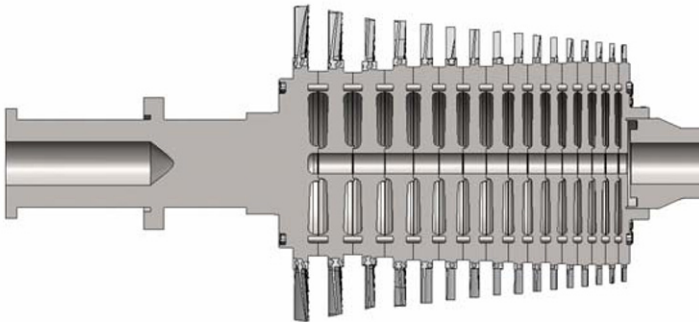


**Fig.17.3:** Constant diameter for a power generation gas turbine, Turbomachinery Design Project, Texas A&M.

Based on the OEM' technology, blades may be attached to individual discs that are connected with each other via a number of tie-bolts as seen in Fig. 17.3, [4]. In this case, a constant mean diameter may be considered as an alternative.

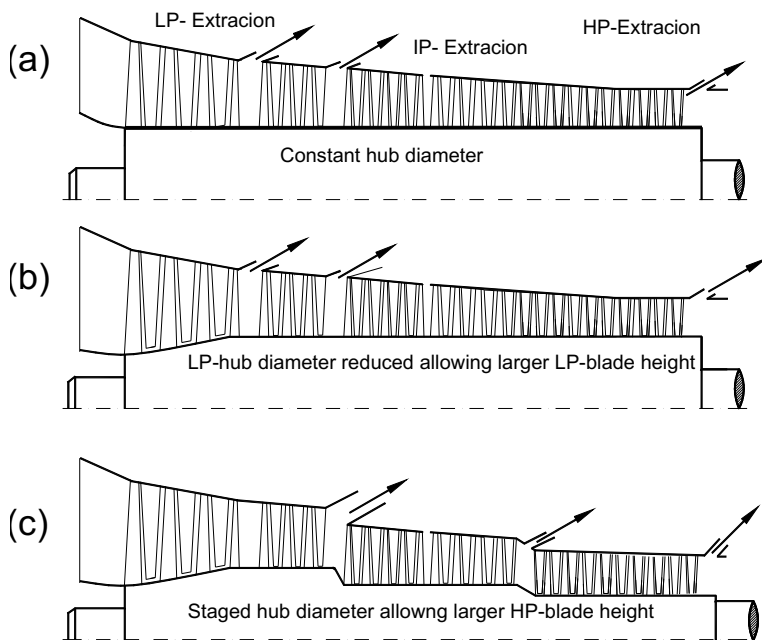


**Fig.17.4:** : Different hub diameter distributions for power generation gas turbines, (a): Constant hub throughout, (b): Contoured hub for LP-part, constant hub for the rest, (c) Three different hub distributions to avoid short blade heights for high pressure ratio gas turbine.

Figure 17.4 (a,b,c) exhibits hub diameter distributions for different compressors. It also shows the positions of the air extractions for cooling purposes as well as surge protection. For compressor pressure ratios  $\pi_c \geq 40$ , the blade height of HP-part substantially reduces causing significant secondary flow losses. This can be prevented by reducing the hub diameter of IP and HP part respectively as shown in Fig. 17.4 (c).

## Step 2: Determine the Number of Stages, Compressor Length

- For a multi-stage subsonic compressor, assume an average stage pressure ratio of  $\pi_{stage}$  (see Chapter 4) and find the stage number from  $\pi_C = \pi_{stage}^n$ . Assuming an initial value of  $\pi_{stage} \approx 1.175$  is acceptable to start with the design. This value

may be changed in the course of an iteration.

- ▶ To obtain the axial length of the compressor stage, the axial chord of the stator  $(c_{ax})_S$ , the axial chord of the rotor  $(c_{ax})_R$  and the axial distance between the stator and the rotor  $\delta_{SR}$  row must be found that determines the stage axial length  $L_{stage} = (c_{ax})_S + (c_{ax})_R + \delta_{SR}$ . The axial chords of stator and rotor are obtained from the optimum solidity  $\sigma = (c/s)_{opt}$  as treated in Chapter 5. Choosing the chord length  $c$ , the optimum spacing is obtained by using the optimum solidity that determines the number of blades for the stator row  $n_S$  and the rotor row  $n_R$  with  $n_S \neq n_R$ . This is to avoid rotordynamic instability that may result in resonance.
- ▶ In choosing the chord length attention must be paid that the stress caused by the centrifugal force at the blade hub is approximately the same for all rotor blades. This leads to larger chords and thicker profiles for the front LP-stages and shorter ones for the rear HP-stages.
- ▶ The axial distance between the stator and the rotor can be assumed as  $\delta_{SR} \approx 0.3 - 0.35$ . This distance determines the degree of interaction between the stator and the rotor blades and the size of the wakes that originate from the upstream stator blade row that impinges on the downstream rotor blade row.
- ▶ Group the LP-, IP- and HP-stages and allow after each stage group a blow-off section as shown in Fig. 17.4.
- ▶ With the information above, draw the first compressor flow path. For power generation gas turbines, a constant hub diameter is the traditionally preferred design, Fig. 17.4(a). However advanced gas turbine designs allow some deviation as shown in Fig. 17.4 (b). For an ultra high efficiency gas turbine with pressure ratio of  $\pi_c = 40.0$  and above, the rotor hub may be designed to have a staged radius distribution as shown in Fig. 17.4(c). This hub radius staging is quite common in aircraft engine. It prevents the blade height from getting too short.

### Step 3: Determine the Stage Parameters as Instructed in Chapter 4 and 15

With the stage pressure ratio  $\pi_{stage}$  determined above, we find:

- ▶ The stage load coefficient  $\lambda$  (note that  $\lambda$  is negative for compressors).
- ▶ The absolute flow angles:  $\alpha_2, \alpha_3$ .
- ▶ The relative flow angles:  $\beta_2, \beta_3$  (for the first iteration set  $r = 50\%$ ).
- ▶ With the known flow path and the blade flow angles, calculate stator and rotor individual blade losses, row total loss coefficient, stage total loss coefficient and the stage efficiency. The losses are calculated from Chapter 6 or Chapter 15. While the loss calculation in Chapter 6 is suitable for low subsonic Mach numbers, the one found in Chapter 15 treats loss calculation for high subsonic

Mach number reasonably well.

- ▶ With the stage/row loss coefficients calculate the isentropic and polytropic efficiency of the compressor and the pressure ratio  $\pi_i$  at the iteration step  $i$ . This may or may not be equal to the  $\pi_{actual}$  obtained from the process calculations. In case  $\pi_i \neq \pi_{actuell}$  adjust the stage load coefficient  $\lambda$  to arrive at the  $\pi_{actuell}$ . This may need a few iterations that would take only a few seconds.
- ▶ Once  $\pi_{actual}$  is reached, use the simple radial equilibrium to adjust the blade metal angles from hub to tip to the flow angles. In this context, calculate incidence and deviation angles.
- ▶ For the final design use the stream line curvature as the radial equilibrium method for the front stages with large span/chord ratios. For the HP-part, free vortex flow can be used as an alternative.
- ▶ For the final design, DCA, MCA blade profiles may be used for the LPC-front stages with high subsonic Mach numbers, for the rest of compressor stages NACA-blade or modified thereof may be used.

### 17.3.2 Compressor Blade Aerodynamics

After the completion of the above steps, CFD-simulation of compressor elements such as the stator and rotor blades need to be conducted. This is to ensure that the compressor design process reflects the expected aerodynamic behavior of the compressor.

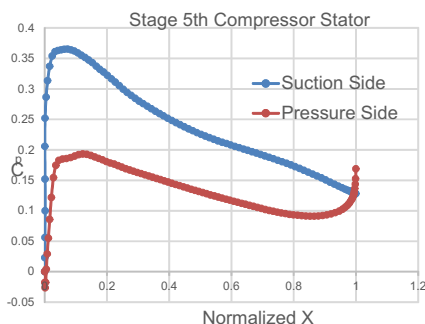


**Fig.17.5** Pressure distribution around the 5<sup>th</sup> stator blade.

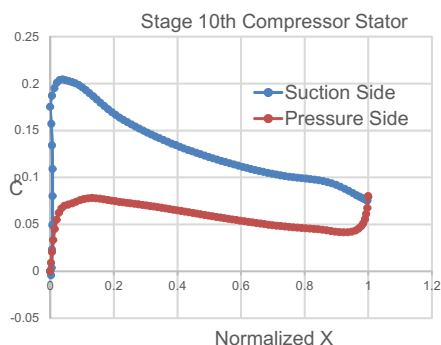


**Fig.17.6:** Pressure distribution around the 10<sup>th</sup> stator blade.

For this purpose, Reynolds Averaged Navier Stokes solvers (RANS) may be used. Since the compressor blades have a low flow deflection, flow separation at the design point is not anticipated. An essential diagram is the pressure distribution as shown in Figs. 17.5 and 6.

### 17.3.3 Controlling the Leakage Flow

As pressure increases from the first to the last stage, the mass flow through the tip clearance becomes increasingly larger. The physics of tip leakage flow and its reduction was discussed in Chapter 6. Recently, the use of brush seal, honeycomb and casing treatment showed additional features for reducing the leakage flow. The application of the casing treatment, not only reduces the leakage flow, but it also positively impacts the rotating stall and surge. These topics are still under intense investigation with a significant number of papers presented every year at the ASME, IGTI conference proceedings.

### 17.3.4 Compressor Exit Diffuser

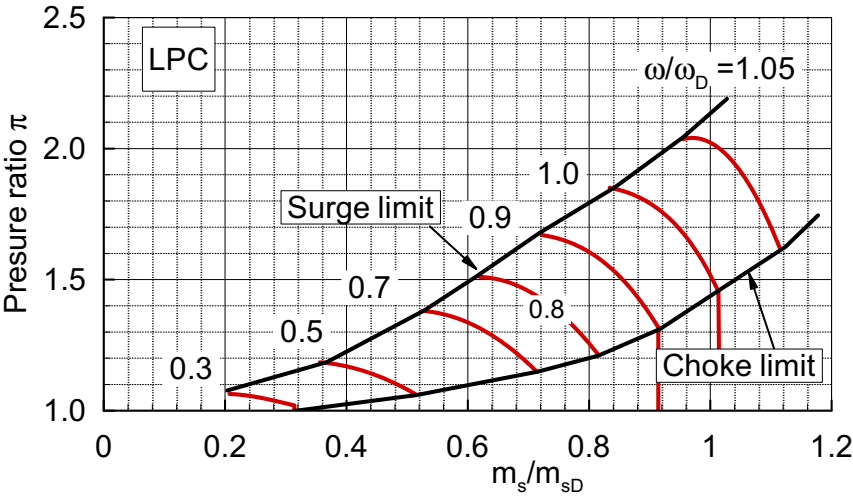
Before exiting the compressor component and entering the combustion chamber, the velocity of air must be substantially reduced. This is accomplished by a diffuser attached to the compressor exit. The diffuser must fulfill the following criteria: (1) its length must be kept as short as possible, (2) the diffuser opening angle must allow an operation without flow separation. The instruction, how to design a short diffuser with a large opening angle is described in detail in Chapter 6.

### 17.3.5 Compressor Efficiency and Performance Maps

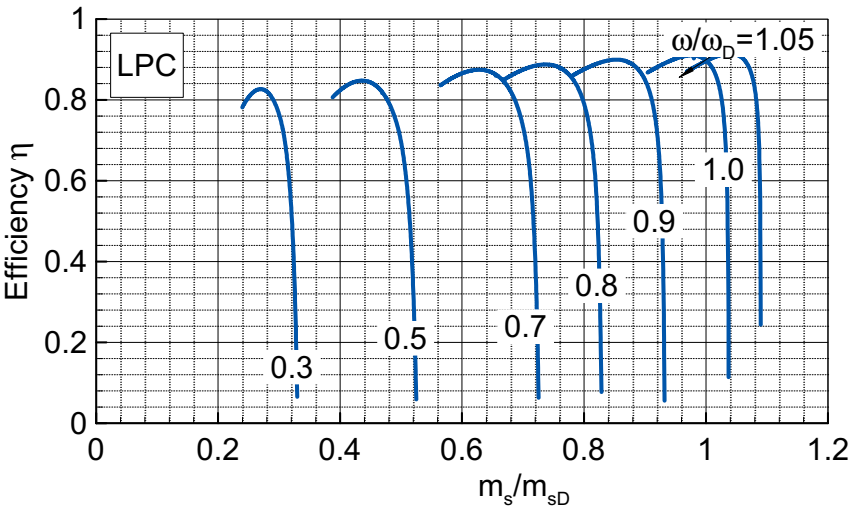
Once the compressor final design work has been completed, the steady performance and efficiency maps have to be generated according to the method described in Chapter 15. Since after each extraction, the mass flow reduces, it is imperative to generate for each section of the compressor, such as LPC-, IPC-, and HPC- its own compressor performance maps. The pressure map must include the surge limit, the choke limit and dimensionless speed lines as shown in Fig. 17.7. As an example, Fig. 17.1 shows a speed line range from  $\omega/\omega_D = 0.4$  to 1.1.

Figure 17.8 shows the efficiency map as a function of dimensionless mass flow with  $\omega/\omega_D$  as a parameter. It reflects the compressor efficiency behavior during design and off-design operation.





**Fig.17.7:** Performance map of a low pressure compressor with angular velocity ratio as a parameter.



**Fig.17.8:** Fig. 17.8: Compressor efficiency map with angular velocity ratio as parameter.

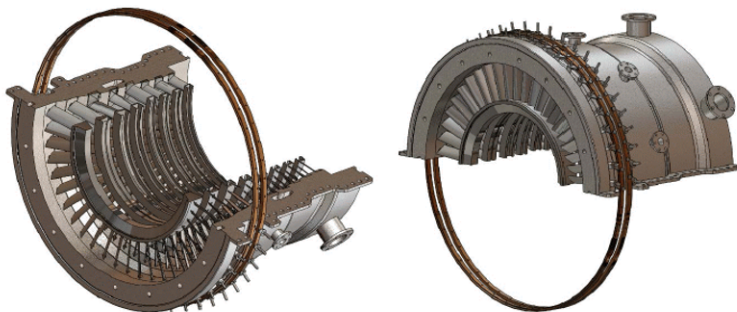
### 17.3.6 Stagger Angle Adjustment During Operation

To operate in an optimized performance envelope, the front compressor stages of advanced gas turbines are connected with a system that allows adjusting the stagger angle of individual stator rows to the incoming flow angle, Fig. 17.9.

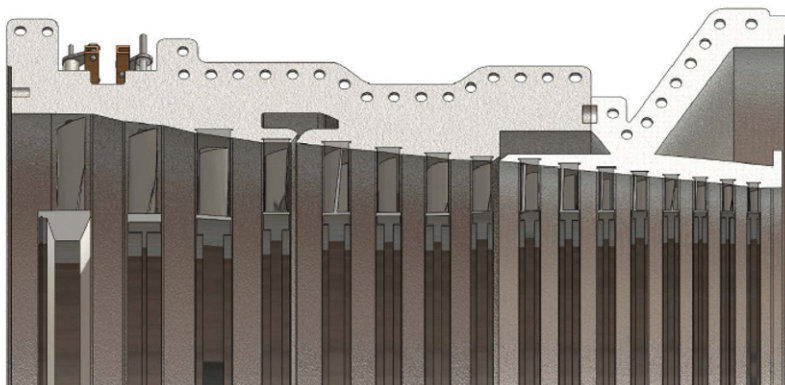


**Fig.17.9:** Compressor with variable stator stagger angle mechanism, Turbomachinery Design Project, Texas A&M.

Details of the adjusting system are shown in Fig. 17.10. The adjustment mechanism is attached to the casing via a ring as shown in the figures. Changing the stagger angle in a pre-determined manner prevents the compressor from entering the rotating stall and surge.



**Fig.17.10:** Details of compressor casing with variable stator stagger angle mechanism, Turbomachinery Design Project, Texas A&M.



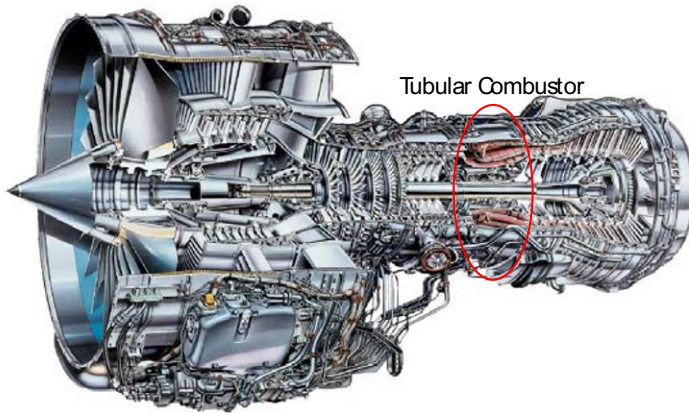
**Fig.17.11:** Details of compressor casing with air extraction pockets, Turbomachinery Design Project, Texas A&M.

Figure 17.11 shows the positions of air extraction slots. Air extracted from the compressor is used for turbine cooling purposes and blow off at the engine start up.

## 17.4 Combustion Chambers

The component combustion chamber follows the compressor. The function of this component was described in Chapter 3. As mentioned, fuel is injected into the combustion chamber primary combustion zone to raise the combustion exit

temperature to the required turbine inlet temperature. While an efficient combustion occurs at the stoichiometric air/fuel ratio of approximately 15:1 (based on the fuel composition), the actual air/fuel ratio of a gas turbine combustion may assume ratios of more than 100:1. For power generation and aircraft engines different designs are used.



**Fig.17.12:** Aircraft gas turbine, note the relatively small size of the combustor compared to the other components.

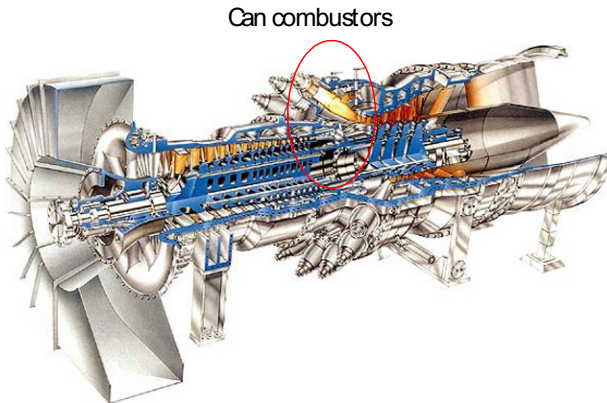


**Fig.17.13:** Power generation gas turbine, note the substantial size of the combustor.

### 17.4.1 Combustion Design Criteria

A modern combustion design, regardless the types and applications, has to fulfill the following combustion criteria:

- 1) High combustion efficiency at different operation conditions.
- 2) Almost complete combustion at all operation conditions.
- 3) Low emission: smoke, carbon monoxide CO, Nitrogen oxides NO<sub>x</sub>
- 4) Maintaining overall low total pressure loss.
- 5) Uniform exit temperature.
- 6) Stable combustion process over a wide range of operating conditions.
- 7) Quasi uniform metal temperature.
- 8) Structural integrity, thermal expansion
- 9) For aircraft engines: Flame blow out, re-ignition

### 17.4.2 Combustion Types

Figures 17.12 and 17.13 reveal structural differences between the stationary gas turbine and the aircraft gas turbine combustors. The can combustion arrangement is characteristic for almost all power generation gas turbines. A representative image of a can combustion chamber is shown in Fig. 17.14 with its essential features.

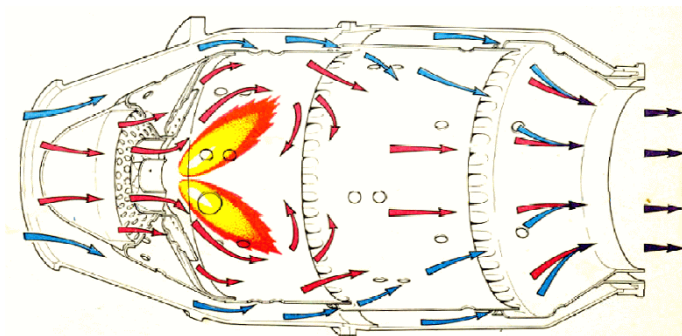


**Fig.17.14:** Sequence of combustion process in a can combustion.

Air enters the combustion and is divided into the primary and secondary portion. The primary air passes through a swirl generator and after injection of the fuel, the highly vortical mixture exit the swirl generator, where a stationary vortex breakdown occurs. The generation of the large vortex and its subsequent breakdown shown in Fig. 17.14, is an essential integral part in a gas turbine combustion process. The purpose of the stationary vortex breakdown is to keep the fuel particle in rotating state to achieve a better mixing of the fuel with the air. The secondary air zone has two



functions: (a) it works as an enclosure to isolate the flame, which might have a temperature exceeding  $2000.0^{\circ}\text{C}$ , from the combustion casing. (b) the secondary air cools the flame holder material and through the holes of the latter injects cold air into the hot primary combustion zone, thereby further reducing the gas temperature. The hardware of a typical combustor is shown in Figs. 17.15 and 17.16.

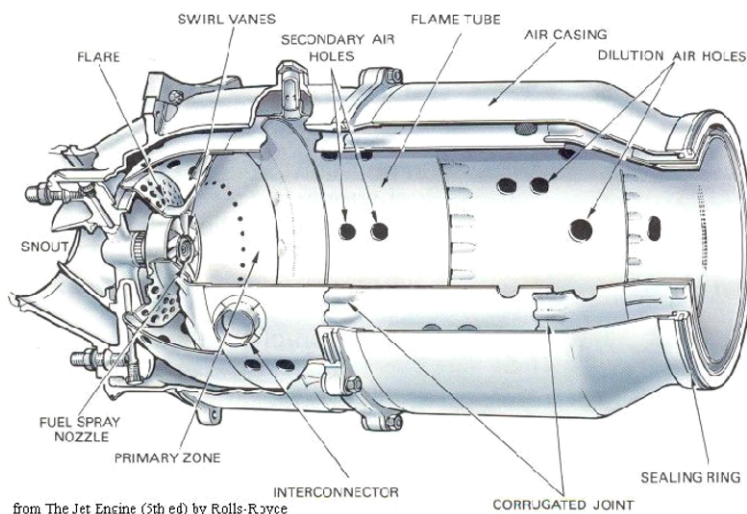


**Fig.17.15:** A can combustor with the elements that realize the features of Fig. 17.9.

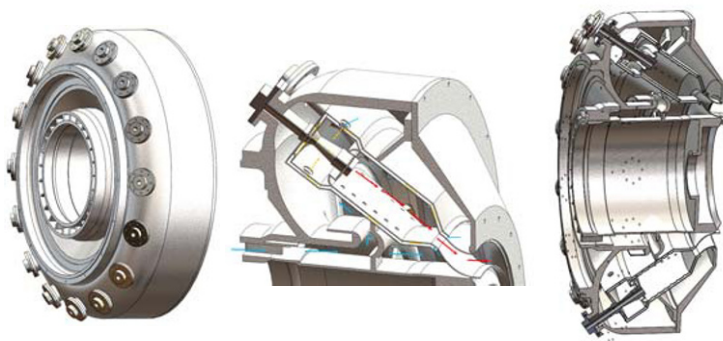


**Fig.17.16:** Views of a can combustor, Turbomachinery Design Project, Texas A&M University.

The annular combustion shown in, Fig. 17.17, has the same essential features mentioned above, but instead of cans, it has injectors that are circumferentially arranged at the inlet of the combustion.

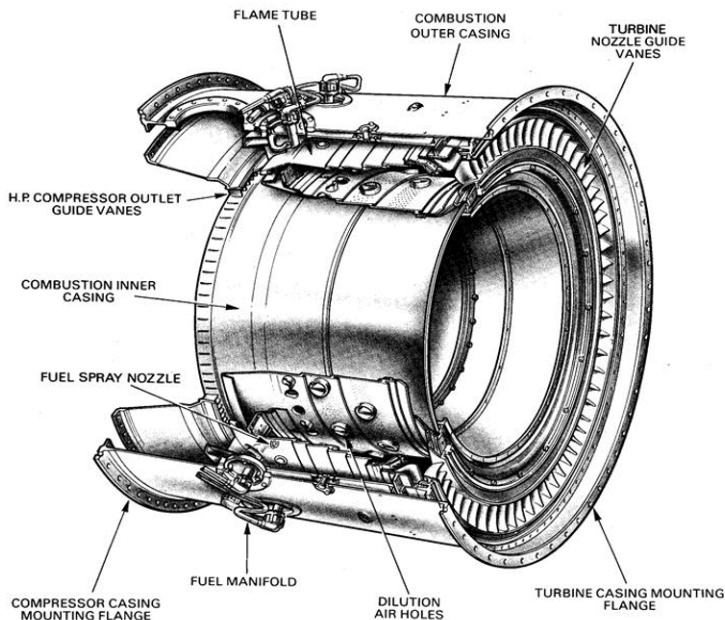


Fig.17.17: Annular combustor

## 17.5 Turbine Design, Boundary Conditions, Design Process

The turbine design process can start using the following given quantities:

- ▶ Turbine mass flow  $\dot{m}$
- ▶ Turbine pressure ratio  $\pi_{act}$
- ▶ Turbine inlet temperature  $T_{inlet}$
- ▶ Turbine rotational frequency  $n$
- ▶ Relative humidity of local air, this goes into calculation of humid air properties.

### 17.5.1 Steps of a Gas Turbine Design Process

To execute the design process, we first use a row-by-row meanline design method detailed in Chapter 16. The computational process is an iterative one that may take only a few seconds on a personal computer. In the following, the design process is explained through a step-by-step approach:

### Step 1: Determine the Turbine Flow Path, Blade Height Distribution

Before starting with the iterative design process, the turbine flow path in terms of hub and tip diameter distribution needs to be determined, from which the distribution of the blade heights is calculated. From previous section we know the following quantities:

- ▶ Turbine mass flow:  $\dot{m}_T = \dot{m}_{Comp} + \dot{m}_{Fuel}$ . For row-by-row design, the amount of cooling mass flow must be considered in mass flow balance.
- ▶ The inlet and exit pressures: Note: the turbine inlet pressure is the compressor exit pressure minus the combustion chamber pressure loss. The turbine exit pressure depends on what follows the turbine component. If the turbine mass flow exits into the environment, the entire kinetic energy of the exiting gas is considered as a major exit loss. To reduce this loss, a diffuser is attached to the exit of the last stage of power generation turbines reducing the exit kinetic energy and thus improving the efficiency of the gas turbine. The design of the an optimum diffuser is described in Chapter 6. Reducing the turbine exit pressure below the atmospheric pressure increases the total enthalpy difference and thus the gas turbine efficiency. Note that in aircraft engine, a nozzle is attached to the turbine exit to increase the kinetic energy resulting in higher exit momentum and thus higher thrust.
- ▶ Assume the flow coefficient in the range of  $\phi = 0.4$  to  $0.8$  from Chapter 4 is a reasonable preliminary assumption. Note: In course of the iteration process all initially assumed values will change.
- ▶ For power generation gas turbines assume a constant hub diameter,

With the above quantities, the application of continuity equation determines the blade height at the inlet and exit. For the power generation gas turbines, the choice of hub or mean diameter is crucial for determining the blade height. These should be chosen such that the blade height does not drop below certain minimum height. This minimum height is dictated by the contribution of the secondary flow loss coefficient. For HP-part, the secondary flow loss coefficient assumes values up to 45% of the entire stage loss coefficient. Shorter blade height causes substantial secondary flow losses that is translated into efficiency reduction.

For power generation gas turbines with welded rotor cylinder such as those manufactured by Alstom, a constant, hub diameter constitutes a standard design process as shown in Fig. 17.2.

### Step 2: Determine the Stage Number

- ▶ With the given inlet and exit pressures as well as an assumed isentropic turbine efficiency, the turbine total enthalpy difference can be estimated. The assumed turbine efficiency will be iteratively replaced by the new efficiency which is the result of a detailed loss and efficiency calculation as detailed in Chapter 6.
- ▶ Within the estimated total enthalpy difference a number of stages can be



embedded, such that the sum of all turbine stage powers equal to the required turbine power. The stage number is directly connected to the specific stage load coefficient  $\lambda$ . For a power generation gas turbine, operation at high efficiency is the primary design objective. In this case a  $\lambda$ -range of  $\lambda = 1.0 - 1.5$  is acceptable. During the iteration process,  $\lambda$  of individual stages will be adjusted to achieve the desirable turbine power.

- ▶ As detailed in Chapter 4, generally the stage is described by nine dimensionless parameters and four equations. To solve the system of four equations with nine unknown, five of the unknowns have to be assumed as given. The given data help to estimate  $\lambda$  and  $\phi$ . Also any three of the following five parameters  $\alpha_2, \beta_3, \mu, v$  and degree of reaction can be chosen to solve the system of four equations.
- ▶ With the known flow path and the blade flow angles, the stator and rotor individual losses, row total loss coefficient, stage total loss coefficient and the stage efficiency are calculated.
- ▶ For preliminary design, use the free vortex radial equilibrium but for the final design use streamline curvature method.
- ▶ For the final design, generate blade profiles from hub to tip.
- ▶ Designing blade profiles, front loaded or aft loaded profiles may be constructed. Important is that the pressure distribution does not have a strong negative followed by equally strong positive pressure gradient. A smooth transition from the negative to positive pressure gradient is favored.

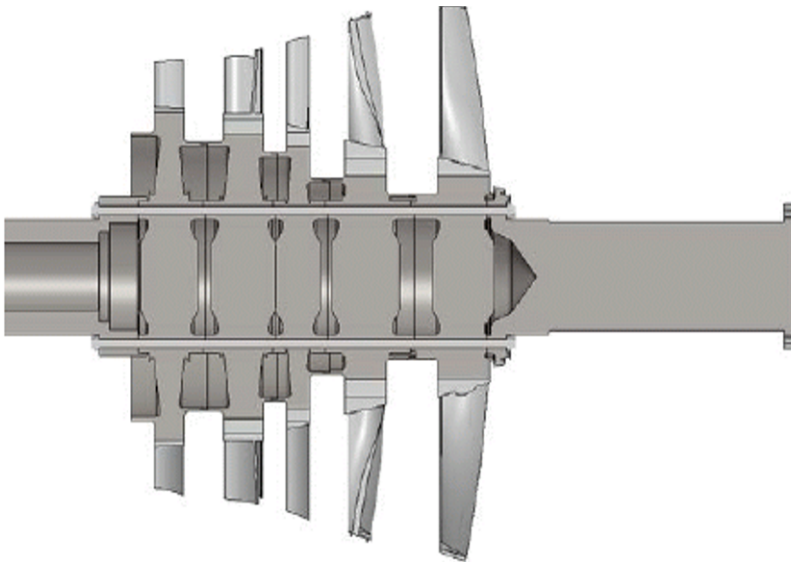


**Fig.17.18:** Cross section of the turbine part of a power generation gas turbine, Turbomachinery Design Project, Texas A&M.

Figure 17.18 shows the cross section of the turbine part of a gas turbine with constant mean diameter and three dimensional blades. The blades are assembled on individual disks that are connected with long anchor bolts. This configuration is just one among many. Note that a simple design with a few parts is always better than a complex design with many parts. As an example Fig. 17.2 shows the Alstom GT-13E with welded rotor. Figure 17.19 shows the same rotor exhibited in Fig. 17.18 in three dimensional form. It shows the assembly details.

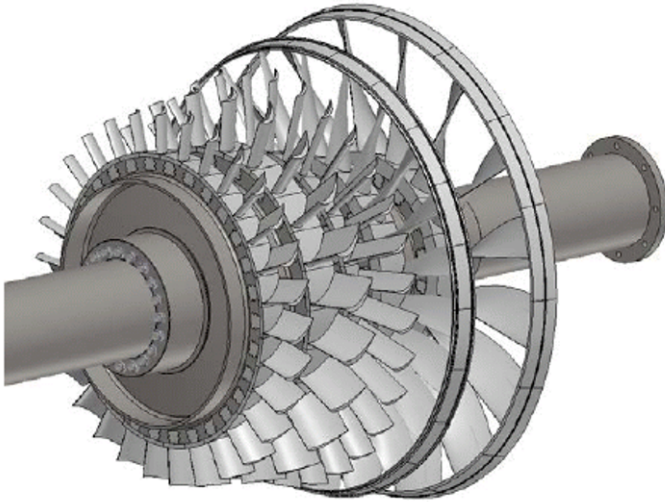


**Fig.17.19:** View of the turbine part, details of the blades assembly, Turbomachinery Design Project, Texas A&M.

The rotor unit with the turbine, compressor and bearings is shown in Fig. 17.20. It is integrated into the casing in Fig. 17.21.

The rotor of a large power size gas turbine is much heavier its aircraft engine counter part. This requires using thrust and journal bearings instead of ball bearings. While the journal bearing, Fig.17.22 is positioned at turbine side, the thrust bearing is attached to the compressor side, Fig. 17.23. This arrangement allows the rotor to expand freely from the compressor relatively cold side to the turbine hot side.

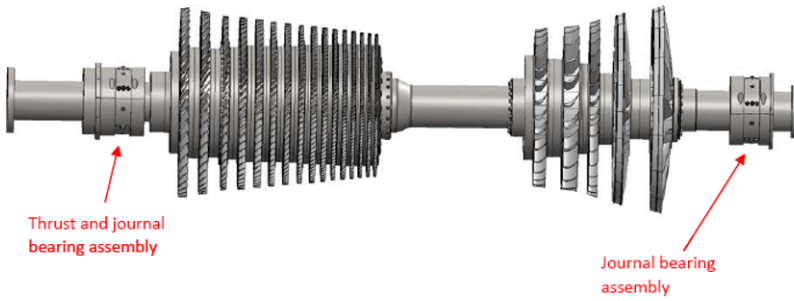


**Fig.17.20:** Gas turbine rotor, Turbomachinery Design Project, Texas A&M.

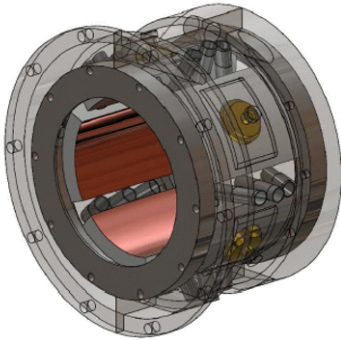


**Fig.17.21:** Journal bearing at the turbine side.

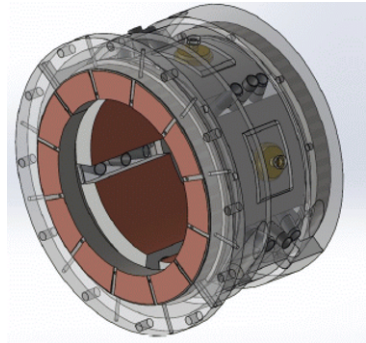


**Fig.17.22:** Thrust bearing at the compressor side.

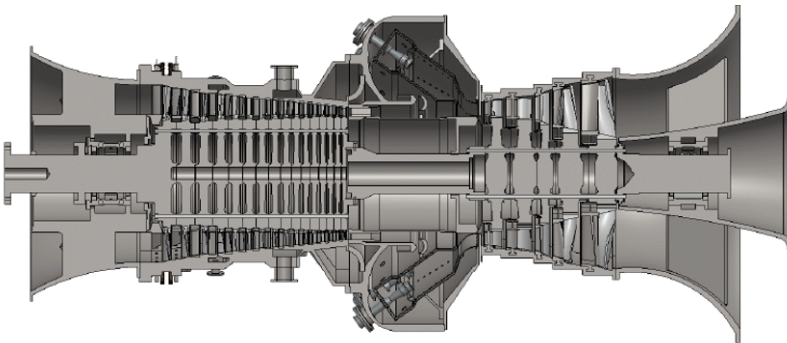


**Fig.17.23:** Gas turbine cross section Turbomachinery Design Project, Texas A&M.

### 17.5.2 Mechanical Integrity, Components Vibrational

Detail calculation of rotordynamic stability, component vibration, interaction of the component mechanical vibration with the rotordynamics are special topics. Their treatments are beyond the scope of this book, which is focused on aerothermodynamic design of components and the entire gas turbine system. Rotordynamics, component vibration and structural integrity are calculated using finite element analysis, rotordynamics and vibration analysis tools. These computational tools are integral parts of any turbomachinery design in general and gas turbine design in particular. Original engine manufacturers may have their own in house developed tools or may use commercially available ones. When using these tools, in the course of preliminary design, particular attention must be paid to the mechanical integrity of the gas turbine components and the system. Components that are particularly subject to vibration are among others LP-compressor blades, LP-turbine blades and the rotor shaft. The first compressor stage and the last turbine stage are particularly sensitive to vibration that may interact with the with the rotordynamics and if precautionary actions are not taken at the stage of design, major damages to the system may result at the first phase of engine shakedown.

### References

1. Yoshiaki, N., 2016 et al., “ Application of Latest Gas Turbine Technologies and Verification Results, GT2016-56520
2. Okui, H., et al. 2009, “Three-Dimensional Design and Optimization of a Transonic Rotor in Axial Flow Compressors”, ASME J. of Turbomachinery, vol.135, Issue 3. Paper031009.
3. Ito, E., et al., 2013, "Development of key technologies for the next generation high temperature gas turbine", ASME Turbo Expo GT2013-45172
4. M.T. Schobeiri, 2016, “Instruction for Mechanical Design of Gas Turbines for Students of Turbomachinery Design Course MEEN-646, Texas A&M University.

## 18 Simulation of Gas Turbine Engines, Design Off-Design and Dynamic Performance

Continuous improvement of efficiency and performance of aircraft and power generation gas turbine systems during the past decades has led to engine designs that are subject to extreme load conditions. Despite the enormous progress in the development of materials, at the design point, the engine components operate near their aerodynamic, thermal, and mechanical stress limits. Under these circumstances, any adverse dynamic operation causes excessive aerodynamic, thermal, and subsequent mechanical stresses that may affect the engine safety and reliability, and, thus, the operability of the engine if adequate precautionary actions are not taken. Considering the above facts, an accurate prediction of the above stresses and their cause is critical at the early stage of design and development of the engine and its components.

This Chapter focuses on the simulation of dynamic behavior of gas turbine engines and their components at design, off-design and adverse operation conditions. The simulation spectrum encompasses single- and multi-spool gas turbine engines, turbofan engines, and power generation gas turbines. The simulation concept is based on a generically modular structured system configurations. In the last six chapters, the gas turbine components were represented by individual modules described mathematically by systems of differential equations. Based on these and other necessary modules, a generic concept is presented. It provides the engine aerodynamicists with the necessary tools for developing computer codes for simulation of arbitrary engine and plant configurations. The spectrum of gas turbine configurations includes power generation and aircraft engines that operate under design, off-design and any arbitrary adverse dynamic operating conditions. The simulation computational tool with its components described in Chapters 12-17 can easily be extended to rocket engines, combined cycles, co-generation cycles and steam power plants. A multi-level system simulation treats different degrees of complexity ranging from global adiabatic simulation to detailed diabatic one. The dynamic behavior of the subject engine is calculated by solving a number of systems of partial differential equations which describe the unsteady behavior of the individual components. Accurate prediction of the dynamic behavior of the engine and the identification of critical parameters by the computational tool enables the engine designer to take appropriate steps using advanced control systems. The method may also be used to proof the design concept of the new generation of high performance engines. The modular structure of the concept enables the user to independently develop new components and integrate them into the simulation code. As representative examples, several different case studies are presented that deal with dynamic simulation of a compressed air energy storage gas turbine,

different transient cases with single- and multi-spool thrust and power generation engines were simulated.

## 18.1 State of Dynamic Simulation, Background

Dynamic behavior of aircraft gas turbine engines was investigated earlier by several NASA researchers among others [1],[2],[3]and [4] using the component performance map. for simulating engines. The engine representation by performance maps exhibits a useful tool for approximating engine behavior within the operation range defined by the component maps. However, the detailed information that is crucial for engine development and design cannot be provided at this simulation level. Furthermore, the above representation is not viable for providing the control system designer with the necessary input parameters, such as those describing the aero-thermodynamic and structural conditions of the compressor and turbine blade rows, shafts and casing. Consequently, the response of the real system to the intervention of the controller cannot be verified. These and other parameters are required inputs to the controller for triggering precautionary actions such as active surge control, prevention of overheating turbine blades due to the cooling failure, to mention just a few. A dynamic simulation that provides details about the behavior of gas turbines during adverse operations enables the engine manufacturer to reduce the number of routine in-house tests.

In order to address the above issues, Schobeiri [5], [6], [7], [8], [9], [10], [11] and [12] developed the modularly structured computer code COTRAN for simulating the nonlinear dynamic behavior of single-shaft power generation gas turbine engines. To account for the heat exchange between the material and the working fluid during a transient event, diabatic processes are employed in COTRAN for combustion chamber and recuperator components. The dynamic expansion process through the turbine component is accomplished by a row-by-row calculation using the stage characteristics. COTRAN reflects real engine configurations and components, and is routinely used at the early stages of design and development of new gas turbine engines. Although COTRAN represents an advanced, nonlinear dynamic code, its simulation capability is limited to single-shaft power generation gas turbine engines and, thus, cannot be used for simulating multi-spool aircraft engines. Considering this circumstance, Schobeiri and his co-workers [3], [12], [13] developed a new computational method with the corresponding, generically modular structured computer code GETRAN for simulating the nonlinear dynamic behavior of single- and multi-spool high pressure core engines, turbofan engines, and power generation gas turbine engines. The code is capable of simulating aircraft engines having up to five spools with variable geometry, with or without additional power generation shafts.

## 18.2 Gas Turbine Configurations

Gas turbines are designed for specific applications that determine their design configurations. For power generation purposes, the gas turbine usually has a *single spool*.

A spool combines a compressor and a turbine that are connected together via a shaft. Fig. 18.1 exhibits a single-spool power generation gas turbine, where a 14-stage compressor shares the same shaft with a 3-stage turbine.

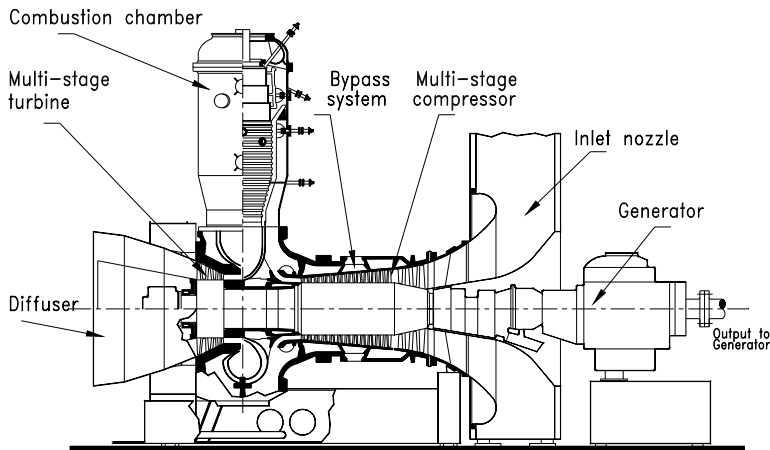


**Fig. 18.1:** A single- spool power generation gas turbine, BBC-GT9.

While in power generation gas turbines the power/weight ratio does not play an critical role, the thrust/weight ratio is a primary parameter in designing an aircraft gas turbine. High performance aircraft gas turbines generally have a twin-spool or a multi-spool arrangements. The spools are usually rotating at different angular velocities and are connected with each other aerodynamically via air or combustion gas. Figure 18.2 exhibits a typical high performance twin spool aircraft gas turbine with a *ducted front fan* as the main thrust generator. Gas turbines with power capacities less than 20 MW might have a *split shaft* configuration that consists of a *gas generation spool* and a *power shaft*. While the turbine of the gas generation spool provides the necessary shaft work to drive the compressor, the power shaft produces the net power. In addition to the above design configurations, a variety of engine derivatives can be constructed using a core engine as shown in Fig. 18.3.

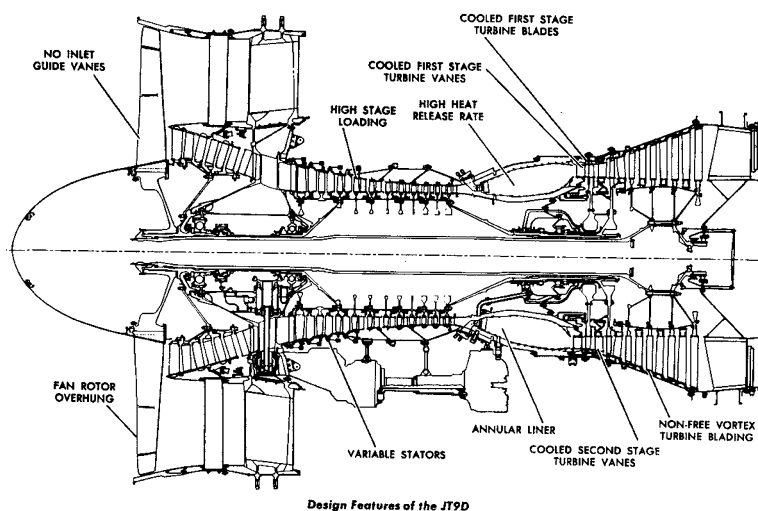


**Fig. 18.2:** A twin-spool Pratt & Whitney high bypass ratio aircraft engine with multi-stage compressors and turbines

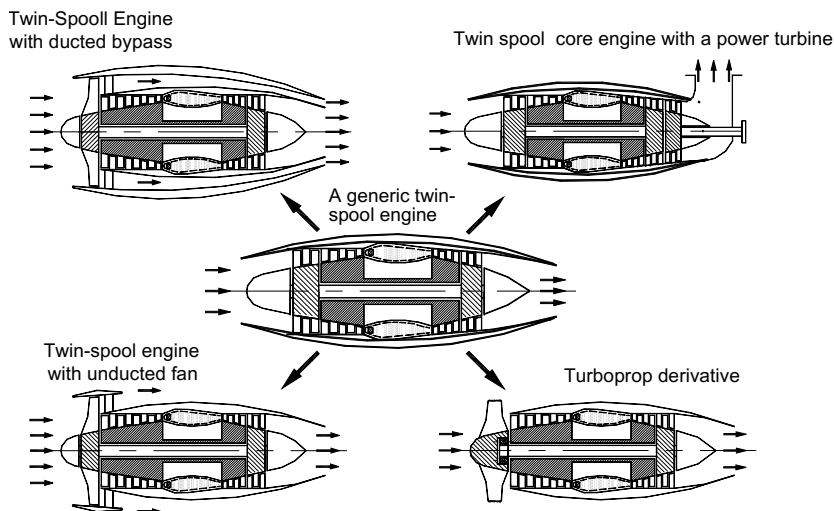


**Fig. 18.3:** Schematic of a twin-spool core engine with its derivatives



### 18.3 Gas Turbine Components, Modular Concept

An overview of power generation and aircraft gas turbines has led to the practical conclusion that any arbitrary aircraft or power generation gas turbine and its derivatives, regardless of configuration, i.e., number of spools and components, can be generically simulated by arranging the components according to the engine configuration of interest. The present nonlinear dynamic method is based on this generic, modularly structured concept that simulates the transient behavior of existing and new engines and their derivatives. The modules are identified by their names, shaft number, and inlet and outlet plena. This information is vital for automatically generating the system of differential equations representing the individual modules. Modules are then combined into a complete system which corresponds to the engine configuration. Each module is physically described by the conservation laws of thermo-fluid mechanics which result in a system of nonlinear, partial differential or algebraic equations. Since an engine consists of a number of components, its modular arrangement leads to a system containing a number of sets of equations. The above concept can be systematically applied to any aircraft or power generation gas turbine engine. The general application of the modular concept is illustrated in Figs. 18.4 and 18.5. The twin-spool engine shown in Fig. 18.4 exemplifies the modular structure of a twin-spool core engine and its component arrangement. The corresponding modules implemented into the engine modular configuration are depicted in Fig. 18.5.

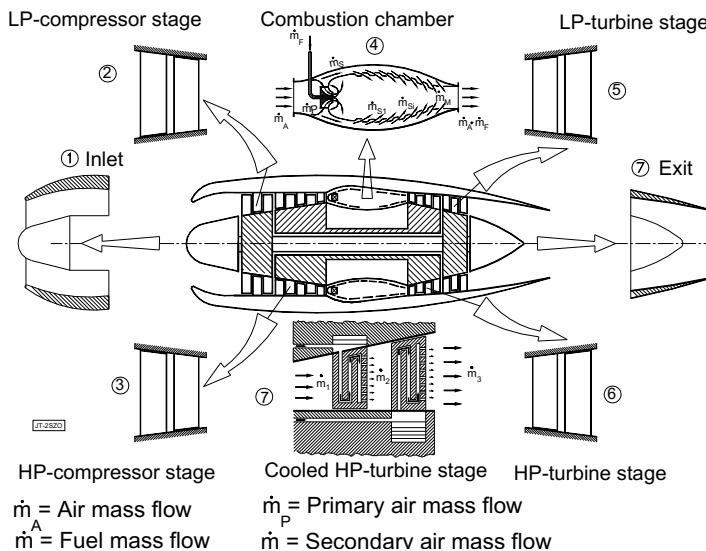


**Fig. 18.4:** Components decomposition of a twin-spool engine.

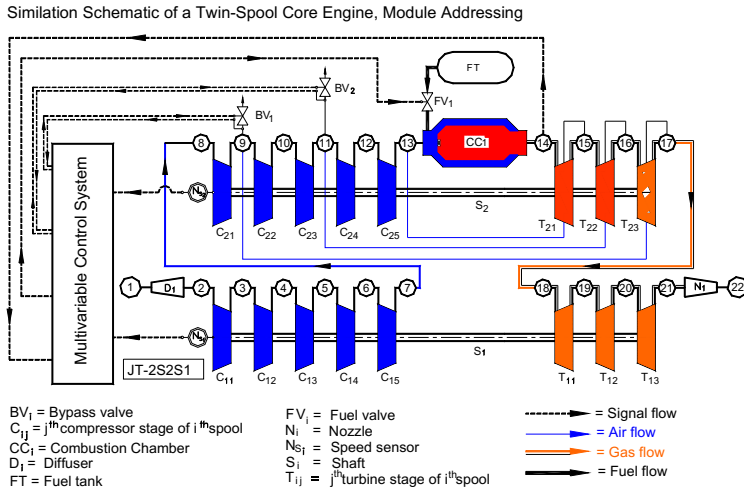


**Fig. 18.5:** Modular configuration of the engine exhibited in Fig.18.4.

It consists of two spools with the shaft  $S_1$  and  $S_2$ , on which the low and high pressure components such as compressors and turbines are assembled. The two shafts are coupled by the working media air and combustion gas. They rotate with different speeds which are transferred to the control system by the sensors  $N_{s1}$  and  $N_{s2}$ . Air enters the inlet diffuser  $D_1$ , which is connected with the multi-stage compressor assembled on  $S_1$ , and is decomposed in several compressor stages  $C_{1i}$ . The first index, 1, refers to the spool number and the second index,  $i$ , marks the number of the compressor stage. After compression in the  $S_1$  compressor stage group, the air enters the second compressor (HP- compressor) assembled on the  $S_2$  shaft that consists of stages  $C_{21}$ - $C_{25}$ . In the combustion chamber ( $CC_1$ ) high temperature combustion gas is produced by adding the fuel from the tank  $FT$ . The gas expands in the high pressure turbine that consists of stages  $T_{21}$  -  $T_{23}$ . By exiting from the last stage of HP-turbine, the combustion gas enters the low pressure turbine consisting of stages  $T_{11}$  -  $T_{13}$  and is expanded through the exit nozzle. Two bypass valves,  $BV_1$  and  $BV_2$ , are connected with the compressor stator blades for surge prevention. The fuel valve,  $FV_1$ , is placed between the fuel tank,  $FT$ , and the combustion chamber,  $CC_1$ . The pipes,  $P_i$ , serve for cooling air transport from the compressor to cooled turbines. The compressor stage pressures, the turbine inlet temperature, and the rotor speed are the input signals to the control system, which controls the valve cross sections and the fuel mass flow.

Figures 18.6 and 18.7 display the lists of components with their corresponding modular representations and symbols that are described by the method presented in Chapters 14 through 17. They exhibit the basic components essential for generically configuring any possible aero- and power generation gas turbine engines.

## Gas turbine Generic Components, Modules, and Symbols

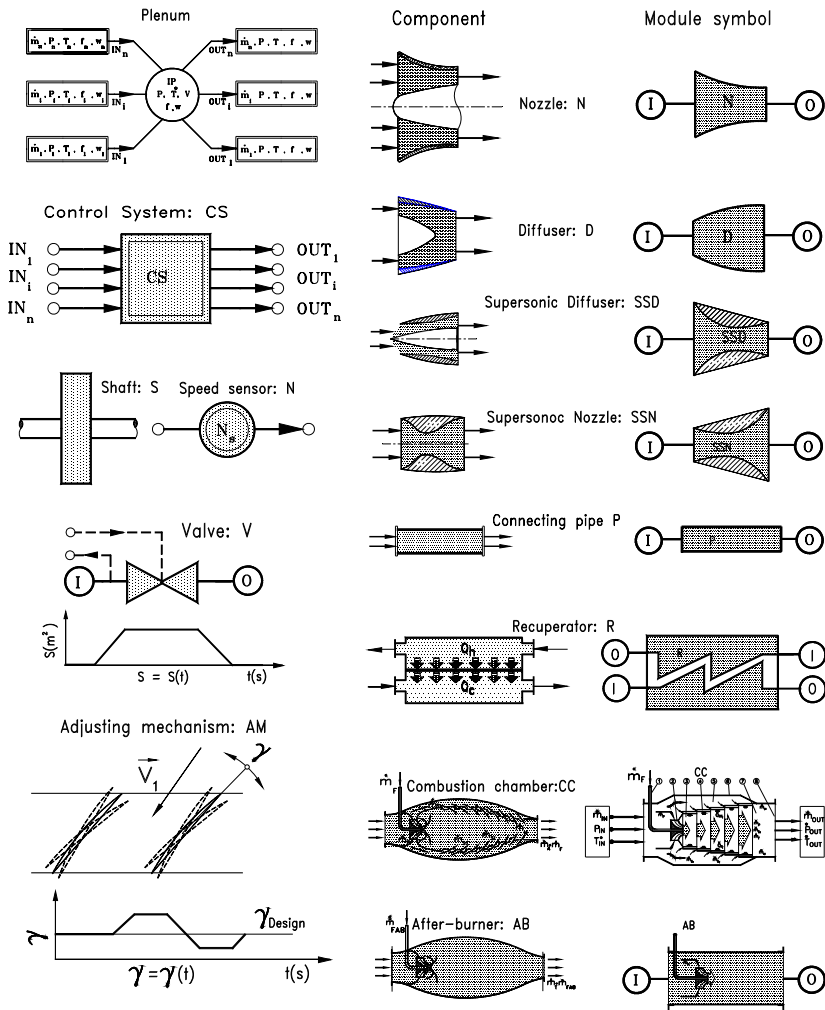


**Fig. 18.6:** Components, modules, and their symbols: Plenum, Control system CS, Shaft S, with moment of inertia  $I$  and the rotational velocity  $\omega$ , Speed sensor N, Valve with an arbitrary ramp for closing and opening the cross section S, Adjusting mechanism AM for stator blade adjustment, Subsonic nozzle N, Subsonic diffuser D, Supersonic Diffuser SSD, Supersonic nozzle SSN, Recuperator R, Combustion Chamber CC, and Afterburner AB.

### Gas turbine Generic Components, Modules, and Symbols

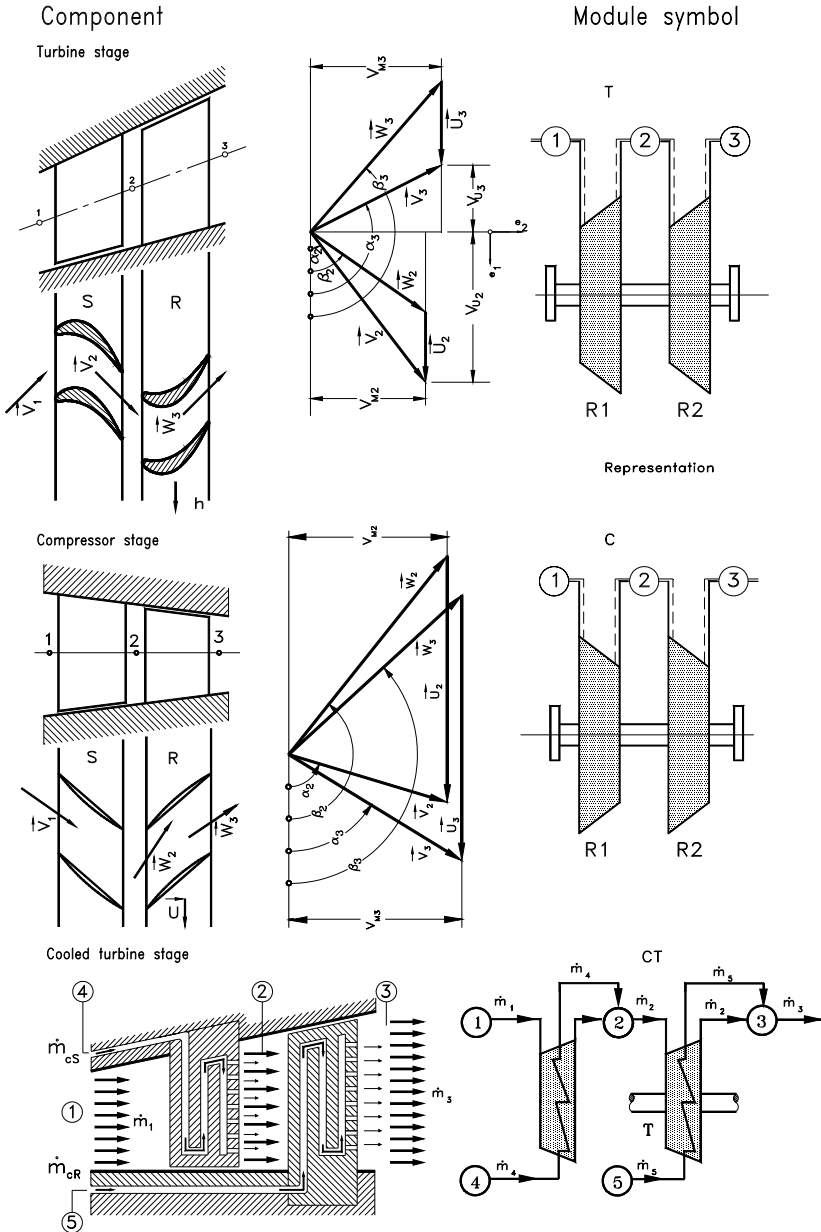


**Fig. 18.7:** Adiabatic turbine stage with the module T, Adiabatic compressor stage with the module C, Cooled turbine stage with the module CT.

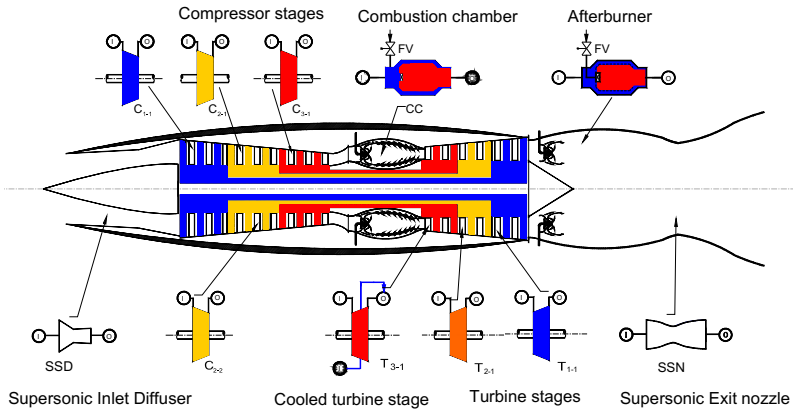


**Fig. 18.8:** Schematic of a 3-spool high performance core engine, component decomposition.

Simulation Schematic of a Three-Spool High Pressure Core Engine  
Module Addressing

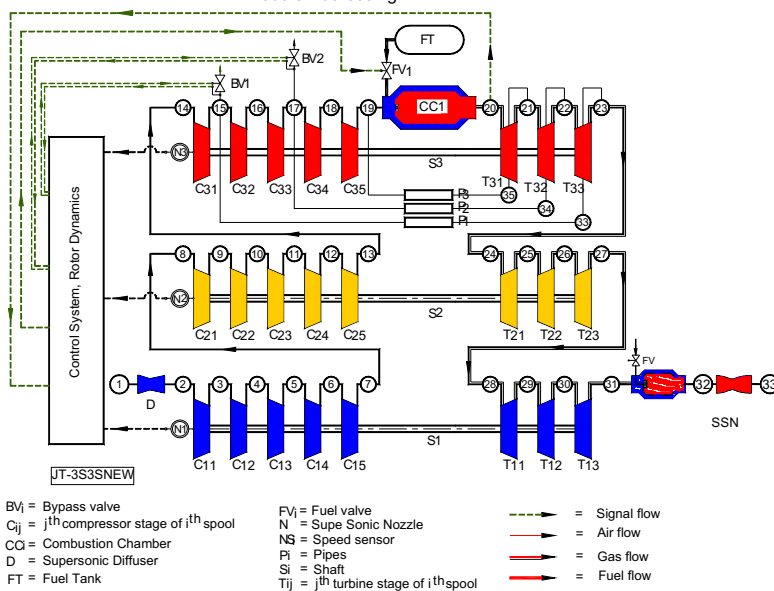


**Fig. 18.9:** Modular configuration of engine exhibited in Fig.18.8.

These modules are connected with each other with a plenum, which is a coupling component between two or more successive components. As briefly explained in Chapters 13, the primary function of the plenum is to couple the dynamic information of entering and exiting components such as mass flow, total pressure, total temperature, fuel/air ratio, and water/air ratio. After entering the plenum a mixing process takes place, where the aforementioned quantities reach their

equilibrium values. These values are the same for all outlet components .

Figure 18.8 shows a more complex example of a three-spool supersonic engine with its modular decomposition. Figure 18.9 exhibits a systematic modular configuration of Fig. 18.8 that is represented by a large system of differential and algebraic equations.

## **18.4 Levels of Gas Turbine Engine Simulations**

Accuracy of gas turbine dynamic simulation is determined by the level of component modeling. It increases by increasing the level of simulation complexity. Four levels of simulation are introduced:

### **18.4.1 Zeroth Simulation Level**

Is applied to simple cases such as those in [4] through [7], utilizing a fixed system configuration with steady state component characteristics that are described by algebraic equations, simplified differential equations, and lookup tables and maps. Furthermore, there is no dynamic coupling between the components. Since this simulation level does not account for engine dynamics, it will not be discussed further.

### **18.4.2 First Simulation Level**

This level uses component global performance map only for turbines and compressors. The maps are generated using the row-by-row adiabatic calculation method detailed in Chapters 18 and 19. The other components such as recuperators, coolers, combustion chambers, pipes, nozzles, and diffusers are simulated according to methods discussed in Chapters 14 through 17. Primary air, secondary combustion gas, and metal temperature of the combustion chamber are calculated. All modules are coupled with plena insuring a dynamic information transfer to all modules involved. Modules are described by algebraic and differential equations.

### **18.4.3 Second Simulation Level**

This level utilizes adiabatic row-by-row or stage-by-stage calculation for compressor and turbine modules. For combustion chamber, primary air, secondary combustion gas, and metal temperature are calculated. Dynamic calculations are performed throughout the simulation, where the modules are coupled by plena. Each module is described by differential and algebraic equations.

### **18.4.4 Third Simulation Level**

This level uses diabatic row-by-row calculation for compressor and turbine modules. This level delivers a very detailed diabatic information about the compressor and turbine component dynamic behavior. It utilizes cooled turbine and compressor stages and simultaneously calculates the blade temperatures. For

combustion chamber, primary air, secondary combustion gas, and metal temperature are calculated. Dynamic calculations are performed throughout the simulation, whereas the modules are coupled by plena. Each module is described by differential and algebraic equations. The details of information delivered by this level and degree of complexity is demonstrated by the following example. The first two stages of a four-stage turbine component of high performance gas turbine engine must be cooled. For the first four turbine rows we use the diabatic expansion process that requires three differential equations for describing the primary flow, three differential equations for describing the cooling flow, and one differential equation for describing the blade temperature. This leads from two cooled turbine stages to 28 differential equations.

The generic structure allows to cross-couple level 1 to 3. For example, we wish to simulate a gas turbine engine with a global compressor performance map, but need to obtain detailed information about turbine blade temperature, which is necessary to calculate the relative expansion between the blades and the casing, then we may use the diabatic calculation method. In this case, we cross-couple the first and third level simulation.

## 18.5 Non-Linear Dynamic Simulation Case Studies

Seven different case studies dealing with 3-completely different gas turbine systems are presented. Table 18.1 shows the matrix of the simulation cases.

**Table 18.1:** Simulation Case Studies

TESTS	DYNAMIC SIMULATION TYPE	ENGINE TYPE
<b>CASE 1.1</b>	Emergency Shutdown of a Compressed Air Energy Storage gas turbine.	Compressed Air Energy Storage GT
<b>CASE 1.2</b>	Dynamics response of a CAES to the fluctuating grid power demand.	Compressed Air Energy Storage GT
<b>CASE 2</b>	Dynamic test of a GT at adverse dynamic operation condition.	Single shaft power generation GT
<b>CASE 3.1</b>	Rotating stall and surge of a GT	Split shaft GT
<b>CASE 3.2</b>	Prevention of rotating stall and surge by adjusting the stator angle	Split shaft GT
<b>CASE 4</b>	Efficiency improvement through adjusting the turbine stator angle	Single shaft power generation GT
<b>CASE 5</b>	Dynamic simulation of Three-Spool, four-shaft aircraft GT-derivative	Three-spool four shaft GT

These studies demonstrate the capability of the generic structured method we discussed in Chapters 13 through 18 to dynamically simulate complex systems with high accuracy. The case studies presented in this chapter are related to the real world engine simulation and are intended to provide the reader with an insight into the non-linear engine dynamic simulation. The selected cases ranging from zero-spool, single shaft power generation to three-spool four shaft thrust and power generation gas turbine engines provide detailed information about the engine behavior during design and off-design dynamic operation. For each engine configuration the simulation provides aero-thermodynamic details of each individual component and its interaction with the other system components. Since the presentation of the complete simulation results of the three cases listed in Table 1 and 2 would exceed the frame of this chapter, only a few selected plots will be displayed and discussed for each case.

### 18.5.1 Case Studies: Compressed Air Energy Storage Plant

The subject of this case study is the dynamic simulation of an emergency shutdown of, single-shaft compressed air energy storage (CAES) gas turbine [14], Fig. 18.10. The CAES is utilized to efficiently cover the peak electric energy demand during the day.

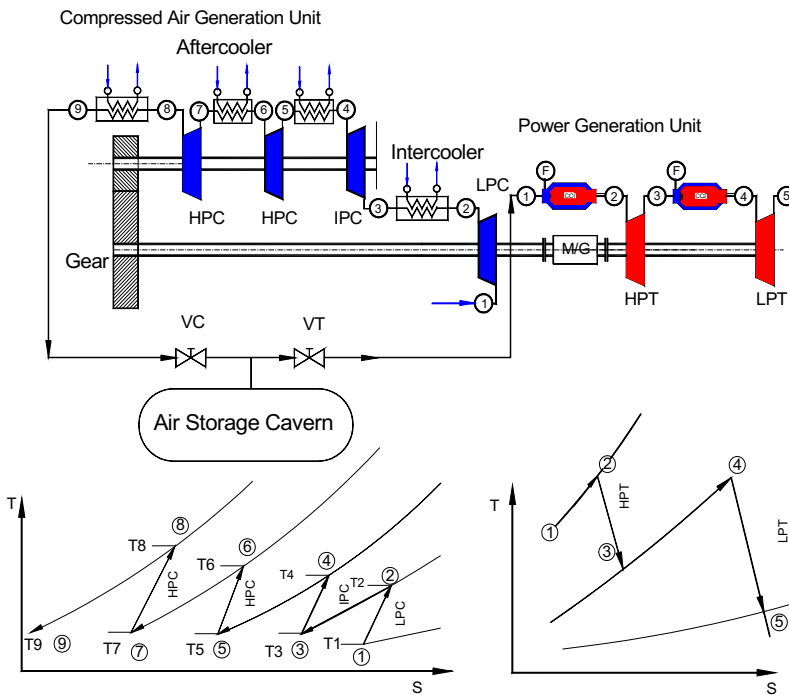


**Fig. 18.10:** Compressed Air Energy Storage Facility plant, located in Huntorf, Germany



Utilities produce excess electrical energy during the period of low electric energy demand that extends up to 8 hours during the night. This excess energy is used to drive the compressor train of the CAES. The compressor with a power of 60 MW operates about 8 hours providing high pressure compressed air to inject into a large underground air storage facility. Figure 18.10 exhibits schematically the working principle of the CAES. As seen, the facility consists of a compressed air generation unit comprising of a LPC, an IPC and two HPCs. The LPC-shaft is connected to the shaft that carries the IPC and two HPCs via a large gear transmission. The power generation unit is a gas turbine that has two large volume combustion chambers and two turbines. During the peak electric energy demand, the compressed air from the underground storage enters the first combustion chamber, where fuel is added and the combustion process starts. The high pressure, high temperature combustion gas expands first in the HP-turbine. After exiting the HP-turbine, the lean combustion gas enters the second combustion chamber, where the remaining fuel is added. The reheated combustion gas expands into the LP-turbine. Both turbines produce about 290 MW of power during the duration of 2 to 4 hours. In contrast to the base load gas turbines, the period of operation of a CAES plant is restricted to a few hours per day resulting in a daily startup followed by shutdown. This relatively high

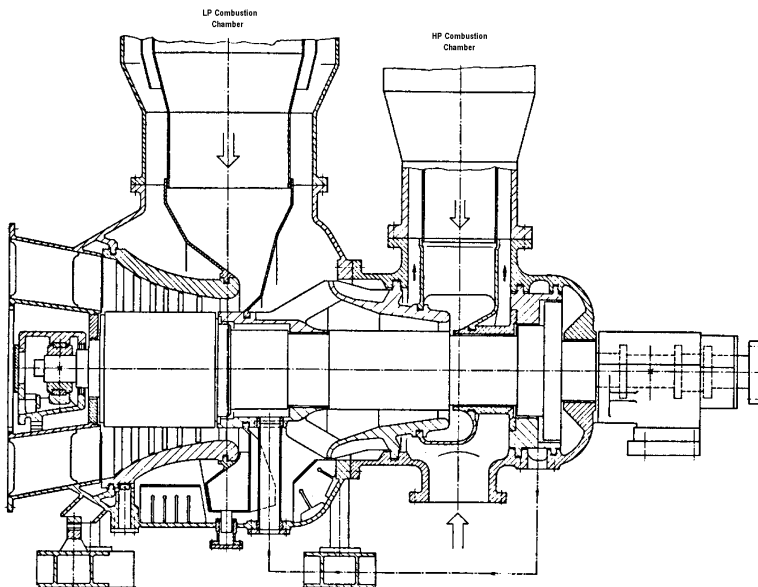


**Fig. 18.11:** The power generation gas turbine unit of Huntorf plant.

frequency of startups and shutdowns may cause structural damages resulting in reduced life time if the startup and shutdown procedures are not performed properly. The CAES gas turbine system, Fig. 18.11, with the simulation schematic shown in Fig. 18.12 features a large volume plenum (8) for storing the compressed air, a high-pressure combustion chamber (HPCC), a high-pressure turbine (HPT), a low-pressure combustion chamber (LPCC), a low-pressure turbine (LPT2), a cold-air pre-heater with a low pressure and a high pressure side (LPP and HPP-side) and a generator (G). During the steady-state turbine operation, cold air from the air-storage facility, plenum 8, passes through the shutdown valve ( $V_1$ ) to the inlet plenum (1), where it is divided into combustion and cooling-air flows.

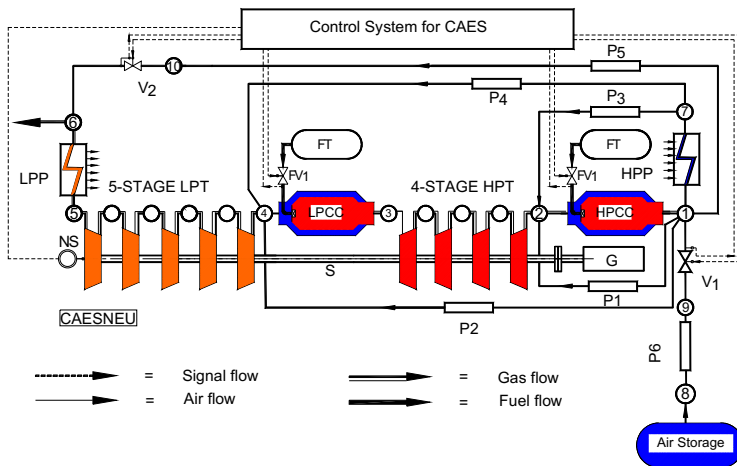


**Fig. 18.12:** Simulation schematic of Air Energy Storage Facility gas turbine Fig.18.11.

The addition of fuel in HPCC causes the combustion air to be heated up to the combustion chamber's exit temperature. Immediately upstream of HPT, the combustor mass flow mixed with a portion of the cooling-air flow, which has already been preheated in HPP. As a result, the gas temperature of the turbine mass flow lies below the combustion chamber's exit temperature. After expansion in HPT, the combustion chamber (LPCC) mass flow is mixed in LPT inlet plenum (4) with the rest of the preheated cooling-air flow and the sealing-air flow. After expansion in LPT, the gas gives off some of its heat in LPP before leaving the gas turbine system. Figure 18.12 shows how the various components are interconnected. Plenum 8, the air storage facility, is connected via two identical pipes (P6) to two shutdown valves ( $V_1$ ). During steady-state operation, the blow-off valve ( $V_2$ ) remains closed. It opens in the event of a disturbance that may cause a rapid shutdown. In such an event, the valve blows off some of the gas, thereby limiting the maximum rotor speed. For the sake of clarity, the pre-heater (P) has been separated into its air and gas sides, designated HPP and LPP, respectively.

### 18.5.1.1 Case Study: Emergency Shutdown

Starting from a steady operating point, a generator trip with rapid shutdown was simulated assuming a failure of the control system. This circumstance necessitates an intervention by the hydraulic emergency system. This incident simulates an extreme transient process within some of the components, as explained briefly. After the generator trip, the rotor is strongly accelerated because of full turbine power acting on it, Fig. 18.13(a).

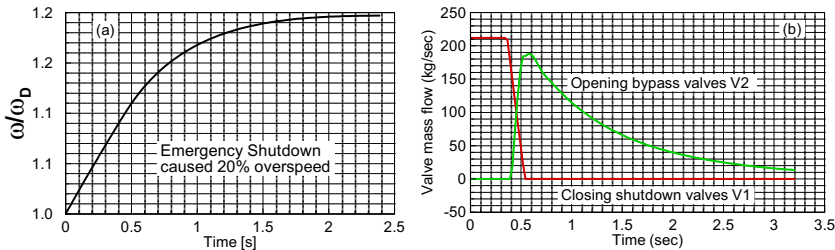


**Fig. 18.13:** Relative angular velocity (a) and mass flows (b) as functions of time.

The hydraulic emergency system intervenes only when the speed corresponding to the hydraulic emergency overspeed trip is reached. This intervention involves closing the fuel valves,  $FV_1$  and  $FV_2$ , and air valves,  $V_1$ , after which the system no longer receives any energy from outside, Fig. 18.13(b). The Inlet-shutdown valves  $V_1$  remain open until the trip speed at  $t = 0.35$  second has been reached. Opening of the bypass/blow-off valve  $V_2$  allows the high pressure air contained in both large volume combustion chambers as well as in the HP-side of pre-heater to discharge. The closing process of the inlet and shutdown valves and the opening of the bypass valves are shown in Fig. 18.13(b). This process results in a steady drop in plena pressures and temperatures.

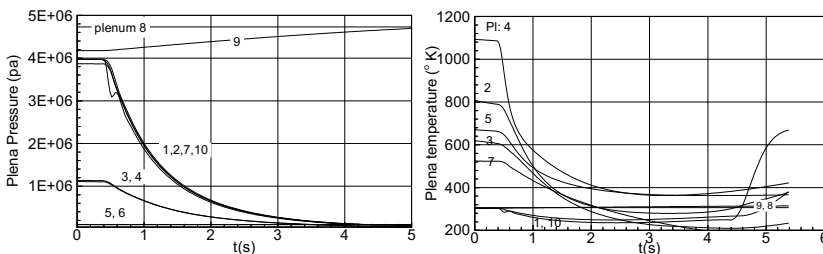


**Fig. 18.14:** Plena pressure and temperature as functions of time. Shutdown process causes rapid depressurization in high pressure plenum 1, 2, 7, and 10.

As Fig. 18.14 shows, the pressure drop in the high-pressure section is initially steeper than in the low-pressure section. This means that the enthalpy difference of the high-pressure turbine is reduced more rapidly than that of the low-pressure turbine. Immediately after the blow-off valve is opened, an abrupt pressure drop takes place in plenum 10, which is connected to plenum 1 via pipe P5. Thereafter, dynamic pressure equalization takes place between the two plena. This drop in pressure and temperature causes a corresponding drop in the shaft power and the mass flow throughout the engine. Figure 18.15 shows the resulting drop in turbine inlet and exit temperature. The continuous decrease in turbine

mass flow causes a strong dissipation of shaft power resulting in the excessive increase of turbine exit temperature. In order to avoid thermal damages to blades, a small stream of cold air is injected into the turbine flow path that causes a reduction in temperature gradient. This is shown in Fig. 18.15 for the exit temperature at  $t = 3.4$  s.

Dynamic behavior of the rotor speed is generally determined by the turbine power acting on the rotor. How the rotor behaves in response to a generator trip depends, in particular, on how long the full turbine power is available, a process monitored by the control and safety monitoring system. When the control system functions normally, trip is signaled without delay to the shutdown valve. Failure of the control system causes the hydraulic emergency system to intervene. The intervention begins only when the speed corresponding to the hydraulic emergency overspeed trip is reached. During this process, and also the subsequent valve dead time, the rotor receives the full turbine power. The closing

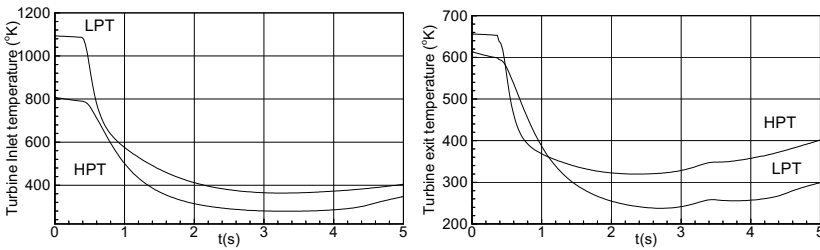


**Fig. 18.15:** Turbine inlet and exit temperature as functions of time. Note changes of the exit temperature at  $t=3.4$  s

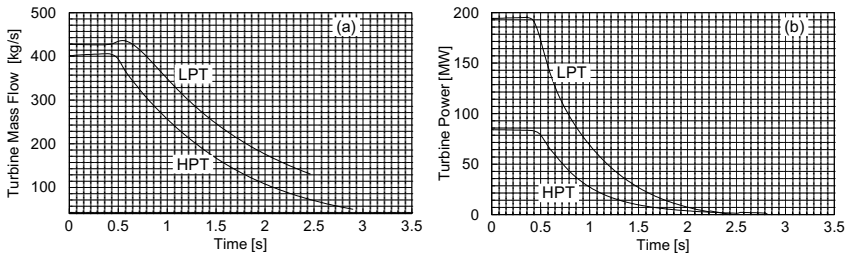


**Fig. 18.16:** Turbine mass flows (a) and power (b) as functions of time.

phase is characterized by a steady reduction in energy input from outside, which finally becomes zero. The total energy of the gases still contained in the system is converted by the two turbines into mechanical energy, causing the rotor speed to increase steadily, Fig. 18.13. When the instantaneous turbine power is just capable of balancing the friction and ventilation losses, the rotor speed reaches its maximum, after which it begins to decrease. Reducing the turbine mass flow, Fig. 18.16 (a), below the minimum value discussed in Chapter 17, causes the shaft power to dissipate completely as heat resulting in negative values as Fig. 18.16 (b) shows. From this point on, the rotational speed starts to decrease. The figure depicts the mass flow through both turbines as representatives for the entire engine as well as the total shaft power.

### 18.5.1.2 Case Study 1: Grid Fluctuation Response

During the operation of a CAES-gas turbine described in the previous section, the power demand by electrical grid may fluctuate. The gas turbine system has to respond correspondingly. In this case, the control system reacts to this event by changing the fuel mass flow to the combustion chambers. Several control scenarios may be applied to change one or both combustion chambers fuel input. In the following simulation, the fuel mass flow of both combustion chambers are changed according to the power demand. Figure 18.17 shows the power schedule (a) with the corresponding fuel reduction in both combustion chambers (b) and the response of the gas turbine to the event. This dynamic event triggers a change the entire aero-thermodynamics as well as the material temperature of all system components. Representative examples, such as turbine powers and inlet temperatures are shown in Fig. 18.8 (a,b)

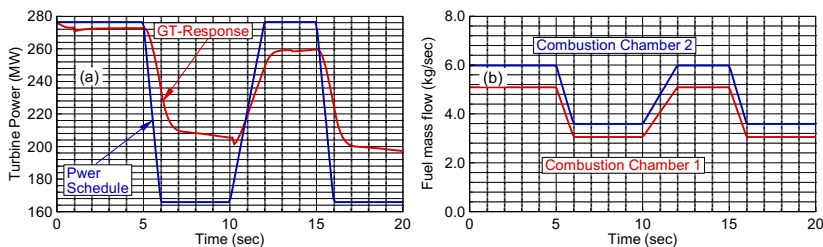


**Fig. 18.17:** Response of the CAES to grid power fluctuation.

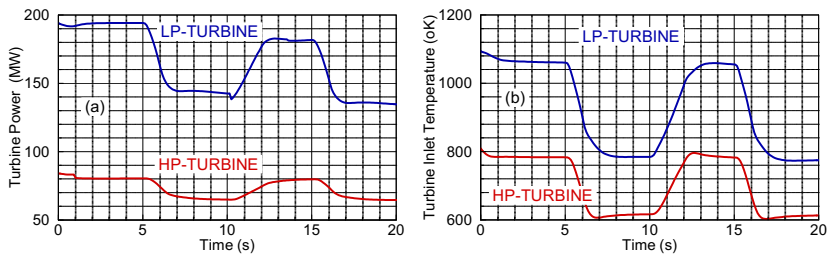


**Fig. 18.18:** Turbine power (a) and inlet temperature (b) as functions of time.

### 18.5.2 Case Study 2: Dynamic Simulation of a Gas Turbine under Adverse Operation condition

The subject of this case study is the dynamic simulation of a BBC-GT9 gas turbine which is a single-shaft power generation gas turbine engine. It is utilized as a stand-alone power generator or in conjunction with combined cycle power generation. The engine shown in Fig. 18.19 consists mainly of three compressor stage groups, a combustion chamber, a turbine, a control system, and a generator. The simulation schematic of this engine is presented in Fig. 18.20. The rotor speed and turbine inlet temperature are the input parameters for the controller, its output parameters are the fuel mass flow (fuel valve opening), and the mass flows of the bypass valves (bypass valve opening). The dynamic behavior of BBC-GT9 was experimentally determined for transient tests with

extreme changes in its load. Its transient data was accurately documented by Schobeiri [3]. Starting from a given network load schedule, the dynamic behavior of the gas turbine is predicted and the results are presented.

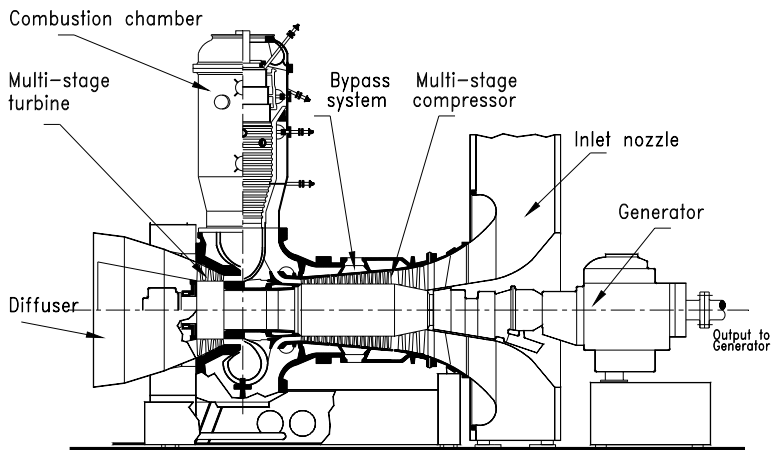


**Fig. 18.19:** A single-shaft power generation gas turbine, BBC-GT9.

The simulation schematic of this engine is shown in Fig. 18.20. For dynamic simulation, the first, second and third stage groups are simulated in row-by-row fashion. A similar row-by-row calculation procedure is applied to the turbine component. The rotor speed and the turbine inlet temperature are the input

Simulation Schematic of the Power Generation Gas Turbine Engine BBC-GT-9, Module Addressing

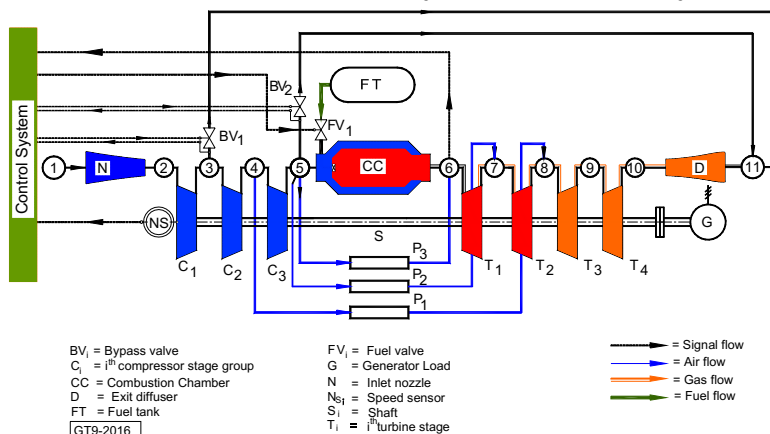


**Fig. 18.20:** Simulation schematic of BBC-GT9 shown in Fig. 18.8.

parameters for the controller, its output parameters are the fuel mass flow (fuel valve opening), and the mass flows of the bypass valves (bypass valve opening).

**Simulation of an Adverse Dynamic Operation:** Starting from the steady state, in accordance with the load schedule shown in Fig. 18.21 (a), curve 1, after one second of operation at design point, a generator loss of load is simulated that lasts for six seconds.

The increase of the rotational speed triggers the intervention of the control system causing a rapid closing of the fuel valve, Fig. 18.21. Furthermore, operating in an idle state with a rotational speed above the design speed causes

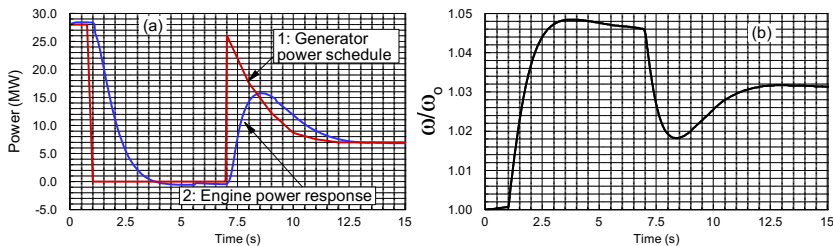


**Fig. 18.21:** (a) generator power schedule and engine power response, (b) relative shaft speed as a function of time.

the compressor and turbine mass flow to increase. The process of control intervention lasts until a constant idling speed is attained. After that, the load schedule in Fig. 18.21 (a, curve 1) applies a sudden load increase to recover the gas turbine power. This sudden increase is followed by a smooth ramp of load reduction to arrive at an approximately 25% of the gas turbine rated power, Fig. 18.21. The rotor first reacts to this addition of load with a sharp decrease in rotational speed, as exhibited in Fig. 18.21(b), causing a quick opening of the fuel valve, Fig. 18.21. After completion of the transient process, the steady off-design state is reached.

**Plena Pressure and Temperature Transients:** The above adverse dynamic operation has triggered temporal changes of flow quantities within individual components. Figure 18.22 shows how the plena pressure and temperature change with time.

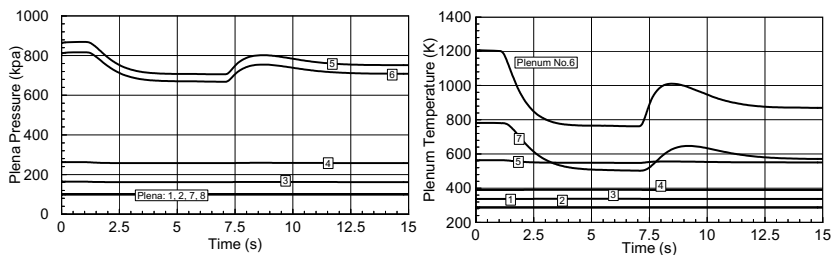


**Fig. 18.22:** Plena pressure and temperature as functions of time. Individual plena are labeled.

Decrease of turbine power and increase of the shaft speed has caused the HP-compressor exit pressure in plenum 5 to decrease. Temperature at combustion chamber exit, plenum 6, and turbine exit, plenum 7, follow the course of fuel injection shown in Fig. 18.23(right). The plena temperature upstream of the

combustion chamber are not affected.

**Compressor and Combustion Chamber Mass Flow Transients:** Figure 18.23 exhibits the mass flow transients through LP-, IP-, and HP-compressors. While IP- and HP-stage groups have the same mass flow, the LP-part has a greater mass flow. The difference of 1 kg/s is due to the cooling mass flow extraction.

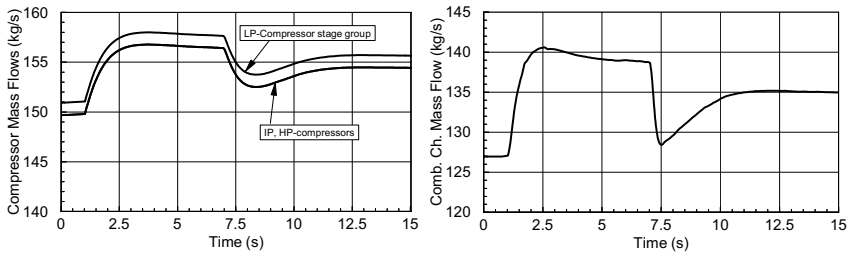


**Fig. 18.23:** Compressor and combustion chamber mass flows as functions of time.

As briefly mentioned, the increase in shaft speed and the simultaneous decrease in compressor power consumption leading to compressor pressure drop has caused an increase in compressor mass flow during the process of loss of load that lasts up to  $t = 6$  sec. The sudden load addition reduces the compressor mass flow. The combustion chamber mass flow shows a similar course with a substantial difference. A substantial portion of compressor mass flow is extracted for combustion chamber exit temperature mixing cooling.

**Combustion Chamber Gas and Metal Temperature Transients:** The Combustion chamber component used in this simulation has three segments that separate the primary combustion zone from the secondary cooling air zone. Its module is shown in Fig. 18.24. Compressed air enters the combustion chamber at station 1, Figs. 18.24. Fuel is added and the segment cooling occurs according to the procedure described in Chapter 14. The secondary mass flow portions  $\dot{m}_{si}$  serve as cooling jets and are mixed with the combustion gas, thus reducing the gas temperature, Fig. 18.25(left). Before exiting, the combustion gas is mixed with the mixing air stream  $\dot{m}_M$ , further reducing the temperature. Figure 18.25 (right) shows the mean segment temperatures. In accordance with the measurements on this gas turbine, the flame length extends from station 1 to 3, which makes the segment number 2 the hottest one.



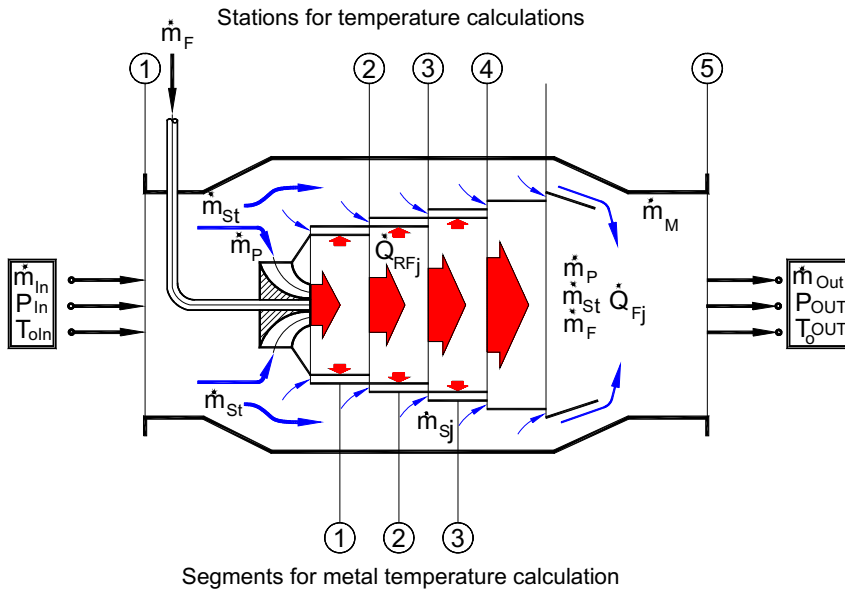


**Fig. 18.24:** Combustion chamber module, stations and segments,  $\dot{m}_P$  = primary air,  $\dot{m}_{Stot}$  = total secondary air,  $\dot{m}_{Sj}$  = individual secondary air.

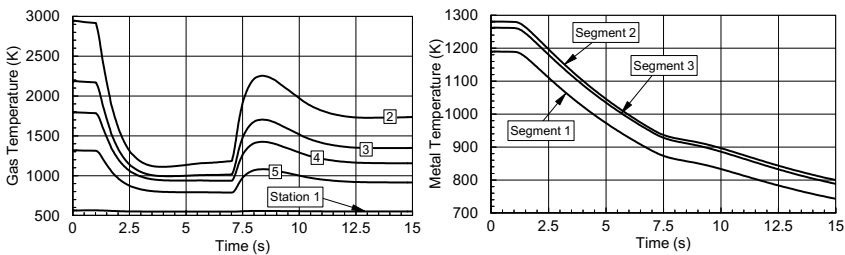


**Fig. 18.25:** Combustion chamber gas and metal temperature at different positions as functions of time.

**Turbine and Fuel Mass Flow Transients:** Figure 18.26 (left) exhibits the turbine mass flow transient, which is dictated by the compressor dynamic operation. Difference between the turbine and the compressor mass flow is the injected fuel mass flow. The particular course of fuel mass flow shown in Fig. 18.26 (right) is due to the intervention of the control system. An increase in rotational speed causes the controller to close the fuel valve. Subsequent addition of generator load results in a steep drop of rotational speed which causes an opening of the fuel valve.

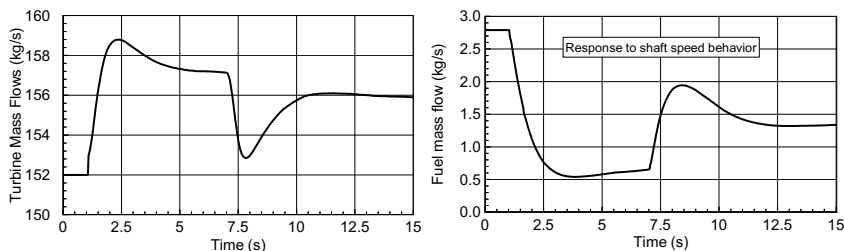


**Fig. 18.26:** Turbine and fuel mass flow as functions of time. The fuel mass flow is controlled by the shaft rotational speed.

### 18.5.3 Case Studies: Dynamic Simulation of a Split-Shaft Gas Turbine under Adverse Operation condition

To force the compressor into an unstable regime, we reconfigured the gas turbine utilized in the previous section by splitting the shaft and connecting the frequency controller to the power shaft. The decomposition of the gas turbine into a gas generator and a power generator part, is shown in Fig. 18.27.

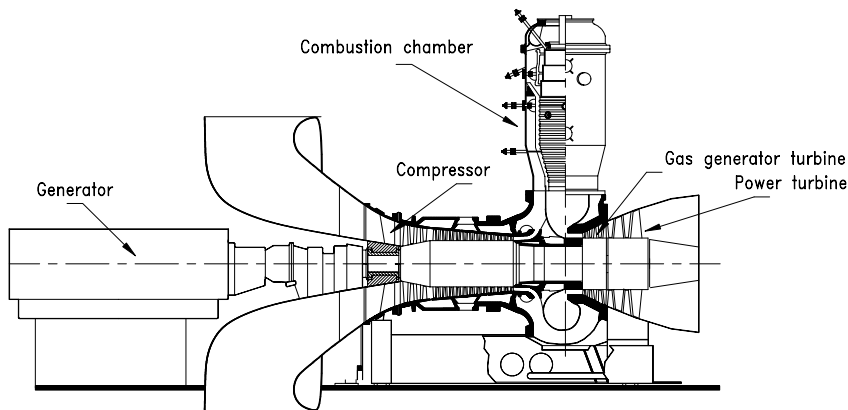


**Fig. 18.27:** A split shaft gas turbine engine for simulating rotating stall and surge.

The gas generator unit incorporates a multi-stage compressor that is decomposed into a low pressure, an intermediate pressure, and a high pressure compressor, as discussed earlier. The compressor is followed by a combustion chamber, a three-stage turbine that drives the compressor, and a two-stage power turbine connected with a generator. The LP, IP, and HP-compressors are modeled using the row-by-row method presented in this paper. The simulation schematic of the engine is shown in 18.28, where the individual components are placed between two successive plena.

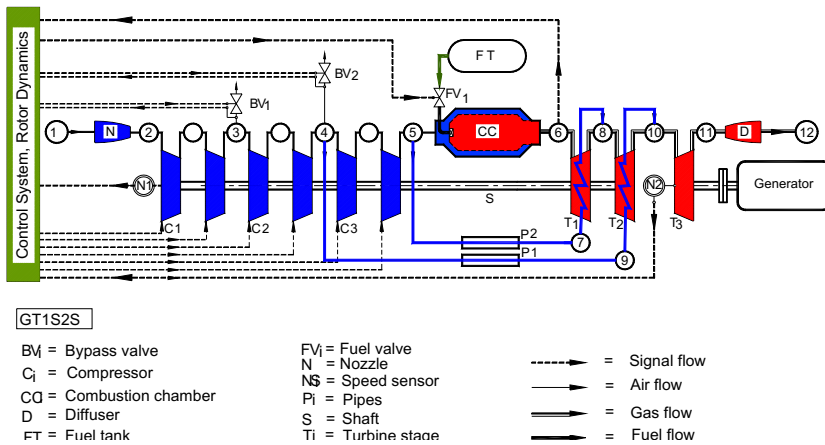


**Fig. 18.28:** Simulation schematic of the split-shaft turbine Fig.18.27.

Figure 18.28 also shows the interaction of individual components with the control system. As seen in Fig. 18.28, the frequency controller is connected to the power shaft, thus sensing the rotational speed and the temperature of the power shaft and its time derivative to control the fuel mass flow.

**18.5.1.1 Simulation of Compressor Surge:** Starting from a steady state operating point, the dynamic behavior of the above engine is simulated for a transient operation which is controlled by a prescribed generator power schedule that acts on the power shaft as shown in Fig.18.29.

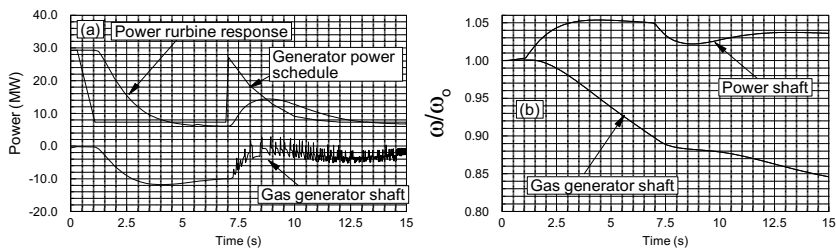


**Fig. 18.29:** (a) Generator load schedule, power shaft response and the response of gas generator shaft, (b) Rotation speed behavior of power and gas generator shaft.

This load schedule is exactly identical with the one described in previous Case. The simulation includes a sudden generator load drop from 100% to 25% that lasts about 7 seconds and is followed by a sudden load addition to 100% and a subsequent incremental load decrease to about 25%. The sudden load drop causes the shaft rotational speed to increase. This increase in rotational speed causes the controller to trigger a rapid throttling of the fuel mass flow. The throttling process

lasts until a constant idling speed of the power shaft is attained. After about seven seconds, full load is suddenly added and then reduced slowly such that after the completion of load addition, the gas turbine is supplying 25% of its rated load, as shown in Fig. 18.29(a). The rotor reacts to this sudden addition of load with a sharp decrease in rotational speed. That, in turn, causes a quick opening of the fuel valve. During this process, the power generation capability of the gas generation turbine deteriorates significantly causing a major power imbalance between the turbine and compressor components. This imbalance results in a continuous decrease of the compressor rotor speed as shown in Fig. 18.29(b), causing the compressor to operate partially in rotating stall and surge regimes.

Reducing the rotor speed below 90% forces the LP-compressor into rotating stall and a short duration surge process with reversal in the mass flow direction, Fig. 18.30. Since the magnitude of the reversed mass flow is relatively small and of very short duration, a total engine mass flow reversal does not occur. Figure 18.29 shows the rotational behavior of power shaft as well as the gas generator shaft. As seen, the rotational speed of the gas generator shaft is not recovering causing the compressor to operate in an unstable operation mode.

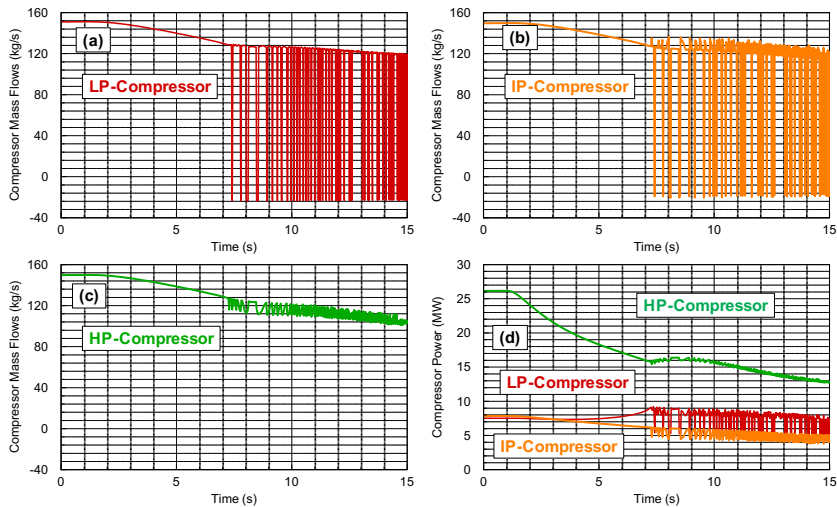


**Fig. 18.30:** (18.30) Mass flow behavior of LP-, IP-, and HP-compressors and their power as functions of time.

The IP-compressor stage group exhibits similar instability behaviors, where the compressor mass flow reversal occurs at slightly lower frequency and almost the same amplitude. The HP-stage group displays a distinctively different behavior. While the mass flow experiences fluctuation at a similar frequency, the amplitude remains always positive. These fluctuations apparently are not caused by the HP-stage group itself and are propagated downstream from the LP- and IP-parts respectively. This behavior is fully consistent with the continuity requirement that leads to an integrally positive mass flow rate because of the high frequency and short duration mass flow reversal in LP- and IP-compressors. The mass flow behavior of the LP, IP, and HP compressors are shown in Fig. 18.30 (a,b,c). The power fluctuation of each compressor is shown in Fig. 18.30 (d). As seen the

mass flow fluctuations of the LP-compressor has caused the major power fluctuations.

### 18.5.3.2 Case 3.2: Surge Prevention by Stator Stagger Angle Adjustment

To prevent the compressor from getting into instability and surge described in Case 3.1, the stagger angles of the LP- and IP-compressor stage groups were dynamically adjusted. Similar to Case 3.1, the engine was forced into an adverse off-design operation condition with the same load schedule as shown in Fig. 18.29. Starting from the steady state point, in accordance with the load schedule displayed in Fig. 18.29, a generator loss of load was simulated first. The power generation shaft responds to this event with a rapid increase in rotational speed, which triggers closing of the fuel valve. As a consequence, without active control, the power of the gas generation turbine would not be sufficient to cover the power consumption of the compressor. As observed in Case 3.1 this imbalance of power has led to a decrease in rotational speed of the gas generation shaft, which forced the first two compressor stage groups into an unstable mode. In order to avoid the power imbalance of the gas generation shaft as in Case 3.1, the stagger angle pertaining to the stator blades of the LP- and IP- stage groups are continuously adjusted according to a prescribed dynamics schedule. The configuration of a multi-stage compressor with adjustable stator blade rows is shown schematically in Fig. 18.31.

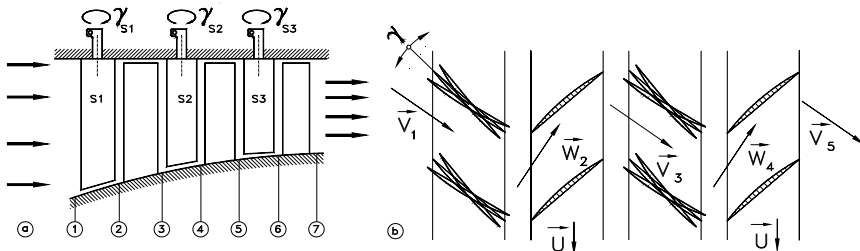


**Fig. 18.31:** (a) Multistage compressor with adjustable stator blades, (b) Stagger angle adjustment.

As shown in Fig. 18.31(a) and 18.31 (b), the stagger angle of each individual stator row  $\gamma_{si}$  can be changed according to a  $\gamma$ -scheme controlled by a multi-variable control system with the row exit pressure as one of its input variables. The effect of the adjustment on the stage velocity diagram is shown in Fig. 18.32. Figure 18.32(a) exhibits the velocity diagram pertaining to the stator row in its design stagger position under an adverse operation condition which is associated with an increase in compressor pressure ratio. This pressure ratio, however, is established by a deflection angle  $\theta$  that may cause a boundary layer separation on stator and rotor blades thus, leading to an inception of rotating stall and surge condition. To prevent this, the stagger angle  $\gamma$  is adjusted resulting in a reduced  $\theta$  as Fig. 18.32(b) shows.

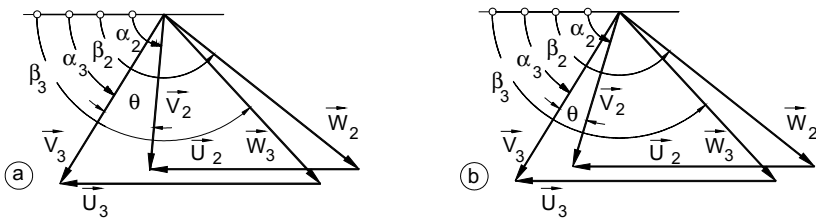


**Fig. 18.32**(a): Velocity diagram with increased flow deflection  $\theta$  as a result of an adverse dynamic operation, (b) adjusted stator blades causing a reduction in flow deflection  $\theta$ , thus preventing rotating stall and surge.

This procedure of stator blade adjustment starts immediately at the time where the loss of load occurs and lasts until the prescribed  $\gamma$ -values at  $t = 4$  s are reached. These values are kept constant for the rest of the simulation. As shown, it is sufficient to reduce the stagger angle of the LP- and IP-compressors, while the stagger angle of the HP-compressor remained unchanged. This intervention causes a substantial shift in the surge limit preventing all three compressor stage groups from entering into the instability regime. As Fig.18.33 shows, the compressor power does not experience any fluctuations. The stable operation of the compressors is also reflected in Fig. 18.33, where the load schedule and the response of the power generator and gas generator turbines are displayed.

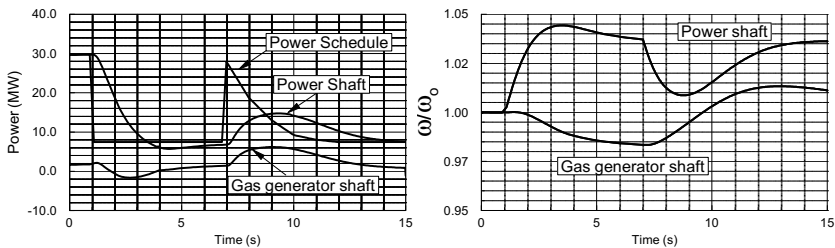


**Fig. 18.33:** (left) Generator load schedule, power shaft response and the response of gas generator shaft, (right) Rotation speed behavior of power and gas generator shaft after stator stagger angle adjustment.

In contrast to the unadjusted **Case 3.1** shown in 18.29, no power fluctuations are encountered. The rotational speed behavior of the gas generator shaft shown in 18.33 is substantially different from the one shown in **Case 3.1**. The positive power difference of the gas generation spool plotted in 18.31 is the result of a decreased compressor load caused by stator angle adjustment. It prevents the rotational speed of the gas generation spool from decreasing and moves the compressor operation into a more stable operation regime.

The compressor mass flow, power, inlet and exit temperature behavior of the LP, IP, and HP parts are shown in Fig. 18.34. As seen, the fluctuation of the above quantities that was characteristic of the compressor component operating close to the surge limit disappeared completely.

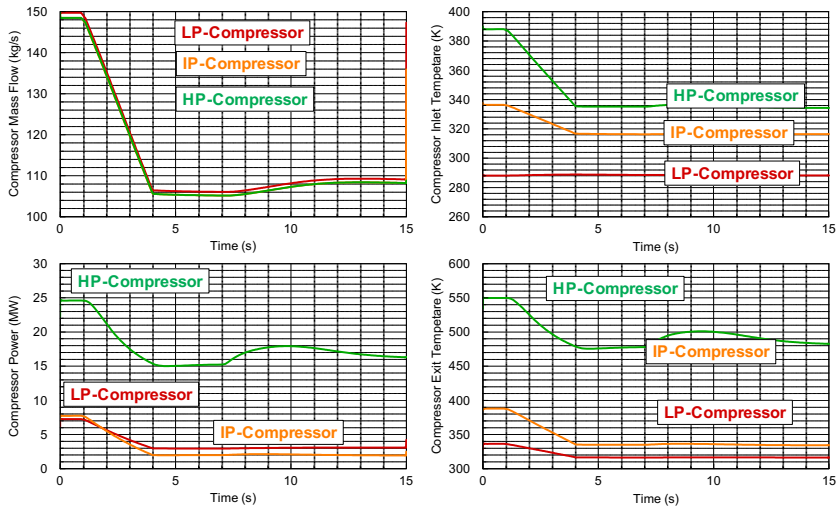


**Fig. 18.34** (18.35): Mass flow behavior of LP-, IP-, and HP-compressors and their power as functions of time. Unlike Fig. 18.30 the compressor is operating in a stable mode.

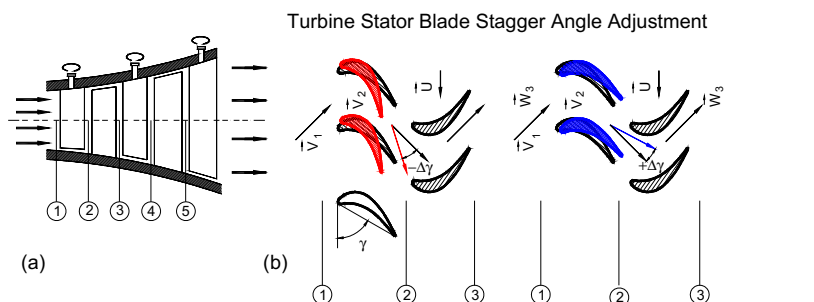
#### 18.5.4 Case Studies: Maximizing the Off-Design Efficiency of a Gas Turbine By Varying the Turbine Stator Stagger Angle

Aero-engines such as those of commuter aircrafts and helicopters are subject to frequent changes of operation conditions. These changes affect the turbine and compressors efficiency and performance. The compressor performance affected by adverse off-design conditions including rotating stall and surge was discussed in the previous section. This section deals with a new method to maximize the turbine efficiency operating at frequently changing the operation conditions. The change of the operation condition may be periodic, a-periodic or random. In general, any off-design operation of a gas turbine is associated with changing the mass flow and thus the blade incidence angles of the turbine component. Incidence change causes an increase of blade losses resulting in lower stage efficiency. Adjusting the blade stagger angle to the incidence changes results in reducing the profile losses and a reduction of the component, thus a decrease of the thermal efficiency of the gas turbine.

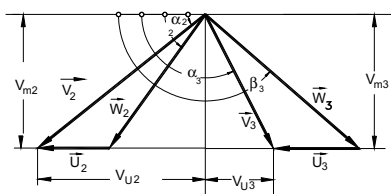
In the following section we discuss a method of adjusting the stator blade stagger angle to achieve higher thermal efficiency at a given off-design condition. Ideally, it would be more effective to adjust both, the stator and the rotor blade stagger angles. However, changing the rotor stagger angle requires a complex adjusting mechanism that is not practical to be implemented, therefore, we consider adjusting the stator stagger angle only. The turbine stage with the velocity diagram with and without adjusting the stator is shown in Fig. 18.35, with the negative and positive changes of the stagger angle  $\Delta\gamma$  (a,b). As seen a negative  $\Delta\gamma$  in Fig. 18.35 causes an increase in specific stage power given by  $V_{u2} + V_{u3}$ , Fig. 18.35(c) compared with the one of the off-design (d). Similarly a positive  $\Delta\gamma$  results in a decrease of the specific stage power.

### 18.5.4.1 Dynamic Change of Stagger Angle, when Engine is Running

To demonstrate the effect of the stator angle change on the efficiency of a gas

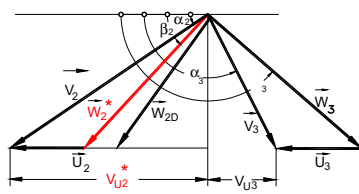


Design point velocity diagram



(c)

Off-design velocity diagram



(d)

**Fig. 18.35:** Turbine blade stagger angle adjustment to reduce the efficiency deterioration at off-design operation conditions.

turbine, we first assume a constant power schedule and change the  $\Delta\gamma$  periodically from  $\Delta\gamma = -3^\circ$  to  $\Delta\gamma = +3^\circ$  as shown in Fig. 18.36.

As seen from Fig. 18.36 (a) The thermal efficiency changes with sinusoidally changing the stagger angle of the first stator. Figure 18.37(b) shows the thermal efficiency as a function of stagger angle. Negative stagger change causes an

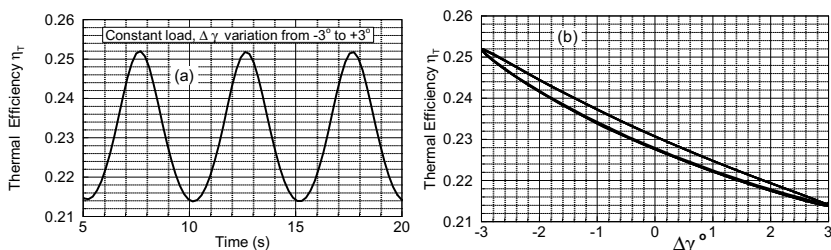


**Fig. 18.36:** Thermal efficiency of the gas turbine BBC-GT-9 as a function of time with stator stagger change  $\Delta\gamma$  as parameter.

increase of the thermal efficiency, while the positive one reduces it. This is in consonance with the change in incidence. Positive incidence (+i) causes an increase of the specific stage power as does negative  $\Delta\gamma$ .

We consider now a power schedule that is changing with time. Arbitrary



dynamic schedule for the turbine power can be applied. As an example, a Gaussian distribution as a function of time is given in Fig. 18.37. This figure exhibits the power ratio  $PR$  which is the ratio of the off-design power  $P_{OD}$  to the design power  $P_D$ . For  $PR = 1$ , the gas turbine is running at its 100% rated output, where as for  $PR = 0.4$  it delivers only 40% of its design power.

Using the scheduled power ratio  $PR$  from Fig. 18.37, the dynamic simulation of the gas turbine BBC-GT-9 used previously is conducted and the efficiency diagram is presented in Fig. 18.38. For each simulation, the  $\Delta\gamma$  was

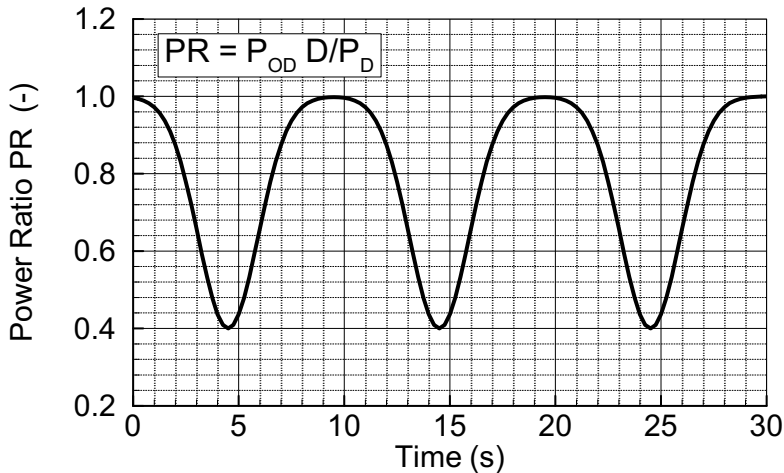


**Fig. 18.37** (18.38) Fig. 18.38: Power ratio  $PR$  as a function of time.

kept constant. Figure 18.38 exhibit the thermal efficiency changes as a function of time for five different stagger angle difference  $\Delta\gamma$  including  $\Delta\gamma = 0$ , which corresponds to the design point. Figure 18.39 shows three transient phenomena: (1) The overall efficiency has increased with negatively increasing  $\Delta\gamma$ . (2) A  $\Delta\gamma = -2^\circ$  has shifted the efficiency distribution by close to 1.5% point. (3) The efficiency distribution region between the two efficiency tips, which is occupied by the off-design, has experienced a significant increase. Thus, the tuning the stagger angle to the power schedule exhibits a practical solution to prevent the efficiency deterioration during adverse off-design operation. This method can be applied to aircraft engine as well as to power generation ones that are exposed to frequent load changes.

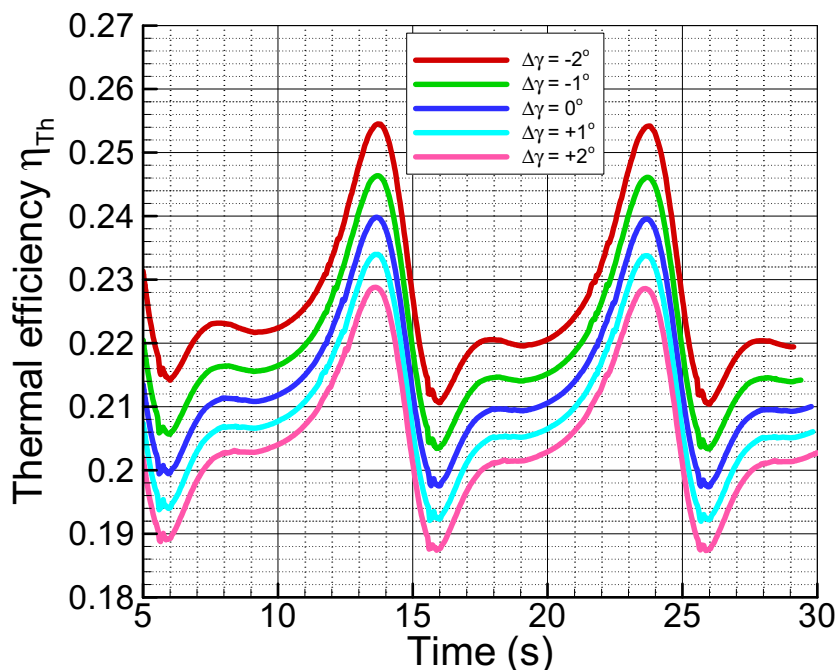


**Fig. 18.38:** Thermal efficiency as a function of time for different  $\Delta\gamma$  as parameter.

### 18.5.5 Case Study 3: Simulation of a Multi-Spool Gas Turbine Engine

The subject of this study is the non-linear dynamic simulation of a gas turbine engine with a higher degree of complexity than the previous cases. For this purpose a three-spool thrust generating gas turbine engine is designed that incorporates advanced components. The three-spool four shaft high performance gas turbine engine consists of a low pressure spool that incorporates the LP-compressor and turbine connected via shaft  $S_1$ . The intermediate pressure spool integrates the IP-compressor and turbine connected via shaft  $S_2$ . The high pressure spool carries the HP-compressor and HP-turbine on shaft  $S_3$ . To increase the level of engine complexity, a fourth shaft,  $S_4$ , with the power generating turbine,  $T_4$ , was attached to the exit of the three-spool gas generating unit as shown in Fig. 18.39. The transient operation is controlled by a given fuel schedule. The component nomenclature for this configuration is the same as for the previous cases. The simulation schematics shown in Fig. 18.39 represents the modular configuration of the gas turbine.

**Fuel Schedule, Rotor Response:** The dynamic behavior of the above engine is simulated for an adverse acceleration-deceleration procedure. The transient operation is controlled by an open loop fuel schedule shown in Fig. 18.40(left). The three- spools and the fourth shaft run independently at different

rotational speed, Fig. 18.40 (right).

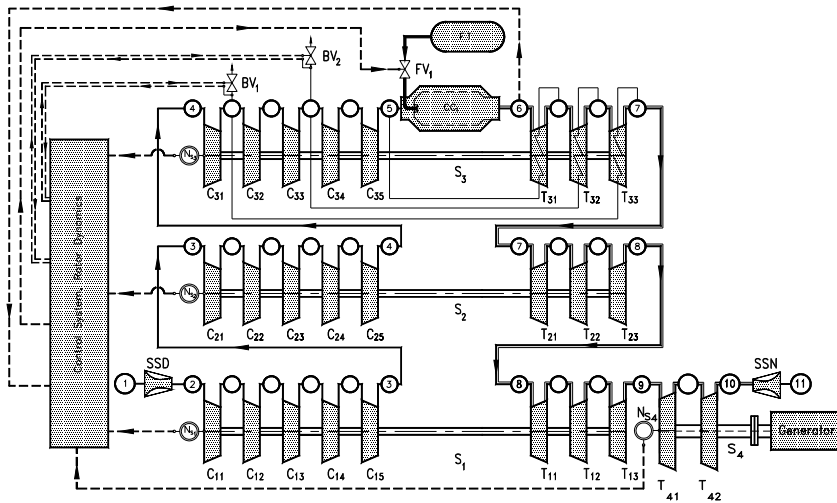


**Fig. 18.39:** Simulation schematic of three-spool four shaft high performance gas turbine engine. Spool 1 incorporates LP-compressor and LP-turbine connected via shaft  $S_1$ ; Spool 2 incorporates IP-compressor and IP-turbine connected via shaft  $S_2$ ; Spool 3 incorporates HP-compressor and HP-turbine connected via shaft  $S_3$ .

The fuel schedule generated fully arbitrarily simulates an acceleration-deceleration procedure with emphasis on deceleration. We start with the steady-state operation and reduce the fuel mass flow to  $\dot{m}_F = 2.8 \text{ kg/s}$  for about two seconds. During this short period of time, the engine operates in a dynamic state which is followed by a cyclic acceleration-deceleration event with the ramps given in Fig. 18.40. The dynamic operation triggers a sequence of transient events within individual components that are discussed in the following sections.

**Rotor Speed Behavior:** The transient behavior of the three spools as well as the power is determined by the net power acting on the corresponding rotor. For each individual spool, the cyclic acceleration-deceleration event has caused a dynamic mismatch between the required compressor power

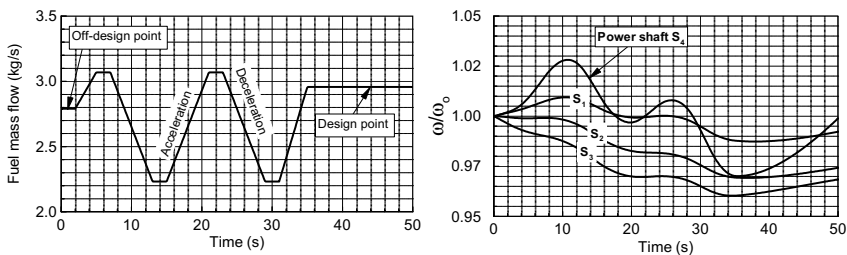


**Fig. 18.40:** Fuel schedule (left) starts with an off-design mass flow followed by a cyclic acceleration-deceleration procedure. Rotational speed of the three spools and the power shaft.(right).

consumption and the turbine power generation as shown in Fig. 18.41. While LP- and IP-spools 2 and 3 decelerate under the influence of negative net power, the HP-spool 3 reacts faster to the acceleration. Since the fuel schedule places special weight upon deceleration, the rotational speeds of all three spools have a decelerating tendency as shown in Fig. 18.41.

**Pressure and Temperature Transients within Plena:** The change in fuel mass flow triggers a chain of transient events within the plena as shown in Fig. 18.41.

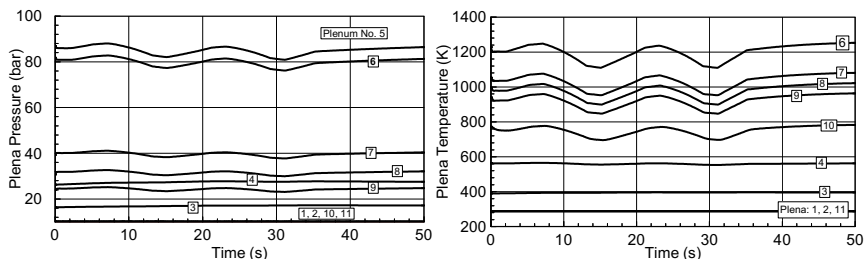


**Fig. 18.42:** Plena pressure (left) and temperature (right) as functions of time.

Plena pressure 5 and 6 which corresponds to the exit pressure of the HP-compressor and the combustion chamber, are strongly affected by the cyclic fuel change, whereas the other plena that correspond to the inlet and exit plena of the remaining components experiences moderate changes. The plena temperature distributions downstream of the combustion chamber shown in Fig. 18.42 (right) reflect the course of the fuel schedule.

**Combustion Chamber Gas and Metal Temperature Transients:** Figure 18.43 exhibits the combustion chamber gas and metal temperatures as functions of time. The combustion chamber component used in this simulation has three segments that separate the primary combustion zone from the secondary cooling

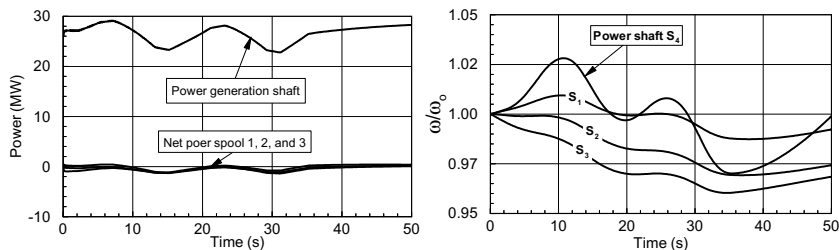


**Fig. 18.41:** Net power acting on the three spools causing a dynamic mismatch; power generated by the fourth shaft (left). Relative rotor speed of three spools and the fourth shaft.

air zone. Its module is shown in Fig. 18.24. Compressed air enters the combustion chamber at station 1, Figs. 18.43 (left). Fuel is added and the segment's cooling occurs according to the procedure described in Chapter 14. The secondary mass flow portions  $\dot{m}_{s_i}$  serve as cooling jets and are mixed with

the combustion gas, thus reducing the gas temperature. Before exiting, the combustion gas is mixed with the mixing air stream  $\dot{m}_M$  further reducing the temperature. Figure 18.43 (right) shows the mean segment temperatures. The flame length extends from station 1 to 3, which makes the segment number 2 the hottest one. As seen, the gas temperature at station 2 follows the sharp changes in the fuel schedule. By convecting downstream, these sharp changes are smoothed out. Wall temperatures shown in Fig. 18.43 (right) exhibit similar tendencies.

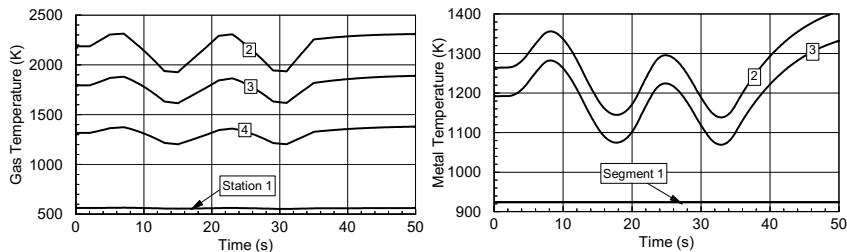


**Fig. 18.43:** Combustion chamber gas and metal temperature as functions of time.

**Compressor and Turbine Mass Flow Transients:** Figure 18.44 (left) exhibits the compressor mass flow transients, which are dictated by the compressor dynamic operation. The difference in compressor mass flow is due to the mass flow extraction for cooling purposes. Turbine mass flows are illustrated in Fig. 18.44 (right). Except for a minor time lag, they show identical distributions. The difference in turbine and compressor mass flow is due to the addition of fuel.

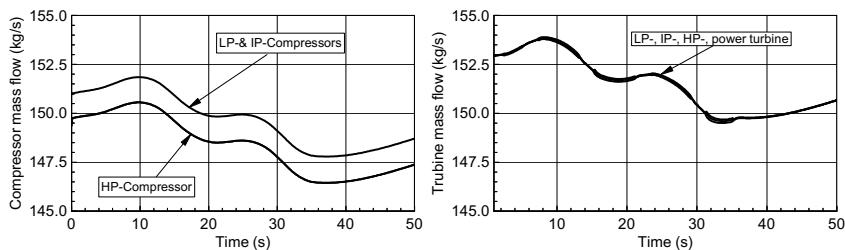


**Fig. 18.44:** Compressor and turbine mass flow as functions of time.

## References

1. Koenig R.W., Fishbach L.H., 1972, " GENENG- A Program for Calculating Design and Off-Design Performance for Turbojet and Turbofan Engines," NASA TN D-6552.
2. Seldner K., Mihailowe J.R., Blaha R.J., 1972, "Generalized Simulation Technique for Turbojet Engine System Analysis," NASA TN D-6610.
3. Szuch J.R., 1974, "HYDES- A Generalized Hybrid Computer Program for Studying Turbojet or Turbofan Engine Dynamics," NASA TM X-3014.
4. Seller J., Daniele C.J., 1975, "DYGEN- A Program for Calculating Steady-State and Transient Performance of Turbojet and Turbofan Engines,"

- NASA TND-7901.
5. Schobeiri M.T., 1985 "Aero-Thermodynamics of Unsteady Flows in Gas Turbine Systems." Brown Boveri Company, Gas Turbine Division Baden Switzerland, BBC-TCG-51.
  6. Schobeiri T., 1985 "COTRAN, the Computer Code for Simulation of Unsteady Behavior of Gas Turbines." Brown Boveri Company, Gas Turbine Division Baden Switzerland, BBC-TCG-53
  7. Schobeiri, T., 1985 "Digital Computer Simulation of the Dynamic Response of Gas Turbines", *VDI- Annual Journal of Turbomachinery*, pp. 381-400, 1985.
  8. Schobeiri T., 1986: "A General Computational Method for Simulation and Prediction of Transient Behavior of Gas Turbines." ASME-86-GT-180.
  9. Schobeiri T., 1987, "Digital Computer Simulation of the Dynamic Operating Behavior of Gas Turbines." *Journal Brown Boveri Review* 3-87.
  10. Schobeiri T., 1987, "Digital Computer Simulation of the Dynamic Operating Behavior of Gas Turbines." *Journal Brown Boveri Review* 3-87.
  11. Schobeiri, H. Haselbacher, H, 1985c, "Transient Analysis of Gas Turbine Power Plants Using the Huntorf Compressed Air Storage Plant as an Example." ASME-85-GT-197.
  12. Schobeiri, M. T., Attia, M, Lippke, C., 1994, "Nonlinear Dynamic Simulation of Single and Multi-spool Core Engines, Part I: Theoretical Method," *AIAA, Journal of Propulsion and Power*, Volume 10, Number 6, pp. 855-862, 1994.
  13. Schobeiri, M. T., Attia, M, Lippke, C., 1994, "Nonlinear Dynamic Simulation of Single and Multi-spool Core Engines, Part II: Modeling and Simulation Cases," *AIAA Journal of Propulsion and Power*, Volume 10, Number 6, pp. 863-867, 1994.
  14. Schobeiri, M. T., 1982, "Dynamisches Verhalten der Luftspeichergasturbine Huntorf bei einem Lastabwurf mit Schnellabschaltung," Brown Boveri, Technical Report, TA-58.